Energy Absorption of Crushable Tubes for Protective Structures under Static, Impact and Blast Loading

Energieabsorptie van buizen en kokers voor bescherming van constructies onder statische, dynamische en explosiebelasting

Sivakumar Palanivelu

Promotoren: prof. dr. ir. W. Van Paepegem, prof. dr. ir. J. Vantomme
Proefschrift ingediend tot het behalen van de graad van
Doctor in de Ingenieurswetenschappen: Werktuigkunde-Elektrotechniek

Vakgroep Toegepaste Materiaalwetenschappen
Voorzitter: prof. dr. ir. J. Degrieck
Faculteit Ingenieurswetenschappen en Architectuur
Academiejaar 2010 - 2011

UNIVERSITEIT GENT

ISBN 978-90-8578-438-8
NUR 929
Wettelijk depot: D/2011/10.500/42

Promoters:

Prof. dr. ir. Wim Van Paepegem
Ghent University
Faculty of Engineering and Architecture
Department of Materials Science and Engineering

Prof. dr. ir. John Vantomme
Royal Military Academy
Polytechnical faculty of the Royal Military Academy
Department of Civil and Materials Engineering

Examination Committee:

Prof. dr. ir. Luc Taerwe (Chairman)	Ghent University
Prof. dr. ir. Jan Vierendeels (Secretary)	Ghent University
Prof. dr. ir. Wim Van Paepegem (Promoter)	Ghent University
Prof. dr. ir. John Vantomme (Promoter)	Royal Military Academy
Prof. dr. ir. Geert De Schutter	Ghent University
Prof. dr. ir. Joris Degrieck	Ghent University
Prof. dr. ir. Danny Van Hemelrijck	Vrije Universiteit Brussel
Prof. dr. ir. Gerald Nurick	Cape Town University
Prof. dr. ir. Theodor Krauthammer	University of Florida

Research Institute:

Ghent University
Department of Materials Science and Engineering
Technologiepark-Zwijnaarde 903
9052 Zwijnaarde

Gent, June 2011

Dedicated to my wife Nalina
and our beloved son Pranav

Acknowledgements

I am extremely thankful to my promoters, Prof. dr. ir. Wim Van Paepegem and Prof. dr. ir. John Vantomme. Without their continuous help and guidance this work would not have been possible and I also would like to thank them for the freedom given on this research. It is an honor to have worked with our head of the department Prof. dr. ir. Joris Degrieck to whom I express my sincere gratitude for all the help given throughout the work. I wish to express my sincere thanks to Prof. dr. ir. Jan Wastiels and Prof. dr. ir Danny Van Hemelrijck from Vrije Universiteit Brussel for their encouragement and advice during the review meetings and procuring composite tubes for the large-scale blast tests. Furthermore, I would like to express my sincere gratitude to the jury members for reading this dissertation. Their suggestions and corrections were a great help to improve the content of this dissertation.

The experimental work presented in this dissertation could not have been done without the help of two persons, ir. Bruno Reymen from Royal Military Academy and Luc Vanden Broecke from Ghent University. I would express my sincere thanks to Bruno for his great support for all blast tests and his idea for using concrete sewage pipes for the large-scale blast tests. He learned me many things about blast loading and measurement and out of that I always remember one thing “to make an omelette one has to break eggs”. I would like to thank Luc for his fantastic and innovative solutions for the manufacturing of composite tubes and his great help during the large-scale blast tests.

I would like to express my sincere gratitude to dr. ir. Jean-Marie Ndambi for introducing me to the world of Autodyn and his great help whenever I needed. I express my sincere appreciation to Capt. ir. Eric Segers and Brasschaat Military Team for their support and coordination for the large-scale blast tests during winter days. Support from Capt. ir. Kathleen De Wolf from Royal Military Academy during the initial months of my PhD is highly appreciated. I would like to express my sincere thanks to my colleagues ir. Dimitrios Kakogiannis and ir. Johan Van Ackeren from Vrije Universiteit Brussel for their support and coordination in all respects.

I would like to express my sincere thanks to the team (ir. Paul Tomas, dr.ir. Geza Nagy, ir. Hans mulder, ir. Fred Jonker and ir. Erik Elzinga) from TATA Steel (earlier Corus), Ijmuiden, The Netherlands, for sharing the material information and suggestions during the meeting. Similarly, the technical input from ir. Hicham Echchgadda, Coca cola, Brussels, Belgium is greatly acknowledged. I express my gratitude for M/s Exel and M/s Acrosoma for supplying the composite tubes and sandwich composite skin plates respectively. This research was sponsored by F.W.O (Fund for scientific research) through grant no: G.0114.07. The financial support of the F.W.O is greatly acknowledged.

I wish also to express my thanks to my colleagues and a kind cooperation and support for these four years; Thanks to Ali, Arun, Amit, Chris, Diederik, Ebrahim, Eli, Geert, Ives, Jan, Jesus, Joachim, Joost, Kamran, Martine, Mathias, Mayank, Nicolas, Patricia, Reddy, Rudy, Sridhar, Stefan and Stijn.

My words will fail to express my deepest heartfelt thanks to my wife, for all what she did, and still does, to help me be at this position and for her continuous support and encouragement. To my parents I am thankful for their dedication and inspiration that enabled me to reach this milestone in my life. I would like to thank my friends dr. ir. Madhavan and dr. ir. Venkat for their support. Last, but not least, I want to thank my son Pranav Naarayan for his persistent understanding and support over the last four years.

Sivakumar Palanivelu
June 2011, Gent.

கேடில் விழுச் செல்வங் கல்வி யொருவற்கு
மாடல்ல மற்றை யவை.

திருக்குறள் (400)

Learning is wealth none could destroy
Nothing else gives genuine joy

Thirukkural (400)

English Summary

Protecting the civilian population against terrorist attacks is a complex and comprehensive task. If critical civil structures (tower buildings, embassies, etc.) are threatened, the main concerns are with the elaboration of an efficient rescue plan and a rapid intervention. The structural integrity of the engineering structure itself is rarely considered. However, since the early nineties (bomb attacks World Trade Centre (1993), Oklahoma (1995), US embassy Kenya (1998) and World Trade Centre (2001)) the protection of civil engineering structures against explosions has become an important research area. Efforts have been made around the globe to propose suitable solutions for this problem. Yet, some of the currently available solutions are expensive and others are not satisfactory. However, few studies from literature demonstrated that the concept of sacrificial cladding structure can be successfully deployed to protect the civil engineering structures from an explosive load with a reasonable cost. Hence, in this research the same concept has been adopted. The proposed sacrificial cladding structure consists of two layers: (i) outer skin panels and (ii) inner core members. The function of the outer skin panel is to distribute the blast pressure more evenly to the inner core which deforms progressively and absorbs most of the energy from the blast load, so that the main load bearing members of the civil engineering structures will be safeguarded. The working principle of the proposed sacrificial cladding structure is to change the blast loading distribution from a high load, short duration impulse to a low load, long duration impulse and thereby reducing damage to the non-sacrificial structure upon which it is mounted. The mechanism by which the sacrificial cladding structure does this, is by absorbing energy through progressive deformation of the inner core.

The objective of this research is study the crushing performance of the materials/structures under different loading rate conditions. In order to identify the suitable energy absorbing material/structure for the inner core and to make a comparison, two types of materials/structures have been chosen based on their load displacement curves: (i) α - type – the load displacement curve falls sharply after the peak crush load and (ii) β - type – the load displacement curve of this type of structure is relatively “flat topped”. Accordingly the empty metal beverage cans (isotropic material) and composite tubes (anisotropic material) have been chosen for α and β - type structures respectively. Before using the aforementioned materials/structures for the inner core, the knowledge of their behaviour for a such high dynamic event should be known. Therefore, a major question arises about the strain rate sensitivity of the materials, structural deformation behaviour and the corresponding energy absorption. Investigation of these factors during blast loading is very difficult. Capturing the strain rate sensitivity and the corresponding structural behaviour is relatively easier during quasi-static and impact tests; results from these tests can be verified further for the blast loading conditions. Furthermore, preliminary blast tests on the aforementioned test specimens at the *Royal Military*

Academy, Brussels showed that the natural frequency of these structures should be high enough, to respond for a very short duration blast load. Hence, to investigate on the above points a systematic approach was adopted. Accordingly this work contains four major parts. Part I studies the quasi-static, impact and small-scale blast loading on empty metal beverage cans (α - type structure). Part II presents a similar approach for large-scale and medium-scale pultruded composite tubes (β - type structure); similarly, Part III is devoted to small-scale in-house composite tubes (β - type structure). Finally, Part IV presents large-scale blast testing on representative sacrificial cladding structures using empty beverage cans and small-scale pultruded composite tubes. To simplify the approach only the axial pressure loading is considered in this dissertation.

Part I starts with axial quasi-static and impact testing on the beverage cans. The axial quasi-static testing of the beverage cans showed a non-uniform crushing deformation pattern. Furthermore, axial impact tests with an impactor mass of 7.6 kg and with an initial impact velocity of 1.4 m/s also showed similar results. However, for higher initial impact velocities such as 2.2 m/s, 3.1 m/s, 3.8 m/s, 4.4 m/s and 4.9 m/s the beverage cans showed controlled and uniform crushing modes with asymmetric or diamond mode deformation patterns. The results from these tests showed that the yield strength of the material increased with increasing initial impact velocities. In addition to that the strain hardening characteristics of the material influenced the mean crush load. The energy balance plot of these cases showed that the allowable deformation length of the beverage cans for the inner core should be limited to 80 mm. If the deformation length goes beyond 80 mm, then the entrapped air inside the beverage can dissipates 3% of the total energy by heat transfer to the atmosphere; furthermore, the elastic strain energy given back to the impactor was increased. In order to confirm this, additional tests have been conducted on the beverage cans with a few holes at the bottom. Similarly, the air inside the beverage can was numerically modelled using the surface based fluid cavity approach. The results from the experimental and numerical studies have confirmed the same conclusion. To predict the energy absorption capability of the beverage cans, an analytical model is formulated including the strain rate and strain hardening effects using *Cowper-Symonds* and *Ludwik* equations respectively. The results from this model provided a very good correlation with the experimental results. Similarly, the developed numerical model using the *Johnson-Cook* material model captured the strain rate and strain hardening effect of the beverage can material. Finally, from the high speed images of axial impact testing of the test specimens, an attempt was made to calculate the dynamic parameters such as deformation length, impact velocity and the reaction force at the crushing end of the test specimen using a contactless method (*Digital Image Correlation technique*). The results from this approach showed promising results. However, the effect of

frame rate and the material/structure deformation behaviour play a significant role for the quality of the results.

As a next step, small-scale blast tests have been conducted on the beverage cans to study the crushing deformation patterns and the corresponding strain rate sensitivity of the beverage cans. A small-scale blast test set-up was designed and manufactured. With the help of this test set-up the effect of finite reflected surface area and the nature of the reflected surface on the reflected blast parameters were evaluated. The experimentally measured reflected parameters were compared with an empirical approach (using *ConWep*). Similarly, the influence of skin plate inertia on the performance of the inner core was captured; the results from all tests showed that this is a very important factor for the design of a sacrificial cladding structure. Besides, the results from all blast tests showed a non-conservation of the linear momentum scenario (a difference was observed between the reflected and transferred impulse). This was unexpected because any sacrificial cladding structure cannot prevent the impulse of the blast being transferred onto the structure upon which it is mounted; rather it changes the force-time distribution. To investigate this case coupled (Eulerian Lagrangian) numerical analyses were carried out. The results from these analyses clearly showed that the interaction of the pressure wave (diffracted and ground reflected) caused the difference in the impulse. The same finding was also validated with decoupled numerical analyses. Similar to the axial impact case, an analytical model was proposed to calculate the crushing parameters of the beverage can for the blast loading. A comparison of the experimental, numerical and analytical models showed that the developed numerical and analytical models can be extended to design a full-scale sacrificial cladding structure. Eventually, the tested cans were collected after usage; hence, the effect of initial geometric imperfections during the usage on the performance of the beverage cans has to be answered. In order to investigate the effect of initial geometric imperfections, decoupled numerical simulations have been conducted using the experimentally measured reflected pressure time histories. The results from two independent numerical approaches (superposition of linear buckling mode shapes and measured geometric imperfections) showed that the initial geometric imperfections of the beverage cans do not influence the crushing performance.

In parallel with the beverage cans, a similar approach was handled for the composite tubes also. Unlike the α - type structure (beverage can), the energy absorption of the β - type structure (composite tubes) is controlled by different variables such as cross-section of the tube, shape of the tube, thickness to diameter ratio (t/D), triggering mechanism, orientation of the fibres etc. Furthermore, the effect of strain rate and the corresponding larger deformation during blast loading on the energy absorption of the composite tubes has to be studied. Understanding these variables is important for the design of composite tubes for the inner core. Most of the studies

from the literature have used circular and square cross-sectional composite tubes. Hence, to start with, impact tests were conducted on large-scale pultruded circular and square cross-sectional glass polyester and vinylester composite tubes for different initial impact velocities (9.3 m/s, 12.4 m/s and 14 m/s). From these tests, in addition to the typical failure modes of brittle composite tubes, the effects of cross-section, triggering, type of resin and strain rate were studied. However, a tool is necessary to transfer the knowledge for the final design of the inner core. The finite element tool can be used for this purpose. A detailed literature review indicated that most of the modelling of the composite tube crushing was done with a single layer of shell or solid elements. However, this approach cannot predict the correct peak force (corresponds to the occurrence of the central major circumferential delamination) and the corresponding crushing variables of uni-directional (pultruded) composite tubes. To prove this point and arrive to an acceptable solution, five different numerical approaches have been handled and the results from these cases are compared with the experimental results. As mentioned in the name itself, the large-scale pultruded composite tubes are larger in geometrical size; hence these composite tubes cannot be crushed in small-scale blast tests where we have more freedom to investigate the different variables. Therefore, alternatively a medium-scale pultruded glass polyester composite tube was chosen. Because of the involved number of variables and their influence on the specific energy absorption quasi-static and impact tests have been conducted on these tubes. The effect of dynamic loading on the energy absorption compared to quasi-static loading was captured. Further, the blast tests on these composite tubes have confirmed that the deformation patterns of the pultruded composite tubes remain the same for all loading conditions (quasi-static, impact and blast). In addition to that these composite tubes (pultruded glass polyester composite tubes) showed strain rate insensitivity which means that the peak crush load approximately remains the same irrespective of the testing condition. The deformation length of the composite tubes from these blast tests gave an indication that the performance of the composite tubes can be further enhanced using less stiff composite tubes.

It was not feasible to obtain a low volume of (lower stiffness) composite tubes with different geometrical shapes from any commercial manufacturer. Hence, it was decided to manufacture them in our laboratory. In order to arrive to an optimum shape for a better energy absorption nine different shapes (circular cross-section, square cross-section, hexagonal cross-section, hourglass type – A, hourglass type – B, hourglass type – X, hourglass type – Y, conical circular type – X and conical circular type – Y) including uniform and non-uniform profiles of uni-directional glass polyester composite tubes have been manufactured. Furthermore, to understand the different variables (thickness to diameter and triggering mechanism) quasi-static test have been conducted with two different wall thicknesses and with two triggering mechanisms. The results from this study showed a clear overview of

the effect of cross-section, shape, thickness to diameter ratio and triggering mechanisms on the specific energy absorption. Motivated by a catastrophic failure of few composite tubes, the effect of polyurethane foam-filling on the composite tube wall strengthening and stability was evaluated for all nine different shapes of the composite tubes. The presence of polyurethane foam inside the composite tube improved the stability and strengthening of the composite tube walls. However, the results from these tests turned out negative for the tubes which can already provide stable and progressive deformation patterns. The difference in the performance was due to a difference in the deformation patterns of hollow and foam-filled composite tubes. The polyurethane foam-filling prevented the delamination and subsequent fibre fracture. Based on the specific energy absorption ranking for quasi-static testing, six qualified shapes have been chosen for the axial impact tests. Axial impact tests with different initial impact velocities such as 3.1 m/s, 3.8 m/s, 4.4 m/s, 4.9 m/s and 5.3 m/s have confirmed very similar results for hollow and foam-filled composite tubes with a lower t/D ratio. However, for a higher t/D ratio the deformation patterns of polyurethane foam-filled composite tubes were very similar to the hollow tubes. This was due to a combined effect of the impactor mass, impact velocity and lateral inertia of the composite tubes. Three qualified composite tubes from the axial impact tests (circular cross-section, hourglass type – A and conical circular type – Y) were considered for the small-scale blast tests. The results from the blast tests further confirmed that the deformation patterns of these tubes (both hollow and foam-filled) remain the same for all loading conditions.

In the last stage of the research, all the gained knowledge from the small-scale blast tests has been applied to conduct large-scale blast tests. To create a perfectly plane shock wave the concept of a shock tube was used using segments of concrete sewage pipes. Coupled numerical simulations have been conducted to calculate the minimum length of the pipe which provides a perfectly plane shock wave. Large-scale blast tests have been conducted on two configurations of the test specimens (empty beverage cans and small-scale pultruded composite tubes) with different charge masses of C4 (75 g, 100 g, 150 g and 200 g). For all tests the beverage cans and the composite tubes showed stable and progressive deformation patterns. The numerically calculated reflected blast parameters are in a very good agreement with the experimental results. Investigations on the transferred load histories and the corresponding transferred impulse showed that the bending stiffness of the rear skin panel was not sufficient enough to transfer all reaction loads through the load cells. Similarly, the load time signals from a decoupled numerical simulation showed a difference in the initial slope to reach the peak crush load compared to the experimental results. Possible reasons for this difference are pointed out.

Nederlandse samenvatting (Dutch summary)

Bescherming van de burgerbevolking tegen terroristische aanslagen is een complexe taak. Wanneer kritische infrastructuur (torengebouwen, ambassades, etc.) bedreigd wordt, gaat de meeste aandacht uit naar een efficiënt reddingsplan en snelle interventie. De structurele integriteit van de constructie zelf wordt niet altijd in beschouwing genomen. Toch is de bescherming van gebouwen tegen explosiebelasting een belangrijk onderzoeksdomein geworden sinds de aanslagen op het World Trade Centre (1993), Oklahoma (1995), de Amerikaanse ambassade in Kenya (1998) en het World Trade Centre (2001).Verschillende oplossingen ter bescherming van gebouwen tegen explosies zijn voorgesteld in de internationale literatuur, maar sommige concepten zijn zeer duur, en andere niet voldoende adequaat. Een concept dat steeds vaker geopperd wordt, is dat van een schokabsorberend paneel dat vóór de dragende elementen van het gebouw wordt geplaatst. Een dergelijk schokabsorberend paneel bestaat uit twee lagen: (i) een buitenhuid, en (ii) het energieabsorberend kernmateriaal. De functie van de buitenhuid is om de explosiedruk meer gelijkmatig te verdelen naar het kernmateriaal, dat op zijn beurt progressief faalt en het grootste deel van de energie in de schokgolf absorbeert, zodat de dragende elementen van de constructie gevrijwaard blijven. Het werkingsprincipe van een dergelijk schokabsorberend paneel bestaat erin om de explosiebelasting om te zetten van een grote kracht – korte duurtijd impuls naar een lage kracht – lange duurtijd impuls, en zo de schade aan de achterliggende constructie te beperken.

Het doel van het voorliggend onderzoek is de studie van de energieabsorptie van geschikte kernmaterialen voor een dergelijk schokabsorberend paneel, en dit onder verschillende belastingssnelheden (van statisch tot hoogdynamisch). Twee sterk verschillende kernmaterialen zijn geselecteerd: (i) recycleerbare gebruikte metalen drankblikjes, en (ii) lichtgewicht composiet buisjes. Zij behoren ook tot twee verschillende categorieën van energieabsorberende materialen op basis van hun typische kracht-verplaatsingscurve bij samendrukking: (i) α - type – de kracht voor samendrukking daalt sterk na de piekkracht (drankblikjes), en (ii) β - type – de kracht voor samendrukking blijft relatief constant over de totale vervormde lengte (composietbuisjes). De belangrijkste factoren voor de beoordeling van de energieabsorptie van de kandidaat kernmaterialen is hun gevoeligheid voor de aangelegde reksnelheid, de vervormingsmechanismen en de hoeveelheid energieabsorptie. Het onderzoek van deze factoren bij explosiebelasting is erg moeilijk. Daarom werd gekozen voor een stapsgewijze aanpak, waarbij de energieabsorptie eerst werd bestudeerd onder quasi-statische belasting, nadien onder impactbelasting en tenslotte onder explosiebelasting. Bovendien hadden preliminaire explosietesten in de Koninklijke Militaire School (KMS, Brussel) aangetoond dat de eigenfrequentie van deze schokabsorberende structuren hoog genoeg moet zijn om enige respons te realiseren onder explosiebelasting. Op basis van deze gegevens werd een systematische aanpak gevolgd, die geresulteerd heeft in de vier grote delen

van dit werk. Deel I beschrijft de studie van de energieabsorptie van de blikjes onder quasi-statische, impact en explosiebelasting (α - type). Deel II stelt een gelijkaardige aanpak voor voor grote en middelgrote composiet buizen en kokers (β - type). Deel III presenteert de studie van de energieabsorptie van kleine composiet buisjes (β - type). Deel IV tenslotte omschrijft de grootschalige explosietesten op representatieve schokabsorberende panelen met drankblikjes en composiet buisjes als respectievelijke kernmaterialen. In alle delen wordt ondersteld dat de schokgolf loodrecht invalt op de structuur.

Deel I start met de quasi-statische en impacttesten op de drankblikjes. De blikjes vertoonden een niet-uniform vervormingspatroon onder quasi-statische drukbelasting. Ook de axiale impacttesten met een impactormassa van 7,6 kg en een initiële valsnelheid van 1,4 m/s leverden gelijkaardige resultaten op. Echter, voor de hogere valsnelheden van 2,2 m/s, 3,1 m/s, 3,8 m/s, 4,4 m/s en 4,9 m/s vertoonden de blikjes zeer gecontroleerde en uniforme vervormingspatronen. De resultaten toonden ook aan dat de vloeigrens van het materiaal toenam met toenemende initiële valsnelheid. Ook de rekversteviging had een invloed op de gemiddelde kracht voor samendrukking. De energiebalans voor deze impacttesten toonde aan dat de vervormde lengte van de blikjes moet beperkt worden tot 80 mm. Als de vervormde lengte groter wordt, begint de ingesloten lucht in het drankblikje een rol te spelen. Dan vergroot ook de elastische energie die wordt teruggegeven aan de impactor. Om dit te valideren, zijn bijkomende impacttesten uitgevoerd waarbij kleine gaten werden aangebracht in de bodem van het blikje. De lucht in het blikje werd bovendien ook meegenomen in de numerieke simulaties. De resultaten van deze experimenten en numerieke modellen bevestigden beide de vooropgestelde hypothese.

Om de energieabsorptie van de blikjes te voorspellen, werd een analytisch model ontwikkeld met inbegrip van de reksnelheid en de rekversteviging op basis van de *Cowper-Symonds* en *Ludwik* modellen. De resultaten van dit model stemden zeer goed overeen met de werkelijkheid. In parallel werd een eindige-elementenmodel opgebouwd en de reksnelheid en de rekversteviging werden gemodelleerd met het *Johnson-Cook* materiaalmodel. Tenslotte werd onderzocht of de digitale beeldcorrelatietechniek, een optische meettechniek voor het contactloos meten van verplaatsingen en rekken, gebruikt kan worden om de dynamische parameters tijdens een impacttest te meten, op basis van de opgenomen digitale hogesnelheidsbeelden. De resultaten van deze aanpak waren veelbelovend, maar tegelijkertijd werd aangetoond dat de opnamefrequentie van de beelden en de structurele respons van het testmateriaal een grote invloed hebben op de kwaliteit van de resultaten.

In een volgende stap zijn kleinschalige explosietesten uitgevoerd op de blikjes, waarbij opnieuw de vervormingspatronen en de gevoeligheid voor reksnelheid werden onderzocht. Voor dit onderzoek werd een kleinschalige explosie-opstelling gebouwd en geïnstrumenteerd, waarbij een topplaat de explosiedruk overdraagt naar één enkel onderstaand blikje. Met behulp van deze proefopstelling werd het effect van de eindige afmetingen van de topplaat en van haar oppervlakteruwheid onderzocht. De experimentele resultaten werden vergeleken met de empirische voorspellingen van het softwarepakket *Conwep*. Ook de invloed van de traagheid van de topplaat werd bestudeerd, een parameter die zeer belangrijk bleek te zijn voor het ontwerp van een schokabsorberend paneel.

Bovendien toonden alle uitgevoerde explosietesten dat er geen behoud van lineair momentum was (er was een systematisch verschil tussen de gereflecteerde en overgedragen impuls). Dit was niet verwacht, want een schokabsorberend element kan niet verhinderen dat de impuls van de explosiebelasting wordt overgedragen op de achterliggende structuur, maar verandert alleen het kracht-tijdsverloop van deze impuls. Om dit nader te onderzoeken, werden gekoppelde Euler-Lagrange simulaties uitgevoerd. De resultaten toonden duidelijk aan dat het verschil in impuls te wijten was aan de diffractie en reflectie van de schokgolven in hun interactie met de topplaat en de bodem van de testopstelling. Ook ontkoppelde Lagrange simulaties bevestigden deze stelling. In analogie met de impacttesten, werd ook voor de explosietesten een analytisch model ontwikkeld. Een vergelijking van de experimentele, numerieke en analytische resultaten toonde aan dat de ontwikkelde modellen zeer bruikbaar zijn voor het ontwerp van schokabsorberende panelen. Tenslotte, aangezien in alle testen leeggedronken drankblikjes werden gebruikt, werd ook het effect van geometrische imperfecties (ten gevolge van het gebruik van het drankblikje) onderzocht. Ontkoppelde numerieke simulaties werden opgebouwd met verschillende types geometrische imperfecties, en op basis van twee modelleringsmethodes (superpositie van lineaire knikmodes en experimenteel opgemeten vormimperfecties). Beide methodes tonen aan dat de geometrische imperfecties geen invloed hebben op de energieabsorptie van de drankblikjes.

Het tweede geselecteerde kandidaat kernmateriaal zijn de composiet buisjes (β - type). In tegenstelling tot de drankblikjes, kunnen hier heel wat parameters gevarieerd worden: het type dwarsdoorsnede, de vorm van het buisje, de verhouding van wanddikte tot diameter (t/D), het triggermechanisme (voor initiatie van het samendrukken), de oriëntatie van de vezels, etc. Het begrip van deze variabelen, ook bij de zeer hoge vervormingssnelheden onder explosiebelasting, is zeer belangrijk. In de literatuur wordt voornamelijk gebruik gemaakt van ronde en vierkante composiet buisjes. Het onderzoek op composiet buisjes werd dan ook gestart met impacttesten op grote gepultrudeerde composiet buizen met ronde en vierkante dwarsdoorsnede. De gebruikte materialen waren glasvezel/polyester en

glasvezel/vinylester en verschillende impactsnelheden (9,3 m/s, 12,4 m/s en 14 m/s) werden getest. Op basis van deze testen werden de typische faalmechanismen van de composiet buizen bestudeerd, alsook het effect van de dwarsdoorsnede, triggermechanisme, type hars en reksnelheid.

Uit de literatuurstudie blijkt duidelijk dat de meeste numerieke simulaties van dergelijke impacttesten gebeuren met één enkele laag schaal- of volume-elementen doorheen de dikte van de composietbuis. Dergelijke aanpak kan echter nooit de correcte piekkracht en energieabsorptie voorspellen, omdat de vervorming gedreven wordt door de centrale delaminatie, die de dikte van de composietbuis in twee helften splijt. Om dit aan te tonen en een alternatieve modellering voor te stellen, zijn vijf verschillende modelleringsmethodes beschreven, en de resultaten ervan zijn stap voor stap vergeleken met de experimentele resultaten. Uit de impacttesten bleek ook duidelijk dat de piekkracht om samendrukking van de grote composietbuizen te initiëren, veel te groot was om te realiseren in de kleinschalige explosietesten. Daarom werd overgegaan op middelgrote gepultrudeerde glas/polyester composiet buizen. Opnieuw zijn eerst quasi-statische en impacttesten uitgevoerd op deze buizen. De energieabsorptie tijdens impact werd vergeleken met deze onder quasi-statische belasting. De correlatie met de explosietesten op deze composiet buizen toonde aan dat de vervormingsmechanismen van de gepultrudeerde composiet buizen dezelfde blijven voor alle belastingsregimes (quasi-statisch, impact en explosiebelasting). Bovendien vertoonden deze buizen geen invloed van reksnelheid, wat betekent dat de piekkracht voor initiatie van samendrukken nagenoeg dezelfde bleef bij alle reksnelheden. De beperkte vervormde lengtes bij explosiebelasting toonden aan dat de composiet buizen nog verder moesten gereduceerd worden in axiale stijfheid (en dus wanddikte).

Aangezien het onmogelijk is om beperkte volumes te bekomen van kleine composiet buizen in verschillende vormen en wanddiktes, werd geopteerd voor eigen vervaardiging van kleine composiet buisjes. In een eerste stap werd de invloed van geometrie bestudeerd onder quasi-statische belasting. Negen verschillende vormen met uniforme en niet-uniforme profielen werden vervaardigd in unidirectioneel glas/polyester. Om ook de invloed van wanddikte/diameter verhouding en triggermechanisme te onderzoeken, werden de quasi-statische testen uitgevoerd met twee verschillende wanddiktes en twee triggermechanismen. De resultaten geven een overzicht van de invloed van dwarsdoorsnede, vorm, wanddikte/diameter verhouding en triggermechanisme op de specifieke energieabsorptie. Het catastrofaal falen van een beperkt aantal buisjes met specifieke wanddikte en vorm vormde de aanleiding om ook het effect van schuimvulling te bekijken. Voor alle negen vormen werd het effect van schuimvulling op de stabiliteit en wandversteviging onderzocht. Het was duidelijk dat het schuim inderdaad bijdroeg tot een verhoogde stabiliteit van de buisjes, maar voor die buisjes die reeds een

stabiel en progressief falen vertoonden, had de schuimvulling een negatieve invloed op de specifieke energieabsorptie. Dat was te verklaren door het vervormingspatroon van de holle en schuimgevulde buisjes. Het schuim binnenin de buisjes verhinderde de centrale delaminatie en daaropvolgende vezelbreuk. Gebaseerd op hun prestaties voor specifieke energieabsorptie werden zes vormen weerhouden voor de impacttesten. Axiale impacttesten werden uitgevoerd met verschillende impactsnelheden (3,1 m/s, 3,8 m/s, 4,4 m/s, 4,9 m/s en 5,3 m/s). Voor de buisjes met geringe wanddikte waren de bevindingen zeer gelijkaardig aan deze onder quasi-statische belasting, maar voor de buisjes met grotere wanddikte waren de vervormingspatronen van de schuimgevulde en holle buisjes zeer gelijkaardig. Dit is te wijten aan het gecombineerd effect van de impactormassa, inertie van de impactor en de laterale inertie van de composiet buisjes. Tenslotte werden drie vormen weerhouden voor de kleinschalige explosietesten. De resultaten van deze testen toonden aan dat de vervormingspatronen van deze buisjes (zowel hol als schuimgevuld) dezelfde blijven voor alle belastingscondities.

In een laatste stap van het onderzoek werd alle verworven kennis van de kleinschalige explosietesten aangewend voor het opzetten van grootschalige explosietesten. Het concept van de schokbuis werd gebruikt voor het creëren van een perfect vlakke schokgolf, met behulp van segmenten van betonnen afvoerbuizen. Gekoppelde numerieke simulaties werden uitgevoerd om de minimumlengte van de schokbuis te berekenen, zodat aan het andere uiteinde een vlakke schokgolf werd opgewekt. Grootschalige explosietesten werden uitgevoerd op twee configuraties van schokabsorberende panelen (met drankblikjes en met kleine gepultrudeerde composiet buisjes), en dit met verschillende explosieve ladingen (75 g, 100 g, 150 g en 200 g). In alle testen vertoonden de kernmaterialen een stabiel en progressief falen. De numeriek berekende explosieparameters waren in goede overeenstemming met de gemeten waarden. Vergelijking van het tijdsverloop van de overgedragen krachten naar de achterliggende betonstructuur en de corresponderende overgedragen impuls toont aan dat de buigstijfheid van de achterzijde van het schokabsorberend paneel niet voldoende was om alle reactiekrachten over te dragen langs de krachtcellen. In de ontkoppelde numerieke simulaties vertoonde het tijdsverloop van de overgedragen kracht ook een andere helling dan in de opgemeten curves. De mogelijke oorzaken van dit verschil worden ook aangehaald. Samenvattend werd aangetoond dat beide kernmaterialen potentieel bieden voor gebruik in een schokabsorberend paneel ter bescherming van gebouwen en andere constructies tegen explosiebelasting.

Curriculum Vitae

Sivakumar Palanivelu was born on June 5, 1976 in Nagapattinam, India. In 2002, he received his M.Tech. degree in Machine Design and Dynamics from Indian Institute of Technology, Madras, India. Immediately after his graduation he started to work for Engineering Research Centre of TATA Motors, Pune, India. After serving more than 5 years in that company, he left to Belgium for his doctorate in the field of the energy absorption assessment of materials and structures. He started his research work in the department of Materials Science and Engineering at Ghent University in May 2007. The work presented in this dissertation has been performed under the guidance of Prof. dr. ir. W. Van Paepegem and Prof. dr. ir. J. Vantomme. His research work entitled "Energy absorption of crushable tubes for protective structures under quasi-static, impact and blast loading" has been financially supported by the PhD grant of F.W.O-Vlaanderen (Grant No: G.0114.07). Sivakumar Palanivelu is author of 9 publications in international journals of the Science citation index and 25 publications in international conference proceedings. He is a reviewer for "Composite structures" and Composite Part B – Engineering" journals. He is also a member of the Society for the Advancement of Materials and Process Engineering (SAMPE).

List of Publications

Publications in international journals of the Science Citation Index (SCI) - a1 papers

[1] **Palanivelu, S.,** Van Paepegem, W., Degrieck, J., Van Ackeren, J., Kakogiannis, D., Van Hemelrijck, D., Wastiels, J. and Vantomme, J., *Experimental study on the axial crushing behaviour of pultruded composite tubes.* **Polymer Testing**, 2010. **29**(2): p. 224-234.

[2] **Palanivelu, S**., Van Paepegem, W., Degrieck, J., Kakogiannis, D., Van Ackeren, J., Van Hemelrijck, D., Wastiels, J. and Vantomme, J., *Comparative study of the quasi-static energy absorption of small-scale composite tubes with different geometrical shapes for use in sacrificial cladding structures.* **Polymer Testing**, 2010. **29**(3): p. 381-396.

[3] **Palanivelu, S**., Van Paepegem, W., Degrieck, J., Kakogiannis, D., Van Ackeren, J., Van Hemelrijck, D., Wastiels, J. and Vantomme, J., *Parametric study of crushing parameters and failure patterns of pultruded composite tubes using cohesive elements and seam, Part I: Central delamination and triggering modelling.* **Polymer Testing**, 2010. **29**(6): p. 729-741.

[4] **Palanivelu, S**., Van Paepegem, W., Degrieck, J., Vantomme, J., Kakogiannis, D., Van Ackeren, J., Van Hemelrijck, D. and Wastiels, J., *Comparison of the crushing performance of hollow and foam-filled small-scale composite tubes with different geometrical shapes for use in sacrificial cladding structures.* **Composites Part B: Engineering**, 2010. **41**(6): p. 434-445.

[5] **Palanivelu, S**., Van Paepegem, W., Degrieck, J., Vantomme, J., Kakogiannis, D., Van Ackeren, J., Van Hemelrijck, D. and Wastiels, J., *Crushing and energy absorption performance of different geometrical shapes of small-scale glass/polyester composite tubes under quasi-static loading conditions.* **Composite Structures**, 2010. **93**(2): p. 992-2007.

[6] **Palanivelu, S**., Van Paepegem, W., Degrieck, J., Van Ackeren, J., Kakogiannis, D., Wastiels, J., Van Hemelrijck, D. and Vantomme, J., *Parametric study of crushing parameters and failure patterns of pultruded composite tubes using cohesive elements and seam: Part II - Multiple delaminations and initial geometric imperfections.* **Polymer Testing**, 2010. **29**(7): p. 803-814.

[7] **Palanivelu, S**., Van Paepegem, W., Degrieck, J., De Pauw, S., Vantomme, J., Wastiels, J., Kakogiannis, D. and Van Hemelrijck, D., *Low velocity axial impact crushing performance of empty recyclable metal beverage cans.* **International Journal of Impact Engineering**, 2011. **38**(7): p. 622-636.

[8] **Palanivelu, S**., Van Paepegem, W., Degrieck, J., Reymen, B., Ndambi, J.-M., Vantomme, J., Kakogiannis, D., Wastiels, J. and Van Hemelrijck, D., *Close-range blast loading on empty recyclable metal beverage cans for use in sacrificial cladding structure.* **Engineering Structures**, 2011. **33**(6): p. 1966-1987.

[9] Kakogiannis, D., Van Hemelrijck, D., Wastiels, J., **Palanivelu, S.,** Van Paepegem, W., Vantomme, J., Kotzakolios, A., Kostopoulos, V. *Assessment of pressure waves generated by explosive loadind.* **Computer Modelling in Engineering and structures**. 2010.**65**(1), p75-92.

Communicated publication in Science Citation Index (SCI) journals (a1 paper)

[1] **Palanivelu, S.,** Van Paepegem, W., Degrieck, J., Reymen, B., Vantomme, J., Kakogiannis, D., Wastiels, J., Van Hemelrijck, D. *Close-range air blast loading on pultruded glass/polyester composite tubes. Part I – Experimental and decoupled numerical study*. Communicated to Polymer testing.

[2] Perumal, V., **Palanivelu, S**., Chouthai, A. *Influence of forging process on fatigue properties of AISI 4140 steel axle component.* Paper under review in Engineering materials and technology.ASME.

Conference proceedings available in ISI Proceedings, Web of science (p1 papers)

[1] **Palanivelu, S.,** Van Paepegem, W., Degrieck, J., De Wolf, K., Vantomme, J., Kakogiannis, D., Van Ackeren, J., Van Hemelrijck, D., Wastiels, J. *Study of blast load on recyclable empty metal cans*. 9th International Conference on Mechanical and Physical Behaviour of Materials under Dynamic Loadings (DYMAT 2009), Brussels, Belgium, 7-11 September 2009.

[2] **Palanivelu, S.,** Van Paepegem, W., Degrieck, J., Vantomme, J., Kakogiannis, D., Van Ackeren, J., Van Hemelrijck, D., Wastiels, J. *Numerical axial impact study of pultruded circular and square composite tubes*. 9th International Conference on Mechanical and Physical Behaviour of Materials under Dynamic Loadings (DYMAT 2009), Brussels, Belgium, 7-11 September 2009.

[3] **Palanivelu, S.,** De Pauw, S., Van Paepegem, W., Degrieck, J., Kakogiannis, D., Van Ackeren, J., Van Hemelrijck, D., Wastiels, J., Vantomme, J. *Validation of digital image correlation technique for impact loading*

applications. 9th International Conference on Mechanical and Physical Behaviour of Materials under Dynamic Loadings (DYMAT 2009), Brussels, Belgium, 7-11 September 2009.

[4] Kakogiannis, D., Van Ackeren, J., Van Hemelrijck, D., Wastiels, J., **Palanivelu, S.,** Van Paepegem, W., Vantomme, J., Nurick, G.N. *Experimenal and numerical study of pultruded composite tubes under blast loading*. 9th International Conference on Mechanical and Physical Behaviour of Materials under Dynamic Loadings (DYMAT 2009), Brussels, Belgium, 7-11 September 2009.

[5] **Palanivelu, S.,** Van Paepegem, W., Degrieck, Reymen, B., Segers, E., Ndambi, J., Vantomme, J., Kakogiannis, D., Van Ackeren, J., Van Hemelrijck, D., Wastiels, J. *Performance of a sacrificial cladding strucutre made of empty recyclable beverage cans under large-scale air blast load.* Protect 2011, 7 – 9 June 2011, Switzerland.

[6] Mookherjee, S.P., **Palanivelu, S**., Jothilingam, C. *Design of Light commercial vehicle with CNG system*, SAE Technical paper, 2005-26-062.

Publications in international conference proceedings (c1 papers)

[1] Kakogiannis, D., De Wolf, K., **Palanivelu, S.,** Van Hemelrijck, D., Vantomme, J., Wastiels, J., Van Paepegem, W. *Blast loading response of typical steel cans*. Proceedings of the International Conference on Structural Analysis of Advanced Materials (ICSAM – 2007), Patras, Greece, September 2-6, 2007.

[2] Kakogiannis, D., Van Hemelrijck, D., Wastiels, J., **Palanivelu, S.,** Van Paepegem, W., De Wolf, K., Vantomme, J. *Experimental and numerical study of the energy absorption capacity of pultruded composite tubes.* Proceedings of the 13th European Conference on Composite Materials (ECCM-13), Stockholm, Sweden, 2-5 June, 2008.

[3] **Palanivelu, S.,** Verhelst, R., Van Paepegem, W., Degrieck, J., Kakogiannis, D., Van Hemelrijck, D., Wastiels, J., De Wolf, K. and Vantomme, J. *Experimental and numerical study on axial crushing behaviour of pultruded composite tubes*. Proceedings of the 13th European Conference on Composite Materials (ECCM-13), Stockholm, Sweden, 2-5 June, 2008.

[4] Kakogiannis, D., De Wolf, K., **Palanivelu, S**., Van Hemelrijck, D., Vantomme, J. and Van Paepegem, W. *Blast Loading Response of Typical*

Coca-Cola Cans. Proceedings of the International Conference on Impact Loading of Lightweight Structures. Trondheim, Norway, 17-19 June 2008.

[5] **Palanivelu, S.,** Van Paepegem, W., Degrieck, J., Vantomme, J., Kakogiannis, D., Van Ackeren, J., Van Hemelrijck, D., Wastiels, J. *Design of sacrificial cladding structures to protect civil engineering structures from blast load.* Sampe students meeting, The Netherlands, 11-12 January, 2009.

[6] **Palanivelu, S.,** Van Paepegem, W., Degrieck, J., Vantomme, J., Kakogiannis, D., Van Ackeren, J., Van Hemelrijck, D., Wastiels, J. *Blast energy absorption of recyclable beverage cans and composite tubes for sacrificial cladding structures*. Deformation and Fracture of Composites Conference (DFC10), Sheffield University, Sheffield, United Kingdom, 15-17 April, 2009.

[7] Van Paepegem, W., **Palanivelu, S.,** Degrieck, J., Vantomme, J., Kakogiannis, D., Van Ackeren, J., Van Hemelrijck, D., Wastiels, J. *Energy absorption of composite tubes: Experimental testing and finite element modelling.* Sampe meeting, The Netherlands, June 02, 2009.

[8] Kakogiannis, D., Van Hemelrijck, D., Van Ackeren, J., Wastiels, J., **Palanivelu, S.,** Van Paepegem, W., Vantomme, J. and Nurick, G.N. *Experimenal and numerical study of pultruded composite tubes under blast loading*. International Conference on SEM (SEM 2009), Albuquerque , New Mexico, US, 1-4 June, 2009.

[9] Kakogiannis, D., Van Hemelrijck, D., Van Ackeren, J., Wastiels, J., **Palanivelu, S.,** Van Paepegem, W., Vantomme, J. and Nurick, G.N. *Experimental and numerical study of pultruded composite tubes under blast loading*. 17th International Conference on Composite Materials (ICCM-17), Edinburgh, United Kingdom, 27-31 July, 2009.

[10] **Palanivelu, S.,** Van Paepegem, W., Degrieck, J., Kakogiannis, D., Van Ackeren, J., Van Hemelrijck, D., Wastiels, J. De Wolf, K., Vantomme, J. *Numerical energy absorption study of composite tubes for axial impact loadings*. 17th International Conference on Composite Materials (ICCM-17), Edinburgh, United Kingdom, 27-31 July, 2009.

[11] Van Ackeren, J., Blom, J., Belkassem, B., Kakogiannis, D., Wastiels, J., Van Hemelrijck, D., **Palanivelu, S.,** Van Paepegem, W., Degrieck, J., Vantomme, J. *Impact study of Textile Reinforced Cementitious materials: test method and experimental results*, 9th Conference on Brittle Matrix Composites (BMC-9), Warsaw, Poland, 25-28 October, 2009.

[12] **Palanivelu, S.,** Van Paepegem, W., Degrieck, J., Vantomme, J., Kakogiannis, D., Van Ackeren, J., Van Hemelrijck, D., Wastiels, J. *Numerical energy absorption study of pultruded composite tubes*, ABAQUS user meeting, The Netherlands, November 11-12, 2009.

[13] **Palanivelu, S.,** Van Paepegem, W., Degrieck, J., Vantomme, J., Kakogiannis, D., Van Ackeren, J., Van Hemelrijck, D., Wastiels, J. *Energy absorption study of recyclable metal beverage cans*, ABAQUS user meeting, The Netherlands, November 11-12, 2009.

[14] Van Ackeren, J., Blom, J., Kakogiannis, D., Wastiels, J., Van Hemelrijck, D., **Palanivelu, S.,** Van Paepegem, W., Degrieck, J., Vantomme, J. *Damage characterisation of a textile reinforce cement composite material under low velocity impact loading*. Proceedings of the 14th European Conference on Composite Materials (ECCM-14), Budapest, Hungary, 7-10 June, 2010.

[15] **Palanivelu, S.,** Van Paepegem, W., Degrieck, J., Reymen, B., Ndambi, J., Vantomme, J., Kakogiannis, D., Van Ackeren, J., Van Hemelrijck, D., Wastiels, J. *Experimental and numerical study of the energy absorption of composite tubes for sacrificial cladding structures under blast loading*. Proceedings of the 14th European Conference on Composite Materials (ECCM-14), Budapest, Hungary, 7-10 June, 2010.

[16] Van Paepegem, W., **Palanivelu, S.,** Degrieck, J., Vantomme, J., Kakogiannis, D., Van Ackeren, J., Van Hemelrijck, D., Wastiels, J. *Effect of tube geometry on the energy absorption and crushing patterns of composite tubes under quasi-static and impact loading*. Proceedings of the 14th European Conference on Composite Materials (ECCM-14), Budapest, Hungary, 7-10 June, 2010.

[17] Kakogiannis, D., Van Hemelrijck, D., Van Ackeren, J., Wastiels, J., **Palanivelu, S.,** Van Paepegem, W., Degrieck, J., Vantomme, J. *Progressive crushing of pultruded tubes under quasi-static and blast loading.* Proceedings of the 14th European Conference on Composite Materials (ECCM-14), Budapest, Hungary, 7-10 June, 2010.

[18] **Palanivelu, S.,** Van Paepegem, W., Degrieck, J., Kakogiannis, D., Van Ackeren, J., Van Hemelrijck, D., Wastiels, J, Vantomme, J. *Measurement of impact parameters using digital image correlation technique.* Photomechanics 2011, Brussels, Belgium, 7 – 9 February, 2011

[19] Kakogiannis, D., Van Hemelrijck, D., Van Ackeren, J., Wastiels, J.,

Palanivelu, S., Van Paepegem, W., Degrieck, J., Vantomme, J. *Measurement of the transmitted impulse under blast loading.* Accepted for 3rd International conference on impact loading of Lightweight structures (ICILLS 2011) (ECCM-14), Valenciennes, France, 28th June – 1st July, 2011.

Invited presentation

[1] **Palanivelu, S.,** Van Paepegem, W., Degrieck, J. *Experimental and numerical axial crushing study of empty recyclable beverage cans for static, impact and blast loading conditions.* TATA Steel Europe (earlier Corus), Ijmuiden, The Netherlands, November 30, 2011.

Awards

[1] Won "**Best poster award**" for the paper entitled "*Blast loading on metal cans*" in UGent PhD symposium, Belgium, December 06, 2008.

[2] Won "**Best presentation poster award"** in 14th European Conference on Composite Materials (ECCM-14), for the significant contribution in the field of composite materials entitled "*Experimental and numerical blast energy absorption study of composite tubes for sacrificial cladding structures under blast loading*" Budapest, Hungary, 7-10 June, 2010.

Contents

PART III

PART IV

Chapter 1

Introduction

Overview

This chapter presents a general overview of the underlying work. A short introduction of the blast effects and the problem statement is presented. Furthermore, the adopted research methodology is given. Finally, the overview of the chapters and the state of the art are shortly introduced.

1. 1. Introduction and background

The entire world faces the problem of security for industrial, military and civil engineering structures due to terrorist activities. Bombs have exploded in and around buildings in many countries causing major threats to people and civil engineering structures. As a result, such events have generated considerable concern about the ability of countries to protect people and civil engineering structures from the continued threat of bombings. When a bomb explodes, a rapid release of stored energy is released with an audible blast. The energy released is divided into two distinct phenomena – thermal radiation, and coupling with air and soil, known as *air blast* and *ground shock*, respectively. Air blast is the principal cause of the damage to buildings. The shock wave from an explosion propagates by compressing the air

molecules in its path, thus producing the *ambient overpressure* or the *incident pressure*. The waves propagate with supersonic velocity and finally hit the building (refer Figure 1-1). They reflect from the building with amplified overpressures (further characteristics of the blast loading are discussed in Chapter 4). If the building components are not capable of resisting the reflected blast wave, they will fracture and be further fragmented (debris) and moved by the dynamic pressure that immediately follows the shock front. The failure of critical load bearing members such as beams, pillars, columns etc., and its debris cause considerable human casualties during this event.

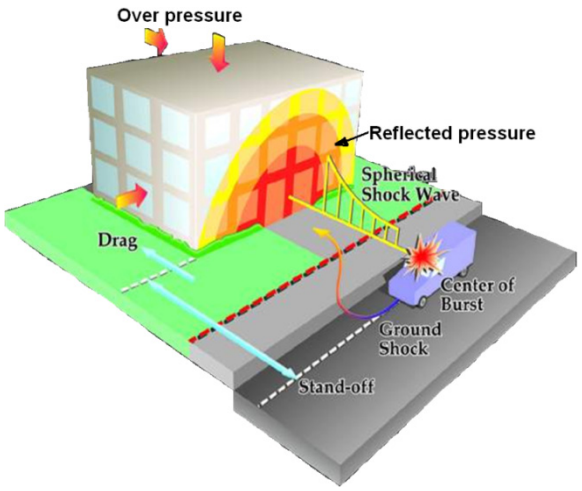

Figure 1-1: Typical blast scenario (reproduced from ref [1]).

Bomb or explosion damage to civil engineering structures depends on the type of structure and the nature of the explosive device and its location relative to the structure. Other factors such as the design of engineering structures and immediate surroundings also determine the damage to the structures. The threat for a conventional bomb to a structure is defined by two equally important parameters: (i) charge mass of the explosive and (ii) the standoff distance (between the blast source and the target). For example, the blast that occurred at the basement of the World Trade Centre in 1993 had the charge mass of 816.5 kg TNT (refer Figure 1-2(a)). The Oklahoma bomb in 1995 had a charge mass of 1814 kg of TNT at a stand-off distance of 4.5 m (Figure 1-2(b)). Assuming the shape of the charge mass for both cases was spherical, a similar blast effect of the latter case (charge mass of 1814 kg of TNT) can be produced by using the previous charge mass (816.5 kg of TNT) with a stand-off distance of 3.45 m. Further details of the scaling law are given in Chapter 4. Terrorist attacks may range from the small letter bomb to a gigantic truck bomb as experienced in Oklahoma City. Based on the stand-off distance the resulting loading on a structure varies. When the stand-off distance increases, a structure will be subjected to a uniform low amplitude and long duration pressure pulse. However, charges situated extremely close to a target structure impose a highly impulsive,

high intensity pressure load over a localized region of the structure. As an example, different damage levels of the buildings exposed to blast loading are shown in Figure 1-2(a-c).

(a) World trade centre bomb blast (1993)

(b) Murrah building Oklahoma city (1995): left – before blast; right – after blast.

(c) Al-khobar building, Saudi Arabia (1996)

Figure 1-2: Example of blast damage to the civil engineering structures (reproduced from ref. [2, 3]).

Over the last few decades the international terrorist attacks have considerably increased (refer Figure 1-3). The increasing terrorist attacks riveted our attention for alternative design methods or improvement in the current design to protect the building and so the people. Few of the currently available solutions are as follows:

(a) Containment of primary steel structures with a thick concrete covering layer; this leads to a large dead weight. Explosion tests have proved that the concrete pulverizes completely and causes a large number of casualties due to shattered granulated material [4].

(b) To increase the structural integrity of critical structural members under blast loading, they are sometimes wrapped with external reinforcement of

composite tape layers. These composite laminates are expensive (the fibre is often carbon and there is currently a supply shortage of carbon fibre worldwide [5]), the adhesive bonding is sensitive to moisture and the fire resistance [6-8].

(c) Another alternative is GLARE, a hybrid composite with alternating aluminium and glass/epoxy layers. This material has been developed by TU Delft and is currently used for the Airbus A380. It has a very good resistance against impact, blast loading (bomb-proof GLARE container) and fire [9-11], however the material is very expensive for application in the construction industry,

(d) Nested structures of sandwich panels have been designed for luggage containers in airplanes, where the exterior sandwich panels sustain the shock wave, while the interior panels preserve the loading capacity [12]. However, again it concerns high-quality composite materials with an inferior fire resistance.

Hence, an alternative and cost effective solution is absolutely necessary to protect the civil engineering structures and to safeguard the human beings from the blast load.

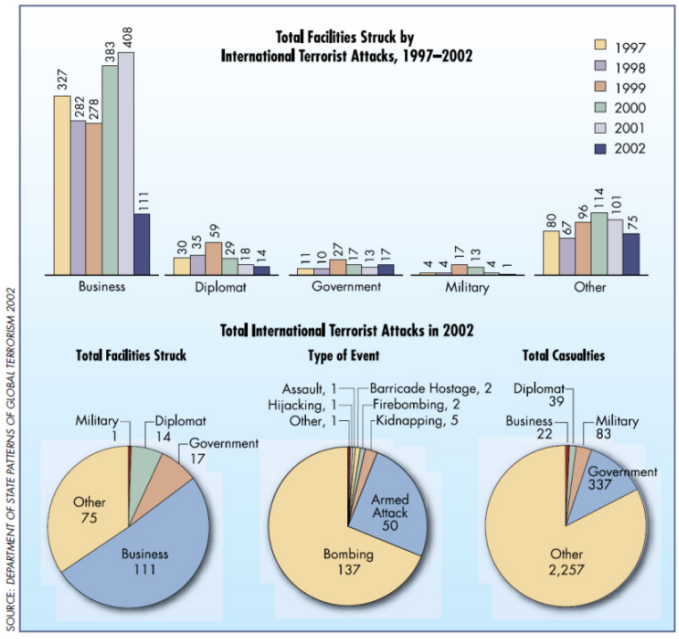

Figure 1-3: Statistical survey on international terrorist attacks (reproduced from ref.[2]).

Recently, the concept of sacrificial cladding design [13-16] has attracted more attention in terms of its functionality and its predictable behaviour. Any sacrificial cladding structure can have two layers (an inner core and outer skin panels). The

function of the skin panel is to distribute the blast pressure more evenly to the inner core which deforms progressively and absorbs most of the energy from the blast load, so that the main load bearing members of the civil engineering structures will be safeguarded. In order to achieve this, the failure load of the sacrificial cladding structure should be kept well below than the failure load of the critical members of the civil engineering structures. Keeping a lower failure load for the inner core may attribute to achieve the plastic deformation/brittle failure during an explosion event and so the transferred peak force to the non-sacrificial structure (civil engineering structures) can be minimised. Based on this objective, in 2007 our consortium (*Ghent University, Royal Military Academy of Belgium and Vrije Universiteit Brussels*) received a research funding from FWO (*Fonds Wetenschappeljik Onderzoek*) to understand the failure mechanisms and the corresponding energy absorption of crushable tubes at different load regimes (Grant No: G.0114.07). Accordingly, one researcher, ir. Dimitrios Kakogiannis started his work around January 2007 at *Vrije Universiteit Brussels,* whereas the author of this dissertation, ir. Sivakumar Palanivelu began his work in May 2007. As per the research proposal, ir. Dimitrios Kakogiannis was continued with contact blast loading and the author of this dissertation continued his work in air blast loading.

1. 2. Objective of this research

In literature, different materials and test specimen shapes [13-17] have been tried out for the sacrificial cladding structures. Generic energy absorption devices are classified into two different categories (α and β types) based on their load-displacement curves [18-24]. The load-displacement curve of the β - type is relatively "flat topped" while for the α - type the curve falls sharply after the peak crush load (refer Figure 1-4). The effect of strain rate and inertia on these structures are explained in refs. [18-24]. The general conclusions of the referred studies are as follows: (i) the deformation of α - type structures is significantly more sensitive to the impact velocity than β - type structures; (ii) when the total kinetic energy remains the same for all test specimens, smaller final deformations result from higher impact velocities and this phenomenon is much more significant for α - type structures than for β - type structure; (iii) strain rate sensitivity and inertia effects must be considered throughout the crushing process during an impact event.

Hence, in order to study the suitability of these structures, two test specimens have been chosen for the inner core of the proposed sacrificial cladding structures: (i) empty metal beverage can (α - type structure) (ii) composite tubes (β - type structure). The advantages of using empty beverage cans are: (i) environment friendly due to recyclable material (ii) it is a waste product and readily available in the market and (iii) non-corrosive due to inner lacquer and outer aesthetic coatings

(iv) dimensionally well controlled (v) these beverage cans can be adopted in different configurations of macro foam depending upon the blast loading magnitudes. As an example, two different configurations (axial and radial) of the macro foam assembly of empty beverage cans are shown in Figure 1-5. Similarly, due to a higher specific strength and modulus, constant crushing force and the corresponding higher specific energy absorption and low strain rate sensitivity of the composite materials, the composite tubes have been chosen for β - type structure. The concept of the proposed sacrificial cladding structure using empty metal beverage cans and composite tubes are shown in Figure 1-6(a) and (b) respectively. The geometry and material details of the used beverage cans and the composite tubes are discussed in the respective chapters.

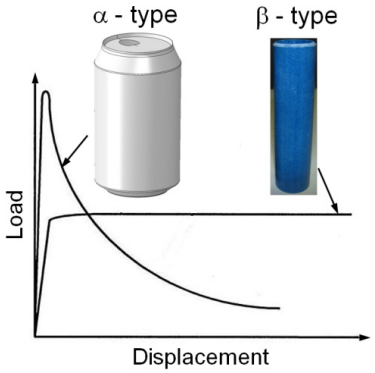

Figure 1-4: General classification of energy absorbing structure.

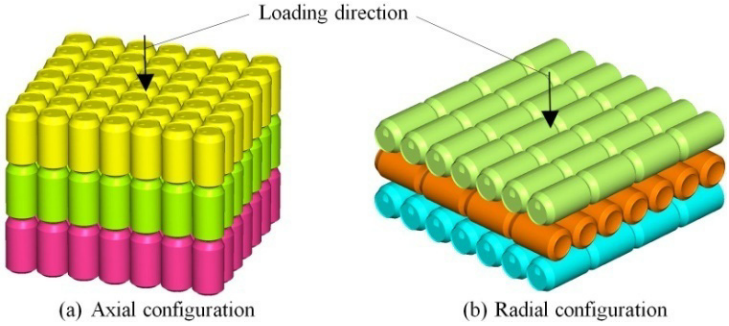

Figure 1-5: Two configurations of macro foam arrangement of empty recyclable metal beverage cans.

1. 3. Hypothesis

The global hypothesis of this research is to check and verify whether the empty metal beverage cans and the composite tubes can be used as inner core members for the proposed sacrificial cladding structure.

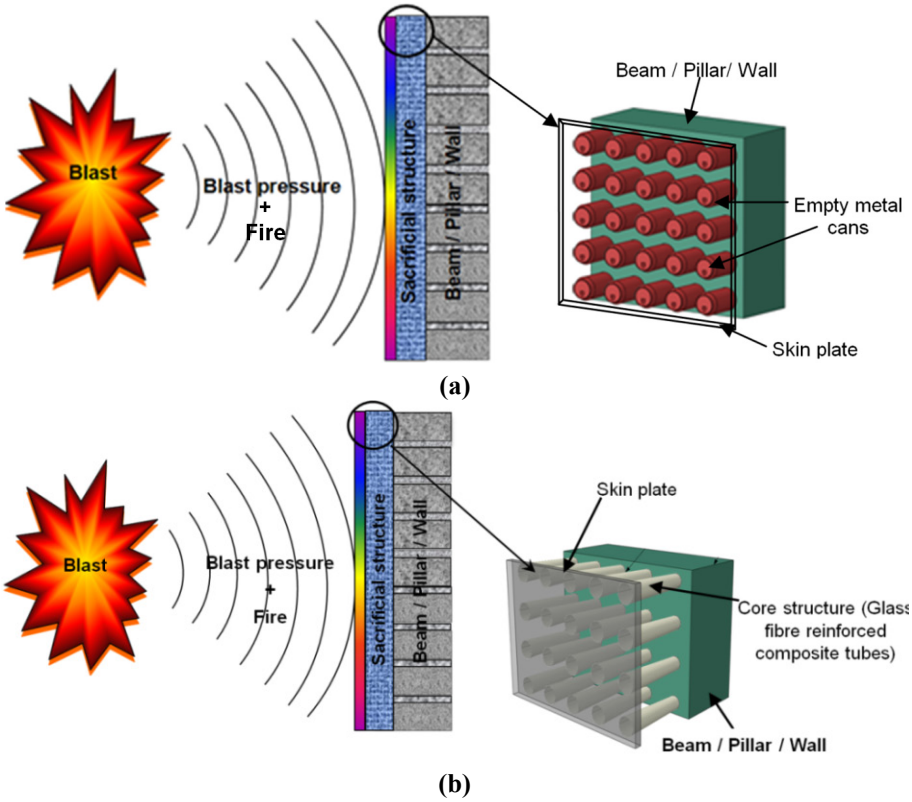

Figure 1-6: Concept of the proposed sacrificial cladding structure **(a)** using empty recyclable metal beverage cans **(b)** using composite tubes.

1. 4. Research methodology

In order to understand the crushing behaviour of the beverage cans and the composite tubes, initial blast tests have been conducted at the *Royal Military Academy*, Brussels, Belgium. The stand-off distance for these experiments was 1.0 m; and different charge masses up to 1.0 kg of C4 were used. The results from these tests showed no permanent deformation of the test specimens (both beverage cans and composite tubes). The beverage cans underwent elastic buckling and hence no plastic deformation was observed. Similarly, the tested pultruded glass polyester composite tubes showed no deformation. As an example, the successive elastic buckling stages of the beverage cans are shown in Figure 1-7. The question of why the beverage cans and the composite tubes did not crush during the blast loading has to be answered.

Furthermore, before designing the inner core of a full-scale sacrificial cladding structure the knowledge of the crushing performance (progressive crushing stages and the corresponding energy absorption) of an individual beverage can or

composite tube is very important. Investigation of these factors during a blast loading is very difficult. Capturing the deformation mechanism, deformation pattern and the corresponding energy absorption during quasi-static and impact tests are relatively easier due to the slow speed of crushing. The results from these tests can be further verified for blast loading conditions. In addition to that, the composite tubes have a significant list of variables which affect the crushing performance and the corresponding energy absorption [25]. A complete list of variables is given in Chapter 7. Understanding the different variables which alter the crushing performance and the corresponding energy absorption of the composite tubes is absolutely necessary. Hence, to understand the above factors a systematic step by step procedure was adopted. The schematic view of the adopted research methodology (applicable to composite tubes) is shown in Figure 1-8.

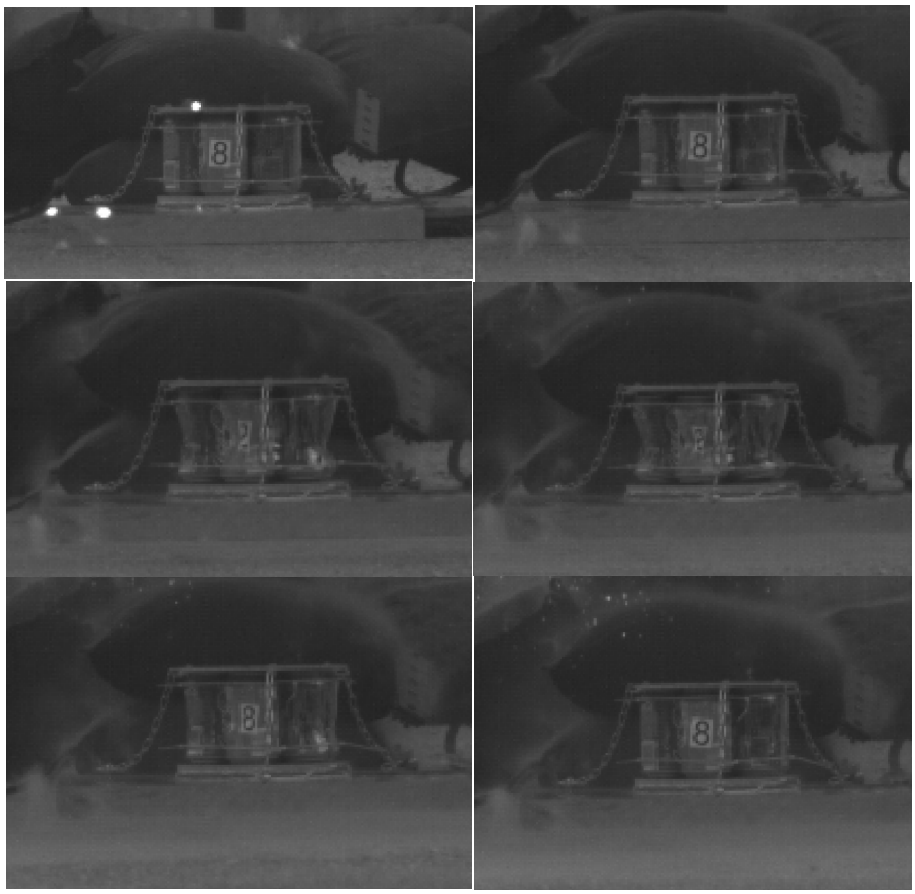

Figure 1-7: Successive elastic buckling stages of beverage cans during air blast loading.

In order to simplify the approach only the axial loading case is considered, i.e. it was assumed that during an explosion event the sacrificial cladding structure receives only axial pressure on the skin panel (at the moment oblique loading on the

sacrificial cladding structure is not considered). In relation with the above assumption only uni-directional composite tubes (pultruded composite tubes) have been investigated. In summary the main focus of this dissertation is to study the crushing performance of the proposed inner core members (empty beverage cans and composite tubes) for different loading conditions such as quasi-static, impact and blast load.

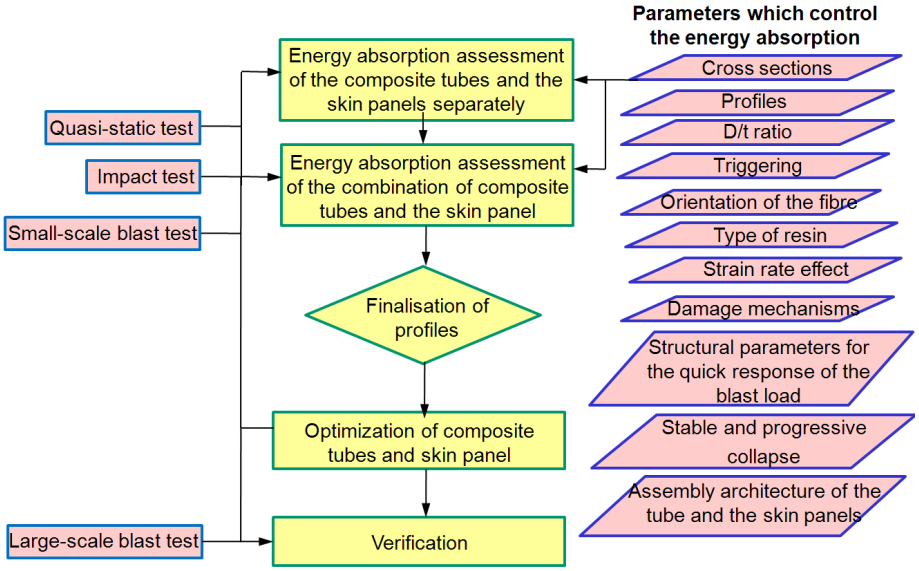

Figure 1-8: Research methodology adopted for this research.

1. 5. Structure of this work

This dissertation consists of four major parts. Part I is dedicated to quasi-static, impact and small-scale blast tests on the α - type structure (empty beverage can); Part II deals with large-scale pultruded composite tubes and medium-scale pultruded composite tubes (β - type structures). Similarly, Part III deals with small-scale in-house composite tubes. Finally Part IV deals with large-scale blast tests on both α - type (empty beverage can) and β - type structures (small-scale pultruded composite tubes). In the following each of them are discussed very shortly.

Part I (α - type structure)
Chapter 2 starts with a literature review on the crushing behaviour of metal tubes. Due to the chosen application (axial blast pressure loading) the study is limited to axial loading of the circular and square cross-sectional metal tubes. A short overview of different failure modes and the corresponding theoretical models are presented. Furthermore, difficulties that arise during dynamic loading and the material modelling are also shortly discussed.

Chapter 3 presents the axial quasi-static and impact crushing performance of the beverage cans. The crushing performance of the beverage can was completely understood from the experimental results. Furthermore, the results from the developed numerical models and analytical model are compared with the experimental results. The effect of entrapped air inside the beverage can during crushing is successfully modelled and the results from the numerical simulation are compared and validated with the experimental results. Finally, this chapter provides a method to calculate the dynamic parameters in a contactless manner using the digital image correlation technique.

In Chapter 4, the experimental and numerical small-scale blast tests on the beverage cans and the corresponding results are presented. The effect of finite surface area and the nature of the reflected surface on the reflected blast parameters are presented. The influence of the inertia of the skin plate on the energy absorption of the inner core is investigated. The results from the experimental tests showed a non-conservation of linear momentum (the transferred impulse to the non-sacrificial structure was significantly lower than the reflected impulse). This problem is investigated in Chapter 5 using a coupled Eulerian and Lagrangian approach. The conducted simulations show that the interaction of pressure waves with the experimental test set-up led to the difference in the impulse. The same finding is also validated with the decoupled numerical analysis.

In Chapter 6, an analytical model is presented to calculate the crushing variables of the beverage can for blast loading. Moreover, the effect of the initial geometric imperfections on the crushing performance of the beverage cans is evaluated numerically. The results from two approaches (using the superposition of linear buckling mode shapes and measured geometric imperfections) are presented.

Part II (β - type structure)

In Chapter 7 a review of the energy absorption of composite tubes is presented. In Chapter 8, the axial impact tests for large-scale pultruded circular and square cross-sectional glass polyester and vinylester composite tubes for three different initial impact velocities (9.3 m/s, 12.4 m/s and 14 m/s) and with two triggering mechanisms are presented. This study concludes the effect of cross-section, triggering geometry, strain rate and resin on the specific energy absorption of the composite tubes.

In Chapter 9, a detailed numerical parametric study is presented for large-scale circular and square cross-sectional pultruded composite tubes with two triggering profiles. The effect of correct modelling of triggering and the inclusion of delamination(s) on the crushing performance of the composite tubes is proved with five different numerical modelling approaches. This study also concludes about the

effect of the initial geometric imperfections and mesh sensitivity on the crushing performance.

Chapter 10 deals with axial impact loading on medium-scale pultruded composite tubes. The question of why the dynamic specific energy absorption decreases compared to the quasi-static specific energy absorption is answered. Similarly, Chapter 11 presents the experimental small-scale blast loading on these composite tubes (medium-scale pultruded glass polyester composite tubes). From these two chapters an interesting finding on strain rate insensitivity of pultruded composite tubes is presented. This chapter also deals with the coupled and decoupled numerical simulations for the charge mass of 40 g C4 with 30 cm and 15 cm stand-off distances.

Part III (β - type structure)

Chapter 12 presents the quasi-static crushing performance of nine different shapes of small-scale in-house glass polyester composite tubes. The results from this study show that the energy absorption of non-standard or special shapes is better than the standard profiles. This study also gives the information about the effect of cross-section, t/D ratio and triggering profiles on the specific energy absorption of the composite tubes. Similarly, the effect of inclusion of polyurethane foam on the specific energy absorption for nine different shapes of the composite tubes is presented in Chapter 13. The qualified shapes have been considered for the axial impact study.

In Chapter 14, the axial impact and blast loading on small-scale in-house glass polyester composite tubes are presented. Axial impact tests have been conducted for different initial impact velocities such as 3.1 m/s, 3.8 m/s, 4.4 m/s, 4.9 m/s and 5.3 m/s with two different t/D ratios. The effect of polyurethane foam-filling on the specific energy absorption for the dynamic loading is presented. The qualified composite tubes from the axial impact testing were also investigated for the small-scale blast tests.

Part IV (both α and β - type structures)

In Chapter 15, large-scale blast tests on two configurations of representative sacrificial cladding structures made of empty beverage cans and sandwich composite skin plates are presented. The concept of shock tubes is successfully employed to create a perfectly plane shock wave using concrete sewage pipes. The coupled numerical simulations have been conducted to calculate a minimum length of the concrete pipes; and the results from the numerical simulations are in very good agreement with the experimental results. The blast mitigation efficiency of the beverage cans for different charge masses such as 75 g, 100 g, 150 g and 200 g of C4 is presented. Furthermore, the results from a decoupled simulation are compared

with the experimental results. Similarly, Chapter 16 presents the large-scale blast tests on small-scale pultruded glass polyester composite tubes. The blast mitigation performance of these tubes is studied for 100 g and 150 g of C4. Also this study captures the importance of having a uniform thickness of the composite tube for the progressive crushing.

Finally, the conclusions of this work are summarized in the last Chapter 17 where besides the achievements of this work also some guidelines are given for the future research work.

1. 6. Innovative aspects

The innovative aspects of this work lie in the combination of systematic experimental approaches and the corresponding numerical simulation validations with the experimental results. The original contributions of this dissertation to the literature are given as follows:

(a) The effect of geometry profile, triggering, strain rate and the type of resin on the energy absorption of square and circular cross-sectional large-scale pultruded glass polyester composite tubes has been published in **Polymer testing [26].**

(b) To predict a correct peak crush load, deformation length, deformation patterns and the corresponding energy absorption of a pultruded composite tube, accurate modelling of triggering and the inclusion of delamination(s) are absolutely necessary. These cannot be achieved using a single layer of shell elements as most of the published works have claimed in the literature. Furthermore, the initial geometric imperfections (within the manufacturing tolerance) of the composite tubes do not influence the overall crushing performance of the composite tube. These results have been published in **two parts in Polymer Testing [27, 28].**

(c) The comparative quasi-static crushing performance of nine different geometrical shapes of the small-scale in-house glass polyester composite tubes showed that the t/D ratio plays a significant role for the progressive crushing and the corresponding specific energy absorption. The specific energy absorption of non-standard or special shapes is significantly higher than the standard profiles. The results from this study have been published in **Polymer Testing [29].**

(d) The quasi-static specific energy absorption of different shapes of the composite tubes with two t/D ratios and triggering showed that the specific energy absorption of composite tubes with tulip triggering was higher than

for the tubes with a bevel triggering. The results from this study have been published in **Composite Structures [30].**

(e) The inclusion of polyurethane foam-filling on the composite tubes has altered the typical failure patterns of brittle composite tubes. Any change in the deformation pattern will influence the energy absorption of the composite tubes. However, this depends on the density of the foam-filling. These results have been published in **Composites Part B [31].**

(f) Axial quasi-static and impact experiments on the beverage can showed a clear evidence for the strain rate and strain hardening dependency. An analytical model for the asymmetric deformation pattern of the beverage can is formulated including strain rate and strain hardening effects. The results from the analytical and experimental results are in very good agreement. The same has been published in **International journal of Impact Engineering [32].**

(g) The crushing performance of the beverage can for small-scale blast tests is captured for 20 g of C4 with 30 cm stand-off distance. The finite reflected surface and its nature play a significant role for the reflected blast parameters. Furthermore, the interaction of the pressure wave with the experimental test set-up was studied using a coupled Lagrangian-Eulerian approach and with moving boundary condition of the skin panel. The results from these simulations are further validated with the decoupled numerical simulation results. All the aforementioned results are published in **Engineering Structures [33].**

(h) The method of conducted large-scale blast testing and the corresponding crushing performance of the empty metal beverage cans are accepted for publication for **Protect 2011** conference which will be held on 7-9 June 2011 at Switzerland.

(i) The pultruded glass polyester composite tubes are insensitive to the strain rate effect. Furthermore, the deformation patterns of these composite tubes remain the same for axial quasi-static, impact and blast loading conditions.

(j) The crushing performance of the polyurethane foam-filled composite tubes is depending upon on the density of the filled foam. A higher density may lead to reduce the specific energy absorption of the composite tubes due to the suppression of few failure modes. However, a low density foam can improve the strengthening and stability of the wall; and subsequently it will improve the specific energy absorption of the composite tubes by allowing all typical failure modes.

(k) The close-range blast testing on the medium-scale pultruded composite tubes and the corresponding results have already been communicated to Polymer testing.

(l) The specific energy absorption of polyurethane foam-filled small-scale in-house composite tubes with lower t/D ratio decreases compared to hollow

tubes. However, for a higher t/D ratio the specific energy absorption of the polyurethane foam-filled composite tubes increases. These results are ready for submission to a journal.

(m) Similarly, the developed analytical model for the blast loading application and the corresponding investigation on the effect of initial geometric imperfections on the crushing performance of the beverage can is ready for submission to a journal.

Bibliography

[1]. Mayes., R. L. and Hinnman, E., *Blast isolation technology and blast loading.* National Park Service.

[2]. Kirk A.Marchand, F. A., *Facts for steel buildings - Blast and progresssive collapse.* American Institute of steel constructioin, Inc.

[3]. http://www.solcomhouse.com/wtc1993.htm (dated 02-06-2011).

[4]. Halleux, F., Art, J., Ndambi, J. M. and Vantomme, J., *Resistance analysis of steel and mixed steel concrete columns subjected to close-contact explosions,* . 16th Technical Dymat Meeting, 27-28/10/2005, Brussels, 2008: p. 145-156.

[5]. Segal, C. L. and Loud, S., *Will There Be Enough Carbon Fiber? - Market Overview & Forecasts.* The Global Outlook for Carbon Fiber 2004, 18-21 October 2004, Hamburg, Germany., 2004.

[6]. Ferrier, E., Lagarde, G. and Hamelin, P., *Concrete beams reinforced by fibre-reinforced plastics: the effect of temperature on the adhesive layer.* Composites Science and Technology, 2001. **61**(3): p. 425-431.

[7]. Matthys, S., *Structural Behaviour and Design of Concrete Members Strengthened with Externally Bonded FRP Reinforcement.* Universiteit Gent, doctoraatsthesis., 2000.

[8]. Ceroni, F., Pecce, M. and Matthys, S., *Tension stiffening of reinforced concrete ties strengthened with externally bonded fiber-reinforced polymer sheets.* Journal of Composites for Construction, 2004. **8**(1): p. 22-32.

[9]. van der Kevie, G., *Glare/FML, the best of both worlds.* SAMPE Benelux meeting, 29 April 2004, Stork Fokker, Papendrecht, The Netherlands, 2004.

[10]. Hooijmeijer, P. A., *Fibre Metal Laminates - New Glare developments.* SAMPE Benelux Meeting, 21, October 2004, SONACA, Gosselies, Belgium, 2004.

[11]. Lemanski, S. L., Nurick, G. N., Langdon, G. S., Simmons, M. S., Cantwell, W. J. and Schleyer, G. K., *Understanding the behaviour of fibre metal laminates subjected to localised blast loading.* Composite Structures, 2006. **76**(1-2): p. 82-87.

[12]. Weerth, D. E., *Blast resistant airline baggage container design.* 15th International Conference on Composite Materials (ICCM-15). Durban, 27 June - 1 July 2005., 2005.

[13]. Guruprasad, S. and Mukherjee, A., *Layered sacrificial claddings under blast loading Part I - analytical studies.* International Journal of Impact Engineering, 2000. **24**(9): p. 957-973.

[14]. Guruprasad, S. and Mukherjee, A., *Layered sacrificial claddings under blast loading Part II - experimental studies.* International Journal of Impact Engineering, 2000. **24**(9): p. 975-984.

[15]. Kotzialis, C., Derdas, C. and Kostopoulos, V., *Blast behaviour of plates with sacrificial cladding.* 5th GRACM International congress on computational mechanics, June 29 - July 1, Limassol, Cyprus., 2005.

[16]. Hanssen, A. G., Enstock, L. and Langseth, M., *Close-range blast loading of aluminium foam panels.* International Journal of Impact Engineering, 2002. **27**(6): p. 593-618.

[17]. Theobald, M. D. and Nurick, G. N., *Experimental and numerical analysis of tube-core claddings under blast loads.* International Journal of Impact Engineering. **37**(3): p. 333-348.

[18]. Zou, Z., Tan, P. J., Reid, S. R., Li, S. and Harrigan, J. J., *Dynamic crushing of a one-dimensional chain of type II structures.* International Journal of Impact Engineering, 2007. **34**(2): p. 303-328.

[19]. Reid, S. R. and Yella Reddy, T., *Experimental investigation of inertia effects in one-dimensional metal ring systems subjected to end impact -I. Fixed end systems.* International Journal of Impact Engineering, 1983. **1(1)**: p. 85-106.

[20]. Oshiro, R. E. and Alves, M., *Scaling impact structures.* Archive of applied mechanics, 2004. **74**: p. 130-145.

[21]. Su, X. Y., Yu, T. X. and Reid, S. R., *Inertia-sensitive impact energy-absorbing structures part I: Effects of inertia and elasticity.* International Journal of Impact Engineering, 1995. **16**(4): p. 651-672.

[22]. Su, X. Y., Yu, T. X. and Reid, S. R., *Inertia-sensitive impact energy-absorbing structures part II: Effect of strain rate.* International Journal of Impact Engineering, 1995. **16**(4): p. 673-689.

[23]. Calladine, C. R. and English, R. W., *Strain-rate and inertia effects in the collapse of two types of energy-absorbing structure.* International Journal of Mechanical Sciences, 1984. **26**(11-12): p. 689-701.

[24]. Gao, Z. Y., Yu, T. X. and Lu, G., *A study on type II structures. Part I:: a modified one-dimensional mass-spring model.* International Journal of Impact Engineering, 2005. **31**(7): p. 895-910.

[25]. Ramakrishna, S., *Microstructural design of composite materials for crashworthy structural applications.* Materials & Design, 1997. **18**(3): p. 167-173.

[26]. Palanivelu, S., Van Paepegem, W., Degrieck, J., Van Ackeren, J., Kakogiannis, D., Van Hemelrijck, D., Wastiels, J. and Vantomme, J., *Experimental study on the axial crushing behaviour of pultruded composite tubes.* Polymer Testing, 2010. **29**(2): p. 224-234.

[27]. Palanivelu, S., Van Paepegem, W., Degrieck, J., Kakogiannis, D., Van Ackeren, J., Van Hemelrijck, D., Wastiels, J. and Vantomme, J., *Parametric study of crushing parameters and failure patterns of pultruded composite tubes using cohesive elements and seam, Part I: Central delamination and triggering modelling.* Polymer Testing, 2010. **29**(6): p. 729-741.

[28]. Palanivelu, S., Van Paepegem, W., Degrieck, J., Van Ackeren, J., Kakogiannis, D., Wastiels, J., Van Hemelrijck, D. and Vantomme, J., *Parametric study of crushing parameters and failure patterns of pultruded composite tubes using cohesive elements and seam: Part II - Multiple*

delaminations and initial geometric imperfections. Polymer Testing, 2010. **29**(7): p. 803-814.

[29]. Palanivelu, S., Van Paepegem, W., Degrieck, J., Kakogiannis, D., Van Ackeren, J., Van Hemelrijck, D., Wastiels, J. and Vantomme, J., *Comparative study of the quasi-static energy absorption of small-scale composite tubes with different geometrical shapes for use in sacrificial cladding structures.* Polymer Testing, 2010. **29**(3): p. 381-396.

[30]. Palanivelu, S., Van Paepegem, W., Degrieck, J., Vantomme, J., Kakogiannis, D., Van Ackeren, J., Van Hemelrijck, D. and Wastiels, J., *Crushing and energy absorption performance of different geometrical shapes of small-scale glass/polyester composite tubes under quasi-static loading conditions.* Composite Structures, 2010. **93**(2): p. 992-2007.

[31]. Palanivelu, S., Van Paepegem, W., Degrieck, J., Vantomme, J., Kakogiannis, D., Van Ackeren, J., Van Hemelrijck, D. and Wastiels, J., *Comparison of the crushing performance of hollow and foam-filled small-scale composite tubes with different geometrical shapes for use in sacrificial cladding structures.* Composites Part B: Engineering, 2010. **41**(6): p. 434-445.

[32]. Palanivelu, S., Van Paepegem, W., Degrieck, J., De Pauw, S., Vantomme, J., Wastiels, J., Kakogiannis, D. and Van Hemelrijck, D., *Low velocity axial impact crushing performance of empty recyclable metal beverage cans.* International Journal of Impact Engineering, 2011. **38**(7): p. 622-636.

[33]. Palanivelu, S., Van Paepegem, W., Degrieck, J., Reymen, B., Ndambi, J.-M., Vantomme, J., Kakogiannis, D., Wastiels, J. and Van Hemelrijck, D., *Close-range blast loading on empty recyclable metal beverage cans for use in sacrificial cladding structure.* Engineering Structures, 2011. **33**(6): p. 1966-1987.

Part I

This part deals with the quasi-static, impact and small-scale blast testing on α - type structure (empty metal beverage cans)

Chapter 2

Metal Tubes for Energy Absorption: a Review

Overview

This chapter presents a literature review on the energy absorption capability of metal tubes. Different failure modes of circular and square cross-sectional metal tubes and the corresponding theoretical models to predict the mean crush load are presented. The effects of dynamic loading on different parameters of these tubes are given. Furthermore, a brief introduction about the models which are used to capture the strain hardening, strain rate and the corresponding damage of the structure is presented.

2. 1. Introduction

The quest for lighter and more efficient energy absorption components for various transportation systems has led to an increased focus in thin-walled high strength metals and their alloys [1-4]. The knowledge of this field of engineering is now available for use in a wide variety of applications, which include crash barrier design [5], collision damage to road bridges, offshore structures [6], oil tankers, personal safety items, packaging material for fragile goods etc. The same concept has been extended to protective structures which are used for the protection of civil engineering and other structures from explosion load [7-12]. The design and analysis of energy absorbing structures are very different from conventional structural design and analysis. The energy absorbing structures have to sustain intense impact loads, so that their deformation and failure involve large geometry changes. Furthermore, the effects of strain rate, strain hardening and various interactions between different

deformation modes have to be accounted for. Based on different applications the selection of the materials and structures can vary; however, some fundamental principles are generally valid for all applications and can serve as guidelines for crashworthy or energy absorbing structures [13]. Therefore, brief definitions of important factors are given below.

(i) *irreversible energy conversion* – the energy conversion by the structures/materials should be irreversible; that is, the structures/materials should be able to convert most of the input (kinetic) energy into inelastic energy by plastic deformation or other dissipation processes, rather than storing it elastically.
(ii) *constant crush force* – the peak crush force of an energy absorbing structure should be kept below a threshold value (this value can be chosen based on the application); and ideally the reaction force should remain constant during the crushing process.
(iii) *long stroke or deformation* – the work done by a force is equal to its magnitude times the displacement/deformation length experienced along the action line of the force. Hence, if the structure has to absorb a large amount of impact energy the stroke should be sufficiently longer.
(iv) *stable, progressive and repeatable deformation mode* – during the crushing process, the energy absorbing structure should exhibit controlled, progressive and repeatable failure patterns for different magnitudes of the loading.
(iv) *high specific energy absorption* – normally an energy absorbing structure is evaluated by the term called "*specific energy absorption',* which means amount of material utilized to absorb a certain energy value (energy absorption capacity per unit mass). Hence, the energy absorbing structure should be light in mass so that the specific energy absorption will be maximum.
(v) *low cost, easy installation and free from maintenance* – the final usage of any energy absorbing structure primarily depends upon the cost related to material, manufacturing, installation and maintenance. Hence, for an easy acceptance in the market the related cost of the energy absorbing element should be low.

In order to achieve the above mentioned requirements, different forms of energy absorption elements and different materials have been tried out and deployed for different applications [14]. Examples of such structures include tubes, frusta, multi-corner columns, struts, sandwich structures, honey comb shells and other special shapes. However, due to the chosen application and its architecture this review is focused only on the circular and square cross-sectional metals tubes. Furthermore, due to an adopted simplification in the approach (axial blast pressure loading on the inner core members) only the axial loading configuration is considered.

2. 2. Circular cross-sectional tubes

2. 2. 1. Collapse modes

The circular tube proves to be a popular energy absorber because it provides a reasonably constant crushing force; furthermore, it has comparatively high energy absorbing capacity and stroke length per unit mass [15]. When a circular thin-walled tube is crushed axially it collapses either *axisymmetrically* or *non-symmetrically* (*asymmetric*), depending primarily on the ratio of diameter to thickness (*D/t*) [16]. The axisymmetric mode is often known as the *ring mode* or *concertina mode* (refer Figure 2-1(a)), while the asymmetric mode is referred to as *diamond mode* (refer Figure 2-1(b)). For certain values of *D/t* a tube may start to collapse with the ring mode and then switch to the diamond mode, hence exhibiting a *mixed mode* (refer Figure 2-1(c)).

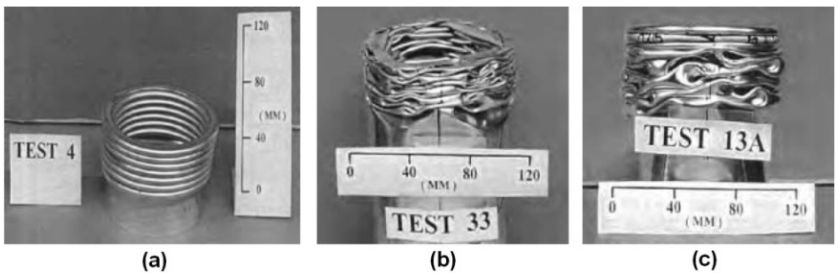

Figure 2-1: Collapse modes of circular tubes under axial loading **(a)** concertina mode **(b)** diamond mode **(c)** mixed mode [16].

Andrews et al. [16] classified the axial crushing of aluminum cylindrical tubes based on the *D/t* (diameter to thickness) and *L/D* (length to diameter) ratios into seven different categories under quasi-static loading: (i) sequential concertina mode (ii) sequential diamond mode (iii) Euler mode (iv) mixed concertina and diamond mode (v) simultaneous concertina mode (vi) simultaneous diamond mode (vii) tilting of the tube axis (refer Figure 2-2).

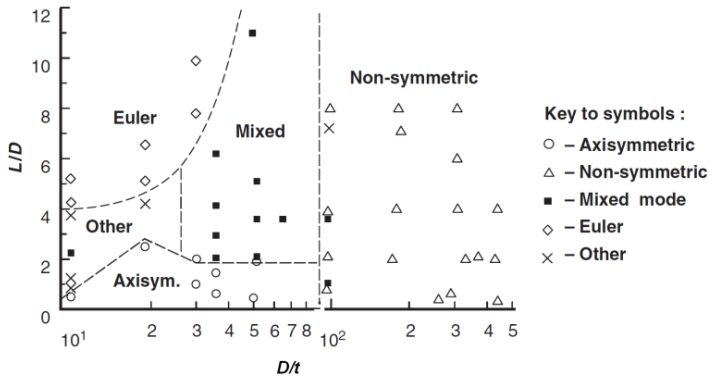

Figure 2-2: Classification of deformation patterns for circular aluminium tubes (reproduced from [16]).

Experimental observations [17-20] showed that thick cylinders (*D/t* ratio < 80 to 90) buckle in the concertina deformation mode, whereas thin cylinders (*D/t* ratio > 90) buckle in the diamond deformation mode. Furthermore, the specific energy absorption of the concertina mode was higher than for the diamond mode [16].

2. 2. 2. Theoretical models for concertina mode

For quasi-static loading

Alexander [21] was the first to provide a theoretical model for quasi-static axial crushing of a circular tube for the ring or concertina model (refer Figure 2-3(a)). During the formation of a single fold, three circumferential plastic hinges occur. Assuming that the fold goes completely outwards, all the material between the hinges experiences circumferential tensile strain. The external work done is dissipated by plastic bending of the three hinges and circumferential stretching of the material in between. Hence, the length of the fold is an important parameter for the calculation of the external work. Furthermore, there is no interaction between bending and stretching of the fold; hence, the material yields either by bending or stretching only. Based on the above assumptions Alxender provided expressions for half fold length and mean crush load (Equation (2.1) and Equation (2.2) respectively [21]),

$$\text{Half fold length} = l = \left(\frac{\pi Rh}{\sqrt{3}}\right)^{1/2} \tag{2.1}$$

$$\text{Mean crush load} = P_{mean} = 6Yh\sqrt{2Rh} \tag{2.2}$$

where h is the thickness of the tube (m); R is the inner radius of the tube (m); Y is the yield stress of the material (Pa). The Equation (2.2) has been most frequently used for the axial crushing of metal tubes. It provides a good prediction of mean crush load for metal tubes when D/t < 30 [22]. Further, this model was modified by Abramowicz and Jones [23]; and their corresponding assumed deformation pattern is shown in Figure 2-3(b). A similar approach was adopted in the Grzebieta model [24] (refer Figure 2-3(d)). They have reported the following equations for half folding length and the mean crush load (Equation (2.3) and Equation (2.4)).

$$\text{Half fold length} = l = 1.76\left(\frac{Rh}{2}\right)^{1/2} \tag{2.3}$$

$$\text{Mean crush load} = P_{mean} = 8.91Yh\sqrt{2Rh}\left(1 - 0.61\sqrt{\frac{h}{2R}}\right) \tag{2.4}$$

To account for the fact that the tube wall deforms both inwards and outwards with respect to the mean diameter of the tube, Wierzbicki et al. [25] introduced a parameter known as the *eccentricity factor*, which defines the outward portion over the whole length (H) (refer Figure 2-3(c)). Based on the experiments they have provided the following equation to calculate the fold length (Equation (2.5)).

$$\text{Half fold lengh} = l = 2.62\left(\frac{Rh}{2}\right)^{1/2} \tag{2.5}$$

Similarly, Jones [26] has provided an equation for the half length using the tangential modulus (E_h) and static yield stress (σ_0) (Equation (2.6)).

$$\text{Half fold} = l = \frac{\pi L}{2}\left(\sqrt{3} - \frac{hE_h}{R\sigma_0}\right)^{-1} \tag{2.6}$$

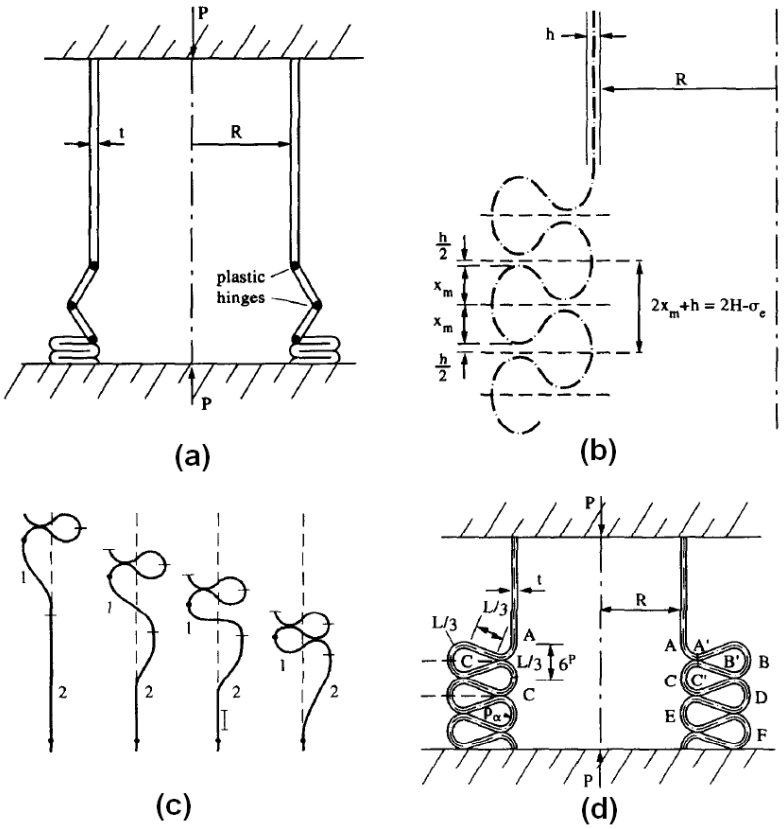

Figure 2-3: Different failure models and their mechanisms for axisymmetric (concertina) failure mode: **(a)** Alexander [21] **(b)** Abramowicz and Jones model [23] **(c)** Wierzbicki et al. model [25] **(d)** Grzebieta model [24].

The above equations are only valid for axial quasi-static crushing without considering the strain hardening effect. The effect of strain hardening should be accounted for materials which have a strong dependency.

For dynamic loading

Similar to quasi-static testing, analytical formulae exist for dynamic mean crush load of circular shells (Equation (2.7)). The effect of strain rate has also to be accounted for dynamic loading cases, because this effect plays a major role to enhance the yield strength of the material.

$$\text{Mean crush load} = P_{mean} = 2(\pi h)^{\frac{3}{2}}\sqrt{R}\sigma_y\left\{1+\left(\frac{V_0}{4RD}\right)^{\frac{1}{q}}\right\}/3^{1/4} \qquad (2.7)$$

where V_0 is the initial impact velocity (m/s): D and q are material constants. Karagiozova and Jones [27] have provided relations to calculate the peak crush load for cylindrical shells which deform in concertina mode during an impact loading based on the *Von-Mises* and *Tresca* stress criterion (Equation (2.8) and (2.9)).

$$P_{Mises}^{\max} = 2\pi Rh\left(2\sigma_0/\sqrt{3}+V_0(\rho E_h)^{1/2}2/\sqrt{3}\right) \qquad (2.8)$$

$$P_{Tresca}^{\max} = 2\pi Rh\left(\sigma_0+V_0(\rho E_h)^{1/2}(2/\sqrt{3})^{1/2}\right) \qquad (2.9)$$

2. 2. 3. Theoretical models for diamond mode

The schematic view and the asymmetric deformation pattern are shown in Figure 2-4(a) and (b) for 3 triangular lobes and 8 triangular lobes respectively; and the corresponding folding mechanism is shown in Figure 2-5 for 3 triangular lobes. It can be noticed from these figures that the fold length is not constant for the asymmetric failure mode in radial direction. In case of the asymmetric deformation mode (diamond mode) the inward part of the fold is found to be bigger than the outward fold [28, 29]. Therefore, the eccentricity factor for a diamond mode deformation can be defined as the ratio of the inward part to the total folding length [28, 29].

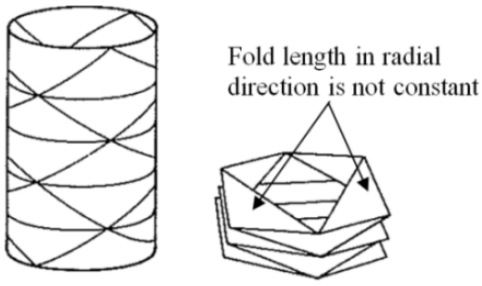

(a) Diamond mode deformation pattern with 3 triangular folds [30]

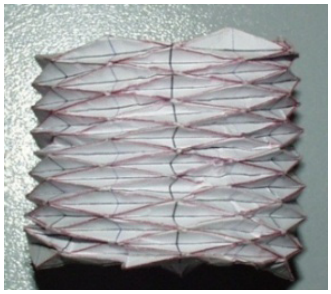

(b) Diamond mode deformation pattern with 8 triangular folds – paper model

Figure 2-4: Asymmetric or diamond mode crushing patterns.

Pugsley and Macaulay [31] studied the diamond deformation mode of thin cylindrical columns. In their analysis, the energy is assumed to be absorbed by plastic bending and shear of the diamond pattern. They proposed a theoretical estimate of the mean crush load of the following form (Equation (2.10)),

$$P_{mean} = Yh(10.05h + 0.38D) \tag{2.10}$$

Further, Pugsley [19] proposed a different model for the diamond deformation mode based on folding of a row of *n* triangular folds. The energy is assumed to dissipate at the plastic hinges during the folding process. Using this approach he proposed that the mean crushing load has the form (Equation (2.11)),

$$P_{mean} = 2.286n^2Yh^2 \tag{2.11}$$

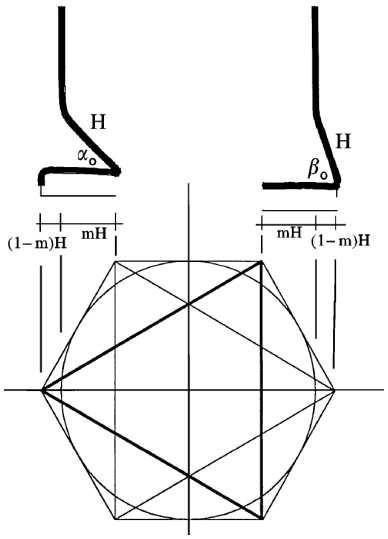

Figure 2-5: Folding mechanism for asymmetry deformation pattern and the corresponding eccentricity factor relationship [14].

Further, theoretical studies have been conducted by Singace [18] and he proposed the following equation (Equation (2.12)) for the mean crush load of the cylindrical tube.

$$\frac{P_{mean}}{M_0} = -\frac{\pi}{3}n + \frac{2\pi^2}{n}\tan\left(\frac{\pi}{2n}\right)\frac{D}{h} \tag{2.12}$$

where M_0 is the plastic bending moment per unit length; n is the number of triangular lobes. There have been a lot of validations done on the concertina mode of deformation mode for quasi-static and impact loading conditions. However, studies and validation on the diamond mode were limited only to quasi-static loading.

Hence, theoretical models for the diamond mode for dynamic loading should be formulated and validated.

2. 2. 4. Splitting and Curling

In 1972, Ezra and Fay [32] identified the combined modes of axial splitting and subsequent curling of the split ends of the metal tubes as an efficient means of energy dissipation. The absorbed energy is dissipated in tearing of the metal of the tube into strips. When tubes are axially split, they are efficient in absorbing energy and can sustain for a long stroke (up to 90% of the length) with a constant crush load. The tube splitting was further studied by other researchers including Reddy and Reid [33]. Examples of such deformation patterns are shown in Figure 2-6 (a-b) for mild steel tubes of diameter 50.8 mm and wall thickness 1.6 mm [33]. These kind of failure modes can be achieved with the help of an inserted conical die into one end of the pre-cut tube while applying compressive load on the other end. A curl stopper (plate) can also be used to fold the petals so that the axial load will be enhanced (refer Figure 2-6(a)); and the corresponding effect on the crushing load can be understood from Figure 2-7.

(a) **(b)**

Figure 2-6: Deformed mild steel tube specimen **(a)** with curling **(b)** without curling (reproduced from ref.[33]).

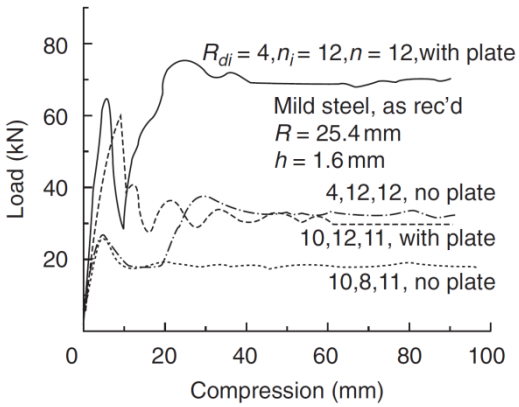

Figure 2-7: Load-deformation curves for mild steel tube specimen with splitting and curling (reproduced from ref.[33]).

Theoretical models have also been proposed to calculate the mean crush load for the above failure modes [33]. There are five energy dissipation mechanisms considered to establish an equilibrium equation for the crushing: (i) stretching ahead of the crack tips (ii) plastic bending in the axial direction (iii) plastic bending in the circumferential direction (iv) crack propagation (v) friction. The work done by the external load is dissipated by the sum of the above five energy components. The final form of the external mean crush load is given by Equation (2.13) [13, 33],

$$P_{mean} = \frac{1}{1-\sqrt{2}\mu}\left[2\pi YhR_o \ln\frac{R_f}{R_0} + \frac{\pi Yh^2}{2}\frac{R_o}{R_{di}} + \frac{\pi Yh^2}{2} + nw_t h\right] \qquad (2.13)$$

where μ is the coefficient of friction; R_o is the inner diameter of the tube (m); R_f is the outer diameter of the tube (m); R_{di} is the radius of the die (m); n is the number of axial cracks; w_t is the fracture energy per unit length (J/m). Further detailed analysis of this type can be found from ref.[33].

2. 2. 5. Tube inversion

One of the interesting energy absorber columns is the tube inversion that basically involves the turning inside out or outside in of a thin circular tube made of ductile material (refer Figure 2-8(a)). This method was introduced by *General Motors* in 1969 as reported by Al-Hassani et al.[34]. The main advantage of this mode of deformation is the constant inversion load that can be obtained for a uniform tube (refer Figure 2-8(b)). Similarly, the characteristics of tube inversion were investigated by Al-Hassani et al.[34], Kinkead [35], Chirwa [36] and Reid [37]. This method is limited by the die radius. If the die radius is small, progressive buckling of the tube will occur, and if the radius is larger than some limiting value, tube splitting will occur.

The mean crush load for the tube inversion can be written as (Equation (2.14)) [13],

$$P_{mean} = \frac{4\pi RhA}{n+1}\left[B + \frac{2}{\sqrt{3}}\ln\left(1+\sqrt{\frac{h}{R}}\right)\right]^{n+1} \qquad (2.14)$$

where R is the radius of the tube; A, B and n are material constants.

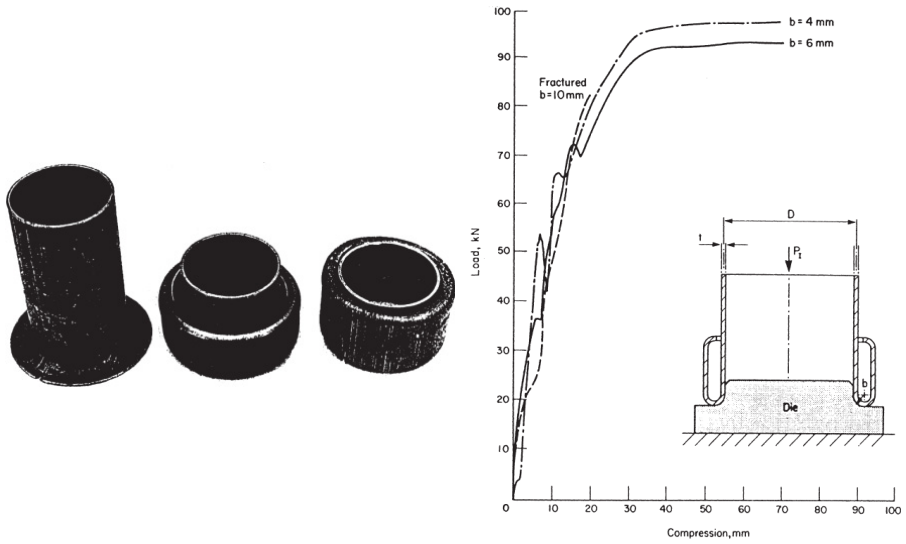

(a) **(b)**

Figure 2-8: Inside-out tube inversion due to axial load (reproduced from ref.[38])
(a) Deformation pattern **(b)** Load-deformation curves.

2. 3. Square cross-sectional tubes

2. 3. 1. Collapse modes

The typical deformation modes of square cross-sectional metal tubes are different from the circular cross-sectional tubes. As an example, a compact (progressive) and non-compact (non progressive) deformation pattern of square cross-sectional tubes are shown in Figure 2-9(a) and (b) respectively.

(a) Compact type **(b)** Non-compact type

Figure 2-9: Collapse modes of square cross-sectional steel and aluminium tubes (reproduced from [39] and [37]).

For the compact type, the tube wall underwent severe inward and outward plastic bending with possible stretching. If the thickness of the square tube is low it may

exhibit a non-contact type collapse mode as shown in Figure 2-9(b). This may be due to a global unstable Euler type buckling phenomenon. The energy absorption level of this crushing mode is significantly lower compared to the compact type mode.

2. 3. 2. Theoretical model

For quasi-static loading

Wierzbicki and Abaramowicz [40] provided a more realistic kinematically admissible folding mechanism for the compact type folding of a square tube (refer Figure 2-10(a-b)). In this model they assumed that the plastic deformation occurs only in the shaded regions of Figure 2-10(b). As shown in Figure 2-10, the four plane trapezoidal plates move as rigid bodies during deformation. Two cylindrical surfaces are bounded by two straight hinge lines which propagate in opposite directions, leading to a wider zone. Two adjacent trapezoidal plates are connected via a conical surface bounded by two straight lines. Finally, the four active deforming zones are connected by a section of a *toroidal shell.* The reader is advised to consult the ref. [40] for further complete details and mathematical relations for the folding mechanisms. The following modes have been considered for the energy dissipation: (i) energy dissipation in the travelling hinge (ii) energy dissipation in a sheet passing over a toroidal surface (iii) energy dissipation in the plastic hinges. Considering the above terms they have provided an expression for the mean crush load (Equation (2.15)):

$$P_{mean} = 9.56Yh^{5/3}c^{1/3} \tag{2.15}$$

where c is the half-width of one side of the square cross-section.

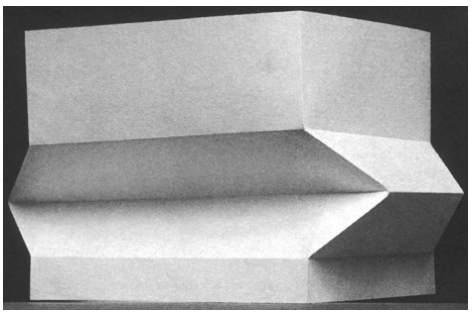

(a) Paper model [41].

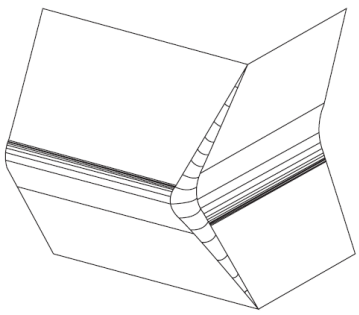

(b) A quarter of a square section during folding [40].

Figure 2-10: Collapse models for the square cross-sectional metal tubes.

For dynamic loading

The mean crush load of square cross-sectional metal tubes can be given as [41],

$$\text{Mean crush load} = P_{mean} = 13.06h^2\left(\frac{C}{h}\right)^{\frac{1}{3}}\sigma_y\left\{1+\left(\frac{0.33V_0}{CD}\right)^{\frac{1}{q}}\right\} \qquad (2.16)$$

where V_0 is the initial impact velocity (m/s): D and q are material constants; and C is width of a square tube.

2. 3. 3. Splitting and curling

The failure modes and the corresponding energy absorption modes are very similar to the circular cross-sectional metal tubes; however, due to the cross-sectional profile only four axial splits were observed at the corners (refer Figure 2-11); The total external work is dissipated by three major mechanisms: (i) tearing of the four corners (ii) plastic bending of the four sidewalls (iii) friction between the tube wall and the die. The final form of the mean crush load is given in Equation (2.17) [13].

$$P_{mean} = \frac{4}{1-\mu}\left(\frac{M_0 b}{R_{di}} + w_t h\right) \qquad (2.17)$$

where M_0 is the plastic bending moment; and b is the side length of a square tube.

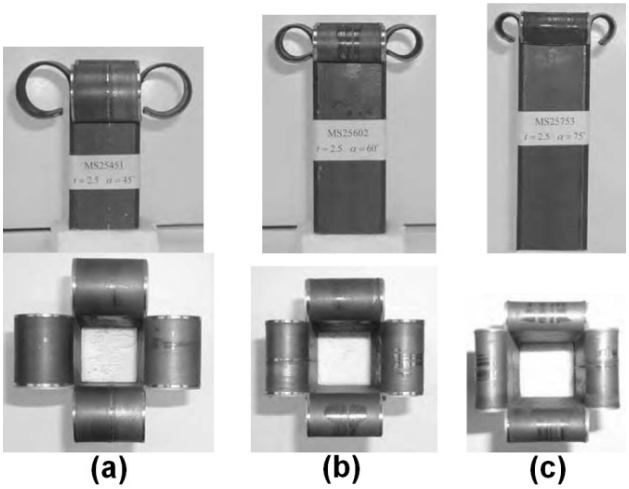

Figure 2-11: Crushed square cross-sectional mild steel tubes (50 × 50 mm; 2.5 mm thick) **(a)** with die semi-angle of 45° **(b)** with die semi-angle of 60° **(c)** with die semi-angle of 75° (reproduced from ref [38]).

2. 4. Effects of dynamic loading

As seen from the previous sections, many studies and design calculations in the field of structural crashworthiness idealise the structural response as quasi-static. However, most of the real-time applications are dynamic in nature. The dynamic load is defined as that load which is applied at high rate and associated with large plastic strains. The deformation pattern of a structure under quasi-static loading may not be necessarily the same for dynamic loading conditions. Out of different cross-sections, the deformation patterns of the circular cross-section remain the same for quasi-static and low velocity impact [42]. Ren et al. [43] investigated the dynamic plastic buckling of cylindrical shells made of aluminium alloy, which showed a considerable strain hardening with strain rate effect; and they reported that the mode of deformation was affected by the impact velocity.

Many experiments [42-44] have proved that the material strain rate sensitivity exercises an important effect on the response of the structures and should be taken into account for strain rate sensitive materials. Among the available empirical relations the *Cowper-Symonds* relation and the *Johnson-Cook* relation are frequently used and provide good agreement with the experiments for crashworthy applications [13, 41] An experimental investigation into the dynamic axial response of top-hat sections made from two different stainless steels and a mild steel has been reported in ref. [45]. It is observed that the use of stainless steel rather than mild steel is not as beneficial to the dynamic energy absorbing performance of top-hat sections as might have been anticipated. This is attributed to a significant enhancement in the dynamic strength of mild steel due to material strain rate effects, while the stress-strain characteristics of the stainless steel have a much lower sensitivity to strain rate. It was observed that at a strain rate of 200 s^{-1}, the yield and ultimate tensile stress of the stainless steel increased by about 25% and 20% compared to their quasi-static values, respectively. The corresponding increases for the mild steel were 116% and 49%. The strength of the mild steel almost was equal to the strengths of the stainless steels under similar dynamic loading conditions. Thus, the improved performance of stainless steel over mild steel for static loadings is not evident to the same degree for the axial impact loadings.

If a thin-walled tube is too long, then it may suffer a global instability, which is an inefficient mode of deformation for an impact energy absorbing system. Abramowicz and Jones [46] presented experimental data and theoretical expressions for circular and square mild steel tubes having various lengths and impacted by a dropping mass. The critical tube length ($L_{critical}$), which marks the transition between progressive buckling and global bending, is larger for impact loadings than for the corresponding static behaviour. There is a fairly distinct transition between progressive buckling and global bending for static loads, whereas it is not so

accurate for impact loads. Another important factor is the inertia effect of the energy absorbing structure. For higher impact velocities this factor plays a significant role [37, 47, 48]. Therefore, the global behaviour of thin-walled tubes is a complex interaction between lateral inertia effects and the axial force, which varies throughout the response. Hsu and Jones [42, 49, 50] reported that the critical initial axial lengths for the transition to global bending of circular tubes under quasi-static loading is $L_{critical}/D$ equal to 5.5, 6.0 and 5.9 for stainless steel 304, aluminium alloy 6063 T6 and ERW mild steel tubes respectively. However, this similarity in critical lengths for static loadings did not occur for axial impact loadings. Karagiozova [51] observed that the critical length at the buckling transition decreases over a small range of increasing impact velocities. It was also observed that the incorporation of a very slight strain rate sensitivity of the aluminium alloy 6063-T6 caused a particular tube to buckle globally rather than progressively as was obtained for the strain rate insensitive material. The influence of the material strain rate sensitivity causes an increased slope of the stress-strain curve during the initial deformation phase thereby increasing the local bending stiffness and presumably, favouring the development of a global bending mode.

Karagiozova and Jones [27, 51] studied the simultaneous influence of both axial and lateral inertia effects of the dynamic buckling of circular and square tubes subjected to axial impact loads. The consumption of energy during the initial uniform dynamic axial compression of tubes can be significant and leaves less energy available in the subsequent folding or wrinkling process, which is the sole energy absorbing mechanism considered in quasi-static methods of analysis. It is shown that the inertia characteristics of a shell together with the material properties determine stress wave propagation patterns, which cause either dynamic plastic buckling or dynamic progressive plastic buckling. Thicker shells made of materials exhibiting large strain hardening tend to buckle in a dynamic plastic buckling pattern in contrast to the thinner shells or shells made of materials with a smaller strain hardening, which buckle progressively even for high impact velocities.

The dynamic behaviour of cylindrical shells subjected to axial impact loads is both velocity and mass sensitive [52]. A larger kinetic energy can be absorbed for higher-velocity impacts when decreasing the striking mass, because larger strains and stresses are accumulated in the shell during the initial compression phase [52]. A localisation of strains leading to progressive buckling develops in thinner tubes, or in tubes made of materials having small strain hardening properties. The shells made of strain rate sensitive materials always buckled progressively. Buckling starts either from the impacted end due to the relaxation properties of the material causing strain localisation near this particular end, or from the distal end due to the increased strains caused by the reflected stress wave [53]. The degree of strain localization

depends on the material viscosity and this effect will decrease for materials exhibiting a smaller viscosity.

Experiments [54] on square cross-sectional tubes showed that the maximum reaction load (peak crush load) occurs at the start of the impact. The magnitude of this load depends on the impact velocity and speed of the plastic waves which propagate along the tube during crushing.

2. 5. Modelling of strain hardening and strain rate

As seen from sections 2. 2. and 2. 3. different analytical formulations have been used to calculate the crushing parameters of the crashworthy structural members. The advantages of this method are simple and fast calculation; however, this approach is limited in terms of availability of detailed results and applicability to complex structures. On the other hand, the finite element methods became a successful tool to solve dynamic impact problems with the advent of explicit integration techniques and modern computers. The ability to model complex structures, availability of different material models, different element formulations etc., have contributed to the widespread use of the finite element methods. As a result many specialized commercial programs are available in the market to solve crashworthiness problems (Abaqus, LS-Dyna, Ansys, Pam-Crash etc.,). Many researchers [55-58] have adopted the finite elements methods for their crashworthiness research.

In both approaches (analytical and finite element method) the choice of constitutive equations affects the ability to accurately predict the behaviour of a structure during a crash event especially if the material has a strong dependency on strain hardening and strain rate [59]. Numerous material models that incorporate strain hardening and strain rate effects have been presented in the literature. Some of the constitutive relations are based on empirical observations on a macro level while others are motivated by micromechanical considerations. One of the most commonly used strain hardening equations is the power law named after *Hollomon* [50, 60] which gives the relation between the yield stress (σ) and total strain (ε) (Equation (2.18)),

$$\sigma = B\varepsilon^{n} \tag{2.18}$$

where B and n are material constants and are usually determined from experimental data. Ludwik proposed [60] a convenient relation between the yield stress and plastic strain which can be modelled by the following equation (Equation (2.19)),

$$\sigma = A + B\varepsilon_p^n \tag{2.19}$$

where A is the initial yield stress of the material and it can be determined along with constants B and n. ε_p is the plastic strain. Out of different material models used to capture the strain rate and strain hardening the *Cowper-Symonds* and *Johnson-Cook* material models are most widely used and currently available in many commercial finite element programs (Equation (2.20) to (2.22))

$$\sigma = \left(A + B\varepsilon_p^n\right).\left[1 + \left(\frac{\dot{\varepsilon}_p}{D}\right)^{1/p}\right] \tag{2.20}$$

$$\sigma_y = \left(A + B\varepsilon_p^n\right)\left[1 + C.\ln\left(\frac{\dot{\varepsilon}_p}{\dot{\varepsilon}_0}\right)\right]\left[1 - T^{*m}\right] \tag{2.21}$$

$$T^* = \frac{T - T_{room}}{T_{melt} - T_{room}} \tag{2.22}$$

where D,C and p are material constants; ε_p is the equivalent plastic strain rate $\dot{\varepsilon}_0$ is the reference strain rate; and T_{melt} is the melting temperature. The availability of such models encourage the users for accurate modelling of structural behaviour. On the other hand, the availability of such sophisticated material models also poses more requirements on experimental programs for the characterisation of materials. The above discussed formulations can be used for the structures which undergo only plastic deformation without any ductile or brittle fracture. However, for the case such as the splitting and curling of metal tubes the fracture (damage) of the tube wall should be captured in addition to the plastic deformation to calculate the correct crushing variables. Hence, a short introduction of damage modelling is given in next section.

2. 6. Damage modelling

In order to formulate a hypothesis on the macroscopic failure/fracture it is necessary to understand the physical mechanism causing the failure. A fracture in a material causes discontinuities and subsequently stress concentrations; further it can be classified into brittle and ductile fractures. Brittle fracture is a fracture of interatomic bonds without any noticeable plastic deformation (occurs when the local strain energy become larger than the energy required to pull the atomic layers apart). Brittle fracture occurs mainly in high-strength metals with poor ductility and toughness. On the other hand, ductile fracture is caused by instability resulting from very large plastic deformations occurring in the surrounding of crystalline defects.

The basic idea of damage mechanics is to translate the underlying microscopic failure phenomena to a macroscopic description that can be used in a phenomelogical model. A number of failure criteria in terms of stresses and strains to characterize the fracture of a body have been proposed by Coulomb, Rankine, Tresca, von Mises [61]. These simple failure models only consider the stress or strain. In recent years, models concerning different types of damage have been studied by Gurson [62], Johnson-Cook [63] and Wilkins [64] which all are trying to describe the new formation, growth and coalescence of micro-voids in terms of the mechanical properties. To use these models a lot of material properties should be known (strain rate dependent properties, temperature dependent properties, stress tri-axiality etc.). Hence, most crashworthy simulations of today do not use damage models due to lack of information.

Damage can be defined as the presence and evolution of cracks and cavities at the microscopic level which may eventually lead to failure (a complete loss of load carrying capacity of the material). While damage manifests itself in the form of irreversible rupture of atomic bonds, deformation can be associated with reversible variations of interatomic spacing (in purely elastic processes) and movement and accumulation of dislocations (in permanent deformation of metals) [65]. Therefore, it should be expected that in order to describe the internal degradation of solids, new variables intrinsically connected with the internal damage process will have to be introduced in addition to the standard variables such as the strain tensor, plastic strain etc. [65]. Based on this principle, many researchers [62, 63, 66, 67] have introduced their own damage models; a brief introduction of a few models is given below.

Wilkins model

The Wilkins [64] damage model assumes that fracture is the result of the history of the strain damage to the material. Two factors enhance strain damage: (i) hydrostatic tension and (ii) asymmetric strain. The expression for the damage variable D can be written as (Equation (2.23) to (2.26)).

$$D = \int w_1 w_2 d\varepsilon_e^p \tag{2.23}$$

$$w_1 = \left(\frac{1}{1 + aP} \right)^{\alpha} \tag{2.24}$$

$$w_2 = (2 - A)^{\beta} \tag{2.25}$$

$$A_D = \min\left(\left| \frac{s_2}{s_3} \right|, \left| \frac{s_2}{s_1} \right| \right), \quad s_1 > s_2 > s_3 \tag{2.26}$$

where P is the hydrostatic pressure; s_1, s_2, s_3 are the principal stress deviators; a, α, β are material constants; the parameter A ranges from 0 to 1 (when the stress field is symmetric $A = 1$ and when it is asymmetric $A = 0$).

Gurson- Tvergaard-Needleman (GTN) model

The original Gurson model [67] considers a damage parameter that describes the porosity (f) of the material. The damage parameter can vary from a value $f = 0$ for undamaged material, to $f = 1$ for a completely damaged material. This model was further modified by Tvergaard and Needleman [66] to predict the instability caused by coalescence of microvoids. The void volume fraction f is replaced by the modified damage parameter f^* in the GTN model to reflect the accelerated void coalescence process after a critical volume fraction f_c is reached. The basic yield function of the GTN model is given as,

$$\Phi = \left(\frac{\Sigma_{eq}}{\sigma_0}\right)^2 + 2q_1 f^* \cosh\left(\frac{3}{2} q_2 \left(\frac{\Sigma_h}{\sigma_0}\right)\right) - 1\left(1 + q_3 f^{*2}\right) = 0 \tag{2.27}$$

where Σ_{eq} and Σ_h denote the macroscopic stress and hydrostatic macroscopic stress respectively; σ_0 is the equivalent tensile yield stress; q_1, q_2, q_3 are model parameters as they influence the form of the yield surface; and f^* is the effective void volume fraction.

Johnson Cook model

The Johnson-Cook failure model [63] is a purely phenomenological model and it is based on the plastic strain. This model uses a damage parameter D and when this parameter reaches the value of 1, the fracture is expected. The damage parameter is defined as (Equation (2.28))

$$D = \int \frac{1}{\varepsilon_p} d\varepsilon_{eq}^p \tag{2.28}$$

where ε_p is the equivalent plastic strain to fracture; $d\varepsilon_{eq}^p$ is the increment in equivalent plastic strain; The expression for the equivalent strain to fracture is given by Equation (2.29). It can be noticed from this equation that this model depends on strain, strain rate, temperature and stress triaxiality.

$$\varepsilon_f = \left(d_1 + d_2 e^{-d_3\left(\frac{\sigma_m}{\sigma_{vM}}\right)}\right)\left[1 + d_4 \ln\left(\frac{\dot{\varepsilon}_{eq}^p}{\dot{\varepsilon}_0}\right)\right]\left[1 + d_5 T\right] \tag{2.29}$$

where d_1, d_2, d_3, d_4 and d_5 are material constants which can be determined from the experiments; σ_m is the average of three normal stresses; σ_{vM} is the von-Mises equivalent stress; $\dot{\varepsilon}_{eq}^{p}$ is the rate of von-Mises equivalent plastic strain; $\dot{\varepsilon}_0$ is the reference strain rate; and T is the corresponding temperature.

2. 7. Conclusions

This chapter presented the progressive and non-progressive failure modes of circular and square cross-sectional metal tubes subjected to axial loading. A brief introduction to the corresponding theoretical models to predict the mean crush force for quasi-static and dynamic loading conditions has also been given. The developed theoretical models for the concertina deformation mode were well proven with the experimental results for both axial quasi-static and dynamic loading conditions. However, very limited work has been done for asymmetric or diamond mode deformation pattern; and the research focused only on quasi-static loading. Furthermore, the number of challenges and difficulties that arise during dynamic loading were introduced. It is very clear that a similar performance of a material/structure cannot always be expected for both quasi-static and dynamic loadings conditions. For dynamic loading cases, the performance of a structure differs due to different effects such as strain rate, strain hardening, impact velocity, wave propagation, global buckling and the corresponding boundary conditions of the structure. Therefore, a thorough investigation is recommended for a material/structure before deploying it for a particular dynamic loading application. In literature, many failure models have been proposed to capture the ductile and brittle damage of metals. However, these models need ample material input data which have to be derived from detailed experimental test programs. Because of this limitation, most of the crashworthiness simulations found in literature do not include damage models.

Bibliography

[1]. Aljawi, A. A. N., *Numerical Simulation of axial crushing of circular tubes.* Engineering science, 2002. **14**(2): p. 101-115.

[2]. Abramowicz, W. and Jones, N., *Dynamic axial crushing of circular tubes.* International Journal of Impact Engineering, 1984. **2**(3): p. 263-281.

[3]. Nagel, G. M. and Thambiratnam, D. P., *Energy absorption and performance of a vehicle impact protection system.* Structures under SHOCK AND IMPACT, 2000. **VII**: p. 229-237.

[4]. Tarigopula, V., Langseth, M., Hopperstad, O. S. and Clausen, A. H., *An experimental and numerical study of energy absorption in thin-walled high*

strength steel sections. WIT Transactions on Engineering Sciences, 2005. **49**(Impact loading of Lightweight structures): p. 495-507.

[5]. Reid, J. D. and Sicking, D. L., *Design and simulation of a sequential kinking guardrail terminal.* International Journal of Impact Engineering, 1998. **21**(9): p. 761-772.

[6]. Kanae, Y., Sasaki, T. and Shimamura, S., *Experimental and analytical studies on the drop-impact test with lead-shielded scale model radioactive shipping casks.* Structural Impact and Crashworthiness, 1984. **2**(2): p. 343-354.

[7]. Kotzialis, C., Derdas, C. and Kostopoulos, V., *Blast behaviour of plates with sacrificial cladding.* 5th GRACM International congress on computational mechanics, June 29 - July 1, Limassol, Cyprus., 2005.

[8]. Bogosian, D. D. and Crawford, J. E., *Energy absorbing retrofit systems for mitigating blast effects on occupants of conventional buildings.* 29th Explosive safety seminar, 2000.

[9]. Nurick, G. N., *Numerical and experimental results of blast loaded strucutres.* VIII International conference on Computational plasticity, 2005. **VIII**.

[10]. Lemanski, S. L., Nurick, G. N., Langdon, G. S., Simmons, M. S., Cantwell, W. J. and Schleyer, G. K., *Understanding the behaviour of fibre metal laminates subjected to localised blast loading.* Composite Structures, 2006. **76**(1-2): p. 82-87.

[11]. Weerth, D. E., *Blast resistant airline baggage container design.* 15th International conference on composite materials, 2005.

[12]. Theobald, M. D. and Nurick, G. N., *Numerical investigation of the response of sandwich panels subjected to blast loads.* WIT Transactions on Engineering sciences **49**(Impact loading of light weight structures).

[13]. Lu, G. and Yu, T. X., *Energy absorption of structures and materials.* Woodhead Publishing Ltd., 2003.

[14]. Alghamdi, A. A. A., *Collapsible impact energy absorpers: an overview.* Thin-Walled Structures, 2001. **39**: p. 189-213.

[15]. Sadeghi., M. M., *Design o heavy duty energy absorbers.* In Davies G, Morten J, editors, Structural impact and Crashworthiness, New York: Elsevier, 1984: p. 588-604.

[16]. Andrews, K. R. F., England, G. L. and Ghani, E., *Classification of the axial collapse of cylindrical tubes under quasi-static loading.* International Journal of Mechanical Sciences, 1983. **25**(9-10): p. 687-696.

[17]. Horton, W., Bailey, S. and Edwards, A., *Nonsymmetric buckle patterns in progressive plastic buckling.* Experimental Mechanics, 1966. **6**(9): p. 433-444.

[18]. Singace, A. A., *Axial crushing analysis of tubes deforming in the multi-lobe mode.* International Journal of Mechanical Sciences, 1999. **41**(7): p. 865-890.

[19]. Pugsley, A., *On the crumpling of thin tubular struts.* Quartely Journal of Mechanics Applied Mathematics, 1979. **32**(1): p. 1-7.

[20]. Johnson, W., Soden, P. and Al-Hassani, S., *Inextensional collapse of thin-walled tubes under axial compression.* The Journal of Strain Analysis for Engineering Design, 1977. **12**(4): p. 317-330.

[21]. Alexander, J. M., *An approximate analysis of the collapse of thin cylindrical shells under axial load.* Quart. J. Mech. App. Math. , 1960. **13**: p. 10-15.

[22]. Johnson., W. and Reid., S. R., *Mettallic energy dissipating systems.* Applied Mechanics Review, 1978. **3**: p. 277-88.

[23]. Abramowicz, W. and Jones, N., *Dynamic progressive buckling of circular and square tubes.* International Journal of Impact Engineering, 1986. **4**(4): p. 243-270.

[24]. Grzebieta, R. H., *An alternative method for determining the behaviour of round stocky tubes subjected to an axial crush load.* Thin-Walled Structures, 1990. **9**(1-4): p. 61-89.

[25]. Wierzbicki, T., Bhat, S. U., Abramowicz, W. and Brodkin, D., *Alexander revisited--A two folding elements model of progressive crushing of tubes.* International Journal of Solids and Structures, 1992. **29**(24): p. 3269-3288.

[26]. Karagiozova, D., *"Dynamic Plastic" and "dynamic progressive" buckling of elastic-plastic circular shells - revisited.* Latin American Journal of Solids and Structures, 2004. **1**(4): p. 423-441.

[27]. Karagiozova, D. and Jones, N., *Influence of stress waves on the dynamic progressive and dynamic plastic buckling of cylindrical shells.* International Journal of Solids and Structures, 2001. **38**(38-39): p. 6723-6749.

[28]. Singace, A. A., Elsobky, H. and Reddy, T. Y., *On the eccentricity factor in the progressive crushing of tubes.* International Journal of Solids and Structures, 1995. **32**(24): p. 3589-3602.

[29]. Singace, A. A., El-Sobky, H. and Petsios, M., *Influence of end constraints on the collapse of axially impacted frusta.* Thin-Walled Structures, 2001. **39**(5): p. 415-428.

[30]. Amdahl, J. and Soreide, T. H., *Energy absorption in axially compressed cylindrical shells with special reference to bulbous bows in collision.* Norwegian Maritime Research, 1981(4): p. 2-11.

[31]. Pugsley, A. and Macaulay, M., *The large-scale crumpling of thin cylindrical columns.* Quarterly Journal of Mechanics Applied Mathematics, 1960. **13**(1): p. 1-9.

[32]. Ezra., A. and Fay., R., *An assessment of energy absorbing devices for prospective use in aircraft impact situation.* In: Herrmann G, Perrone N, editors. Dynamic response of structures. New York: Pergamon Press, 1972: p. 225-34.

[33]. Reid, S. R. and Yella Reddy, T., *Experimental investigation of inertia effects in one-dimensional metal ring systems subjected to end impact -I. Fixed end systems.* International Journal of Impact Engineering, 1983. **1(1)**: p. 85-106.

[34]. Al - Hassani, S. T. S., Johnson, W. and Lowe, W. T., *Characteristics of inversion tube under axial loading.* International Journal of Mechanical Sciences, 1972. **14**: p. 372-81.

[35]. Kinkead, A. N., *Analysis for inversion load and energy absorption of a circular tube.* Journal of Strain analysis, 1983. **18**: p. 177-88.

[36]. Chirwa, W. C., *Theoretical analysis of tapered thin-walled metal inverbucktube.* International Journal of Mechanical Sciences, 1993. **35**((3/4)): p. 325-51.

[37]. Reid, S. R., *Plastic deformation mechanisms in axially compressed metal tubes used as impact energy absorpers.* International Journal of Mechanical Sciences, 1993. **12**: p. 1035-52.

[38]. Huang, X., Lu, G. and Yu, T. X., *On the axial splitting and curling of metal tubes.* International Journal of Mechanical Sciences, 2002. **44**(5-6): p. 2369.

[39]. Peroni, L., Avalle, M., Petrella, V. and Monacelli, G., *Strain-rate effects on the energy absorption capability of crash boxes with different geometry.* Structures under SHOCK AND IMPACT, 2002. **11**: p. 259-268.

[40]. Wierzbicki, T. and Abramowicz, W., *On the crushing mechanism of thin-walled structures.* ASME Journal of Applied mechanics, 1983. **50**: p. 727-34.

[41]. Jones, N., *Structural Impact.* Cambridge University Press, Cambridge, 1989.

[42]. Hsu, S. S. and Jones, N., *Quasi-static and dynamic axial crushing of circular and square stainless steel tubes.* Structures under SHOCK AND IMPACT, 2000. **VII**: p. 169-178.

[43]. Wang, R., Han, M., Huang, Z. and Yan, Q., *An experimental study on the dynamic axial plastic buckling of cylindrical shells.* International Journal of Impact Engineering, 1983. **1**(3): p. 249-256.

[44]. Jones, N., *Energy absorption effectiveness of thin-walled strucutres under static and dynamic axial crushing loads.* WIT Transactions on Engineering Sciences, 2005. **49**: p. 273-287.

[45]. Schneider, F. and Jones, N., *Impact of thin-walled high-strength steel structural sections.* Proceedings of the Institution of Mechanical Engineers, Part D: Journal of Automobile Engineering, 2004. **218**(2): p. 131-158.

[46]. Abramowicz, W. and Jones, N., *Transition from initial global bending to progressive buckling of tubes loaded statically and dynamically.* International Journal of Impact Engineering, 1997. **19**(5-6): p. 415-437.

[47]. Su, X. Y., Yu, T. X. and Reid, S. R., *Inertia-sensitive impact energy-absorbing structures part I: Effects of inertia and elasticity.* International Journal of Impact Engineering, 1995. **16**(4): p. 651-672.

[48]. Su, X. Y., Yu, T. X. and Reid, S. R., *Inertia-sensitive impact energy-absorbing structures part II: Effect of strain rate.* International Journal of Impact Engineering, 1995. **16**(4): p. 673-689.

[49]. Hsu, S. S. and Jones, N., *Dynamic axial crushing of aluminium alloy 6063 - T6 circular tubes.* Latin American Journal of Solids and Structures, 2004(1): p. 277-296.

[50]. N.Jones., *Structural Impact.* Cambridge University Press, Cambridge, 1989.

[51]. Karagiozova, D. and Jones, N., *On the dynamic collapse of circular and square tubes under axial impact.* in: C.A .Brebbia and G. N. Nurick (Eds.) Advances in Dynamics and Impact Mechanics, 2003: p. 1-22.

[52]. Karagiozova, D., Alves, M. and Jones, N., *Inertia effects in axisymmetrically deformed cylindrical shells under axial impact.* International Journal of Impact Engineering, 2000. **24**(10): p. 1083-1115.

[53]. Karagiozova, D. and Jones, N., *Dynamic effects on buckling and energy absorption of cylindrical shells under axial impact.* Thin-Walled Structures, 2001. **39**(7): p. 583-610.

[54]. Karagiozova, D. and Jones, N., *Dynamic buckling of elastic-plastic square tubes under axial impact--II: structural response.* International Journal of Impact Engineering, 2004. **30**(2): p. 167-192.

[55]. Kim, H.-S., *New extruded multi-cell aluminum profile for maximum crash energy absorption and weight efficiency.* Thin-Walled Structures, 2002. **40**(4): p. 311-327.

[56]. Chen, W. and Wierzbicki, T., *Relative merits of single-cell, multi-cell and foam-filled thin-walled structures in energy absorption.* Thin-Walled Structures, 2001. **39**(4): p. 287-306.

[57]. Chiandussi, G. and Avalle, M., *Maximisation of the crushing performance of a tubular device by shape optimisation.* Computers & Structures, 2002. **80**(27-30): p. 2425-2432.

[58]. Li, Q. M. and Jones, N., *Response and failure of a double-shear beam subjected to mass impact.* International Journal of Solids and Structures, 2002. **39**(7): p. 1919-1947.

[59]. Simunovic., S. and Shaw., J., *Material modelling effects on impact deformation of ultrilight steel autobody.* SaE Technical paper No: 2000-01-2715, 2000.

[60]. Samuel, K. and Rodriguez, P., *On power-law type relationships and the Ludwigson explanation for the stress-strain behaviour of AISI 316 stainless steel.* Journal of Materials Science, 2005. **40**(21): p. 5727-5731.

[61]. Dieter, G., *Mechanical Metallurgy.* McGraw-Gill, 1986.

[62]. Feucht, M., Sun, D.-Z., Erhart, T. and Frank, T., *Recent developements and applications of the Gurson model.* LS-DYNA Anwenderforum, Ulm, Germany, 2006.

[63]. Johnson, G. R. and Cook, W. H., *Fracture characteristics of three metals subjected to various strains, strain rates, temperatures and pressures.* Engineering fracture mechanics, 1985. **21**(1): p. 31-48.

[64]. Wilkins, M. L., Streit, R. D. and Reaugh, J. E., *Cumulative strain-damage model of ductile fracture: Simulation and fracture of engineering fracture test.* University of California, 1980.

[65]. De Souza Neto, E. A., Peric, D. and Owen, D. R. J., *Computational methods for plasticity - theory and applications.* John Wiley & Sons Ltd, 2008.

[66]. Needleman, A. and Tvergaard, V., *An analysis of ductile rupture in notched bars.* Journal of the Mechanics and Physics of Solids, 1984. **32**(6): p. 461-490.

[67]. Gurson, A. L., *Continuum theory of ductile rupture by void nucleation and growth, 1. Yield criteria and flow rules for porous ductile media.* Journal of Engineering Materials and Technology-Transactions of the ASME 99(1), 1977: p. 2-15.

Chapter 3

Axial Crushing Study of Recyclable Empty Metal Beverage cans

Overview

This chapter presents the axial quasi-static and impact crushing behaviour of recyclable empty metal beverage cans available in the market. Axial drop weight tests have been conducted to understand the crushing characteristics and the corresponding energy absorption of a single empty beverage can in detail. To conduct such tests a small-scale drop weight test set-up has been used. The deformation mechanisms and the corresponding energy absorption of the beverage cans were studied in detail for different initial impact velocities (1.4 m/s, 2.2 m/s, 3.1 m/s. 3.8 m/s, 4.4 m/s and 4.9 m/s). An analytical model is proposed to calculate the crushing parameters of empty metal beverage cans. The results from the analytical model are compared and validated with the experimental results. Furthermore, finite element models have been developed to study the performance of these beverage cans in detail and the results of these analyses are also compared and validated with the experimental results. Finally, to measure the dynamic parameters such as deformation length, impact velocity and the corresponding reaction force at the crushing end of the impactor a contactless method using Digital Image Correlation (DIC) is proposed. The DIC derived results are compared with the signals which were measured by using sensors.

3. 1. Introduction

The concept of the proposed sacrificial cladding structure and the details of the adopted inner core structures (α and β structures) and their details have been discussed in Chapter 1. Before deploying any structure for the proposed sacrificial cladding the knowledge of the crushing performance (progressive crushing stages and the corresponding energy absorption) of an individual inner core member is very important. Investigation of these factors during a blast loading is extremely difficult. Capturing the deformation mechanism, deformation pattern and the corresponding energy absorption during quasi-static and impact tests are relatively easier due to a slow speed of crushing. Therefore, to understand the above factors detailed axial crushing tests were conducted for first the "α" type structure (empty metal beverage can). However, the effect of strain rate on the deformation mechanisms and the corresponding deformation patterns of the beverage cans are further studied and verified for blast loading conditions (which are discussed in Chapter 4 for blast testing on a single beverage can).

Many studies have been conducted to study the crushing mechanism of circular and square cross-sectional thin-walled structures. The influence of impact velocity and the material characteristics on the dynamic buckling response of circular tubes during axial loading (quasi-static and impact) were studied in [1, 2]. In this work, the buckling mode to global bending was explained in terms of the material yield stress, strain hardening and the strain-rate sensitivity. This paper also proved that the energy absorption performance of cylindrical ductile tubes with high yield stress and low strain hardening is better than the one with low yield stress and high strain hardening. Similarly, the transition from initial global bending to progressive buckling on square and circular geometries was studied in [3]. Investigations of dynamic progressive crushing of cylindrical tubes indicate that the deformation is mainly started and concentrated at the end of the cylinder subjected to impulsive loading [4]. Furthermore, it deforms either axisymmetrically (concertina or ring mode) or asymmetrically (diamond mode), depending on the D/t ratio (diameter – thickness) [5]. Experiments have shown that tubes with $D/t < 80$ and rigid-perfectly plastic behaviour (low strain-hardening) deform in concertina mode and the tubes with higher D/t (> 80) and sensitive to strain-hardening will deform into diamond mode [5-8]. Andrews et al. [9] further gave a guideline to predict the mode of deformation based on tube length to wall thickness ratio *(L/t)* and diameter to wall thickness ratio *(D/t)*. Few studies also focussed on the switch of deformation pattern from concertina mode to diamond mode and mixed collapse of diamond and concertina modes [7, 9, 10]. Pugsley [7] concluded that the transition from concertina to diamond mode occurs for $D/t = 91$. The influence of other parameters on the switching of deformation patterns such as heat treatment and end constraints was also studied in ref. [11] and [10] respectively.

The mean crush load is the most important parameter in evaluating the energy absorption capacity of any structure. Hence, many theoretical models have been developed to study the mean crush load of the circular and square cross-sectional tubular structures exhibiting axisymmetric and asymmetric deformation modes [5, 12-16]. Alexander [12] was the first to provide an analytical model for the circular cross-sectional tubes for axisymmetric failure mode. This model assumed the formation of three circumferential plastic hinges during the formation of a single fold; and when the fold goes outwards the material experiences circumferential tensile strain. Furthermore, the external work done is dissipated by plastic bending and circumferential stretching. In order to predict the occurrence and the position of the second peak within each fold Wierzbicki et al. [17] introduced a parameter known as the eccentricity factor (the ratio of outward fold to the whole fold length). This work has been further refined by Singace et al. [18] and Singace and Elsokby [19]. Similarly, few researchers have worked on diamond deformation mode [5, 20, 21]. Pugsley and Macaulay [7, 22] were the first researchers who initiated the work on diamond crushing mode. Later Johnson et al. [8] tried to develop a theoretical model for the diamond mode crushing based on the experiments with PVC tubes. Later Singace [5] proposed an improved solution to calculate the mean crush load of tubular structures. Most of the above analyses have focused on the quasi-static crushing of tubular structures. However, during a dynamic loading condition the strain-rate effect plays a key role to enhance the yield stress of the material. Abramowicz and Jones [13] suggested a method to extend the quasi-static mean crush load expression to dynamic loading conditions considering the strain-rate effects.

This chapter presents the axial quasi-static and impact crushing behaviour of recyclable empty metal beverage cans available in the market. Axial drop weight tests have been conducted to understand the crushing characteristics and the corresponding energy absorption of a single empty beverage can in detail. To conduct such tests a small-scale drop weight test set-up has been used. The deformation mechanisms and the corresponding energy absorption of the beverage cans were studied in detail for different initial impact velocities (1.4 m/s, 2.2 m/s, 3.1 m/s. 3.8 m/s, 4.4 m/s and 4.9 m/s). An analytical model is proposed to calculate the crushing parameters of empty metal beverage cans. The results from the analytical model are compared and validated with the experimental results. Furthermore, finite element models have been developed to study the performance of these beverage cans in detail and the results of these analyses are also compared and validated with the experimental results. Finally, to measure the dynamic parameters such as deformation length, impact velocity and the corresponding reaction force at the crushing end of the impactor a contactless method using Digital Image Correlation (DIC) is proposed. The DIC derived results are compared with the signals which were measured by using sensors.

3. 2. Test specimen

Used empty recyclable metal beverage cans were selected for this experimental study. Special care was taken to choose cans without defects such as indents and scratches. The details of the geometry of an empty metal beverage can are shown in Figure 3-1(a). The metal beverage cans available in the European market can be classified into two types based on the type of material they are made with. Type A is made of a combination of two materials; the entire body is made of steel and the top cover is made of aluminium (Figure 3-1(b)). Type B is completely made of aluminium. Due to the larger availability especially in Belgium, Type A was chosen for the experimental study. The measured average mass of a beverage can for this study was 26 g. The raw material used for the manufacturing of the beverage can is Steel TH340 [23]. However, during the manufacturing process which involves 9 stages of deep drawing and wall ironing, the properties of Steel TH430 are changing throughout the process. The material properties of final manufactured beverage cans are very close to Steel 4340 grade [23]. The corresponding material properties of the top cover and body of the beverage can are adopted from literature and the same are given in Table 3-1. A complete information on the different stages of the beverage can manufacturing can be found from ref.[24, 25].

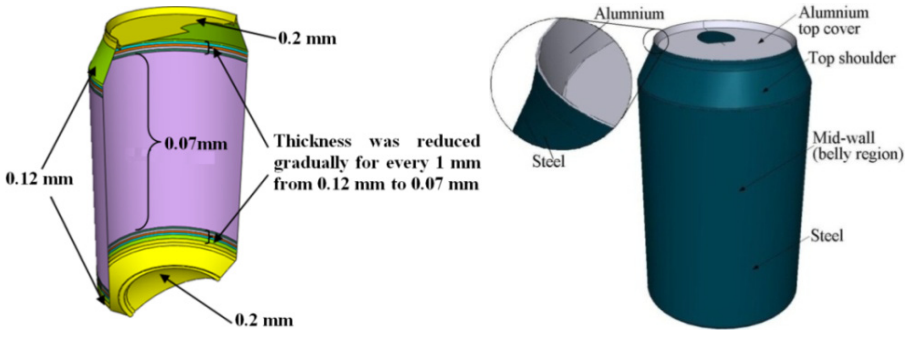

Figure 3-1:(a) Nomenclature and material details **(b)** Geometry details

3. 3. Quasi-static study

The deformation patterns and the corresponding load-deformation histories of the beverage cans were studied for quasi-static axial compressive loading condition. An electro-mechanical Instron 4505 machine was used for conducting all the quasi-static crushing tests. The quasi-static study of the empty beverage cans clearly indicated the strain-rate dependency on their material deformation and their peak crush load (refer Figure 3-2). The peak crush load of an empty beverage can varied from 1.1 to 1.4 kN for 0.002 to 0.037 s^{-1} rate of loading. In this complete

dissertation, for the simplification the crushing compressive load and the deformation length are shown in positive values in all load-deformation graphs. The peak crush load corresponded to the initiation of local wall buckling at the mid-wall region of the beverage can (refer Figure 3-3). For lower strain rate (0.002 s^{-1}) the crushing was not progressive. As the deformation progressed, one side of the beverage can lost its contact with the upper crushing platform of the Instron machine. This was due to the lower thickness (~70 μm) and the corresponding instability of the mid-wall region of the beverage can. However, for higher strain rates (0.018 s^{-1} and 0.037 s^{-1}) no such offset loading was noticed. From the quasi-static experimental results it can be concluded that these structures perform as α - type structure which we discussed in the Chapter 1. The quasi-static investigation on the beverage cans was limited due to the fact that these beverage cans will be eventually deployed for blast loading applications.

Table 3-1: Material, elastic and strength parameters for top cover and body of the beverage can [23, 26-29].

	Unit	**Steel 4043** (for body of the can)	**Aluminium 2024** (for top cover)
Material and elastic properties			
Density (ρ)	*(kg/m^3)*	7830	2770
Elastic modulus (E)	*(GPa)*	200	73
Poisson's ratio (υ)	-	0.29	0.33
Shear modulus (G)	*(GPa)*	77	28
Bulk modulus (K)	*(GPa)*	159	72
Strength parameters (*Johnson-Cook material parameters)*			
A	*(MPa)*	792	265
B	*(MPa)*	510	426
n	-	0.26	0.34
c	-	0.014	0.015
m	-	1.03	1.0
Strength parameters (*Cowper-Symonds material parameters)*			
C	*(s^{-1})*	200000	6500
p	-	3.3	4
Thermal parameters			
Conductivity (k)	*$W/m^{\circ}K$*	38	121
Specific heat (C_p)	*$J/kg^{\circ}K$*	477	875
Expansion coefficient (α)	*(K^{-1})*	13×10^{-6}	22×10^{-6}
Melting temperature (T_{melt})		1793	775

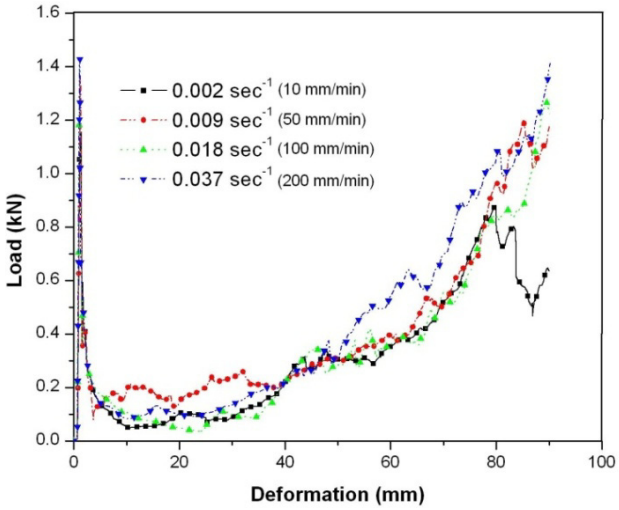

Figure 3-2: Quasi-static load-deformation curves of empty beverage cans at different strain rates.

Figure 3-3: Quasi-static deformation patterns of recyclable empty metal beverage cans.

3. 4. Axial impact study

3. 4. 1. Experimental set-up

The schematic representation of the experimental test set-up is shown in Figure 3-4. The vertical guides along which an impactor slides were fixed to a wall by means of horizontal supports. The impactor assembly slides on the vertical guides by roller ball bearings. The maximum drop height of the impactor for this set-up is 2 m. The mass of the impactor, support structure for the test specimens and the end crushing part of the impactor can be varied as per the test specimen's requirement. An impactor mass of 7.7 kg was chosen for all tests. The experimental test set-up is fully instrumented with a dynamic force sensor and an accelerometer at the crushing end of the impactor to measure the reaction force and the acceleration of the impactor respectively. Furthermore, an inductive displacement sensor is also used to

measure the drop height, instantaneous displacement of the impactor and the residual deformation length of the test specimen. The view of the experimental test set-up and the corresponding location of the sensors are shown in Figure 3-5(a) and (b) respectively. A brief introduction and the specification of these three sensors are given in next section.

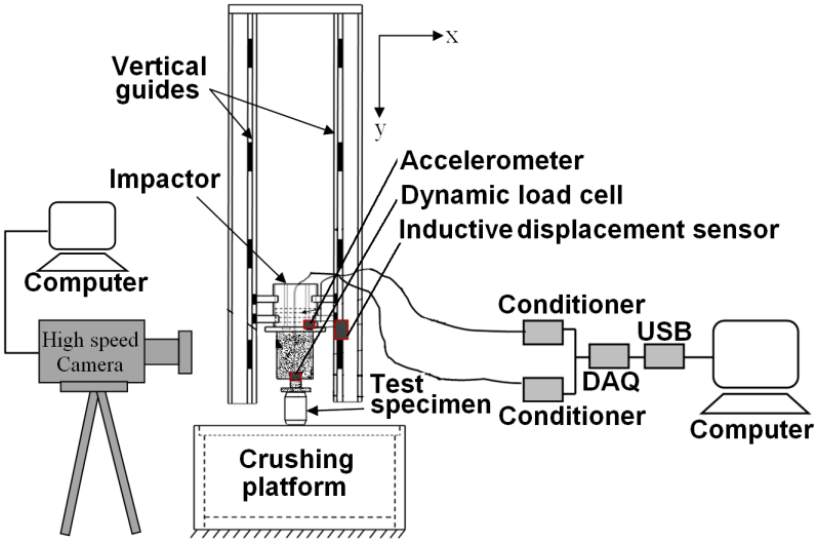

Figure 3-4: Schematic representation of the experimental set-up.

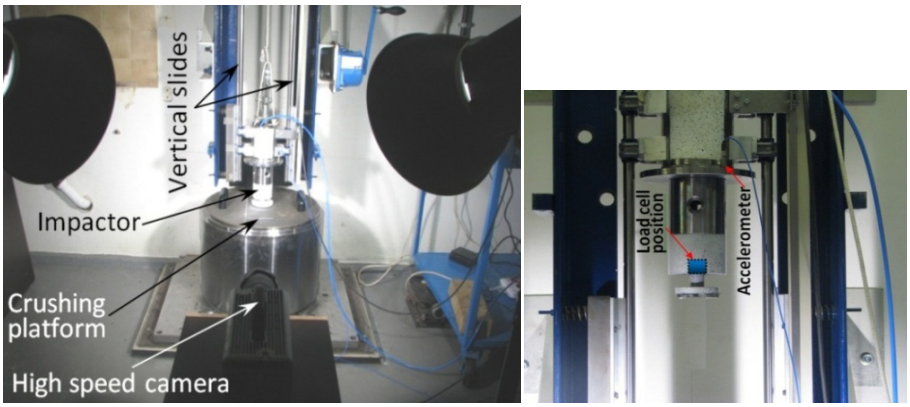

(a) **(b)**

Figure 3-5: (a) Experimental test set-up **(b)** Close view of the impactor.

3. 4. 2. Instrumentation

Force Sensor

The used force sensor for all impact experiments is the *Endevco Isotron* force sensor *model 2311* and the corresponding specification is given in Table 3-2. It is a uniaxial

force sensor of the Integrated Electronic Piezoelectric (IEPE) type. In this sensor a charge collection electrode is sandwiched between quartz crystal elements which in their turn are clamped between two mounting plates, held together and preloaded by an elastic stud (refer Figure 3-6(a)). This ensures linearity by producing intimate contact between the components and also provides the capability for tensile force measurements. When axial force is applied, the quartz crystals generate an electrostatic charge, which is proportional to the force applied. This high impedance, electrostatic charge signal is converted within the sensor by a built-in amplifier to a low impedance voltage signal. This dynamic sensor cannot be used for static loading application because the generated electrical signal decays rapidly after the application of the force due to the leakage of electrostatic charge [30].

Table 3-2: Specification of the Endevco Isotron force sensor model 2311.

Sensitivity	0.2293 mV/N
Measurement range	2 kN in tension; 22 kN in compression
Resonance frequency	75 kHz

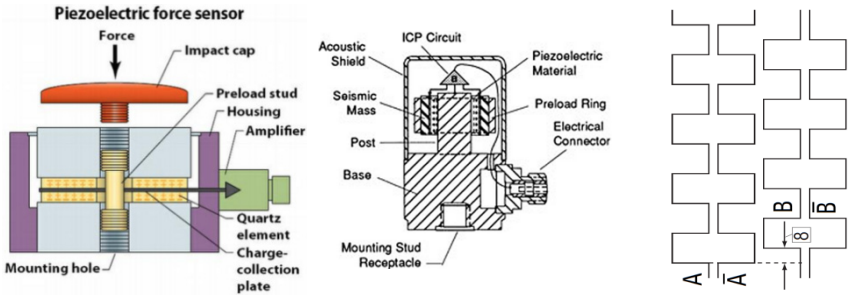

(a) **(b)** **(c)**

Figure 3-6: Piezoelectric force sensor [30]. (b) Piezoelectric accelerometer [31]. (c) Displacement sensor [32].

Accelerometer

The PCB 350 B02 *axial shear mode accelerometer* was used for all the impact tests. The working principle of the accelerometer is very similar to the force sensor. The internal construction of the PCB accelerometer is shown in Figure 3-6(b) [31]. Two equivalent masses are attached on both sides of the piezoelectric crystal. Under acceleration, the masses cause a shear force which is proportional to the acceleration; due to this shear the piezoelectric material generates the electrostatic charge. The corresponding specification of the accelerometer is given in Table 3-3.

Table 3-3: Specification of the PCB 350 B02 accelerometer.

Sensitivity	0.103 mV/g
Measurement range	50000 g
Usable frequency	± 1 dB: 4 to 10000 Hz
Resonance frequency	≥ 100 kHz

Displacement sensor

The Limes *linear magnetic measurement system* by Kubler, consisting of a sensor L150 and a magnetic band B2 was used for all impact tests. The resolution of this sensor is 25 µm and can measure speeds up to 16.25 m/s. It is used in combination with an electronic counter type 572. The working principle is shown in Figure 3-6(c). When the magnetic sensor is guided across the magnetic band, it sends out two block signals A and B. The block signals are used to measure the displacement. The direction of the displacement can be determined based on the phase shift between the both signals [33]. To acquire the signals from these sensors (dynamic force sensor, accelerometer and the displacement sensor) during the experiments, the M and C series data acquisition (DAQ) boards (NI-USB 6251 and NI-CDAQ 9172), NI-SCB-68 connector block and Labview 8.2 commercial code were used.

Axial impact tests have been conducted with different impact heights which correspond to different initial impact velocities ranging from 1.4 m/s to 4.9 m/s. A high speed camera (Photron APX RS 250K capable of recording 250,000 fps) was also used to capture the images during the test. A frame rate of 5000 fps was used for these tests. A sampling frequency of 2 MHz was chosen for all sensors (load cell, accelerometer and the inductive displacement sensor). In order to compare the deformation mechanism with the corresponding load-deformation curve all sensors and the high speed camera were triggered at the same time for recording the data.

For all tests, the data from the different sensors have been checked and validated against each other. The integrated displacement from the accelerometer signal was validated with the signal from the inductive displacement sensor. As an example, one of the cases is presented here. Figure 3-7(a) shows the measured acceleration signal from the accelerometer for the initial impact velocity of 3.1 m/s (only the relevant portion of the signal is shown here). To calculate the velocity and the corresponding displacement (equivalent to the deformation length of the test specimen) of the impactor the acceleration signal was integrated using the trapezoidal integration rule without filtering the signal (the filtered signal also provided the same results). The corresponding integrated velocity and the displacement of the impactor are given in Figure 3-7(b) and (c) respectively. Furthermore, Figure 3-7 (c) also shows the recorded signal from the inductive displacement sensor during the impact event. It can be noticed that the results from these two measurements provided almost the same result.

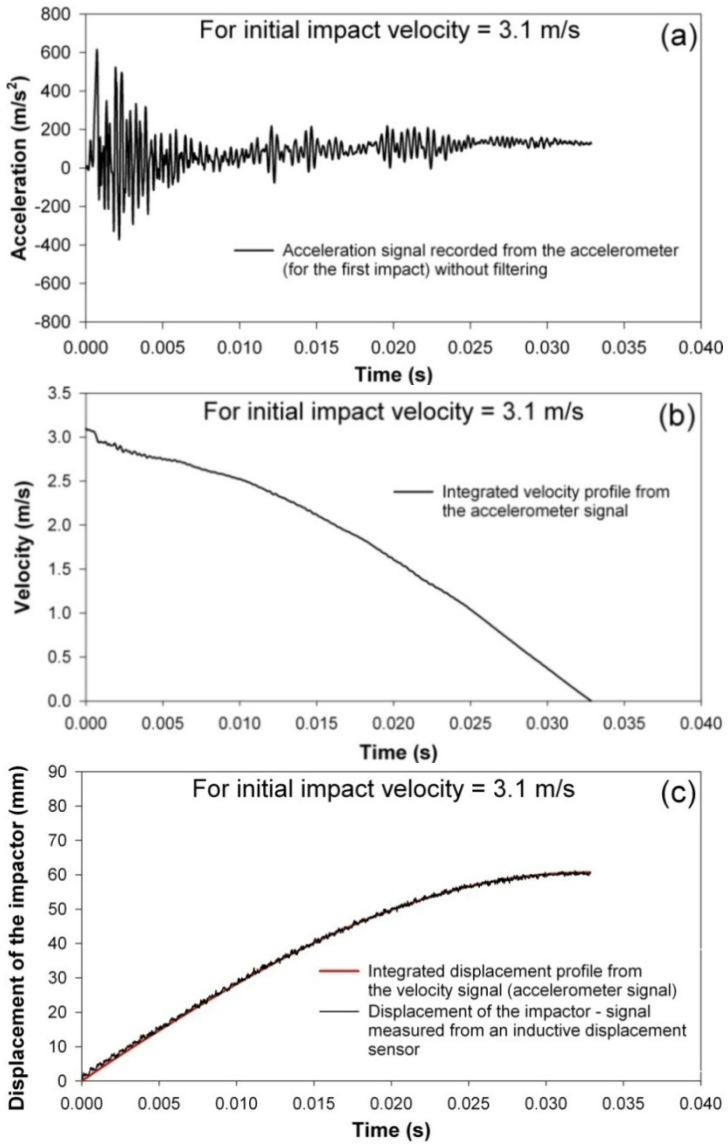

Figure 3-7: (a) Measured accelerometer signal (without filtering). **(b)** Integrated velocity profile from the accelerometer signal **(c)** Comparison of the displacement (equivalent to the deformation length of the test specimen) profile from the integrated accelerometer signal and from an inductive displacement sensor.

Similarly, the load signal from the force sensor was validated with the load signal calculated from the accelerometer signal assuming that the impactor is a rigid body. It can be noticed from Figure 3-7(a) that the acceleration signal contains high frequency noise. Hence, the measured accelerometer signal was numerically filtered with a low-pass filter (with a cut-off frequency of 1500 Hz and a slope of -100 dB/decade). To calculate the force signal the filtered accelerometer signal was multiplied by the mass of the impactor (7.7 kg). A comparison of these two signals

is given in Figure 3-8. Similar to the displacement signals there was a good correlation observed for the force signals.

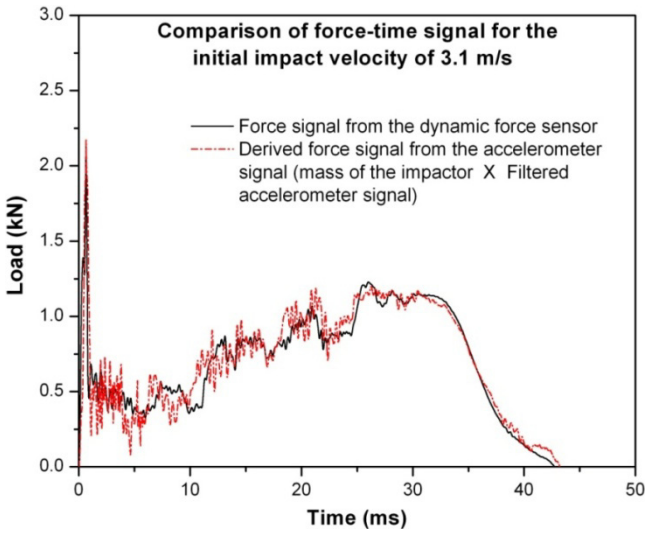

Figure 3-8: Comparison of force-time signal from the dynamic force sensor and the derived signal from the accelerometer for the case with the initial impact velocity of 3.1 m/s.

3. 5. Experimental results and discussions

The crushing performance of empty beverage cans was studied for different initial impact velocities such as 1.4 m/s, 2.2 m/s, 3.1 m/s, 3.8 m/s, 4.4 m/s and 4.9 m/s. For each case a minimum of ten tests have been carried out and the average of all the parameters were taken into account to calculate the performance parameters which are discussed in the next section. The empty beverage cans showed a controlled and progressive failure pattern for all cases. As an example, the different phases of empty beverage can crushing subjected to an initial impact velocity of 4.9 m/s are shown in Figure 3-9.

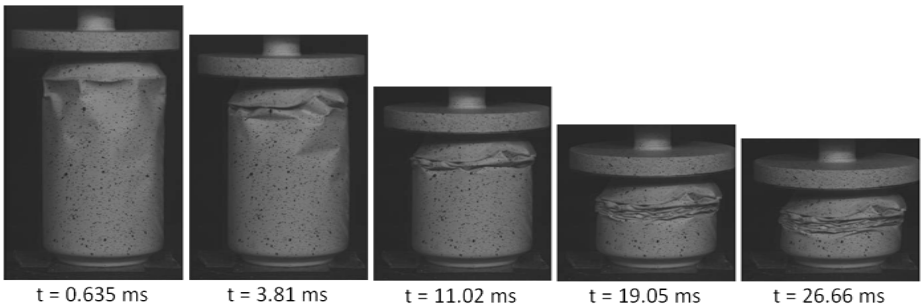

Figure 3-9: Progressive crushing stages of empty beverage can for an initial impact velocity of 4.9 m /s.

3. 5. 1. Collapse modes

The final deformation patterns of the empty beverage cans for different initial impact velocities are shown in Figure 3-10(a – f).

(a) Deformation patterns for initial impact velocity of 1.4 m/s.

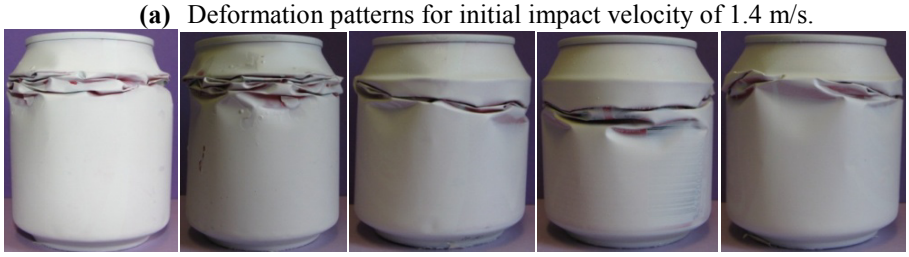

(b) Deformation patterns for initial impact velocity of 2.2 m/s.

(c) Deformation patterns for initial impact velocity of 3.1 m/s.

(d) Deformation patterns for initial impact velocity of 3.8 m/s.

(e) Deformation patterns for initial impact velocity of 4.4 m/s.

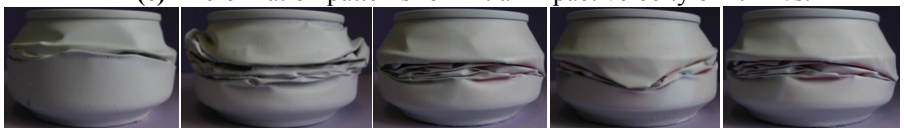

(f) Deformation patterns for initial impact velocity of 4.9 m/s

Figure 3-10: Final deformation patterns of empty recyclable metal beverage cans for different impact velocities. **(a)** 1.4 m/s **(b)** 2.2 m/s **(c)** 3.1 m/s **(d)** 3.8 m/s **(e)** 4.4 m/s **(f)** 4.9 m/s.

These cans are painted after the test (except the one which is shown in Figure 3-9). Based on the thickness distribution of an empty beverage can, it can be concluded that the initial deformation should occur at the mid-wall location (belly portion) of the can due to its lower thickness (0.07 mm). However, for the case with an initial impact velocity of 1.4 m/s the deformation occurred at different points of the can along its length (plastic local wall buckling and folding). The difference in the deformation pattern of the cans may be influenced by a combination of two effects: (i) the initial geometry imperfections induced during the manufacturing process and during usage and (ii) a lower impact velocity of the impactor. The average deformation length of the beverage can for this case was 17.5 mm.

The deformation patterns of the beverage cans for all other impact velocities (2.2 m/s, 3.1 m/s, 3.8 m/s, 4.4 m/s and 4.9 m/s) are different from the earlier case (refer Figure 3-10(b - f)). The chronological order of the initiation of the folding process and the corresponding collapse mode can be understood from the high speed images (refer Figure 3-11). For these cases, an initial elastic local wall buckling started below the top shoulder region which caused to form few fold legs around the circumference (indicated in Figure 3-11). The initial elastic local wall buckling (towards the inside of the can) was always axisymmetric. Furthermore, the location of local wall buckling and the corresponding fold legs below the top shoulder region was consistent for these cases (2.2 m/s, 3.1 m/s, 3.8 m/s, 4.4 m/s and 4.9 m/s). This was due to the combined effect of higher impact velocity, inertia of the impactor and a lower geometrical thickness of the beverage can at that location. The formation of fold legs removed the cylindrical curvature of the beverage can and converted it into a ring of triangles. During further crushing the base of the triangular fold inclined towards the axis of the beverage can and the apex started to move away from the axis of the beverage can. When the fold legs reach a critical angle the elastic hinge became plastic which facilitated axial bending and subsequent fold formation. Due to the presence of loading, the de-curving process continues for all triangle folds until the distance from the apex to the base of the triangle (called as half fold length H) becomes invariable. During the above process an initiation of another set of fold legs occurred below. At later crushing phases the deformation propagated downwards along its length and crushed progressively in a diamond mode which caused an asymmetric failure pattern (refer Figure 3-9, Figure 3-11 and Figure 3-12). The occurrence of the diamond mode deformation depends upon the combined effect of D/t ratio (~ 937 for beverage can) and material strain hardening characteristics [5]. During the crushing process, the diamond folding of the wall of the beverage can occurred partially inside and partially outside the mean diameter. Experiments have shown that the wall of a concertina mode deformed tube will be laid down partly to the inside and partly to the outside of the mean diameter; furthermore, it was proved that the outward part is usually bigger than the inward part [17]. However, in case of asymmetric deformation mode (diamond mode) the

inward part of the fold is found to be bigger than the outward fold. Similar evidence can be noticed from Figure 3-12, where the inward fold or lobes are bigger than outwards. Therefore, the eccentricity factor for a diamond mode deformation can be defined as the ratio of the inward part to the total folding length [10, 18].

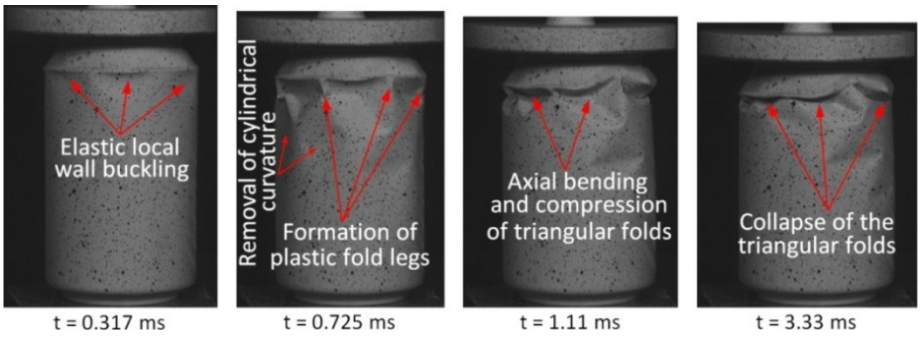

Figure 3-11: Chronological order of initiation and folding of fold legs and triangular folds during crushing of an empty beverage can.

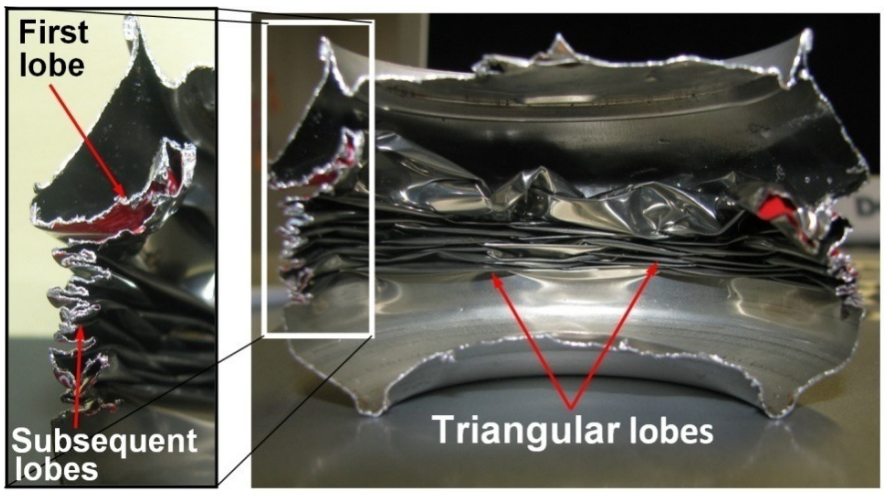

Figure 3-12: Cut sectional view of beverage cans for initial impact velocity of 4.4 m/s.

The number of circumferential triangular segments or lobes varied from a minimum of 5 to a maximum of 8. The higher *D/t* ratio of the beverage can facilitated to form a larger number of triangular lobes [5]. As an example, the geometric relationships for an empty beverage can that deformed into six circumferential lobes are given in Figure 3-13(a) and (b). For the case with an initial impact velocity of 2.2 m/s the formation of triangular lobes occurred for 2 rows simultaneously. For all cases, the length of the first lobe was always longer than for the others. The longitudinal cut-section of these test specimens confirmed the same (refer Figure 3-12). This may be due to the combined effect of initial impact velocity and impactor inertia on the initial compression phase of the beverage can. The average half folding length of

each lobe and the corresponding numbers were increased with increasing initial impact velocities (refer Figure 3-12). The average half folding length varied from a minimum of 2.1 mm to a maximum of 4.5 mm. For higher initial impact velocities such as 3.8 m/s, 4.4 m/s and 4.9 m/s, the impactor rebounded after reaching the maximum deformation length of the test specimen; subsequently, successive impacts were observed for these cases. This was due to the densification of lobes and the corresponding strain hardening of the material. However, the successive impacts were not taken into account for the energy absorption calculation. Compared to the thickness of a bright can (can without any coating) the thickness of the aesthetic coating on the outer surface and lacquer coating (used to prevent the contact of beverage with metal) at the inner surface was negligible. Hence, it can be concluded that the effect of these coatings on the deformation mechanisms and the corresponding energy absorption was negligible. However, a detailed study on bright cans is needed for the final conclusion of this statement. For all cases, no significant deformation was noticed at top and bottom shoulder and end caps (refer Figure 3-10(a-f)).

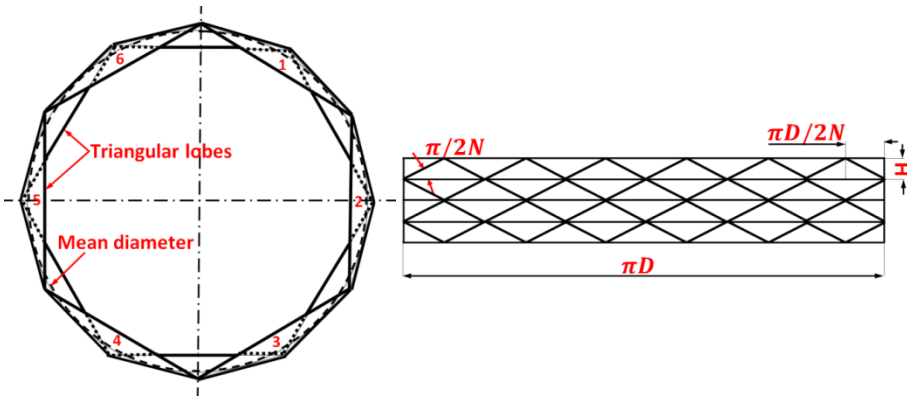

(a) **(b)**

Figure 3-13: Deformed view of a beverage can with six lobes (a) Top view (b) Developed view.

3. 5. 2. Typical load-deformation curves

The measured crushing load of the beverage cans can be expressed in terms of the impactor acceleration as (Equation 3.1),

$$F_c(t) = M_I \cdot [a(t) + g] \tag{3.1}$$

where $F_c(t)$ is the instantaneous crushing load of an empty beverage can which was measured by a dynamic load cell at the crushing end; M_I is the mass of the impactor (7.7 kg); $a(t)$ is the acceleration of the impactor (m/s^2); g is the acceleration due to

gravity (m/s^2). The velocity of the impactor *(v(t))* and the corresponding displacement *(l(t))* which is equivalent to the deformation length of the test specimen can be written as (Equation 3.2 and 3.3),

$$v(t) = \int_0^t a(t) \cdot dt \qquad v(0) = v_0 \quad \text{(m/s)} \tag{3.2}$$

$$l(t) = \int_0^t v(t) \cdot dt \qquad l(0) = 0 \quad \text{(m)} \tag{3.3}$$

where v_0 is the initial impact velocity which varied from a minimum of 1.4 m/s to a maximum of 4.9 m/s. From equations 3.1 and 3.3 the total absorbed energy *(E_{abs})* by an empty beverage can for each initial impact velocity can be calculated from the following relation (Equation 3.4),

$$E_{abs} = \int_0^{l_{\max}} F(l) \cdot dl \quad \text{[J]} \tag{3.4}$$

where *F(l)* is the instantaneous crushing load corresponding to the instantaneous crushing deformation length of the beverage can *dl*. l_{max} is the maximum or total deformation length of the test specimen (for the first impact). Similarly, the total energy given by the impactor can be calculated from the following relation (Equation 3.5):

$$E_{given} = \frac{1}{2} M_I \cdot v_0^2 + \int_0^{l_{\max}} M_I \cdot g \cdot dl \quad \text{[J]} \tag{3.5}$$

In Equation 3.5, the first term on the right hand side of the equation corresponds to the initial kinetic energy given by the impactor before impact and the second term corresponds to the additional potential energy due to the travelling mass of the impactor during the crushing process. The calculated average values (from 10 experiments for each case) are given in Table 3-4. From Table 3-4, it can be noticed that there was a difference in the energy levels between the total energy given by the impactor *(E_{given})* and the energy absorbed by the beverage can *(E_{abs})* (varied from approximately 2 to 3.5 % for the initial impact velocity of 1.4 m/s to 4.4 m/s). The reason for the difference can be attributed to: (i) the friction between the roller ball bearing of the impactor and the supporting guides (ii) air resistance to the impactor (iii) energy loss due to the impacting sound (iv) friction between the impactor and the test specimen during crushing (v) energy absorbed by the impactor by elastic deformation (vi) heat dissipation during the plastic deformation of the can. However, for the case with the initial impact velocity of 4.9 m/s the difference (E_{given} - E_{abs}) was higher compared to other cases (approximately 7.7 %). An investigation and the corresponding reason for this difference are presented in section 3. 5. 3.

Table 3-4: Summary of average crushing parameters (from 10 tests of each category).

Drop height *(h)*	Initial impact velocity (v_0)	Mass of the impactor (M_I)	Mass of empty beverage can (m_{bc})	Length of an empty beverage can (l_{bc})	Total energy given by the impactor (E_{given}) (initial kinetic energy before impact + additional potential energy due to the mass of the impactor during the crushing process)	Energy absorbed by the beverage can (E_{abs})	Peak crush load (P_{max})	Mean crush load (P_{mean})	Standard deviation for mean crush load	Deformation length of the test specimen (l_{max})	Standard deviation for deformation length	Crushing efficiency (η_c)	Specific energy absorption (SEA)
(m)	(m/s)	(kg)	(g)	(mm)	(J)	(J)	(kN)	(kN)	(kN)	(mm)	(mm)	(%)	(kJ/kg)
Experimental													
0.1	1.4	7.7	26	117	8.9	8.7	1.69	0.413	0.045	18.1	4.7	24.4	2.16
0.25	2.2				21.8	21.1	1.72	0.446	0.072	42.1	7.3	25.9	2.25
0.5	3.1				41.5	40.2	2.19	0.610	0.094	60.6	8.6	27.8	2.98
0.75	3.8				60.9	59.0	2.28	0.774	0.131	71.8	12.3	33.9	3.69
1.0	4.4				80.5	77.5	2.37	0.918	0.149	80.0	10.8	38.7	4.37
1.25	4.9				98.9	91.3	2.46	1.060	0.161	86.7	14.3	43.0	4.75
1.25*	4.9*				100.0*	95.4*	2.47*	0.998*	0.170*	95.5*	13.5	38.8*	4.49*
*Tests have been conducted with beverage cans having 4 holes (ϕ 3.5 mm each) at the bottom (refer Figure 15).													
Analytical using Equation (3.20)													
0.25	2.2	7.7	26	117	21.9	21.9	-	0.495	-	44.2	-	-	2.22
0.5	3.1				41.6	41.6	-	0.673	-	61.8	-	-	3.02
0.75	3.8				61.2	61.2	-	0.808	-	74.5	-	-	3.70
1.0	4.4				80.7	80.7	-	0.968	-	83.3	-	-	4.35
1.25	4.9				99.0	99.0	-	1.120	-	88.4	-	-	5.03

Drop height *(h)*	Initial impact velocity *(v_0)*	Mass of the impactor *(M_I)*	Mass of empty beverage can *(m_{bc})*	Length of an empty beverage can *(l_{bc})*	Total energy given by the impactor *(E_{given})* (initial kinetic energy before impact + additional potential energy due to the mass of the impactor during the crushing process)	Energy absorbed by the beverage can *(E_{abs})*	Peak crush load *(P_{max})*	Mean crush load *(P_{mean})*	Standard deviation for mean crush load	Deformation length of the test specimen *(l_{max})*	Standard deviation for deformation length	Crushing efficiency *(η_c)*	Specific energy absorption (SEA)
(m)	(m/s)	(kg)	(g)	(mm)	(J)	(J)	(kN)	(kN)	(kN)	(mm)	(mm)	(%)	(kJ/kg)
Numerical simulation													
0.1	1.4	7.7	26	117	8.94	8.92	2.20	0.479	-	18.6	-	22.0	2.15
0.25	2.2				21.6	20.1	2.31	0.499	-	40.3	-	21.6	2.24
0.5	3.1				41.5	40.6	2.48	0.680	-	59.7	-	27.4	3.06
0.75	3.8				60.9	59.3	2.59	0.841	-	70.2	-	32.5	3.78
1.0	4.4				80.6	76.5	2.61	0.953	-	80.3	-	36.7	4.28
1.25	4.9				99.7	95.1	2.75	1.008	-	94.2	-	36.7	4.54
1.25^{Δ}	4.9^{Δ}				99.0^{Δ}	91.0^{Δ}	2.75^{Δ}	1.054^{Δ}	-	86.3^{Δ}	-	38.3^{Δ}	4.75^{Δ}
$^{\Delta}$ Numerical simulations considering air inside the beverage can.													

As an example, one of the load-deformation profiles of the empty beverage cans for each initial impact velocity is given in Figure 3-14(a – f). The initial peak crush load corresponds to the initial formation of fold legs which altered the cylindrical curvature of the can and subsequent plastic folding into a certain number of triangular lobes. Immediately after the peak load there was a reduction in the load noticed; this stage corresponded to the complete collapse or rotation of the triangular lobes about their base. At the end of this process, the subsequent formation of another set of fold legs occurred and these processes continued. This phenomenon can be noticed from Figure 3-14 (b – f); after the peak crush load the load fluctuated in the form of a triangle. The increase in load corresponds to the formation of new fold legs and the drop in the load corresponds to the collapse or compression of triangular lobes. The number of triangles in the curve indicates the number of folds along its length. Furthermore, it can be noticed from these figures that the fold length increases with increasing initial impact velocities (refer Figure 3-14 (c) and (e)). In all load – deformation curves (except 1.4 m/s initial velocity) the crush load of the can increased considerably after achieving 20 mm of deformation length; this was due to the onset collapse and the corresponding compression of triangular lobes. Furthermore, the strain hardening characteristics of the material significantly contributed for this increasing crush load. From the load-deformation curves of successive tests, it can be noticed that the peak crushing load of an empty beverage can varied from 1.8 kN to 2.4 kN (a minimum of 10 tests for each case) and it is increasing with higher initial impact velocities (Figure 3-14). These values are significantly higher than from quasi-static results (1.1 to 1.4 kN for 0.002 to 0.037 s^{-1} rate of loading). This shows a clear evidence of strain-rate dependency of the material.

When characterizing the energy absorption capacity of a material or structure the following three important parameters have to be considered. The first parameter is the mean load (P_{mean} - can be calculated using Equation 3.6); it is a measure of average force required to deform the material in a progressive manner. The second important parameter is the specific energy absorption (SEA - energy absorbed per unit mass of the crushed material) which provides a measure of the energy absorption ability of a structural component (Equation 3.7). The third parameter crushing efficiency (η_c) gives an idea about how ideal a structural component for energy absorption behaves (Equation 3.8). The ideal value is 100% which means that after the initiation of crushing (peak crush load) the load will remain the same (mean load). A low percentage is not desirable because a higher initial force (acceleration) will be transferred to the mounting structure.

$$P_{mean} = \frac{\int_0^{l_{\max}} F(l) \cdot dl}{l_{\max}} \quad [\text{kN}] \tag{3.6}$$

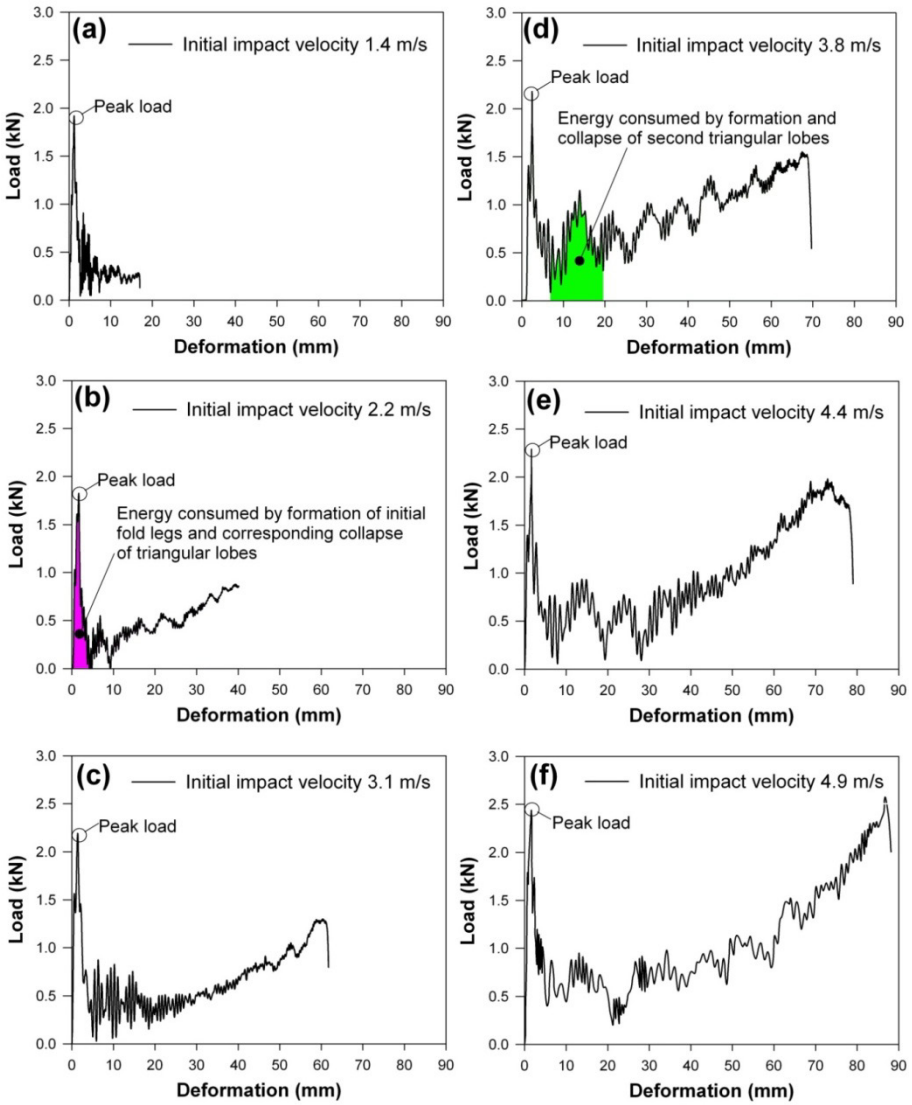

Figure 3-14: Load-deformation histories of empty beverage cans: **(a)** for initial impact velocity of 1.4 m/s. **(b)** for initial impact velocity of 2.2 m/s. **(c)** for initial impact velocity of 3.1 m/s. **(d)** for initial impact velocity of 3.8 m/s. **(e)** for initial impact velocity of 4.4 m/s. **(f)** for initial impact velocity of 4.9 m/s.

$$SEA = \frac{\int_0^{l_{\max}} F(l) \cdot dl}{m_{bc}} \quad [\text{kJ/kg}] \tag{3.7}$$

$$\eta_c = \frac{P_{mean}}{P_{\max}} \quad (\%) \tag{3.8}$$

where m_{bc} is the mass of an empty beverage can for maximum length of deformation (an equivalent mass over length was considered); P_{max} is the peak crush load of each empty beverage can.

The calculated average values of the peak crush load (from 10 test specimens) for each case are given in Table 3-4. The results from these tests provided clear guidelines for the deployment of beverage cans for the sacrificial cladding structure. For the case with initial impact velocity of 4.9 m/s the crush load (~ 2.68 kN) was increased beyond the initial peak crush load (~ 2.46 kN) after reaching the deformation length of about 83 mm. Hence, a higher acceleration could be transferred at the end of the crushing. Therefore, limiting the deformation length below 80 mm would provide a tolerable acceleration to the mounting structure. However, the deformation mechanism and mode are to be further verified for blast loading conditions (discussed in Chapter 4 and Part IV). Furthermore, as noticed, the peak crush load increased with increasing the initial impact velocities which corresponds to a higher acceleration to the mounting structure.

3. 5. 3. Effect of air inside the beverage can during crushing

As mentioned earlier, the difference in the energy levels (E_{given} - E_{abs}) for the case with the initial impact velocity of 4.9 m/s was higher compared to other cases (approximately 7.7%). In order to investigate the difference the high speed images of this particular case were examined; as an example the high speed images from one of the tests are presented in Figure 3-15. After reaching the maximum deformation length during the first impact the elastic strain energy from the test specimen was given back to the impactor (spring back). In addition to the elastic strain energy given by the test specimen the air entrapped inside the test specimen played a role for the energy loss. When the deformation length of the beverage can reached its maximum value the compressed air inside the beverage can provided an additional resistance to the impactor (refer Figure 3-15). Due to this combined effect, the impactor bounced back and dropped once more on the test specimen and the combined spring back energy (elastic strain energy + energy from compressed air) was absorbed by the beverage can in subsequent impacts. The developed internal pressure inside the beverage can caused an upward force, leading to a longer contact time between the impactor and the beverage can during rebound, and a higher rebound height. This phenomenon was noticed only for 50% of the tests. The occurrence of air entrapping and its resistance depend upon the perfect contact between the crushing platform and the test specimen. During the compression process the temperature of the compressed air should have increased; consequently, a part of the thermal energy from the compressed air was lost to the atmosphere (by convection through the beverage can wall and discharge of air from the top opening

of the beverage can). For the remaining 50% of the tests the air escapes due to a minor gap between the test specimen and the crushing platform and hence the height of bounce back of the impactor was shorter.

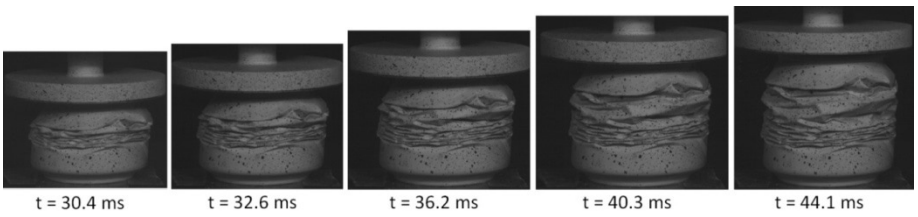

Figure 3-15: Spring back of the test specimen due to elastic strain energy and the entrapped and compressed air inside the test specimen for the initial impact velocity of 4.9 m/s.

In order to confirm the influence of air inside the beverage can additional tests have been conducted. To avoid the entrapping and consequent compression of the air during the crushing process, holes were drilled at the bottom of the beverage cans at four locations without deforming the beverage can (refer Figure 3-16). Experiments on these beverage cans (for the initial impact velocity of 4.9 m/s) showed a higher deformation length and corresponding energy, compared to the test specimen without holes. However, there was no difference in the deformation pattern compared to the ones without holes. Furthermore, there was a very minor spring back of the test specimen observed (refer Figure 3-17).

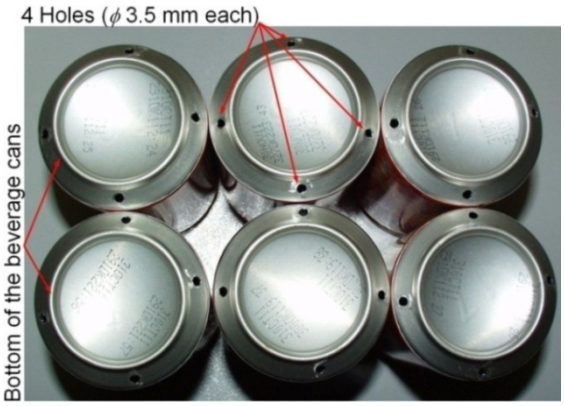

Figure 3-16: Beverage cans with holes at the bottom (to remove the air inside the beverage can during the crushing process).

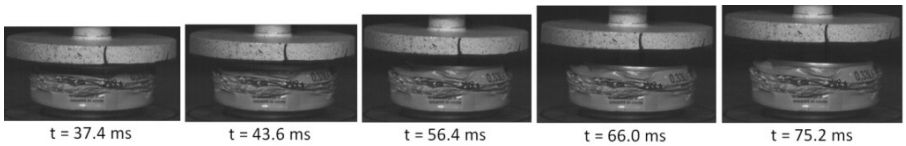

Figure 3-17: Separation and rebound of the impactor after crushing the beverage can with 4 holes (ϕ 3.5 mm each) for the initial impact velocity of 4.9 m/s.

As an example, a comparison of the load time histories of the cases with air and without air inside the beverage can is shown in Figure 3-18. The total duration of the impact was significantly different for both cases. The case without air inside the beverage can (with holes at the bottom) showed a shorter duration (34.6 ms) compared to the case with entrapped air inside the beverage can (43.9 ms). The reason for this difference was already explained in the previous section with Figure 3-15. Furthermore, the magnitude of the load increased significantly around 25 ms for the case with entrapped air inside the beverage can (refer Figure 3-18). As a result, the total impulse measured by the dynamic load cell (integrated load time histories) for the case with entrapped air inside the beverage can was higher than for the case without air (42.5 kN.ms and 56.4 kN.ms for with and without air respectively (refer Figure 3-19)). It can be noticed from Figure 3-19 that a significant part of the impulse was measured during the bounce back of the impactor (due to a longer contact between the impactor and the beverage can).

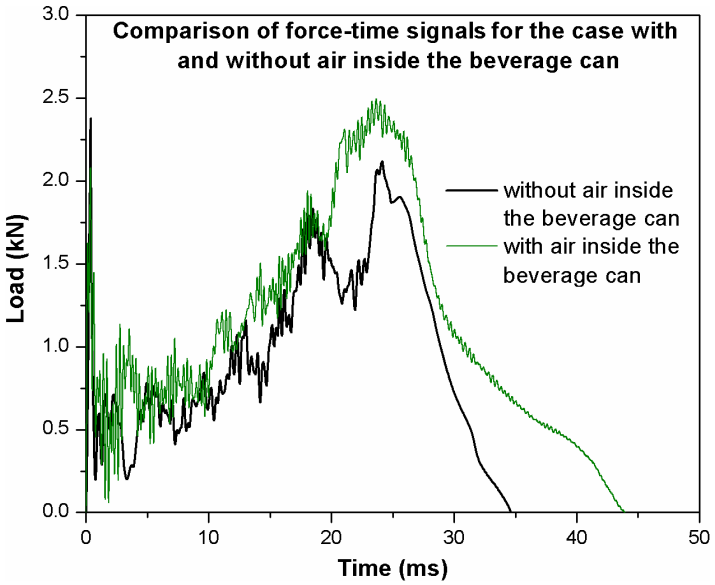

Figure 3-18: Comparison of load time histories for the case with and without air inside the beverage can (for the initial impact velocity of 4.9 m/s).

The average crushing parameters (from 10 experiments) are reported in Table 3-4. It can be noticed that for the case with holes the difference in the energy levels (E_{given} - E_{abs}) was approximately reduced to 4.5%. A comparison of the energy balance for the cases without and with holes is also shown in Figure 3-20(a) and (b) respectively. The total energy absorption of these cases was very close to the respective experimental average values. From these figures it can be noticed that the total energy given by the impactor (initial kinetic energy + additional potential energy due to the travelling mass of the impactor) for both cases was approximately the same (99.9 J). However, the total energy absorbed by the beverage can for the

case without holes (89.9 J) was lower than for the case with holes (96.1 J). Due to this there was a difference in the energy loss observed for these two cases (refer Figure 3-20(a) and (b)). An additional evidence for the influence of the entrapped and compressed air can be observed from these figures. Due to the resistance provided by the compressed air the duration at which the beverage can reached its maximum deformation length was shorter (26.9 ms) than for the one with holes (31.4 ms). Therefore, it can be concluded from the results that the remaining 3% of energy loss was caused by the entrapped and compressed air inside the beverage can during the crushing process. This phenomenon is also proved numerically and the details of the analysis are discussed in section 3. 8. In order to check the influence of air inside the beverage cans similar tests have been conducted for other impact velocity cases (1.4 m/s to 4.4 m/s). The results from these tests showed no significant difference in the crushing performance of these beverage cans (compared to the one without holes).

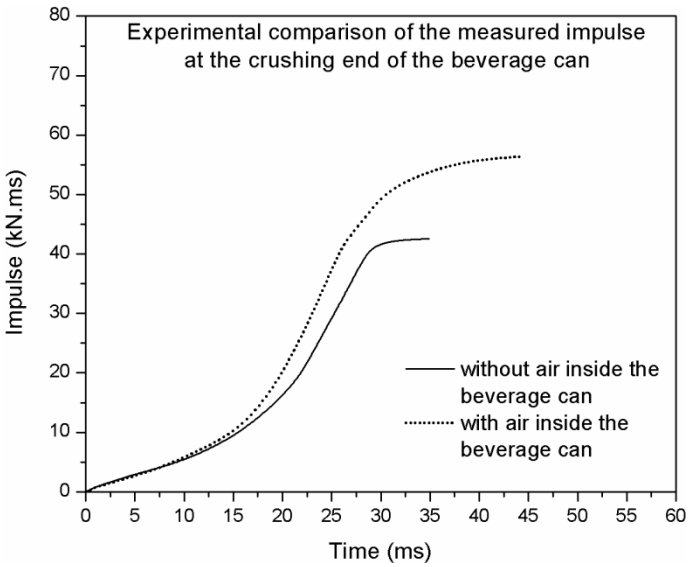

Figure 3-19: Comparison of the experimentally measured impulse histories for the case with and without air inside the beverage can (for the initial impact velocity of 4.9 m/s).

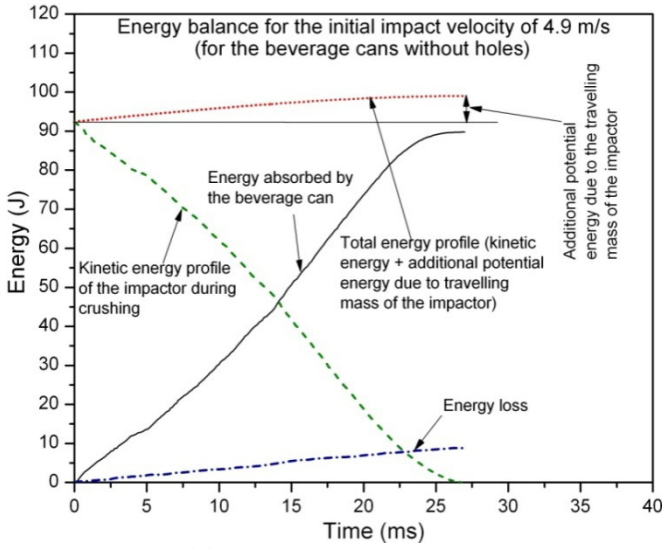

(a) Beverage can without holes

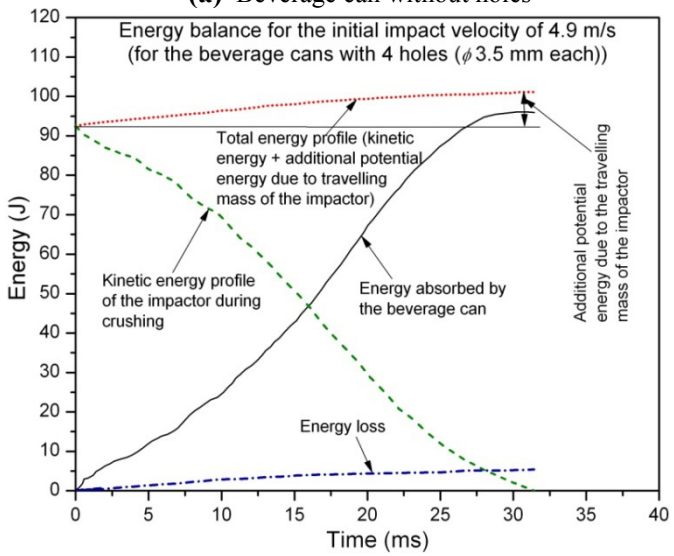

(b) Beverage can with holes at the bottom

Figure 3-20: Comparison of the experimental energy balance for the case with the initial impact velocity of 4.9 m/s (for the test on beverage cans with and without holes).

3. 5. 4. Effect of initial impact velocity on the performance parameters

The effect of initial impact velocity on the performance parameters can be understood from Figure 3-21(a) and (b). It can also be noticed that the variation in SEA and peak crush load is quite low for these tests. The mean crush load of the beverage can was increased with increasing initial impact velocity. The mean crush load varied from a minimum of 413 N (for the case with 1.4 m/s initial impact

velocity) to a maximum of 1060 N (for the case with 4.9 m/s initial impact velocity). The strain hardening of the material during onset collapse and folding process significantly contributed to increase the mean crush load. Consequently, the corresponding total energy absorption and the specific energy absorption of the beverage can was increased (1.86 kJ/kg, 2 kJ/kg, 2.74 kJ/kg, 3.48 kJ/kg, 4.13 kJ/kg and 4.72 kJ/kg for 1.4 m/s, 2.2 m/s, 3.1 m/s, 3.8 m/s, 4.4 m/s and 4.9 m/s initial impact velocities respectively). Furthermore, the initial peak crush load was increased with increasing initial impact velocity (1.69 kN, 1.72 kN, 2.19 kN, 2.28 kN, 2.37 kN and 2.46 kN for 1.4 m/s, 2.2 m/s, 3.1 m/s, 3.8 m/s, 4.4 m/s and 4.9 m/s initial impact velocities respectively). This clearly indicates the strain rate dependency on the material behaviour.

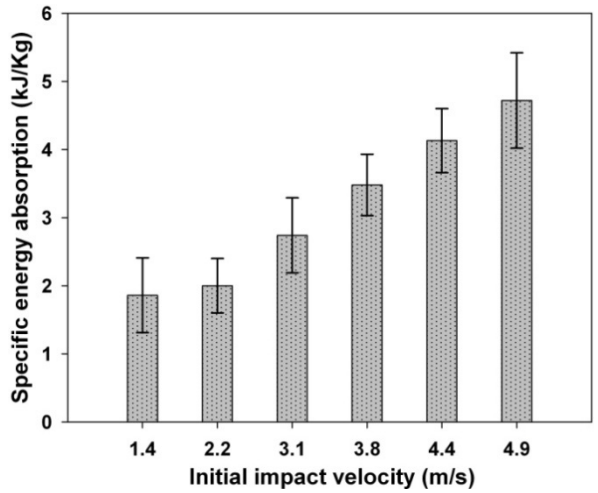

(a) Specific energy absorption of beverage cans without holes.

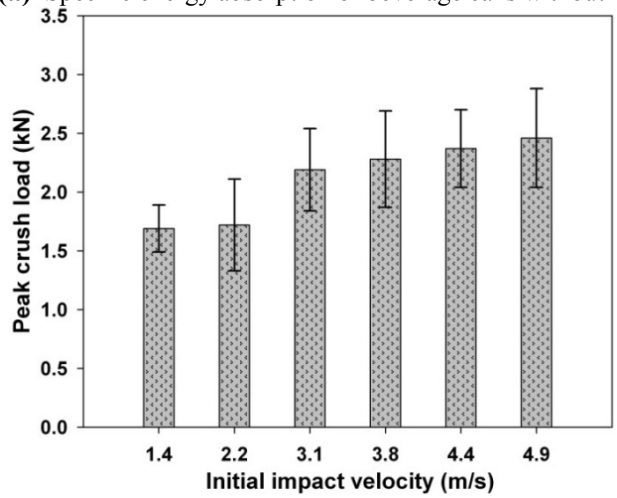

(b) Peak crush load of beverage cans without holes.

Figure 3-21: Effect of initial impact velocity on the specific energy absorption and peak crush load of an empty beverage can (error bar indicates the standard deviation).

3. 6. Analytical model

In this section a new analytical model is established to calculate the deformation length and the corresponding energy absorption of the empty beverage can subjected to the axial impact loading condition. The total kinetic energy of the impactor before impact (equal to the potential energy for certain drop height having an initial impact velocity) and the additional potential energy due the travelling mass of the impactor during the crushing process has been used to deform the empty beverage can. Hence, we write the force equilibrium for this system as (Equation 3.9),

$$F_c(t) = M_I \cdot \left(\frac{dv}{dt} + g \right) = \frac{d}{dx}\left(E_{abs}\right) \tag{3.9}$$

where $\frac{dv}{dt} = a(t)$ is the acceleration of the impactor (m/s^2); $\frac{d}{dx}\left(E_{abs}\right)$ is the energy absorbed per crushed empty beverage can length (J/m); $E_{abs}(x)$ is the energy absorbed by the beverage can (J) as a function of crushing length using a qualitative term called "dynamic mean crush load" (Equation 3.10).

$$E_{abs}(x) = P_{mean} \cdot x \tag{3.10}$$

where x is the deformation length of the beverage can. The expression to calculate the dynamic mean crush load of the empty beverage can considering diamond mode is discussed later. Equation 3.9 can be integrated by means of the "*Runge-Kutta*" integration scheme where the second order differential equation can be split in two single order equations using the "*Odesolve*" function of MathCAD [34]. The initial condition for velocity and displacement of the impactor are as follows:

$$v(0) = v_0 = \sqrt{2gh}; \qquad x(0) = 0 \tag{3.11}$$

where h is the drop height of the impactor (m).

Expression for dynamic mean crush load

As noticed from Figure 3-10(a-f) there was no significant deformation noticed for top and bottom shoulders and end caps. Hence, for simplification the beverage can can be considered as a cylindrical structure and subsequently the stability provided by the top and bottom end caps can also be neglected. The diamond mode crushing characteristics of thin-walled structures by the formation of triangular lobes considering total bending and the corresponding membrane energies (contributing in

converting the tube into collated and flattened triangles) are well studied in ref. [5]. Furthermore, the development of initial and successive lobes and their corresponding angle relationship for inward and outwards fold are given. The triangular formation at the start of this impact event (for an initial impact velocity of 2.2 m/s) and during crushing (for an initial impact velocity of 4.4 m/s) and the corresponding geometrical relationships are given in Figure 3-22(a) and (b).

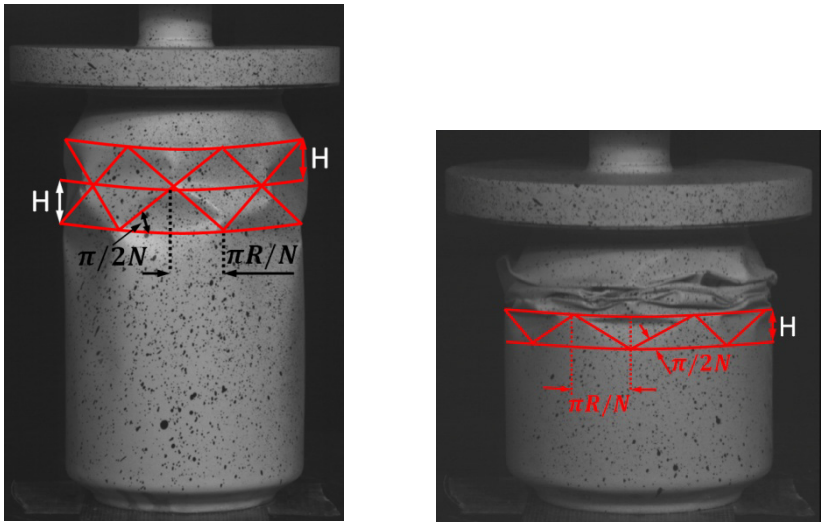

(a) **(b)**

Figure 3-22: (a) Formation of triangular lobes at the start of the impact process for an initial impact velocity of 2.2 m/s. (b) Formation of triangular lobes during the crushing process for an initial impact velocity of 4.4 m/s.

Singace [5] has proposed an expression to calculate the mean crush load of a tubular structure (which exhibits asymmetric or diamond deformation pattern) under quasi-static compressive loading condition. The following modes of deformation were accounted for to calculate the mean crush load:

(i) bending energy – which comprises the de-curving of the tube wall into triangles and the rotation of the triangles about their base and side edges.

(ii) membrane energy at the base of the triangle (i.e.) the energy required to compress an element of the tube wall towards the axis of the tube.

(iii) membrane energy at the apex of the triangle, i.e. the energy required to push an element of the tube wall outwards (away from the axis of the tube). The mean crush load of a tubular structure that exhibits asymmetric or diamond mode is given by [5],

$$\frac{P_{mean}}{M_p} \cong \frac{4\pi H}{t} - \frac{\pi N}{3} \tag{3.12}$$

where H is the half fold length (m); N is the number of lobes; t is the thickness of the tubular structure (m); M_p is the full plastic bending moment per unit length which can be written as follows [5],

$$M_p \cong \frac{\sigma_y t^2}{2\sqrt{3}} \tag{3.13}$$

where σ_y is the yield stress of the tubular structure (MPa). The above model (Equation 3.12) can be extended to the impact loadings with the method used by Abramowicz and Jones [13]. Among rate-dependent constitutive equations, the *Cowper-Symonds* equation has been most popularly employed in structural impact problems. This relation represents a rigid, perfectly plastic material with dynamic yield or flow stress that depends on strain rate. The ratio of dynamic yield stress σ_y^d and static yield stress σ_y is [13],

$$\frac{\sigma_y^d}{\sigma_y} = 1 + \left(\frac{\dot{\varepsilon}}{C} \right)^{1/p} \tag{3.14}$$

where C (characteristic strain rate) and p (measure of the strain rate sensitivity) are material constants; $\dot{\varepsilon}$ is the strain rate. Using Equation 3.13 and 3.14, the Equation 3.12 can be written as follows (Equation 3.15),

$$P_{mean} \cong \frac{\sigma_y t^2}{2\sqrt{3}} \left(\frac{4\pi H}{t} - \frac{\pi N}{3} \right) \cdot \left[1 + \left(\frac{\dot{\varepsilon}}{C} \right)^{1/p} \right] \tag{3.15}$$

To estimate the strain rate over collapse process, a simple estimate for the mean circumferential strain (ε) for a completely flattened fold of the circular tube is [5],

$$\varepsilon \cong \frac{H}{D} \tag{3.16}$$

where D is the average diameter of the beverage can at mid-wall region (65.63 mm). It was assumed that the empty beverage can deforms with an initial impact velocity of v_0 and this velocity decreases linearly with time (this assumption is experimentally supported by the integrated velocity-time profile of the impactor from the acceleration signal – refer Figure 3-7(b)). This corresponds to a constant deceleration of the impactor during the crushing process. For the simplification, the effect of additional potential energy during the crushing process on the strain rate was neglected. Furthermore, the air resistance inside the can for the 50% of the cases with the initial impact velocity of 4.9 m/s was not considered. The time taken to

deform one complete fold *(T)* and the corresponding average strain rate ($\dot{\varepsilon}$) can be given as Equation 3.17 and 3.18 respectively.

$$T = \frac{2H}{v_0} \tag{3.17}$$

$$\dot{\varepsilon} \cong \frac{\varepsilon}{T} = \frac{v_0}{2D} \tag{3.18}$$

Now, substituting Equation 3.18 into Equation 3.15 gives the mean crush load of that structure including the strain rate effect for a particular initial impact velocity (Equation 3.19),

$$P_{mean} \cong \frac{\sigma_y t^2}{2\sqrt{3}} \left(\frac{4\pi H}{t} - \frac{\pi N}{3} \right) \cdot \left[1 + \left(\frac{v_0}{2DC} \right)^{1/p} \right] \tag{3.19}$$

Experimental studies have proved that structures with high *D/t* ratio and/or material sensitive to strain hardening would generally deform in diamond mode [5-8]. Further, as noticed from the experimental results the mean crush load of the beverage can significantly increases after 30 mm of deformation length for 3.8 m/s, 4.4 m/s and 4.9 m/s. This was due to strain hardening of the material during the onset collapse, flattening and subsequent compression of each lobe. Therefore, to capture the appropriate mean crush load of beverage cans for these impact velocities the effect of strain hardening has to be included in the above expression. The effect of strain hardening of any material can be captured with yield stress and plastic strain using *Ludwik* equation. Assuming the mean circumferential strain as the plastic strain, the final form of the dynamic mean crush load of a thin tubular structure subjected to impact loading can be written as follows (Equation 3.20),

$$P_{mean} \cong \frac{\sigma_y + B(H/D)^n t^2}{2\sqrt{3}} \left(\frac{4\pi H}{t} - \frac{\pi N}{3} \right) \cdot \left[1 + \left(\frac{v_0}{2DC} \right)^{1/p} \right] \tag{3.20}$$

where B and n are material constants (usually calculated from experimental data). The final material parameters of the manufactured steel beverage cans are very close to the steel grade 4340 [23]. The corresponding values for steel 4340 were given in Table 3-1 [26, 29]. Substituting the value obtained from Equation 3.20 for a particular initial impact velocity in Equation 3.10 and subsequently, solving of Equation 3.9 provides the total deformation length and the corresponding energy absorption of the tubular structure (beverage can). The choice of calculating the mean crush load from equation 3.19 or 3.20 should be based on the initial impact velocity and the corresponding strain rate and strain hardening properties of the material. For lower impact velocities the consideration of Equation 3.19 can provide reasonable results; however for the impact velocities where the chances of strain hardening of the material are more, consideration of Equation 3.20 can yield close results compared to the experimental values.

3. 7. Comparison of analytical and experimental results

3. 7. 1. Comparison of dynamic mean crush load

Due to the inconsistent failure pattern, the case with an initial impact velocity of 1.4 m/s was not considered for the calculation of dynamic mean crush load. A comparison of dynamic mean crush loads for the remaining cases is given in Figure 3-23.

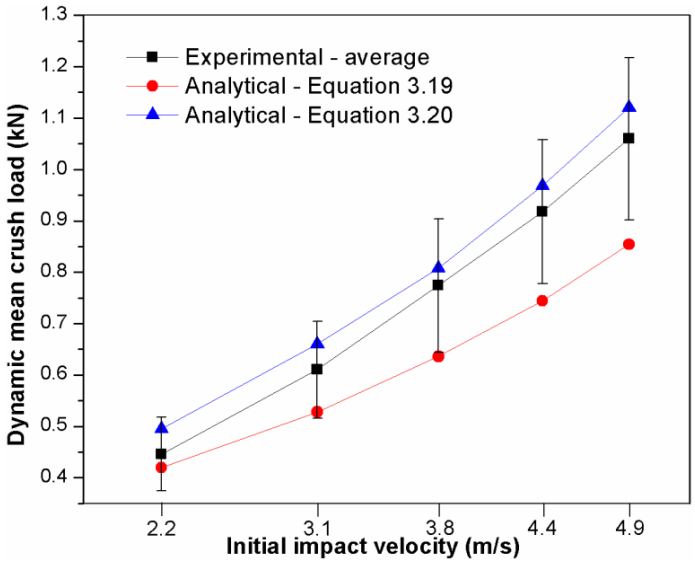

Figure 3-23: Comparison of the experimental and analytical dynamic mean crush load for different skin plates (error bar indicates the standard deviation).

The dynamic mean crush load using Equation 3.19 yielded a good correlation for the case with an initial impact velocity of 2.2 m/s. For the remaining cases (from 3.1 m/s to 4.9 m/s), there was a significant difference noted from the experimental data. Equation 3.19 predicted lower values compared to the experimental data. The major reason for this difference is the absence of the strain hardening effect which was observed in all cases. On the other hand, Equation 3.20 provided reasonable results for all impact velocities. The difference between the experimental and analytical solution was gradually reduced for higher impact velocities. Hence, it can be concluded that the consideration of strain rate and the corresponding hardening characteristics of the beverage can material is absolutely necessary to calculate the dynamic mean crush load.

3. 7. 2. Comparison of crushing parameters

The crushing performance of an empty beverage can can be calculated considering the values from Figure 3-23. Substituting these values of dynamic mean crush load in Equation 3.10 and solving Equation 3.9, the corresponding crushing performance (deformation, velocity and energy histories with respect to time) of the beverage can were calculated. The calculated performance values for all cases are given in Table 3-4. As an example, the initial impact velocity of 3.8 m/s case is discussed here. Figure 3-24(a), Figure 3-24(b) and Figure 3-24(c) show a comparison of deformation, velocity and the corresponding energy absorption of experimental and analytical solutions respectively.

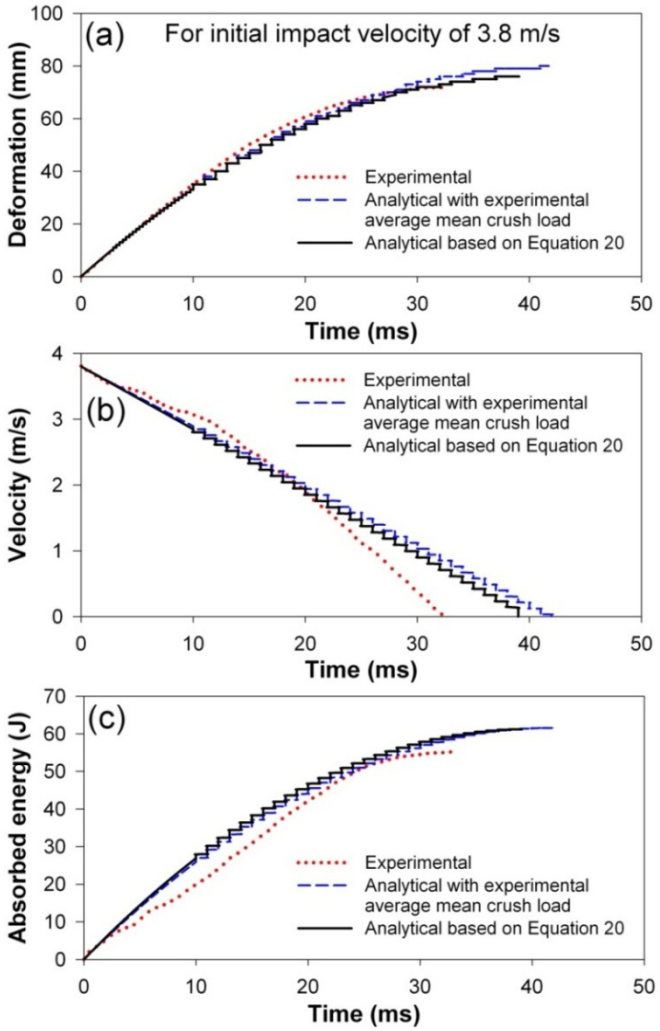

Figure 3-24: Comparison of crushing parameters of experimental and analytical solutions. (a) deformation-time history (b) velocity-time history (c) energy absorption history.

The dotted line is an experimental curve (one of the tests with the deformation length close to the average deformation length from 10 tests); the second curve (dashed line) represents the analytical solution considering the average dynamic mean crush load from the experiments; and the third solid curve shows the analytical solution considering Equation 3.20. The results from these three cases showed a good correlation of parameters such as deformation length, velocity and the corresponding energy absorption. Compared to the experimental data there was a difference in the total impact duration noticed (Figure 3-24(a-c)). This was due to the change in crush load and the corresponding deceleration of impactor during the experimental crushing process. However, the analytical formulation uses a constant mean crush load (the decrease in velocity and the corresponding deceleration were linear).

Similarly, Figure 3-25 shows the energy balance during the crushing process. It can be noticed that the total energy given by the impactor is increased due to the travelling mass of the impactor during the crushing process. The initial kinetic energy and the total energy given by the impactor were 55.6 J and 61.2 J respectively. An incremental energy value of 4.6 J was obtained for the additional potential energy from the travelling mass of the impactor during the crushing process.

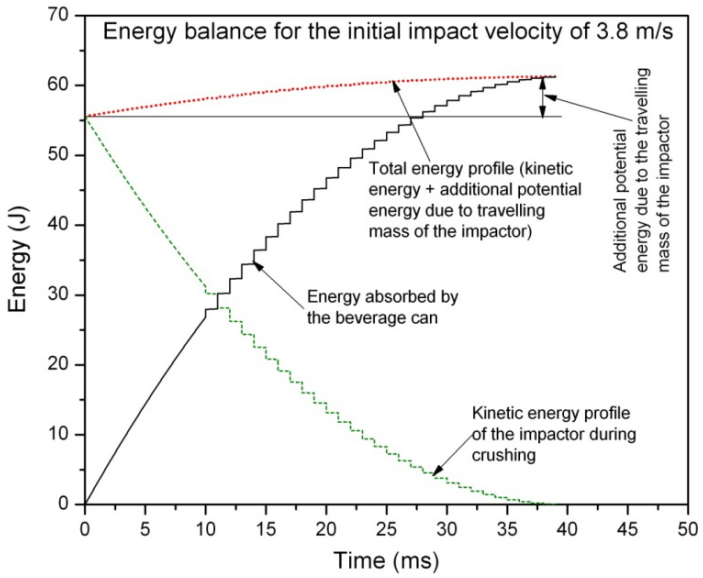

Figure 3-25: Energy balance for the case with the initial impact velocity of 3.8 m/s.

3. 7. 3. Conclusions

In this section the axial impact energy absorption characteristics and the corresponding deformation mechanism of empty recyclable metal beverage cans were presented. Axial impact tests have been conducted for different initial impact velocities ranging from 1.4 m/s to 4.9 m/s. An analytical model is also developed to predict the performance parameters of the beverage cans. From the conducted experiments the following conclusions can be made:

- For all initial impact velocities (2.2 m/s, 3.1 m/s, 3.8 m/s, 4.4 m/s and 4.9 m/s) the empty beverage cans showed controlled and uniform crushing failure modes. Furthermore, these beverage cans exhibited a diamond mode deformation pattern (formation of fold legs around the circumference and collapse and fold of triangular folds) (except for the case with an initial impact velocity of 1.4 m/s).
- The peak crush load of beverage cans with different initial impact velocities showed the strain rate sensitivity consistently. Hence, the effect of strain rate on increasing yield strength should be taken into account for dynamic investigations.
- The mean crush load and the corresponding specific energy absorption of these cans increased with increasing initial impact velocities. Furthermore, this test has given a guideline that these cans should be deployed for the maximum allowable deformation length of 80 mm.
- For the tests with the initial impact velocity of 4.9 m/s the air entrapped inside the beverage can consumed 3% of the total energy given during the impact process.
- An analytical solution including the strain rate and strain hardening effects of the material provided the mean crush loads which are very close to the experimental results. Furthermore, the other parameters such as deformation length, velocity and the corresponding energy absorption are very close to the experimental data.

3. 8. Numerical simulations

The numerical simulation part has been divided into two parts. The first part deals with the modelling of impact without considering the entrapped air inside the beverage cans. This is applicable to all impact velocities (and 50% cases with the initial impact velocity of 4.9 m/s). The second part accounts for the effect of entrapped and compressed air inside the beverage can and the corresponding influence on the crushing performance particularly for the case with the initial impact velocity of 4.9 m/s.

3. 8. 1. Modelling of impact without considering air inside the beverage can

The commercially available finite element code ABAQUS™ V6.7-3 Explicit was used to study the energy absorption characteristics of the empty beverage can. The details of the finite element model are shown in Figure 3-26. The beverage can was modelled with shell elements (4-node, quadrilateral, stress/displacement shell element with reduced integration and with finite membrane strain formulation) as per the geometry which was shown in Figure 3-1. The used size of the element for the beverage can was 1 mm. In order to reduce the computation time the impactor and the bottom resting plate were modelled as analytical rigid surfaces. To simulate the axial impact load only in vertical direction (along "Y" direction), all degrees of freedom of the top analytical rigid body were arrested apart from the vertical translation. To represent the fixed supporting base plate, all degrees of freedom of the bottom rigid body were also arrested. During the experimental test the bottom of the beverage can was glued to the supporting base plate. Hence, in order to simulate the same experimental conditions the bottom face of the beverage can (which contacts with the base plate) was constrained with the base plate using "*tie*" constraints. In order to include the additional potential energy due to the travelling mass of the impactor during impact the entire model was assigned with acceleration due to gravity (9.81 m/s^2). A "*surface-to-surface*" master-slave contact algorithm was established between the beverage can and the impactor with a friction coefficient equal to 0.2. In addition to that, a self-contact algorithm was also introduced for the beverage can. The analysis was carried out for different initial impact velocities ranging from 1.4 m/s to 4.9 m/s. The deformation of the beverage can was obtained from the displacement of the impactor (top rigid body) and the reaction load was extracted from the interface load between the beverage can and the impactor (analytical rigid surface).

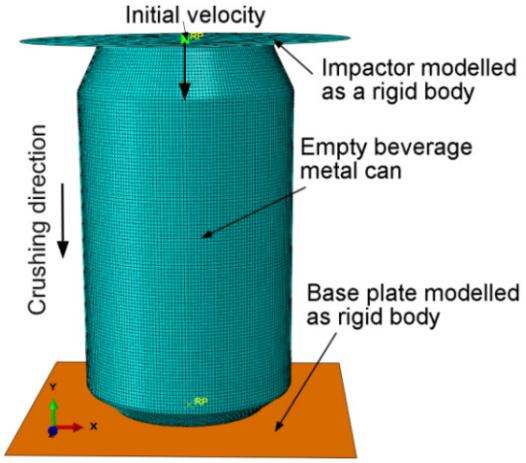

Figure 3-26: Details of the numerical model.

3. 8. 2. Material Model

As have noticed from the experimental test results, the peak crush load and the corresponding mean crush load of the beverage can strongly depend on the strain rate and strain hardening effect. The same was proved by the analytical model using *Cowper-Symonds* material model. Hence, in order to compare the numerical results with the experimental and analytical results the use of the same material model (*Cowper-Symonds*) would be an ideal choice. However, the *Cowper-Symonds* material model is not available in the chosen commercial code (ABAQUS^{TM} V6.7-3 Explicit). Therefore, an equivalent standard material model (*Johnson-Cook*) which can very well capture the strain rate and the strain hardening effects was used for all the numerical simulations. The *Johnson-Cook* material model is well developed and deployed in the area of automobile crashworthiness applications [35]. The corresponding equations are reproduced below (Equations 3.21 to 3.23). The material of the entire body of the beverage can (except the top cover) was modelled with steel 4340; the top cover of the beverage can was modelled with aluminium (grade 2024 T3) material.

$$\sigma_y = \left(A + B\bar{\varepsilon}^{p^n}\right)\left[1 + C.\ln \overset{\bullet *}{\varepsilon}\right]\left[1 - T^{*m}\right] \tag{3.21}$$

$$\overset{\bullet *}{\varepsilon} = \bar{\varepsilon}^{\bullet p} \Big/ \dot{\varepsilon}_p = \text{effective plastic strain rate} \tag{3.22}$$

$$T^* = \frac{T - T_{room}}{T_{melt} - T_{room}} \tag{3.23}$$

The details of the used constants and the corresponding material properties for the body and the top cover of the beverage can were given in Table 3-1. The experimental test results for all impact velocities showed no fracture of the beverage can. However, in order to check and validate the developed finite element model the *Johnson-Cook ductile damage model* was included in the simulation. This damage model is a special case of the ductile criterion in which the equivalent plastic strain at the onset of damage (fracture strain), ε^f is assumed to be of the form (Equation 3.24),

$$\varepsilon^f = \left[D_1 + D_2 \cdot \exp^{D3.\sigma^*}\right]\left[1 + D_4.\ln \overset{\bullet *}{\varepsilon}\right]\left[1 + D_5.T^*\right] \tag{3.24}$$

where D_1 to D_5 are failure parameters (D_1 = 0.54; D_2 = 4.89; D_3 = -3.03; D_4 = 0.014; D_5 = 1.12). The used failure parameters are adopted from ref. [26].

3. 8. 3. Comparison of experimental and numerical results

Deformation pattern

The numerical simulations have been performed for all impact velocities (1.4 m/s, 2.2 m/s, 3.1 m/s, 3.8 m/s. 4.4 m/s and 4.9 m/s). A comparison of deformation patterns from the experimental and numerical simulation of the beverage can for the initial impact velocity 4.4 m/s are given in Figure 3-27(a) and Figure 3-27(b) respectively. It can be noticed from these figures that the initiation and the corresponding deformation patterns from the numerical simulation correlated very well with the experimental results (the initiation and the subsequent crushing stages of the beverage can were well discussed in the experimental part). Similarly, the final deformation patterns of the beverage can for all impact velocities are shown in Figure 3-28(a-f). The use of the *Johnson-Cook* material model accurately predicted the deformation patterns of the beverage cans very close to the experimental deformation patterns. Furthermore, there was a very good correlation observed for the total deformation lengths of the beverage cans for all cases. The calculated final deformation lengths from the numerical simulations for all cases were given in Table 3-4. Similar to the experimental results, for all cases except the case with an initial impact velocity of 4.9 m/s there was no significant deformation observed at top and bottom portion of the beverage cans.

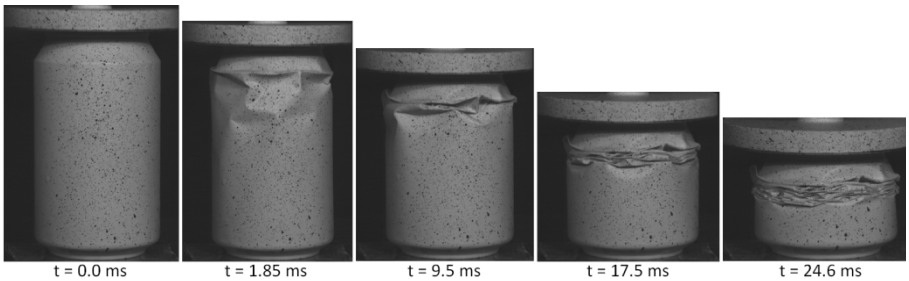

(a) Experimental deformation patterns for an initial impact velocity of 4.4 m/s

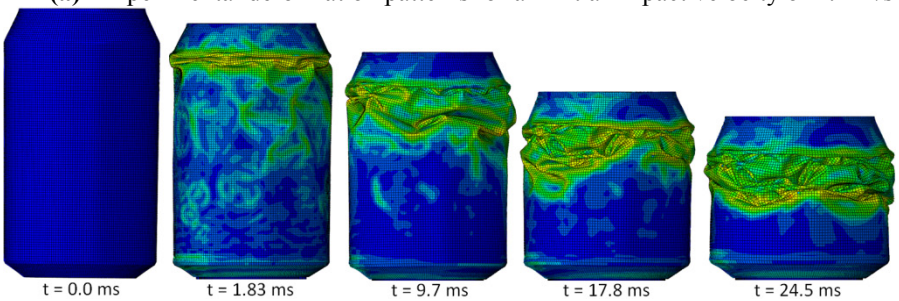

(b) Numerical deformation patterns for an initial impact velocity of 4.4 m/s

Figure 3-27: Comparison of the experimental and numerical deformation patterns of a beverage can subjected to an initial impact velocity of 4.4 m/s.

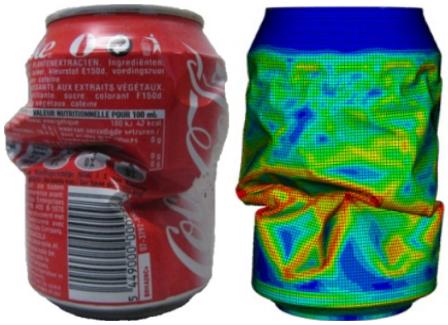

(a) Deformation patterns for initial impact velocity 1.4 m/s

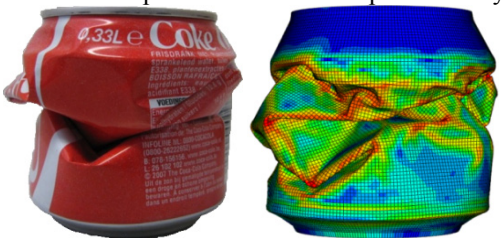

(b) Deformation patterns for initial impact velocity 2.2 m/s

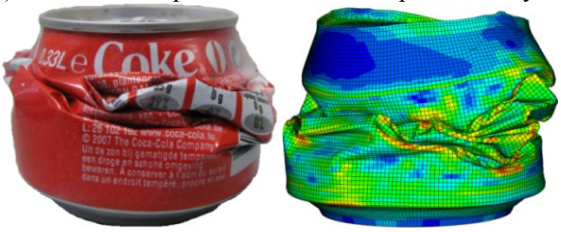

(c) Deformation patterns for initial impact velocity 3.1 m/s

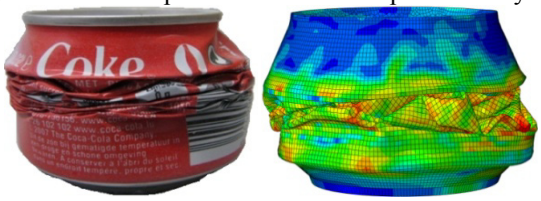

(d) Deformation patterns for initial impact velocity 3.8 m/s

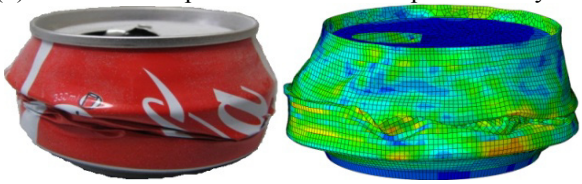

(e) Deformation patterns for initial impact velocity 4.4 m/s

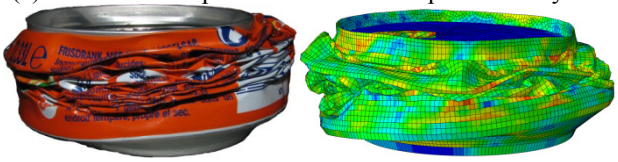

(f) Deformation patterns for initial impact velocity 4.9 m/s

Figure 3-28: Comparison of final deformation patterns of empty recyclable metal beverage cans for different impact velocities. (a) 1.4 m/s (b) 2.2 m/s (c) 3.1 m/s (d) 3.8 m/s (e) 4.4 m/s (f) 4.9 m/s.

As mentioned earlier, for the case with the initial impact velocity of 4.9 m/s the influence of entrapped air inside the beverage can was noticed only for 50% of the cans which reduced the total deformation length; subsequently, around 7.7% of the total energy was lost during the impact process. Due to the compressed air inside the beverage can, the height of the bounce back of the impactor was higher after achieving the maximum deformation length of the test specimen and the corresponding impulse of this case was significantly higher. However, for the remaining 50% of the tests air escaped due to a minor gap between the test specimen and the crushing platform; and hence the height of bounce back (only due to elastic strain energy of the test specimen) of the impactor was shorter. This evidence can be further proved from the numerical simulation results. Figure 3-29 shows the bounce back of the impactor (rigid body) after reaching the maximum deformation length of the test specimen. It can be noticed that the rebound height of the impactor was very similar to the one which was shown in Figure 3-17 (experimental case). Furthermore, an important evidence that can be noticed from the same figure is that the impactor is completely separated from the test specimen unlike the one which was shown in Figure 3-15 (beverage can had a very good contact with the impactor due to the compressed air inside the beverage can).

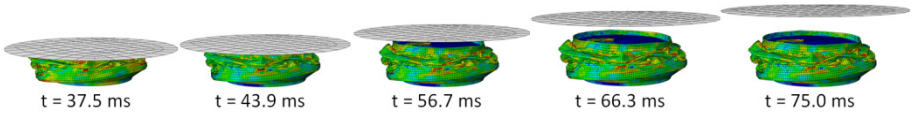

Figure 3-29: Spring back of the test specimen due to elastic strain energy and the corresponding rebound back of the impactor for the initial impact velocity of 4.9 m/s.

Load-deformation curves

Similar to the deformation patterns, a comparison of the experimental and numerically calculated load-deformation curves are shown in Figure 3-30(a-f). The crushing load figures show a clear evidence of capturing the strain rate and strain hardening effect of the material. The local strain rates varied from a minimum of 17 s^{-1} to 133 s^{-1} corresponding to the initial impact velocities of 1.4 m/s and 4.9 m/s respectively. However, for all cases the peak crush load from the numerical simulations was slightly higher than from the experimental values. This may be due to considering a perfect structure of the beverage can. The peak crush load varied from a minimum of 2.2 kN to a maximum of 2.75 kN. However, the total deformation length and the corresponding mean crush load for all cases were very close the experimental results (refer Table 3-4). Although the crush load curves from the numerical simulations do not show a form of triangle (which corresponds to the formation of triangular lobes and consequent folding) the crushing load curve for each case followed the experimental mean crush load profile (refer Figure 3-30(a-f)). The calculated mean crush load and the corresponding total energy absorption for each case was close to the experimental results (refer Table 3-4). Due to the

higher peak crush load the calculated crushing efficiency from the numerical simulations was lower than for the experimental results (refer Table 3-4).

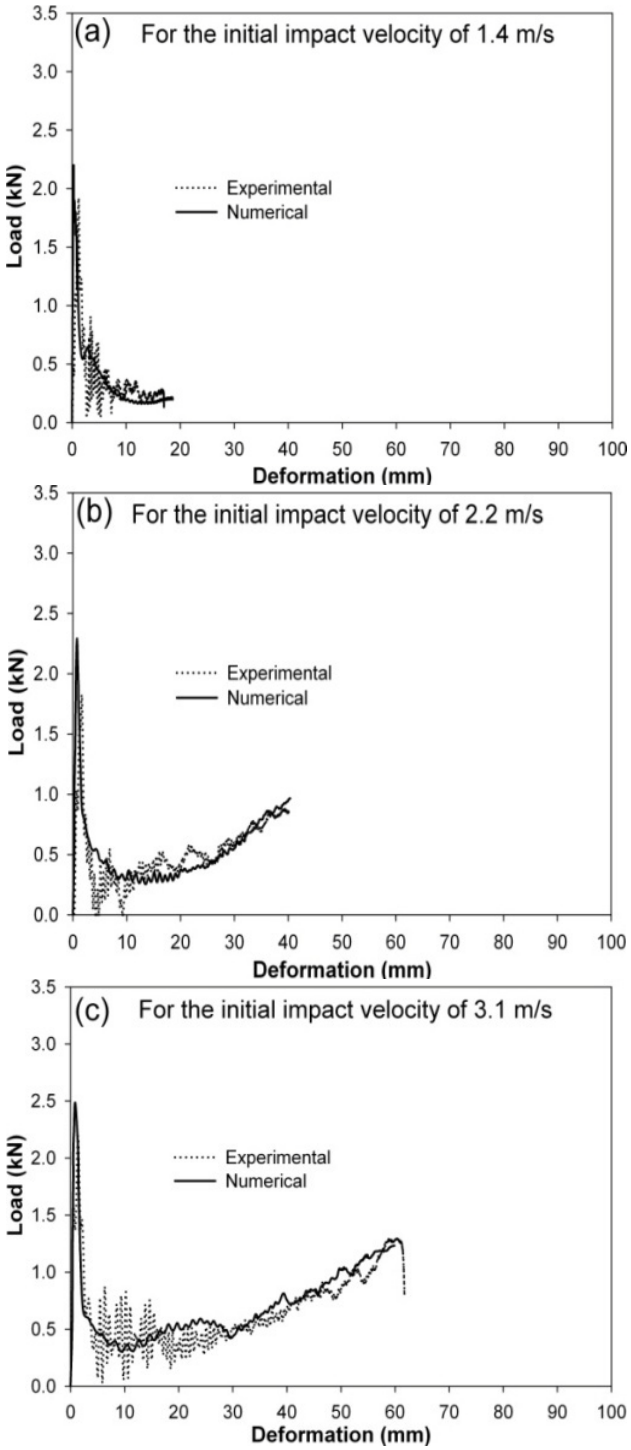

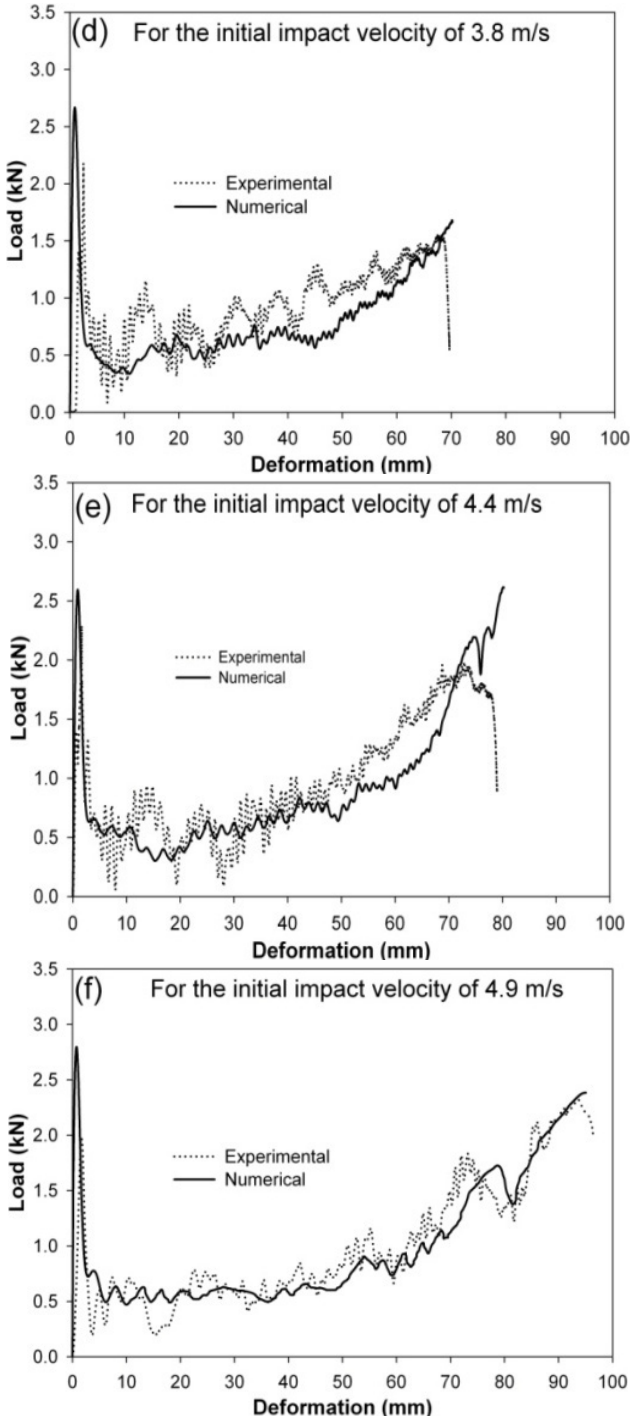

Figure 3-30: Comparison of the experimental and numerical load-deformation histories of empty beverage cans: **(a)** for initial impact velocity of 1.4 m/s. **(b)** for initial impact velocity of 2.2 m/s. **(c)** for initial impact velocity of 3.1 m/s. **(d)** for initial impact velocity of 3.8 m/s. **(e)** for initial impact velocity of 4.4 m/s. **(f)** for initial impact velocity of 4.9 m/s.

Energy equilibrium

In order to understand the relation between the different parameters during an impact process, the displacement of the impactor, velocity of the impactor, reaction force and the corresponding change in kinetic energy with respect to time (for the case with the initial impact velocity of 2.2 m/s) are plotted in Figure 3-31. This figure shows complete information of a total of 6 impacts. The first impact took place when time t = 0 sec (for the numerical simulation the impactor was placed just above the test specimen with an initial assigned impact velocity). During the first impact the maximum deformation length of the test specimen was achieved around 0.04 s (the negative values of the deformation length and the corresponding velocity show that the impactor precedes in negative "Y" axis). During this time the (total) energy of the impactor was brought to zero which means that the impactor lost all its energy (initial kinetic energy + additional potential energy due to the travelling mass of the impactor which is not shown in the figure) to the test specimen. The total energy from the impactor was absorbed by the test specimen in the form of (i) elastic energy (ii) plastic dissipation (iii) frictional energy. After reaching the maximum deformation length of the test specimen, the impactor started to move upwards (opposite to the direction of the impact) due to a part of elastic strain energy (spring back) given by the test specimen (refer Figure 3-31). However, the impactor was still in contact with the test specimen; after some time the separation of the impactor and the test specimen took place (which is the end of the first impact). Because of the spring back the impactor further travelled in the opposite direction of the impact and dropped on the test specimen again due to the gravity. The total available energy for the test specimen to absorb during the second impact was equivalent to the elastic strain energy given by the test specimen at the end of the first impact. Again during the second impact the total energy from the impactor was absorbed by the test specimen and a part of the elastic strain energy was given back to the impactor. This process continued till that the time the total energy from the impactor was absorbed by the test specimen. To calculate the crushing efficiency of the test specimen the information from the first impact is sufficient enough, because the available energy for the subsequent impacts and the corresponding peak crushing loads were very low compared to the first impact. Furthermore, the plastic residual deformation length from the subsequent impact was negligible compared to the total deformation length from the first impact. Hence, similar to the experimental results the very first impact was taken into account to calculate the crushing performance of empty metal beverage cans.

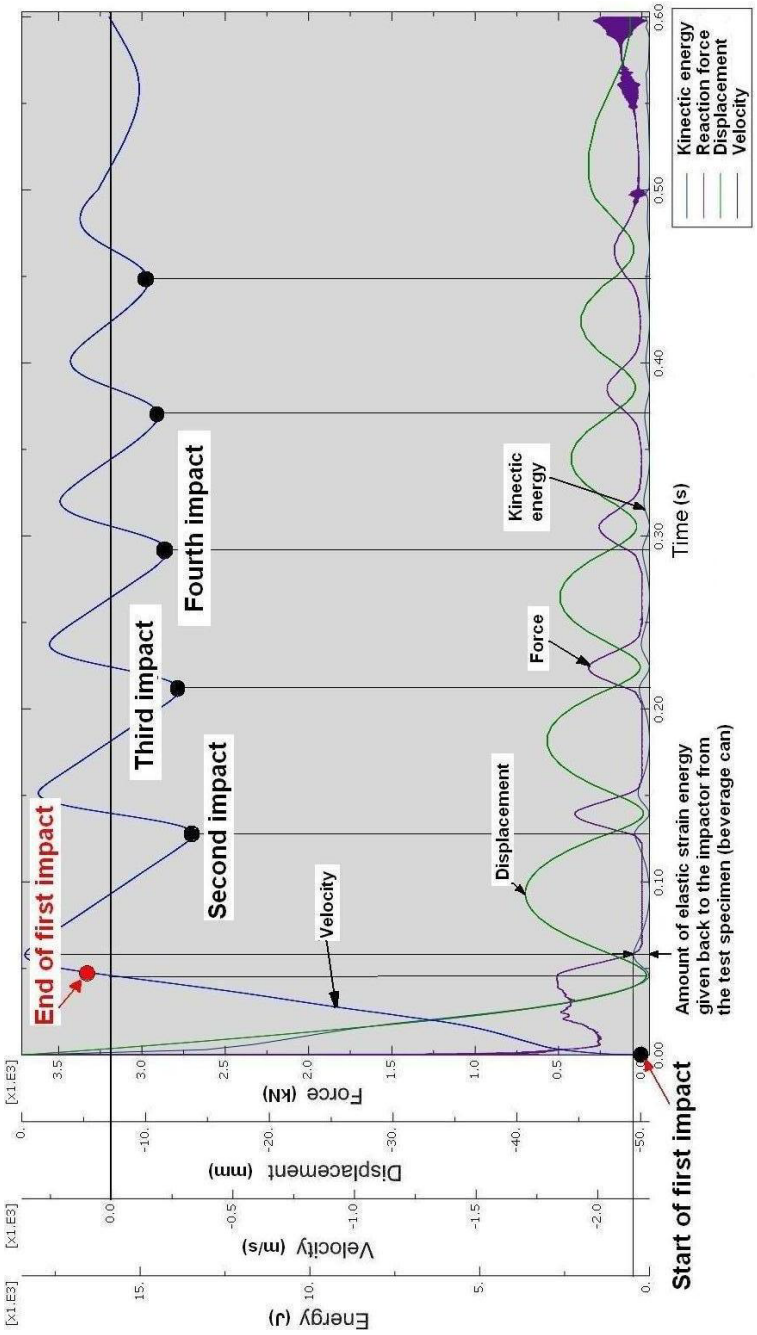

Figure 3-31: Displacement, velocity, force and kinetic energy histories for the case, with an initial impact velocity of 2.2 m/s.

Now, to understand the different modes of the energy dissipation an energy balance plot is illustrated in Figure 3-32 for the first two impacts for the initial impact velocity of 2.2 m/s. Similarly, Figure 3-33 shows the energy balance for the first impact for the case with the initial impact velocity of 4.9 m/s.

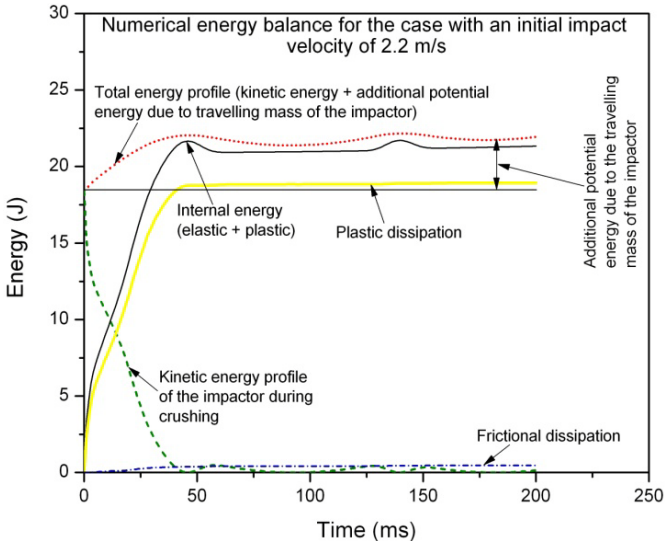

Figure 3-32: Numerical energy balance for the case with an initial impact velocity of 2.2 m/s.

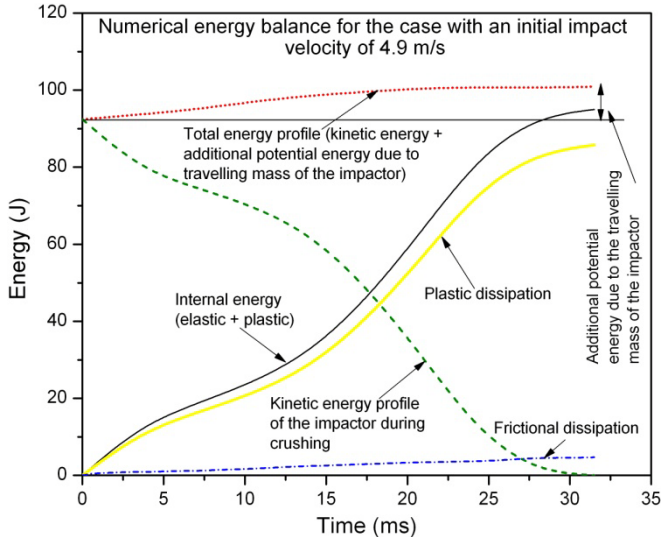

Figure 3-33: Numerical energy balance for the case with an initial impact velocity of 4.9 m/s (without considering air inside the beverage can).

The total energy given by the impactor was increased with increasing deformation length of the test specimen (due to the potential energy given by the impactor). The kinetic energy of the impactor reaches zero when the test specimen achieves its maximum deformation length; at that moment the internal energy of the test specimen (comprises of elastic and plastic dissipation) reaches its maximum value. Similarly these figures also show the plastic and frictional energy dissipation. For both cases the frictional energy was increased with increasing deformation length. The total elastic energy can be calculated by subtracting the plastic and frictional

dissipation from the internal energy. An important validation can be noticed from Figure 3-33 regarding the difference in the given and absorbed energy levels. As discussed earlier for the experimental results, there was a difference in the energy levels ($E_{given} - E_{abs}$) noticed for all cases. For the case with 4.9 m/s the difference was 4.5 % and 7.7 % for the tests conducted with and without holes at the bottom of the beverage cans respectively (refer Table 3-4). The numerical evidence for the difference in the energy level (7.7%) for the beverage cans without holes is discussed in the subsequent section. The difference in the energy level for the case with holes (no influence of air inside the beverage can) can be verified from Figure 3-33. The total energy given (initial kinetic energy + additional potential energy) by the impactor was 99.7 J; and the total energy absorbed by the beverage can by elastic and plastic deformation modes was 95.1 J. The remaining 4.6 J was dissipated in terms of friction (refer Figure 3-33). This value is very close to the experimental result for this case (refer Figure 3-20(b) and Table 3-4). Furthermore, this value was significantly increased with increasing deformation length of the test specimen, which means a considerable amount of energy has been spent by the friction during the crushing process (sliding lobes). Hence, it can be concluded that approximately 4.5 % of the total energy (for the case with the initial impact velocity of 4.9 m/s) was lost due to frictional dissipation. A similar evidence was also observed for the case with the initial impact velocity of 2.2 m/s (refer Figure 3-32).

Verification of load measurement from the numerical model

As discussed earlier, in the numerical model, the entire impactor was modelled as a rigid body and the corresponding reaction load at the crushing end was extracted from the centre of the rigid body. However, during the experimental testing the dynamic load cell was assembled at the top of the crushing plate (refer Figure 3-5(a) and (b)). Although the inertia of the crushing plate (~300g) was negligible compared to the total mass of the impactor (7.7 kg), an additional numerical simulation was conducted to check the effect of the inertia of the crushing plate on the load measurement,. The details of the numerical modelling are the same as for the previous case. However, in addition to the impactor the crushing plate was also modelled as per its geometry (refer Figure 3-34) using 8 node brick elements. Accordingly, the load was measured at two points: (i) reference point of the rigid body (impactor) which corresponds to the location of the load cell similar to the experimental test (ii) load measurement at the interface point between the crushing plate and the empty metal beverage can (refer Figure 3-34). Out of different initial impact velocity cases, the energy loss for the case with 4.9 m/s was higher compared to other cases. Hence, the same case was considered to check the effect of the inertia of the crushing plate on the load measurement. However, the results from this analysis showed no significant difference in the load time histories measured at these two locations. The impulse (integration of load time history) and the

corresponding energy absorption (integration of load deformation history) at the load cell location was 1.2% lower than from the interface point between the crush plate and the test specimen. Hence, the inertia effect of the crushing plate on the load measurement can be neglected.

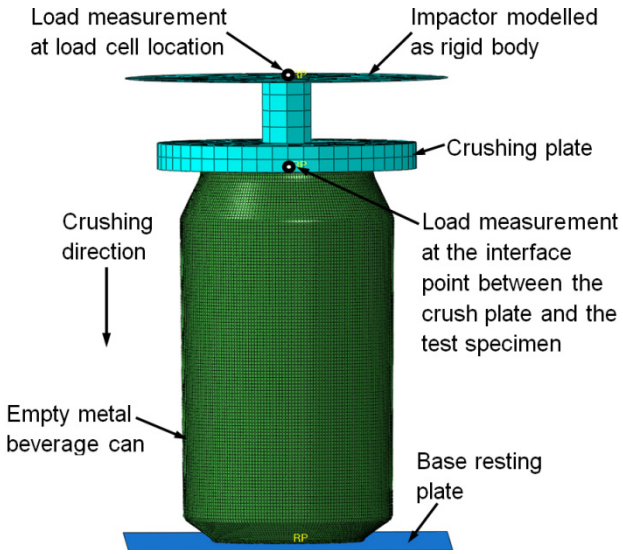

Figure 3-34: Details of the finite element modelling to check the effect of the inertia of the crushing plate on the load measurement.

3. 8. 4. Modelling of impact with considering air inside the beverage can

As discussed earlier, for the case with the initial impact velocity of 4.9 m/s the influence of entrapped air inside the beverage can was noticed only for 50% of the cans which reduced the total deformation length. Subsequently, around 7.7% of the total energy was lost due to the friction and the compressed air inside the beverage can. In order to check and validate the experimental results, a numerical simulation has been conducted considering the air inside the beverage can. Therefore, this section presents the numerical modelling details and the corresponding results of this numerical study. The modelling of air inside the beverage can during the crushing process is basically a fluid structure interaction problem. ABAQUS^{TM} provides many options to deal with such problems: (i) Eulerian approach (ii) hydrostatic fluid modelling (iii) surface-based fluid cavities. The first choice was ruled out due to a longer computation time and limitations for the thermal coupling. Among the remaining two the third option was chosen due to a relatively easy implementation. This approach is very suitable to couple stress/displacement and temperature fields. Therefore, the approach of surface based fluid cavity was used to predict the mechanical response of the air-filled beverage can.

3. 8. 5. Surface-based fluid cavities – an introduction

When a fluid-filled structure is subjected to an external loading, the response of that structure depends not only on the external loads but also on the pressure exerted by the fluid which in turn affected by the deformation of the structure (refer Figure 3-35(a)). In ABAQUS^{TM}, the surface-based fluid cavity capability provides the coupling needed to analyse such situations. The cavity is assumed to be filled with fluid with the same properties and Equation Of State (EOS) which means sloshing and wave propagation through the fluid cannot be modelled with this option [36].

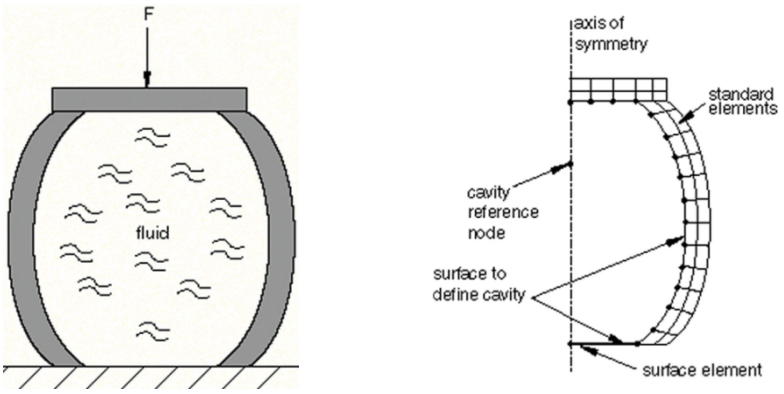

(a) (b)

Figure 3-35: (a) Fluid-filled structure [36]. **(b)** Example of a model [36].

3. 8. 6. Modelling

The modelling details of this case are very similar to the one which was discussed in section 3. 8. 1. However, the opening at the top cover of the beverage can (slit opening to drink the beverage) was not considered. Modelling the slit opening on the top cover of the beverage can calls for an additional input, (i.e.) the mass or volume flux of air during venting. This data cannot be calculated without the knowledge of the developed air pressure inside the beverage can during crushing. Hence, in order to reduce the complexity in the numerical model the top cover of the beverage can was assumed completely closed. This assumption was based on the following experimental observation. After achieving the maximum deformation length of the test specimen the impactor started to move upwards (opposite to the direction of impact). Figure 3-15 showed a perfect contact between the impactor and the test specimen, and it was continued (due to the entrapped and compressed air inside the beverage can) until the time of separation. In addition to a minor elastic strain energy of the test specimen, the spring back of the test specimen and the corresponding bounce back of the impactor continued till all the energy from the compressed air has been transferred to the impactor and the beverage can. The

pressure of the entrapped air inside the beverage can should have reduced to the moment when all the energy from the compressed air transferred to the impactor and the beverage can. The bounce back of the impactor is further continued due to the acquired momentum from this process. On the other hand, if we assume that the separation of the impactor and the test specimen will take place before transferring all the energy from the compressed air to the impactor and the beverage can, even then this assumption will not affect the calculation of the maximum built up in pressure inside the beverage can and the corresponding effect on the crushing characteristics. Indeed, this can only affect the time taken for the beverage can to reach thermal equilibrium (with atmospheric temperature). The following discussion can support the above statement. During the crushing process the air pressure inside the beverage can reaches a maximum value corresponding to the maximum deformation length of the beverage can (minimum volume). Due to this process, the rise in temperature will be transferred to the beverage can wall and to the impactor. If the contact time is long enough then a large part of the energy from the compressed air will be transferred to the beverage can (in the form of heat transfer and work against the plastic deformation of the can) and to the impactor (in the form of heat transfer and rebounding the impactor); subsequently, at the time of separation the vented air from the beverage can will carry the remaining temperature and pressure to the atmosphere. After this event the beverage can will take its own time to reach its thermal equilibrium state. On the other hand, if we assume that the contact between the impactor and the beverage can will be shorter, then a significant quantity of energy (in the form of pressure and temperature) will be taken away by the vented air before it transfers to the beverage can and the impactor. The only difference among these two assumptions is the time to reach the thermal equilibrium for the beverage can and the height of rebounding of the impactor; and there will not be any change in the percentage of energy (pressure + thermal) loss from the whole process. As noticed from Figure 3-15 that the contact between the impactor and the beverage can and subsequent bounce back of the impactor was significant, the latter assumption may not be valid. Now, a major interest is to calculate the built in air pressure and temperature and subsequent effect on the crushing characteristics of the beverage can corresponding to its maximum deformation length. Hence, the assumption of closed top cover is valid to check whether the entrapped air inside the beverage can plays a role for the energy loss (in terms of an increasing temperature of the beverage can wall and the corresponding heat dissipation to the atmosphere during the crushing process).

The boundary of the fluid cavity inside the beverage can was defined by an element based surface with normals pointing to the inside of the cavity (refer Figure 3-35 (b)). The initial volume of the cavity will be calculated based on the chosen surface elements. As per the procedure instructed by ABAQUS^{TM}, this fluid cavity should be associated with a single reference node. This reference node has a single degree

of freedom representing the pressure inside the fluid cavity. The behaviour of air within the cavity can be based on a hydraulic or a pneumatic model. In order to capture the compressibility of air, the *Ideal gas* Equation Of State was used for this analysis; furthermore, the initial state of the atmospheric condition of air was taken into account (atmospheric pressure = 101.325 kPa; temperature = 20° C). The used properties of air are given in Table 3-5.

Table 3-5: Used properties of air.

Equation of state	Ideal gas
Density	1.127 kg/m^3
Specific heat at constant pressure	1000 J/kg °K
Universal gas constant	287 J/kg °K
Absolute zero temperature	-273.16 °K
Thermal expansion	3.43 × 10^{-3}/°K
Thermal conductivity	2.71 × 10^{-2} W/m/°K

3. 8. 7. Results and discussions

Deformation patterns

The progressive deformation patterns of the empty beverage can were very similar to the earlier cases. However, there was a significant difference noticed during the rebounding stages of the impactor. After reaching the maximum deformation length of the beverage can the impactor started to move upwards (opposite to the direction of crushing) due to the elastic strain energy and the compressed air inside the beverage can. The rebounding or spring back energy from the compressed air was very significant compared to the elastic energy from the beverage can. This difference can be understood from a comparison of Figure 3-29 (without air) and Figure 3-36 (with air).

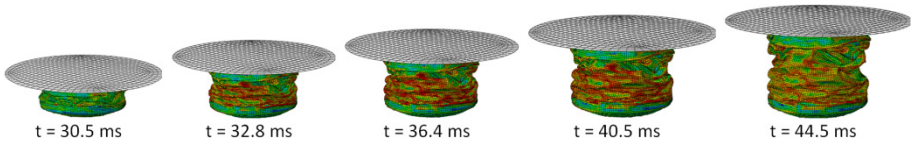

Figure 3-36: Numerical evidence for spring back of the test specimen due to elastic strain energy and the entrapped and compressed air inside the beverage can for the initial impact velocity of 4.9 m/s.

As compared to the previous case (without air inside the beverage can) the contact between the test specimen and the impactor continued for a long time. (refer Figure 3-36). The extended duration of contact between the test specimen and the impactor was due to the built up in air pressure inside the beverage can. Due to the

accumulated plastic deformation of the beverage can the contact between the impactor and the beverage can was terminated around 57.7 ms (Figure 3-37). Moreover, the later time increments showed a clear evidence of rebounding of the impactor for a longer duration and a higher height compared to the case without air inside the beverage can (refer Figure 3-37).

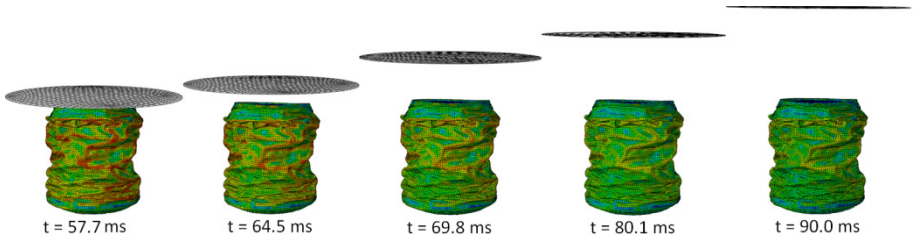

Figure 3-37: Numerical evidence for a higher bounce back of the impactor due to the entrapped and compressed air inside the beverage can for the initial impact velocity of 4.9 m/s.

In order to understand the properties of compressed air inside the beverage can during the crushing process, the pressure-time history and the corresponding change in volume are plotted in Figure 3-38(a). The pressure and the corresponding volume are measured from the reference point which represented the entire air cavity. The reduction in volume of air cavity throughout the crushing process was approximately uniform (directly proportional to the deformation length). Similarly, the change in air pressure inside the beverage can was uniform till 12.5 ms; at later time increments the magnitude of the pressure increased steeply to a higher value. A maximum pressure of 6.5 bar (relative to the atmospheric pressure) corresponded to the maximum deformation length of the beverage can. Because of the rise in pressure, the temperature of air inside the beverage can increased; and consequently it transferred to the beverage can wall. The calculated average temperature for the whole beverage can at different time steps is shown in Figure 3-38(b). A maximum temperature value of 7.5 $^{\circ}$C (with respect to the atmospheric temperature) was noticed when the beverage can reached its maximum deformation length.

As an example, the temperature distributions on the beverage can for a few time steps are shown in Figure 3-39. It can be noticed that in addition to the temperature from the compressed air, the heat generated due to the plastic work also has significantly contributed to increase the beverage can wall temperature. Due to the rise in air pressure inside the beverage can there was no fracture or tearing of the beverage can wall noticed. This pressure is lower than the pressure which is used for testing the integrity of the top cover seam with the body of the can (6.9 bar) during the production process [23].

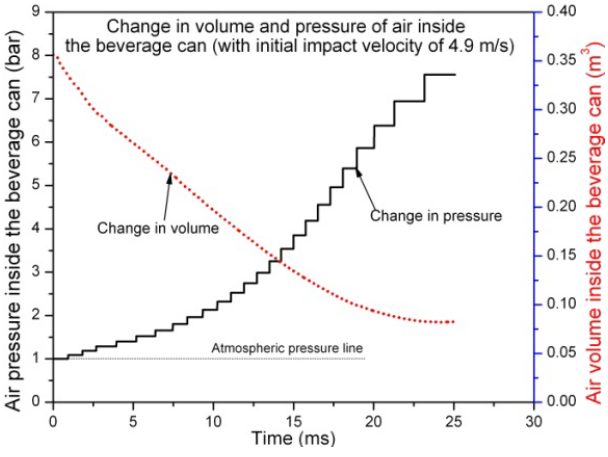

(a)

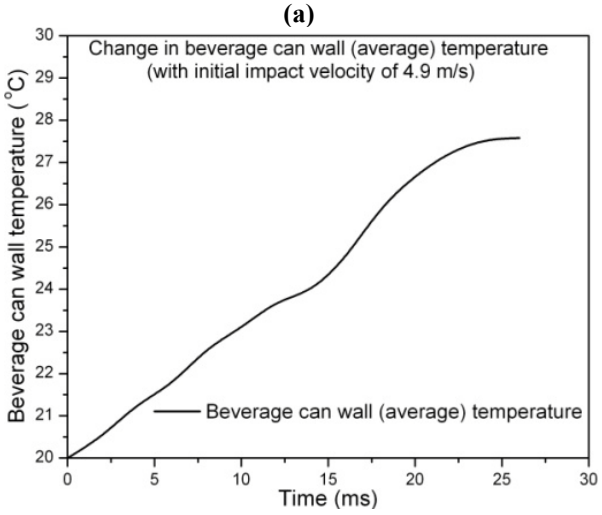

(b)

Figure 3-38: (a) Change in volume and the corresponding pressure inside the beverage can during crushing.**(b)** Change in beverage can wall temperature.

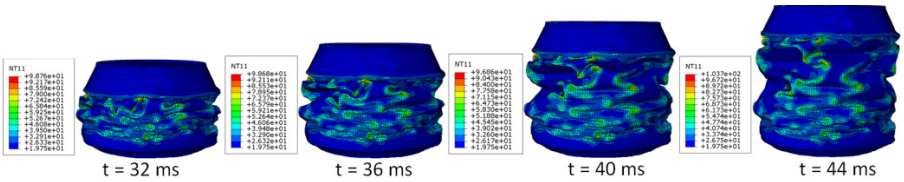

Figure 3-39: Temperature distribution on the wall surface of the beverage can.

Load-deformation curve

A comparison of the experimental and numerical load-deformation curves is shown in Figure 3-40. It can be noticed that a good correlation of crushing parameters is observed. However, the peak crush load of this case was the same as previous case (without air inside the beverage can) and it was slightly higher than the experimental

value (2.47 kN and 2.75 kN for experimental and numerically calculated values respectively). Similar to the experimental results the crush load significantly increased after reaching a deformation length of 80 mm. This was due to the additional resistance offered by the compressed air inside the beverage can. Furthermore the calculated total deformation length of the beverage can was very close to the experimental value (86.7 mm and 86.3 mm for experimental and numerical results respectively). The calculated mean crush load from the numerical simulation (1.054 kN) was very close to the experimental value (1.060 kN). The calculated crushing parameters are presented in Table 3-4.

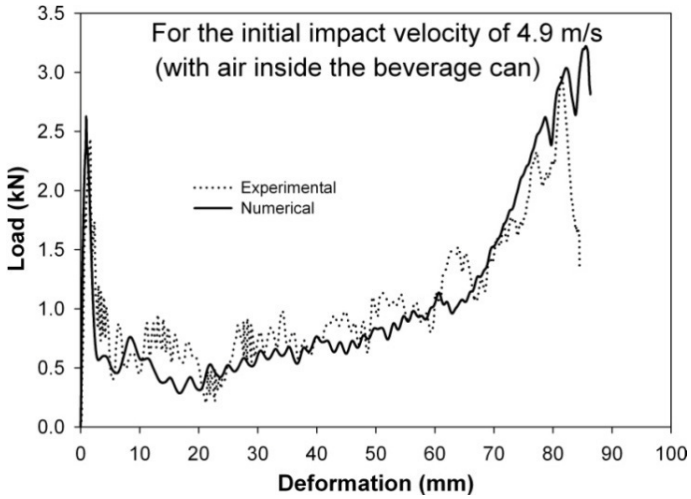

Figure 3-40: Comparison of the experimental and numerical load-deformation curves for the beverage can filled with air for the initial impact velocity of 4.9 m/s.

Comparison of transferred impulse

In order to understand the effect of entrapped air inside the beverage can, the transferred impulse to the bottom of the beverage can during the crushing was compared. Figure 3-41 shows a comparison of the transferred impulse for the cases with and without air inside the beverage can. Similar to the experimental results, it can be noticed that the magnitude of the transferred impulse for the case with air inside the beverage can was significantly higher (61.2 kN.ms and 45.8 kN.ms for the cases with and without considering air inside the beverage can respectively). Furthermore, the total duration of the impact was significantly longer (48.3 ms) compared to the case without considering air inside the beverage can (32.5 ms). Due to the built-up air pressure inside the beverage can and the elastic spring back of the beverage can, the contact between the impactor and the beverage can was continued for a long time during the restitution phase of the impactor. However, as seen from the previous section the total energy absorption for the case with air inside the beverage can was lower (refer Table 3-4). In addition to the energy loss the total

transferred impulse also proves that entrapping of air inside the beverage can is not desirable.

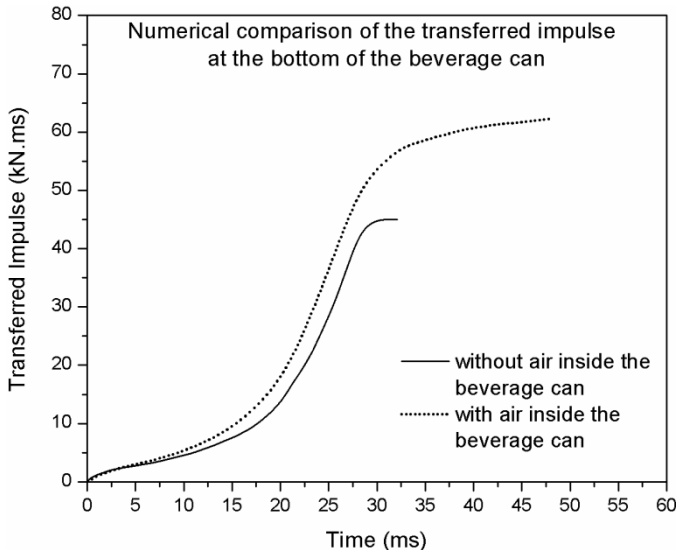

Figure 3-41: Comparison of the transferred impulse at the bottom of the beverage can for the cases with and without air inside the beverage can.

Energy equilibrium

The change in different modes of energy for this case was very similar to the previously discussed cases. The total energy given by the impactor (E_{given}) was 99 J. The energy absorbed by the beverage can (E_{abs}) was 91 J (refer Table 3-4). The remaining 8 J energy was lost during the crushing process. As explained for the experimental case, this difference ($E_{given} - E_{abs}$) was 7.7 J. It can be noticed that the experimental and the numerical results are close to each other. However, the numerically predicted frictional energy for the case with air inside the beverage can (2.6 J) was lower than for the case without air inside the beverage can (4.5 J). One of the major reasons for reduction in the frictional energy was the presence of compressed air inside the beverage can. The developed air pressure inside the beverage can might have reduced the hard contact between the lobes of the beverage can during crushing. The remaining energy (8 J – 2.6 J = 5.4 J) might have been lost by in the form of thermal energy to the atmosphere. To calculate the amount of thermal energy transferred from the compressed air to the beverage can wall and subsequently to the atmosphere, the heat flux density on the beverage can wall was calculated (refer Figure 3-42). The heat flux density was measured for the whole length of the beverage can at different time intervals from zero to the maximum deformation length (Figure 3-42). The calculated average value of the heat flux density was 5.51 mW/mm^2. Now, the thermal energy can be calculated taking into account the total time to reach the maximum deformation length (26.1 ms) and the

corresponding total surface area of the beverage can (32.17×10^3 mm^2). The calculated total thermal energy was 4.6 J. As explained earlier, either this energy might have lost by thermal conduction or by the vented air from the opening end of the beverage can during the separation of the impactor and the beverage can. Deducting the frictional energy and the thermal loss to the atmosphere from the total loss gives 0.8 J .Therefore a difference of 0.8 J (8 J – 2.6 J – 4.6 J) was noticed. One possible answer for this difference was the energy spent on to extend the beverage can and its plastic folding during the rebounding of the impactor.

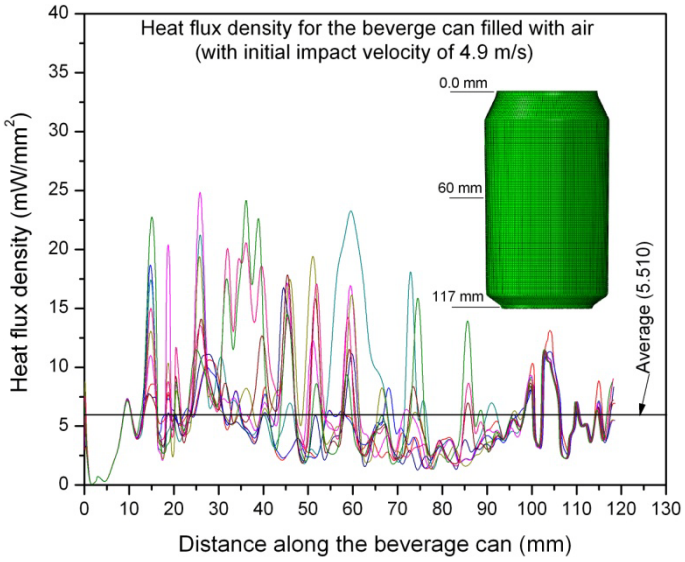

Figure 3-42: Heat flux density distribution on the beverage can wall.

3. 8. 8. Conclusions

In this section the numerical axial impact energy absorption characteristics and the corresponding deformation mechanisms (initiation and progressive crushing modes) are well studied using ABAQUS^{TM} Explicit V6.7-3. In order to capture the effect of strain rate and strain hardening during the crushing process the *Johnson-Cook* material model was used. The developed numerical models captured very well the crushing characteristics of the beverage cans subjected to different initial impact velocities. The initiation and the corresponding progressive crushing stages of the beverage can correlated very well with the experimental results. To understand the different forms of energy during the impact process a complete energy balance is presented. The different forms of energy such as kinetic energy, potential energy from the impactor and subsequently different forms of the dissipation were studied in detail. The calculated load-deformation curves and the corresponding energy absorption values are very close to the experimental results. Furthermore, in order to confirm the effect of entrapped and compressed air inside the beverage can a

numerical simulation was carried out for the case with an initial impact velocity of 4.9 m/s. The air inside the beverage can was modelled with a surface based fluid cavity approach using an *Ideal gas* Equation Of State. The results from this analysis showed that the entrapped air inside the beverage can reduced the total deformation length of the test specimen; consequently, the bounce back of the impactor was also high compared to the case without air inside the beverage can. Finally, it was proved that the percentage of energy loss increased from 4% to 7.5% for the case with entrapped air inside the beverage can.

3. 9. Application of Digital Image Correlation technique for measuring dynamic parameters during impact loading

As described above, many contact sensors have been employed to collect the data during the impact tests. Often, prior knowledge of the magnitude of the peak crushing parameters and the duration of the crash event is important to select the appropriate data acquisition equipments and sensors. However, this is not an easy task. Any improper selection would lead to loss of sensors and equipments. Furthermore, the level of accuracy of these sensors can be affected by the selection and working environment variables such as sensitivity, mechanical interface, wiring harness, disturbing frequencies in the vicinity, coupling losses, operating temperature etc,. So a contact-less method is an interesting alternative to collect the data during such dynamic events. In this section, we deal with the *Digital Image Correlation technique* (DIC) for measuring the impact parameters such as deformation length of the test specimen, impactor velocity and the corresponding reaction force at the crushing end. In order to validate this method axial impact tests have been carried out on polyurethane foam with different densities in addition to the metal beverage cans. The effect of frame rate and subset size on the derived parameters (deformation length, velocity and force time profiles) was also evaluated. The DIC derived results are compared with the signals which were measured by using sensors. The commercially available code Vic-2D was used for carrying out DIC calculations.

3. 9. 1. Digital image correlation technique – an introduction

Digital Image Correlation is an optical-numerical full-field displacement measuring technique. The technique is based on a comparison between the images taken during loading of a specimen. For an optimal use of this method the object of interest should be covered with non-repetitive, isotropic and high-contrast speckle patterns. Normally the random textures fulfil this requirement. To calculate the displacement

of a feature in images (vector difference between two images coordinates of the same physical point) the signature of a pixel is tracked. The signature of the pixel can be the pixel grey value or grey value derivatives or colour value of that pixel which differentiates from the other pixels. In practice, a single value is not a unique signature of a point; hence, the neighbouring pixels are used. Such a collection of pixel values is called a *subset*. Another parameter is the *step size* which defines the number of pixels over which the subset is shifted in "x" and "y" directions to calculate the displacement field. With the given parameters of subset and step size, these pixels can be tracked by checking the possible matches at several locations and grade them by using a correlation function. The classic correlation function using a *sum of squared differences* (SSD) of the pixel values is extensively used for many applications. Using this correlation function the entire subset can be tracked from the reference image to the deformed images. Subsequently, an average displacement value of that subset can be calculated for each image. Furthermore, the strains can also be computed from the gradients of a set of displacements. The basic principle of this DIC technique is illustrated in Figure 3-43.

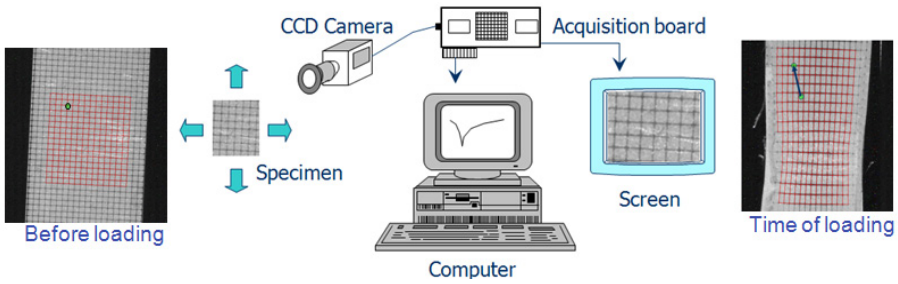

Figure 3-43: Basic principle of digital image correlation technique.

Many investigations have been made to use this technique for different applications and the results of those experiments showed promising results. Li et al. [37] adopted this technique to measure the various rolling parameters such as neutral point location, neutral angle, forward and backward slips, the length of the contact arc and the coefficient of friction. Vanlanduit et al. [38] proved that the DIC technique can be used to monitor the crack length from the displacement field during a fatigue test. Huang et al. [39] demonstrated this technique to measure the real-time monitoring of clamping force during fastening. Tarigopula et al. [40] used this technique to study strain localization in tensile specimens at high rates of strain. They showed that the in-plane displacement and strain fields during non-uniform deformation of the gauge section and accordingly the strains associated with diffuse and localized necking can be determined.

3. 9. 2. Test specimens

In addition to the metal beverage cans, polyurethane foam with two densities (40 kg/m^3 and 55 kg/m^3) has been chosen for this study. The dimensional and material details (quasi-static compressive stress-strain curve for the polyurethane foam with 55 kg/m^3) of the polyurethane test specimens are given in Figure 3-44(a) and (b) respectively.

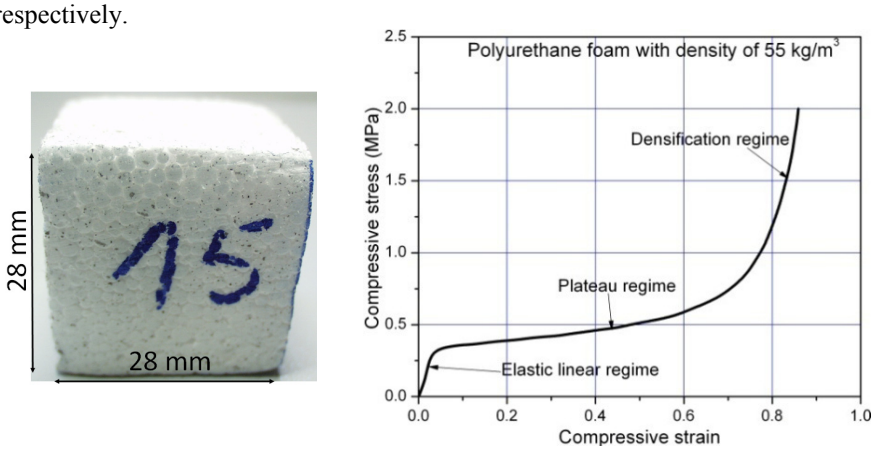

(a) **(b)**

Figure 3-44: (a) Polyurethane foam **(b)** Quasi-static compressive stress-strain curve for polyurethane foam with density of 55 kg/m^3.

The details of the used axial experimental test set-up and high speed camera can be found from section 3. 4. For optimal use of the digital image correlation technique a random speckle pattern (black speckles on the white background) was applied to the impactor and its base (refer Figure 3-45). Special care was taken to align the axis of the camera perpendicular to the impactor front surface. The tracking area by the high speed camera covered the entire impact basement. A special metal – halide lamp was used to maintain the light intensity at the area of the impact basement.

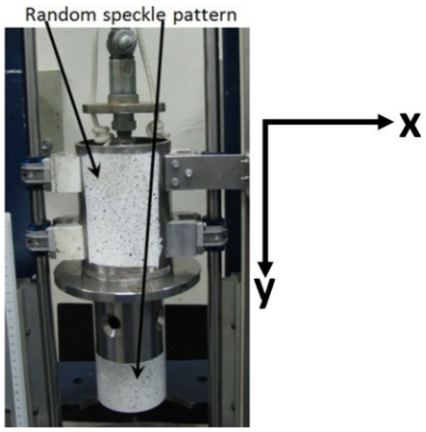

Figure 3-45: Random speckle pattern on the impactor.

Axial impact tests have been conducted with different impact heights which correspond to different initial impact velocities ranging from 1 to 4.4 m/s and with different frame rates. The used mass of the impactor for all tests with empty metal beverage cans was 7.33 kg. These tests were conducted before incorporating a winch mechanism to lift the impactor in the experimental test set-up. Hence, the mass of the impactor for this case was slightly lower than from the previous tests (7.7 kg) which were discussed in section 3. 4. Due to the requirement of a different end crushing part for polyurethane foam the used mass of the impactor was further lower (7.1 kg).

3. 9. 3. Method of calculation using DIC

As in the Introduction section, the displacement-time history can be calculated by performing correlation between the high speed images which were taken before and during loading. It was assumed that the vertical displacement (crushing direction of the test specimen (along "y" axis)) of the quasi-rigid impactor was equivalent to the deformation length of the test specimen. Hence, the DIC correlation was carried out to calculate the displacement-time history of the quasi-rigid impactor. The commercially available digital image correlation code "Vic-2D" was used for this calculation. Around a centre point on the quasi-rigid impactor surface (x, y) we have chosen a subset (n=21) of pixels (i × j = 441) from the reference image and consequently the classic correlation based on *sum of squared difference* (SSD) function was employed to calculate the displacement field (Equation 3.25). The effect of the subset size on the quality of the results is discussed later.

$$C(x,y,u,v) = \sum_{i,j=-n/2}^{n/2} (I(x+i,y+i) - I^*(x+u+i,y+v+j))^2 \qquad (3.25)$$

where "*C"* is a correlation function; (*x,y*) is the pixel coordinate of the reference image; (*u,v*) is the displacement in x and y directions; "*n"* is the subset size; "*I"* is the image before impact (reference image); (*x+i, y+j*) is the pixel value at (*x+i; y+j*); "I^**"* is the image during impact; (*x+u+i, y+v+j)* is the pixel value at (*x+u+i; y+v+j*). A step size of 5 was used for all the analyses. Subsequently, the displacement field in the area of the subset of the quasi-rigid impactor along "y" direction of the successive images was calculated. Due to the very small clearance between the vertical slide and the impactor, the displacement of the impactor perpendicular to the impact direction (along "x" direction) was neglected. The DIC correlations of the displacement field of the quasi-rigid impactor for one of the tests with the recyclable empty beverage cans are shown in Figure 3-46. The average displacement value of the pixels at the centre of the quasi-rigid impactor was considered from each image to calculate the displacement-time history of the quasi-

rigid impactor which is equivalent to the deformation length of a test specimen with respect to time. Subsequently, the impact velocity and the acceleration were calculated by differentiating the displacement-time history (Equation 3.26 and 3.27). In order to avoid the effect of accumulated error due to the differentiation process, the velocity profile of the impactor was filtered using "*Bi-square*" method. The filtered velocity signal was further differentiated to get the acceleration signal.

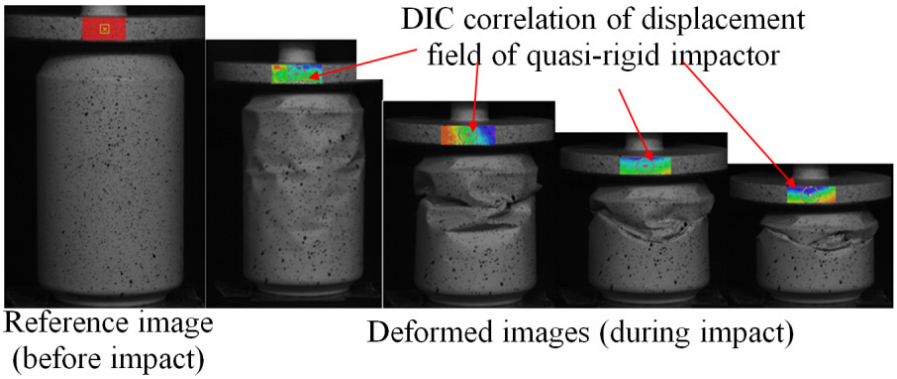

Figure 3-46: Digital image correlation of crushing of recyclable beverage can.

$$Velocity = \vec{w} = \left(\frac{d\vec{s}}{dt}\right)_k = \frac{s_{k+1} - s_{k-1}}{2\Delta t} \quad \text{(m/s)} \tag{3.26}$$

$$Acceleration = \vec{a} = \left(\frac{d\vec{w}}{dt}\right)_k \quad \text{(m/s}^2\text{)} \tag{3.27}$$

where "S" is the displacement of the quasi-rigid impactor, "*k*" is the image number and "*Δt"* is the time interval between the two successive images. It was assumed that the acceleration of the quasi-rigid impactor was constant during a time interval. Based on this assumption the reaction force at the impactor end was calculated by multiplying the mass of the quasi-rigid impactor (M_I) with the acceleration data (Equation 3.28) at every time interval. (7.1 kg and 7.33 kg for polyurethane foam and empty metal beverage cans respectively).

$$F = M_I \times \vec{a} \quad \text{(kN)} \tag{3.28}$$

3. 9. 4. Comparison of results

Empty metal beverage cans

Since the approach of calculating the dynamic parameters is the same for all tests, only a few cases of the recyclable empty beverage can results are presented. The DIC derived results corresponded to a frame rate of 5000 fps; a subset value of 21 and with step size of 5. Figure 3-47(a) shows the experimentally measured and DIC derived displacement-time histories of the quasi-rigid impactor for one of the tests with the initial impact velocity of 3.1 m/s. The measured signal from the accelerometer sensor was integrated twice to get the displacement time history. It can be noticed that the time to achieve the maximum deformation for both cases is comparable. However, the DIC reported a slightly higher displacement value than the experimental data. This may be due to the minor variation in the reference scale distance on the reference image. Subsequently, the comparison of velocity-time histories of experimental and DIC derived signals for the same experiment is shown in Figure 3-47(b). It can be noticed that there was a good correlation obtained for the magnitude of initial impact velocity and the time to reach zero magnitude. Furthermore, the reaction force at the impactor end was calculated as per Equation (3.28) and correspondingly the force-deformation history of the same experiment (initial velocity impact is 3.1 m/s) is shown in Figure 3-47(c). The peak crush force derived from DIC was very close to the experimentally measured value and subsequently the average crush force remained also the same till 45 mm of deformation length. However, after 45 mm deformation there was a fluctuation in the force noticed. Similarly, the comparison of transferred impulse to the quasi-rigid impactor for the test with an initial impact velocity of 4.13 m/s is shown in Figure 3-47(d).

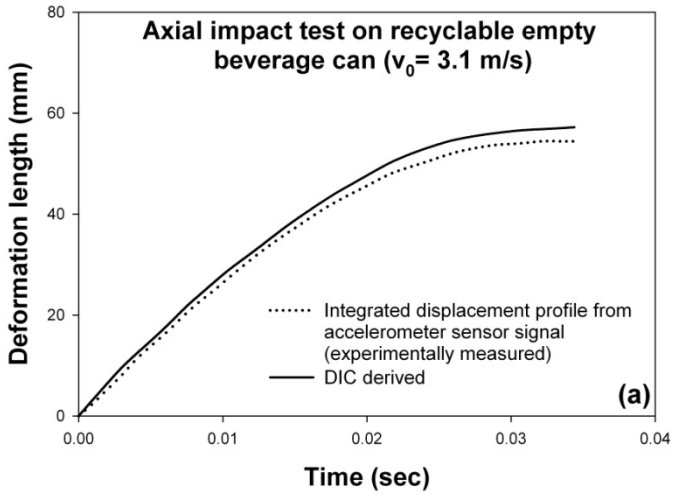

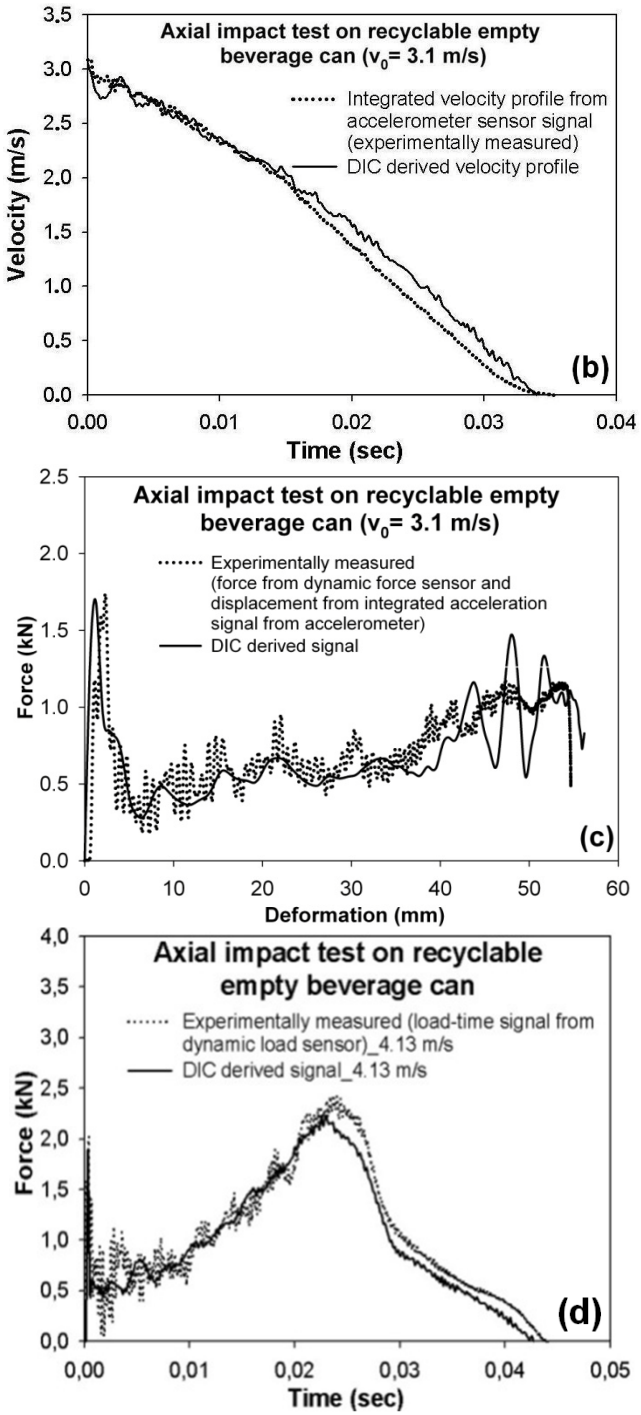

Figure 3-47: **(a)** Comparison of deformation histories for the initial impact velocity of 3.1 m/s. **(b)** Comparison of impact velocity profiles for the initial impact velocity of 3.1 m/s **(c)** Comparison of force-deformation curves for the initial impact velocity of 3.1 m/s **(d)** Comparison force-time histories for the initial impact velocity of 4.13 m/s.

3. 9. 5. Effect of frame rate

The experiments with a frame rate of 5000 fps showed a significant scatter in the peak crush load. Hence, in order to investigate the effect of frame rate on the peak crush load and the corresponding parameters an initial impact velocity of 3.1 m/s case was chosen. Tests have been conducted for different frame rates such as 7500 fps, 10000 fps, 15000 fps, 21000 fps and 31500 fps. The DIC processing was done on the high speed images using the subset of 21 and step size of 5. The results from this analysis are shown in Figure 3-48 and Figure 3-49. Figure 3-48(a) shows a comparison of the deformation length measured from the accelerometer sensor and the corresponding DIC derived data. The average deformation length and the corresponding standard deviation for 5 tests in each case are reported in this figure.

Irrespective of the used frame rate the DIC derived deformation length for each case was very close to the experimentally measured sensor data (integrated displacement from the accelerometer data). Similarly, there was a very good correlation observed for the initial impact velocity (refer Figure 3-48(b)). However, there was a significant difference in the peak crush load noticed between the experimentally measured sensor data and the DIC derived data (refer Figure 3-49(a)). For lower frame rates such as 5000 fps, 7500 fps and 10000 fps the difference was higher. The experimentally measured average peak crush load from the force sensor was 2.19 kN, 2.0 kN, 2.23 kN, 2.2 kN and 2.31 kN for the tests with 5000 fps, 7500 fps, 10000 fps, 15000 fps, 21000 fps and 31500 fps respectively. The corresponding DIC derived average peak crush load was 1.7 kN, 1.65 kN, 1.85 kN, 1.75 kN, 1.9 kN and 2.1 kN. It can be noticed that the difference was higher for a lower frame rate.

The standard deviation for the experimentally measured and DIC derived data for each case is shown in Figure 3-49(a). Furthermore, the same figure also shows the linear regression curves for both cases (experimental and DIC derived). It can be noticed that the difference in the peak crush was reduced for higher frame rates; this means that the probability of capturing a frame which corresponds to the peak crush load was higher for higher frame rates. The capturing of the peak crush load with lower frame rates also depends on the material and/or structure behaviour during the crushing process. As seen earlier from the beverage can experimental results, the load fluctuated abruptly before and after reaching a peak value. Hence, capturing the frame which corresponds to the occurrence of peak crush load is difficult. However, if the material or structure exhibits a smooth crushing behaviour then the chances of capturing the frame corresponding to the peak crush load will be easy. This point is further supported with the results from the polyurethane foam (discussed in next section). Although there was a significant difference in the peak crush load for the beverage cans, the calculated values of the total energy absorption and the corresponding specific energy absorption (energy absorption normalized with

respect to the mass of crushed material of the beverage can) from DIC showed no significant difference. Due to the fact that the peak crush load corresponded to a very short deformation length the integrated total energy absorption was very close to the experimental results.

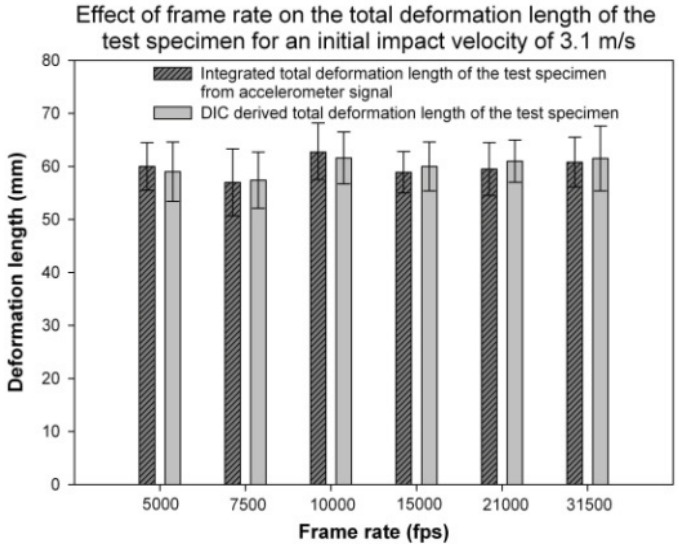

(a)

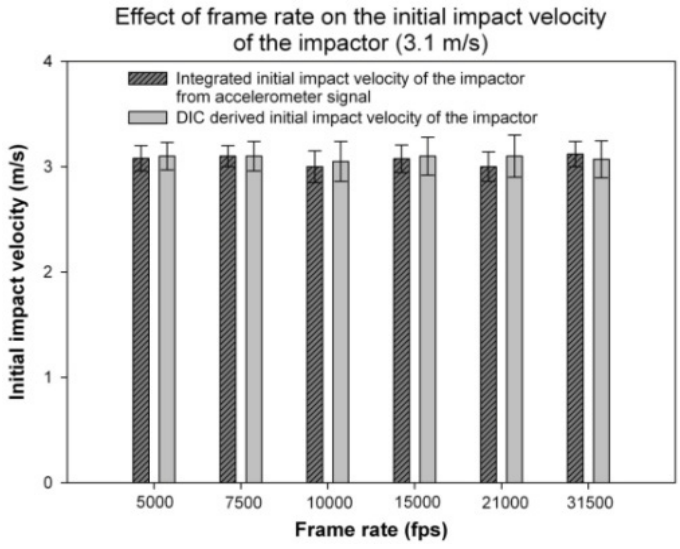

(b)

Figure 3-48: (a) Comparison of deformation length of the test specimen (error bar indicates the standard deviation). **(b)** Comparison of initial impact velocity (error bar indicates the standard deviation).

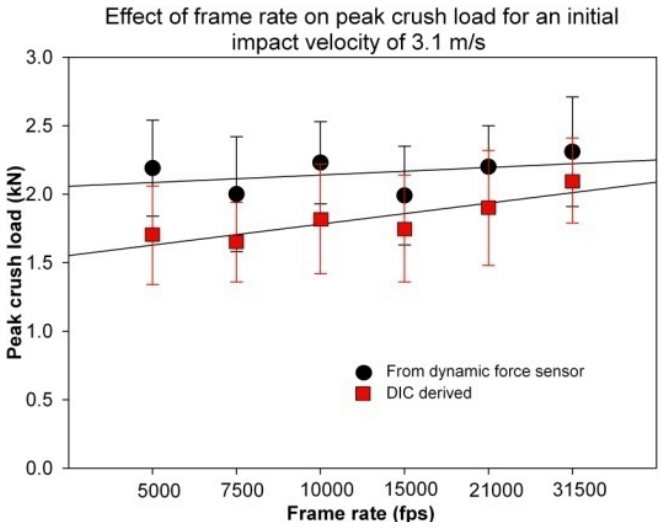

(a)

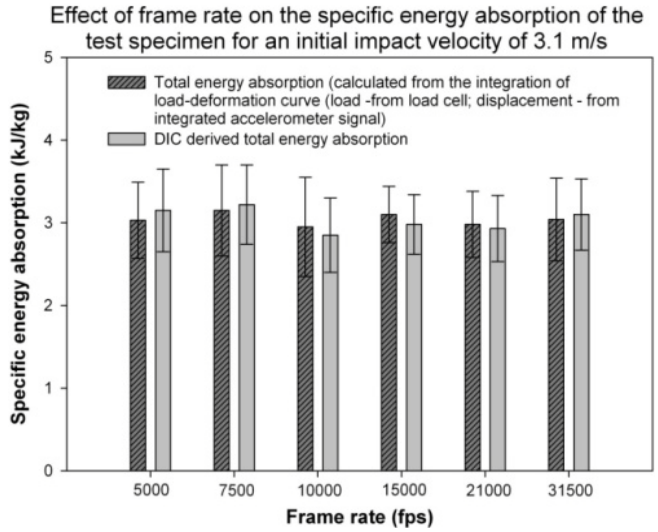

(b)

Figure 3-49: **(a)** Comparison of the peak crush load (error bar indicates the standard deviation). **(b)** Comparison of the specific energy absorption (error bar indicates the standard deviation).

3. 9. 6. Effect of subset

Many studies [41-43] have shown that the subset value is a critical parameter during the correlation process. Lecompte et al. [44] proved that the size of the speckles in a given speckle pattern in combination with the subset size have an influence on the accuracy of the measured results. Furthermore, they suggested that the subset has to be chosen in accordance with the expected deformations. However, for this test the

quasi-rigid impactor does not undergo any deformation other than the pure translation in "y" direction (crushing direction). Hence, the influence of subset on the derived parameters may be neglected. Nevertheless, investigations have been carried out to study the effect of subset on the crushing parameters for different initial impact velocities (1.1 m/s, 2.4 m/s and 3.1 m/s) with a frame rate of 5000 fps. Two subsets of 21 and 25 have been chosen with the step size of 5. Similarly, a minimum of 5 tests have been carried out for each initial impact velocity and the corresponding comparison of results is shown in Figure 3-50(a-c) .The results from this analysis showed no significant difference in the average deformation length, initial impact velocity and the corresponding specific energy absorption for these two subsets. However, the case with subset of 25 showed a minor increase in the scatter of the results (refer Figure 3-50 for the corresponding standard deviation in the results).

Polyurethane foam

As mentioned earlier, the probability of capturing the frame which corresponds to the peak crush load also depends on the material and/or structural deformation behaviour. This can be further explained by the deformation behaviour of polyurethane foam. The high speed deformation images of polyurethane foam for an initial impact velocity of 1.6 m/s are shown in Figure 3-51. The used frame rate for all experiments with polyurethane foam was 5000 fps. It can be noticed that the compressive deformation mode of polyurethane foam was very uniform. The corresponding measured force-time histories of the polyurethane foam with different densities subjected to different initial impact velocities are shown in Figure 3-52(a-d). The load-time profiles for different initial impact velocities are smooth.

Similar to the beverage cans, the DIC correlation was carried out for polyurethane foam. A subset size of 21 and a step size of 5 were used for all digital image correlations. For all cases, the results from the analyses showed a very good correlation with the experimentally measured sensor results. (refer Figure 3-52(a-d)). Hence, it can be stated that apart from the frame rate the material and/or structural behaviour during a dynamic loading also plays a role.

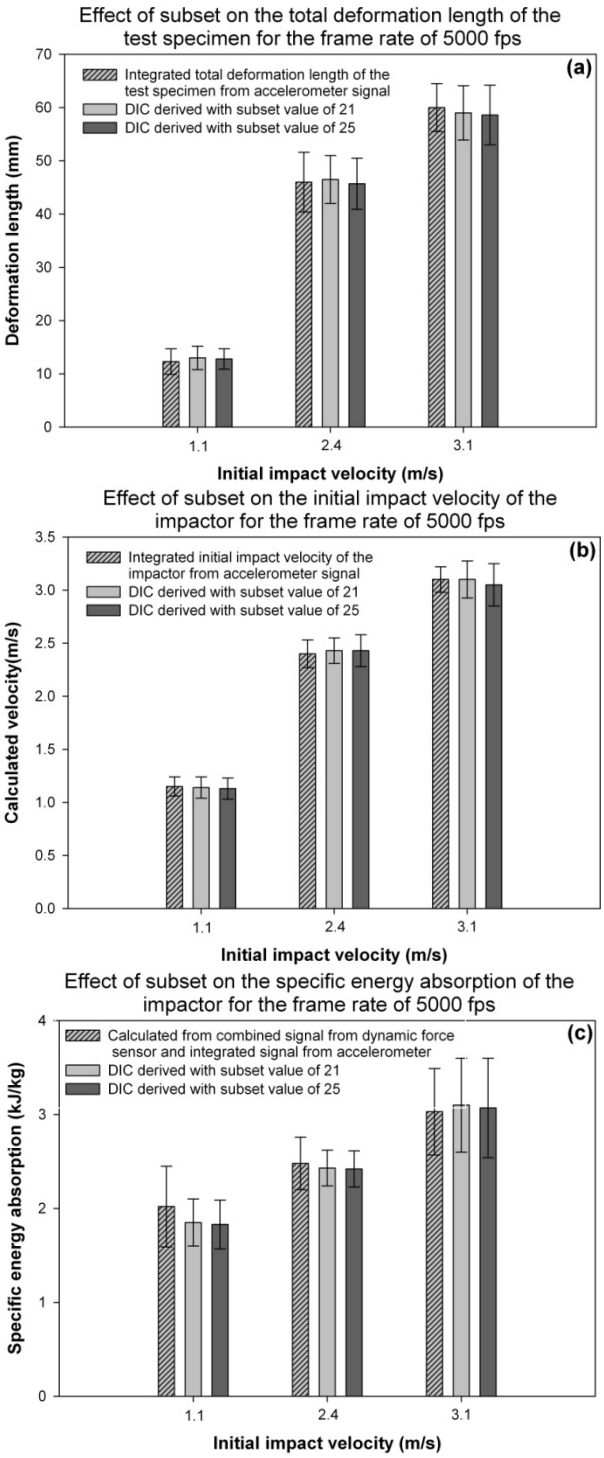

Figure 3-50: (a) Comparison of deformation length of the test specimen (error bar indicates the standard deviation). **(b)** Comparison of initial impact velocity (error bar indicates the standard deviation)**. (c)** Comparison of force-deformation histories of the test specimen (error bar indicates the standard deviation)**.**

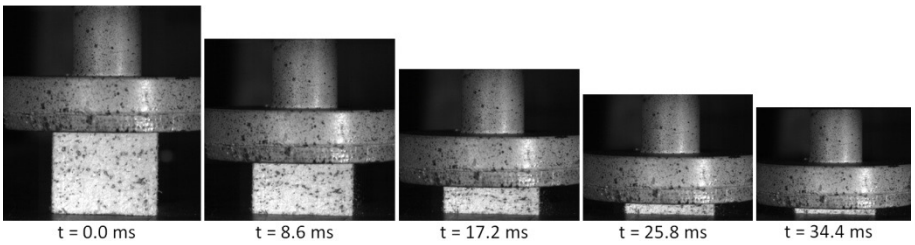

Figure 3-51: Progressive deformation stages of polyurethane foam subjected to an initial impact velocity of 1.6 m /s.

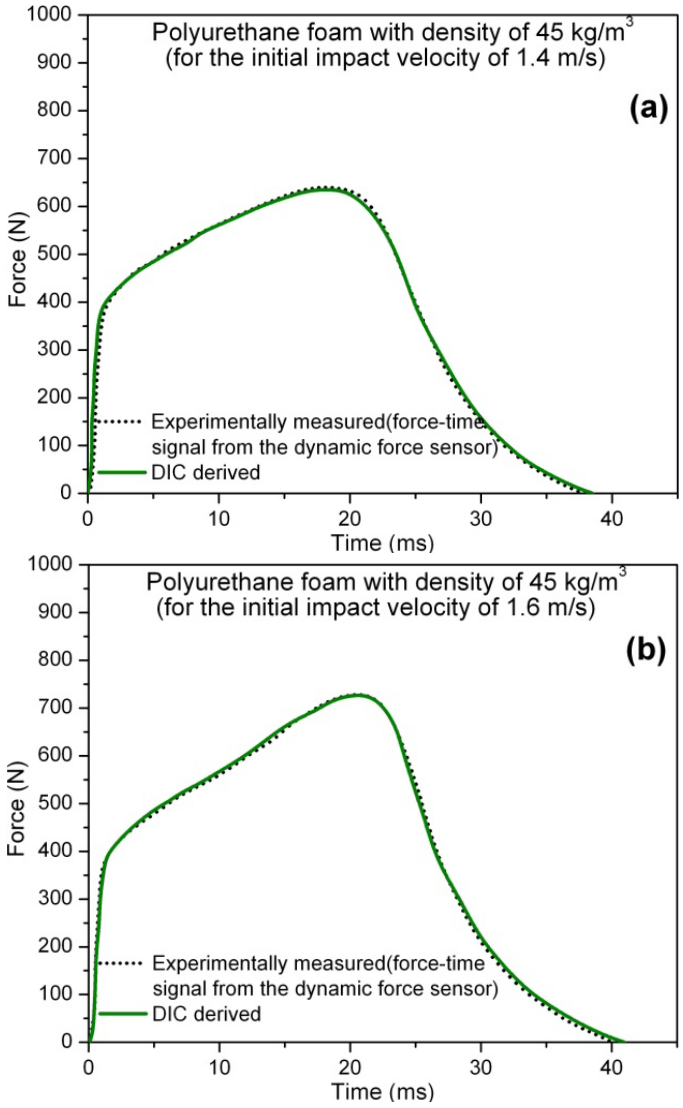

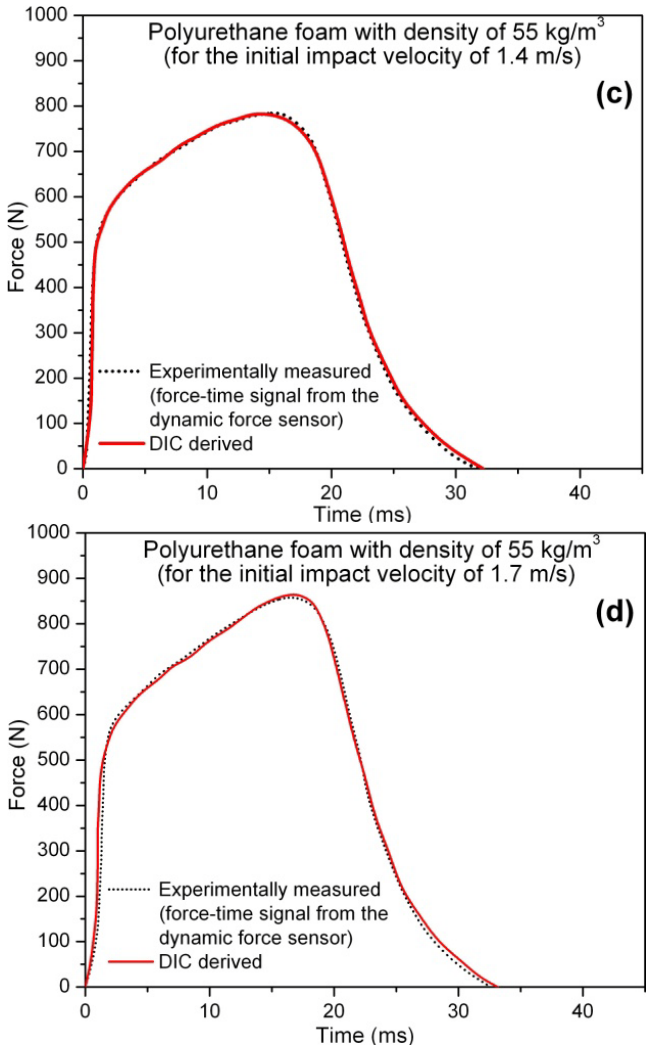

Figure 3-52: (a) Comparison of force-time history for polyurethane foam with density of 45 kg/m^3 subjected to an initial impact velocity of 1.4 m/s. **(b)** Comparison of force-time history for polyurethane foam with density of 45 kg/m^3 subjected to an initial impact velocity of 1.6 m/s. **(c)** Comparison of force-time history for polyurethane foam with density of 55 kg/m^3 subjected to an initial impact velocity of 1.4 m/s. **(d)** Comparison of force-time history for polyurethane foam with density of 55 kg/m^3 subjected to an initial impact velocity of 1.7 m/s.

3. 9. 7. Conclusions

In this section we demonstrated that the digital image correlation technique can be adopted for axial impact loading applications to calculate the test parameters such as deformation length of the specimen, impact velocity and the corresponding reaction force at the impactor end in a contactless manner. In order to prove this, axial impact tests were conducted with different test specimens (recyclable empty beverage cans

and polyurethane foam with different densities). The calculated results from the digital image correlation technique were compared with the experimentally measured data. A good correlation was obtained between these two cases. The effect of frame rate and the subset size on the quality of derived parameters are studied. It was found that the frame rate plays a role to capture the peak crush load of the beverage cans which showed a high fluctuation in the load-time history. However, the DIC results for polyurethane foam with different densities showed a very good correlation with the experimental results for a lower frame rate of 5000 fps. Hence, the DIC technique can be used to measure the dynamic parameters for an axial impact testing condition.

3. 10. Conclusions and future developments

To conclude a short overview is given what has been discussed in this chapter. To understand the crushing characteristics of empty recyclable metal beverage cans (failure modes and the corresponding energy absorption) axial quasi-static and impact experiments have been conducted. The failure patterns and the corresponding performance of the beverage can were well studied by using experimental, analytical and numerical approaches. Because of a very high D/t ratio (~937), quasi-static results showed non-uniform crushing patterns (local wall buckling and folding). However, the results from the impact tests showed a progressive crushing failure pattern for all initial impact velocities (2.2 m/s, 3.1 m/s, 3.8 m/s, 4.4 m/s and 4.9 m/s). The failed beverage can showed an asymmetric (diamond mode) deformation pattern consistently. Furthermore, throughout the crushing process the material of the beverage cans showed a strong dependency for strain rate and strain hardening effects. The influence of these two parameters is evident from all the experimentally measured load-deformation curves.

In order to predict the energy absorption capability of the beverage can an analytical model is proposed including the strain rate and strain hardening effects using *Cowper-Symonds* and *Ludwik* equations respectively. The results from this model provided a very good correlation with the experimental results. However, for a particular initial impact velocity this model requires few inputs such as folding length and the number of triangular folds. If the experimental failure patterns are established, then an accurate prediction of the crushing parameters is possible. If not, these parameters can be varied and accordingly a range of crushing parameters can be proposed.

Further investigation with the finite element simulations for the impact of beverage cans gave an opportunity to understand the impact process in detail. The developed numerical model using the *Johnson-Cook* material model captured the strain rate

and strain hardening effect of the material. There was a good correlation observed for the mean crush load and the specific energy absorption values. However, the numerical models predicted a slightly higher peak crush load for all cases. This may be due to the effect of considering a perfect structure of the beverage can. The effect of geometric imperfection on the peak crush load was evaluated for blast loading condition and this is presented in Chapter 6. Similarly, the investigation with entrapped and compressed air inside the beverage can confirmed the same results from the experiments. When the deformation length reaches more than 80 mm, the entrapped and compressed air inside the beverage can provided an additional resistance to the impactor and hence, further deformation was restricted. The entrapped air inside the beverage can increased the energy loss. Finally, a contactless method using *Digital Image Correlation (DIC)* technique is proposed to measure the dynamic parameters such as deformation length, impact velocity and reaction force at the crushing end of the test specimen. The DIC derived parameters are compared with the experimentally measured sensor results. Furthermore, the effect of frame rate and the subset on the quality of the results are explored. The results from the analyses showed promising results. Hence, we propose this technique to measure the impact parameters for such axial impact loading applications.

Besides all of the above mentioned works, the deployment of the beverage cans for the impact and blast loading application needs further investigations on the macro-foam structure. As mentioned in the Chapter 1, these beverage cans can be arranged in two different macro-foam configurations (axial and radial). Hence, understanding the behaviour of such macro-foams for impact loading is very important for the final usage in the sacrificial cladding structure. The developed analytical and numerical models can be used as a start point for this investigation. Furthermore, these approaches have inherent advantages such as faster and less infrastructure to carry out the analyses.

Bibliography

[1]. Karagiozova, D. and Alves, M., *Transition from progressive buckling to global bending of circular shells under axial impact--Part I: Experimental and numerical observations.* International Journal of Solids and Structures, 2004. **41**(5-6): p. 1565-1580.

[2]. Karagiozova, D. and Alves, M., *Transition from progressive buckling to global bending of circular shells under axial impact--Part II: Theoretical analysis.* International Journal of Solids and Structures, 2004. **41**(5-6): p. 1581-1604.

[3]. Abramowicz, W. and Jones, N., *Transition from initial global bending to progressive buckling of tubes loaded statically and dynamically.* International Journal of Impact Engineering, 1997. **19**(5-6): p. 415-437.

[4]. Jones, N. and De Oliveira, J. G., *Impulsive loading of a cylindrical shell with transverse shear and rotatory inertia.* International Journal of Solids and Structures, 1983. **19**(3): p. 263-279.

[5]. Singace, A. A., *Axial crushing analysis of tubes deforming in the multi-lobe mode.* International Journal of Mechanical Sciences, 1999. **41**(7): p. 865-890.

[6]. Horton, W., Bailey, S. and Edwards, A., *Nonsymmetric buckle patterns in progressive plastic buckling.* Experimental Mechanics, 1966. **6**(9): p. 433-444.

[7]. Pugsley, A., *On the crumpling of thin tubular struts.* Quartely Journal of Mechanics Applied Mathematics, 1979. **32**(1): p. 1-7.

[8]. Johnson, W., Soden, P. and Al-Hassani, S., *Inextensional collapse of thin-walled tubes under axial compression.* The Journal of Strain Analysis for Engineering Design, 1977. **12**(4): p. 317-330.

[9]. Andrews, K. R. F., England, G. L. and Ghani, E., *Classification of the axial collapse of cylindrical tubes under quasi-static loading.* International Journal of Mechanical Sciences, 1983. **25**(9-10): p. 687-696.

[10]. Singace, A. A., El-Sobky, H. and Petsios, M., *Influence of end constraints on the collapse of axially impacted frusta.* Thin-Walled Structures, 2001. **39**(5): p. 415-428.

[11]. Reddy, T. Y. and Zhang, E., *Effect of strain-hardening on the behaviour of axially crushed cylindrical tubes.* In:WB Lee, Editor. Advances in engineering plasticity and its applications. London:Elsevier, 1993: p. 755-762.

[12]. Alexander, J. M., *An approximate analysis of the collapse of thin cylindrical shells under axial load.* Quart. J. Mech. App. Math. , 1960. **13**: p. 10-15.

[13]. Abramowicz, W. and Jones, N., *Dynamic axial crushing of circular tubes.* International Journal of Impact Engineering, 1984. **2**(3): p. 263-281.

[14]. D.Karagiozova, N. J., *Inertia effects in square tubes sujected to an axial impact, in: N.Jones, C.A .Brebbia and A.M. Rajendran (Eds.).* WIT Transactions on Engineering Sciences, 2005. **49**(Structures under Shock and Impact VII): p. 531-540.

[15]. Jones, N., *Energy absorption effectiveness of thin-walled strucutres under static and dynamic axial crushing loads.* WIT Transactions on Engineering Sciences, 2005. **49**(Impact Loading of Light Weight structures): p. 273-287.

[16]. Jones, N. and Hsu, S. S. *Quasi-static and dynamic axial crushing of circular and square stainless steel tubes.* Structures under SHOCK AND IMPACT, 2000. **VII**: p. 169-178.

[17]. Wierzbicki, T., Bhat, S. U., Abramowicz, W. and Brodkin, D., *Alexander revisited--A two folding elements model of progressive crushing of tubes.* International Journal of Solids and Structures, 1992. **29**(24): p. 3269-3288.

[18]. Singace, A. A., Elsobky, H. and Reddy, T. Y., *On the eccentricity factor in the progressive crushing of tubes.* International Journal of Solids and Structures, 1995. **32**(24): p. 3589-3602.

[19]. Singace, A. A. and Elsobky, H., *Further experimental investigation on the eccentricity factor in the progressive crushing of tubes.* International Journal of Solids and Structures, 1996. **33**(24): p. 3517-3538.
[20]. Abramowicz, W. and Jones, N., *Dynamic progressive buckling of circular and square tubes.* International Journal of Impact Engineering, 1986. **4**(4): p. 243-270.
[21]. Amdahl, J. and Soreide, T. H., *Energy absorption in axially compressed cylindrical shells with special reference to bulbous bows in collision.* Norwegian Maritime Research, 1981(4): p. 2-11.
[22]. Pugsley, A. and Macaulay, M., *The large-scale crumpling of thin cylindrical columns.* Quarterly Journal of Mechanics Applied Mathematics, 1960. **13**(1): p. 1-9.
[23]. *Private communication from TATA Steels (earlier Corus), in The Netherlands to the Department of Materials Science and Engineering, Ghent University, Belgium.* 2010.
[24]. http://www.ball-europe.com (dated 02-06-2011).
[25]. http://www.mpma.org.uk (dated 02-06-2011).
[26]. Johnson, G. R. and Cook, W. H., *Fracture characteristics of three metals subjected to various strains, strain rates, temperatures and pressures.* Engineering fracture mechanics, 1985. **21**(1): p. 31-48.
[27]. Lesuer, D., *Experimental Investigations of Material Models for Ti-6Al-4V Titanium and 2024-T3 Aluminum.U.S. Department of Transportation.DOT/FAA/AR-00/25,Sept. 2000*
[28]. Markiewicz, E., Ducrocq, P. and Drazetic, P., *An inverse approach to determine the constitutive model parameters from axial crushing of thin-walled square tubes.* International Journal of Impact Engineering, 1998. **21**(6): p. 433-449.
[29]. Gonzales., M. A. C., Barrios., D. B. i., Lima., N. B. d. and Goncalves., E., *Importance of considering a material micro-failure criterion in the numerical modelling of the shot peening process applied to parabolic leaf springs* in *Latin American journal of Solids and Structures*. 2010. **7:**. p. 21-40.
[30]. http://machinedesign.com/article/sensor-sense-piezoelectric-force-sensors-0207 (dated 02-06-2011).
[31]. http://www.pcb.com/techsupport/tech_accel.php (dated 02-06-2011).
[32]. *Linear magnectic measurement system Limes L150/B2 data sheet by Kubler 2008.*
[33]. http://www.directindustry.com/prod/kubler/linear-measurement-systems-1934-62193.html (dated 02-06-2011).
[34]. *User manual MathCad.* Mathsoft Engineering & Education, 2005.
[35]. Soderberg, A. and Sellgren, U., *A report on " Modelling of strain hardening and strain rate hardening of dual phase steels in finite element analysis of energy-absorbing components".* Machine Design, Royal Institute of Technology (KTH), Sweden.
[36]. *ABAQUS User manual.* ABAQUS, Inc. and Dassault Systèmes 2007.
[37]. Li, E. B., Tieu, A. K. and Yuen, W. Y. D., *Application of digital image correlation technique to dynamic measurement of the velocity field in the deformation zone in cold rolling.* Optics and Lasers in Engineering, 2003. **39**(4): p. 479-488.

[38]. Vanlanduit, S., Vanherzeele, J., Longo, R. and Guillaume, P., *A digital image correlation method for fatigue test experiments.* Optics and Lasers in Engineering. **In Press, Corrected Proof**.

[39]. Huang, Y. H., Liu, L., Yeung, T. W. and Hung, Y. Y., *Real-time monitoring of clamping force of a bolted joint by use of automatic digital image correlation.* Optics & Laser Technology, 2009. **41**(4): p. 408-414.

[40]. Tarigopula, V., Hopperstad, O. S., Langseth, M., Clausen, A. H. and Hild, F., *A study of localisation in dual-phase high-strength steels under dynamic loading using digital image correlation and FE analysis.* International Journal of Solids and Structures, 2008. **45**(2): p. 601-619.

[41]. Knauss, W.G. C. I. and Huang, Y. *Mechanical measurements at the micron and nanometer scales.* Mech Matter, 2003(35): p. 217-31.

[42]. Sutton M. A, Mingqi, C., Peters, W. H, Chao, Y. J. and McNeil, S.R, *Application of an optimized digital image correlation method to planar deformation analysis.* Image Vision Comput, 1986. **4(3)**: p. 143-50.

[43]. Vendroux, G. and Knauss. W.G, *Submicron deformaiton field measurements. Part 2: improved digitial image correlation.* Exp Mech, 1998. **38(2)**: p. 86-91.

[44]. Lecompte, D., Smits, A., Bossuyt, S., Sol, H., Vantomme, J., Van Hemelrijck, D. and Habraken, A. M., *Quality assessment of speckle patterns for digital image correlation.* Optics and Lasers in Engineering, 2006. **44**(11): p. 1132-1145.

Chapter 4

Close-range Air Blast Loading on Recyclable Empty Metal Beverage cans

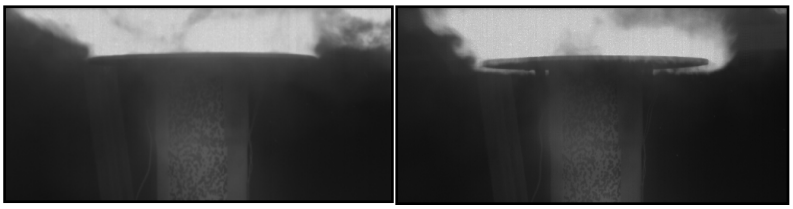

Overview

This chapter deals with the experimental and (decoupled) numerical study on empty metal beverage cans. Close-range free air blast tests have been conducted to understand the crushing behaviour and the energy absorption of a single empty beverage can in detail. To conduct such an air blast test a special small-scale test set-up was designed and manufactured. The effect of skin plate surface area and its nature on the blast parameters is studied. Furthermore, the effect of inertia of the skin plate on the crushing performance of the beverage can is evaluated. Tests have been conducted with different plates (made of aluminium and sandwich composite materials) with different masses which represented the skin plate of the proposed sacrificial structure. The measured blast parameters from the experimental tests were compared with ConWep predicted data. Furthermore, the influence of the finite surface area of the skin plate on the clearing of the reflected pressure waves was also studied. The deformation behaviour and the corresponding energy absorption of empty beverage cans were captured. From the experimental blast results, it was observed that a part of the impulse was lost before it transfers to the non-sacrificial structure (non-conservation of linear momentum). In order to study this phenomenon in detail a decoupled numerical analysis was carried out using the experimentally measured reflected pressure time histories. The results from this analysis are compared with the experimental results

4. 1. Introduction to blast or explosive load

An *explosion or blast* phenomenon is a rapid release of stored potential energy characterized by a bright flash and an audible blast which expands the shock wave in radial direction. Explosions can be categorized on the basis of their nature as physical, nuclear or chemical events. There are a number of possible situations that may cause an explosion such as that of a sudden relief of compressed air in a tire, a sudden release of pressurized steam in a boiler, mixing of two liquids at different temperatures or that from detonation of solid high explosives. Explosive materials can be classified based on their physical state as *solid, liquid and gases*. Out of that the effects of solid explosives are well characterized or best known. Due to this fact the solid explosives are used for many different purposes. They can also be classified on the basis of their sensitivity to ignition as *primary* and *secondary* explosive. The former explosive can be easily detonated by simple ignition from a spark, flame or impact. Examples of such materials are lead azide, lead styphnate, mercury fulminate and silver azide etc., Secondary explosives can be detonated less easily than primary explosives. When a secondary explosive is detonated, it creates *shock waves* which can result in widespread damage to the surroundings. Examples of such materials are tri-nitrotoluene (TNT), nitroglycerine, RDX (cyclonite) etc.

4. 1. 1. Air blast parameters

A *shock wave* is defined as a discontinuity in pressure, temperature and density in air or another medium [1-4]. The detonated shock wave has a very high magnitude of pressure (in the order of 10 – 30 GPa) proceeding outwards at approximately 7000 - 8000 m/s [1-3]. This violent release of energy will be followed by the spherical expansion of the blast wave into the surrounding air. As the shock front propagates the air particles are accelerated in the direction of the travelling front, which results in a net particle velocity. As a consequence, a layer of compressed air (blast wave) forms in front of the air volume containing most of the energy released by the explosion. The blast wave instantaneously increases to a value of pressure above the ambient atmospheric pressure. This is referred to as the *side-on overpressure or incident pressure* that decays as the shockwave expands outward from the explosion source (refer Figure 4-1). Furthermore, Figure 4-2 shows an idealistic representation of a blast wave profile at a given distance from the centre of explosion.

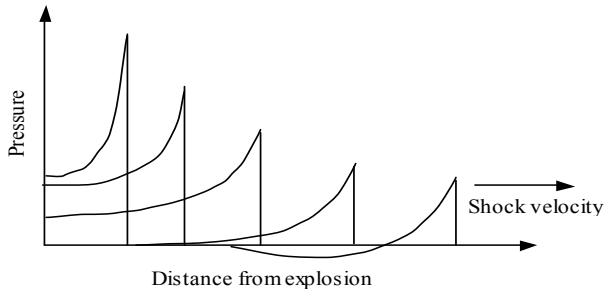

Figure 4-1: Blast wave propagation.

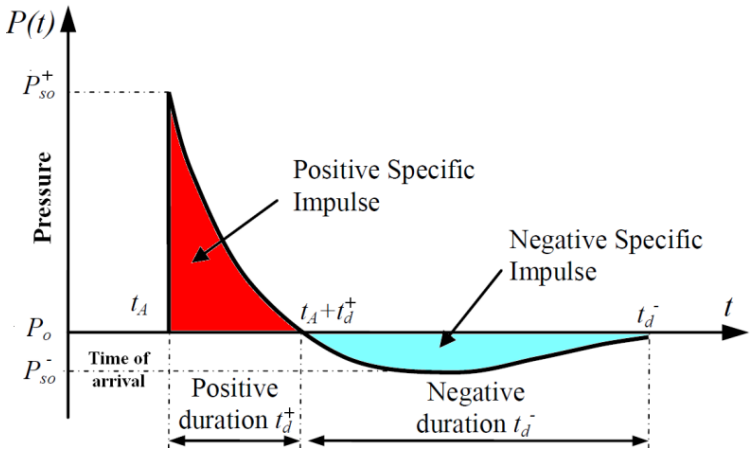

Figure 4-2: Typical pressure-time profile of air blast wave.

The peak incident pressure decays exponentially till it reaches atmospheric pressure. The first part of the blast wave is termed as the *positive phase*. Consequently, there is a *negative phase* where the pressure drops below the atmospheric pressure. This negative phase can be understood as an elastic rebound of the air mass behind the shock. Usually, the negative phase will have a longer duration and a lower intensity than the positive duration. For sacrificial cladding structure design, the negative phase is normally less important compared to the positive phase. However, in some cases it is important to consider the effects of the negative phase, e.g. when considering damage of windows or in a case with heavy structures having a response time longer than the positive phase. Furthermore, it may also be applicable to sacrificial cladding structure; but further details about this statement can be found in Part IV of this dissertation. The entire blast phenomenon can be modelled using the following *Friedlander* equation (Equation (4.1)),

$$p(t) = p_{\max}\left(1-\frac{t}{t_p}\right)\exp\left(-\frac{at}{t_p}\right) \tag{4.1}$$

where "t_p" is the positive phase duration and parameter "a" is the wave number (decay rate) which corresponds to the maximum pressure $p_{\max}$. While encountering an obstruction in their path the incident blast waves get reflected and the total magnitude of the *reflected pressure* is much higher than the incident pressure. Very often in literature the total pressure (incident + reflected) is mentioned as the reflected pressure only [5-8]. Hence, in this dissertation also the same terminology is used. The nature of the reflection depends upon the magnitude of the *incident pressure* (which depends on the size and shape of the charge), *angle of incidence, stand-off distance* and the *nature of the reflected surface* [1, 2]. The nature of the reflected pressure is very similar to the incident pressure (Figure 4-2) and it can be modelled using Equation (4.1) with different decay rate. The increase in the magnitude of the reflected pressure will be the largest for the *normal reflection* case (where the direction of motion of the wave is perpendicular to the surface at the point of incidence). For a longer stand-off distance the normal reflection of blast waves will result in a reflected pressure of about twice of its incident value. However, for a shorter stand-off distance the reflected blast waves can reach values several times larger in magnitude compared to that of its incident value. In extreme cases, the reflected pressure has the ability to reach up to 20 times of its incident value [1]. Figure 4-3 illustrates the incident and reflected pressure values for both the positive and the negative phase of a blast wave at different scaled distances. The pressure increase during reflection is due to the conversion of the kinetic energy of the air immediately behind the shock front into internal energy as the moving air particles are decelerated at the surface [7]. A shock front striking a surface at an angle differing from that of normal reflection is termed as *oblique reflection*. As the stand-off distance increases, the duration of the positive-phase blast wave increases resulting in a lower-amplitude, longer-duration shock pulse. Charges situated extremely close to a target structure impose a high intensity pressure load over a localized region of the structure; charges situated further away produce a lower-intensity, longer-duration uniform pressure distribution over the entire structure. Besides considering the magnitude of the peak incident and reflected pressures and the corresponding positive duration it is very important to consider the *specific impulse* from the respective pressure-time profiles. The specific impulse from the positive and negative phase can be calculated by using the following equations.

$$I_s^+ = \int_{t_a}^{t_a+t^+} p(t) \cdot dt \quad [\text{kN} \cdot \text{s}] \tag{4.2}$$

$$I_s^- = \int_{t_a+t^+}^{t_a+t^++t^-} p(t) \cdot dt \quad [\text{kN} \cdot \text{s}] \tag{4.3}$$

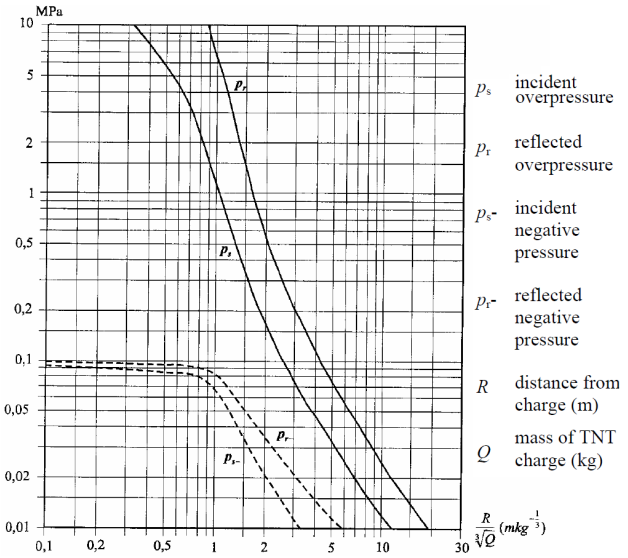

Figure 4-3: Incident and reflected overpressure and negative pressure, respectively, as a function of the scaled distances for detonation of a spherical TNT charge in free air (reproduced from ref.[8]).

4. 1. 2. Types of blast loading

Based on the location of the charge and the corresponding detonation and interaction with engineering structures, blast loading can be classified into the following categories.

(i) ***free air blast*** – detonation takes place in air. The interaction of blast pressure with the ground surface can be neglected compared to the interaction with engineering structures.

(ii) ***air blast*** – the blast pressure interacts with structure(s) before it reaches to the ground surface.

(iii) ***surface blast*** – the detonation takes place just above the ground surface. The pressure wave will be reflected and reinforced by the ground surface. The incident and the reflected waves travel as a single wave in the form of a hemisphere into the undisturbed atmosphere. Because of the above process the surface blast creates a higher pressure compared to the case of a free air explosion.

(iv) ***tunnel blast*** **–** a blast inside a tunnel will initially give a complicated event due to the blast wave reflections against all sides of the tunnel (walls, floor and roof). However, at a certain distance from the centre of explosion the propagation of the two shock fronts propagating in opposite longitudinal directions will be mainly one-dimensional and planar. In a tunnel with a constant cross-section this one-dimensional propagation of

the blast waves leads to higher pressures, and longer durations of the blast waves compared to the case with a spherical expansion of the shock front.

Apart from the above stated cases there are other kinds of explosions such as underground explosion and underwater explosion. The details of those explosions are not covered in this dissertation. For the clarification, the contents of this dissertation deal with the severe dynamic loads that arise from the detonation of air blast and tunnel blast loading of C4. The air blast approach was used for the tests which were conducted with a single test specimen (empty beverage can or composite tube). For representative sacrificial cladding structures (an array of beverage cans or composite tubes) the tunnel blast approach was used to create a perfectly plane high pressure shock wave at the other end. The details of this study are presented in Part IV of this dissertation.

4. 1. 3. Blast wave scaling laws

In blast wave analysis, the approach of scaling of blast waves is a common practice. Among the available scaling laws the "*Hopkinson-Cranz*" or "*cube-root*" scaling law is widely used. This scaling principle states that "*when two explosive charges of identical geometry and of the same explosive but of different size are detonated in the same atmosphere and at identical scaled distances, then the same blast overpressures are produced*". The scaled distance (Z) can be given in the form (Equation (4.4)) [2, 9].

$$Z = {}^{R}\!/_{W^{1/3}} \tag{4.4}$$

where "*R*" is the distance from the centre of the explosive charge (m); *W* is the *equivalent mass of TNT* which is widely used for military applications (refer section 4. 1. 4. Using this scaling law the experimental test results are generalized and can be utilized in the general blast wave analysis and blast loading of varying explosive powers and distances. Figure 4-4 shows schematic implications of the Hopkinson-Cranz blast wave scaling law. An observer located at a distance "R" from the center of an explosive source of characteristic dimension "D" will be subjected to a blast wave with amplitude "p_{s0}", duration "t_0", and a characteristic time history. The integral of the pressure-time history is the impulse, designated as "I" (refer Figure 4-4). As shown in the same figure, most of the parameters are multiplied with a length scale factor, λ. The length scale ratio, λ= R′/R. The Hopkinson-Cranz scaling law states that an observer stationed at a distance "λR" from the center of a similar explosive source of characteristic dimension "λD" detonated in the same atmosphere will feel a blast wave of 'similar' form with amplitude "p_{s0}", duration "λt_0" and impulse of "λI". One important point is that the assumption of this scaling is valid

for spherical charge mass and may not be applicable for stronger shock waves that arise from very close-range detonations due to neglecting the effect of gravity and viscosity of the wave front.

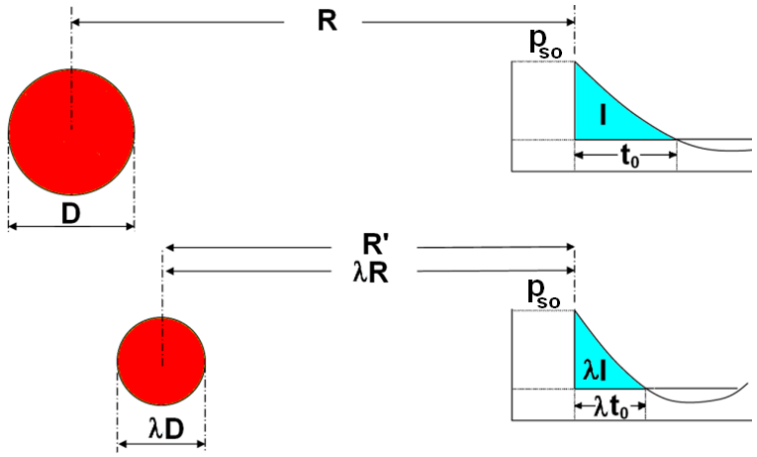

Figure 4-4: Basis of the "*Hopkinson-Cranz*" scaling law.

4. 1. 4. TNT equivalent

All blast parameters are primarily dependent on the amount of energy released by the detonation in the form of a blast wave. The energy release rate for an explosive material depends on the specific energy of that material. Furthermore, other important parameters such as detonation pressure and velocity are different for different explosive materials. Therefore, a common scale to assess the effectiveness of the explosive materials is necessary. Most of the carried out blast investigations and the corresponding developed knowledge were based on using TNT. Hence, to evaluate the effectiveness of an explosive material other than TNT, the term "TNT equivalent" is used. Examples of a few explosive materials and the corresponding TNT equivalent are given in Table 4-1.

Table 4-1: Physical properties and TNT equivalent of various explosive materials [2, 3, 9].

Name of the explosive	TNT equivalent	Specific energy (kJ/kg)	Density (kg/m^3)	Detonation velocity (m/s)	Detonation pressure (GPa)
TNT	1.0	4520	1600	6730	21.0
Pentolite	1.129	5110	1660	7470	28.0
HMX	1.256	5680	1900	9110	38.7
Comp.B	1.148	5190	1690	7990	29.5
C4	1.185	5360	1650	8700	34.0

4. 1. 5. Equivalent triangular pulse

For engineering analysis, the exponentially decaying reflected pressure wave can be modelled as an *equivalent triangular* pressure wave. The reflected pressure magnitude and duration of the simplified pulse is usually chosen such that the impulse (i.e. the area under the reflected pressure time history curve) is equal to the total impulse (or specific impulse) on the structure (Equation 4.5).

$$p(t) = p_{\max}\left(1 - \frac{t}{t_p}\right) \tag{4.5}$$

The shape of the triangular pulse depends on whether a structure experiences *diffraction* or *dragging* type loading (load imposed on a structure is largely due to drag of the blast wind) [3, 9]. For diffraction loading (or engulfing), the actual peak pressure is taken as the peak of the equivalent impulse load, and the equivalent duration is selected to give the same impulse per unit area as that of the actual pulse [3, 9]. For example, Figure 4-5(a) shows a typical reflected pressure time history measured from one of the explosion test. The corresponding equivalent triangular impulse loads for diffraction type or engulfing type is shown in the same figure (Figure 4-5(a)). Similarly, for dragging type loading, the actual positive duration is taken as the equivalent duration of the impulse load, and the equivalent pressure peak is selected to give the same impulse per unit area as that of the actual pressure pulse [3, 9]. As an example, a representative pressure profile and the corresponding equivalent triangular impulse is given in Figure 4-5(b).

4. 1. 6. Interaction with structures

While encountering a structure, the incident pressure wave gets reflected. The interaction of blast pressure waves with that structure is depending upon the radius of the pressure wave and the dimension of the structure. Based on this a brief introduction of three possible combinations are given below; and for all cases the structure is assumed to be fixed rigidly to the ground.

(a) ***large blast wave and large structure*** – pressure wave completely will engulf the structure. In addition to the higher crushing forces some translational forces will be generated (refer Figure 4-6 (a)).

(b) ***large blast wave and small structure*** – the entire structure will be engulfed and crushed by the blast wave. The overpressure acting on the structure will be more or less the same. A significant magnitude of drag force will be generated on the structure (refer Figure 4-6(b)).

(c) ***small blast wave and large structure*** – the loading on the structure will not be uniform. Analysis should be carried out separately to identify the response of the structure (refer Figure 4-6(c)).

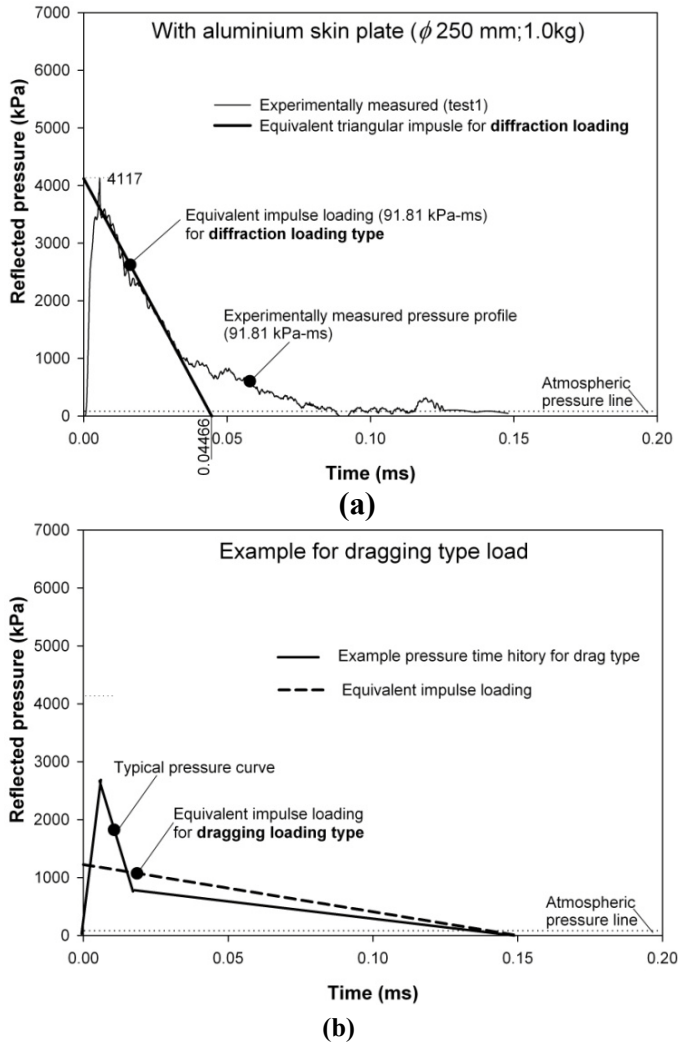

Figure 4-5: Equivalent triangular impulse load **(a)** for diffraction type and **(b)** drag type loading.

The natural period of the structure is another important factor which plays a major role during the interaction of blast pressure. From Equation (4.5), the total impulse and the corresponding positive duration can be calculated using Equation (4.6) and Equation (4.7) respectively.

$$I_{tot} = \frac{1}{2} \cdot p_{\max} \cdot t_p \quad [\mathrm{kN \cdot s}] \tag{4.6}$$

$$t_p = 2 \cdot I_{tot} / p_{\max} \quad [\text{s}] \tag{4.7}$$

If the structure is designed for blast resistance then the natural period of that structure should be greater than the positive duration of the blast which it is targeted for. Based on the positive duration and the natural period of a structure the following three loading regimes can be classified [2]:

$$40 < \omega \cdot t_p \qquad \left[\propto \frac{t_p(long)}{T(short)} \right] \Rightarrow \text{Quasi - static loading} \tag{4.8}$$

$$0.4 < \omega \cdot t_p < 40 \qquad \left[\frac{t_p}{T} \approx 1 \right] \Rightarrow \text{Dynamic loading} \tag{4.9}$$

$$0.4 > \omega \cdot t_p \qquad \left[\propto \frac{t_p(short)}{T(long)} \right] \Rightarrow \text{Impulse loading} \tag{4.10}$$

where ω is the natural frequency of the structure (Hz); T is the natural period of the structure (s); t_p is the positive duration of the blast (s).

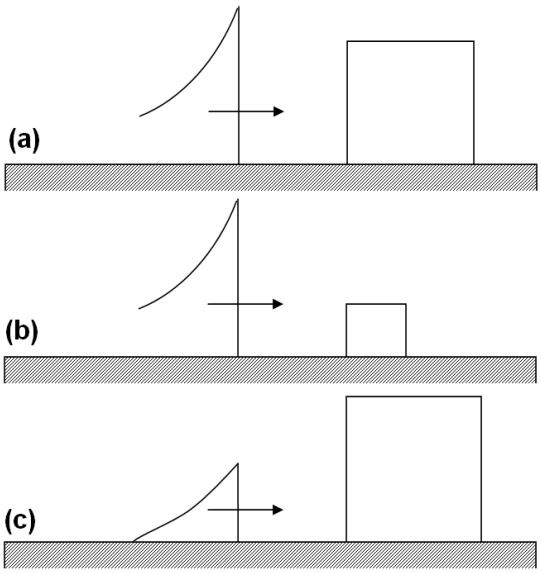

Figure 4-6: (a) Large blast wave large structure **(b)** large blast wave with small structure (c) small blast wave with large structure (reproduced from [2]).

4. 2. Working principle of a sacrificial cladding structure – an example

4. 2. 1. Working principle

The schematic representation of the proposed sacrificial cladding structure and the corresponding function of the front skin panel and the inner core members were well explained in Chapter 1. To limit the focus only on the sacrificial cladding structure, the emphasis is given only to the sacrificial cladding structure and not to the non-sacrificial structures such as concrete elements. In this section, the working principle of a sacrificial cladding structure is presented with a numerical simulation example. As seen in the previous section, out of three different loading regimes most civil engineering structures and sacrificial cladding structures will receive an impulse load during an explosion event. The reason is that the positive duration of the blast load will be much shorter than the natural period of the structure. Furthermore, to simplify the analysis only the axial blast pressure loading is considered throughout this dissertation (where the direction of the striking shock front is perpendicular to the surface of the front skin plate). In order to protect civil engineering structures from the blast load the proposed sacrificial cladding structure should be mounted or assembled in front of those structures. During a blast loading the sacrificial cladding structure will receive a high load (p_0), short duration impulse (refer Figure 4-7). The function of the sacrificial cladding structure as a whole is to change the force-time distribution from a high load, short duration to impulse to a low load, long duration impulse (refer Figure 4-7). To avoid permanent damage in the main structure (non-sacrificial structure), the failure load of the sacrificial cladding structure (F_{max}) should be kept well below the minimum elastic capacity of the non-sacrificial cladding structure. By doing so, the transferred peak force to the non-sacrificial structure can be minimised (Figure 4-7). The mechanism by which a sacrificial cladding structure does this, is absorbing energy through elastic, plastic or brittle deformations. During this process the *conservation of (linear) momentum* should be satisfied (which is explained in detail in the next section).

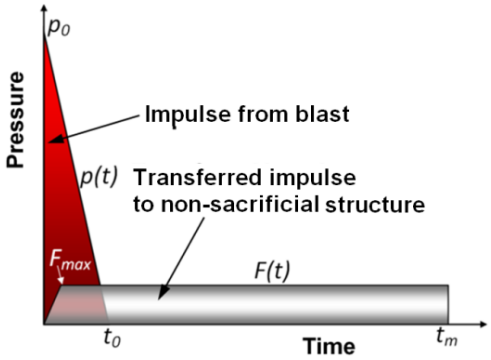

Figure 4-7: Working principle of a sacrificial cladding structure.

Furthermore, the blast loads typically produce very high strain rates (refer Figure 4-8). The strain rate and the corresponding strain hardening and its rate alter the dynamic mechanical properties of the target structures (sacrificial cladding structure). Hence, these factors should be thoroughly studied and taken into account while deploying a material for the inner core of a sacrificial cladding structure.

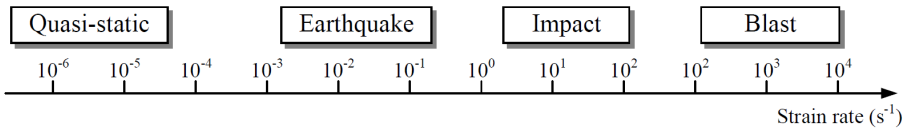

Figure 4-8: Strain rates associated with different types of loading [2].

4. 2. 2. Example

In order to explain the function of the sacrificial cladding structure in detail, the numerical simulation of a single inner core member is presented in this section. The important aspect during a blast loading on a (sacrificial) structure is the *conservation of (linear) momentum,* i.e. the impulse from the blast should be conserved with the impulse transferred to the non-sacrificial structure. The following example will give a detailed understanding of this point. Let us consider a cylindrical inner core member (cylindrical tube) which is made of aluminium 2024 (outer diameter ϕ 25 mm; wall thickness 0.25 mm; length 100 mm). To capture the strain rate and the strain hardening characteristics the *Johnson-Cook* material model was used; the corresponding *Johnson-Cook* material properties were adopted from [10]. To reduce the computation time the top skin plate and the non-sacrificial structure were modelled as rigid bodies. The mass and the diameter of the skin plate were assumed to be 0.55 kg and ϕ 250 mm respectively (refer Figure 4-9(a)). In order to simulate the blast pressure, a time dependent simplified equivalent pressure profile was applied on the top face of the skin plate (refer Figure 4-9(b)). An equivalent loading of 20g C4 with a stand-off distance of 30 cm was considered (corresponds to a peak reflected pressure of 4775 kPa and a positive duration of 0.066 ms). These data were derived from *ConWep*, a commercial tool available to calculate the blast parameters. The details of this tool are discussed later. It was assumed that the aluminium tube was rigidly fixed to the non-sacrificial structure. The displacement of the skin plate was allowed only in vertical crushing direction (axial pressure loading). The contact between the skin plate and the aluminium tube was assumed to be frictionless (hypothetical case). In order to limit the length, the further modelling details are not discussed in detail. All modelling details for a very similar loading case using empty beverage cans are discussed in Section 4. 6. To calculate the transferred impulse to the non-sacrificial structure, the force-time history was calculated at the interface between the aluminium tube and the non-sacrificial structure. It was assumed that the displacement of the skin plate was equivalent to the deformation length of the

test specimen (aluminium tube). Accordingly, the displacement and the corresponding velocity of the skin plate were measured from the skin plate.

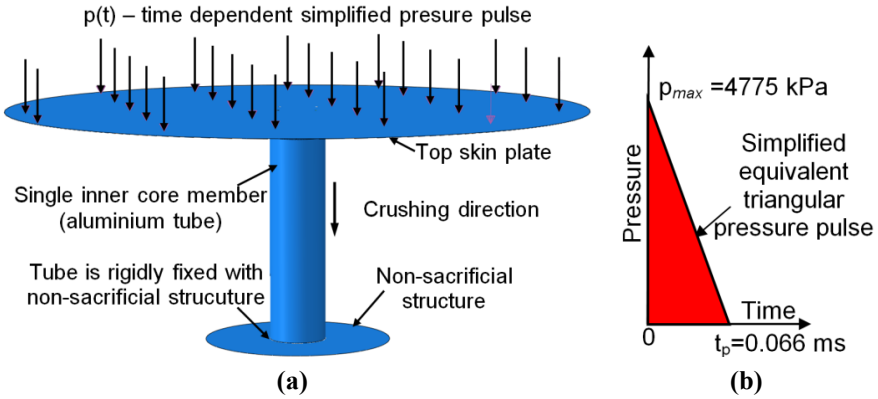

Figure 4-9: (a) Finite element modelling details of an aluminium tube subjected to blast loading **(b)** Simplified equivalent triangular pressure pulse.

Displacement and velocity of the skin plate

The finite element simulation was carried out for a total time period of 5 ms. Because of the applied time dependent blast pressure the momentum of the skin plate changed after overcoming its inertia and acquiring velocity. The maximum velocity of the skin plate (14 m/s) is achieved after the positive phase duration of the applied blast pressure (t_p = 0.066 ms); subsequently, the velocity of the skin plate was brought to zero due to the resistance offered by the aluminium tube at time t_{md} (refer Figure 4-10(a)). The skin plate velocity phase from zero to maximum and to t_{md} can be stated as the "*crushing phase"*. During this crushing phase the aluminium tube had undergone elastic and plastic deformation failure modes. The corresponding deformation-time history is shown in Figure 4-10(b). After achieving the maximum deformation length of the aluminium tube a very small quantity of elastic strain energy from the test specimen was given back to the skin plate. Due to this, the contact between the skin plate and the test specimen continued for a little while. As a result the velocity of the skin plate was recovered (to the direction opposite to the crushing) and reached a maximum value of approximately 1.0 m/s (refer Figure 4-10(a)). At that moment the contact between the skin plate and the test specimen was terminated. This phase can be stated as "*restitution phase"* of the skin plate. The restitution phase of the skin plate purely depends on the material behaviour of the inner core structure. If the inner core material is a purely elastic material all the absorbed energy during the crushing process will be given back to the skin plate. Then the velocity during the crushing phase will be equal to the velocity in the restitution phase. On the other hand, if the inner core material exhibits a perfectly plastic behaviour then the test specimen will not give any elastic

strain energy back to the skin plate. In that case the restitution velocity of the skin plate will be zero.

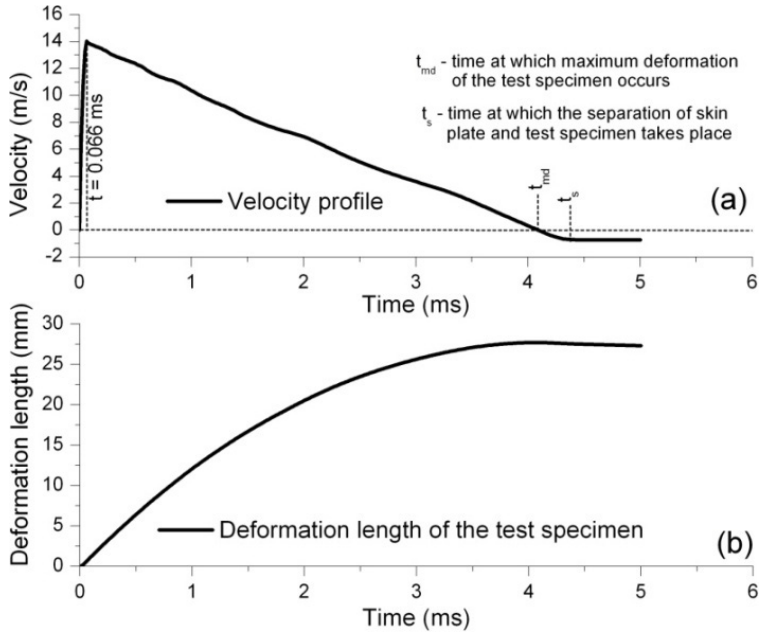

Figure 4-10: (a) Deformation – time history of the test specimen **(b)** Velocity profile of the impactor.

Although the purpose of this example is not to deal with a detailed initiation and progressive deformation of the test specimen the global plastic deformation failure modes of the test specimen are shown in Figure 4-11. The initial crushing stages of the aluminium tube showed an axisymmetric failure mode (concertina failure mode). However, the later time increments exhibited an asymmetric deformation mode (diamond crushing mode). The change in failure mode was due to the higher *D/t* ratio (100) of the aluminium tube [11-13].

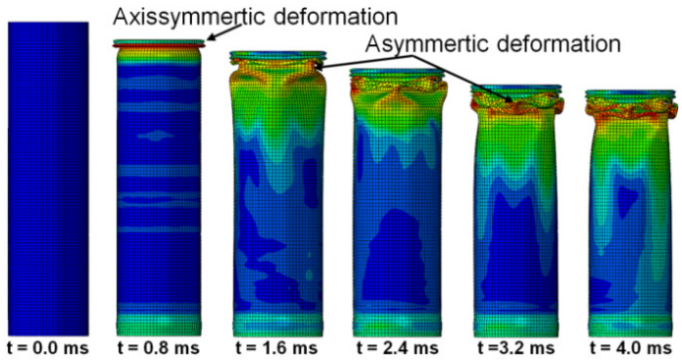

Figure 4-11: Deformation sequence of the aluminium tube.

Impulse and energy transfer

In order to understand the change in parameters the delivered impulse (I_{refl}) and the corresponding energy (E_{refl}) from the blast were calculated for the example by the following relations (Equation (4.11) and Equation (4.12)).

$$I_{refl}(t) = \int_0^{t_p} p(t) \cdot A_p \cdot dt \quad [\text{kN} \cdot \text{s}] \tag{4.11}$$

$$E_{refl}(t) = \int_0^{t_p} p(t) \cdot A_p \cdot v(t) \cdot dt \quad [\text{J}] \tag{4.12}$$

where t_p is the positive duration of the blast (0.066 ms); $p(t)$ is the time dependent reflected pressure applied to the top face of the skin plate (Pa); A_p is the area of the skin plate (m^2); $v(t)$ is the time dependent velocity of the skin plate (m/s). Similarly, the transferred impulse to the non-sacrificial structure (I_{trans}) and the corresponding energy absorbed by the aluminium tube (E_{abs}) were calculated using Equations (4.13) and Equation (4.14) respectively.

$$I_{trans}(t) = \int_0^{t} p(t) \cdot dt \ [\text{kN} \cdot \text{s}] \tag{4.13}$$

$$E_{abs}(t) = \int_0^{l_{\max}} F(l) \cdot dl \ [\text{J}] \tag{4.14}$$

where $F(l)$ is the instantaneous crushing load corresponding to the instantaneous crushing deformation length of the aluminium tube, dl (kN); l_{max} is the maximum or total deformation length of the aluminium tube (m). Now the calculated parameters with respect to time are presented in Figure 4-12(a-d). Figure 4-12(a) shows the force from the blast pressure delivered to the top face of the skin plate and the same figure also shows the corresponding delivered impulse (I_{refl}) with respect to time. This figure shows that a total of 7.8 N.s was applied to the top face of the skin plate during the positive duration 0.066 ms. The corresponding calculated energy profile from the blast using Equation (4.12) is shown in Figure 4-12(b). From this figure it can be seen that a total of 53 J was delivered to the skin plate. Similarly, the transferred impulse to the non-sacrificial structure and the corresponding absorbed energy by the aluminium tube are presented in Figure 4-12(c) and Figure 4-12(d) respectively. As mentioned earlier, the purpose of the sacrificial cladding structure is to alter the high force, short duration impulse to a low force and longer duration pulse. It can be noticed that the use of the aluminium tube changed the peak force from the blast (234 kN) to approximately 5 kN (refer Figure 4-12(a) and (c)); furthermore, the duration of the pressure pulse (0.066 ms) was stretched to a longer time (approximately 4.36 ms).

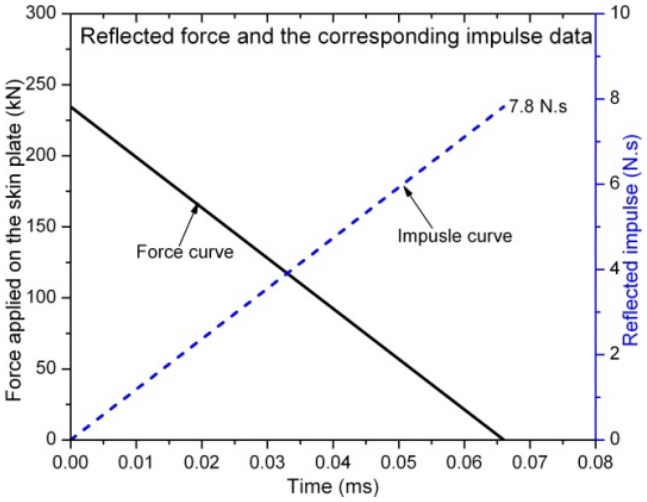
Reflected force and the corresponding impulse data
Force applied on the skin plate (kN)
Reflected impulse (N.s)
Time (ms)
7.8 N.s
Force curve
Impusle curve

(a)

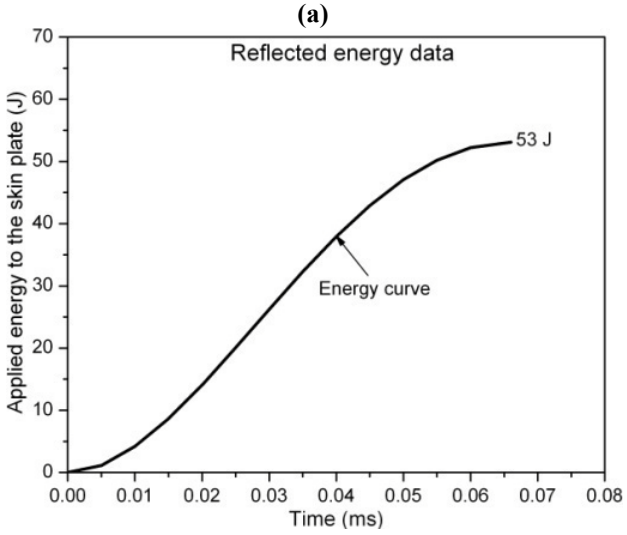
Reflected energy data
Applied energy to the skin plate (J)
Time (ms)
53 J
Energy curve

(b)

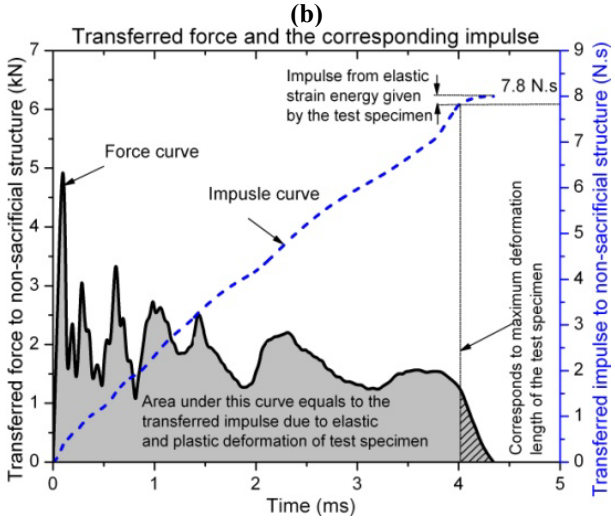
Transferred force and the corresponding impulse
Transferred force to non-sacrificial structure (kN)
Transferred impulse to non-sacrificial structure (N.s)
Time (ms)
Impulse from elastic strain energy given by the test specimen
7.8 N.s
Force curve
Impusle curve
Area under this curve equals to the transferred impulse due to elastic and plastic deformation of test specimen
Corresponds to maximum deformation length of the test specimen

(c)

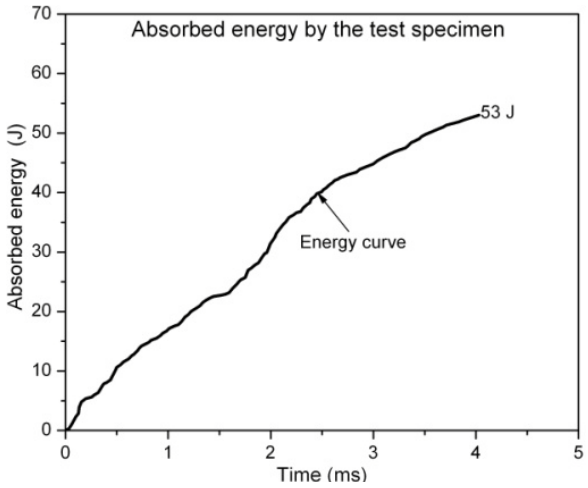

(d)

Figure 4-12: (a) Reflected impulse (load-time history) of the skin plate (ϕ 250 mm; 0.55 kg of mass) **(b):** Energy delivered by the reflected pressure wave to the skin plate (ϕ 250 mm; 0.55 kg). **(c):** Transferred impulse (load-time history) to the non-sacrificial structure due to the aluminium tube crushing. **(d)**: Energy absorbed due to the crushing of aluminium tube.

Comparing Figure 4-12(a) and Figure 4-12(c) shows that the reflected impulse and the transferred impulse are equal to the moment when the test specimen reaches its maximum deformation length. However, the total transferred impulse (8.0 N.s) was slightly higher than the total reflected impulse (7.8 N.s). Actually, the non-sacrificial structure experienced a higher impulse compared to the total impulse from the blast. The increase in impulse was due to an additional impulse from the restitution phase. Figure 4-12(c) shows the transferred force-time history to the non-sacrificial structure. The area below this complete curve equals to the total impulse transferred to the non-sacrificial structure. The shaded area equals to the impulse due to elastic and plastic deformation of the aluminium tube; the remaining area (shaded area covered with 45° inclined lines) corresponds to the impulse from the restitution phase. Hence the conservation of momentum equation for this can be written as Equation (4.15); assuming that the skin plate and the test specimen are separated by an infinitesimal distance before the start of crushing.

$$m_{sp} v_{sp,1} = (m_{sp} + m_{tube}) v_{sp,2} - m_{sp} v^{*}_{sp,1} \tag{4.15}$$

where m_{sp} is the mass of the skin plate (kg); $v_{sp,1}$ is velocity of the skin plate just before the start of crushing (m/s); m_{tube} is the mass of the aluminium tube (kg); $v_{sp,2}$ is the velocity of the skin plate during crushing (equivalent to the velocity of the crushing end of the test specimen)(m/s); $v^{*}_{sp,1}$ is the restitution velocity (opposite to

the crushing direction) (m/s) of the skin plate. The magnitude of $v^*_{sp,1}$ is depend upon the material and/or structural behaviour. If the material and/or structure of the inner core exhibits a perfectly plastic behaviour then the restitution phase of the skin plate can be avoided. However, for most of the cases the impulse transferred during the restitution phase is insignificant compared to the total transferred impulse. Furthermore, the effectiveness of a sacrificial cladding structure is determined based on the peak force and the corresponding force duration transferred to the non-sacrificial structure. The magnitude of the force and the corresponding duration of the restitution phase were very small compared to the total magnitude during the crushing phase. Hence, the impulse from the restitution phase will not make any adverse effect on the non-sacrificial structure. Furthermore, the amount of elastic strain energy stored during the crushing phase which will be given back to the skin plate during the restitution phase cannot be calculated easily using analytical methods. Hence, a validation of the impulse corresponding to the maximum deformation length for a structure which undergoes a large plastic deformation and/or brittle fracture can give enough information. Finally, it can be stated that impulse transfer is simply a conservation of momentum, thus the sacrificial cladding cannot prevent the impulse of the blast being transferred onto the structure upon which it is mounted. Its purpose is to spread out the blast impulse.

Similarly, the total absorbed energy by the aluminium tube was equal to the total energy delivered from the blast (53 J). An important point should be noted here that in the numerical simulation there was no friction included (between the skin plate to the aluminium tube; and self contact of the aluminium tube). Furthermore, the skin plate was modelled as a rigid body which means the bending stiffness of the skin plate is infinite and so, no elastic energy will be absorbed by the skin plate during blast loading. However, in real life events achieving the above assumptions is impossible. Hence, a part of energy will be utilised for different modes of energy dissipation. Therefore, the energy is not necessarily conserved during a blast event. Furthermore, apart from the available impulse from the blast the amount of energy transferred to the inner core highly depends on the inertia of the skin plate. This point is well discussed in experimental blast results section 4. 5. 7.

4. 3. Experimental close-range air blast loading on recyclable empty metal beverage cans

In literature, different materials and test specimen shapes have been tried out for the blast protection applications. Few researchers have proposed versatile solutions to the above problem. Guruprasad and Mukherjee [14, 15] have suggested a solution with layered mild steel plates. The results of their air blast experiments showed the perfect plastic collapse behaviour of mild steel plates. Furthermore, they have given

guidelines for the parameters which control the performance of a sacrificial structure (mode of deformation, impulse transfer to the non-sacrificial structure, energy absorption in plastic deformation and collapse space efficiency). Hanssen et al. [16] demonstrated that the ideal control of the impulse or pressure transferred to the main load bearing structure (non-sacrificial structure) is achieved by using perfectly plastic material as the sacrificial part. They have used aluminium foam with different densities as a sacrificial member. The general conclusion of this study was that the energy and impulse transfer to the non-sacrificial member increased by the surface effects of the plane panel.

Karagiozova et al.[17] studied the influence of inertia effects on circular and square shells subjected to explosive loads. They showed that the initial compression phase is important for the energy absorption of these structures when the blast load was transmitted by a small attached mass. Furthermore, the inertia interaction between the attached mass and the structure was greatly influenced by the dynamic mean load of crushing. Similarly, the influence of impact velocity and the material characteristics on the dynamic buckling response of circular tubes during an axial loading (quasi-static and impact) case were studied in [18, 19]. In this work, the buckling mode to global bending was explained in terms of the material yield stress, strain hardening and the strain-rate sensitivity. This paper also proved that the energy absorption performance of circular ductile tubes with high yield stress and low strain hardening is better than the one with low yield stress and high strain hardening. Similarly, the transition from initial global bending to progressive buckling on square and circular geometries was studied in [20]. Nurick et al. [21] studied the response of circular plates with clamped boundary conditions for contact blast loading. This work explained the onset thinning and subsequent tearing of plates at the boundary location. Longdon et al. [22, 23] conducted localised blast loading experiments on fibre-metal laminates with aluminium alloy and glass fibre reinforced polypropylene. They reported different failure modes such as diamond and cross-shaped back face damage, pitting, global displacement and ring buckling of the front face. These failure modes were correlated with material and geometric parameters and wave propagation effects.

Before designing any sacrificial structure in full-scale, the knowledge of the performance characteristics (peak crush load, energy absorption, deformation pattern, strain rate effect on material, etc.) of the individual sacrificial member is very important. Furthermore, the effect of skin plate variables such as the surface area, inertia and the surface roughness on the performance of the inner core has to be understood. To study the performance parameters, researchers often use shock tube apparatus to create a controlled pressure load on the structure [24, 25]. The advantage of this approach is that the pressure load is well controlled over the surface of the test specimen. Furthermore, phenomena such as diffraction and

reflections from the boundary structures can be avoided. Considering the development time this option was left out. Hence, an alternate small-scale test set-up was developed to understand the performance characteristics of an individual test specimen (empty beverage can) for an air blast loading. Close-range free air blast tests have been conducted with 20g of C4 with a stand-off distance of 30 cm. These parameters are constant for all blast tests conducted with empty metal beverage cans. The crushing characteristics and the corresponding energy absorption of the individual beverage can were studied in detail. All the tests were performed at *The Royal Military Academy of Brussels*, Belgium.

Normally during the analysis of a blast event, the blast reflected surfaces are considered to be infinite which will not allow any diffraction of pressure waves. Furthermore, for the simplification of analysis the exponentially decaying blast pressure can be modelled as an equivalent triangular impulse load [2, 14-16]. Calculating the specific impulse without considering the clearing of the reflected pressure waves (associated with the finite surface area of the reflected surface) will over predict the efficiency of the inner core structure. Hence, in this chapter the effect of clearing of the reflected pressure waves on the specific impulse is addressed by using different surface areas of the skin plates having the same mass. As seen in the previous section, an impulse loading will be transferred from the skin plate to the inner core when a sacrificial cladding structure is exposed to a blast pressure. The transferred impulse is depending upon the surface area, inertia and bending stiffness of the skin plate.

Often during the design of a sacrificial cladding structure, the above mentioned parameters are not considered. Furthermore, the effect of the nature of the reflected surface on the reflected pressure parameters is an open research area where considerable amount of study is needed. Understanding the effect of these parameters is very important for designing the sacrificial cladding structure. Hence, to study the above parameters close-range blast tests (20g of C4 with a stand-off distance of 30 cm) have been conducted with different skin plates (made of aluminium and sandwich composite materials). The measured blast parameters from the experimental tests were compared with *ConWep* predicted data. From the experimental blast results, it was observed that a part of the impulse was lost before it transfers to the non-sacrificial structure (*non-conservation of linear momentum*). In order to study this phenomenon in detail a decoupled numerical analysis was carried out in Abaqus v6.7-3 explicit code using the experimentally measured reflected pressure time histories. The results from this analysis are compared with the experimental results.

4. 4. Experimental test set-up

The geometry and material details of the used beverage cans have already been mentioned in Chapter 3. The schematic representation of the small-scale air blast test set-up which was used for conducting the blast tests is shown in Figure 4-13(a).

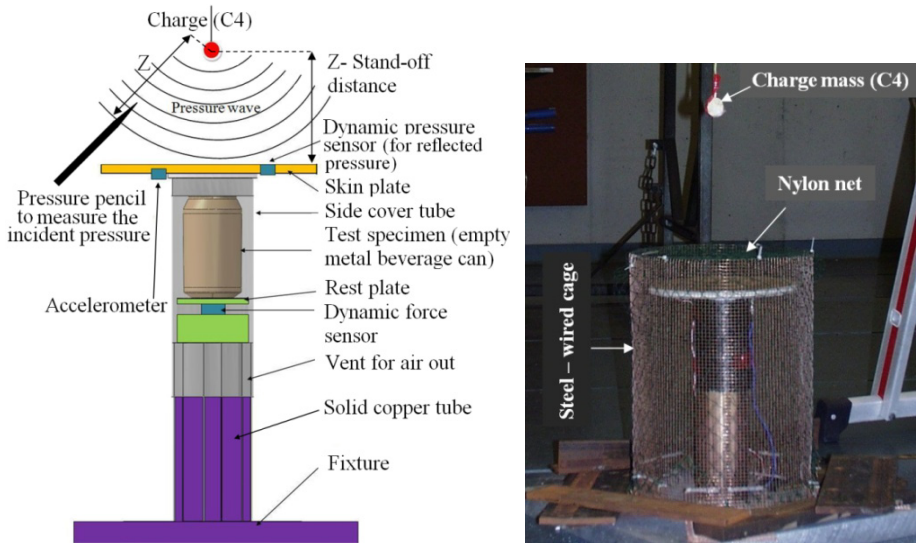

(a) **(b)**

Figure 4-13: (a) Schematic view of small-scale air blast test set-up. **(b):** Small-scale air blast set-up with steel wired cage.

An empty beverage can was mounted on a resting plate below which a dynamic load cell was connected to measure the transferred impulse (force-time history) to a solid copper tube. The details of the used sensors are given in the subsequent section. The solid copper tube which represented the non-sacrificial member was rigidly fixed to a heavy metal panel. The top cover which represents the skin panel of the sacrificial cladding structure was mounted over an empty beverage can. The skin panel was completely instrumented with an accelerometer and a pressure sensor to measure the acceleration of the skin plate and the reflected pressure from the top face of the skin plate respectively. The positions of the accelerometer and the pressure sensor were chosen close to the centre of the skin plate (70 mm from the centre of the skin plate). To simulate the real condition of air blast loading and to avoid the effect of side pressure (diffracted pressure) on the test specimen, a side cover tube was attached to the skin plate. When the test specimen deforms, the side cover tube can slide over the solid copper shaft. The outer diameter of the copper tube and the inner diameter of the side tube were chosen to have an adequate clearance to avoid excessive friction between them. Semi-circular cross-sectional vents were made at three locations on the copper tube throughout its length to eliminate the resistance offered by the air inside the set-up during blast loading. A steel-wired cage was made to

protect the data measuring sensors. The top of the cage was covered with a nylon net which is shown in Figure 4-13(b).

4. 4. 1. Skin plates

The diameter and thickness of the skin plates were chosen to restrict the maximum deflection to 10 and 20 mm at the free end for aluminium and sandwich composite skin plates respectively. Totally, five skin plates have been manufactured to study the effect of surface area, nature of reflected surface and the inertia of the skin plate on the deformation length and the corresponding energy absorption of an empty beverage can. To study the effect of surface area on the blast parameters and the clearing of reflected pressure waves, two skin plates have been used with different surface area (ϕ 200 mm and ϕ 250 mm) having the same mass (1.0 kg). These skin plates were made with aluminium grade 2024 T3 (refer Figure 4-14(a) and Figure 4-14 (b)). In order to study the effect of the nature of the reflected surface and the inertia, in addition to the aluminium skin plate with ϕ 250 mm, two other skin plates (ϕ 250 mm) have been used. These skin plates were made with sandwich composite materials. The materials used for manufacturing the composite skin plates were bi-axially balanced glass fibre mat, epoxy resin and polyurethane foam. The thickness of the top and bottom composite skin plates was in the range of 1.5 to 2.5 mm based on the mass requirement. Between the top and bottom composite plates a polyurethane foam with 7 mm thickness was used (Figure 4-14(c) and Figure 4-14 (d)). The used materials for the side covers were flexi-glass and carbon-epoxy composite for the aluminium and composite sandwich skin plates respectively. The length of the side tube was chosen 180 mm to have an adequate protection for the test specimen from the side pressure and to avoid oblique or offset loading during a blast event. To have a rigid crushing surface for the sandwich composite skin plates, a circular aluminium plate (ϕ 97 mm; 2 mm thick) was fixed to the bottom face of the skin plate in contact with the metal beverage can. The combined inertia of the sandwich composite skin plate and the side cover tube which represented the skin plate of the sacrificial structure was 0.53 kg and 0.36 kg (Figure 4-14). Apart from the above mentioned skin plates, an additional aluminium skin plate (fifth skin plate) was manufactured to study the effect of surface roughness of the reflected surface. The total mass of this skin plate was slightly higher than the rest (1.187 kg).

4. 4. 2. Instrumentation

Force Sensor

The used force sensor for all blast experiments is the *PCB force sensor model 202B*. A brief specification of this model is given in Table 4-2. The working principle of

this force sensor is very similar to the one which was discussed for the axial impact tests (refer Chapter 3).

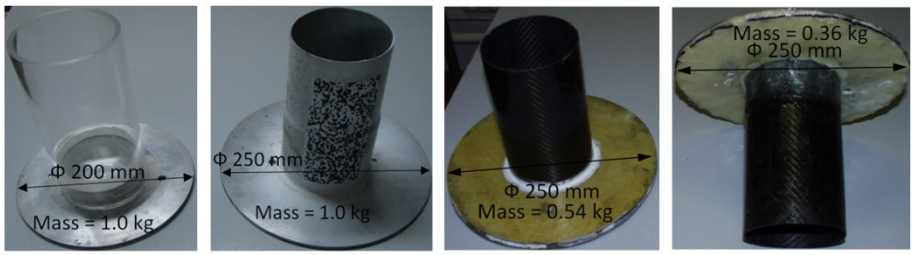

Figure 4-14: Aluminium and sandwich composite skin plates.

Table 4-2: Specification of the *PCB 202B force sensor* [26].

Sensitivity	0.112 mV/N
Measurement range	44.48 kN in compression; 5 kN in tension
Resonance frequency	60 kHz

.

Pressure Sensors

Two pressure sensors, namely, the *PCB 102A quartz* pressure sensor and *KUlite HKS-375(M)* pressure sensor were used to measure the reflected pressure from the conducted blast experiments. The internal construction and a view of PCB pressure sensors are shown in Figure 4-15(a) and Figure 4-15(b) respectively. The working principle of these pressure sensors is very similar to the force sensor. When the quartz crystal is stressed, a charge is generated. This high-impedance output must be routed through a special low-noise cable to an impedance-converting amplifier, such as a laboratory charge amplifier or source follower. High insulation resistance must be maintained in the cables and connections [26]. The corresponding specifications of these sensors are given in Table 4-3 and Table 4-4 for *PCB* and *KUlite* pressure sensors respectively. Similarly, to measure the side-on overpressure (incident pressure) the *PCB probe Model 137A24* was used for all tests (refer Figure 4-15(c)); and the corresponding technical specifications can be found from Table 4-5.

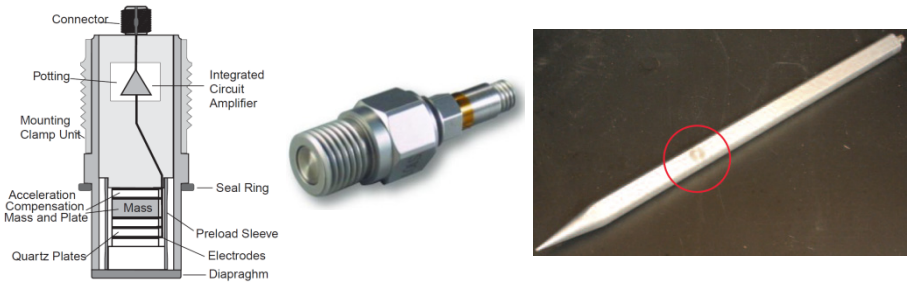

Figure 4-15: (a) Internal construction of the *PCB* pressure sensor **(b)** View of *PCB* 102A pressure sensor **(c)** Pressure pencil probe (*PCB 137A24*).

Table 4-3: Specification of the *PCB 102A* pressure sensor [26].

Sensitivity	0.2293 mV/N
Measurement range (± 5V)	344 bar
Maximum pressure	1034 bar
Resonance frequency	> 500 kHz

Table 4-4: Specification of the *Kulite HKS-375* pressure sensor [27].

Sensitivity	0.287 mV/bar
Measurement range (± 5V)	140 bar
Maximum pressure	210 bar
Resonance frequency	650 kHz

Table 4-5: Specification of the *PCB 137A24* pressure probe [26].

Sensitivity	2.90 mV/kPa
Measurement range (± 5V)	17.24 bar
Maximum pressure	344.75 bar
Resonance frequency	>500 kHz

Accelerometer

The PCB 350 B02 *axial shear mode accelerometer* was used for all blast tests. The working principle and the corresponding technical data are already discussed in Chapter 3.

4. 5. Experimental results and discussion

In order to understand the crushing behaviour of a single empty beverage can, a series of close-range free-air blast tests have been conducted with 20g of C4 and a stand-off distance of 30 cm. The charge was made spherical in shape. To achieve a zero incidence angle of the pressure waves, the charge was placed perpendicular and positioned to the centre of the top face of the skin plate. Due to the short duration of the pressure pulse loading, a sampling frequency of 5 MHz was chosen for all sensors (pressure sensors, accelerometer and the dynamic load cell). In order to have consistent results, a minimum of five tests have been conducted for each case. The measured values of blast and material response parameters are discussed systematically in the subsequent sections.

4. 5. 1. Pressure profiles and clearing effect

Pressure profiles

As discussed earlier, the typical pressure-time histories (incident and reflected) of a spherically charged free-air explosion can be modelled using *Friedlander equation*

(Equation 4.1). Out of two phases (positive and negative), often the negative phase is not considered for design of sacrificial cladding structures. Varying the input parameters of blast (mass of charge, stand-off distance and orientation to the target) and correspondingly conducting the tests for the measurement of output parameters is an expensive process which needs ample of resources. Alternatively, some commercial tools (*ConWep, ATBlast, BlastX*, etc.,) are available to predict the incident and reflected blast parameters for a given set of input values. However, the fully reflected blast parameters given by these programs do not include the effects of clearing of the reflected pressure wave associated with a limited size of the reflected surface. To study this effect a comparison was made between the *ConWep* and measured blast data with different skin plates (refer Table 4-6). The peak reflected pressure and the corresponding positive duration from the experiments reported in Table 4-6 were measured with the *PCB 102A* pressure sensor; and the corresponding incident pressure was measured with the *PCB 137A24* pressure probe. It can be seen from Table 4-6 that the measured blast parameters (peak reflected pressure and the corresponding positive duration) from all the skin plates do not correlate with *ConWep* data (Table 4-6). Before conducting the blast tests with sandwich composite skin plates an analysis was carried out for the incident pressure measurement values with both aluminium skin plates (ϕ 200 mm and ϕ 250 mm). The standard deviation and the corresponding coefficient of variation were calculated for these 10 experiments. The calculated mean, standard deviation and the corresponding coefficient of variation (in percentage) for these experiments are 577 kPa, 10 kPa and 1.7 % respectively. These values indicated the consistency of the results for such a close-range free air blast loading conditions. However, the measured values of the incident pressure magnitudes were much lower than the *ConWep* predicted data. Furthermore, for the design of sacrificial cladding structures the incident pressure value is not considered. Hence, we decided to measure the incident pressure for only few experiments for the remaining skin plates such as the sandwich composite skin plates.

Similarly, to check the scattering in blast parameters an analysis was carried out for the reflected blast parameters (reflected pressure and its positive duration). The mean, standard deviation and the corresponding coefficient of variation were calculated for each case (each skin plate with five experiments). The results of this analysis are presented in Figure 4-16(a-b). It can be noticed that the scatter in the reflected pressure and the positive duration is low for such close-range free air blast loading conditions. The scatter in the calculated parameters such as energy, velocity and deformation length of the test specimen are presented later. It can be noticed that the scatter in these parameters is also low. Hence, it can be stated that the number of tests performed with each skin plate is sufficient enough to understand the behaviour of the test set-up and the corresponding performance of the test specimen.

Table 4-6: Summary of blast parameters (incident and reflected).

Test No	Area of circular skin plate (A_p)	Mass of the skin plate (m_p)	Average surface roughness (R_a)	Mass of C4 (m_c)	Stand-off distance (Z)	Maximum incident overpressure (p^I_{max})	Maximum reflected overpressure (p^R_{max})	Coefficient of variation (C_v) for p^R_{max}	Positive duration (t_p)	Coefficient of variation (C_v) for t_p	Average deformation length of the test specimen(l)
	m^2	Kg	μm	g	cm	kPa	kPa	%	ms	%	mm
Conwep (Incident angle is zero)				20	30	898.7	4755	-	0.5321	-	-
Test 1	0.0314 (ϕ200mm)	1.0	0.18	20	30	579	3016	8.6	0.115	10.7	8.67
Test 2						585	2819		0.127		8.23
Test 3						568	3002		0.119		8.00
Test 4						580	2863		0.140		10.0
Test 5						588	3558		0.101		9.71
Test 1	0.0491 (ϕ250mm)	1.0	0.186	20	30	590	4120	3.7	0.150	2.2	15.8
Test 2						590	3880		0.147		16.3
Test 3						572	4016		0.144		19.6
Test 4						560	4206		0.154		16.2
Test 5						567	3790		0.151		15.9
Test 1	0.0491 (ϕ250mm)	0.54	1.502	20	30	500	6553	2.0	0.263	9.3	48.7
Test 2						Not measured	6529		0.232		45.4
Test 3						550	6902		0.291		41.2
Test 4						Not measured	6572		0.225		41.0
Test 5						Not measured	6701		0.258		50.0

Test No	Area of circular skin plate (A_p)	Mass of the skin plate (m_p)	Average surface roughness (R_a)	Mass of C4 (m_c)	Stand-off distance (Z)	Maximum incident overpressure (p^I_{max})	Maximum reflected overpressure (p^R_{max})	Coefficient of variation (C_v) for p^R_{max}	Positive duration (t_p)	Coefficient of variation (C_v) for t_p	Average deformation length of the test specimen(l)
	m^2	Kg	μm	g	cm	kPa	kPa	%	ms	%	mm
Test 1	0.0491 (ϕ250mm)	0.36	0.8	20	30	590	5053	11.0	0.236	5.4	58.0
Test 2						Not measured	4204		0.216		61.5
Test 3						Not measured	5745		0.205		60.5
Test 4						600	4788		0.208		57.0
Test 5						Not measured	5594		0.229		62.0

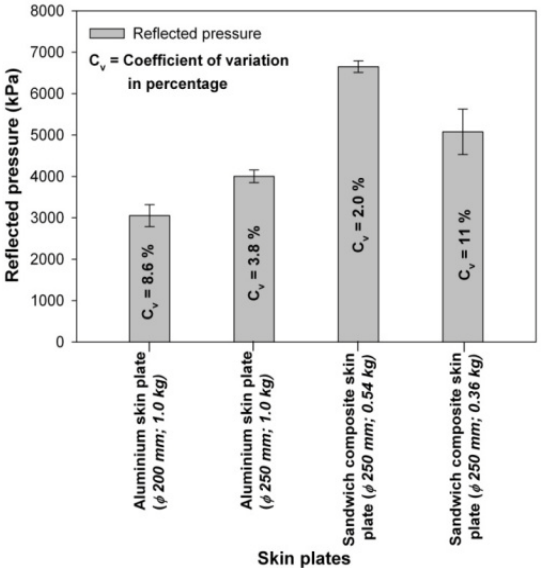

(a)

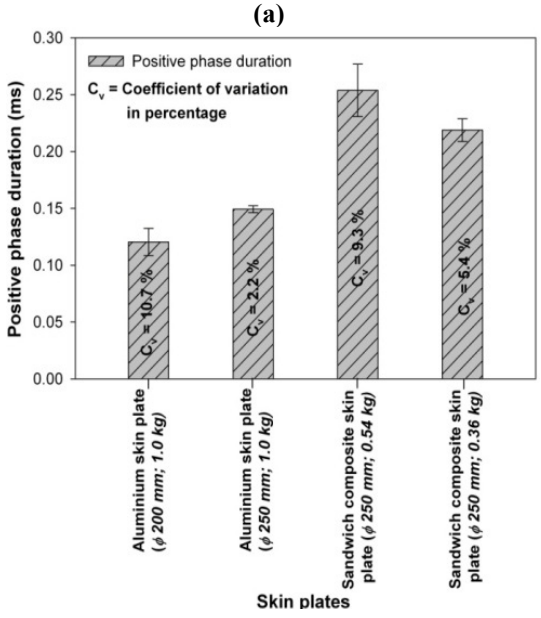

(b)

Figure 4-16: Scattering of blast parameters from five tests with different skin plates **(a)** Reflected pressure **(b)** Positive phase duration.

4. 5. 2. Effect of surface area and nature of reflected surface

Figure 4-17(a) and Figure 4-17(b) show a comparison of the experimentally measured reflected overpressure-time histories for the tests with aluminium skin plates (having the same mass 1.0 kg and surface roughness (0.18 μm) and different surface area (ϕ 200 mm and ϕ 250 mm)) with the *ConWep* pressure profile. Due to

the limited scatter, the first three tests are shown and for the simplification, only the positive phase of the reflected pressure profile is considered. The influence of surface area on the peak reflected pressure and the corresponding positive phase duration can be understood from these figures. Although the mass of both aluminium skin plates is the same (1.0 kg), a 50 mm increase in diameter attributed to an increase of the average maximum reflected pressure from 3050 kPa to 4000 kPa. Subsequently, the average positive phase duration was increased from 0.12 ms to 0.145 ms. However, these values are significantly lower than the values predicted by *ConWep* (4755 kPa and 0.5321ms). Figure 4-17(c) and Figure 4-17(d) show the reflected overpressure-time histories for sandwich composite skin plates with mass of 0.54 kg (ϕ 250 mm) and 0.36 kg (ϕ 250 mm) respectively. The peak reflected pressures from few experiments with sandwich composite skin plates were comparable with *ConWep* data (Table 4-6). However, most of the experiments showed higher values of the peak reflected pressure than the *ConWep* predicted values (Figure 4-17(c) and Figure 4-17(d)).

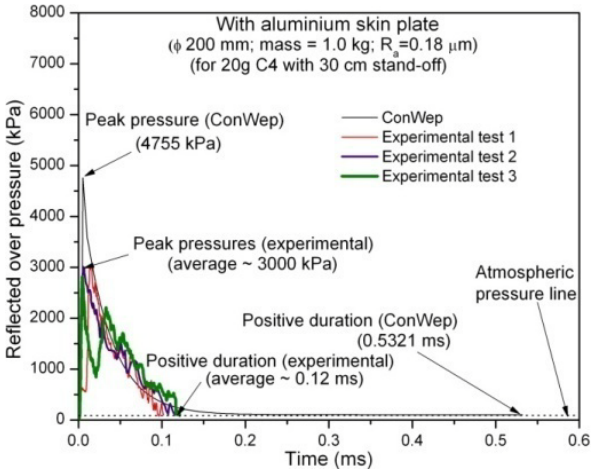

(a)

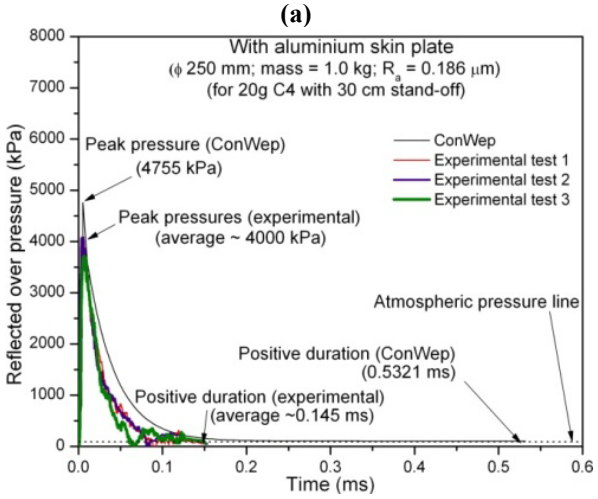

(b)

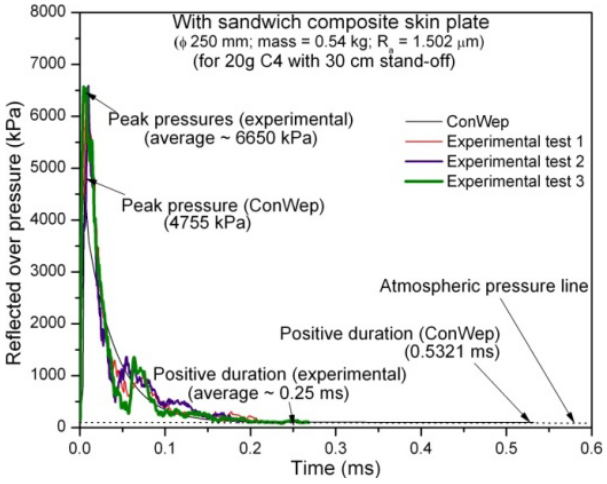

(c)

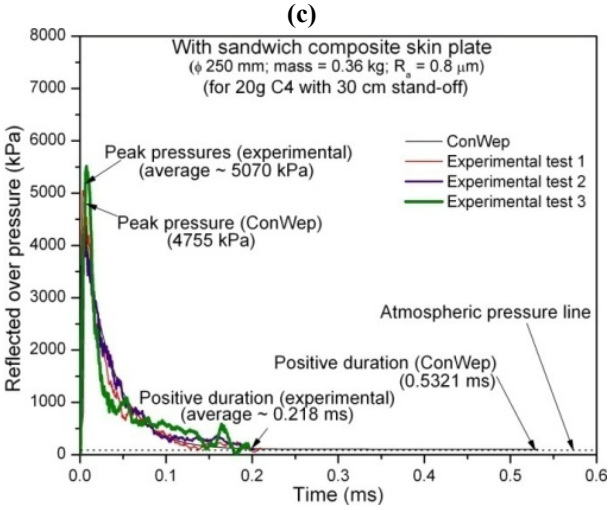

(d)

Figure 4-17: Comparison of experimentally measured pressure-time histories with *ConWep* data for 20g of C4 with a stand-off distance of 30 cm: **(a)** with aluminium skin plate (ϕ 200 mm; 1.0 kg of mass; R_a = 0.18 μm). **(b)** with aluminium skin plate (ϕ 250 mm; 1.0 kg of mass; R_a = 0.186 μm) **(c)** with sandwich composite skin plate (ϕ 250 mm; 0.54 kg of mass; R_a = 1.502 μm). **(d)** with sandwich composite skin plate (ϕ 250 mm; 0.36 kg of mass; R_a = 0.8 μm).

Although the surface area of the two sandwich composite skin plates (ϕ 250 mm) was the same, a significant difference in the magnitude of the peak reflected pressure was noticed consistently. The difference in average maximum reflected pressure between these two sandwich composite skin plates may be due to the nature of the reflected surface, mass of the skin plate and the non-homogeneous pressure cloud formation. The later explanations are not likely, because the chance of recording a consistent pressure with each sandwich composite skin plate would be very small. Furthermore, the magnitudes of peak pressure measured from the

aluminum skin plate (ϕ 250 mm) should also have indicated the same range of peak pressure magnitudes compared to the values from the sandwich composite skin plates. However, the magnitudes of pressure were lower than from the sandwich composite skin plates (Table 4-6). Secondly, the numerically calculated natural time period of these skin plates (9.0 ms, 4.09 ms and 5.021 ms for aluminium (ϕ 250mm; 1.0 kg) and sandwich composite skin plates respectively) is much higher than the positive phase duration of the blast (refer Table 4-7).

So according to the general blast load regime [2, 9] these skin plates will be subjected to impulsive loading. Therefore, the influence of the mass of the skin plate on the peak reflected pressure can be eliminated. Hence, it can be stated that the surface roughness of the reflected surface may play a significant role for the blast parameters. The surface roughness was measured at different locations of the reflected surfaces and the average is reported here. The average maximum reflected pressure of 6650 kPa corresponds to the sandwich composite skin plate (ϕ 250 mm; 0.54 kg) with an arithmetic average surface roughness of 1.502 µm. The average maximum reflected pressure 5076 kPa corresponds to the sandwich composite skin plate (ϕ 250 mm; 0.36 kg) reflected surface with the arithmetic average surface roughness of 0.8 µm. Similarly, the average maximum 4000 kPa corresponds to the aluminium skin plate (ϕ 250 mm) with the arithmetic average surface roughness of 0.186 µm. Furthermore, the influence of surface roughness can be observed from the positive phase duration values. The average values of the positive phase duration were 0.25 ms and 0.21 ms for the sandwich composite skin plates (ϕ 250 mm) with surface roughness of 1.502 µm and 0.8 µm respectively. Due to a smooth surface the positive phase duration of the aluminium skin plate with 250 mm diameter (0.145 ms) was lower than for the sandwich composite skin plates. These values indicate that the interaction period of the pressure waves increases with rough surface structures.

Table 4-7: Natural time period of different skin plates.

S. No	Type of skin plate	Natural time period of skin plate without beverage can (ms)	Natural time period of skin plate with beverage can (ms)
1.	Aluminium skin plate (ϕ 200mm, 1.0 kg)	4.95	10
2.	Aluminium skin plate (ϕ 250mm, 1.0 kg)	9.0	13.88
3.	Sandwich composite skin plate (ϕ 250mm, 0.54 kg)	4.09	9.52
4.	Sandwich composite skin plate (ϕ 250mm, 0.36 kg)	5.21	9.25

4. 5. 3. Study of surface roughness on blast parameters

Although the mass of the skin plate does not play any role for the peak reflected parameters for the above cases, the skin plates were manufactured with different materials. Use of different materials for the skin plates will not influence the reflected blast parameters provided having the same boundary conditions. However, in order to reduce the number of variables such as the mass and material of the skin plate, additional blast tests have been conducted on a single skin panel having two different surface roughness values. For ease of manufacturing the aluminum skin panel was chosen; accordingly an additional aluminium skin panel was manufactured. The mass of the complete manufactured aluminium skin panel assembly was 1.187 kg. Out of two surface roughness values, one value was chosen to have a much higher arithmetic average surface roughness of 7.0 μm than the previously reported values (0.186 μm, 0.8 μm and 1.502 μm). However, the second value (arithmetic average of 0.545 μm) was chosen in the same range of the previously used values. At first stage the top face of the skin plate (which was subjected to pressure loading) was sand blasted to have a rough surface (average surface roughness of 7.0 μm). After conducting the blast tests on the rough skin plate the rough surface was sanded into a smooth surface using sandpapers (6 stages from coarser to smoother). During this process the mass of the skin plate was reduced by 4 g (1.184 kg).

Usually the spherical shape of the charge used for blast load testing is made by hand. Any distortion in the shape may lead to a significant change in the blast parameters for such a close-range blast loading (20g C4 with a stand-off distance of 30 cm). The distortion in the final spherical shape of the charge is difficult to avoid due to the insertion of the detonator. Hence, in order to avoid the influence of the change in shape of C4 (characteristics have nowhere been mentioned), a mould was made (refer Figure 4-18). This mould contains two parts (bottom and top mould) with an insert for the detonator (Figure 4-18). With this mould the spherical shape of the C4 was ensured.

Air blast experiments have been conducted with the above mentioned aluminium skin plate. A minimum of 5 tests have been conducted for each case. The experimental reflected pressure time history was measured with the *Kulite HKS-375* pressure sensor; and the corresponding incident pressure was measured with the *PCB 137A24* pressure probe. However, the used pressure probe (*PCB 137A24*) was a brand new sensor.

(a) Bottom mould **(b)** Top mould

Figure 4-18: Mould for C4.

Similar to earlier approaches, the mean, standard deviation and the corresponding coefficient of variation for reflected pressures are calculated. The calculated mean, standard deviation and the corresponding coefficient of variation (in percentage) for the experiments with rough surface were 11287 kPa, 828 kPa and 7.3 % respectively. The corresponding positive duration also showed similar values (0.2116 ms, 0.008 ms and 4.1% for mean, standard deviation and the coefficient of variation respectively). However, the blast tests conducted with the smooth surface showed a scatter in the peak reflected pressure values (5673 kPa, 1663 kPa and 29.3 % for mean, standard deviation and the coefficient of variation respectively). Therefore, 5 more tests have been repeated with the smooth surface skin plate (a total of 10 experiments). The experimentally measured incident and the corresponding reflected parameters are given in Table 4-8. It can be noticed that the magnitude of the peak reflected pressures from the rough surface provided very high values compared to the experiments with the smooth surface (11287 kPa (from 5 experiments) and 5555 kPa (from 10 experiments) for rough and smooth surfaces respectively). In addition to that, these values are significantly higher than the values measured with other skin plates which were discussed in the previous section. The corresponding experimentally measured reflected pressure time histories (5 tests from each case) are shown in Figure 4-19(a) and (b) for rough and smooth surfaces respectively. For the case with smooth surface, even after increasing the number of tests from 5 to 10, a significant scattering of the peak reflected pressure was noticed. The calculated coefficient of variation for this case was 23.9 % which is a much higher value compared to other cases.

If we consider the average magnitude of the peak reflected pressure, it can be concluded that for such close-range blast loading (30 cm stand-off distance) the surface roughness plays a major role for the reflected blast parameters. The consolidated average reflecting parameters (reflected pressure and its positive duration) are given in Table 4-9 for different skin plates. From this table it can be concluded that the surface roughness plays a role for close-range blast loading.

Nevertheless, the scattering of the reflected parameters with the smooth surface and the physics behind the rise of reflected pressure with rough surface should be investigated further. Unlike the experimental tests which were discussed in the previous section, the average peak incident pressure from these experiments (964.5 kPa) (refer Table 4-8) was close to the *ConWep* predicted value (898.7 kPa). This shows that sensors which are used for the blast loading applications should be calibrated of course periodically (the used pressure pencil for these tests was a brand new one). The calculated crushing parameters (energy absorption, mean crush load and the specific energy absorption) of the beverage cans from these experimental tests are presented in section 4. 5. 6.

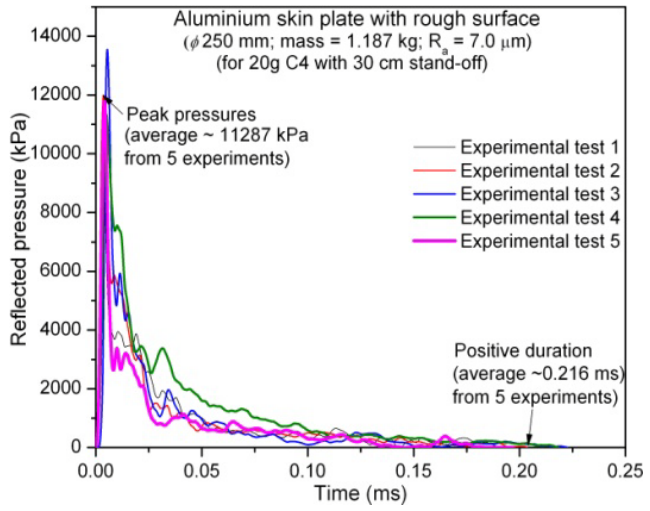

(a)

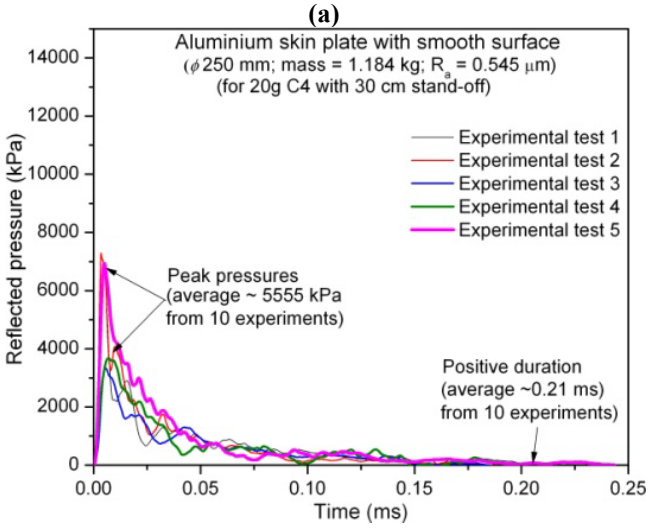

(b)

Figure 4-19: Comparison of experimentally measured pressure-time histories **(a)** with aluminium skin plate (ϕ 250 mm; 1.187 kg of mass; R_a = 7.0 μm). **(b)** with aluminium skin plate (ϕ 250 mm; 1.184 kg of mass; R_a = 0.545 μm).

Table 4-8: Summary of blast parameters (incident and reflected) for the tests conducted with rough and smooth surfaces.

Test No	Area of circular skin plate (A_p)	Mass of the skin plate (m_p)	Average surface roughness (R_a)	Mass of C4 (m_c)	Stand-off distance (Z)	Maximum incident overpressure (p^I_{max})	Coefficient of variation (C_v) for p^I_{max}	Maximum reflected overpressure (p^R_{max})	Coefficient of variation (C_v) for p^R_{max}	Positive duration (t_p)	Coefficient of variation (C_v) for t_p
	m^2	Kg	µm	g	cm	kPa	%	kPa	%	ms	%
With aluminium top skin plate (ϕ 250 mm; m_p= 1.187 kg; R_a= 7.0 µm;) – rough surface											
Test 1	0.0491 (ϕ 250mm)	1.187	7.0	20	30	923	3.5	9687	7.3	0.210	4.1
Test 2						1001		12010		0.210	
Test 3						925		11592		0.223	
Test 4						909		11356		0.218	
Test 5						963		11792		0.197	
With aluminium top skin plate (ϕ 250 mm; m_p= 1.187 kg; R_a= 0.545 µm;) – smooth surface											
Test 1	0.0491 (ϕ 250mm)	1.184	0.545	20	30	994	7.5	6755	23.9	0.207	9.6
Test 2						968		7358		0.189	
Test 3						1053		3633		0.190	
Test 4						1036		3678		0.200	
Test 5						891		6944		0.230	
Test 6						809		5442		0.240	
Test 7				20	30	1035		6881		0.200	
Test 8						956		4232		0.242	
Test 9						1046		5005		0.184	
Test 10						959		5623		0.214	

Table 4-9: Consolidated average blast parameters for the tests with different surface roughness values of the skin plates (for 20g C4 with a stand-off distance of 30 cm).

S. No	Type of skin plate	Reflected pressure (kPa)	Positive duration (ms)
1.	Aluminium skin plate (ϕ 250mm, 1.0 kg; **R_a= 0.186 µm**)	4000	0.145
2.	Aluminium skin plate (ϕ 250mm, 1.0 kg; **R_a= 0.545 µm**)	5555	0.209
3.	Sandwich composite skin plate (ϕ 250mm, 0.54 kg; **R_a= 0.8 µm**)	5070	0.218
4.	Sandwich composite skin plate (ϕ 250mm, 0.36 kg; **R_a= 1.502 µm**)	6650	0.250
5.	Aluminium skin plate (ϕ 250mm, 1.0 kg; **R_a= 7.0 µm**)	11688	0.211

4. 5. 4. Effect of clearing phenomenon on the equivalent load

Figure 4-20 shows one of the experimental recordings of reflected pressure-time profile measured with sandwich composite skin plate (ϕ 250 mm; mass = 0.36 kg; R_a = 0.8 µm). The peak reflected pressure magnitude (4788 kPa) of this test (refer test 4 from Table 4-6) was very close to the *ConWep* value (4755 kPa). The equivalent triangular impulse load (area below the reflected pressure curve) for the experimental curve is shown in solid line (Figure 4-20). This equivalent triangular impulse load was calculated based on the diffracting (engulfing) load case [9]. The approximate new positive duration for this equivalent triangular impulse load is 0.069 ms. Next, the equivalent triangular impulse load calculated from the predicted positive duration from *ConWep* is also shown in the same figure (dashed-line). The difference between these two load cases is indicated by the 45° inclined lines. The equivalent triangular impulse load from *ConWep* accumulates a higher amount of energy compared to the experimental curve. The reason for the significant difference between these two load cases is due to a considerable difference in positive duration. The measured and *ConWep* predicted positive phase duration of this case were 0.2081 ms and 0.5321 ms respectively. Considering the *ConWep* predicted load for this case definitely will over predict the efficiency of the core structure. Hence, the effect of clearing has to be taken into account for the correct efficiency calculation of core structures. The above discussion is valid for other skin plate cases also. Furthermore, the calculation of clearing time (the time at which the reflected pressure becomes equivalent to the incident pressure) using the standard relation may not yield the correct value for such a close-range blast loading application with finite surface area. The approximate clearing time can be calculated using the following relation [2].

$$t_c = 3 \cdot S / U_s \tag{4.16}$$

where "*S*" is the smallest distance at which the pressure wave can pass around the edges; "U_s" is the blast front velocity. Taking "*S*" as the radius of the skin plate (100 mm and 125 mm) and assuming the value of "U_s" is approximately 440 m/s [2], the calculated clearing time was 0.68 ms and 0.85 ms for ϕ 200 mm and ϕ 250 mm skin plates respectively. The calculated clearing time was significantly higher than the positive duration of the blast (refer Table 4-6 and Table 4-8) which is physically impossible (refer Figure 4-17 and Figure 4-20).

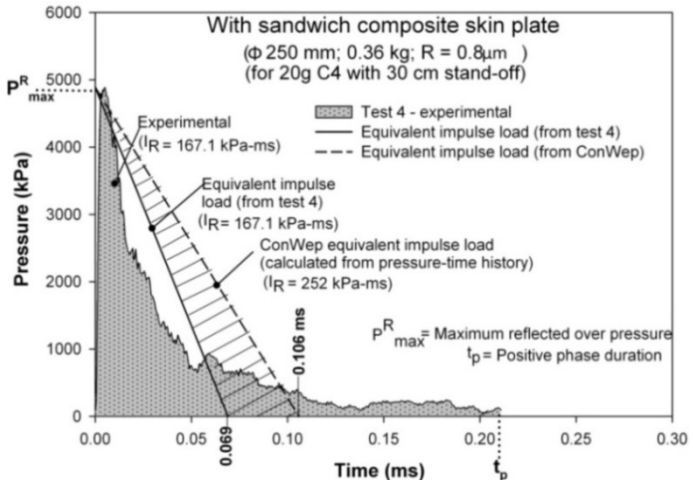

Figure 4-20: Effect of clearing phenomenon on the equivalent triangular impulse load (comparison of experimental and *ConWep* values).

4. 5. 5. Deformation patterns

With aluminium skin plates (ϕ 200 mm and ϕ 250 mm; mass = 1.0 kg)

The deformation patterns of the empty beverage cans from different blast tests with the aluminium skin plate (ϕ 200 mm; 1.0 kg) are shown in Figure 4-21(a); Based on the thickness distribution of an empty beverage can, it can be concluded that the initial deformation should occur at the mid-wall location (belly portion) of the can due to its lower thickness. However, it can be noticed from Figure 4-21(a) that the initial deformation occurred at different points of the can along its length (similar to the axial impact loading case with an initial impact velocity of 1.4 m/s discussed in Chapter 3). The difference in the deformation pattern of the cans may be influenced by a combination of two effects: (i) the initial geometry imperfections induced during the manufacturing process and during usage and (ii) a lower impact velocity of the skin plate. Due to the very small thickness at the mid-wall location (0.07 mm), plastic local wall buckling and folding occurred at different points along the length of each empty can. However, no significant deformation was noticed at top and bottom shoulder and end caps. Compared to the thickness of a blank can the thickness of the aesthetic coating on the outer surface and lacquer coating (used to

prevent the contact of beverage with metal) at the inner surface was negligible. Hence, there was no significant effect on the deformation from these coatings. However, a detailed study is needed for the final conclusion of this statement. For a few cans, the deformation was local folding which occurred at the mid-length of the belly portion of the can. The average deformation length of the beverage can for this case was 8.9 mm.

Figure 4-21: Deformation patterns of empty beverage cans. **(a)** with aluminium skin plate (ϕ 200 mm; 1.0 kg of mass; R_a = 0.18 µm). **(b)** with aluminium skin plate (ϕ 250 mm; 1.0 kg of mass; R_a = 0.186 µm). **(c)** with sandwich composite skin plate (ϕ 250 mm; 0.54 kg of mass; R_a = 1.502 µm). **(d)** with sandwich composite skin plate (ϕ 250 mm; 0.54 kg of mass; R_a = 0.8 µm).

Similarly, Figure 4-21(b) shows the deformation patterns of beverage cans with the other aluminium skin plate (ϕ 250 mm and 1.0 kg of mass). However, this deformation pattern is quite different from the previous case. For this case, the initial deformation started at the interface location of top shoulder and mid-wall region consistently (Figure 4-21 (b)). This may be due to a higher impact velocity of the skin plate and the lower thickness reduction at that location. Subsequently, the deformation progressed by local wall buckling which resulted into a formation of lobes around the circumference (Figure 4-21 (b)). The average deformation length of the can for this case was 16 mm.

With sandwich composite skin plates (ϕ 250 mm; mass = 0.54 kg and 0.36 kg)

The deformation patterns of the empty beverage cans with sandwich composite skin plate (ϕ 250 mm; 0.54 kg of mass; R_a = 1.502 µm) are shown in Figure 4-21(c). Similar to the aluminium skin plate with ϕ 250 mm, the initial deformation started below the top shoulder region. Consequently, the deformation propagated downwards along its length. Similar to the axial impact experimental tests, the longitudinal cut-section of these specimens showed a clear evidence of forming of triangular lobes. However, the number of triangular lobes around the circumference was lower (varied from 3 to 4) and the corresponding half folding length of each lobe was longer (refer Figure 4-21). The formation of lobes was uniform for the test specimens which were subjected to co-axial loading (longitudinal axis of test specimen and skin plate was aligned) during the blast event. For a few cases, there was an offset noticed between the skin plate and the test specimen during the pressure loading. Due to this effect the crushing of the cans was not uniform around their circumference and a few bigger lobes were formed on one side of the can. This phenomenon can be noticed from the third test specimen shown in Figure 4-21(c). Furthermore, due to offset loading there was no significant deformation observed at the top shoulder region. In case of co-axial loading of cans, the top shoulder of the cans showed a considerable deformation. This can be noticed from the first two test specimens shown in Figure 4-21(c). However, in all cases there was no deformation observed at top and bottom end cover locations. The deformation length of these samples varied from a minimum of 41.2 mm to a maximum of 50.01 mm. The deformation patterns of the empty beverage can specimens with sandwich composite skin plate of mass 0.36 kg are shown in Figure 4-21(d). The deformation length of these samples was higher than from the other cases. The maximum deformation length for this case was 62 mm and the minimum was 57 mm. The effect of offset loading was clearly seen on this case also. Due to the offset loading the plastic local wall buckling occurred, followed by the formation of lobes. In all cases, due to plastic wall buckling, the wall of the can on the other side was stretched. As a result of that the can profile was changed from a concave to planar surface at that location. This process altered the shape of the can significantly. The deformation patterns of

the beverage cans tested to study the effect of surface roughness were very similar to the ones which are presented in Figure 4-21(b).

4. 5. 6. Load-deformation curves

The measured load-deformation curves for the first three blast tests for different skin plates are shown in Figure 4-22(a-d). Similar to the axial impact experiments which were discussed in Chapter 3, it was assumed that the vertical displacement of the skin plate was equivalent to the deformation length of the test specimen. The measured signal from the accelerometer was integrated twice to get the displacement of the skin plates. From the load-deformation curves of successive tests, it can be noticed that the peak crushing load of an empty beverage can varied from 3 to 3.3 kN with aluminium skin plates (Figure 4-22 (a) and (b)). For sandwich composite skin plates this value varied between 4.48 and 4.104 kN (refer Figure 4-22(c) and (d)). This value shows a clear evidence of strain-rate dependency (the quasi-static values varied from 1.1 kN to 1.4 kN and impact test values varied from a minimum of 1.69 kN to a maximum of 2.47 kN). The total energy absorption, mean crush load and the corresponding specific energy absorption for each test specimen during the blast event were calculated. The relations which were used to calculate the above parameters have already been discussed in Chapter 3. The mean crushing load of the test specimen oscillated from a minimum of 0.4 kN to a maximum of 0.75 kN with different top skin plates. The mean crush load of the test specimen with 0.54 kg mass of the skin plate varied from a minimum of 0.523 kN to a maximum of 0.712 kN. However, the mean crush load of test specimens with 0.36 kg mass of skin plate showed consistent values (more than 0.7 kN) which is a good indicator for better energy absorption than the other cases [17]. The calculated crushing efficiency (the ratio of the mean crush load to the peak crush load which indicates the efficiency of the crushing (η_c)) of all tests is given in Table 4-10. The summary of crushing parameters (peak crush load, mean crush load and the energy absorption) for all cases is also given in Table 4-10. To understand the energy absorption efficiency of each test specimen, the specific energy absorption (SEA - normalized with respect to mass) was calculated. The average mass of each metal beverage can was 26 g. The test specimens which were tested with higher skin plate mass exhibited a lower SEA. The average SEA of test specimens which were tested with aluminium skin plates was 1.95 kJ/kg and 2.32 kJ/kg for 200 mm and 250 mm diameter respectively. Empty beverage cans tested with the sandwich composite skin plate showed higher values. The average values of SEA were 2.64 and 3.25 kJ/kg for test specimens with 0.54 and 0.36 kg of skin plates respectively (refer Table 4-10).

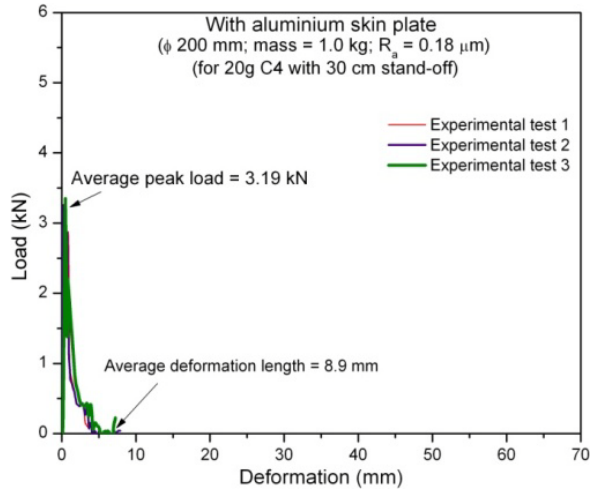
With aluminium skin plate
(ϕ 200 mm; mass = 1.0 kg; R$_a$ = 0.18 μm)
(for 20g C4 with 30 cm stand-off)
Experimental test 1
Experimental test 2
Experimental test 3
Average peak load = 3.19 kN
Average deformation length = 8.9 mm
Load (kN)
Deformation (mm)

(a)

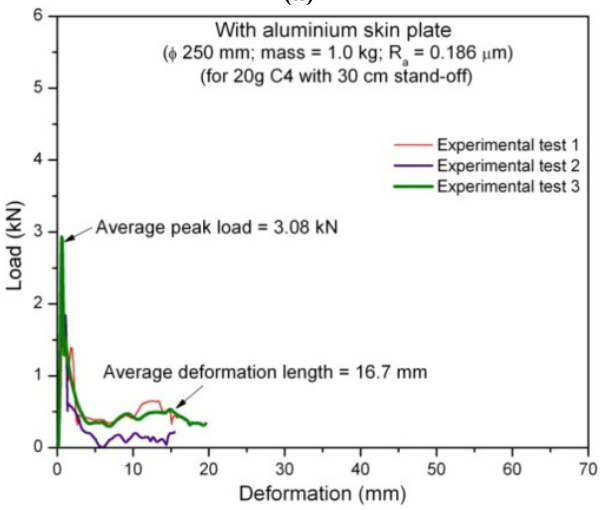
With aluminium skin plate
(ϕ 250 mm; mass = 1.0 kg; R$_a$ = 0.186 μm)
(for 20g C4 with 30 cm stand-off)
Experimental test 1
Experimental test 2
Experimental test 3
Average peak load = 3.08 kN
Average deformation length = 16.7 mm
Load (kN)
Deformation (mm)

(b)

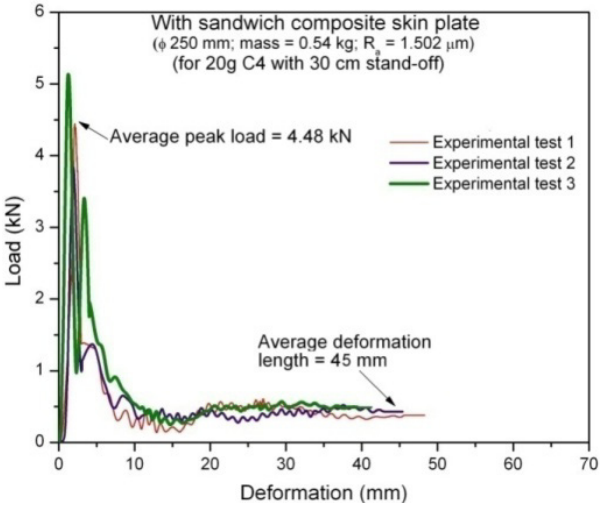
With sandwich composite skin plate
(ϕ 250 mm; mass = 0.54 kg; R$_a$ = 1.502 μm)
(for 20g C4 with 30 cm stand-off)
Average peak load = 4.48 kN
Experimental test 1
Experimental test 2
Experimental test 3
Average deformation
length = 45 mm
Load (kN)
Deformation (mm)

(c)

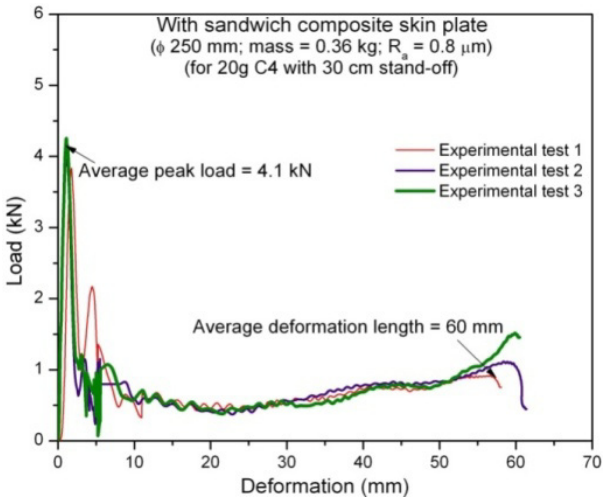

(d)

Figure 4-22: Force-deformation histories of beverage cans **(a)** with aluminium skin plate (ϕ 200 mm; 1.0 kg of mass; R_a = 0.18 μm). **(b)** with aluminium skin plate (ϕ 250 mm; 1.0 kg of mass; R_a = 0.186 μm). **(c)** with sandwich composite skin plate (ϕ 250 mm; 0.54 kg of mass; R_a = 1.502 μm). **(d)** with sandwich composite skin plate (ϕ 250 mm; 0.36 kg of mass; R_a = 0.8 μm).

Similarly, the load-deformation curves for the tests which were conducted to study the effect of surface roughness are very similar to the ones which are shown in Figure 4-22(b). The corresponding calculated crushing parameters are given in Table 4-11. The measured average mean crush load of the test specimens were 0.531 kN and 0.496 kN for the tests with rough (R_a= 7.0 μm) and smooth surface (R_a= 0.545 μm) respectively. Due to this there was a difference in SEA observed (average SEA of 2.39 kJ/kg and 2.21 kJ/kg for rough and smooth surfaces respectively).

Table 4-10: Summary of crushing parameters.

Test No	Reflected (total) impulse delivered to the skin plate (I_{refl})	Impulse transferred to non-sacrificial structure (I_{trans})	Impulse difference	% difference in impulse (ΔI)	Available energy to the skin plate for beverage can crushing (E_{refl})	Energy absorbed by the beverage can (E_{abs})	Energy difference	Peak (crush) load (F_{max})	Mean crush load (F_{mean})	Deformation length of test specimen (l_{max})	Crush efficiency (η_d)	SEA
	kN-s	kN-s	kN-s	%	J	J	J	kN	kN	mm	(%)	(kJ/kg)
With aluminium top skin plate (ϕ 200 mm; m_p= 1.0 kg; R_a= 0.18µm;)												
Reference test	0.00385	0.00258	0.00127	33	-	-	-	12.32	-	-	-	-
Test 1	0.00392	0.00266	0.00126	32	7.54	3.84	3.70	2.98	0.443	8.67	14.9	1.99
Test 2	0.00381	0.00251	0.00130	34	7.07	3.32	4.22	3.34	0.403	8.23	12.1	1.82
Test 3	0.00404	0.00286	0.00118	29	8.03	4.01	4.02	3.40	0.501	8.00	14.7	2.25
Test 4	0.00393	0.00263	0.00130	33	7.47	3.95	3.52	2.95	0.394	10.03	13.4	1.77
Test 5	0.00400	0.00288	0.00112	28	7.87	4.16	3.71	3.28	0.428	9.71	13.0	1.92
With aluminium skin plate (ϕ 250 mm; m_p= 1.0 kg; R_a= 0.186µm)												
Reference test	0.00478	0.0032	0.00158	32	-	-	-	16.97	-	-	-	-
Test 1	0.00451	0.0029	0.00161	35	11.10	8.75	2.35	2.92	0.47	15.80	18.8	2.49
Test 2	0.00516	0.0031	0.00206	39	13.23	7.78	5.45	2.94	0.48	16.32	16.3	2.15
Test 3	0.00532	0.0034	0.00192	36	14.02	8.66	5.36	3.01	0.44	19.60	14.6	2.00
Test 4	0.00430	0.0028	0.00150	34	13.67	8.80	4.87	3.30	0.54	16.20	16.3	2.44
Test 5	0.00481	0.0030	0.00181	37	11.49	7.35	4.14	3.23	0.46	15.89	14.2	2.08

Test No	Reflected (total) impulse delivered to the skin plate (I_{refl})	Impulse transferred to non-sacrificial structure (I_{trans})	Impulse difference	% difference in impulse (ΔI)	Available energy to the skin plate for beverage can crushing (E_{refl})	Energy absorbed by the beverage can (E_{abs})	Energy difference	Peak (crush) load (F_{max})	Mean crush load (F_{mean})	Deformation length of test specimen (l_{max})	Crush efficiency (η_d)	SEA
	kN-s	kN-s	kN-s	%	J	J	J	kN	kN	mm	(%)	(kJ/kg)
With sandwich composite skin plate (ϕ 250 mm; m_p= 0.54 kg; R_a= 1.502µm)												
Reference test	0.00912	0.00637	0.00275	30	-	-	-	7.25	-	-	-	-
Test 1	0.01032	0.00756	0.00276	27	92.89	25.94	66.95	4.44	0.533	48.7	12.0	2.40
Test 2	0.00954	0.00656	0.00298	31	82.50	24.47	58.03	3.83	0.539	45.4	14.0	2.43
Test 3	0.01020	0.00629	0.00391	38	92.36	29.35	63.01	5.13	0.712	41.2	13.9	3.20
Test 4	0.00976	0.00673	0.00303	31	84.78	25.00	59.78	4.62	0.610	41.0	13.2	2.74
Test 5	0.01079	0.00640	0.00439	40	102.1	26.14	75.96	4.39	0.523	50.0	11.9	2.35
With sandwich composite skin plate (ϕ 250 mm; m_p= 0.36 kg; R_a= 0.8µm)												
Reference test	0.00879	0.00633	0.00246	28	-	-	-	6.01	-	-	-	-
Test 1	0.00823	0.00592	0.00231	28	90.8	41.96	48.84	3.95	0.723	58.0	18.3	3.26
Test 2	0.00870	0.00629	0.00241	27	102.1	44.49	57.61	4.48	0.723	61.5	16.1	3.26
Test 3	0.00845	0.00657	0.00198	22	92.3	45.42	46.88	4.25	0.750	60.5	17.6	3.38
Test 4	0.00864	0.00625	0.00239	28	97.6	40.01	57.59	4.01	0.702	57.0	17.5	3.16
Test 5	0.00901	0.00635	0.00266	30	106.2	43.98	58.62	3.83	0.709	62.0	18.5	3.19

Table 4-11: Summary of crushing parameters (for the tests conducted with rough and smooth surfaces).

Test No	Reflected (total) impulse delivered to the skin plate (I_{refl})	Impulse transferred to non-sacrificial structure (I_{trans})	Impulse difference	% difference in impulse (ΔI)	Available energy to the skin plate for beverage can crushing (E_{refl})	Energy absorbed by the beverage can (E_{abs})	Energy difference	Peak (crush) load (F_{max})	Mean crush load (F_{mean})	Deformation length of test specimen (l_{max})	Crush efficiency (η_d)	SEA
	kN-s	kN-s	kN-s	%	J	J	J	kN	kN	mm	(%)	(kJ/kg)
With aluminium top skin plate (ϕ 250 mm; m_p= 1.187 kg; R_a= 7.0 µm;) – rough surface												
Test 1	0.00927	0.00620	0.00307	33	23.1	10.3	12.8	2.53	0.512	20.1	20.2	2.31
Test 2	0.00976	0.00641	0.00335	34	24.4	9.87	14.53	3.01	0.533	18.5	17.7	2.40
Test 3	0.00943	0.00650	0.00293	31	22.6	10.9	11.7	3.22	0.560	19.6	17.3	2.50
Test 4	0.00982	0.00662	0.00320	32	21.5	9.12	12.38	2.89	0.541	16.9	18.7	2.43
Test 5	0.00899	0.00646	0.00253	28	20.3	9.08	11.22	3.33	0.510	17.8	15.3	2.29
With aluminium top skin plate (ϕ 250 mm; m_p= 1.184 kg; R_a= 0.545 µm;) – smooth surface												
Test 1	0.00751	0.00525	0.00226	30	17.8	7.79	10.01	2.82	0.501	15.5	17.7	2.26
Test 2	0.00690	0.00462	0.00228	33	18.9	7.28	11.62	3.20	0.489	14.9	15.2	2.19
Test 3	0.00704	0.00485	0.00219	31	15.3	7.69	7.61	3.04	0.472	16.3	15.5	2.12
Test 4	0.00558	0.00396	0.00162	29	16.1	8.45	7.65	3.25	0.500	16.9	15.3	2.25
Test 5	0.00633	0.00417	0.00216	34	14.9	10.0	4.9	3.23	0.550	18.3	17.0	2.45
Test 6	0.00657	0.00459	0.00198	30	17.9	7.43	10.47	2.78	0.492	15.1	17.6	2.21
Test 7	0.00843	0.00590	0.00253	30	18.8	7.01	11.79	2.98	0.479	14.8	16.0	2.13

Test No	Reflected (total) impulse delivered to the skin plate (I_{refl})	Impulse transferred to non-sacrificial structure (I_{trans})	Impulse difference	% difference in impulse (ΔI)	Available energy to the skin plate for beverage can crushing (E_{refl})	Energy absorbed by the beverage can (E_{abs})	Energy difference	Peak (crush) load (F_{max})	Mean crush load (F_{mean})	Deformation length of test specimen (l_{max})	Crush efficiency (η_d)	SEA
	kN-s	kN-s	kN-s	%	J	J	J	kN	kN	mm	(%)	(kJ/kg)
Test 8	0.00743	0.00534	0.00209	28	16.5	7.05	9.45	3.06	0.507	13.9	16.5	2.28
Test 9	0.00764	0.00504	0.0026	34	19.0	6.59	12.41	2.88	0.455	17.0	15.7	1.74
Test 10	0.00651	0.00449	0.00202	31	16.9	8.89	8.01	3.00	0.523	15.7	17.4	2.54

4. 5. 7. Effect of skin plate inertia

The efficiency of the energy absorption of the inner core will be reduced if the skin plate interacts with the blast pressure over a significant duration of the blast time. Furthermore, the inertia of the skin plate is another parameter which controls the amount of energy transferred to the inner core. A significant amount of blast energy has to be spent on the skin plate if the inertia of the skin plate is larger. Hence, a comparison was made only for three skin plates (one aluminium skin plate and two sandwich composite skin plates) having the same surface area (ϕ 250 mm). The available energy for the crushing of the beverage can or the energy transmitted from the blast wave to the skin plate and subsequently to the empty beverage can was calculated using Equation (4.12). Figure 4-23(a) shows the available energy from the skin plate to the beverage can for absorption.

It is very clear that a significant amount of energy has been spent to overcome the inertia of the skin plates. The average energy given by the sandwich composite skin plates was 90 J and 97 J for 0.54 kg and 0.36 kg respectively. However, the energy delivered by the aluminium skin plate (ϕ 250 mm; 1.0 kg of mass; R_a = 0.186 μm) was much lower (12.5 J) than for the sandwich composite skin plates. The maximum attained velocity of the skin plates (integrated acceleration signal measured from the skin plate during the experimental tests) depends on the peak reflected pressure and the mass of the skin plate. A higher peak pressure and a lower mass of the skin plate will provide a higher attained velocity of the skin plates which has an influence on the crushing response of the test specimens. As a result, the maximum velocity attained by the aluminium skin plate was lower than for the other two cases (refer Figure 4-23(b)). Due to the different levels of the attained velocity of the skin plates, a significant difference in the deformation length (integrated twice from the acceleration signal) of the test specimens was noticed. The average maximum deformation length achieved with the aluminium skin plate (ϕ 250 mm; 1.0 kg of mass; R_a = 0.186 μm) was 16.7 mm. Skin plates with lower masses attributed to a higher crushing length of the test specimens. The sandwich composite skin plate with 0.54 kg yielded an average deformation length of 45.25 mm. Similarly, the sandwich composite skin plate with 0.36 kg provided an average deformation length of 60 mm (refer Figure 4-23(b) and Figure 4-21(c-d)).

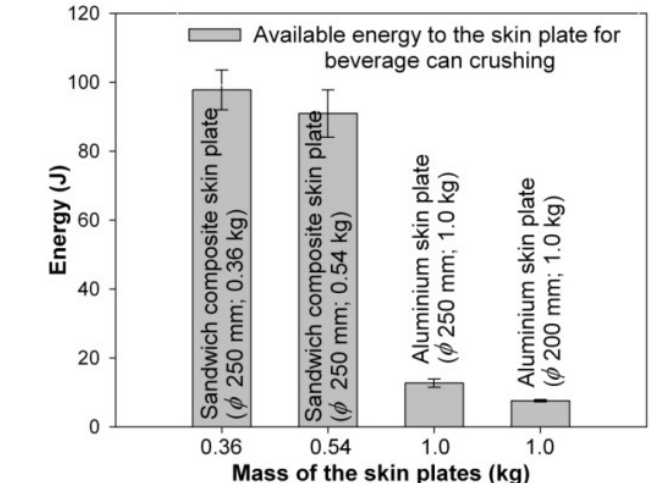

(a)

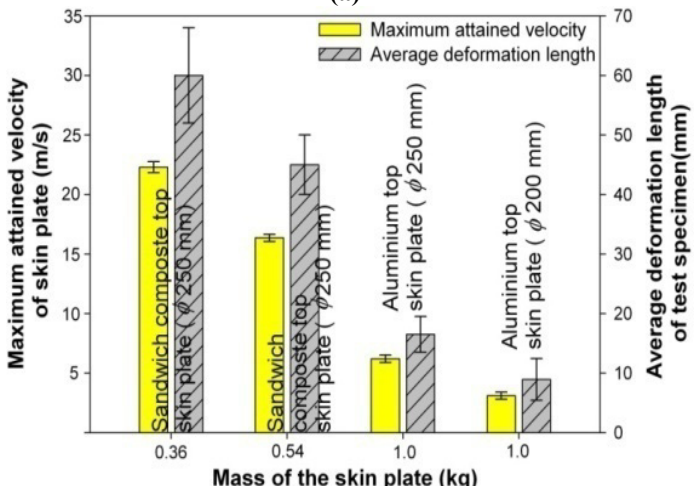

(b)

Figure 4-23: (a) Effect of inertia of skin plate on the available energy to the skin plate for beverage can crushing (error bar indicates the standard deviation). **(b)** Effect of inertia of skin plate on the maximum attained velocity of skin plate and the corresponding deformation length achieved by the beverage cans (error bar indicates the standard deviation).

4. 5. 8. Impulse and energy transfer

In order to understand the effectiveness of the empty beverage can, the impulse delivered to the top face of the skin plate (reflected impulse) and the corresponding transferred impulse at the bottom of the beverage can to the non-sacrificial member (integration of measured force-time history at the bottom of the beverage can) are compared. The reflected impulse and the transferred impulse were calculated using Equation (4.11) and Equation (4.13) respectively.

The calculated values of I_{refl} and I_{trans} for all cases are given in Table 4-10 and Table 4-11. It can be observed that the linear momentum is not conserved for any of the cases. One of the reasons might be the recording of the transferred force signal for a shorter duration compared to the complete event of beverage can crush. However, even after increasing the recording duration significantly, the same difference was observed for all cases. The difference between the reflected impulse and the transferred impulse for all cases is given in Table 4-10 and Table 4-11. This result is unexpected, because any sacrificial cladding structure cannot prevent the impulse of the blast being transferred onto the structure upon which it is mounted, rather it changes the force-time distribution from a high load, short duration impulse to a low load, long duration impulse and thereby avoiding or reducing the damage to the non-sacrificial structure upon which it is mounted. As an example, one of the cases with sandwich composite skin plate (ϕ 250 mm; 0.54 kg of mass; R_a = 0.8 µm) is presented here. The delivered load and the corresponding (reflected) impulse given to the top face of the sandwich composite skin plate are shown in Figure 4-24(a); and the corresponding transferred load and impulse to the non-sacrificial structure are shown in Figure 4-24(c). Furthermore, the peak load from the reference test (average of two tests conducted without test specimen and only with skin plate directly placed on the dynamic load cell for the same loading parameters (20 g C4 with 30 cm stand-off distance)) is also given in Table 4-10. It can be noticed that the use of the beverage can reduced the peak load from 7.25 kN to about 4 kN considerably and the corresponding positive duration was extended significantly (11.8 ms – refer Figure 4-24(c)). However, the same figures (Figure 4-24 (a)) and (c)) also show the difference in the impulses. Similarly, there was a significant difference noticed between the available energy to the skin plate for beverage can crushing (90.8 J) and the corresponding energy absorbed by the beverage can (refer Figure 4-24(b) and Table 4-10). If we assume that, the difference might be due to the energy absorbed by the top skin plate; then one can expect a significant deformation of the skin plates during the experiments. However, there was no significant deformation observed during these tests. Hence, the question of why such a difference occurs for both impulse and energy is to be answered. In order to understand the difference in impulse and energy and to capture the crushing phenomena of the beverage can in detail, a (decoupled) blast simulation was carried out in ABAQUS V6.7-3 Explicit using the experimentally recorded reflected pressure-time histories at the top face of the skin plates. The details of the finite element modelling and the corresponding results are presented in next section.

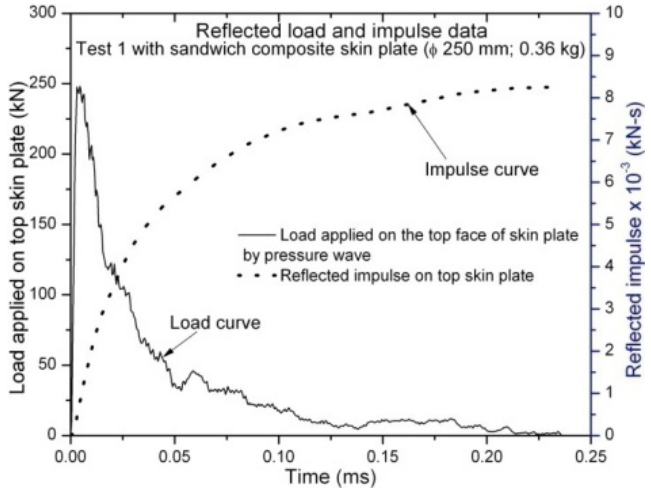
Reflected load and impulse data
Test 1 with sandwich composite skin plate (ϕ 250 mm; 0.36 kg)
Load applied on top skin plate (kN)
Reflected impulse x 10^{-3} (kN-s)
Time (ms)
Impulse curve
Load curve
Load applied on the top face of skin plate by pressure wave
Reflected impulse on top skin plate

(a)

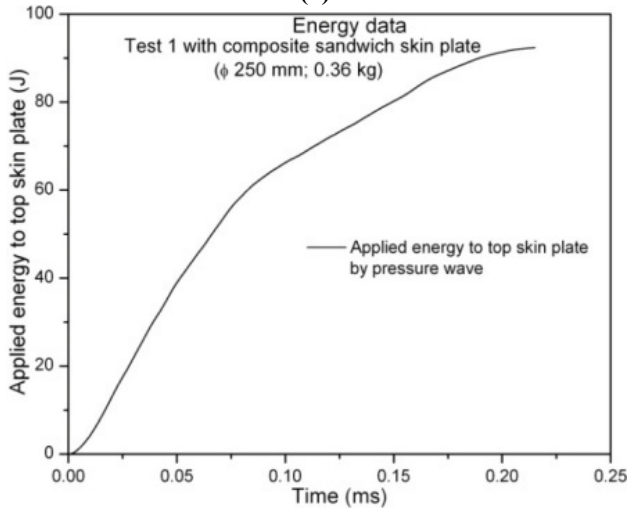
Energy data
Test 1 with composite sandwich skin plate
(ϕ 250 mm; 0.36 kg)
Applied energy to top skin plate (J)
Time (ms)
Applied energy to top skin plate by pressure wave

(b)

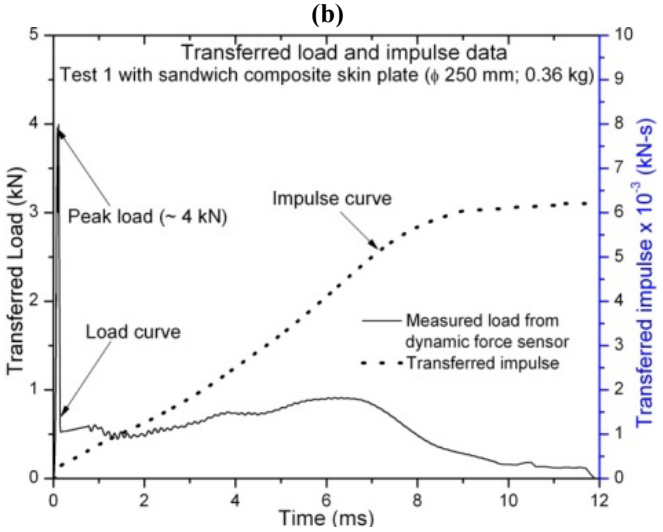
Transferred load and impulse data
Test 1 with sandwich composite skin plate (ϕ 250 mm; 0.36 kg)
Transferred Load (kN)
Transferred impulse x 10^{-3} (kN-s)
Time (ms)
Peak load (~ 4 kN)
Impulse curve
Load curve
Measured load from dynamic force sensor
Transferred impulse

(c)

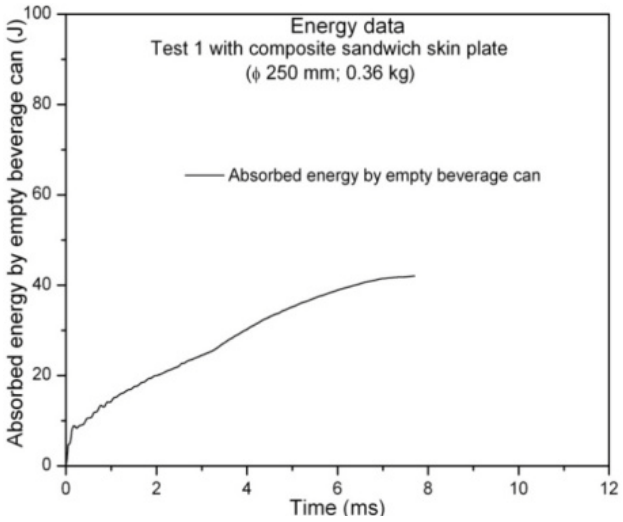

(d)

Figure 4-24: (a) Reflected impulse (load-time history) of sandwich composite skin plate (ϕ 250 mm; 0.54 kg of mass; R_a = 0.8 µm) **(b):** Energy delivered by the reflected pressure wave to the sandwich composite skin plate (ϕ 250 mm; 1.0 kg). **(c):** Transferred impulse (load-time history) to the non-sacrificial structure due to the beverage can crushing. **(d)**: Energy absorbed due to the crushing of beverage can.

4. 6. Decoupled numerical simulation with measured pressure-time histories

4. 6. 1. Modelling

With aluminium skin plate (ϕ 200 mm; mass = 1.0 kg)

The details of the finite element model are shown in Figure 4-25(a). The modelling details of the beverage can (used elements, geometry and the materials details, used material model (*Johnson-Cook*)) were similar to the one which was discussed in Chapter 3 (for axial impact loading simulation). The aluminium skin plate and the side tube were modelled with solid C3D8R elements (8 node, linear brick elements with reduced integration and hourglass control). For simplification, the side tube was also modelled with aluminium material (grade 2024 T3). The equivalent mass of the flexi-glass was considered for the modelling of the aluminium side tube. The bottom resting plate (non-sacrificial structure) was modelled as an analytical rigid surface. To simulate the axial blast load only in vertical direction (along "Y" direction) the translational degrees of freedom of the aluminium skin plate in "X" and "Z" axis were arrested; the rotational degree of freedom with respect to the "Y" axis was also arrested and the bending of the aluminium skin plate with respect to

the "X" and "Z" axis were allowed. To represent the fixed supporting plate at the bottom, all degrees of freedom of the bottom rigid body were also arrested. To simulate the same experimental condition, a "*surface-to-surface*" master-slave contact algorithm was established between the beverage can and the top and bottom plates with a friction coefficient equal to 0.2. In addition to that, a self-contact algorithm was also introduced for the beverage can.

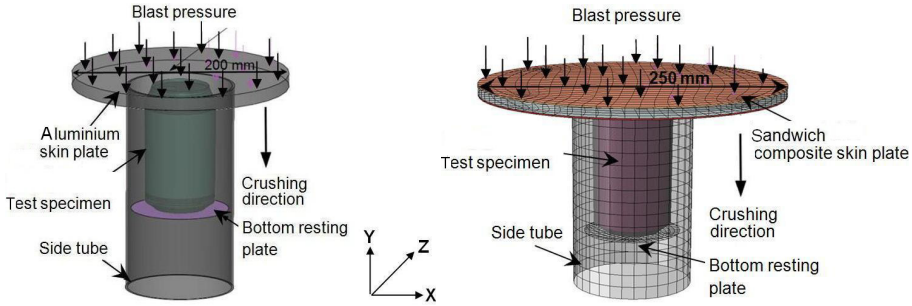

(a) Finite element model with aluminium skin plate (ϕ 200 mm; 1.0 kg).

(b) Finite element model with sandwich composite skin plate (ϕ 250 mm; 0.54 kg).

Figure 4-25: Details of the finite element models.

The analysis was carried out for the equivalent triangular impulse load for one of the measured pressure-time profiles (Test 1) which was shown in Figure 4-17(a). The deformation of the beverage can was obtained from the displacement of the skin plate and the reaction load was extracted from the interface load between the beverage can and the bottom analytical rigid surface. The commercially available explicit code ABAQUS V6.7-3 was used to carry out all these analyses.

With sandwich composite skin plate (ϕ 250 mm; mass = 0.54 and 0.36 kg)

The numerical modelling of the sandwich composite skin plate was done as per the assembly sequence. The top and bottom composite skin faces were modelled with shell elements (Figure 4-25 (b)). The meshed shell elements were located at the centre of the thickness of each composite laminate. It was assumed that the thickness of each individual ply of the composite plate is 0.5 mm. The integration points representing all layers were located evenly through the thickness of the plates using *Simpson* integration rule. A minimum of 3 integration points was allocated for each layer in the shell element. The material properties of the shell sections in principal directions were defined by introducing a local *Cartesian* coordinate system. The adopted material properties for the glass epoxy laminates are given in Table 4-12. Subsequently, the *Hashin failure criterion* was used to capture the failure in the composite laminates. The corresponding composite plate strengths are given in Table 4-12. To simplify the numerical model the side tube was also modelled with glass-epoxy material and the equivalent mass of the carbon epoxy tube was

considered for the modelling. Furthermore, the aluminium plate (ϕ 97 mm; 2 mm thick) used in the contact between the sandwich composite skin plate and the top end of the beverage can was also modelled by shell elements.

Table 4-12: Material properties of glass epoxy composite laminates in principal directions.

Parameters	Symbol	Values
Material and elastic data		
Density (kg/m^3)	ρ	1870
Longitudinal modulus in warp direction (GPa)	E_{11}	24.25
Transverse modulus in weft direction (GPa)	E_{22}	24.25
In-plane shear modulus (GPa)	G_{12}	4.83
Poisson's ratio	v_{12}	0.153
Glass-epoxy composite strength		
Failure criteria	-	Hashin
Tensile strength in warp (MPa)	X_1^T	390.7
Compressive strength in warp (MPa)	X_1^C	345.1
Tensile strength in weft (MPa)	X_2^T	390.7
Compressive strength in weft (MPa)	X_2^C	345.1
In-plane shear strength (MPa)	S^L	100.6

For the polyurethane foam (used in between the top and bottom composite skin plates) the strength model can be represented by means of the crush characteristics. The compressive stress-strain curve of polyurethane foam can often be simplified into three regimes, namely the linear elastic regime, the plateau regime and the densification regime. In order to acquire the crushing characteristics of the used foam, quasi-static compressive tests have been conducted as per ASTM 1621-91. The typical compressive behaviour of the polyurethane foam is presented in Figure 4-26. The same compaction curve was defined as a strength input for the polyurethane foam.

It was assumed that the top and bottom composite plates, polyurethane foam, aluminium plate and the side tube are rigidly connected. Accordingly a rigid connection was established at the interfaces of all these parts. The boundary conditions of the composite sandwich skin plate were the same as for the aluminium skin plate. A "*surface-to-surface*" master-slave contact algorithm was established between two pairs with a friction coefficient equal to 0.2. The first pair consists of the aluminium plate (ϕ 97 mm; 2 mm thick) and the beverage can and the second pair consists of the bottom resting plate and the beverage can. The analysis was carried out for the equivalent triangular impulse load for one of the measured pressure-time profiles (Test 1) which was shown in Figure 4-17(c). The deformation of the beverage can was obtained from the displacement of the lower aluminium

contact plate and the reaction load was extracted from the interface load between the beverage can and the bottom analytical rigid surface.

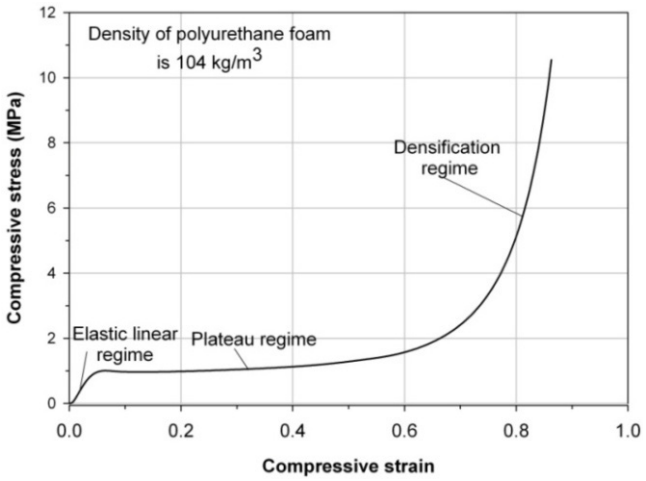

Figure 4-26: Crushing characteristic of the polyurethane foam.

4. 6. 2. Results

The numerical results of these cases showed that the applied impulse (on the top face of the skin plate) was equivalent to the transferred impulse (at the bottom of the beverage can). As an example, the aluminium skin plate case (ϕ 200 mm; 1.0 kg) is discussed here. Figure 4-27(a) shows the comparison of the applied equivalent triangular impulse (0.00392 kN-s) and the transferred impulse (0.00392 kN-s) at the bottom of the beverage can. The same figure also shows the predicted load-time history measured at the bottom of the beverage can. Similarly, Figure 4-27(b) shows the comparison of energy. It can be noticed that the energy absorbed by the beverage can (7.48 J) was slightly lower than the applied energy to the skin plate by the equivalent triangular impulse load (7.65 J). The difference between these two energy levels was the energy absorbed by the aluminium skin plate and energy loss due to friction. Furthermore, it can be noticed from these figures that the short duration impulse load was stretched to a longer duration with a lower peak load (Figure 4-27(a) and Figure 4-27(b)). However, the predicted deformation length (13 mm) of the test specimen of this case is much higher than the experimental result (8.67 mm). The corresponding deformation pattern of the beverage can is shown in Figure 4-28(a). For the cases with the sandwich composite skin plates the test specimens were crushed completely in the simulations (Figure 4-28(b)).

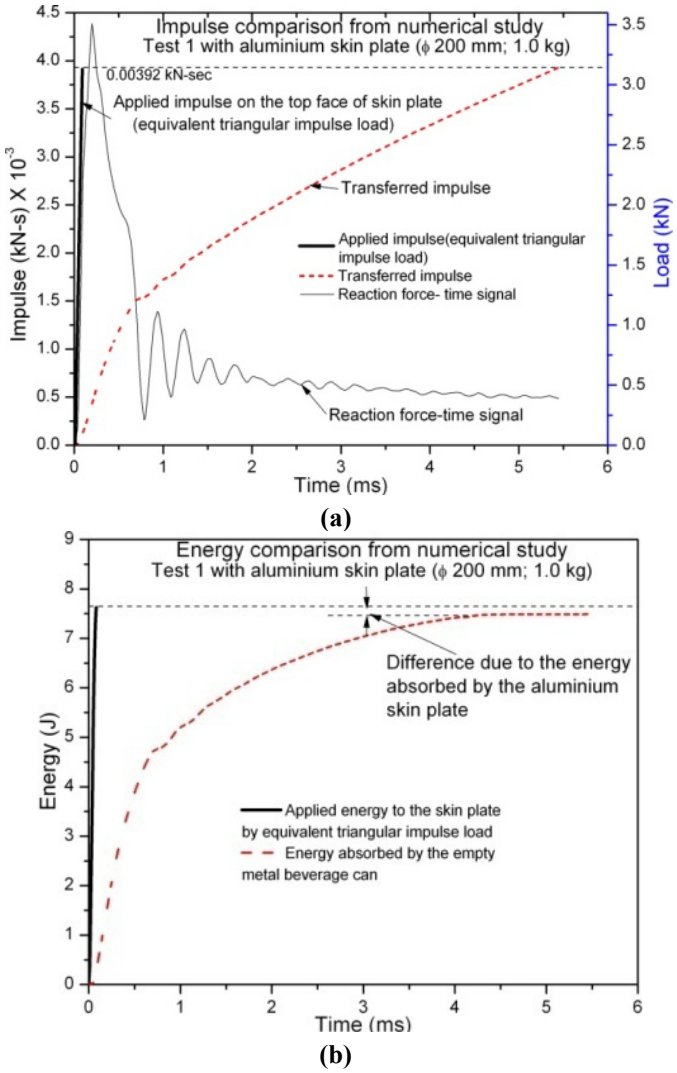

Figure 4-27: For aluminium skin plate (ϕ 200 mm; 1.0 kg). **(a)** Comparison of impulses **(b)** comparison of energies.

The reasons for those very large deformation lengths could be the inadequate geometry modelling of the beverage can, material modelling (*Johnson-Cook* material parameters) and the improper interaction of the pressure waves. However, the current model (geometry modelling and the *Johnson-Cook* material parameters) was already validated for axial impact loading of the beverage cans and the results of these analyses were in very good agreement with the experimental results (refer Chapter 3). This gives an indication that the interaction of pressure waves (pressure wave load) is the only parameter which affects the deformation length for this case. Hence, the study of interaction of pressure waves with the complete experimental set-up is absolutely necessary. Therefore, a coupled analysis was carried out to study the interaction of the pressure waves with the test set-up using Hydrocodes. The

influence of different parameters such as the diffraction of pressure waves due to the clearing effect and reflected pressure from the ground surface on the net impulse acting on the skin plate and the corresponding energy absorption of the test specimen are studied in detail. The details of this analysis are presented in Chapter 5.

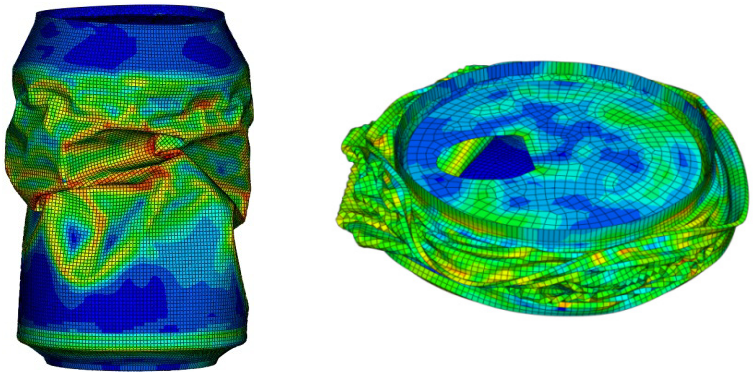

(a) **(b)**

Figure 4-28: Numerical deformation pattern of beverage can **(a)** with aluminium skin plate (ϕ 200 mm; 1.0 kg). **(b)** with sandwich composite skin plate (ϕ 250 mm; 0.54 kg).

4. 7. Conclusions

In this chapter, the blast energy absorption characteristics and the corresponding crushing mechanisms of empty recyclable metal beverage cans were investigated. Close-range free-air blast tests have been conducted with 20g of C4 with a stand-off distance of 30 cm. Experiments were carried out with different top skin plates to understand the effect of inertia of the skin plates on the energy absorption of a sacrificial core structure. Furthermore, the effect of the surface area and the nature of the reflected surface on the reflected blast parameters were also evaluated. The experimentally measured blast parameters were compared with predicted values from *ConWep*. The importance of the clearing effect of reflected pressure with a finite surface of skin plate was studied. The failure patterns of the empty beverage cans and the corresponding energy absorption levels were studied in detail. From the conducted experiments the following conclusions can be made:

- The measured values of the peak reflected pressures from different skin plates (with different surface roughness values) showed that the surface roughness largely influenced the reflected blast parameters. A comparison of blast parameters with *ConWep* for all cases showed a significant difference in the peak reflected pressure and its positive duration. The

positive duration of the blast event was significantly lower than *ConWep* predicted data. The difference in the pressure was due to the clearing of the reflected pressure waves associated with the finite surface area of the skin plates.

- The effect of clearing of the pressure waves has to be considered for the energy absorption evaluation of a sacrificial cladding structure with a finite surface area of the skin plate. Energy absorption prediction with an equivalent triangular impulse load based on empirical relations overestimate the capacity of the inner core of a sacrificial structure.
- The inertia of the skin plate of a sacrificial cladding structure plays a vital role for the crushing length of the test specimens. A lower mass with adequate bending stiffness of the skin plate would maximize the energy absorption of the inner core structure. The specific energy absorption of an empty beverage can was increased with lower mass of the skin plates.
- The peak crush load of beverage cans with different skin plate mass showed the strain-rate sensitivity. The peak crush load of the beverage cans was approximately three times higher than the quasi-static value. Hence, the effect of increasing strength should be accounted for further investigations.
- The deformation patterns of the empty beverage cans with different skin plate masses were evaluated and they were very similar to the impact loading cases. However, the number of triangular lobes decreased and the corresponding half fold length increased compared to the axial impact tests. Tests with higher inertia and lower surface area of the skin plate showed plastic local wall buckling along the length of the can. However, tests with lower skin plate masses exhibited uniform formation of triangular lobes around the circumference of the can.
- In order to understand the observed non-conservation of linear momentum, the decoupled finite element analysis was carried out using experimentally measured reflected pressure-time profiles. Although the results from the finite element analysis showed the conservation of linear momentum the predicted deformation length of the beverage cans was much higher than observed from the experimental results. Hence, a detailed coupled numerical study is needed to understand why the deformation length should be higher in order to achieve the conservation of linear momentum.

As seen from the experimental results, it is clear that the surface roughness plays a role for the reflected blast parameters for such a close-range blast loading case. However, the physics behind the increase in the blast parameters was not studied in this dissertation. Therefore, a thorough analysis to study this phenomenon is recommended. Furthermore, the deployment of the beverage cans for the higher blast pressure loading needs further investigations on the macro-foam structure.

Hence, a study on a single unit of macro-foam (consists of few beverage cans assembled in axial or radial configuration) is also recommended.

Considering the reflected pressure for the numerical simulation only on the top face of the skin plate yielded a much higher deformation length for all cases. Hence, in order to study the interaction of the blast pressure wave with the experimental set-up a 3D computational model was developed using Hydrocodes. The results of this analysis are presented in Chapter 5.

Bibliography

[1]. Mays, G. C. and Smith, P. D., *Blast effects on buildings.* Thomas Telford Publications, London, 1995.

[2]. Smith, P. D. and Hetherington, J. G., *Blast and ballistic loading of structures.* Butterworth-Heinemann Ltd., 1994.

[3]. Krauthammer, T., *Modern protective structures.* CRC Press, New York, 2008.

[4]. Ngo, T., Mendis, P., Gupta, A. and Ramsay, J., *Blast loading and Blast effects on Structures - An Overview.* EJSE Special Issue: Loading on Structures, 2007.

[5]. Luccioni, B., Ambrosini, D. and Danesi, R., *Blast load assessment using hydrocodes.* Engineering Structures, 2006. **28**(12): p. 1736-1744.

[6]. Zhu, F., Zhao, L., Lu, G. and Gad, E., *A numerical simulation of the blast impact of square metallic sandwich panels.* International Journal of Impact Engineering. **In Press, Corrected Proof**.

[7]. Glasstone, S. and Dolan, P. J., *The effects of nuclear weapons.* United states of Defence, Washington. D.C, 1977.

[8]. *US Department of Army Technical Manual (TM5-855-1). Fundamentals of protective design for conventional weapons, Washington, DC.* 1986.

[9]. Kinney, G. F. and Graham, K. J., *Explosive shocks in air.* Springer-Verlag, 1985.

[10]. Lesuer, D., *Experimental Investigations of Material Models for Ti-6Al-4V Titanium and 2024-T3 Aluminum.U.S. Department of Transportation.DOT/FAA/AR-00/25,Sept. 2000*

[11]. Hsu, S. S. and Jones, N., *Quasi-static and dynamic axial crushing of circular and square stainless steel tubes.* Structures under SHOCK AND IMPACT, 2000. **VII**: p. 169-178.

[12]. Hsu, S. S. and Jones, N., *Dynamic axial crushing of aluminium alloy 6063 - T6 circular tubes.* Latin American Journal of Solids and Structures, 2004(1): p. 277-296.

[13]. Jones, N., *Structural Impact.* Cambridge University Press, Cambridge, 1989.

[14]. Guruprasad, S. and Mukherjee, A., *Layered sacrificial claddings under blast loading Part I -- analytical studies.* International Journal of Impact Engineering, 2000. **24**(9): p. 957-973.

[15]. Guruprasad, S. and Mukherjee, A., *Layered sacrificial claddings under blast loading Part II -- experimental studies.* International Journal of Impact Engineering, 2000. **24**(9): p. 975-984.
[16]. Hanssen, A. G., Enstock, L. and Langseth, M., *Close-range blast loading of aluminium foam panels.* International Journal of Impact Engineering, 2002. **27**(6): p. 593-618.
[17]. Karagiozova, D., Nurick, G. N. and Chung Kim Yuen, S., *Energy absorption of aluminium alloy circular and square tubes under an axial explosive load.* Thin-Walled Structures, 2005. **43**(6): p. 956-982.
[18]. Karagiozova, D. and Alves, M., *Transition from progressive buckling to global bending of circular shells under axial impact--Part I: Experimental and numerical observations.* International Journal of Solids and Structures, 2004. **41**(5-6): p. 1565-1580.
[19]. Karagiozova, D. and Alves, M., *Transition from progressive buckling to global bending of circular shells under axial impact--Part II: Theoretical analysis.* International Journal of Solids and Structures, 2004. **41**(5-6): p. 1581-1604.
[20]. Abramowicz, W. and Jones, N., *Transition from initial global bending to progressive buckling of tubes loaded statically and dynamically.* International Journal of Impact Engineering, 1997. **19**(5-6): p. 415-437.
[21]. Nurick, G. N., Gelman, M. E. and Marshall, N. S., *Tearing of blast loaded plates with clamped boundary conditions.* International Journal of Impact Engineering, 1996. **18**(7-8): p. 803-827.
[22]. Langdon, G. S., Lemanski, S. L., Nurick, G. N., Simmons, M. C., Cantwell, W. J. and Schleyer, G. K., *Behaviour of fibre-metal laminates subjected to localised blast loading: Part I--Experimental observations.* International Journal of Impact Engineering, 2007. **34**(7): p. 1202-1222.
[23]. Lemanski, S. L., Nurick, G. N., Langdon, G. S., Simmons, M. C., Cantwell, W. J. and Schleyer, G. K., *Behaviour of fibre metal laminates subjected to localised blast loading--Part II: Quantitative analysis.* International Journal of Impact Engineering, 2007. **34**(7): p. 1223-1245.
[24]. Tekalur, S. A., Shukla, A. and Shivakumar, K., *Blast resistance of polyurea based layered composite materials.* Composite Structures, 2008. **84**(3): p. 271-281.
[25]. Wang, E., Gardner, N. and Shukla, A., *The blast resistance of sandwich composites with stepwise graded cores.* International Journal of Solids and Structures, 2009. **46**(18-19): p. 3492-3502.
[26]. http://www.pcb.com/techsupport/tech_pres.php (dated 02-06-2011).
[27]. http://www.kulite.com/products.aspdated (date 02-06-2011).

Chapter 5

Numerical Study of Diffraction and Ground Reflection using Hydrocodes

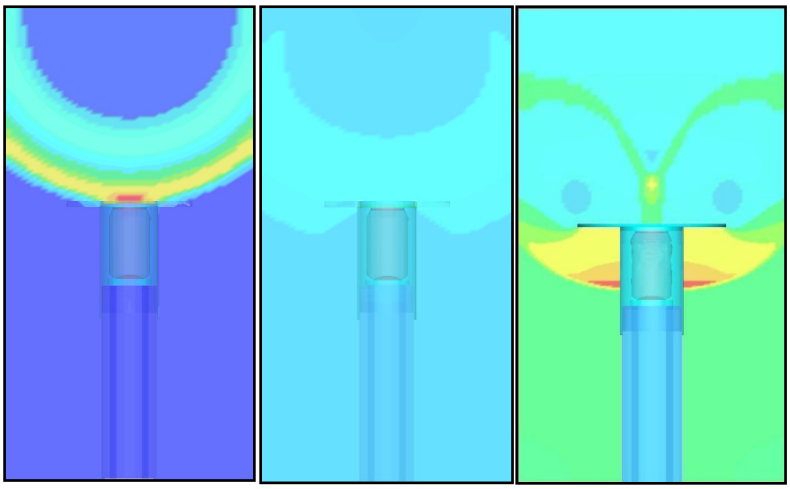

Overview

This chapter proves the effect of clearing of the reflected pressure waves due to the finite surface area of the skin plate. The effect of clearing on the reflected pressure-time history is evaluated with the aid of Hydrocodes using the coupled Eulerian and Lagrangian approach. 2D and 3D blast simulations were carried out for 20 g C4 with a stand-off distance of 30 cm. Furthermore, using the 3D computational model, the interactions of diffracted and ground reflected pressure waves with the bottom face of the skin plate are studied. The effect of these parameters on the crushing performance of the test specimens is explained. The commercially available codes AUTODYN V-11.0 2D and 3D were used for conducting the numerical simulations. The results obtained from these analyses are validated with the experimental results.

5. 1. Introduction

The behaviour of a structure exposed to a blast wave load can be analyzed by dealing with three main issues [1, 2]. Firstly, the interaction of pressure waves with the structure; secondly the blast loading effects, i.e., forces that result directly from the action of the blast pressure; thirdly, the structural response, or the expected damage criteria associated with such loading effects and the corresponding failure modes. The above mentioned issues are critically important for the design of any structure which is subjected to blast loading [3]. However, the interaction of pressure waves and subsequent effects on a structure are quite complicated to study for structures which have complex configurations. A better understanding of the complex interactions between structures and pressure waves can guide to develop better design codes and so an adequate protection can be created for the civil engineering structures. Therefore, dedicated computer programs with modern advances in computing technology can be a valuable tool for this problem.

Blast loading effects on real life structural members may produce both local and global responses associated with different failure modes. The type of structural response depends mainly on the loading rate, the orientation of the target with respect to the direction of the blast wave propagation, mass and the boundary conditions. The prediction of all the failure modes and mechanisms for a complex structural geometry is highly tedious. However, it is possible to consider an equivalent simplified geometry. Accordingly, two types of structures can be considered for analyzing the dynamic response to blast loading: they are (i) diffraction-type and (ii) drag type structures. As these names imply, the former structures would be affected mainly by diffraction (engulfing) loading and the latter by drag loading. It should be emphasized that actual civil engineering structures will respond to both types of loading and the distinction can be made to simplify the analysis [3-6]. Existence of openings in a structure is also an important factor to be considered for the structural response. Few tools are available based on experimental measurement results to predict the response of a structure with some assumptions [6-8].

Computational methods in the area of blast mitigation are generally classified into two categories. The first one is used for prediction of blast loads on the structure and the second one is used for calculation of the structural response to the blast loads. Computational programs for blast prediction and structural response use empirical methods [3, 9], computational fluid dynamics (CFD) and Hydrocodes [7]. Computational programs using empirical methods do not include important effects such as multiple blast wave reflections, Mach effect and diffraction of pressure waves etc. On the other hand, the CFD and Hydrocodes can handle the above mentioned effects. Using these approaches, coupled and uncoupled analyses are

possible to study blast loading on a structure. The uncoupled analysis calculates blast loads as if the structure and its components were rigid and then applies these blast loads to a responding model of the structure. The loads (reflected pressure and its duration) on the structure are often over-predicted, particularly if significant motion or failure of the structure occurs during the loading period. For a coupled analysis, the blast simulation module is linked with the structural response module. In this type of analysis the CFD model for blast load prediction is solved simultaneously with the CSM (computational solid mechanics) model for structural response. By accounting for the motion of the structure while the blast calculation proceeds, the pressure that arises due to motion and failure of the structure can be predicted more accurately. The consideration of the latter approach is very important and accurate because most of the real life engineering structures respond (motion, deflection or deformation) at the time of blast loading. A few commercially developed computer codes (Autodyn, Abaqus and LS-Dyna) are available to carry out such calculations.

Few studies [3, 10-13] have been carried out using Hydrocodes to study the pressure wave interaction with fixed structures. Luccioni et al. [8] studied the interaction of pressure waves for complex urban conditions. They have concluded that the use of empirical and semi-empirical expressions is not enough to predict the accurate evolution of incident pressure distributions and associated impulses in complex urban environments. Furthermore, they added that neglecting the reflections and the Mach effect of the blast wave could lead to underestimation of peak values in far field and the empirical relations are not applicable with confidence in the near field. Similarly, Baylot et al. [10] studied (experimentally and numerically) the structural response of main load bearing columns with and without masonry walls. Remiennikov et al. [11] proved the shadowing or enhancing effect of pressure due to the presence of other buildings in an urban environment. Silva et al. [14] demonstrated experimentally that retrofitting of carbon and steel fibre reinforced polymers on both sides of concrete slabs increased the blast resistance significantly. The finite element modelling of composite materials for a high speed impact was studied in a few cases using Autodyn [15-17]. In most of the above studies, fixed boundary conditions are considered for the reflected structures. However, in the present study the effect of skin plate boundary movement on the interaction of pressure waves and the corresponding loading are not known. Therefore, to understand the experimental impulse loss scenario, the moving boundary condition for the skin plate has to be considered similar to the experimental testing conditions.

The knowledge of interaction of pressure waves is very important to predict the load experienced by the structure. As explained in Chapter 4, in order to meet the linear conservation of momentum the results from the decoupled finite element analysis (with the experimentally measured reflected pressure-time profile on the top face of

the skin plate) showed a higher deformation length compared to the experimental result. Therefore, apart from the clearing effect some other factors which significantly contribute to reduce the impulse and subsequently, the deformation length of the test specimens, should be present. In order to investigate the loss of impulse, 2D and 3D computational models were developed using Hydrocodes. The commercially available codes "Autodyn V-11.0 2D and 3D" were used for the simulations. Using this model the interaction of explosive pressure waves with the skin plate (clearing and diffracted pressure on the bottom face of the skin plate), reflection from the boundary structures (ground reflected pressure on the bottom face of the skin plate) and the corresponding effect on the loading are well captured. The influence of these two parameters on the crushing length of the test specimen and the corresponding transferred impulse are evaluated. The simulated blast parameters are compared with the experimental data and empirical relations (*ConWep*).

5. 2. A brief introduction to Hydrocodes

Hydrocodes are large computer programs used to simulate shock hydrodynamics problems [7]. They differ from Computational Fluid Dynamics (CFD) codes in that they must be applicable to solid materials as well as to liquids and gases. The hydrocodes are specifically suitable to carry out time dependent non-linear dynamic analyses using a combination of finite difference, finite volume and finite element techniques. Any given problem is governed by the conservation of mass, energy and momentum. In order to obtain a complete solution, it is necessary to define a further relation between the flow variables in addition to appropriate initial and boundary conditions. This can be found from a material model which relates stress to deformation and internal energy or thermodynamic properties of the material; and ideally should not require any dynamic data to build up the relationship. However, in practice, the only practical way of obtaining the data on the behaviour of the material at high strain rate is to carry out well-characterized dynamic experiments. In most cases, the stress may be separated into a uniform hydrostatic pressure and a stress deviator associated with the resistance of the material to shear distortion. Then, the relation between the hydrostatic pressure, the local density (or specific volume) and local specific internal energy is known as the Equation Of State (EOS). Constitutive strength models are used to represent the material resistance to shear distortion. The major advantage of using this code is interfacing of different solvers. It allows the user to interface the coupling of different solvers such as Lagrangian and Eulerian to obtain the numerical solution for a complex problem involving fluid structure interaction. In this work, a commercial hydrocodes named "Autodyn V-11-0" was used. Using this code, the coupled Eulerian and Lagrangian approach was

adopted to study the blast pressure interaction with the skin plates and the corresponding loading effect on the skin plate.

5. 3. Salient features of blast simulation

In order to reduce the computational time the blast simulation for the discussed experimental set-up (discussed in Chapter 4) was done in two stages. The first stage is the analysis of initiation of the explosion of C4 from the detonation point and propagation of the pressure waves. In Autodyn V-11.0 this analysis can be done using a 2D approach. The simulation was done for 20g of C4 with a stand-off distance of 30 cm. The second part deals with the propagation of blast pressure in a 3D computational model using 2D data. The remapping option of Autodyn provides this feature. As mentioned in Chapter 4, the predicted peak reflected pressure and its positive duration from the aluminium skin plate (ϕ 200mm, 1.0 kg; R_a= 0.186 μm) were significantly lower than from the ConWep values. On the other hand, for most of the cases the peak reflected pressure from the sandwich composite skin plates was higher than the ConWep predicted values. Furthermore, in order to meet the conservation of linear momentum the decoupled numerical analyses with the aluminium (ϕ 200 mm; 1.0 kg; R_a= 0.186 μm) and sandwich composite (ϕ 250 mm; 0.54 kg) skin plates showed higher deformation lengths compared to the experimental data. Hence, similar to Chapter 4 both cases (aluminium skin plate with ϕ 200 mm and 1.0 kg; sandwich composite skin plate with ϕ 250 mm and 0.54 kg) have been chosen for this study.

Secondly, with the help of the developed computational model the pressure distribution on the bottom face (diffraction associated with clearing of reflected pressure waves due to the finite surface area) of the skin plate was studied. This measurement is highly tedious during a blast experiment. Subsequently, the effect of this pressure on the crushing length of the test specimens and the corresponding energy absorption were also studied. Furthermore, the effect of reflected pressure from the ground surface was observed during the experiments. Hence, few experiments have been conducted with a longer copper tube (representing the non-sacrificial structure during the blast experiments) (refer Figure 5-1(a-b)). After the assembly of the test specimen, the height from the top face of the skin plate to the ground surface was 450 mm and 950 mm for the original and modified test set-ups respectively (refer Figure 5-2(a-b)). The idea was to delay the ground reflected pressure acting on the bottom face of the skin plate during the crushing of the test specimen. The results from these tests showed a higher deformation length of test specimens for the same loading (20g of C4 with a stand-off distance of 30 cm).

(a) (b)

Figure 5-1: (a) Original configuration of the copper tube **(b)** Modified copper tube to delay the ground reflection.

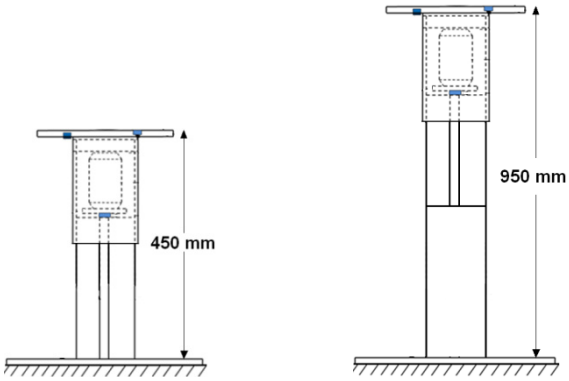

(a) (b)

Figure 5-2: Original and modified configurations of the non-sacrificial structures.

In order to study the effect of ground reflection on the total deformation length of the test specimen numerical analyses were conducted "*with*" and "*without*" ground reflection boundary conditions. Out of many factors (mesh or grid size, mesh pattern and the aspect ratio) which control the accuracy of the results of blast numerical analysis, the grid or element size of the air model plays an important role [8, 18]. Hence a mesh sensitivity study was conducted (only on the Eulerian air model) to study the change in blast parameters such as the peak reflected pressure and the positive phase duration.

5. 4. 2D Blast simulation and its results

The unique capability of remapping of Autodyn is well studied in ref. [18] and the advantages of this approach are well explained in [8, 18]. This approach greatly reduced the number of grids or elements to achieve accurate blast parameters. In order to study the detonation of the C4 explosive, a wedge model was used (Figure

5-3). Accordingly 1000 grids (elements) were chosen along the "Y" axis in the air medium. The air and C4 were modelled using *multi-material Euler formulation*. The initiation, detonation and the expansion of C4 was modelled using the *Jones-Wilkins-Lee* (JWL) Equation of state (EOS) which can be written as

$$p = C_1\left(1-\frac{\omega}{r_1\upsilon}\right)\exp^{-r_1\upsilon} + C_2\left(1-\frac{\omega}{r_2\upsilon}\right)\exp^{-r_2\upsilon} + \frac{\omega e}{\upsilon} \tag{5.1}$$

where p is the hydrostatic pressure (Pa), ρ is the density (kg/m^3); $\upsilon = 1/\rho$ is the specific volume (m^3/kg); e is the specific internal energy (J); and C_1, C_2, r_1, r_2 and ω are adiabatic constants (these constants can be determined from dynamic experiments and values are available for most commonly used explosives such as C4). The adopted values of the constants of C4 are C_1 = 6.097699 x 10^8 kPa; C_2 = 1.2950 x 10^7 kPa; r_1 = 4.5; r_2 = 1.4 and ω = 0.25 [7]. For large expansion ratios of the explosive, the first and second terms of Equation (5.1) become negligible [8, 12] and the behaviour of the explosive can be considered as an ideal gas. Hence, similar to the approaches handled in [7, 8, 12] when the volume of the explosive has expanded by a factor 10, the EOS of the explosive (JWL equation) changes into the EOS of an ideal gas which can be written as

$$p = (\gamma - 1)\rho e \tag{5.2}$$

The standard properties of air (ρ= 1.225 kg/m^3; adiabatic gas constant γ= 1.4) were used for this simulation. The internal energy of air (e) was assumed to be 2.068 × 10^5 kJ/kg [7]. Moreover, the adiabatic constant of the explosive, ω was related to the adiabatic exponent γ of an ideal gas by the following relation [7, 8, 12]

$$\gamma = \omega + 1 \tag{5.3}$$

Using the above Equation Of States, the spherical charge of 20g C4 was modelled with an equivalent radius of 14 mm in the 2D model. Similarly, the wedge area filled with ambient air was modelled using the ideal gas equation (Equation (5.2)). Two wedge models have been created. The wedge length of the first model was 60 cm and the wedge length of the second model was 30 cm. Using the first model, the complete incident pressure-time history at a distance of 30 cm from the centre of detonation of C4 was calculated. Similarly from the second model the overpressure data was captured for remapping into a 3D air model. The contours of the simulated incident pressure at 30 cm from the detonation centre are shown in Figure 5-3.

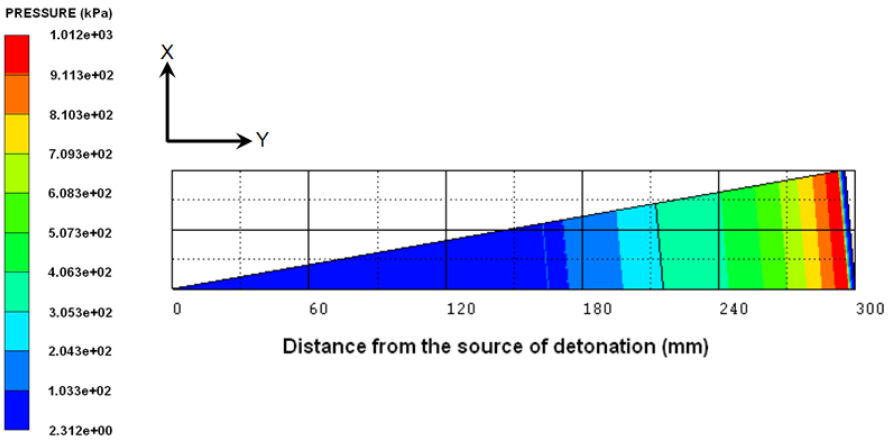

Figure 5-3: Wedge model (incident overpressure contours for 20g of C4 at 30 cm stand-off distance).

The magnitude of the pressure wave at that location (30 cm) was approximately 920 kPa. These symmetric (about the "Y" axis) spherical data were written into a remap file and then imported into the 3D air model. The details of the 3D modelling are discussed in the next section. As discussed in Chapter 4, few commercial tools are available to predict the blast parameters based on the empirical formulae. In order to compare the incident blast parameters the results from the Hydrocodes calculation was compared with *ConWep* data for the same input parameters (mass of the C4 = 20 g and stand-off distance is 30 cm). Figure 5-4 shows a comparison of the incident blast parameters (arrival time, peak incident pressure and the positive phase duration) from Autodyn, *ConWep* and experimentally measured data. For the simplification only the positive phase of the pressure-time history is considered.

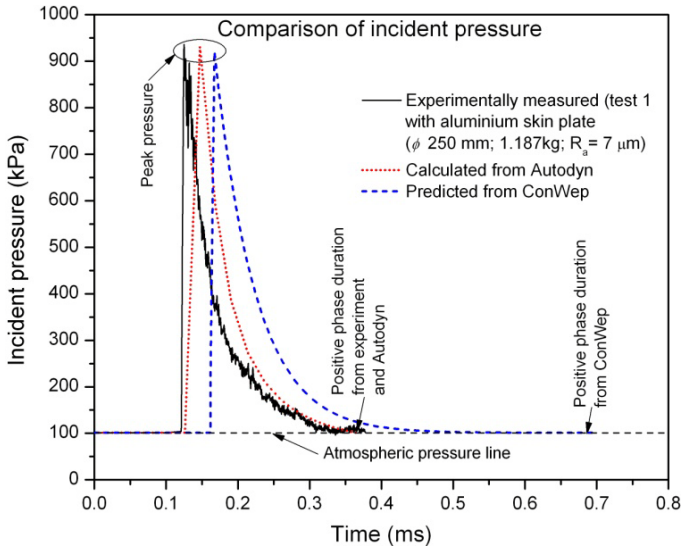

Figure 5-4: Comparison of incident pressure-time histories.

The magnitude of peak incident overpressure from the experimental measurement and the calculated value from Autodyn were very close to the *ConWep* predicted data (923 kPa, 920 kPa and 898.7 kPa from the experimental, Autodyn and *ConWep* respectively). Furthermore, there was a good correlation observed for arrival time and positive phase duration between the experimentally measured data (0.121 ms and 0.378 ms respectively) and Autodyn simulated values (0.126 ms and 0.37 ms respectively). However, the predicted time of arrival and the positive phase duration from the ConWep showed longer durations (0.162 ms and 0.6941 ms for arrival time and positive duration of the blast respectively).

5. 5. 3D Blast simulation with aluminium skin plate

In order to study the interaction of the blast pressure wave with the skin plates and to understand the clearing effect of reflected pressure waves, a detailed 3D computational model was created. The numerical modelling details of the complete experimental set-up (and its individual components) with aluminium skin plate are presented in this section.

5. 5. 1. Air model

The air was modelled as a rectilinear box with Eulerian grid. The boundary of the air model was chosen to have adequate air space in all directions from the centre of detonation. The dimensional details and the 3D computational modelling of the experimental set-up are shown in Figure 5-5.

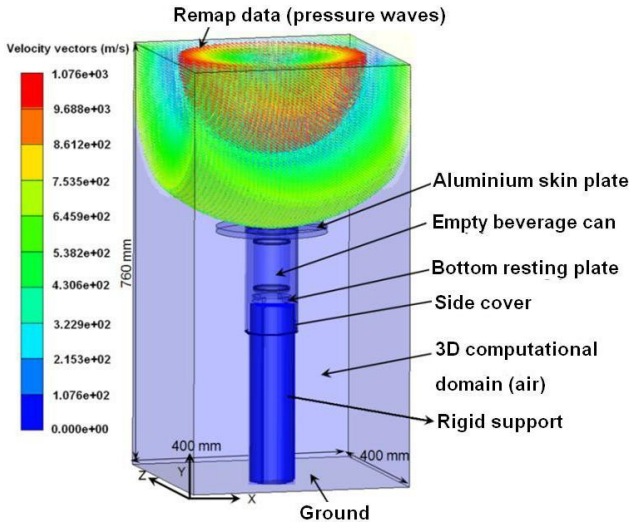

Figure 5-5: 3D computational model for simulating blast waves with aluminium skin plate.

The propagation of blast pressure from the 2D simulation was fed into the 3D air model by "remapping". Remapping allows the user to take the solution of one analysis and impose it on a selected region(s) of another model and to start a new analysis. The remapping file stores the field data of the initial spherically symmetric expanding blast wave. Accordingly the field data which were created from the 2D simulation were remapped (symmetrical about "Y" axis and 30 cm away from the top face of aluminium skin plate) into the 3D air model. The Equation of state (Equation (5.2)) and the corresponding air properties are the same as used in the 2D simulation.

5. 5. 2. EOS and material model for aluminium skin plate and side tube

For the experimental set-up the aluminium skin plate was integrated with a side flexi -glass. Similar to the decoupled analysis (discussed in Chapter 4), the side tube was also modelled as an aluminium tube to eliminate the complexity in the EOS and material model. The equivalent mass of the flexi-glass was considered to model the side aluminium tube. The aluminium skin plate and the side tube were modelled by solid brick elements with eight nodes. For a close stand-off air blast loading, the air molecules at the centre of the pressure wave interact initially with the structure due to the shorter distance of travelling. This central spherical wave can have a significant influence on the overall behaviour of the structure. To capture this effect, a uniform and fine mesh was introduced at the centre of the aluminium skin plate. In order to avoid the spurious reflection of pressure waves at the interface of fine/coarse mesh [19-22], the size of the elements was increased gradually (adjacent elements size was chosen in such a way that the size ratio of these elements should not go beyond 1.5 as suggested in ref. [22]).The mesh patterns of the skin plate and the side tube are shown in Figure 5-6.

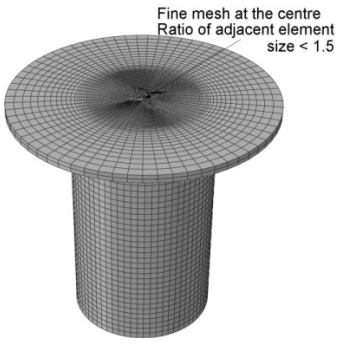

Figure 5-6: Mesh pattern of aluminium skin plate assembly.

The volumetric response or compression response of the skin plate and the side tube were modelled using Mie-Gruneisen EOS which is given by (Equation (5.4))

$$p = p_H + \Gamma_\rho (e - e_H) \tag{5.4}$$

where e is the energy (J); the constant Γ_ρ and the variables p_H and e_H are given by the following equations (Equations (5.5) to (5.7)),

$$\Gamma_\rho = \Gamma_0 \rho_0 \tag{5.5}$$

$$p_H = \frac{\rho_0 C_0^2 \mu (1+\mu)}{[1-(S-1)\mu]^2} \tag{5.6}$$

$$e_H = \frac{1}{2} \frac{p_H}{\rho_0} \left(\frac{\mu}{1+\mu} \right) \tag{5.7}$$

where ρ_0 is the initial density (kg/m^3); Γ_0 is the Gruneisen coefficient (2.1 [7]); $\mu = \rho / \rho_0 - 1$; C_0 (5380 m/s [7]) and S (1.337 [7]) are material constants based on a linear relationship between particle velocity and shock velocity. Similar to the decoupled analysis, to include the effect of strain-rate and strain hardening on the aluminium skin plate, the Johnson-Cook material model was used and the material parameters for aluminium 2024 were adopted from ref. [23] and the same were already given in Chapter 3.

5. 5. 3. EOS and material model for empty beverage can

The geometry, material details, used finite elements for the modelling of the beverage can are very similar to the ones which were discussed in Chapter 4. For the empty beverage can, it was assumed that the influence of the change in entropy is not significant and so the pressure (p) was considered to be only a function of density or specific volume (μ). An alternative approach is to consider the initial elastic behaviour expressed by *Hooke's* law. Hence the linear equation of state is given by (Equation (5.8)),

$$p = K\mu \tag{5.8}$$

where K is the bulk modulus of the material. The choice of constitutive equation controls the ability to accurately predict the behaviour of an empty beverage can during a blast loading case. Similar to Chapter 4, to capture the strain hardening and strain rate hardening, the Johnson-Cook material model was used and the corresponding material parameters ([23, 24]) were already introduced in Chapter 3.

5. 5. 4. Bottom resting plate and non-sacrificial structure (rigid support)

In the experimental set-up a copper tube was used to represent the non-sacrificial structure (refer Figure 5-1(a)). A bottom resting plate was placed above the load cell which was connected to the non-sacrificial structure. Similar to the experimental conditions, the length of the copper tube (320 mm) is important to study the effect of ground reflection of the pressure waves. In order to reduce the computation time the bottom resting plate and the copper tube were modelled as rigid bodies and subsequently, all translational and rotational degrees of freedom were arrested.

5. 5. 5. Applied boundary conditions and contact controls

On the rectilinear air flow domain, the "*flow-out"* boundary condition was assigned to all boundary planes of the 3D domain except the base plane, which represented the ground surface. This boundary condition is needed to simulate the reflection of pressure waves from the ground surface. To compare the results a separate analysis "*without*" ground reflection was carried out. For this case the ground surface was also assigned with "flow-out" boundary condition. The interaction of blast pressure waves with the aluminium skin plate and the side tube was defined by a fully coupled feature available in Autodyn V-11.0. The fully coupled algorithm allows the *Lagrange and the Euler-FCT (Flux Corrected Transport)* formulation to be coupled in a single problem. With help of this approach a high order solution is computed wherever possible in the flow field. This coupled algorithm automatically detects the interfacing faces of aluminium skin plate, side tube and the rigid support. These interfacing faces act as a physical constraint to the fluid domain. Consequently, the resultant shock from the pressure waves on the aluminium skin plate will be transferred to the test specimen.

In the experimental set-up the side tube was used to guide the translational movement of the skin plate (axial direction to the test specimen) during the interaction of pressure waves and the crushing of the test specimen. To simulate the same experimental condition, the translational degrees of freedom of the aluminium skin plate in "X" and "Z" directions were arrested. Similarly, the rotation of the aluminium skin plate with respect to the "Y" axis was also arrested. The bending of the skin plate with respect to "X" and "Z" axis was allowed. A "*surface-to-surface*" master-slave contact algorithm was established with a friction coefficient equal to 0.2 for two pairs. The first pair consists of the aluminium skin plate and the beverage can and the second pair consists of the bottom resting plate and the beverage can. In addition to that a self contact algorithm was also incorporated for the empty beverage can model.

5. 6. 3D Blast simulation with sandwich composite skin plate

As mentioned in Chapter 4, a lower inertia and an adequate bending stiffness can be achieved with a sandwich composite skin plate. To account for the energy absorbed by the composite skin faces (top and bottom) and the polyurethane foam during the blast loading, the modelling of the concerned materials is absolutely necessary. Hence, similar to Chapter 4 the finite element modelling of the sandwich composite plate was done as per the assembly sequence which is shown in Figure 5-7. The EOS and material models for air, empty beverage can, aluminium plate (ϕ 97 mm; 2 mm thick – refer Figure 5-7), bottom resting plate and rigid support are similar to the ones discussed for the aluminium skin plate. The top and bottom composite faces were modelled with shell elements. To capture the compression behaviour the polyurethane foam was modelled with solid 8 node brick elements.

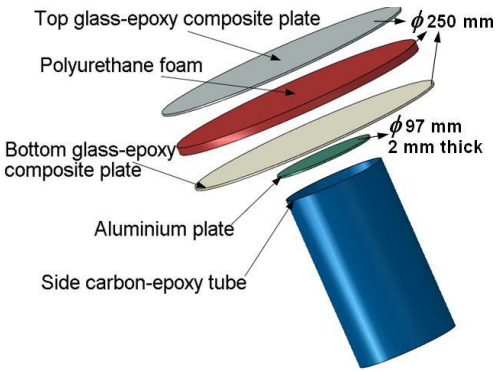

Figure 5-7: Assembly sequence of the sandwich composite skin plate.

5. 6. 1. EOS for glass-epoxy composite plates (top and bottom faces and the side tube)

The behaviour of the top and bottom glass-epoxy composite faces was modelled by using "*Orthotropic"* material model. This model is suitable for high dynamic loading applications and it is able to calculate the contributions to the pressure from the isotropic and deviatoric strain components. Secondly, it provides deviatoric stresses from the deviatoric strains. Furthermore, using this method the non-linear effects such as shock effects can be incorporated. For any linear orthotropic material the stress and strain relation can be written in terms of the orthotropic stiffness matrix C_{ij} which is a function of material constants E_{ij}, υ_{ij} and G_{ij} (E is Young's modulus, υ is the Poisson's ratio and G is the shear modulus of that material). The incremental linear stress-strain relationship is given by (Equation (5.9)),

$$\begin{bmatrix} \Delta\sigma_{11} \\ \Delta\sigma_{22} \\ \Delta\sigma_{33} \\ \Delta\sigma_{23} \\ \Delta\sigma_{31} \\ \Delta\sigma_{12} \end{bmatrix} = \begin{bmatrix} C_{11} & C_{12} & C_{13} & 0 & 0 & 0 \\ C_{21} & C_{22} & C_{23} & 0 & 0 & 0 \\ C_{31} & C_{32} & C_{33} & 0 & 0 & 0 \\ 0 & 0 & 0 & C_{44} & 0 & 0 \\ 0 & 0 & 0 & 0 & C_{55} & 0 \\ 0 & 0 & 0 & 0 & 0 & C_{66} \end{bmatrix} \begin{bmatrix} \Delta\varepsilon_{11} \\ \Delta\varepsilon_{22} \\ \Delta\varepsilon_{33} \\ \Delta\varepsilon_{23} \\ \Delta\varepsilon_{31} \\ \Delta\varepsilon_{12} \end{bmatrix} \tag{5.9}$$

To include the non-linear effect of shock waves in the above linear equation it is desirable to separate the thermodynamic response (volumetric response) of the material from its ability to carry the shear loads (strength). For this, it is convenient to separate the strain increments $\Delta\varepsilon_{ij}$ into their volumetric (average) and deviatoric components $\Delta\varepsilon_{ij}^{d}$ which is given as (Equation (5.10)),

$$\Delta\varepsilon_{ij} = \Delta\varepsilon_{ij}^{d} + \Delta\varepsilon_{average} \tag{5.10}$$

where $\Delta\varepsilon_{average}$ is the average direct strain and can be stated as follows (Equation (5.11)),

$$\Delta\varepsilon_{average} = \frac{1}{3}(\varepsilon_{11} + \varepsilon_{22} + \varepsilon_{33}) \tag{5.11}$$

where ε_{11}, ε_{22} and ε_{33} are the three principal strains. For small strain increments the volumetric strain increment can be defined as (Equation (5.12)),

$$\Delta\varepsilon_{vol} = \varepsilon_{11} + \varepsilon_{22} + \varepsilon_{33} \tag{5.12}$$

The total strain increments can be expressed in terms of the volumetric and deviatoric strain increments resulting in the following orthotropic constitutive equation (Equation (5.13)).

$$\begin{bmatrix} \Delta\sigma_{11} \\ \Delta\sigma_{22} \\ \Delta\sigma_{33} \\ \Delta\sigma_{23} \\ \Delta\sigma_{31} \\ \Delta\sigma_{12} \end{bmatrix} = \begin{bmatrix} C_{11} & C_{12} & C_{13} & 0 & 0 & 0 \\ C_{21} & C_{22} & C_{23} & 0 & 0 & 0 \\ C_{31} & C_{32} & C_{33} & 0 & 0 & 0 \\ 0 & 0 & 0 & C_{44} & 0 & 0 \\ 0 & 0 & 0 & 0 & C_{55} & 0 \\ 0 & 0 & 0 & 0 & 0 & C_{66} \end{bmatrix} \begin{bmatrix} \Delta\varepsilon_{11}^{d} + 1/3\,\Delta\varepsilon_{vol} \\ \Delta\varepsilon_{22}^{d} + 1/3\,\Delta\varepsilon_{vol} \\ \Delta\varepsilon_{33}^{d} + 1/3\,\Delta\varepsilon_{vol} \\ \Delta\varepsilon_{23} \\ \Delta\varepsilon_{31} \\ \Delta\varepsilon_{12} \end{bmatrix} \tag{5.13}$$

If the above equation is expanded and the deviatoric and volumetric terms are grouped, the following expressions for the direct stress increments can be written (Equation (5.14)).

$$\begin{aligned}\Delta\sigma_{11} &= \tfrac{1}{3}(C_{11}+C_{12}+C_{13})\Delta\varepsilon_{vol} + C_{11}\Delta\varepsilon_{11}^{d} + C_{12}\Delta\varepsilon_{22}^{d} + C_{13}\Delta\varepsilon_{33}^{d}\\ \Delta\sigma_{22} &= \tfrac{1}{3}(C_{21}+C_{22}+C_{23})\Delta\varepsilon_{vol} + C_{21}\Delta\varepsilon_{11}^{d} + C_{22}\Delta\varepsilon_{22}^{d} + C_{23}\Delta\varepsilon_{33}^{d}\\ \Delta\sigma_{33} &= \tfrac{1}{3}(C_{31}+C_{32}+C_{33})\Delta\varepsilon_{vol} + C_{31}\Delta\varepsilon_{11}^{d} + C_{32}\Delta\varepsilon_{22}^{d} + C_{33}\Delta\varepsilon_{33}^{d}\end{aligned} \tag{5.14}$$

To find the equivalent pressure increment, firstly the pressure as a third of the trace of the stress increment tensor is defined (Equation (5.15))

$$\Delta p = -\tfrac{1}{3}(\Delta\sigma_{11} + \Delta\sigma_{22} + \Delta\sigma_{33}) \tag{5.15}$$

Substituting Equation (5.14) into Equation (5.15) results in an expression for the pressure of the form, from which the contributions to the pressure from volumetric and deviatoric components of strain can be clearly identified (Equation (5.16)).

$$\begin{aligned}\Delta p = &-\tfrac{1}{9}[C_{11}+C_{22}+C_{33}+2(C_{12}+C_{23}+C_{31})]\Delta\varepsilon_{vol}\\ &-\tfrac{1}{3}[C_{11}+C_{12}+C_{13}]\Delta\varepsilon_{11}^{d} - \tfrac{1}{3}[C_{21}+C_{22}+C_{23}]\Delta\varepsilon_{22}^{d}\\ &-\tfrac{1}{3}[C_{31}+C_{32}+C_{33}]\Delta\varepsilon_{33}^{d}\end{aligned} \tag{5.16}$$

For an isotropic material the first term on the right-hand side of Equation (5.16) is equivalent to the linear equation of state. For an orthotropic material the first term can be replaced with the Mie-Gruneisen equation of state, and the remaining terms act as a correction due to deviatoric strains:

$$\begin{aligned}\Delta p = p_r(\varepsilon_{vol}) + \frac{\Gamma(\upsilon)}{\upsilon}[e_r - e_r(\varepsilon_{vol})] - \tfrac{1}{3}[C_{11}+C_{12}+C_{13}]\Delta\varepsilon_{11}^{d}\\ -\tfrac{1}{3}[C_{21}+C_{22}+C_{23}]\Delta\varepsilon_{22}^{d} - \tfrac{1}{3}[C_{31}+C_{32}+C_{33}]\Delta\varepsilon_{33}^{d}\end{aligned} \tag{5.17}$$

The parameters $p_r(\varepsilon_{vol})$ and $e_r(\varepsilon_{vol})$ define the material pressure, volume and energy relationship along the Hugoniot shock reference curve (refer Figure 5-8). The Gruneisen gamma $\Gamma(\upsilon)$ allows to identifying the material state of the reference curve and is a thermodynamic property of the material. The used orthotropic material parameters for glass/epoxy were already given Chapter 4.

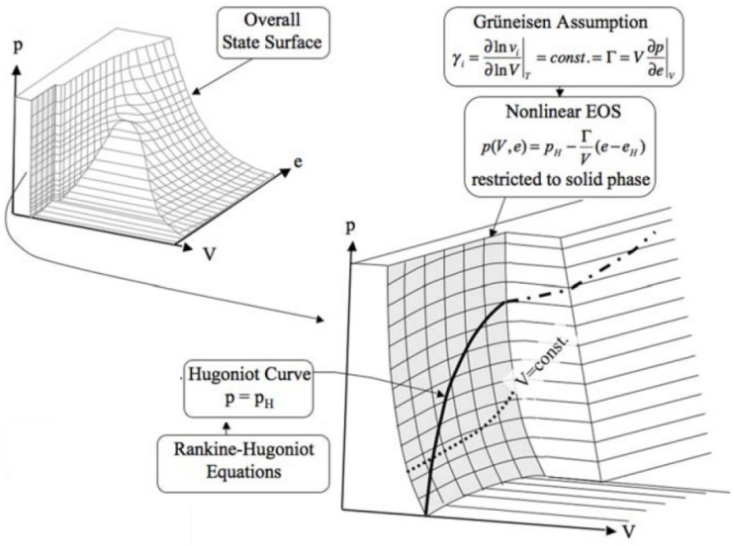

Figure 5-8: Construction of a non-linear equation of state for shock propagation processes based on the Rankine-Hugoniot equations and Gruneisen theory [25].

5. 6. 2. Material model for glass-epoxy composite plates

Similar to Chapter 4, the bottom and top faces of the skin plate was modelled with shell elements. To capture the damage in these shell layers the standard available failure criteria in Autodyn (Tsai-Wu failure) [26] were used. For plane stress, the Tsai-Wu polynomial failure criteria can be expressed as (Equation (5.18)),

$$F_1\sigma_1 + F_2\sigma_2 + F_{11}\sigma_1^2 + F_{22}\sigma_2^2 + F_{66}\tau_{12}^2 + 2F_{12}\sigma_1\sigma_2 = 1 \tag{5.18}$$

All parameters of the Tsai-Wu criterion, other than F_{12}, can be expressed in terms of the basic strengths

$$\begin{aligned} F_1 &= \frac{1}{X_1^T} - \frac{1}{X_1^C}; F_{11} = \frac{1}{(X_1^T X_1^C)}; F_{22} = \frac{1}{X_2^T} - \frac{1}{X_2^C} \\ F_{22} &= \frac{1}{(X_2^T X_2^C)}; F_{66} = 1/S_6^2 \end{aligned} \tag{5.19}$$

F_{12} is a strength interaction parameter that has to be determined from a bi-axial experiment. Alternatively, this can be estimated from the following relationship suggested by Tsai and Hahn [26].

$$F_{12} = -\frac{1}{2}\sqrt{F_{11}F_{22}} \tag{5.20}$$

The details of used symbols and their material strengths for the analysis were already discussed in Chapter 4.

5. 6. 3. Polyurethane foam

The polyurethane foam strength model was represented by means of the crush characteristics (refer Figure 4-25 of Chapter 4). The strength model was accompanied with a linear equation of state and with the following incremental elastic update of pressure and stress deviator used,

$$p^{n+1} = p^n + K\dot{\varepsilon}^{n+1/2}\Delta t^{n+1/2} \tag{5.21}$$

$$S_{ij}^{n+1} = S^n + 2G\left(\varepsilon_{ij}^{n=+1/2} - \delta_{ij}\dot{\varepsilon}^{n+1/1}\right)\cdot\Delta t^{n+1/2} \tag{5.22}$$

where p is the pressure; K is the shear modulus; S is the stress deviator; G is the bulk modulus; ε is the volumetric strain; Δt is the incremental time and n is the number of increments. The magnitude of the resulting principal stresses is compared against the allowable principal compaction stress for the current volumetric strain. If the principal stress exceeds the maximum allowable then it is reduced to the allowable value.

5. 7. Results and discussions

A blast simulation with fully coupled Lagrangian and Eulerian formulation for the empty beverage can (20g of C4 and a stand-off distance of 30 cm) was carried out. The interaction of the pressure waves with the skin plates was studied. The magnitude of the reflected pressure wave was calculated at the air grid which was closer to the top and bottom faces of the skin plates (1 μm away from the faces). A few researchers [8, 18] have concluded that the grid size of the air model plays an important role to predict the blast parameters. In order to study the effect of the grid size on the blast parameters, a mesh sensitivity study was conducted for the air model with the aluminium skin plate (ϕ 200 mm; 1.0 kg). The different grid sizes (1 mm to 15 mm) of air models are shown in Figure 5-9(a-d). The effect of grid or element size on the peak reflected pressure values can be easily understood from Figure 5-10. For a smaller element size (0.25 mm and 0.5 mm) the magnitude of the peak reflected pressures (4849 kPa and 4745 kPa respectively) were very close to the ConWep value (4755 kPa). The corresponding positive phase durations are also shown in the same figure. There was no significant difference in the positive duration noticed due to the change in size of the element (minimum 0.18 ms; maximum 0.183 ms). However, these values are significantly higher than the experimental values which were presented in Chapter 4 (refer Table 4-6 and Table 4-8). The reason for this difference is the surface roughness of the skin plates which

cannot be included in the present numerical analysis. An element size of 0.25 mm was used for all the analyses.

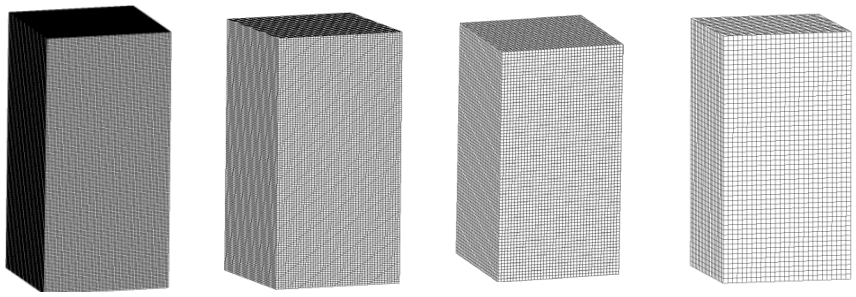

(a) **(b)** **(c)** **(d)**

Figure 5-9: Air models with different grid sizes **(a)** 1 mm air grid size **(b)** 5 mm air grid size **(c)** 10 mm air grid size **(d)** 15 mm air grid size.

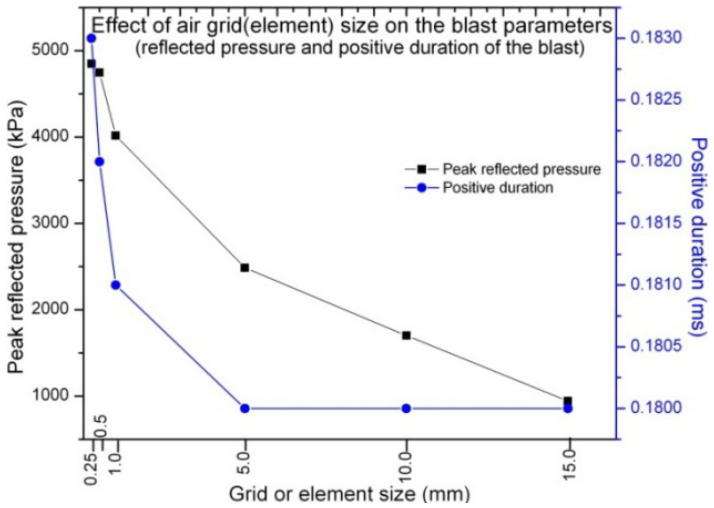

Figure 5-10: Mesh sensitivity study on the peak reflected pressure and its positive duration.

5. 8. Reflected blast parameters for aluminium and sandwich composite skin plates

5. 8. 1. Reflected pressure profiles at the top face of the skin plates

The calculated pressure profiles from the top face of the aluminium skin plate (ϕ 200 mm; 1.0 kg) and the sandwich composite skin plate (ϕ 250 mm; 0.54 kg) are shown in Figure 5-11 and Figure 5-12 respectively. The reflected pressure profile was measured at five locations on the top face of the skin plates (Figure 5-11 and Figure

5-12). For the simplification, only the positive phase of the reflected pressure profile is considered for discussion. It can be noticed that the peak magnitude of the reflected pressure wave from the centre (4849 kPa for aluminium skin plate and 4960 kPa for sandwich composite skin plate) was gradually reduced to the periphery (4006 kPa for aluminium skin plate and 3948 kPa for sandwich composite skin plate) for both skin plates. Correspondingly, the positive phase duration varied from 0.1998 ms to 0.1686 ms for the aluminium skin plate; and for the sandwich composite skin plate it varied from 0.223 ms to 0.188 ms.

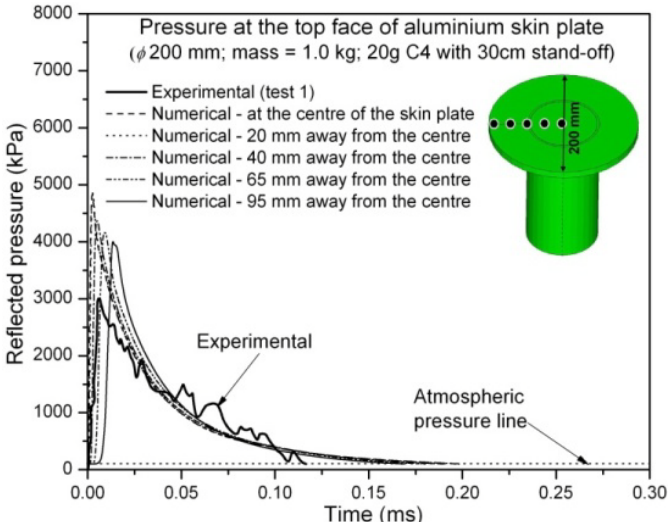

Figure 5-11: Reflected pressure time histories at the top face of the aluminium skin plate (ϕ200 mm; 1.0 kg).

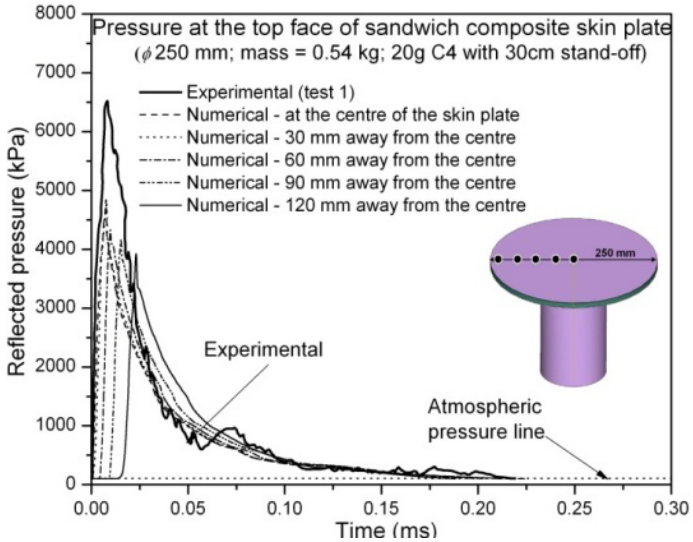

Figure 5-12: Reflected pressure time histories at the top face of sandwich composite skin plate (ϕ250 mm; 0.54 kg).

In order to understand the difference in results between the coupled simulation (Autodyn) and the empirical relation (*ConWep*), a comparison was made for the reflected pressure and the corresponding positive duration. Figure 5-13 shows the pressure distribution and its positive phase duration from ConWep (for 20g of C4 with a stand-off distance of 30 cm) for the plates with ϕ 200 mm (diameter of the aluminium skin plate) and ϕ 250 mm (diameter of the sandwich composite skin plate).

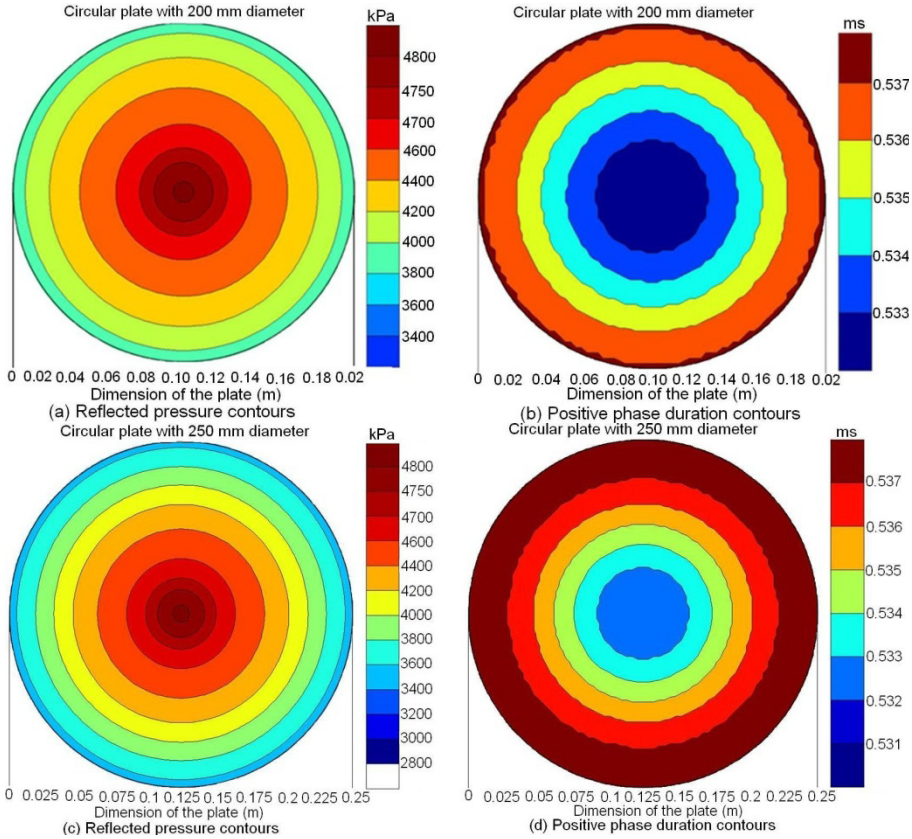

Figure 5-13: Contour plots from ConWep for 20g C4 with a stand-off distance of 30cm - **(a) & (b)** Reflected pressure contours and positive phase duration for a circular plate of ϕ 200 mm respectively. **(c) & (d)** Reflected pressure contours and positive phase duration for a circular plate of ϕ 250 mm respectively.

The peak reflected pressure at the centre and the average reflected pressure on the surface of the skin plates from the Autodyn simulations (4849 kPa and 4429 kPa for aluminium skin plate; 4960 kPa and 4483 kPa for sandwich composite skin plate) were very close to the ConWep values (4755 kPa and 4492 kPa for ϕ 200 mm plate; 4755 kPa and 4225 kPa for ϕ 250 mm plate). On the other hand, the average positive phase duration from the numerical simulation (0.187 ms for the aluminium skin plate; 0.2089 ms for the sandwich composite skin plate) was much lower than the

ConWep predicted values (0.532 ms for ϕ 200 mm plate; 0.535 ms for ϕ 250 mm plate). This difference is due to the fact that *ConWep* (based on empirical relations) does not take into account the finite reflected surface area. However, for the aluminium skin plate the peak reflected pressure and the positive duration values from these two approaches (*ConWep* and Autodyn) were higher than for the experimental data (refer Figure 5-11 and Figure 5-13(a)). On the other hand, the peak reflected pressures for the sandwich composite skin plate from Autodyn and ConWep (4960 kPa and 4755 kPa respectively) were lower (refer Figure 5-12 and Figure 5-13(b)) than the experimental value (average is 6650 kPa). The reason for the significant differences in the peak reflected pressure is the surface roughness of the top face of the skin plates which cannot be included in the present numerical simulation analyses. As a result of the different peak reflected pressure, the calculated average impulse from the Autodyn simulation for the aluminium skin plate (153.7 kPa-ms (0.00482 kN-s)) was higher than the average experimental impulse (125.41 kPa-ms (0.00394 kN-s)). The calculated average impulse from the Autodyn simulation for the sandwich composite skin plate (155.7 kPa-ms (0.00764 kN-s)) was lower than the average experimental impulse (206.2 kPa-ms (0.0101 kN-s)).

5. 8. 2. Diffraction associated clearing of reflected pressure waves

The clearing of reflected pressure waves and the consequent diffraction phenomenon can be explained by investigating the propagation and interaction of blast pressure waves with respect to time. As an example, one of the cases (aluminium skin plate) is discussed here. Figure 5-14(a-d) show the interaction of the pressure waves (at the mid-plane representing X = 0 and Z = 0) with top and bottom faces of the aluminium skin plate. These figures show a chronological event of interaction and diffraction of the pressure waves around the edges of the aluminium skin plate. As mentioned earlier the remapping of the 2D blast wave was fed into the 3D computational model. After remapping the analysis was started when the pressure reached 1 mm above the top face of the aluminium skin plate (this corresponds to time t = 0 ms). The magnitude of the pressure wave increased suddenly when the incident pressure was obstructed by the top face of the aluminium skin plate (refer Figure 5-11 and Figure 5-14(a)). Due to the spherical wave front a higher magnitude was observed at the centre of the top face of the aluminium skin plate. This event started approximately 1.1 μs after the start of the simulation at the centre of the top face of the aluminium skin plate; and it lasted for approximately 0.01 ms. After that the amplitude reduced exponentially. During this period a significant amount of pressure waves (especially the pressure wave at the periphery of the top face of the aluminium skin plate) diffracted around the top edge of the aluminium skin plate. Due to the limited surface of the aluminium skin plate (radius is 100 mm) the

reflected pressure wave reached the edges in a very short time. This event of diffraction is called "*clearing*" of the reflected pressure waves. Due to this clearing the magnitude of the reflected pressure wave was reduced significantly in short time. Furthermore, a clear evidence of the diffracted pressure waves acting on the bottom face of the aluminum skin plate can be noticed in Figure 5-14(c-d). The calculated pressure-time history of the pressure waves at the top and bottom faces (70 mm from the centre) of the aluminum skin plate is shown in Figure 5-15.

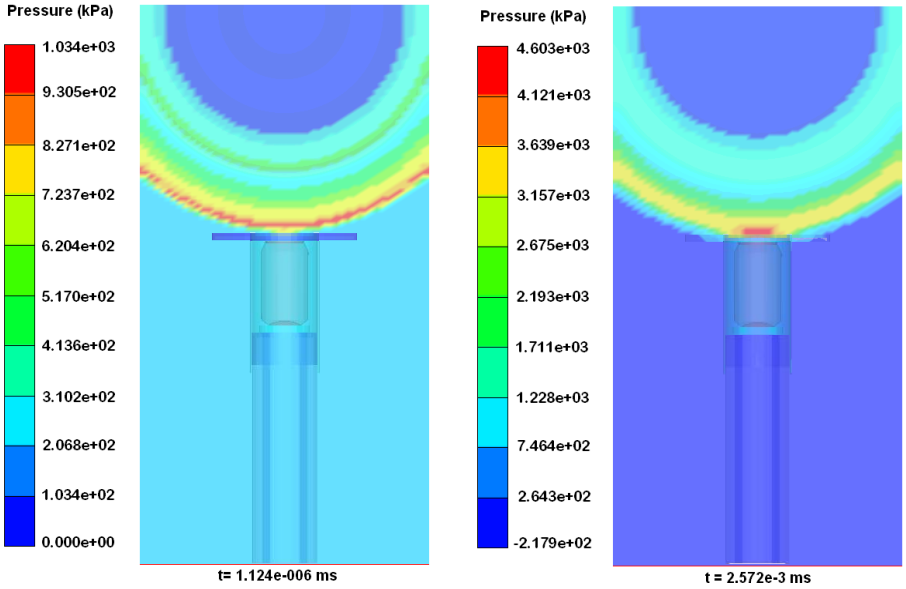

(a)

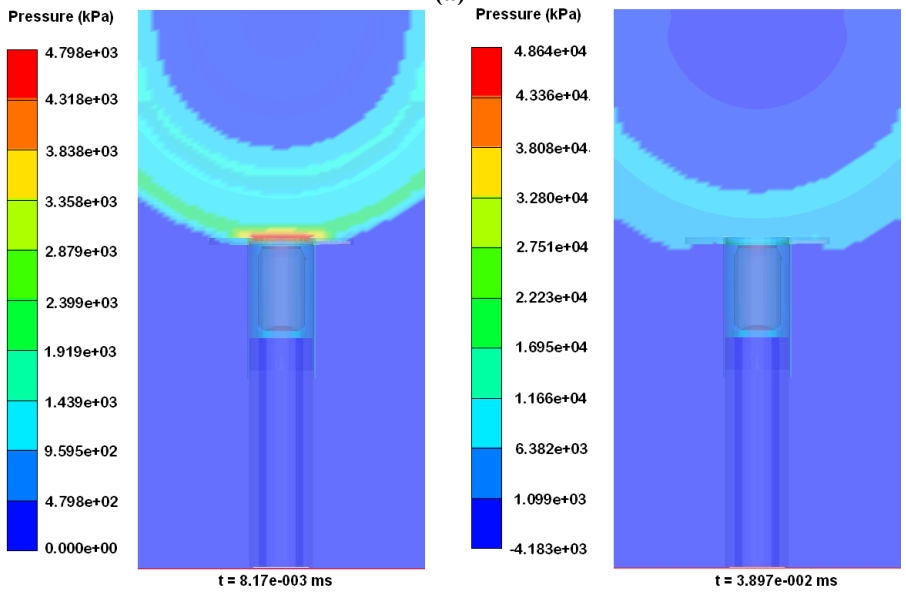

(b)

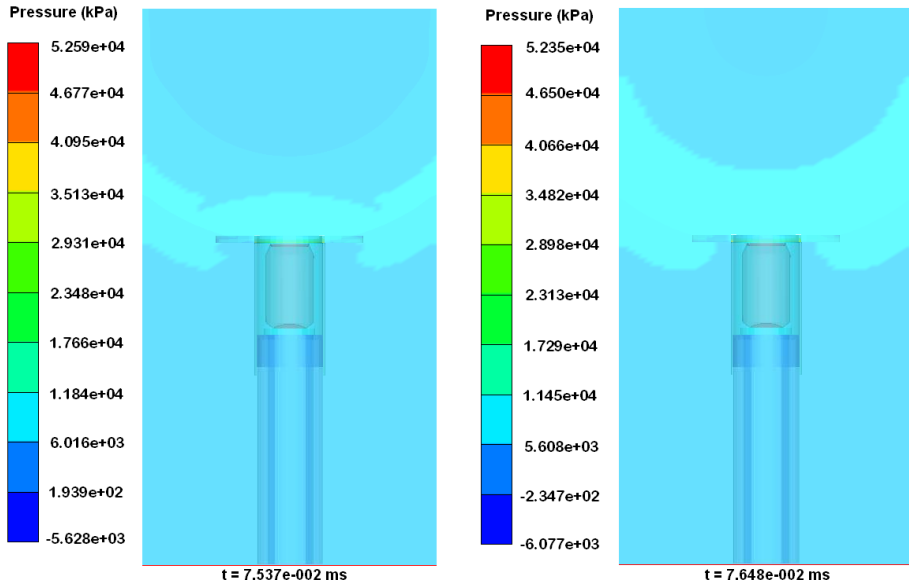

(c)

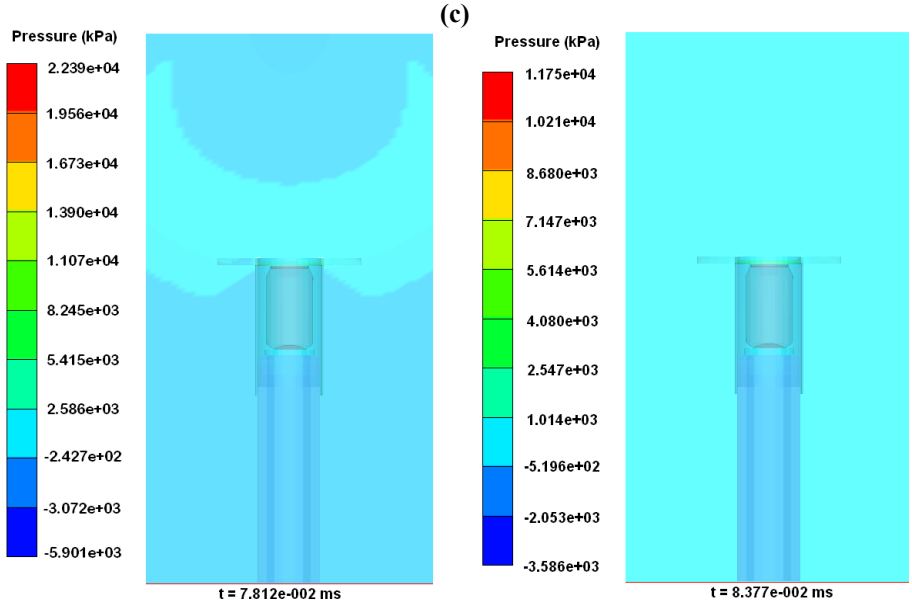

(d)

Figure 5-14: (a-d) Interaction of blast pressure waves with the aluminium skin plate.

It can be noticed that the magnitude of the diffracted pressure and its duration at the bottom face was significant compared to the peak reflected pressure at the top face of the aluminium skin plate. The rise in pressure at the bottom face was noticed approximately 0.008 ms later than the rise in pressure at the top face of the aluminium skin plate. This was due to the time taken for the pressure waves to reach the edges and to create the subsequent diffraction phenomenon. The maximum magnitude of the diffracted pressure acting at the bottom face was approximately

743 kPa (Figure 5-15). In addition to the diffracted pressure, the direct pressure waves from the explosion at the boundary of the skin plate also contributed to increase the pressure at the bottom face of the skin plate (engulfing phenomenon). Subsequently, the magnitude of the pressure wave was exponentially reduced to the atmospheric pressure due to the undisturbed air volume below the skin plate. Similar interaction of the pressure waves was also observed for the sandwich composite skin plate (refer Figure 5-16). However, the magnitude and the corresponding duration was much lower. The calculated average impulse from the diffraction (area below the diffracted pressure curves in Figure 5-15 and Figure 5-16) for these cases was 41.89 kPa-ms (0.0013 kN-s) and 40.82 kPa-ms (0.002 kN-s) for the aluminium and sandwich composite skin plates respectively.

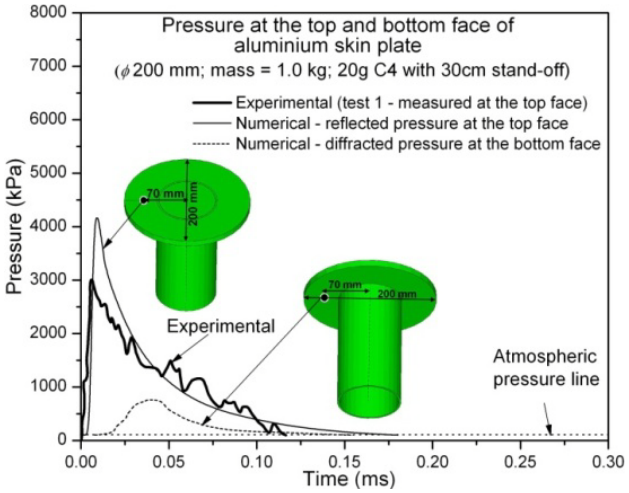

Figure 5-15: Pressure interaction at top and bottom faces of the aluminium skin plate (ϕ200 mm; 1.0 kg).

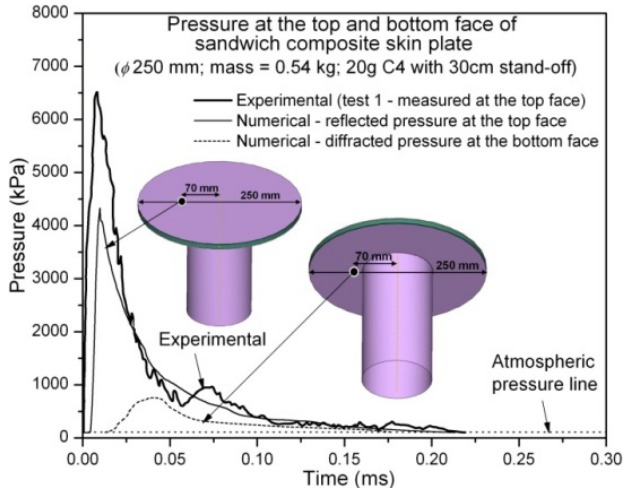

Figure 5-16: Pressure interaction at top and bottom faces of the sandwich composite skin plate (ϕ250 mm; 0.54 kg).

5. 8. 3. Experimental validation

In order to observe the diffraction phenomenon during the experimental testing, a few experimental tests were conducted with a high speed camera (Photron APX RS 250K capable of recording 250,000 fps). A frame rate of 10,000 fps was used for these tests. High speed images from the experiments showed a clear evidence of diffraction and subsequent pressure acting on the bottom face of the skin plates (refer Figure 5-17). Concluding from the values observed from this 3D computational model, less than one sixth of the reflected pressure was acting at the bottom face due to the diffraction associated with the clearing of the pressure waves. However, this magnitude is also depending upon the area of the reflected surface and the distance from the edges of the reflected surface to its centre. The major advantage of carrying out such a numerical simulation is obtaining a clear picture of the interaction of blast pressure waves. In addition to that, it provides an opportunity to measure the reflected blast parameters at the locations where the experimental measurement is highly tedious or impossible. The measurement of blast pressure at the bottom face of the skin plates has a high risk for the pressure transducer and its couplings from the blast pressure. Indeed, to measure the pressure at the bottom face a major part of the pressure transducer and its couplings has to be assembled on the top face of the skin plates. As mentioned in Chapter 4, the (decoupled) numerical study based upon the experimentally measured reflected pressure-time profiles at the top face predicted too high deformation lengths of the test specimens. The reason is that in the numerical model the pressure acting on the bottom face of the skin plates due to the diffraction effect was not accounted for.

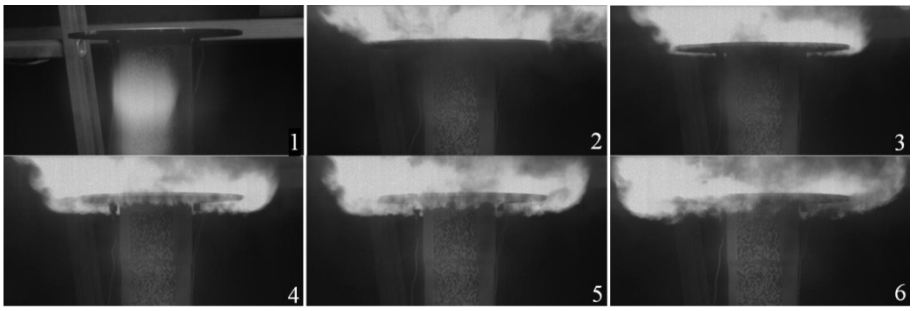

Figure 5-17: High speed image evidences for diffraction of blast waves during blast loading (with aluminium skin plate).

5. 8. 4. Ground reflection

As mentioned earlier, experiments with a longer length of the supporting copper tube which represented the non-sacrificial member, showed a higher deformation length than the shorter one. After assembling the test specimen in the experimental

test set-up, the measured distance from the top face of the skin plates to the ground surface was 450 mm. To investigate the effect of ground reflection, numerical simulations were carried out "*with*" and "*without*" ground reflection boundary condition. For both analyses the same 3D air domain was used. As an example, the calculated pressure-time histories at the bottom face of the aluminium skin plate are shown in Figure 5-18 and Figure 5-19 for cases "*with*" and "*without*" ground reflection respectively.

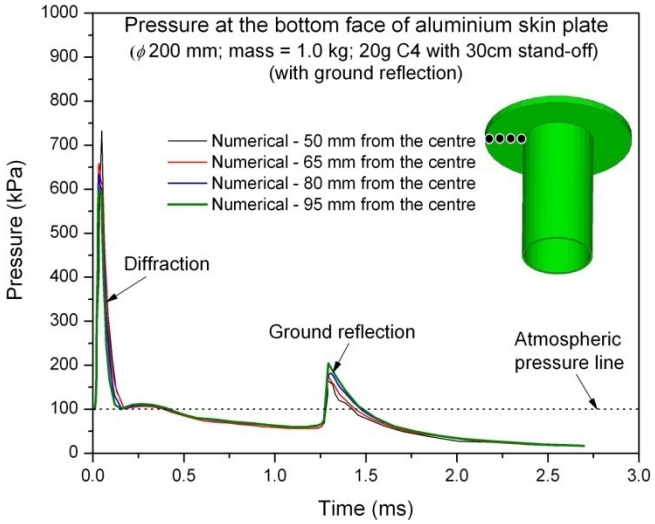

Figure 5-18: Pressure- time histories at the bottom face of the aluminium skin plate with ground reflection

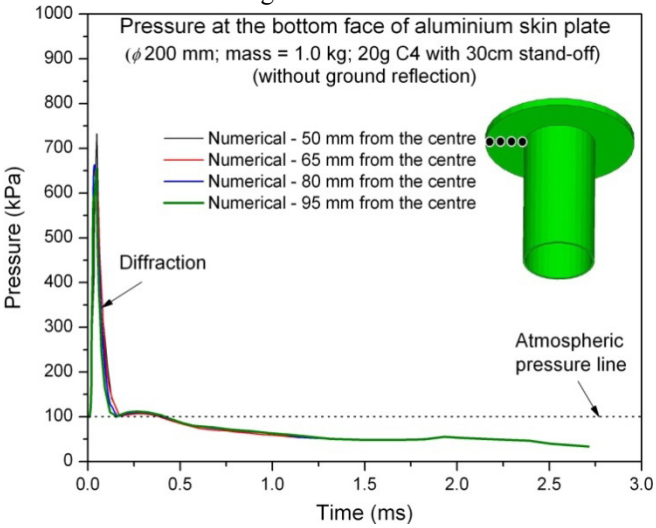

Figure 5-19: Pressure- time histories at the bottom face of aluminium skin plate without ground reflection.

As discussed in the earlier section the pressure was increased at the bottom face for both cases suddenly due to the diffracted pressure wave from the top face and direct

blast wave from the explosion (Figure 5-18). The later time increments show that the downward propagated waves acted on the side tube and subsequently, at the bottom face of the skin plate. However, the magnitude of this pressure wave was much lower (refer Figure 5-18 and Figure 5-19); subsequently there was a suction phase noticed for both cases. This was due to the applied "*flow-out*" boundary condition to the surrounding planes of the 3D computational air domain. Next, the case "*with ground reflection"* showed a sudden rise in pressure around 1.25 ms compared to the case "*without reflection"*. This phenomenon can be noticed from Figure 5-18. The increase in pressure was more than 100 kPa above the atmospheric pressure. This effect can be clearly understood from the interaction of the pressure waves with the aluminium skin plate in Figure 5-20(a-d).

The reflection of the pressure waves at the ground surface lasted about 0.7 ms. The magnitude of the pressure wave at the ground reflection was approximately 328 kPa (Figure 5-20(a)). This reflected pressure wave propagated rapidly back to the bottom face of the aluminium skin plate and during the propagation the magnitude was reduced to approximately 130 kPa (refer Figure 5-20(b)). The rapid propagation of this reflected pressure wave to the aluminium skin plate might be accelerated by the negative pressure (below atmospheric pressure) below the aluminium skin plate. The reflected pressure wave from the ground acts on the bottom face of the aluminium skin plate around 1.24 ms; subsequently, the diffraction of this pressure wave occurred around the edge of the aluminum skin plate (Figure 5-20(c-d)). However, due to the lower magnitude of this diffracted pressure wave there was no significant effect observed on the top face of the aluminium skin plate. Due to the reflection phenomenon the magnitude of the pressure wave was increased to twice of its incident value (Figure 5-20(c)). The case "*without ground reflection*" showed a continuous negative phase due to the applied "flow-out" boundary condition to all the boundary planes of the 3D computational air domain. The calculated average impulse due to the ground reflection was 9.23 kPa-ms (0.00029 kN-s).

Similar results were also observed for the sandwich composite skin plate case. However, there was a difference in the arrival time noticed. The arrival time for this case was approximately 1.4 ms; this value was higher compared to the aluminium skin plate case which showed 1.24 ms. The increased size of the sandwich composite skin plate (ϕ 250 mm) attributed to a longer time for the pressure waves to reach the edges of the skin plate and subsequently to the ground surface. The calculated average impulse due to the ground reflection was 9.18 kPa-ms (0.00045 kN-s) for this case.

The combined impulse from diffraction and ground reflection at the bottom face of the skin plate was approximately 33% and 30% of the total reflected impulse at the top face of aluminium (ϕ 200 mm; 1.0 kg) and sandwich composite skin (ϕ 250 mm;

0.54 kg) plates respectively. Now, these values can be compared with the average difference in impulse ($\Delta I = I_{refl} - I_{trans}$) observed during the experimental testing (refer Table 4-10 and Table 4-11 of Chapter 4). The combined effect of diffraction and ground reflection on the crushing performance of the test specimen is discussed in the subsequent sections.

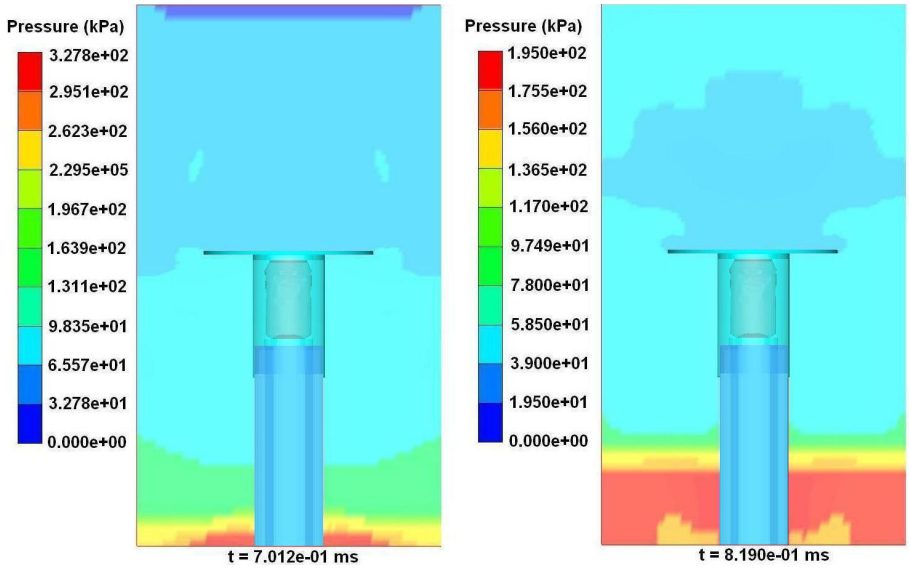

(a)

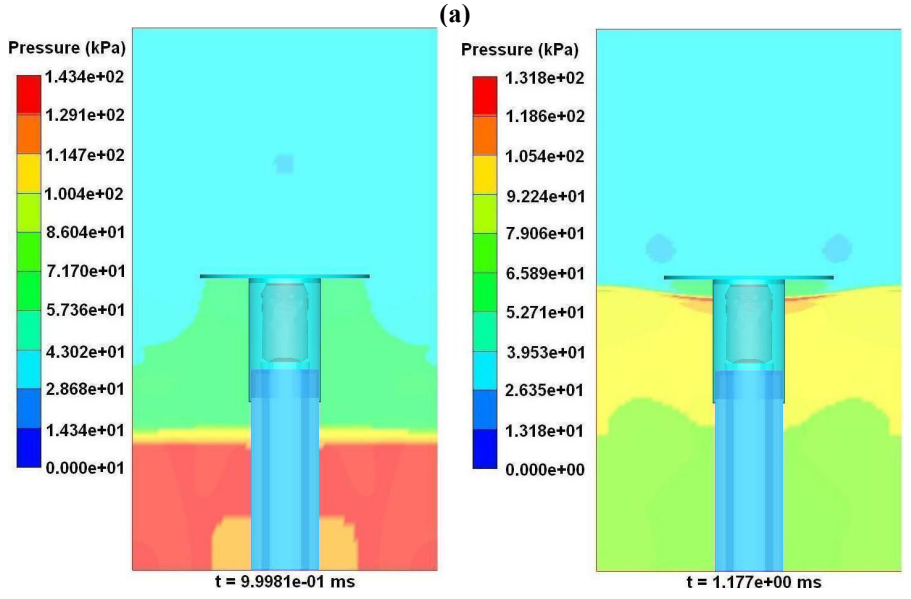

(b)

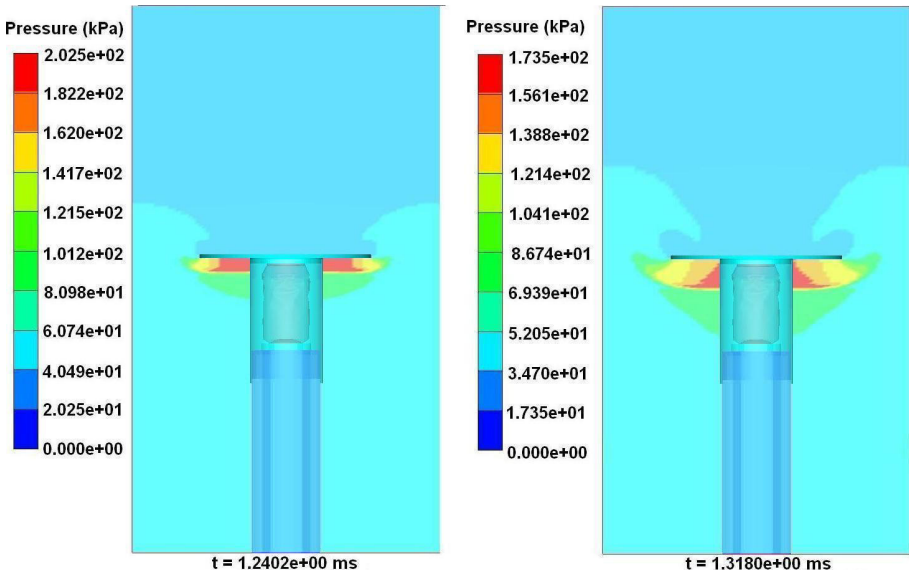

(c)

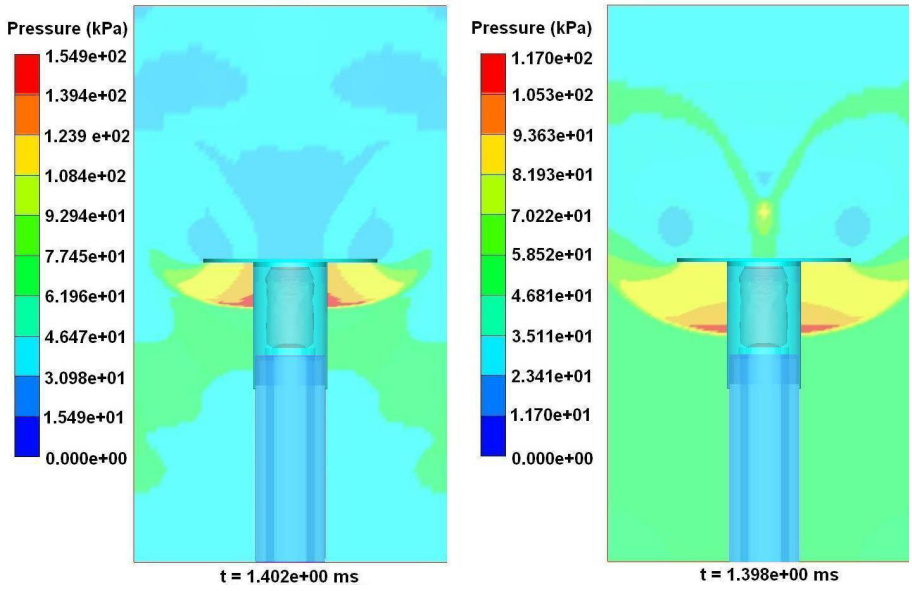

(d)

Figure 5-20: (a-d) Interaction of blast pressure waves with the aluminium skin plate.

5. 9. Crushing characteristics of empty beverage can

The deformation patterns of the empty beverage can from Autodyn simulations (coupled analysis with 0.25 mm grid size considering the diffraction and ground reflection) are shown in Figure 5-21 and Figure 5-22 for aluminium and sandwich

composite skin plates respectively. For both cases (aluminium and sandwich composite skin plates) the initial deformation started at the interfacial line of the top shoulder and the mid-wall. However, the experimental deformation patterns of the beverage can with aluminum skin plate (ϕ 200 mm; 1.0 kg) showed the initiation of deformation at different points along the length. This may be due to a higher reflected pressure (impulse) and the corresponding velocity of the skin plate. Consequently, a local wall buckling mode was observed throughout the length of the can which caused the circumferential progressive folding (lobes) of the mid-wall especially with the sandwich composite skin plate. A similar phenomenon was noticed from the experimental results also.

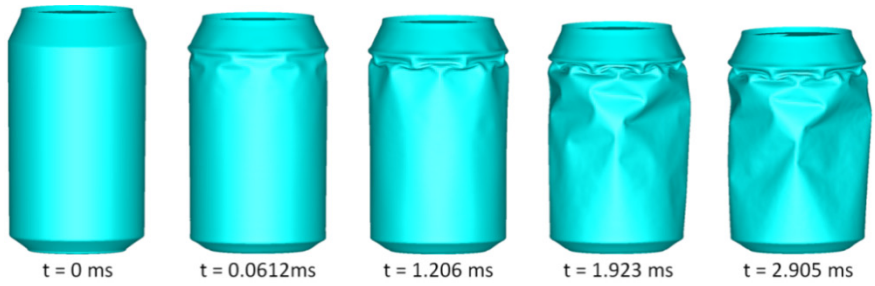

Figure 5-21: Deformation patterns of empty beverage can with the aluminium skin plate (ϕ 200 mm; 1.0 kg).

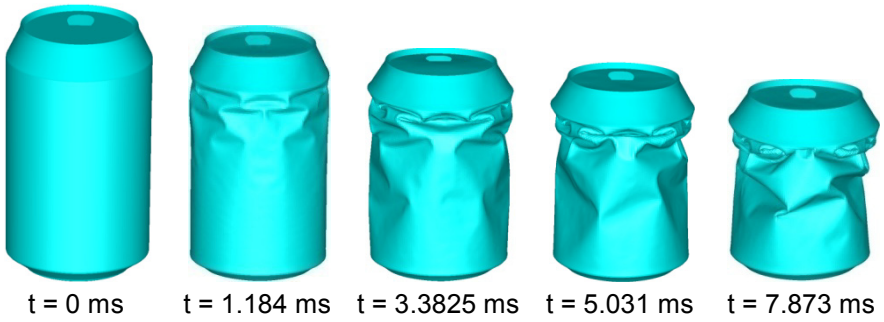

Figure 5-22: Deformation patterns of empty beverage can with sandwich composite skin plate (ϕ 250 mm; 0.54 kg).

The corresponding force-deformation histories are shown in Figure 5-23(a-b). The magnitude of the peak crush load from these cases (3.1 kN and 3.5 kN for aluminium and sandwich composite skin plates respectively) clearly indicates the strain-rate sensitivity (Figure 5-23(a-b)). The crushing load of the can fluctuated throughout its crushing length. This may be corresponding to the local-wall buckling associated with the formation of lobes during the crushing process. Although the linear momentum and energy are conserved for these cases the predicted deformation lengths were different from the experimental results. The deformation length of the beverage can (32.4 mm) with sandwich composite skin plate (ϕ 250 mm; 0.54 kg) was lower than the experimental value (48.7 mm). This was due to the

difference in the attained maximum reflected pressure (due to the surface roughness of the skin plate discussed in Figure 5-12) and the corresponding impulse (155.7 kPa-ms (0.00764 kN-s)) compared to the experimental value (268 kPa-ms (0.010 kN-s)).

On the other hand, the deformation length and the corresponding energy absorption of the beverage can with the aluminium skin plate (13 mm and 5.3 J) were higher due to a higher reflected impulse (153.7 kPa-ms (0.0048 kN-s)) compared to the experimental data (8.67 mm, 3.84 J and 124.7 kPa-ms (0.00392 kN-s)). Hence, in order to validate this finding (diffraction and ground reflection) with the experimental results (deformation length and the corresponding energy absorption) the consideration of experimentally recorded pressure time history is absolutely necessary and this is discussed in the next section.

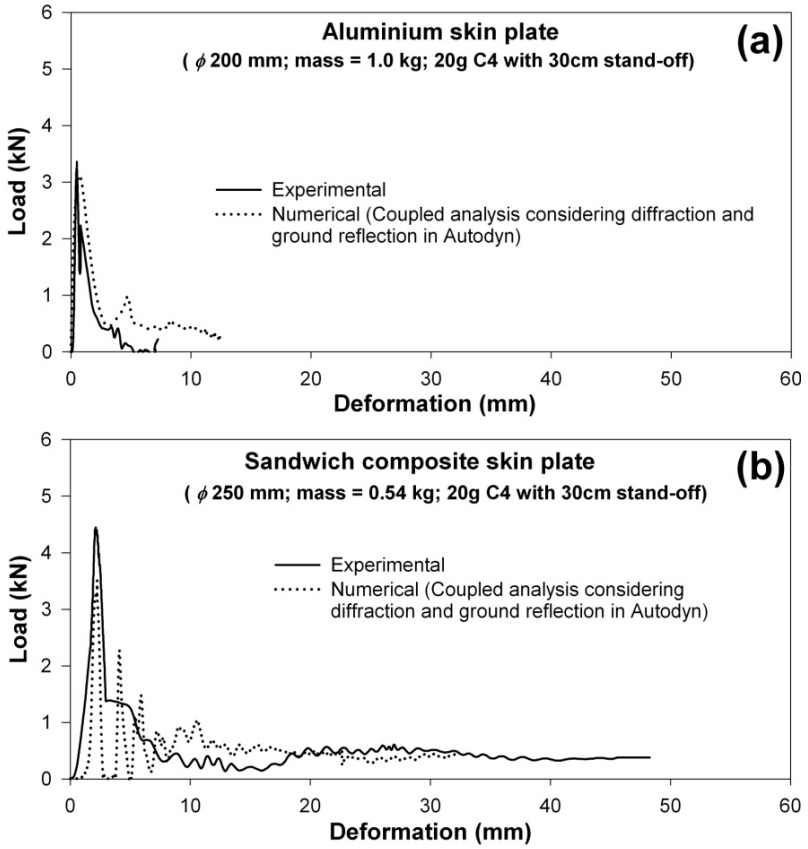

Figure 5-23: Comparison of load-deformation histories of the empty beverage cans from Autodyn simulation (considering the diffraction and ground reflection). (**a)** with aluminium skin plate (ϕ 200 mm; 1.0 kg); **(b)** with sandwich composite skin plate (ϕ 250 mm; 0.54 kg)).

5. 10. Validation of Hydrocodes simulation results

The results from the Autodyn simulations showed that the total impulse from the diffraction and the ground reflection phenomenon acting at the bottom face of the skin plates was approximately 33% and 30 % of the total reflected impulse for aluminium and sandwich composite skin plates respectively. In order to validate this finding a decoupled analysis was carried out for all cases considering experimentally recorded pressure time histories. Due to the similarity in approach the results of one of the cases (sandwich composite skin plate (ϕ 250 mm; 0.36 kg)) are discussed in this section. It was assumed that the proportion of the impulse due to diffraction and ground reflection phenomena (30%) is constant. The modelling details of the decoupled analysis were very similar to the ones which were discussed in Chapter 4. Figure 5-24 shows one of the experimentally measured reflected pressure-time profiles (test 1) on the top face of the sandwich composite skin plate (ϕ 250 mm; 0.36 kg). The calculated reflected impulse from this curve (area below the reflected pressure time profiles) was 167.7 kPa-ms (0.00823 kN-s). This impulse can be modelled as an equivalent triangular impulse loading as discussed in Chapter 4; and the same is shown in Figure 5-24 (dashed line). This equivalent triangular impulse load was calculated based on the diffracting (engulfing) load case [27]. The approximate new positive duration for this equivalent triangular impulse load is 0.0663 ms (refer Figure 5-24). Now, subtracting 30% of the impulse (for diffraction and ground reflection) from the reflected impulse can provide the resultant equivalent triangular impulse (117.4 kPa-ms (0.00576 kN-s)) loading curve; and the corresponding calculated equivalent duration of the resultant triangular impulse load is 0.04645 ms. This resultant load is indicated by the solid line in Figure 5-24.

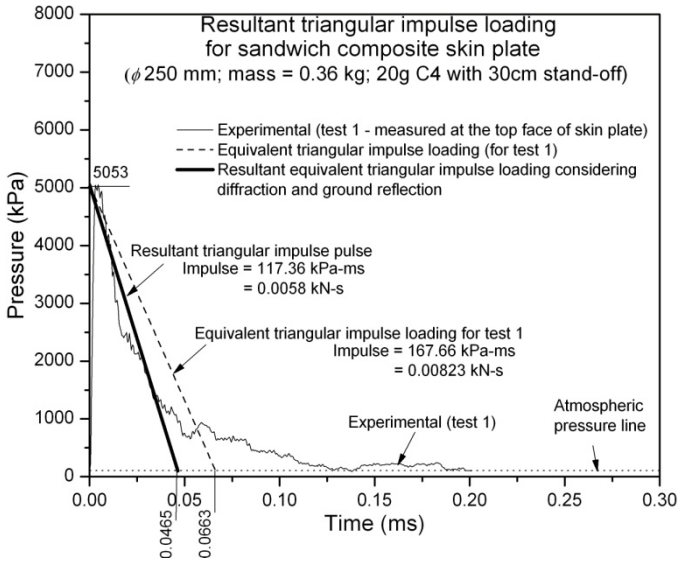

Figure 5-24: Simplified equivalent triangular loading.

Numerical analyses have been conducted for these two load cases (dashed line and solid line). The effect of diffraction and ground reflection can be understood from the velocity profile of the sandwich composite skin plate (Figure 5-25). The velocity profile of the sandwich composite skin plate considering diffraction and ground reflection was close to the experimental data. The corresponding deformation length and its pattern were very close to the experimental data (refer Figure 5-26(a) and Figure 5-26(b)). However, the case without considering diffraction and ground reflection showed a higher peak velocity (25.9 m/s) and a lower time (5.32 ms) to reach the zero velocity position (Figure 5-25). Furthermore, the test specimen crushed completely which is entirely different from the experimental results (refer Figure 5-26(c)).

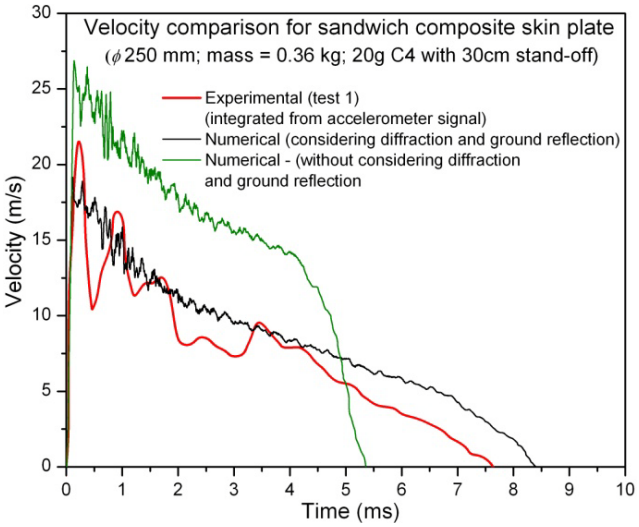

Figure 5-25: Comparison of velocity profiles.

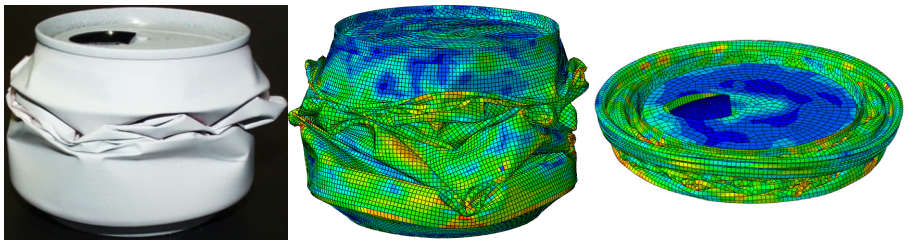

(a) **(b)** **(c)**

Figure 5-26: Deformation patterns of empty recyclable beverage cans with sandwich composite skin plate (ϕ 250 mm; 0.36 kg); **(a)** Experimental **(b)** Numerical (considering diffraction and ground reflection) **(c)** Numerical (without considering diffraction and ground reflection).

The force-deformation curve for the case with diffraction and ground reflection is also shown in Figure 5-27. The peak crush load from the numerical simulation (3.7

kN) was closer to the experimental data (3.95 kN). This shows that the *Johnson-Cook* material model captured the strain rate and the corresponding strain hardening effect of the beverage can material. A maximum local strain rate value of 337 s^{-1} was noticed for this case. Similarly, the calculated total absorbed energy for both cases is comparable (41.96 J and 45.2 J for experimental and numerical respectively). Furthermore, the numerical results of this case showed the conservation of impulse and energy. Figure 5-28 shows the comparison of the applied equivalent triangular impulse (117.4 kPa-ms (0.0058 kN-s)) and the numerically calculated transferred impulse at the bottom of the beverage can (0.0058 kN-s) corresponding to its maximum deformation length. The same figure also shows the comparison of energy.

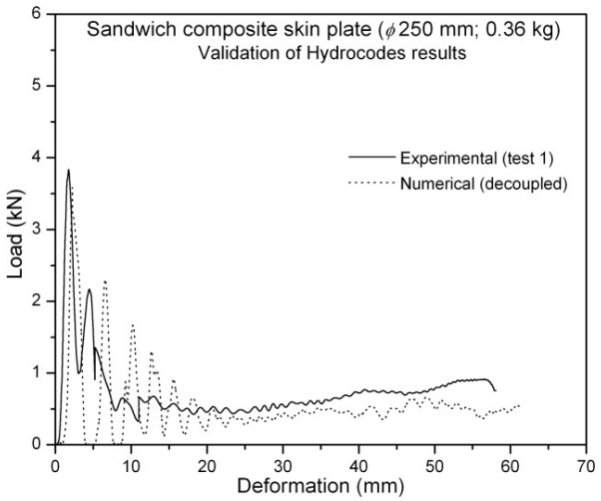

Figure 5-27: For sandwich composite skin plate (ϕ250 mm; 0.36 kg): **(a)** Comparison of force-deformation histories.

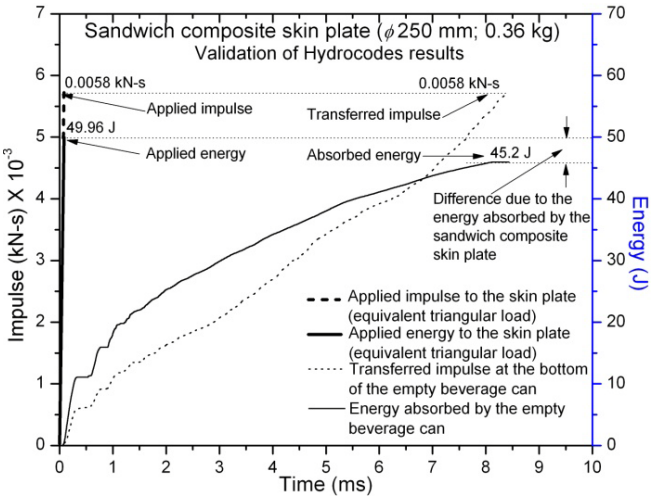

Figure 5-28: Comparison of impulse and the energy.

It can be noticed that the energy absorbed by the beverage can (45.2 J) was lower than the applied energy to the skin plate by the equivalent triangular impulse load (49.96 J). The difference between these two energy levels was the energy absorbed by the sandwich composite skin plate (by elastic bending of composite skin plates and the compression of polyurethane foam). From the above results it can be concluded that the results yielded by the Autodyn simulations are appropriate.

5. 11. Conclusions

In this chapter, the numerical simulation of blast loading for 20g of C4 with a stand-off distance of 30 cm was carried out. 2D and 3D computational models were developed using Hydrocodes. The pressure-time histories from the numerical simulation were compared with experimentally measured profiles and the ConWep predicted values. The clearing of the reflected pressure wave with finite surface area of the skin plates was explained using coupled Eulerian and Lagrangian approach. The combined effect of diffracted pressure on the bottom face of the skin plates and the influence of ground surface reflection on the crushing performance of the test specimens were studied. The crushing mechanism and the numerical failure patterns of the empty beverage can were presented. The above parameters were studied with aluminium and sandwich composite skin plates (ϕ 200 mm; 1.0 kg and ϕ 250 mm; 0.54 kg respectively). From the numerical simulation results it can be concluded that:

- The magnitude of the peak incident and reflected blast pressures from the 2D and 3D computational models were very close to the ConWep predicted values. However, a significant difference in the positive phase duration was noticed. The predicted value from ConWep is always higher than the numerically calculated value. For a close-range blast loading (20g C4 with a stand-off distance of 30 cm) the calculated reflected pressure and its positive duration from ConWep and Autodyn V-11.0 showed a non-uniform distribution of these parameters on the top face of the skin plates. The magnitude of the peak reflected pressure from the 3D computational model with aluminium skin plate showed a higher value than the experimental data. On the other hand, the sandwich composite skin plate showed a lower value compared to the experimental value. The reason for the differences is the surface roughness of the reflected surface (top face) of the skin plates which cannot be included in the present numerical analyses.
- The 3D computational model showed a clear evidence of clearing of the reflected pressure waves with finite surface area of the reflected surface (aluminium and sandwich composite skin plates). The diffracted pressure

from the top face quickly passed around the edges and acted on the bottom face of the skin plates. In addition to the diffracted pressure, the incident pressure wave at the boundary of the skin plates also contributed to increase the pressure at the bottom face of the skin plates (engulfing phenomenon). High speed images from the experimental tests also confirmed the same. The magnitude of the diffracted pressure was less than one sixth of the reflected pressure.

- The effect of ground surface reflection on the bottom face of the skin plates was also studied. Approximately 100 kPa (above the atmospheric pressure) was acting on the bottom face of the skin plates due to ground reflection.
- The effective impulse from the diffraction and ground reflection was significant compared to the reflected impulse; an average value of 30% of the reflected impulse acted on the bottom face due to diffraction and ground reflection. The same finding was also validated with a decoupled numerical analysis using the experimentally measured pressure time history.
- The failure patterns of the empty beverage can were studied using the same 3D computational model. The failure initiation of the test specimen was very similar to the experimental results. The failure was initiated at the interfacial line of the top shoulder and the mid-wall region. Furthermore, the peak crush load of the beverage can showed strain rate sensitivity.

Bibliography

[1]. *US Department of Army Technical Manual (TM5-855-1). Fundamentals of protective design for conventional weapons, Washington, DC.* 1986.

[2]. *US Department of Army Technical Manual (TM5-1300). Design of structures to resist the effects of accidential explosions, Washington, DC.* 1900.

[3]. Smith, P. D. and Hetherington, J. G., *Blast and ballistic loading of structures.* Butterworth-Heinemann Ltd., 1994.

[4]. Krauthammer, T., *Modern protective structures.* CRC Press, New York, 2008.

[5]. Bulson, P. S., *Explosive loading of engineering structures.* E & FN SPON (Am imprint of Chapman & Hall), London, 1997.

[6]. Bangash, M. Y. H., *Shock, impact and Explosion.* Springer, London, 1993.

[7]. Autodyn, *Theory manual.* M/s Century Dynamics, 2007.

[8]. Luccioni, B., Ambrosini, D. and Danesi, R., *Blast load assessment using hydrocodes.* Engineering Structures, 2006. **28**(12): p. 1736-1744.

[9]. Smith, P. D. and Rose, T. A., *Blast loading and building robustness.* Progress in Structural Engineering and Materials, 2002. **4**(2): p. 213-223.

[10]. Baylot, J. T. and Bevins, T. L., *Effect of responding and failing structural components on the airblast pressures and loads on and inside of the structure.* Computers and Structures, 2007. **85**: p. 891-910.

[11]. Remennikov, A. M. and Timothy, R. A., *Modelling blast loads on buildings in complex city geometries.* Computers & Structures, 2005. **83**(27): p. 2197-2205.

[12]. Tham, C. Y., *Numerical simulation on the interaction of blast waves with a series of aluminum cylinders at near-field.* International Journal of Impact Engineering, 2009. **36**(1): p. 122-131.

[13]. Rose, T. A. and Smith, P. D., *Influence of the principal geometrical parameters of straight city streets on positive and negative phase blast wave impulses.* International Journal of Impact Engineering, 2002. **27**(4): p. 359-376.

[14]. Silva, P. F. and Lu, B., *Improving the blast resistance capacity of RC slabs with innovative composite materials.* Composites Part B: Engineering. **38**(5-6): p. 523-534.

[15]. Grujicic, M., Bell, W. C., Thompson, L. L., Koudela, K. L. and Cheeseman, B. A., *Ballistic-protection performance of carbon-nanotube-doped poly-vinyl-ester-epoxy matrix composite armor reinforced with E-glass fiber mats.* Materials Science and Engineering: A, 2008. **479**(1-2): p. 10-22.

[16]. Silva, M. A. G., Cismasiu, C. and Chiorean, C. G., *Numerical simulation of ballistic impact on composite laminates.* International Journal of Impact Engineering, 2005. **31**(3): p. 289-306.

[17]. Tham, C. Y., Tan, V. B. C. and Lee, H. P., *Ballistic impact of a KEVLAR® helmet: Experiment and simulations.* International Journal of Impact Engineering, 2008. **35**(5): p. 304-318.

[18]. Chapman, T. C., Rose, T. A. and Smith, P. D., *Blast wave simulation using AUTODYN2D: A parametric study.* International Journal of Impact Engineering, 1995. **16**(5-6): p. 777-787.

[19]. Adelman, S. A. and Doll, J. D., *Generalized Langevin equation approach for atom/solid–surface scattering: General formulation for classical scattering off harmonic solids.* Journal of Chemical Physics, 1976. **64**: p. 2375-2388.

[20]. Doll, J. D. and Dion, D. R., *Generalized Langevin equation approach for atom/solid–surface scattering: Numerical techniques for Gaussian generalized Langevin dynamics.* Journal of Chemical Physics, 1976. **65**(9): p. 3762-3766.

[21]. Holmes, N. and Belytschko, T., *Post processing of finite element transient response calculations by digital filters.* Computers & Structures, 1976. **6**(3): p. 211-216.

[22]. Zekai, C. and Zdenek, P. B., *Spurious reflection of elastic waves due to gradually changing finite element size.* International journal of Numerical methods in engineering, 1983. **19**(5): p. 631-646.

[23]. Lesuer, D., *Experimental Investigations of Material Models for Ti-6Al-4V Titanium and 2024-T3 Aluminum.U.S. Department of Transportation.DOT/FAA/AR-00/25,Sept. 2000*

[24]. Johnson, G. R. and Cook, W. H., *Fracture characteristics of three metals subjected to various strains, strain rates, temperatures and pressures.* Engineering fracture mechanics, 1985. **21**(1): p. 31-48.

[25]. Hiermaier, S. J., *Structures Under Crash and Impact - Continuum mechanics, discretization and experimental characterization.* Springer, 2007.

[26]. Tsai, S. W. and Hahn, H. T., *Introduction to composite materials.* Technomic, Lancaster, PA, 1980.

[27]. Kinney, G. F. and Graham, K. J., *Explosive shocks in air.* Springer-Verlag, 1985.

Chapter 6

Analytical Model and Effect of Initial Geometric Imperfections under Blast Loading

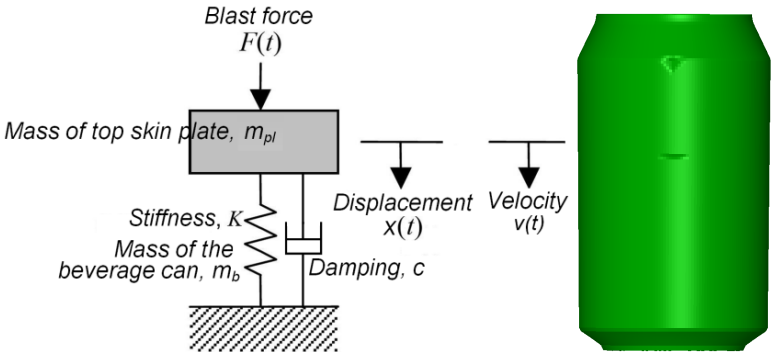

Overview

This chapter presents an analytical model to predict the blast energy absorption behaviour of empty beverage cans. The results from the analytical model were validated with the experimental and numerical results. Secondly, a numerical study was conducted to understand the effect of initial geometric imperfections on the crushing mechanism of the beverage cans in detail. Two different approaches of finite element modelling of initial geometric imperfections were considered. The first approach deals with a combination of Eigen vectors of the linear buckling prediction; and the second case deals with the finite element modelling of measured initial geometric imperfections from used beverage cans. From these studies, the deformation patterns and the corresponding crushing performance of the beverage cans are presented.

6. 1. Introduction

The dynamic behaviour of a structure subjected to a blast loading depends upon the material, geometry, inertia, magnitude of loading, rate of loading, boundary conditions etc. Though the behaviour of a structure subjected to an explosive loading is predictable, the complexity of this kind of problems is still not resolved completely due to the factors such as multiple degrees of freedom, wide range of strain rates and its corresponding non-linear inelastic material behaviour. However, to resolve these issues some simplifications can be adopted in the approach. A widely accepted simplification in the area of blast load calculations is replacing an actual structure by an equivalent Single Degree Of Freedom (SDOF) structure and applying the blast load as an equivalent triangular pressure pulse [1-4]. The major advantage of these simplifications is to identify the global response of the structure subjected to blast loading.

Materials such as steels are greatly affected by dynamic loads and will exhibit different degrees of increasing strength depending on their grade. Both the yield strength and ultimate strength increase during dynamic loading; however, the behaviour of a structure is significantly affected by the increase of yield strength [5]. The reasons for increasing the strength is due to the dislocation effects originating from the crystalline structure of the steel under shear stresses [6]. The strength enhancement during the dynamic loading can be defined as "*Dynamic Increase Factor* (*DIF*)". The DIF can be calculated in terms of yield strength and the average strain rate [5]. This DIF factor should be considered for energy absorbing structures which are subjected to higher rates of strain [7-10]. Norris et al. [11] tested steel with two different static yield strengths of 330 and 278 MPa under tension at strain rates ranging from 10^{-5} to 0.1 s^{-1}. Strength increases of 9 - 21% and 10 - 23 % were observed for the two steel types respectively. Another tensile experiments study by Dowling and Harding [6] with split Hopkinson's Pressure Bar (SHPB) on mild steel using strain rates varying between 10^{-3} s^{-1} and 2000 s^{-1} concluded that the materials of body-centered cubic (BCC) structure (such as mild steel) showed a high strain rate sensitivity. It has been found that the lower yield strength of mild steel can almost be doubled; the ultimate tensile strength can be increased by about 50%; and the upper yield strength can be considerably higher. In contrast, the ultimate tensile strain decreases with increasing strain rate. Malvar et al. [5] also studied strength enhancement of steel reinforcing bars under the effect of high strain rates. This was described in terms of the dynamic increase factor (DIF), which can be evaluated for different steel grades and for yield stresses ranging from 290 to 710 MPa. For any analytical and numerical approach the inclusion of above factors is very important to predict the accurate behaviour of a structure. Many studies [12-15] have proven that the assessment of structures subjected to blast loading can be done using analytical and numerical tools. As discussed in Chapter 4 and 5 the peak crush load of an

empty beverage can was increased during the blast loading to approximately three times of its quasi-static value. This shows a large dependency on the strain rate during blast loading. Hence, similar to the approach used for axial impact testing (refer Chapter 3) an analytical model is proposed to assess the energy absorption capacity of empty beverage cans for blast loading including the strain rate and strain hardening effects. The results from this analytical model were validated by experimental and numerical results.

Further, the performance of these structures can be affected by the material and the geometric imperfections conceived during the manufacturing process. However, quantifying these imperfections is not an easy task. Dynamic buckling and the energy absorption behaviour of metallic cylindrical shells were well studied using the buckling and folding process in ref. [16]. Furthermore, the effect of geometric imperfections in the form of sine wave on the energy absorption was also explained. Studies on different structures [17-20] have proved that traditional (geometric tube – wall mid-surface imperfections) and non-traditional imperfections (tube wall thickness variation, tube end geometric imperfections, non-uniform loading of tubes and variations in the boundary condition) have a large influence on the performance of shell structures, especially on the buckling load. Non-traditional imperfections such as variation in the boundary conditions and loading can be avoided with proper care during experimental testing. However, the initial imperfections caused during the manufacturing process such as a variation in structural dimensions cannot be avoided during an experimental test. Hence, during an analytical study or a finite element calculation it is advisable to consider the above factors to predict the correct performance parameters. As seen from Chapter 5, the Hydrocodes simulation results showed that the failure initiation of the beverage can was not similar to the experimental results for the case with the aluminium skin plate (ϕ 200 mm; 1.0 kg). This may be due to non-consideration of geometric imperfections in the numerical model. Therefore, the effect of geometric imperfections on the initiation of failure and the corresponding crushing performance has to be understood. In order to study the effect of initial geometric imperfections on the performance of the beverage cans two approaches have been handled: (i) the first approach is based on the linear combination of *Eigen vectors* of the linear buckling prediction. The initial geometric imperfections were accounted for as the linear buckling mode shapes of the beverage can (ii) the second method dealt with the finite element modelling of measured initial geometric imperfections from the used beverage cans. However, the conceived initial geometric imperfections during the manufacturing process are not considered, because, the magnitude of imperfections caused during the usage is higher than the imperfections caused during the manufacturing process. The effect of geometric imperfections on the deformation patterns and its corresponding energy absorption are evaluated and compared with the experimental results.

6. 2. Analytical Model for blast loading

6. 2. 1. Equilibrium equation

In this section, an equilibrium equation is established to find the energy absorption of an empty beverage can subjected to an axial blast loading. It was assumed that the lateral movement (translation and rotation) of the top skin plate and its effect on the crushing mechanisms and the corresponding energy absorption of the test specimen are negligible. This assumption was confirmed by the observations during the experimental testing. The entire experimental system can be represented by a single degree of freedom (SDOF) with damping (energy dissipation) as shown in Figure 6-1.

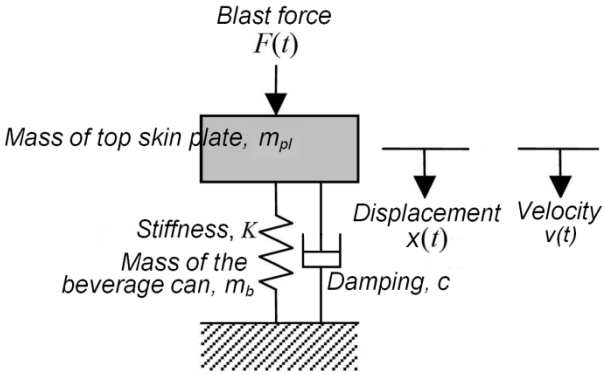

Figure 6-1: Simplified model (SDOF) of the experimental test set-up.

As seen in Chapter 4 and 5, the exponential decayed pressure can be modelled as an equivalent triangular impulse loading. For diffraction type loading on a structure the actual peak load is taken as the peak of the equivalent pulse load and the equivalent duration is selected to give an impulse per unit area the same as that of the actual [21]. Hence, the resulting blast pressure (in the crushing direction of the specimen) acting on the top face of the skin plate can be written as (Equation (6.1)),

$$p(t) = \begin{cases} p_{\max}^{R}\left(1-\dfrac{t}{t_p}\right) & for\ t \le t_p \\ 0 & otherwise \end{cases} \tag{6.1}$$

where *p(t)* is the time dependent blast pressure (Pa); $p_{\max}^{R}$ is the peak reflected pressure (Pa); t_p is the equivalent positive duration of the blast (s); The total reflected impulse (I_{refl}) delivered to the top face of the skin plate can be approximated by the following equation (Equation (6.2)),

$$I_{refl} = \frac{1}{2} p^{R}_{\max} \cdot t_p \quad [\text{Pa} \cdot \text{s}] \tag{6.2}$$

As discussed in Chapter 5, the combined effect of diffraction and the ground reflection was significant (which acted on the bottom face of the skin plate and opposite to the crushing direction of the test specimen). Due to that, approximately 30% of the total impulse was lost (I_{loss}) from the total reflected impulse delivered to the skin plate (I_{refl}). Hence, the resultant impulse which was actually utilized to crush the test specimen can be written as

$$I_{res} = I_{refl} - I_{loss} \quad [\text{Pa} \cdot \text{s}] \tag{6.3}$$

From the above resultant impulse, considering the same peak pulse, a new positive duration can be calculated (discussed in Chapter 5). It was assumed that the energy absorbed by the skin plate is insignificant and the power from this pressure wave is utilized for the top skin plate acceleration; and subsequently for the deformation of the test specimen (empty beverage can). Hence, the force equilibrium of the skin plate due to the blast pressure can be written as:

$$F_{bl}(t) = m_{pl} \cdot a(t) + \frac{d}{dx} E_{abs} \cdot x(t) \tag{6.4}$$

where m_{pl} is the mass of the skin plate including the side tube, while the mass of the beverage can can be neglected compared to the mass of the skin plate (kg); $a(t)$ is the acceleration of the skin plate (m/s^2); $\frac{d}{dx} E_{abs} \cdot x(t)$ is the energy absorbed per unit of crushed beverage can length (J/m). Considering the effective area of the top skin plate (A_{pl}) the magnitude of the force transmitted to the top skin plate from the blast pressure can be written as

$$F_{bl}(t) = p(t) \cdot A_{pl} \tag{6.5}$$

$E_{abs}(x)$ is the energy absorbed by the beverage can crushing as a function of crushed length of the beverage can (J) and can be expressed using a qualitative term called dynamic mean crush load" (Equation (6.6)).

$$E_{abs}(x) = P_{mean} \cdot x \tag{6.6}$$

where P_{mean} is the "dynamic mean crush load" of the empty beverage can and the detail of this value is discussed in the latter part of this section. The equilibrium Equation (6.4) can also be modified (which represents the power delivered by the

pressure waves for the acceleration of the top skin plate and the corresponding deformation of an empty beverage can) as follows:

$$F_{bl}(t)\cdot v = m_{pl}\cdot v\left(\frac{d}{dt}v\right)+\frac{d}{dt}\cdot E_{abs}\left(\frac{d}{dx}x\right) \tag{6.7}$$

where v is the velocity attained by the top skin plate (m/s). Equation (6.4) or (6.7) can be integrated by means of the "*Runge-Kutta*" integration scheme where the second order differential equation can be split into two single order equations using the "*Odesolve*" function of MathCAD [22]. The equation for displacement and velocity of the top skin plate and their initial conditions are as follows:

Equations for initial conditions:

$$\frac{d}{dt}x(t) = v(t) \qquad \mathrm{x}(0) = 0 \tag{6.8}$$

$$m_{pl}\cdot a(t) = m_{pl}\cdot\frac{d}{dt}v(t) \qquad \mathrm{v}(0) = 0 \tag{6.9}$$

6. 2. 2. Dynamic mean crush load

As discussed in Chapter 3, the quality of the energy absorption can be defined by a "*dynamic mean or average crush load*" of any test specimen or structural element. Furthermore, a relation was introduced for the dynamic mean crush load including the strain rate and strain hardening effects for an empty beverage can. The same equation can be extended to blast loading applications (the same equation is reproduced below (Equation (6.10)).

$$P_{mean} \cong \frac{\sigma_y + B(H/D)^n t^2}{2\sqrt{3}}\left(\frac{4\pi H}{t}-\frac{\pi N}{3}\right)\cdot\left[1+\left(\frac{v_0}{2DC}\right)^{1/p}\right] \tag{6.10}$$

However, the calculation of the dynamic mean crush load of the beverage can for blast loading application involves two steps, because of two unknown variables in Equation (6.10) (P_{mean} and v_0). As per Equation (6.10), to include the strain rate effect in the analytical model the maximum impact velocity of the skin plate during the blast loading should be known. For an axial impact loading case this value can be calculated from the drop height of the impactor (initial impact velocity of the impactor). However, using Equation (6.10) (for blast loading case), the maximum velocity of the skin plate cannot be calculated directly without knowing the dynamic mean crush load. Hence, in order to circumvent this problem two steps have been adopted. As discussed in Chapter 5, the skin plate attains its maximum velocity

corresponding to the positive duration of the blast. Compared to the total crushing duration of the test specimen the positive duration of the blast is negligible. As an example, the case with the sandwich composite skin plate (ϕ 250 mm; 0.36 kg) is discussed here. Figure 6-2 shows the velocity profiles of the skin plate from three experimental tests; and the same figure also shows the average numerically calculated velocity profile. From this figure it can be noticed that the maximum velocity of the skin plate corresponds to the positive duration of the blast (approximately 0.05 ms); after that the velocity decreases approximately linearly with respect to time. This corresponds to the constant deceleration of the skin plate. Hence, the maximum attained velocity of the skin plate can be calculated (using Equation (6.4)) assuming an arbitrary value of the dynamic mean crush load. The maximum velocity of the skin plate will not be affected by the dynamic mean crush load of the test specimen (because of the assumption of constant dynamic mean crush load) rather it will be affected only by the inertia of the skin plate. To explain this point two arbitrary values of the dynamic mean crush load were chosen (0.75 kN and 1.5 kN). Using these values the velocity profile of the skin plate was estimated.

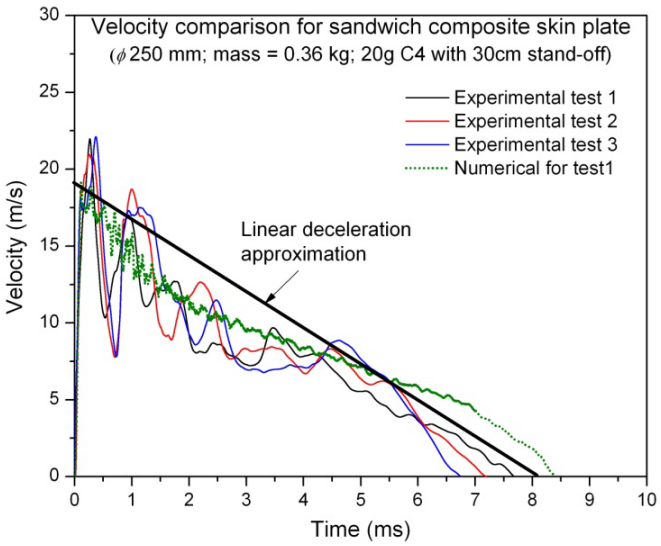

Figure 6-2: Experimental and numerical velocity profiles of the skin plate.

To calculate the maximum attained velocity of the skin plate the reflected pressure loading from the experimental test 1 for the case with the sandwich composite skin plate (ϕ 250 mm; 0.36 kg) was considered. The maximum reflected pressure and the corresponding positive duration after considering the diffraction and ground reflection were 5053 kPa and 0.0465 ms respectively (refer Figure 5-24 of Chapter 5). The calculated velocity profiles of these two cases from Equation (6.4) are presented in Figure 6-3. It can be noticed that the maximum attained velocity of the skin plate for both cases is the same (15.8 m/s). However, based on the chosen

dynamic mean crush load the total crushing time differs (3.85 ms and 7.69 ms for the case with 0.75 kN and 1.5 kN dynamic mean crush load respectively). Furthermore, the skin plate achieved its maximum velocity corresponding to the positive duration of the blast (0.0465 ms). Hence, to include the strain rate effect during the blast loading the maximum velocity of the skin plate from the analytical model can be considered. Now, the strain rate and the corresponding strain hardening effect can be included by substituting v_0 = 15.8 m/s into Equation (6.10). The used parameters and the details of Equation (6.10) have already been discussed in Chapter 3 in detail. The calculated P_{mean} from Equation (6.10) for the same loading case (test 1 with sandwich composite skin plate (ϕ 250 mm) with 0.36 kg) was 0.893 kN. This value is higher than the average value reported from experimental results (0.72 kN – refer Table 4-10 of Chapter 4 for more details). The reason for this difference may be due to the inconsistent failure modes from the experimental testing. As mentioned in Chapter 4, an offset loading of the beverage can was observed for a few test specimens. However, the analytical model assumes a perfectly axisymmetric blast loading.

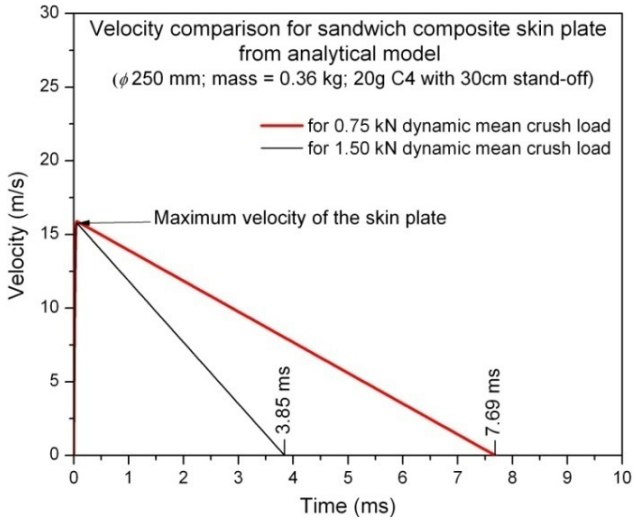

Figure 6-3: A comparison of velocity profiles from the analytical model using different mean crush load.

6. 3. Comparison of analytical, experimental and numerical results

6. 3. 1. Comparison of dynamic mean crush load

Substituting the calculated maximum velocity in Equation (6.10) provided the dynamic mean crush load. The aluminium skin plate with ϕ 200 mm and 1.0 kg provided inconsistent failure patterns; hence, this case was not considered to

calculate the dynamic mean crush load. A comparison of dynamic mean crush loads for the remaining cases is given in Figure 6-4 (aluminium skin plate (ϕ 250 mm and 1.0 kg); sandwich composite skin plate (ϕ 250 mm) with 0.54 and 0.36 kg). For all cases the calculated dynamic mean crush load from the analytical model was approximately 16% higher than the experimental results. This may be due to the difference in the considered analytical deformation pattern and the experimental deformation patterns. The analytical deformation pattern assumed a perfectly asymmetric deformation pattern. However, during the experimental testing for a few test specimens for each case showed an offset loading. This has already been discussed in Chapter 4 (refer Figure 4-20). Furthermore, the dynamic mean crush load from the numerical simulations also showed similar results. The numerical modelling approach and its subsequent analysis were very similar to the one which was discussed in Chapter 4 and 5. The numerical dynamic mean crush load for the aluminium plate (ϕ 250 mm; 1.0 kg) was very close to the experimental value (0.478 kN and 0.492 kN for experimental and numerical results respectively). However, for the sandwich composite skin plates the calculated average dynamic mean crush load was always higher than from the experimental results

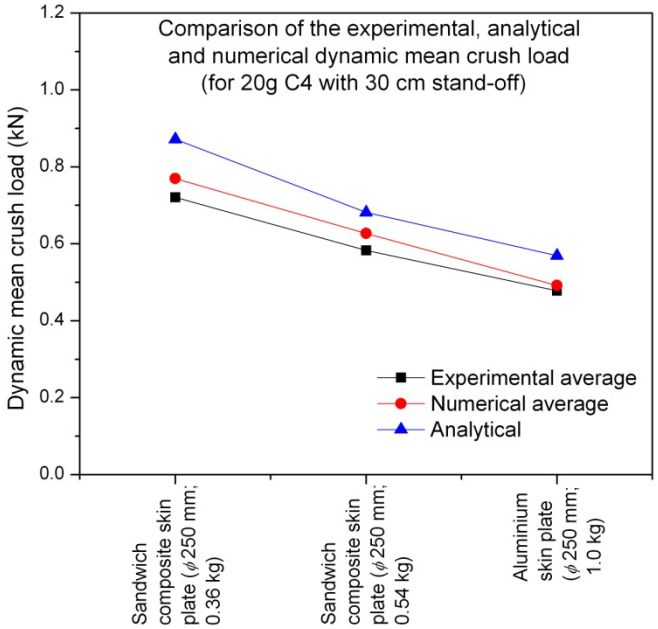

Figure 6-4: Comparison of dynamic mean crush load from experimental, numerical and analytical solutions.

6. 3. 2. Comparison of crushing parameters

The crushing performance of an empty beverage can during blast loading can be calculated considering the values from Figure 6-4. Substituting these values of dynamic mean crush load in Equation (6.6) and solving Equation (6.4), the corresponding crushing performance (deformation, velocity and energy histories with respect to time) of the beverage can was calculated. As an example, one of the cases is presented here (sandwich composite skin plate with ϕ 250 mm and 0.36 kg). Figure 6-5(a), Figure 6-5(b) and Figure 6-5(c) show a comparison of deformation, velocity and the corresponding energy absorption of experimental, numerical and analytical solutions respectively. The dotted line is an experimental curve (test 1 for sandwich composite skin plate with ϕ 250 mm and 0.36 kg); the second curve (dashed line) represents the numerical solution for the same test which was discussed in Chapter 5; and the third solid curve shows the analytical solution considering Equation 6.4. The results from these three cases showed a good correlation of parameters such as deformation length, velocity and the corresponding energy absorption. Due to a higher dynamic mean crush load, the total deformation length predicted by the analytical model was slightly lower than the experimental and numerical values (58 mm, 62 mm and 56 mm for experimental, numerical and analytical respectively). Furthermore, there was a difference in the total impact duration noticed (Figure 6-5(a-c)). This was due to the assumption of constant deceleration of the skin plate during the crushing process.

Similarly, the maximum velocity of the skin plate was lower than the experimental and numerical values. Furthermore, the energy absorption profiles of these three cases are shown in Figure 6-5(c). The results from the experimental and numerical model captured the fluctuation in the energy absorption during the initial phase of crushing. This was due to a cumulative effect of compression and bending behaviour of the sandwich composite skin plate and the corresponding crushing performance of the beverage can. The total absorbed energy from the analytical model was higher than the experimental and numerical values (42 J, 45.2 J and 49 J for experimental, numerical and analytical model respectively). During the experimental testing and in the numerical model the energy absorbed by the skin plate and the energy dissipated by friction were captured. Due to the rigid top plate assumption and the constant mean crush load the energy absorption profile from the analytical approach showed no fluctuation in the energy absorption. Furthermore, the energy dissipated by friction was also not included in the analytical model.

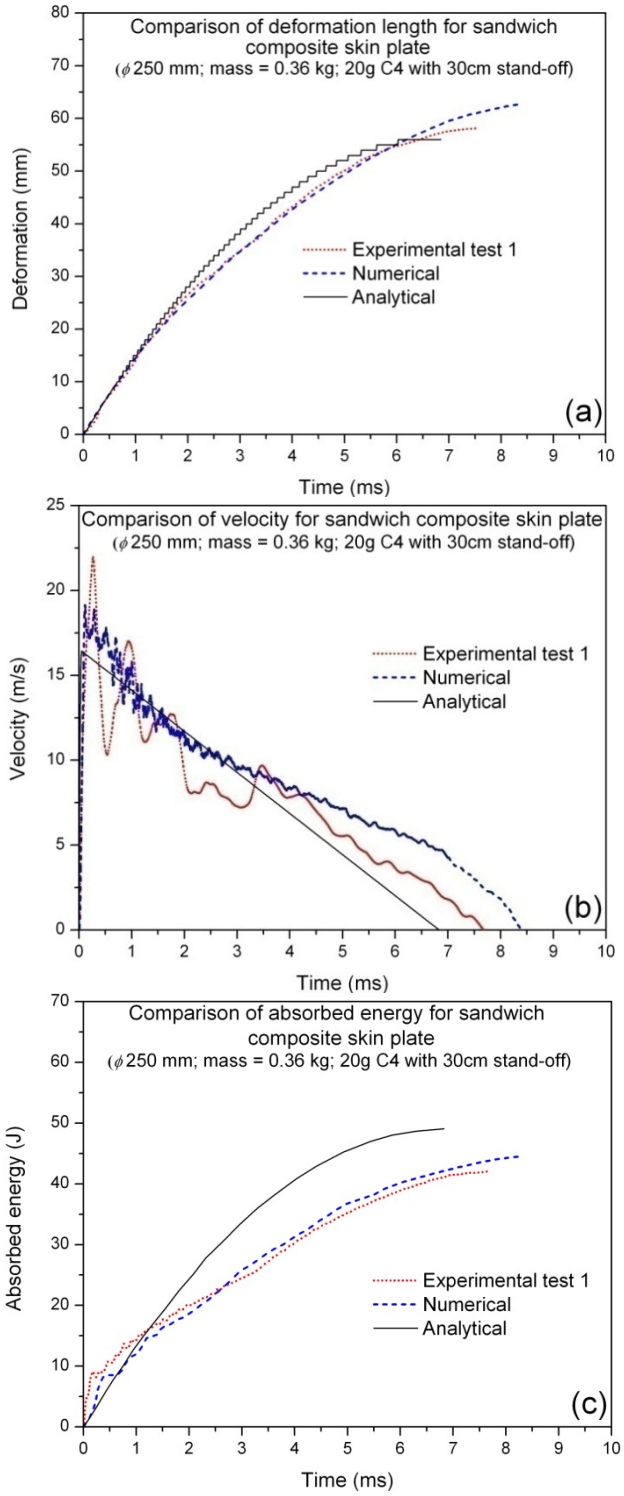

Figure 6-5: Comparison of crushing parameters of experimental, numerical and analytical solutions. **(a)** deformation time history **(b)** velocity time history **(c)** energy absorption time history.

6. 3. 3. Conclusions

In this section, an analytical model was developed to study the energy absorption behaviour of an empty beverage can subjected to an axial blast loading condition. This model was validated by comparing the results from experimental and numerical results (deformation length of test specimen, velocity profile of the top skin plate and the corresponding energy absorption). The predicted dynamic mean crush load from the analytical model was higher compared to the average experimental results. This was due to the difference in the deformation patterns of the beverage can. The analytical deformation pattern assumed a perfectly asymmetric deformation pattern. However, during the experimental testing a few test specimens of each case showed an offset loading. Finally, the predicted results of deformation length, velocity-time history of the top skin plate and the energy absorption history of the test specimen from the analytical solution were correlated very well with the experimental and numerical solutions. Hence, this analytical model can be used to design a sacrificial cladding structure with empty beverage cans as an inner core.

6. 4. Effect of geometric imperfection – numerical study

The details of the materials and their properties, geometric profile and the used material models for the finite element analysis of the beverage can were discussed in Chapter 4 and 5. As discussed in Chapter 5, the failure initiation of the beverage cans from the Hydrocodes simulation was not similar to the experimental results for the case with the aluminium skin plate (ϕ 200 mm; 1.0 kg). Hence, to evaluate the influence of initial geometric imperfections on the deformation pattern, peak crush load and the corresponding energy absorption, numerical simulations were carried out. Out of different initial imperfections (loading, boundary conditions, material and geometry) the initial geometric imperfections greatly influence the performance parameters of a structure [17, 23]. However, quantification of these initial geometric imperfections is a tedious task due to the variance of control parameters of a continuous production process and different usage conditions. For the beverage cans, the imperfections caused during the usage are another important parameter (especially at the mid-wall region of the can due to a lower thickness) which should be accounted for the imperfections analysis.

There are several ways to study the effect of geometric imperfections in a structure. Out of that the "*linear superposition of buckling Eigen modes*" is one of the most appreciated methods for structures whose manufacturing geometric imperfection is not known [24, 25]. Secondly, if the magnitude of the geometric imperfections is known then it can be applied directly in the numerical model and subsequently the performance of a structure can be evaluated [17, 23, 26, 27]. Therefore, the

numerical simulations were carried out to compare the results of these two approaches and to study the effect on peak crush load and the corresponding energy absorption. For the axisymmetric structures such as circular cross-sectional tubes, it was proved that the *Eigen* modes associated with the linear buckling problem will be either (i) axisymmetric modes associated with a single *Eigen* value, including the possibility of *Eigen* modes that are axially symmetric or (ii) non-axisymmetric modes associated with a repeated *Eigen* value [28, 29]. However, in most of the practical applications, it was found that the buckling mode shapes of the cylindrical tubes are non-axisymmetric. However, the geometry of an empty beverage can is very complex and it can be expected that the buckling mode shapes are similar to circular tubes with a thin section. Due to the above facts and similar to the previous analyses the complete 3D model of the beverage can was considered for the linear buckling study. The commercially available finite element code ABAQUS V6.7-3 Standard and Explicit were used for this study.

6. 5. Geometric imperfections based on linear buckling approach

In order to calculate the linear buckling modes of an empty beverage can the finite element simulation of linear *Eigen* value buckling analysis was conducted. Consequently, the imperfections were introduced in a perfect can geometry by adding these buckling modes. This perturbated can geometry was used to study the effect on the peak crush load and the corresponding energy absorption of the empty beverage can for the axial air-blast loading cases.

6. 5. 1. Buckling analysis

Assuming that the empty beverage can is a perfectly stiff structure when it is loaded in axial direction, the theoretical buckling mode shapes and the corresponding buckling loads can be calculated using linear buckling prediction approach. The advantage of this method is a lower computational cost and it provides likely failure modes of a structure. This result can be used as a basic guideline to conduct non-linear analyses. The linear buckling finite element calculation looks for the loads for which the model stiffness matrix becomes singular. If an incremental loading pattern (Q^N) is applied on the model, the *Eigen* values can be calculated based on the following equation [29],

$$\left(K_0^{NM} + \lambda_i K_\Delta^{NM}\right)\vartheta_i^{NM} = 0 \tag{6.11}$$

where K_0^{NM} is the matrix corresponding to the initial state, which includes the effect of the preload (mass of the top skin plate). K_Δ^{NM} is the differential initial stress and load stiffness due to the incremental loading pattern and λ_i are the *Eigen* values. ϑ_i^{NM} are the buckling mode shapes (*Eigen* vectors), *M* and *N* refer to the degrees of freedom of the whole model and *i* refers to the i^{th} buckling mode. The combined mass of the skin plate and the side tube (1.0 kg for aluminium skin plate and 0.36 kg for sandwich composite skin plate) represent the base or initial state of loading on the beverage can structure. An incremental loading (Q^N) of 250 N is applied at the centre point of the top face of the skin plate (refer Figure 6-6).

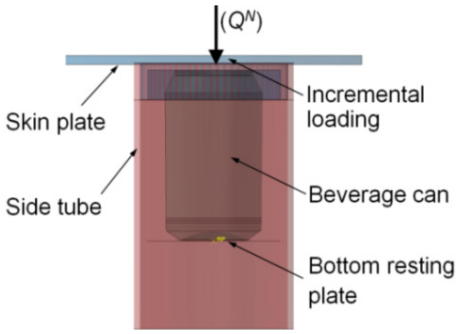

Figure 6-6: Finite element model of the beverage can for linear buckling prediction.

6. 5. 2. Results

In order to handle the complex contact pairs between the skin plate and the beverage can, the "*subspace*" solver method was used to predict the *Eigen* values. The first two buckling mode shapes of an empty beverage can and its corresponding *Eigen* values are shown in Figure 6-7(a-b). The beverage can exhibited axisymmetric mode shapes associated with a single *Eigen* value. From the result it can be concluded that the beverage can structure is imperfection sensitive especially at the mid-wall location; and the first mode will characterize the deformation that leads to the lowest buckling load. The corresponding buckling loads can be calculated from the Equation (6.12).

$$F_i = P_D + \left(\lambda_i Q^N\right) \tag{6.12}$$

where F_i is the buckling load corresponding to the i^{th} buckling mode and P_D is the dead load (mass of the skin plate) applied to the beverage can. The calculated lowest buckling load for the perfect geometry of the beverage can is 3.94 kN.

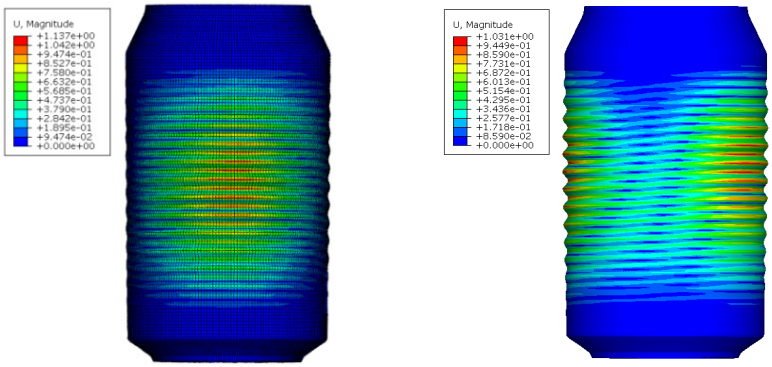

(a) First mode (f= 15.707 Hz) **(b)** Second mode (f= 15.709 Hz)

Figure 6-7: Buckling mode shapes of the empty beverage can.

6. 5. 3. Blast analysis

Perturbation of mesh to introduce geometric imperfections

Similar to the cases which were discussed in Chapter 4 and 5, the aluminium skin plate (ϕ 200 mm; 1.0 kg) and the sandwich composite skin plate (ϕ 250 mm; 0.36 kg) were chosen for the analysis. The details of the finite element models with the aluminium and sandwich composite skin plates are shown in Figure 6-8(a) and Figure 6-8(b) respectively. The modelling approaches of these cases are very similar to the ones which were discussed in Chapter 4 (decoupled numerical analysis). However, the perturbated geometry of the beverage can was considered for this analysis. The perturbation was done by introducing a mesh as a linear superposition of buckling mode shapes on the perfect structure of the beverage can. For that the normalized nodal data of the *Eigen* mode was written to an output file; subsequently, the perfect structure mesh was perturbated only at the mid-wall location due to its lower thickness. Generally, the lowest buckling mode is frequently assumed to provide the most critical imperfection in a stiff structure. In this study also the same assumption was made. The imperfection of the mesh was introduced based on the following relation (Equation (6.13)),

$$\Delta x_i = \sum_{i=1}^{M} \omega_i \phi_i \tag{6.13}$$

where ϕ_i is the i^{th} mode shape and ω_i is the associated scale factor. In order to analyze the effect of imperfections, different scale factors have been chosen and their results are discussed in the subsequent section. The scale factor was chosen based on a few selected percentages of the nominal thickness of the beverage can at mid-wall location.

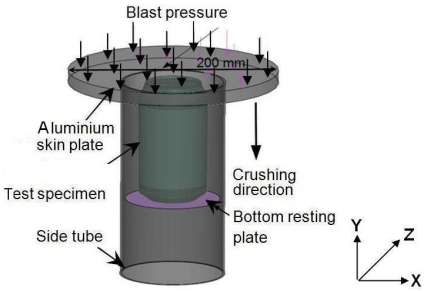

(a) Finite element model with aluminium skin plate (ϕ200 mm; 1.0 kg).

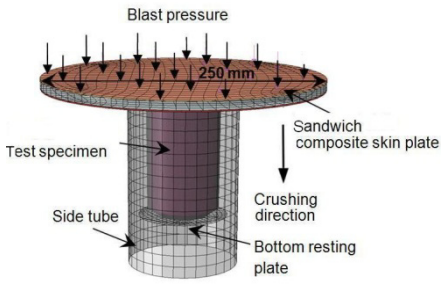

(b) Finite element model with sandwich composite skin plate (ϕ250 mm; 0.36 kg).

Figure 6-8: Finite element models.

6. 5. 4. Results and discussions

With aluminium skin plate (ϕ200 mm; 1.0 kg)

Different scale factors (ω = 1%, 2.5%, 5%, 10% and 100 % of mid-wall thickness) were considered for the blast analysis study. The final deformation patterns of the beverage cans for different scale factors with the aluminium skin plate (ϕ200 mm; 1.0 kg) are shown in Figure 6-9. As an example the sequence of deformation patterns with a scale factor of ω = 10 % (of mid-wall thickness) is shown in Figure 6-10. Due to the sine-wave profile of imperfection the initiation of the failure was started at the mid-wall region of the beverage can. Scale factors of 1 to 10 % provided realistic deformation patterns and are comparable with the experimental results (during the experimental testing it was observed that the initiation of deformation was started at different points on the mid-wall region for different test specimens discussed in Chapter 4).

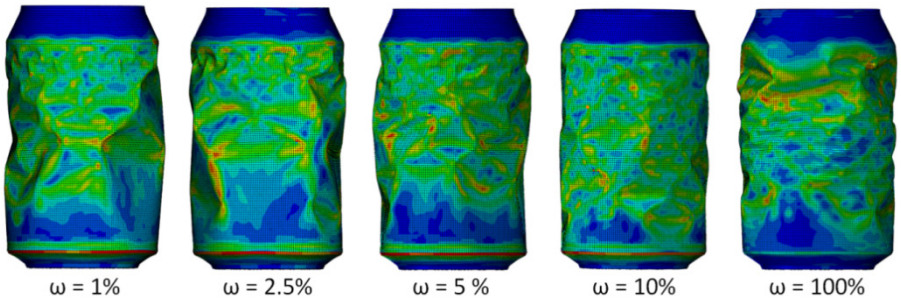

Figure 6-9: Final deformation patterns of beverage cans with different scale factors.

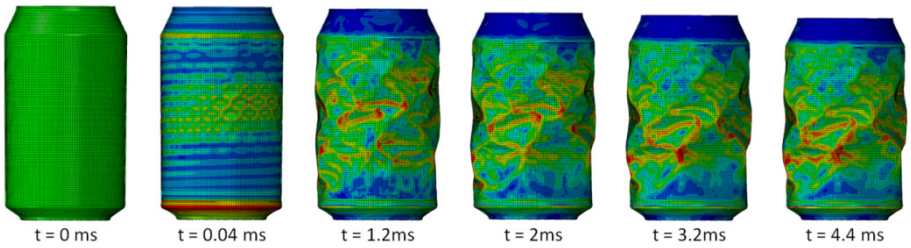

Figure 6-10: Deformation sequence of a beverage can with the scale factor ω = 10 % of mid-wall thickness.

In addition to that there was no reduction in the peak crush load noticed for the cases with scale factor from 1 to 10 % of mid-wall thickness. As an example, the load-deformation histories of the case with initial geometric imperfection scale factor ω = 2.5 % and 100% are shown in Figure 6-11.

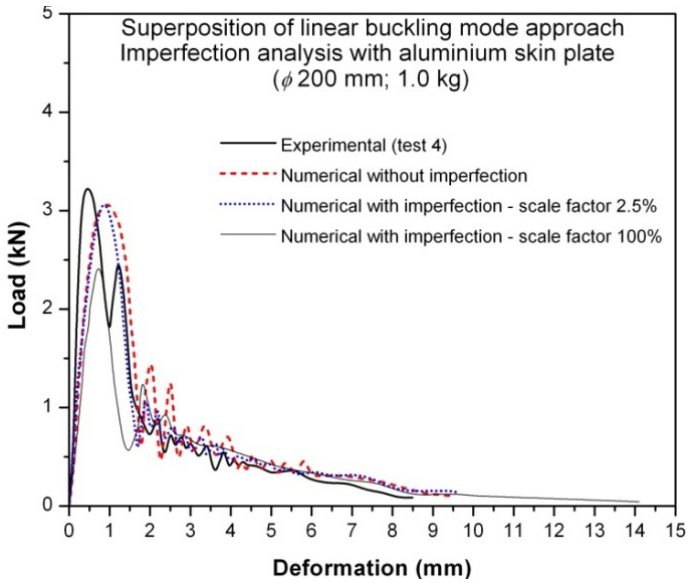

Figure 6-11: Load-deformation histories of beverage can with geometric imperfection (superposition of linear buckling modes).

The peak crush load for the cases with scale factor ω = 1%, 2.5%, 5% and 10% showed no difference compared to the perfect case (refer Table 6-1). The case with 100 % scale factor provided a 20 % reduction in the peak crush load compared to a perfect can geometry analysis (refer Figure 6-11 and Table 6-1). However, during the experimental testing a similar reduction in the peak crush load was not noticed for any of the beverage can. This shows that even though the thickness of the mid-wall is lower (0.07 mm) the attributed imperfection with 100 % scale factor may not occur during the manufacturing process and in due course of usage. Due to a higher amplitude of imperfection (for 100 % scale factor) the total deformation length of the can was increased compared to the experimental results (Table 6-1).

Furthermore, with higher scale factors the fluctuation in the crush load was reduced considerably. This is obvious due to the higher amplitude of introduced imperfections. The energy absorption of all cases with scale factors 1 to 100 % was remained approximately the same. This was due to a higher deformation length and a lower mean crush load of the test specimens with large scale factors (refer Table 6-1). The summary of the numerical parameters such as peak crush load, mean crush load, the energy absorption and the corresponding specific energy absorption is given in Table 6-1. It can be noticed that due to the same level of absorbed energy the specific energy absorption of all cases remained the same.

With sandwich composite skin plate (ϕ 250 mm; 0.36 kg)

Similar results have been obtained for the case with the sandwich composite skin plate (ϕ 250 mm; 0.36 kg). The peak crush load was not affected for the scale factors from 1% to 10% (refer Figure 6-12).

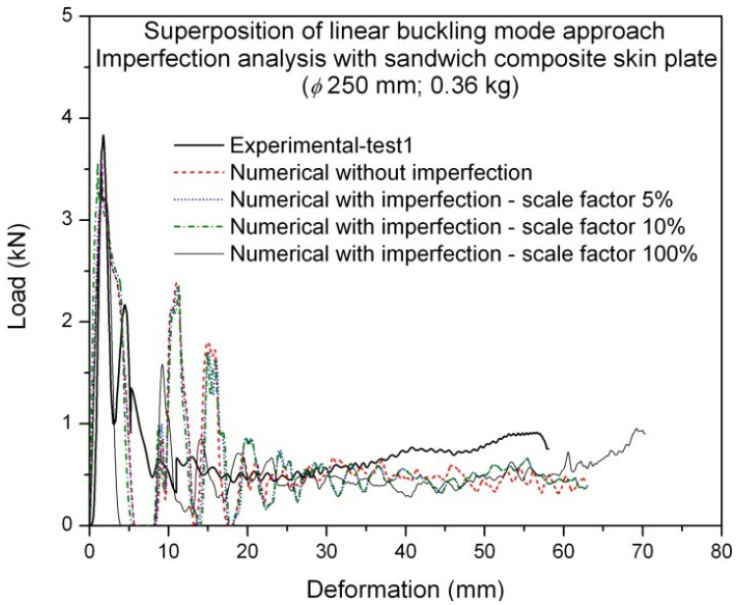

Figure 6-12: Force-deformation histories of beverage can with geometric imperfections (superposition of linear buckling modes) and with sandwich composite skin plate (ϕ 250 mm; 0.36 kg).

Unlike the case with the aluminium skin plate (ϕ 200 mm; 1.0 kg) the scale factor with ω = 100% showed a 10% reduction in the peak crush load compared to the perfect geometry analysis of the beverage can. However, the total deformation length of this case was higher than the remaining cases (70.5 mm). The calculated parameters such as the peak crush load, mean crush load, deformation length and the corresponding energy absorption for all cases are given in Table 6-2. The deformation patterns of all cases (except the case with a scale factor ω = 100%) were the same. For all cases (ω = 1%, 2.5%, 5% and 10%) the initiation of crushing

started at the interface location of top-shoulder and mid-wall region (refer Figure 6-13) similar to the experimental results. However, for the case with the scale factor ω = 100%, the initiation of progressive crushing was started at the mid-wall region of the beverage can. This evidence can be noticed from the second image of Figure 6-13.

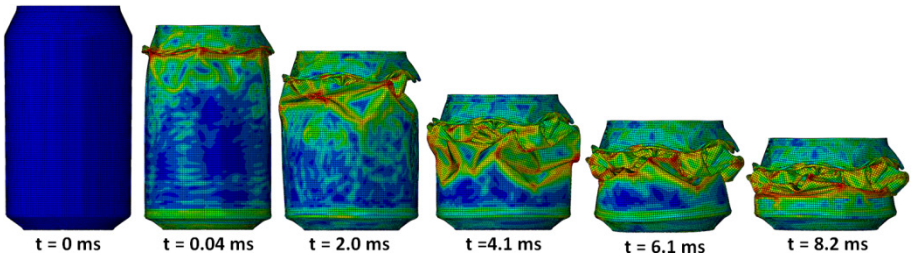

Figure 6-13: Deformation sequence of a beverage can with scale factor ω= 10 % of mid-wall thickness.

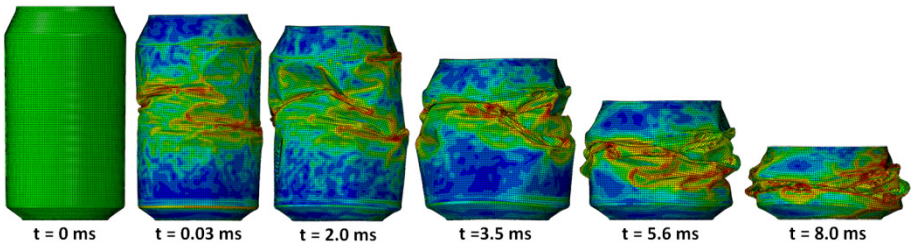

Figure 6-14: Deformation sequence of a beverage can with scale factor ω= 100 % of mid-wall thickness.

Table 6-1: Summary of numerical crushing parameters for an empty beverage can with initial geometric imperfections (with aluminium skin plate (ϕ 200 mm; 1.0 kg))

Cases	Peak crush load P_{max} (kN)	Mean crush load P_{avg} (kN)	Deformation length l_{max} (mm)	Absorbed energy E_d (J)	SEA (kJ/kg)
With aluminium skin plate (ϕ 200 mm; 1.0 kg)					
Experimental average	3.19	0.434	8.93	3.85	1.940
Numerical results without imperfection	3.10	0.418	9.41	3.93	1.879
Numerical results with imperfection – linear superposition of *Eigen* vectors					
Scale factor 1 % of mid-wall thickness	3.10	0.418	9.41	3.93	1.879
Scale factor 2.5 % of mid-wall thickness	3.10	0.418	9.41	3.93	1.879
Scale factor 5 % of mid-wall thickness	3.10	0.407	9.65	3.93	1.833
Scale factor 10 % of mid-wall thickness	3.10	0.402	9.78	3.93	1.808
Scale factor 100 % of mid-wall thickness	2.49	0.284	14.1	4.00	1.277
Numerical results with imperfection - measured initial geometric imperfection approach					
Case (i) – Initial geometry imperfection only at top - shoulder location	3.06	0.415	9.50	3.94	1.866
Case (ii) – Initial geometry imperfection only at mid-wall location	3.05	0.442	8.90	3.94	1.992
Case (iii) – Initial geometry imperfection on both locations - 180° opposite configuration	3.01	0.431	9.01	3.89	1.943
Case (iv) – Initial geometry imperfection on both locations – in-line configuration	3.04	0.422	9.30	3.93	1.901

Table 6-2: Summary of numerical crushing parameters for an empty beverage can with initial geometry imperfections (with sandwich composite skin plate (ϕ 250 mm; 0.36 kg))

Cases	Peak crush load P_{max} (kN)	Mean crush load P_{avg} (kN)	Deformation length l_{max} (mm)	Absorbed energy E_d (J)	SEA kJ/kg)
With sandwich composite skin plate (ϕ 250 mm;0.36 kg)					
Experimental average	3.95	0.723	58.0	41.96	3.26
Numerical results without imperfection	3.73	0.673	62.3	41.93	3.03
Numerical results with imperfection – linear superposition of *Eigen* vectors					
Scale factor 1 % of mid-wall thickness	3.73	0.674	62.3	42.0	3.02
Scale factor 2.5 % of mid-wall thickness	3.73	0.667	62.8	41.9	3.00
Scale factor 5 % of mid-wall thickness	3.73	0.667	62.8	41.9	3.00
Scale factor 10 % of mid-wall thickness	3.73	0.661	63.2	41.8	2.98
Scale factor 100 % of mid-wall thickness	3.32	0.581	70.5	41.0	2.62
Numerical results with imperfection - measured initial geometric imperfection approach					
Case (i) – Initial geometry imperfection only at top - shoulder location	3.67	0.672	62.4	41.91	3.02
Case (ii) – Initial geometry imperfection only at mid-wall location	3.67	0.672	62.4	41.91	3.02
Case (iii) – Initial geometry imperfection on both locations – in-line configuration	3.66	0.665	63.0	41.94	3.00
Case (iv) – Initial geometry imperfection on both locations – 180° opposite configuration	3.66	0.669	62.6	41.90	3.01

6. 6. Measured geometric imperfections approach

If the details of the initial geometric imperfections during the manufacturing process and during the usage are known then accurate results can be predicted using this information. However, quantification of the initial geometric imperfections from a production process is a tedious task due to the variance of control parameters. Hence, in this study only the initial geometric imperfections caused during the usage were considered. Furthermore, a comparison can be made for these approaches (linear superposition of buckling mode shapes approach and measured initial geometric imperfections approach). The initial geometric imperfections during the usage were captured and the same was utilized to study the crushing performance of the beverage can. The investigation of the tested beverage cans before the blast tests showed two major initial geometric imperfections. The majority of the beverage cans had a dimple at the interfacial line of top-shoulder and the mid-wall region (refer Figure 6-15). This kind of imperfection was predominant for the beverage cans which were drawn from vending machines. The dimension of this initial geometric imperfection was measured from 10 beverage cans. The average geometric details of this imperfection are shown in Figure 6-16. Secondly, few cans had a dimple at the mid-wall region of the can. This kind of imperfection can occur during the usage. The details of this imperfection and the corresponding location on a beverage can are shown in Figure 6-17. There was no significant imperfection found on any other part of the beverage can. To study the effect of these measured initial geometric imperfections, four different analyses were conducted. The effect of an individual and combinations of these imperfections were studied in detail.

6. 6. 1. Results and discussions

Similar load cases are considered to compare the results with the linear superposition of buckling analysis. The results of these four cases are reported here.

i. *case 1* - deals with the initial geometric imperfection only in the top-shoulder region.
ii. *case 2* - deals with the initial geometric imperfection only in the mid-wall region.
iii. *case 3* - deals with a combination of both imperfections (above) located at opposite side (180° opposite) of the beverage can.
iv. *case 4* - deals with a combination of both imperfections (above) located at the same side of the beverage can (in-line).

Figure 6-15: Examples of initial geometric imperfections at top - shoulder locations

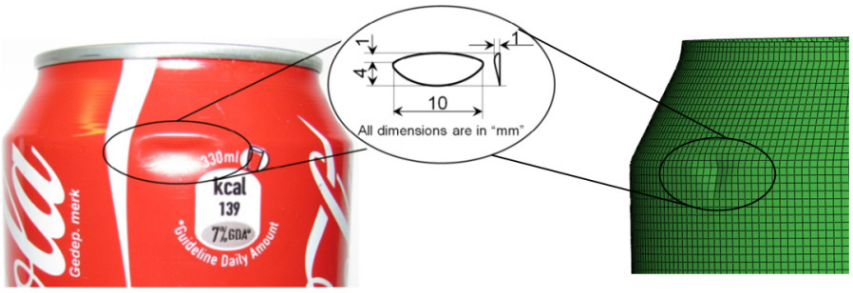

(a) Initial geometry imperfection at top shoulder –test specimen. (b) Finite element modelling

Figure 6-16: Details of an initial geometric imperfection (at top - shoulder location) of an empty beverage can.

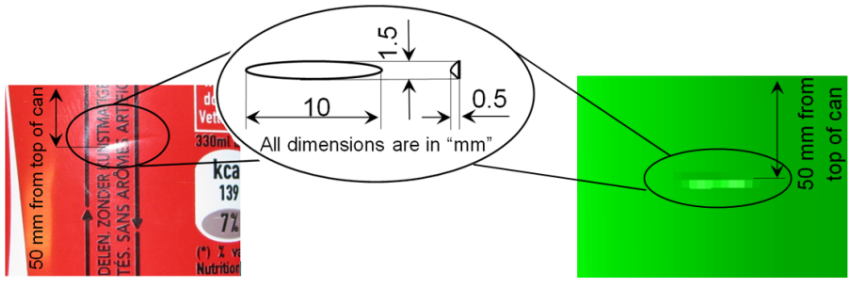

(a) Initial geometry imperfection at midwall – test specimen (b) Finite element modelling

Figure 6-17: Details of an initial geometric imperfection (at mid-wall location) of an empty beverage can.

6. 6. 2. Case 1 – Initial geometric imperfection only in the top – shoulder region

With aluminium skin plate (ϕ 200 mm; 1.0 kg)

The sequence of deformation patterns of a beverage can with initial geometric imperfection only on the top shoulder are shown in Figure 6-18. The initial time increments of the simulation showed a stress concentration around the imperfection area at the top-shoulder region. Consequently, the deformation of the can was started

from that point and spread around in circumferential direction. This phenomenon can be noticed from Figure 6-18 around 0.24 ms. Due to this phenomenon the local wall failure mode of the beverage can occurred and it was different from the earlier cases (superposition of buckling mode shapes). Subsequently, the failure of the can further propagated downwards. This evidence can be noticed from the same figure at time t = 3.03 ms. However, there was no significant failure noticed at the point of imperfection. This was due to a higher thickness and the corresponding stiffness of the beverage can at that location. The corresponding load-deformation history of this case is shown in Figure 6-19.

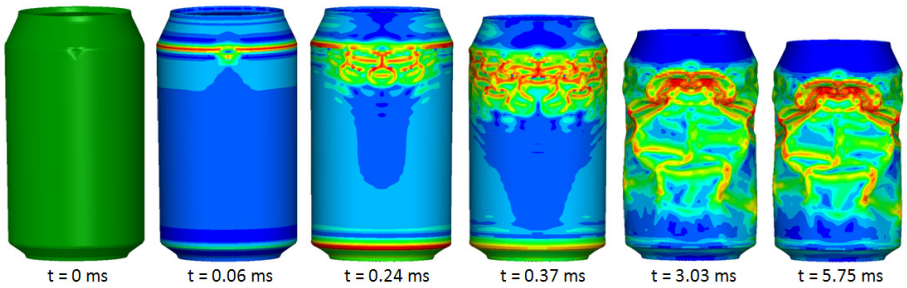

Figure 6-18: Deformation sequence of beverage can with geometric imperfection only at top - shoulder region (with aluminium skin plate; ϕ 200 mm; 1.0 kg).

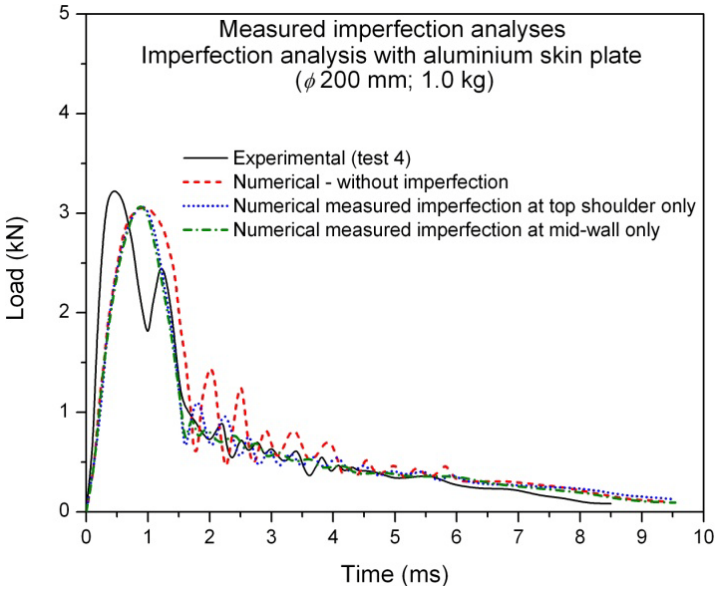

Figure 6-19: Comparison of load-deformation histories without and with geometric imperfection only in top-shoulder region (with aluminium skin plate; ϕ 200 mm; 1.0 kg).

The load-deformation history of this case showed no difference in the peak crush load. However, the imperfection at the top-shoulder region attributed to a drop in the

crush load after the peak (refer Figure 6-19). The later time increments of this analysis showed a minor fluctuation in the crush load. The predicted deformation length of this case was very close to the experimental result. The summary of the crushing parameters is presented in Table 6-1.

With sandwich composite skin plate (ϕ 250 mm; 0.36 kg)

The deformation sequence of this case was very similar to the one which is shown in Figure 6-13. Furthermore, the presence of the imperfection in the top-shoulder region did not alter the peak crush load and the corresponding energy absorption of the beverage can. This may be due to a higher rate of loading (and the corresponding maximum impact velocity of this case was approximately 18 m/s). Furthermore, the initiation of the triangular lobes formed just below the dimple portion (imperfection); hence, the presence of an imperfection in the top shoulder region did not influence the peak and post crushing load of the beverage can. The calculated crushing parameters for this case are presented in Table 6-2.

6. 6. 3. Case 2 – Initial geometry imperfection at mid-wall location only

With aluminium skin plate (ϕ 200 mm; 1.0 kg)

The deformation patterns of a beverage can with an initial geometric imperfection only in the mid-wall region are shown in Figure 6-20. Similar to the earlier case there was a stress concentration noticed around the imperfection during the initial stages of crushing. Subsequently, a significant deformation occurred at the imperfection location. One difference must be noticed for this case compared to the earlier case. For Case 1 (imperfection only on top-shoulder region) below the top-shoulder region, a significant deformation in the mid-wall region was noticed around the circumference. However, for Case 2 there was no significant deformation noticed at that location. This can be noticed from Figure 6-20 which corresponded to the crushing time of 0.37 ms. The later time increments of this analysis showed a squeezing of the mid-wall (at imperfection location) towards the axis of the can. Furthermore, on the opposite side of the beverage can there was no local wall buckling mode observed. On the other hand, a considerable local wall buckling was observed at the top-shoulder region. This may be due to the combined effect of squeezing of the mid-wall on one side (subjected to compression) and stretching on other side (subjected to tension). However, the above difference in the deformation mode did not alter the magnitude of the peak crush load; rather it changed the crush load after the peak (refer Figure 6-19) similar to the case with the imperfection only in top shoulder region. Similar to Case 1, the load-deformation history of this analysis showed no considerable difference in the peak crush load. The predicted total deformation length of this case was also very close to the experimental value.

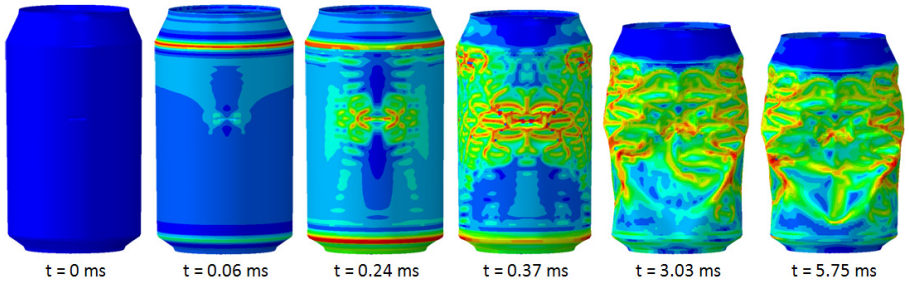

Figure 6-20: Deformation sequence of beverage can with geometric imperfection only at mid-wall region (with aluminium skin plate; ϕ 200 mm; 1.0 kg).

With sandwich composite skin plate (ϕ 250 mm; 0.36 kg)

The deformation sequence of the case with sandwich composite skin plate (ϕ 250 mm; 0.36 kg) is shown in Figure 6-21. Although the initial stages of the crushing showed a stress concentration in the mid-wall (imperfection) region, the initiation of the triangular lobes started at the top shoulder region. This evidence can be noticed from Figure 6-21 which corresponded to time t = 0.2 ms. Hence, there was no influence of this mid-wall imperfection on the peak and post crushing load of the beverage can. The calculated crushing parameters of this case were very close to the experimental results (refer Table 6-2).

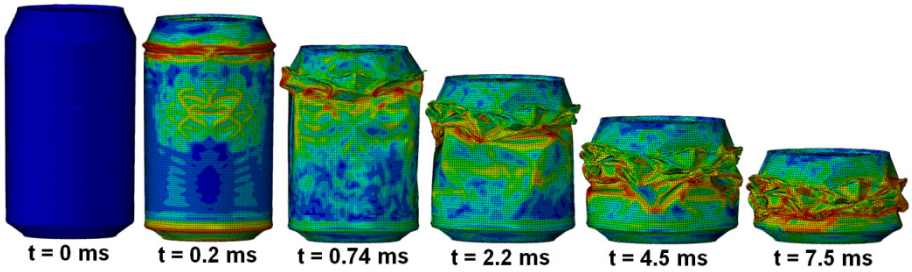

Figure 6-21: Deformation sequence of beverage can with geometric imperfection only at mid-wall region (with sandwich composite skin plate; ϕ 250 mm; 0.36 kg).

6. 6. 4. Case 3 and 4 – Initial geometric imperfections at both locations

For aluminium skin plate (ϕ 200 mm; 1.0 kg)

In this case a combination of imperfections in the top-shoulder and the mid-wall regions was considered for the analysis. There was no experimental testing done with this type of cans. However, a combination of these two imperfections on a beverage can is very much possible. Therefore, a study on this combination of imperfections is necessary. The location of these two imperfections on the beverage cans was arbitrary. However, two instances are considered for the study. The first case (case 3) considers both imperfections (at top-shoulder and mid-wall) opposite

in location (180° opposite). The second analysis (case 4) assumes both imperfections in line. However, the positions of the imperfections on the can were the same. (i.e., one at top shoulder and other is 50 mm from the top cover of the beverage can). The influence of a combination of these two imperfections on the deformation patterns and the corresponding energy absorption was evaluated. The deformation patterns from case 3 (assumed both imperfections are located at 180° opposite) are shown in Figure 6-22. Similarly case 4 is shown in Figure 6-23. It can be noticed that the deformation patterns of the first case very well correspond to the individual cases (imperfection only at top-shoulder and mid-wall locations). The initial stages from case 4 showed a difference compared to the individual cases. However, the later time increments and final deformation patterns showed no significant difference. Similar to the individual cases, the load-deformation history of this analysis showed a small reduction in the peak crush load (3.01 kN and 3.04 kN for case 3 and case 4 respectively). However, the magnitude was not significant. The total deformation length of the in-line configuration was slightly higher than the opposite configuration (9.01 mm and 9.30 mm for case 3 and 4 respectively). Due to the same mean crush load and higher deformation length the in-line configuration showed a higher value of energy absorption (3.89 J and 3.93 J for case 3 and case 4 respectively). The calculated values of all crushing parameters are given in Table 6-1.

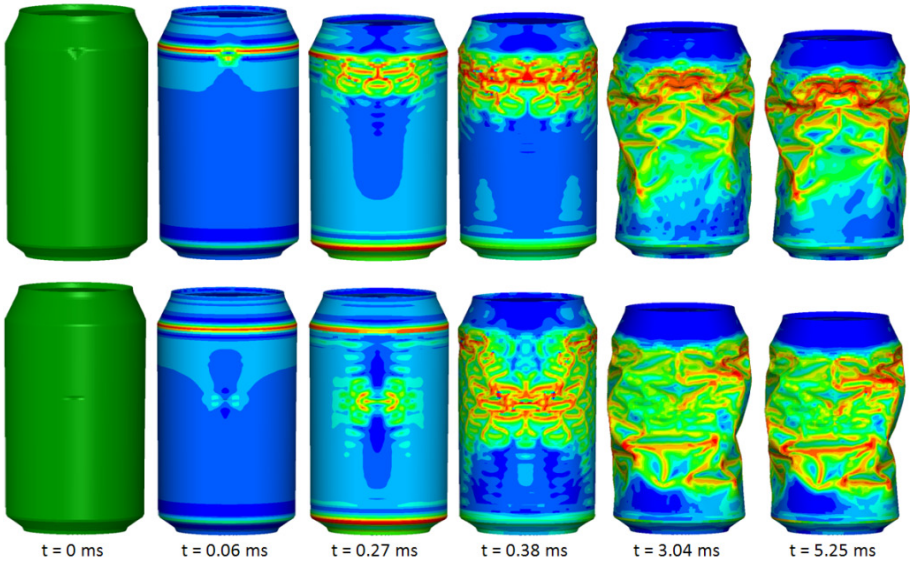

Figure 6-22: Deformation sequence of beverage can with geometric imperfections in the top - shoulder and mid-wall regions (180° opposite) with the aluminium skin plate (ϕ200 mm; 1.0 kg).

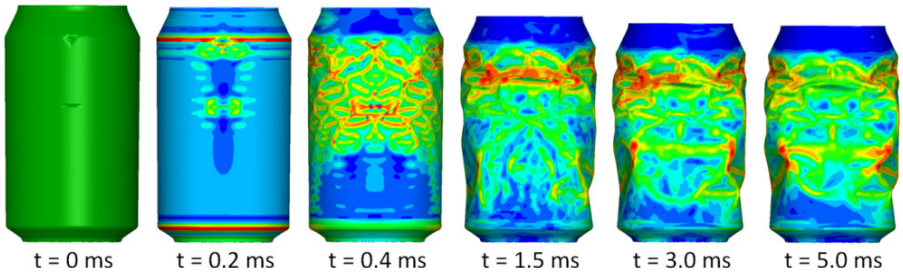

Figure 6-23: Deformation sequence of beverage can with geometric imperfections at top - shoulder and mid-wall regions (in-line) with the aluminium skin plate (ϕ 200 mm; 1.0 kg).

With sandwich composite skin plate (ϕ 250 mm; 0.36 kg)

For both cases (case 3 and 4), similar results have been observed with the sandwich composite skin plate. As an example, the deformation patterns of case 4 (in-line configuration) are presented in Figure 6-24. The calculated crushing parameters of these cases are presented in Table 6-2.

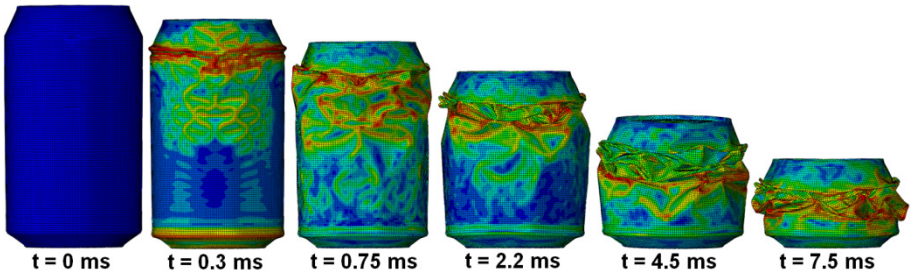

Figure 6-24: Deformation sequence of beverage can with geometric imperfections at both locations (with the sandwich composite skin plate; ϕ 250 mm; 0.36 kg).

6. 6. 5. Conclusions

In order to understand the influence of initial geometric imperfections on the deformation patterns and the corresponding crushing parameters an imperfection study was conducted. Two different approaches have been adopted to study the effect of the initial geometric imperfections. The first approach dealt with a superposition of linear combinations of typical buckling modes. The second approach was based on the measured initial geometric imperfections (due to usage). The commercially available code ABAQUS V6.7-3 Implicit and Explicit were used for the analysis. From the conducted numerical studies and their results the following conclusions can be made:

- Buckling analysis of an empty beverage can exhibited axisymmetric mode shapes associated with a single *Eigen* value. From the results it can be

concluded that the beverage can structure is imperfection sensitive especially at the mid-wall location; and the first mode will characterize the deformation that leads to the lowest buckling load.

- The approach of superposition of linear buckling modes with different scale factors (ω = 1%, 2.5%, 5% and 10%) provided realistic deformation patterns compared to experimental data. Similarly, the predicted deformation length from these cases correlated well with the experimental results. Furthermore, there was no significant difference in the peak crush load observed due to the imperfections. Hence, the energy absorption values of these cases remained the same.
- The approach of measured initial geometric imperfections (in the top-shoulder and mid-wall locations) accurately predicted the deformation lengths and deformation patterns compared to the experimental results. However, there was no significant reduction in the peak load and the energy absorption values compared to the perfect geometry analysis.
- Results from the combination of imperfections (at top-shoulder and mid-wall regions) analyses showed no significant difference in the peak crush load and the energy absorption. The deformation patterns of these two cases (180° opposite and in-line) can be very well compared with individual imperfection results.

The magnitude of the discussed geometric imperfections (superposition of buckling mode shapes and measured geometric imperfections) did not influence the crushing performance of the beverage can significantly. Therefore, these geometric imperfections can be neglected for an analysis to predict the crushing performance of the beverage cans. However, any other imperfections with magnitudes higher than the discussed ones should be studied thoroughly and to be accounted for accordingly.

Bibliography

[1]. Krauthammer, T., *Modern protective structures.* CRC Press, New York, 2008.

[2]. Bangash, M. Y. H., *Shock, impact and Explosion*. Springer, London, 1993.

[3]. Smith, P. D. and Hetherington, J. G., *Blast and ballistic loading of structures.* Butterworth-Heinemann Ltd., 1994.

[4]. Ngo, T., Mendis, P., Gupta, A. and Ramsay, J., *Blast loading and Blast effects on Structures - An Overview.* EJSE Special Issue: Loading on Structures, 2007.

[5]. Malvar, L. J., *Review of static and dynamic properties of steel reinforcing bars.* ACI Materials journal, ACI, Detroit, Michigan., 1998. **95**(5): p. 609-616.

[6]. Dowling, A. R. and Harding, J., *Tensile properties of mild steel under high strain rates.* Proceedings of the 1st HERF conference, University of Denver, Colorado, 1967.

[7]. Calladine, C. R. and English, R. W., *Strain-rate and inertia effects in the collapse of two types of energy-absorbing structure.* International Journal of Mechanical Sciences, 1984. **26**(11-12): p. 689-701.

[8]. Su, X. Y., Yu, T. X. and Reid, S. R., *Inertia-sensitive impact energy-absorbing structures part II: Effect of strain rate.* International Journal of Impact Engineering, 1995. **16**(4): p. 673-689.

[9]. Tam, L. L. and Calladine, C. R., *Inertia and strain-rate effects in a simple plate-structure under impact loading.* International Journal of Impact Engineering, 1991. **11**(3): p. 349-377.

[10]. Zou, Z., Tan, P. J., Reid, S. R., Li, S. and Harrigan, J. J., *Dynamic crushing of a one-dimensional chain of type II structures.* International Journal of Impact Engineering, 2007. **34**(2): p. 303-328.

[11]. Norris, G. H., Hansen, R. J., Holly, M. J., Biggs, J. M., Namyet, S. and Minami, J. K., *Structural design for dynamic loads.* McGraw-Hill, New York, USA, 1959.

[12]. Guruprasad, S. and Mukherjee, A., *Layered sacrificial claddings under blast loading Part I - analytical studies.* International Journal of Impact Engineering, 2000. **24**(9): p. 957-973.

[13]. Hanssen, A. G., Enstock, L. and Langseth, M., *Close-range blast loading of aluminium foam panels.* International Journal of Impact Engineering, 2002. **27**(6): p. 593-618.

[14]. Karagiozova, D., Nurick, G. N. and Langdon, G. S., *Behaviour of sandwich panels subject to intense air blasts - Part 2: Numerical simulation.* Composite Structures, 2009. **91**(4): p. 442-450.

[15]. KazancI, Z. and Mecitoglu, Z., *Nonlinear dynamic behavior of simply supported laminated composite plates subjected to blast load.* Journal of Sound and Vibration, 2008. **317**(3-5): p. 883-897.

[16]. Garcia, J. G., Marsolek, J. and Reimerdes, H. G., *Determination of the Energy Absorption of Cylinderical shells under Axial Loading by Analysis of the Dynamic Buckling and Folding Process.* International Journal of Crashworthiness, 1999(4:4): p. 351-364.

[17]. Hilburger, M. W. and Starnes, J. H., *Effects of imperfections of the buckling response of composite shells.* Thin-Walled Structures, 2004. **42**(3): p. 369-397.

[18]. Arbocz, J. and Hol, J. M. A. M., *Collapse of axially compressed cylindrical shells with random imperfections.* Thin-Walled Structures, 1995. **23**(1-4): p. 131-158.

[19]. Koiter, W., *On the stability of elastic equilibrium, Ph.D. Thesis,.* Polytechnic Institute Delft, English Translation: NASA TT F-10,, 1945 (1967) 833.

[20]. Chryssanthopoulos, M. K., Giavotto, V. and Poggi, C., *Characterization of manufacturing effects for buckling-sensitive composite cylinders.* Composites Manufacturing, 1995. **6**(2): p. 93-101.

[21]. Kinney, G. F. and Graham, K. J., *Explosive shocks in air.* Springer-Verlag, 1985.

[22]. *User manual MathCad.* Mathsoft Engineering & Education, 2005.

[23]. Arbocz, J. and Babcock, C. D., *The effect of general imperfections on the buckling of cylinderical shells.* Journal of Applied mechanics, 1969. **36**(Series E(1)): p. 28-38.

[24]. Arbocz, J., *The effect of general imperfections on the buckling of cylinderical shells. Ph.D thesis.* California Institute of Technology, Pasadena, California, 1968.

[25]. W.Schneider, *Stimulating Equivalent Geometric Imperfections for the Numerical Buckling Strength Verification of Axially Compressed Cylinderical Steel Shells.* Cimputational Mechanics, 2006. **37**: p. 530-536.

[26]. Bisagni, C., *Numerical analysis and experimental correlation of composite shell buckling and post-buckling.* Composites Part B: Engineering, 2000. **31**(8): p. 655-667.

[27]. Tsouvalis, N. G., Zafeiratou, A. A. and Papazoglou, V. J., *The effect of geometric imperfections on the buckling behaviour of composite laminated cylinders under external hydrostatic pressure.* Composites Part B: Engineering, 2003. **34**(3): p. 217-226.

[28]. Wohlever, J. C., *Some computational aspects of a group theoretic finite element approach to the buckling and postbuckling analyses of plates and shells-of-revolution.* Computer Methods in Applied Mechanics and Engineering, 1999. **170**(3-4): p. 373-406.

[29]. *ABAQUS User manual.* ABAQUS, Inc. and Dassault Systèmes 2007.

Part II

This part deals with the quasi-static, impact and small-scale blast testing on β - type structure (large-scale pultruded and medium-scale pultruded composite tubes)

Chapter 7

Composite Tubes for Energy Absorption: a Review

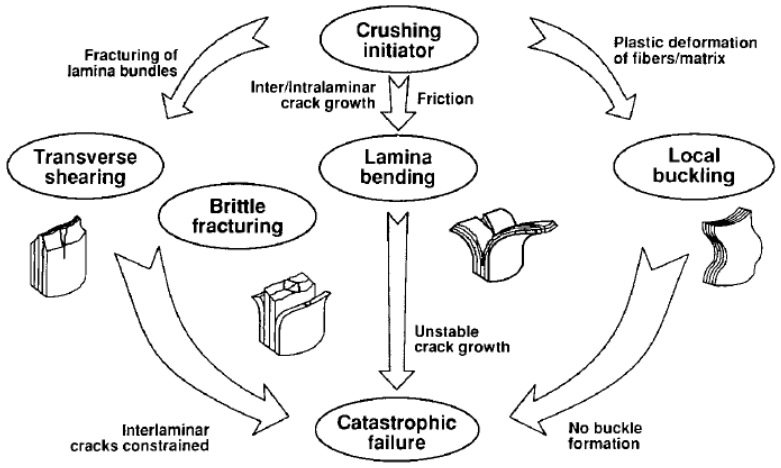

Overview

This chapter presents a literature review on the energy absorption capability of polymer composite tubes. Different failure mechanisms (macro and micro) which are related to the progressive and catastrophic failure patterns of composite tubes are presented. The list of variables which influence the (specific) energy absorption of composite tubes are presented. Furthermore, a brief introduction of all these parameters and their effect on the specific energy absorption are given. Finally different methods of assessing the energy absorption of composite tubes are introduced briefly.

7. 1. Introduction

Numerous experimental and simulation studies have been conducted in the area of energy absorption with different metals and non-metals for impact and blast loading applications. In case of impact loading most of the studies concentrated on the energy absorption of the frontal collision system [1-6] and frontal protection system for automobiles. Crashworthy efficient structures must be able to dissipate large

amounts of energy in the event of a crash. The structures which were used to investigate energy absorption for the automobiles were mostly metals and their alloys. Different shapes and profiles were tried out, to get maximum energy absorption during the impact loading. Similarly, the usage of metals in the area of protection of civil engineering and other structures has also been studied by some of the researchers [7-12]. However the use of metals, for the energy absorption for civil engineering structures is costly in terms of investment and maintenance [13, 14].

On the other hand a considerable amount of work has been done on the energy absorption of composite materials [15-41]. Different profiles of the energy absorbing tubes, their architecture, failure modes, and the triggering mechanisms which induce the progressive failure are studied. Properties of composite materials can be tailored to provide specific energy absorption capabilities superior to metals [13, 42]. This chapter presents a literature survey, on the area of energy absorption of polymer composite materials. However, the interest of this literature study is to focus only on the composite tubes which are relevant to the proposed application. From the success stories in the aerospace industry it is widely accepted that polymer composite materials offer a number of technical advantages. Some of them are high specific mechanical properties such as stiffness and strength, design flexibility, reduced weight and less maintenance. Due to the above factors, the interest in composites has been increased much in the area of impact and blast loading applications. One of the main reasons for the above fact is the higher specific energy absorption of composites over metals and their alloys. From Figure 7-1, it is well evident that composites are superior compared to metals in terms of specific energy absorption.

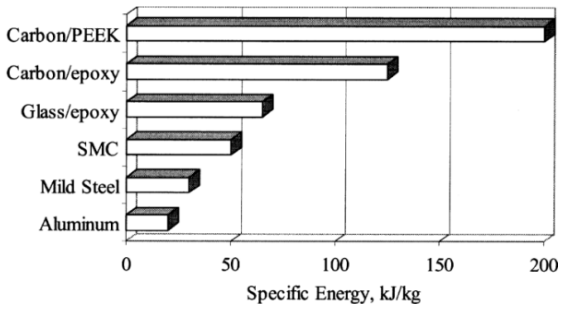

Figure 7-1: Comparison of specific energy absorption [42].

However unlike metals, composite materials display inherent brittle behavior and do not exhibit either plasticity or high elongation prior to failure. For example, the glass fibres are very brittle and fail after elastic deformation of approximately 1.5 to 2.0% elongation [42]. Similarly the polyester matrix suitable for structural composites is brittle and fails in tension after elongation between 1.5 and 3.5%. So special design approaches are required to provide an energy absorption capability comparable to that of metal structures. Some researchers investigated the energy absorption

behavior for multi-material systems such as the combination of metal and composite materials [43, 44].

The failure modes of composite materials are entirely different from those of the typical metals. One can notice multiple energy absorption mechanisms during the crushing of composite tubes. Each energy absorption mechanism is a function of the material properties of the tubes; and the architecture of the tubes or structures which are employed. Because of the complexity of the energy absorption process and to evaluate the suitability of composite material for crashworthy and blast loading applications, one should understand the energy absorption mechanisms of the composite structures and their corresponding failure patterns. The failure of composites structures during the energy absorption may be catastrophic or progressive. Some of the composite tubes made from brittle materials likely fail by brittle fracture either by compressive shear or lamina bending of the tube wall. During the crush process, the load increases to a peak value followed by a low post failure load. This kind of catastrophic failure results in a low energy absorption; moreover the energy is absorbed suddenly (refer Figure 7-2(a)). On the other hand the progressive crushing of composite tubes yields higher energy absorption (refer Figure 7-2(b)). The area under the load displacement curve gives the absorbed energy during the crush process.

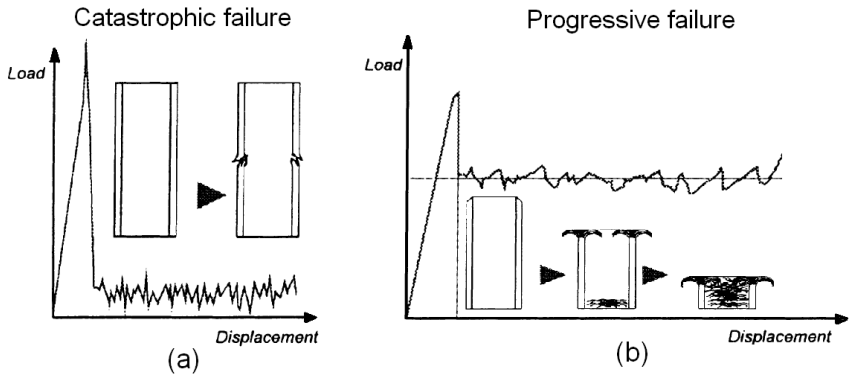

Figure 7-2: (a) Catastrophic failure **(b)** Progressive failure (reproduced from ref. [45]).

7. 2. Macroscopic failure modes of composite tubes

Composite tubes with thin walled geometries undergo different failure modes during an axial loading. The brittle nature of both fibre and matrix ensures that tubes do not undergo plastic deformation like ductile materials. However, the failure modes which dominate in case of axially loaded composite tubes are fracture and fragmentation. The failure modes are greatly affected by the geometry of the tube,

type of fibre and matrix, stacking sequence, etc. [42, 46]. The macroscopic collapse modes of the composite tubes which are subjected to axial loading can be broadly classified into two categories: (i) stable collapse mode associated with controlled crushing (ii) catastrophic failure or unstable mode associated with brittle fracturing. Based on the deformation patterns Mamalis [33, 34, 37, 47, 48] has classified the macroscopic failure modes of composite tubes as discussed below.

7. 2. 1. Progressive end crushing (Mode I)

Progressive crushing with micro fragmentation dissipates more energy (refer Figure 7-3). Furthermore, this mode can be classified into:

(i) *Mode I-a* is called the "*mushroom*" failure mode which is characterized by progressive collapse through the formation of continuous petals which spread outwards and inwards.

(ii) *Mode I-b* is characterized by fracturing and folding of the tube wall inside the tube. This mode of collapse is observed when the circular and square conical tubes with larger semi-apical angle are subjected to axial loading.

(iii) *Mode I-c* is characterized by the outward fracturing and folding of the shell wall.

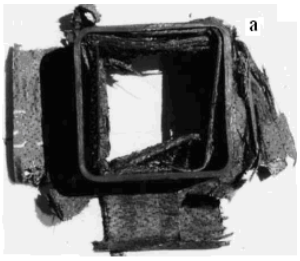

Figure 7-3: Progressive end crushing [48].

7. 2. 2. Brittle fracturing or Local tube wall buckling (Mode II & III)

Brittle fracturing modes lead to catastrophic failures which are classified either as *Mode II* or *Mode III* based on the crack form. Mode II is characterized by the development of a spiral crack propagating along the shell circumference (Figure 7-4(a)). Mamalis reported that this mode was observed in the conical shell specimen with 20° -30° semi-apical angle [48]. Mode III is called the mid-length collapse mode. This mode is characterized by the formation of circumferential fracturing of the material at a distance from the loaded end of the tube specimen approximately equal to the mid height of the tube. Composite tubes with a small semi-apical angle and less thickness undergo this mode of failure [48].

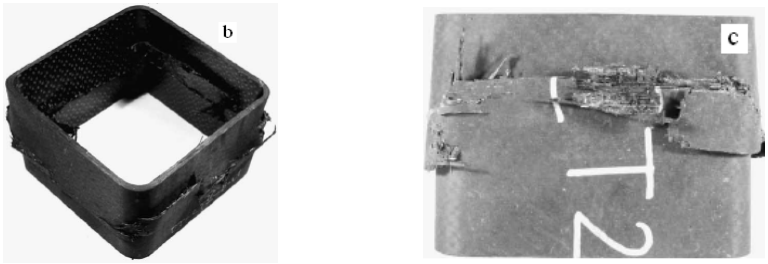

(a) **(b)**

Figure 7-4: (a) Local wall buckling **(b)** Mid-length collapse [48].

7. 2. 3. Progressive folding and hinging (Mode IV)

This mode is very similar to the crushing behaviour of thin-walled ductile material and plastic tubes. This mode dissipates much less crushing energy (Figure 7-4(b)). This mode of failure is associated with tubes having very less wall thickness and with a semi-apical angle not more than 15˚ [48].

7. 3. Microscopic failure modes of composite tubes

The crushing process of ductile and brittle continuous fibres composites well explained in Figure 7-5 [21, 43]. Since most of the composite materials are brittle in nature, the transverse shearing and lamina bending are two major energy absorbing modes. In addition to the above stated, some of the brittle composites may exhibit local buckle crushing behavior also. The details of the individual failure mechanisms are explained briefly below.

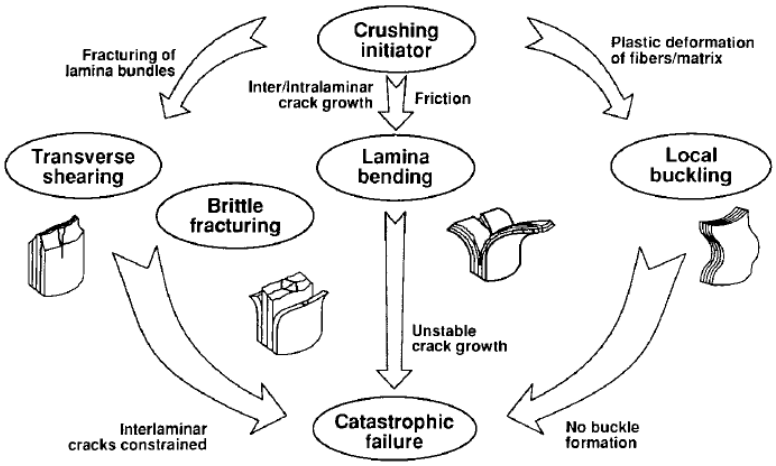

Figure 7-5: Crushing process of continuous fibre composite tubes [21].

7. 3. 1. Transverse shearing

Composite tubes which are made up of brittle fibres having high modulus and low failure strain can exhibit the transverse shearing mode. When the load is transferred to the edges of the tubes, longitudinal cracks are formed whose length is less than the thickness of the laminate (refer Figure 7-6). The interlaminar cracks grow further, when the load is present. The two major mechanisms which control the transverse shearing are: (a) i*nterlaminar growth* and (b) *lamina fracture.*

Interlaminar Growth: The interlaminar growth depends on the mechanical properties of the matrix, orientation of the fibres, stiffness and failure strain of the fibres. This crack grows by either Mode-I or Mode-II (refer Figure 7-7). The ability of a crack to grow in either mode is purely depending upon the toughness of the matrix and up to some extent the orientation of the plies [21].

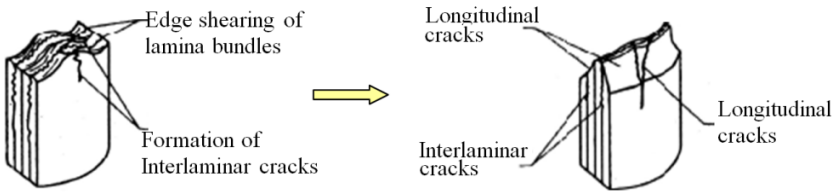

Figure 7-6: Transverse shearing crushing mode [21].

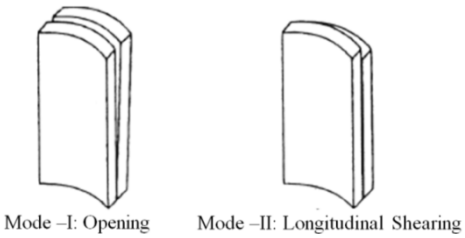

Figure 7-7: Different Modes of failure [21].

Lamina Fracture*:* This process absorbs the major amount of energy. When a considerable amount of cracks are developed, the laminae or lamina bundles are separated from each other. These are subjected to transverse bending load, where the bending moment will be maximum at the base of the lamina. During this process the lamina bundle fracture occurs, when the stress on the tensile portion of the bundle exceeds the fracture strength.

7. 3. 2. Lamina Bending

Separation of fibre bundles occurs due to the formation of interlaminar (cracks grow at the interface of the adjacent layer) and intralaminar cracks followed by matrix

cracking. The primary energy absorber for this mechanism is the significant bending of the lamina without fracture. During this process, the laminae slide against each other and the loading surface. Some amount of energy is also spent on this process. The characteristics of the lamina bending crushing mode are shown briefly in Figure 7-8.

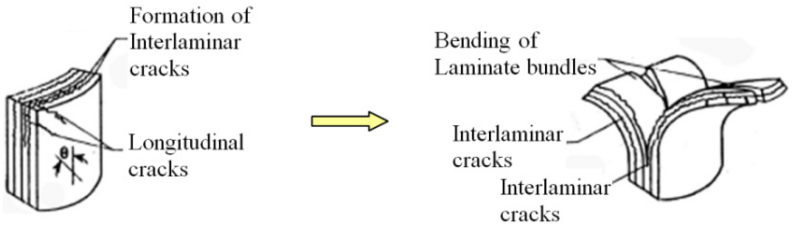

Figure 7-8: Lamina bending crushing mode [21].

7. 3. 3. Brittle Fracture

Most brittle fibre composite tubes exhibit brittle fracturing failure modes. Lamina bundles in this mode can exhibit the combination of transverse shearing and lamina bending at the base of the bundles. During this phenomenon, a cyclic process of crack growth, lamina bending and fracture occurs. The schematic representation of brittle fracturing is shown in Figure 7-9.

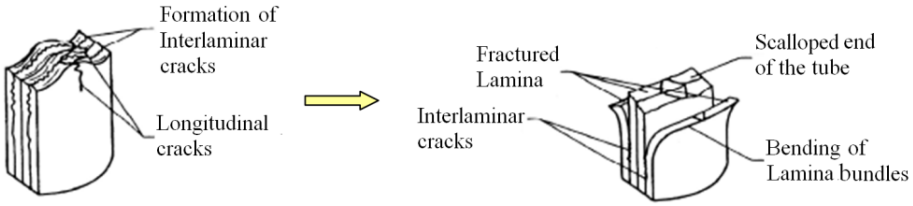

Figure 7-9: Brittle fracturing crushing mode [21].

7. 3. 4. Local Buckling

Local buckling is a common failure mode for ductile and brittle fibre tubes. However, the failure phenomena are slightly different for ductile and brittle fibre tubes. In case of ductile fibre tubes, local buckling causes the delamination between the plies at those locations. Most ductile fibre tubes exhibit post-crushing integrity. This is due to the considerable amount of deformation of fibre and matrix without crushing. However, the brittle fibre tubes exhibit the local buckling failure mode only when the matrix yields. The yielding of the matrix occurs in the tube, if any one of the following phenomena occurs.

(i) The matrix has a higher failure strain than the fibre.
(ii) The interlaminar stresses are smaller compared to the strength of the matrix.
(iii) The matrix exhibits plastic deformation under high stress.

The amount of interlaminar cracks is less due to the higher failure strain of the matrix. This effect causes the tubes to fail in local buckling mode. The crushing characteristic of the local buckling mode is shown in Figure 7-10.

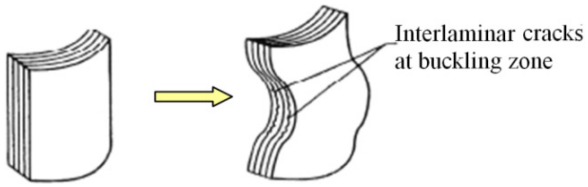

Figure 7-10: Local buckling crushing mode [21].

7. 4. Microscopic fracture mechanisms

Mamalis reported a conceptual model of the crush-zone based on a microscopic analysis of thin-walled square tubes and hourglass rail beams subjected to static axial loading [47, 49]. Fairfull and Hull reported similar results for circular tubes [38, 50]. Based on the performed microscopic observations [38, 47, 49], the chronological events occurred during the axial loading of a composite tube can be summarized as follows:

(i) An annular wedge of highly fragmented material forced down axially through the shell wall.
(ii) An intra-wall micro crack which develops ahead of the crush-zone at the apex of the annular wedge and propagates at a rate equivalent to the compression or strain rate.
(iii) Due to the delaminations two continuous petals or fronds radially spreads, one is inwards and another is outwards.
(iv) A severely strained area which extends between the central crack and the shell wall edges showing a combined tensile–compressive type of deformation.

The above mechanisms can be clearly noticed from Figure 7-11(a) and similarly a configuration of the internal fracture is also shown in Figure 7-11(b). The deformation behaviour of the tube depends on the fibre orientation. The fibres which are aligned parallel to the axis of the tube bend inwards and outwards. However, fibres arranged in the circumferential direction (90°) can only expand outwards. Delamination occurs due to the shear and the tensile stress between the plies. The

axial laminae split into progressively thinner layers, thus forming trans-laminar cracks normal to the fibre direction. During the axial loading the cracks propagate preferably through the area where the stress concentration is more. For example, the matrix rich area and interface between the different fibre orientation. The resistance to the crack propagation along the central region of the shell depends upon the compressive stiffness of intact internal material, tensile strength of the outer plies and the bonding between these two.

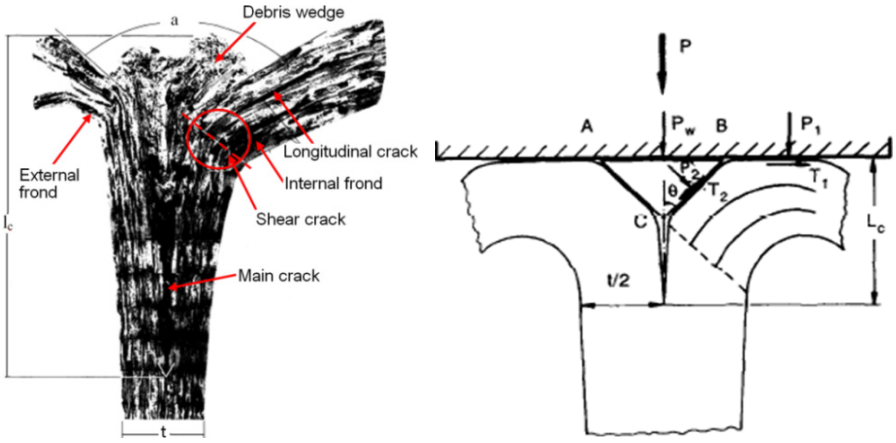

(a) **(b)**

Figure 7-11: (a) Micrographs showing micro-failures in the crush zone **(b)** Configuration of internal fracture [47, 49].

7. 5. Specific energy absorption

Due to the absence of a standard test protocol, researchers have adopted different geometries and profiles to compare the energy absorption of the tubes. The specific energy absorption (E_s), is defined as the amount of energy absorbed per unit mass of the crushed material [29, 42, 45] (Equation (8.1),

$$E_s = \frac{\overline{P}}{\rho A} = \frac{\overline{\sigma}}{\rho} = \frac{\int_0^{l_{\max}} F(l) \cdot dl}{m} \quad \text{[kJ/kg]} \tag{7.1}$$

where $\overline{P}$ is the mean crush load which can be obtained from the load-displacement curve (kN); $\overline{\sigma}$ is the mean crush stress (Pa); A is the cross-sectional area of the tube (m^2); ρ is the density of the tube (kg/m^3); *F(l)* is the instantaneous crushing load corresponding to the instantaneous crushing deformation length of the composite tube *dl* (kN); l_{max} is the maximum or total deformation length of the test specimen (m); *m* is the mass of the crushed material (kg).

7. 6. Comparison of specific energy absorption

The specific energy absorption of different composite materials from literature is presented in Table 7-1 [38]. One can observe that the specific energy absorption of the same material differs in a range. This is due to the fact that the specific energy absorption of composite tubes is depending upon so many parameters. The influence of the different factors and their corresponding roles on the energy absorption of composite materials is discussed in the subsequent sections.

7. 7. Variables influencing the energy absorption

The energy absorption characteristics of various composite structural elements have been experimentally and numerically studied by several researchers. Different cross-sections of the tubes are employed to get the maximum energy absorption with the least material investment. However, the energy absorption characteristics of the tubes are not only depending on the shape of the tubes [42, 43]. Various variables that influence the energy absorption characteristics of the composite tube are shown in Figure 7-12 [42]. A brief introduction of the effect of these variables on the specific energy absorption is given below.

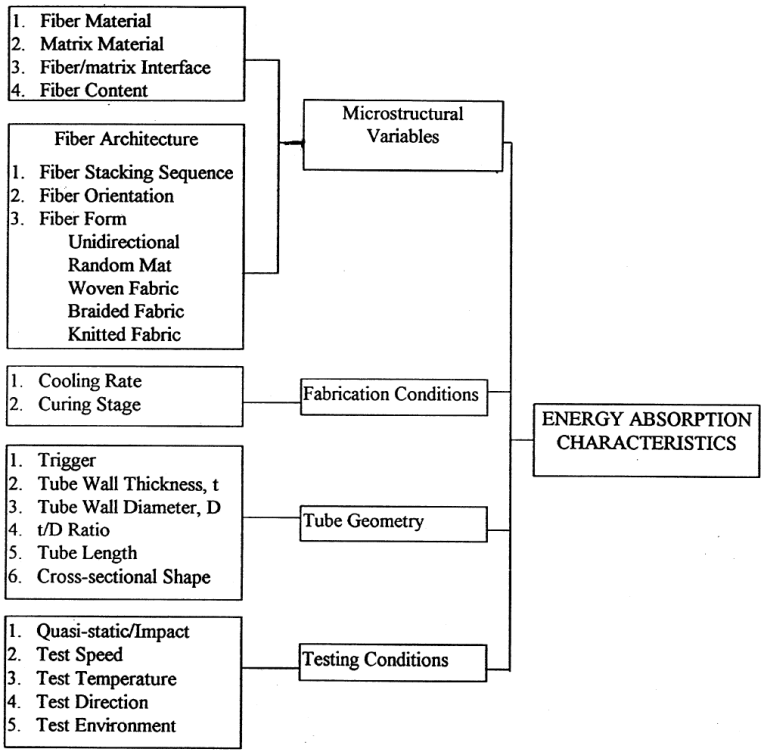

Figure 7-12: Variables altering the energy absorption of the composite tubes[42].

Table 7-1: Comparison of the specific energy absorption of different composite materials [38].

Authors	Thronton and Magee [51]	Thronton [41]	Thronton and Edwards [52]	Farley [22]	Farley [53]	Farley [23]	Farley [54]	Farley and Jones [24]	Hamada et al. [27]	Mamalis et al. [55, 56]
Material	**Specific energy absorption kJ/kg (t/D ratio)**									
Carbon-epoxy [0±15]				99 (0.033)		75 (0.0045)				
Carbon-epoxy [0/±45]				46 (0.032)		55 (0.051)	65 (0.02)			
Carbon-epoxy [±45]			55 (0.062)		55 (0.036)	58 (0.048)	50 (0.021)	60 (0.031)	53 (0.05)	
Carbon-PEEK [0]									180 (0.05)	
Carbon-PEEK [±30]									127 (0.05)	
Aramid-epoxy [0/±15]				31 (0.036)				9 (0.020)		
Aramid-epoxy [0/±45]				30 (0.033)				21 (0.020)		
Aramid-epoxy [±45]		60 (0.066)	31 (0.042)		33 (0.035)		23 (0.022)	22 (0.03)		
Aramid-epoxy [0/±90]				50 (0.033)						
Glass-epoxy [0/±15]				30 (0.060)						
Glass-epoxy [0/±45]			30 (0.028)	31 (0.059)						
Glass-epoxy [0/±75]				53 (0.070)						
Glass-vinylester [90/0/2R_c/2R_c/0/0/90/R_c.75]										54 (0.05)
Glass-polyester $[R_c]_n$										54 (0.162)
Aluminium 6061	75 (0.060)	72 (0.060)		90 (0.057)						
1015 Mild steel	33 (0.060)	33 (0.060)								

7. 8. Micro-structural variables

7. 8. 1. Fibre and matrix materials

Fibre material

Typically, the failure modes of the composite tube depend upon the type of fibre material which is made up. As discussed previously, brittle fibres like carbon and glass exhibit transverse shearing and lamina bending; however, most of the ductile fibres exhibit the local buckling mode. This difference in behavior is attributed to the lower failure strain of carbon and glass which fail at approximately 1% strain compared to aramid fibres which fail at approximately 8% strain. The specific energy absorption of the fibre depends on the density also. Investigation on PEEK matrix composite tubes [42] with different types of fibres (AS4 carbon, IM7 carbon and S2 glass) showed that the failure modes of all the composite tubes exhibited progressive crushing with lamina bending mode. However, the specific energy absorption of S2 glass fibre tubes was approximately 20% less than the carbon varieties. The difference in the specific energy absorption is attributed to the direct difference between the density of glass and carbon. Carbon has less density than glass. Although AS4 carbon fibres are more ductile than IM7, the specific energy levels of both tubes were the same. So it was concluded that, unlike the thermoset composite tubes, the fibre failure strain has less effect on the energy absorption of the thermoplastic tubes, as the fibre failure strain is much smaller than that of thermoplastic matrix. Warrior [57] concluded that if the energy absorption levels are normalized by mass and stiffness, the high strength and low density of carbon fibres leads to the highest rating.

Matrix material

Polyester resins are used widely in most of the applications. Their properties vary strongly with chemical formulation but generally they offer a high performance per cost ratio. Epoxies offer an increased modulus and strain to failure, but they are two times costlier than polyester. Vinylester resins are gaining popularity as they have better adhesion and fatigue properties than polyester whilst costing less than epoxy. The effect of matrix and the processing properties on the crushing performance of composites is significant. Warrior [57] combined glass fibre (engineered as well as random mat) with different matrices such as polyester, vinylester and epoxy. The dimensions of the tubes were outer diameter 90 mm, thickness 3.75 mm and 100 mm long. He reported that the specific energy absorption of epoxy tubes (80 kJ/kg) is higher than vinylester tubes (78 kJ/kg) and the SEA of vinylester tubes larger than for polyester tubes (58kJ/kg). Another combination tried out by him was 50:50 of vinylester and polyester. However the SEA results of this fall halfway between the

optimal results obtained with the two resins separately. The energy absorption of the matrix depends on the

(i) interlaminar fracture toughness (G_{IC})
(ii) matrix failure strain

Ramakrishna [42] compared the energy absorption characteristics of thermoset and thermoplastic matrices. The energy absorption of carbon/epoxy (thermoset matrix) was compared with carbon/polyetheretherketone (PEEK, thermoplastic matrix). The superior specific energy absorption (180 kJ/Kg) of carbon-PEEK is attributed to the higher interlaminar fracture toughness (1.6 ~ 2.4 kJ/m^2), compared to carbon/epoxy (53 kJ/kg). The same trend was observed with the other thermosetting matrices. The order of specific energy absorption of different matrices is as follows [42].

Polyetheretherketone (PEEK)> Polyetherimide (PEI) > Ploymide (PI) > polyarylsulfone (PAS)

Farley [58] studied the effect of strain rate in case of circular carbon/epoxy tubes. He reports that the energy absorption capability of those composite tubes is dependent on the strain at failure of both fibre and matrix. Further he suggested that to obtain the maximum energy absorption from a particular fibre, the strain rate of the matrix at failure should be more than the fibre material. In case of low tensile strain carbon fibres, changing the matrix from low to high failure strain resulted in an increase in specific energy absorption [59]. A linear correlation of in-plane properties to specific energy absorption was conducted in ref. [57]. The specific energy absorption results were correlated to each in-plane property in both directions. Compressive and tensile modulus showed a weaker correlation with specific energy absorption whereas the strongest correlation was observed for ultimate compressive strength [57]. Farley [60] conducted experiments on hybrid composites tubes to get the best energy absorption. However, he reported that the energy absorption characteristics of those hybrid specimens were not significantly better than single fibre type with the same ply orientation. Hamada [27] reported carbon PEEK gave a very good specific energy absorption value of 180 kJ/kg. This is due to the high resistance of PEEK for the crack initiation and propagation. However the cost of the thermoplastic matrix is higher than the thermoset.

7. 8. 2. Fibre and matrix interface

It has been well accepted that the interface between the fibres and matrix is important and it affects the mechanical behavior of composite materials. The fibre and matrix interface strength can be altered by the type of surface treatment. Ramakrishna [42] studied two varieties of composite tubes. One type contained

glass cloth treated with aminosilane (γ -aminopropyltriethoxysilane) coupling agent and the other was treated with acrysilane (γ - methacryloxypropyltrimethoxysilane). He reported that aminosilane treated tubes absorbed the specific energy of 66.6 kJ/kg compared to 53 kJ/kg for acrysilane treated tubes. Moreover the aminosilane treated tubes exhibited lamina bending mode and acrysilane treated tubes exhibited transverse shearing mode. Further a microscopic study of the crush zones showed that, the fracture occurred at the matrix region in case of aminosilane treated tubes; whereas in case of acrysilane tubes the fracture occurred at the fibre matrix interface. For aminosilane treated tubes, the cracks developed in the matrix zone is due to the better bonding between fibre and matrix. The smoother fracture surfaces caused the lower frictional force between the crushing plate and the tube and it facilitated easy sliding of frond against the crushing plate which resulted in the lamina bending mode. In case of acrysilane treated tubes, rough fracture surfaces resulted due to poor bonding between the fibre and matrix. This caused the higher frictional force.

7. 8. 3. Volume fraction of fibre and matrix

Berry and Hull [56] investigated the effect of increasing fibre content on the specific energy absorption. It was found that increasing the volume fraction from 13 to 18% had given an increase in specific energy from 39 kJ/kg to 54 kJ/kg. Further, this effect was studied by Tao et al. [40]. The fibre percentage varied from 10 to 60% in glass/epoxy composite material and further reported that the specific energy increased with increasing percentage of fibre content. However, this reached the saturation condition when it was 50% and above. Assuming the fibre density always larger than the matrix density, the density of the tube also increases when the fibre percentage increases. If the specific energy is to increase, then the crush load has to be increased by the same amount that exceeds the increase in material density. Hence, it should be noted that the increase in the fibre content may not always improve the specific energy.

7. 8. 4. Fibre Architecture

Fibre stacking sequence

In energy absorbing structures, the stacking sequence of the fibres plays an important role for the energy absorption. A lot of research has been done to study the effect of stacking sequence [21]. The change in the stacking sequence would give a variation in the energy absorption of 5 to 25%. The position of the 0° lay-up could change the magnitude of energy absorption. When it is exterior of the stacking sequence, it will give less energy absorption, than when it is inside. This is due to

the fact that, when the stacking is inside, the 0 layers crush in transverse shearing mode, whereas in case of outside stacking the fibres would exhibit lamina bending mode. Farley [22, 38] studied the effect of ply orientation on energy absorption of carbon epoxy circular tubes. From his study he concluded that considerable variation in the energy absorption was observed with respect to the ply orientation. For the composite tubes with $0^{\circ} < \theta < 45^{\circ}$, the energy absorption decreased with increasing θ. Similarly, Thornton and Edwards [38, 41] reported that composite tubes with $(45/45)_n$ lay-up give consistent lower values of specific energy absorption than tubes with $(0/90)_n$ lay-ups.

Fibre orientation

Ramakrishna [42] investigated the effect of fibre orientation on energy absorption of carbon/PEEK and carbon/epoxy composite tubes. He noted that, for $\theta = 0^{\circ}$, carbon/PEEK tubes failed progressively, whereas carbon/epoxy failed catastrophically. This clearly shows that the matrix material plays a vital role in case of energy absorption. The difference is attributed to the lower fracture toughness of the epoxy matrix. The variation of specific energy of carbon/PEEK tubes with respect to the fibre orientation is shown in Figure 19 [42].

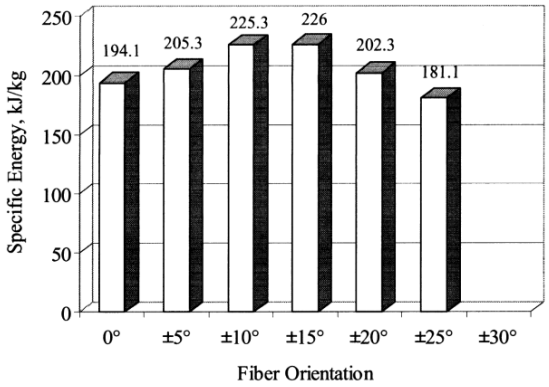

Figure 7-13: Effect of fibre orientation on the energy absorption [42].

Fibre architecture

Many investigations have been done to study the effect of architecture form on the energy absorption of composite tubes. Hull [61] investigated the effect of hoop (H) and axial (A) fibres (which are parallel to warp and weft yarns) in a woven fabric (Figure 7-14(a)). The ratio of hoop to axial (H:A) fibres ratio was varied from 8.5:1 to 1:8.5. The tubes with H:A = 8.5:1 and 7:1 showed the transverse shearing failure mode, whereas tubes with 1:1 ratio displayed the lamina bending mode crushing with interlaminar fracture between the woven cloth layers. He reported that when the H: A ratio changed from 8.5:1 to 1:4, the specific energy was increasing. However, a further increase of axial fibre (H:A = 1:8.5) content leads to reduction in specific

energy of the tube. Composites with large amount of hoop fibres fail by transverse shearing mode whereas tubes with less hoop constraint fail by lamina bending mode.

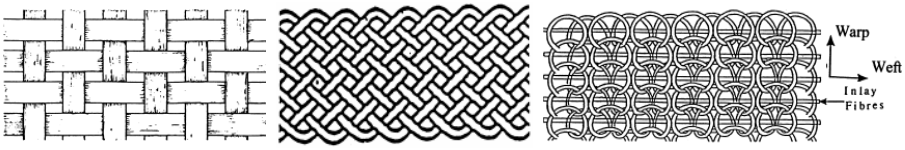

(a) Woven fabric **(b)** Braided fabric **(c)** Knitted fabric

Figure 7-14: Different forms of fabric.

A typical example of braided fabric is shown in Figure 7-14(b). This is made from intertwining of fibre yarns. Hamada [28] investigated the energy absorption behavior of braided glass/epoxy composite tubes with fibre volume fraction of 60%. He reported that the specific energy absorption of these tubes was 70 kJ/kg for the static test. Han et al. [62] studied the effect of adding braided (carbon and glass) composite layers on glass pultruded tubes. From the quasi-static and dynamic numerical simulations, it was stated that the response of the tube with braiding is sensitive to tube length, braid thickness and loading conditions. It was concluded that the thickness of the braiding affects the energy absorption. Tao Zeng [63] numerically studied the effect of braid angle (the absolute angle between the yarn direction and the braid direction) on the energy absorption. He reported that the total energy is decreased with increasing braid angle. The total energy absorption was minimum when the braid angle is 45°.

Similarly Ramakrishna and Hull [46] studied the energy absorption characteristics of knitted carbon/epoxy tubes (made by interlooping of fibre yarns as shown in Figure 7-14(c)). The fibre content of the tubes increased with increasing tow size of the inlay fibres. Composite tubes are categorized based on the orientation of knitted fabric with respect to the axis of the tube. Two cases, warp (inlay fibres are oriented in hoop direction) and weft (inlay fibres are oriented in axial direction), were tried out. The warp tubes were crushed by transverse shearing mode whereas the weft ones exhibited the lamina bending mode. The hoop stiffness of the tube increases with the increasing percentage of inlay fibres. In addition to that, the transverse shear strength of the composite material decreases. Therefore, the tendency of lamina bending mode reduces considerably. The specific energy of the tube increases with increasing percentage of fibre content. Maximum specific energy of 85 kJ/kg was observed with fibre content 22.5% (volume fraction). This value can be comparable with the highest specific energy of 120 kJ/kg for woven carbon/epoxy tubes.

7. 9. Tube geometry

7. 9. 1. Cross-sectional shape

Various cross-sectional shapes have been investigated by many researchers to find out the optimum cross-sectional shape which yields maximum energy absorption. Some of the cross-sectional shapes are shown in Figure 7-15(a-h).

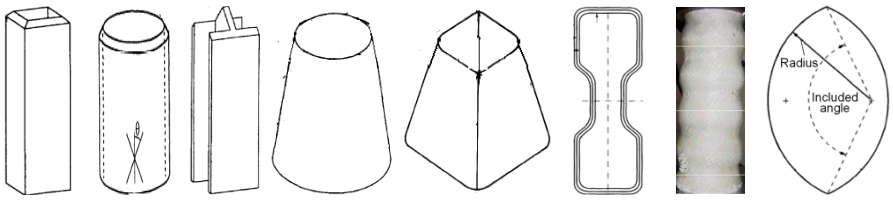

Figure 7-15: Different cross-sections and shape of the composite tubes **(a)** Square cross-section **(b)** Circular cross-section **(c)** "I" cross-section **(d)** Conical circular **(e)** Conical square **(f)** Hourglass cross-section **(g)** Corrugated shape.**(h)** Elliptical cross-section.

Thronton [52] and Thronton et al. [64] demonstrated experimentally that composite tubes with circular cross-section display higher energy absorption capability than tubes with rectangular or square cross-sections (Figure Figure 7-15(a-b)). Mamalis [38, 48] reported that the square and rectangular cross-sectioned tubes have 0.8 and 0.5 times the specific energy absorption of circular specimens. A very limited research has been carried out in "I" section profiles [45]. The comparison was made with square tubes showing that the energy absorption capability of the "I" section profile is 15% smaller than the square cross-sectional tube (Figure 7-15(c)). Mamalis [34, 38] reported that in case of conical tubes which were subjected to axial loading, the specific energy absorption decreases as the semi-apical angle of the frusta increases (Figure 7-15(d-e)). Furthermore he mentioned that the transition point between stable and unstable collapse with respect to the semi-apical angle is lying in the range of 15 to 20 degrees. Mamalis [49] investigated the energy absorption characteristics of an automotive rail frame with hourglass cross-section made of glass/vinylester composite (Figure 7-15(f)). He reported that the hourglass sections gave higher specific energy than the square tubes with the same material and loading conditions. Elagalai et al. [20] investigated the crushing response of composite corrugated tubes (made of carbon and glass fibres) in quasi-static axial loading (Figure 7-15(g)). It was reported that in case of carbon tubes, a positive trend for the specific energy absorption was observed with increasing helix angle of the tube. However in case of glass fibre tubes the maximum specific energy absorption was obtained for a helix angle $\beta = 20^{\circ}$. Farley and Jones [24, 38] investigated the effect of reducing the included angle in elliptical carbon/epoxy

composite tubes (Figure 7-15(h)). It was found that the specific energy absorption of the elliptical tube increases with decreasing the included angle. The specific energy absorption improved about 10 to 30% by reducing the included angle from 180° (circular) to 90°.

7. 9. 2. Triggering geometry

Why it is necessary?

When the load is applied on the tubes, some kind of failure initiator (preferably sharp edges) is needed to initiate the local failure in the material at relatively low load to create small interlaminar and intralaminar cracks. Generally this is achieved by chamfering one end of the tube. When the compressive load is applied to the chamfered end of the tube, the stresses at the tip of the chamfer are very high compared with the stresses in the rest of the tube. This process causes micro-cracks at those locations (refer Figure 7-16). Due to the presence of load, these cracks split the integrity of the laminates, which leads to the circumferential delamination at the middle of the tube thickness (refer Figure 7-16). This further results into transverse shearing, lamina bending, brittle fracturing and local buckling failure modes.

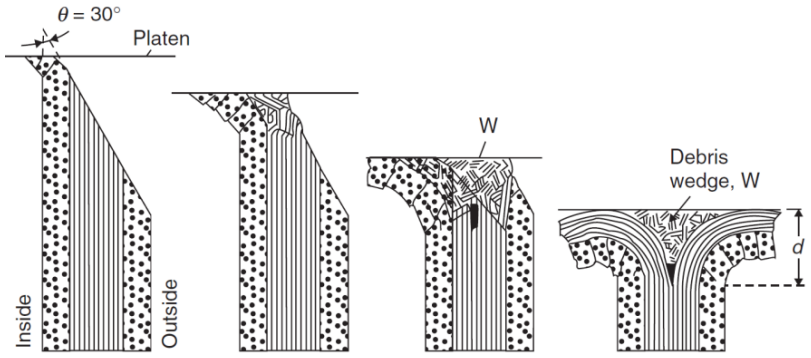

Figure 7-16: Initiation of progressive crushing due to triggering profile [61].

The effect of triggering on the load-deformation curve is also depicted in Figure 7-17. Crushing of composite tubes without triggering can provide a very high peak crush load (load at which the damage initiates) and in most of the situations the composite tube will end up in catastrophic failure mode.

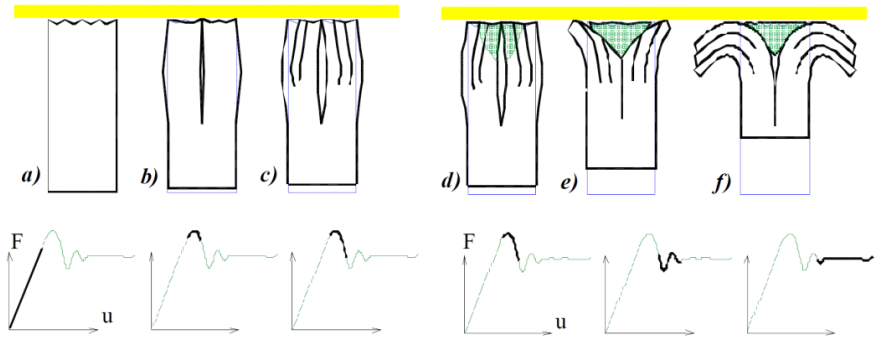

Figure 7-17: Effect of triggering on the load-deformation curve [65].

Types of triggering

Different types of triggering profiles which induce the initial failure are shown in Figure 7-18. Jimenez [45] studied the effect of triggering on the specific energy absorption of square and "I" sectional tubes (refer Figure 7-15(a) and (c)) using two triggering profiles (external bevel and tulip). He reported that, the specific energy absorption of the "I" sectional profile is independent of the angle of the triggering profile. However, in case of square section the triggering type and the angle showed an important influence on the specific energy absorption. For bevel triggering the specific energy absorption increased with increasing angle from 30°. The maximum value of the energy absorption was noticed for 60°.

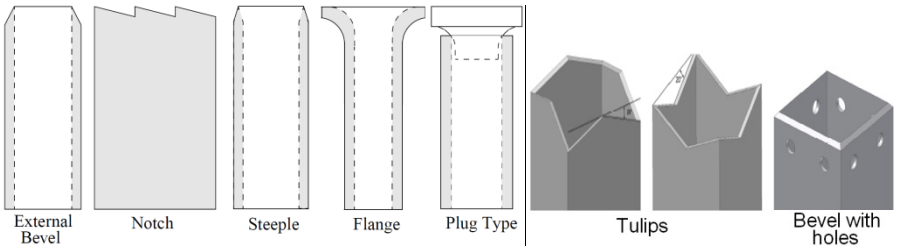

Figure 7-18: Different types of triggering profiles.

7. 9. 3. Tube wall thickness

Tao Zeng [63] investigated the effect of tube wall thickness for 3D braided tubes. He investigated this with fixed inner radius of the tube 28.5 mm and with varying thickness from 1 mm to 3.5 mm. He reported that the specific energy absorption steadily increased from 1 mm to 3 mm wall thickness; after that it remains the same.

7. 9. 4. Tube diameter

Fairfull and Hull [66] investigated the effects of specimen dimensions on the specific energy absorption of glass/epoxy tubes. Five sets of tubes with D (outer

diameter of the tube) ranging from 16 to 50 mm were investigated. The specific energy absorption capability increased with increasing D. For a given value of D, the specific energy initially increased with increasing t/D ratio up to 0.20, above which it decreased. The reasons for this variation of energy were not clearly identified and it was concluded that there can be no universal relationship to predict energy absorption capability. Further research by Tao Zeng [63] on the braided tubes showed that the specific energy absorption of the tube increased with increasing diameter from 13.5 to 29 mm with wall thickness of 1.5 mm. He reported that the value of SEA for inner radius of 29 mm is 45% higher than the tube with inner radius of 13.5 mm. When the ratio of inner radius to the thickness increases, buckling becomes the main failure mode of composite tubes and this causes less specific energy absorption.

7. 9. 5. Thickness to the diameter ratio (t/D ratio)

Hamada and Ramakrishna [29] have worked on the progressive crushing of circular cross-sectional tubes and proved that composite tubes with a t/D ratio less than 0.015 will fail catastrophically. However the tubes with a t/D ratio in the range 0.015 to 0.25 will crush progressively. Further it was reported that the specific energy absorption of the tubes increased with decreasing diameter. For constant diameter, the specific energy absorption increased with increasing thickness up to some extent. The values of specific energy absorption of the tubes increase with thickness up to some extent, but after that the SEA decreased. The composite tubes with 2-3 mm thickness exhibited the highest energy absorption. Investigations on the carbon/epoxy and Kevlar/epoxy tubes ($[\pm 45^{\circ}]_N$ fibre architecture) with a thickness from 12.7 mm to 101 mm showed a non-linear variation of SEA with t/D ratio [66].

7. 10. Experimental prediction of energy absorption

To investigate the energy absorption of composite tubes, most of the researchers have adopted *quasi-static testing.* Since the speed of the entire process is very slow it helps to capture the deformation behaviour of the composite tubes. Although a considerable amount of static tests has been conducted to study the energy absorption, but most of the real time applications are dynamic in nature (*axial and oblique impact*). Very few researchers [21, 43, 54, 67] have investigated the effect of strain rate on the energy absorption of tubes. The mechanism which controls the failure of the composite tube is a function of the strain rate or speed of crushing. In general, the crushing speed affects the energy absorbing capability of the fibre and the matrix. Hamada et al. [28] studied the energy absorption difference between the

static and dynamic modes. It was reported that the energy absorption of the same composite tube was less in case of dynamic loading compared to static.

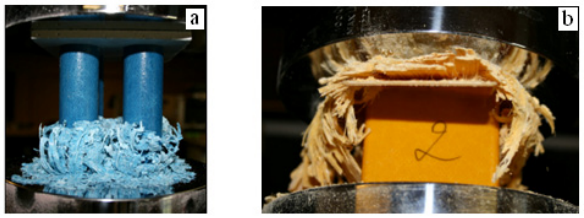

Figure 7-19: Quasi-static testing of composite tubes **(a)** Circular cross-sectional tube **(b)** Square cross-sectional tube.

Farley [21, 54] investigated the effect of strain rate on the energy absorption using carbon/epoxy and aramid/epoxy tubes. He reported that the matrix stiffness and failure strain can be a function of strain rate. Hence the major energy absorption associated with the interlaminar crack growth may be a function of crushing speed. However generally, the mechanical properties of brittle fibres are insensitive to the strain rate. Mamalis [34] reported that for glass/polyester square and circular tubes the energy absorption levels during dynamic tests are lower than for the static tests. Thornton [41, 52] investigated the effect of testing temperature on the performance of composite tubes. He reported that the specific energy absorption of graphite and glass composite tubes generally decreases with increasing temperature above 0° C.

7. 11. Analytical prediction of energy absorption

Conducting a destructive test to analyze the energy absorption characteristics of a composite material is an expensive affair. Hence alternative methods to find out the energy absorption capability of the composite tube are necessary. The analytical and numerical simulation techniques are more popular among the scientists for prediction of energy absorption in case of composites. These methods are relatively cheaper.

7. 11. 1. Farley and Jones model

Farley and Jones [68] described a simplified procedure based on the buckling load equation. The sustained crushing load equation is given as,

$$P_{sus} = \sum_{i=1}^{n} \frac{N_i (EI)_i \varepsilon_{ci} + \dfrac{K_{fi}.\varepsilon_{fi}}{M_i}}{L_i (G/t)_i} \tag{7.2}$$

where *G/t* is the internal tube diameter to wall thickness ratio; *L is* the lamina bundle length; *n is* the number of lamina bundles; *EI is* the bending stiffness; ε_c is the failure strain; K_f is the foundation stiffness and ε_f is the foundation failure strain. The value of N depends on the type of failure mode. It is used to define the general crushing mode. For lamina bending and crushing mode, the value of N is between 0 and 1; tubes that fail in a local buckling mode would have an N value of approximately 1.

7. 11. 2. Mamalis and Melonakos model

Mamalis and Melonakos [35] provided a method to calculate the total energy absorbed by a composite tube. The method is based on the stable collapse mechanism of a thin walled circular structure under axial static and dynamic loading (refer Figure 7-11(b)). The total energy absorbed by the tube for a crush distance "s" is given by (Equation (7.3)),

$$\begin{aligned} W_T = {} & [1/(1-\mu_1+\mu_1 \cdot s_2/s][\pi(d-t)t \cdot k \cdot \sigma_\theta \{(s-s_2)\times \\ & [\mu_2/\cos(\alpha/2)-\mu_1[\tan(\alpha/2)+.\mu_2]]+[(\alpha/2)/\cos(\alpha/2)]\times \\ & [0.25 \cdot t/\cos(\alpha/2)+s-s_2]\}+R_{ad} \cdot \pi(d-t)(s-s_1+L_c) \\ & +n(t/2) \cdot G_s] \end{aligned} \tag{7.3}$$

where μ_1 is the coefficient of friction (static or dynamic) between the plate and the frond; μ_2 is the coefficient of friction (static or dynamic) between the wedge and the frond; *t* is the tube thickness; *k* is a constant; σ_0 is the tensile fracture stress; α_1 is the angle formed by the height and external side of the wedge; α_2 is the angle formed by the height and internal side of the wedge; s_2 is the related shell shortening corresponding to the completion of the wedge formation; θ is the semi-apical angle of the frustum; L_c is the crack height; d_c is the frustum diameter at the crack tip; R_{ad} is the fracture energy required to fracture a unit area of the adhesive at the interface between two adjacent layers and it is calculated using fracture theory; *n* is the number of splits of petals or fronds and G_s is the fracture toughness.

7. 11. 3. Solaimurugan and Velmurugan model

Solaimurugan and Velmurugan reported [69, 70] that mode I delamination in a thin wall of axially collapsed shell is one of the major energy modes; contribution of G_{IC}

to the specific energy absorption of tubes is significant during crushing. Increasing G_{IC} up to a certain value leads to a controlled progressive crushing failure modes. The idealized crush zone model of a circular cross-sectional tube wall is shown in Figure 7-20.

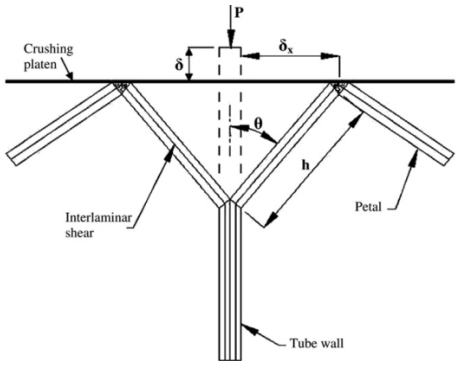

Figure 7-20: Idealized crush zone model of cylindrical tube wall [69, 70].

During the crushing process, the energy is absorbed or dissipated by the following modes [69, 70]: (i) energy required for circumferential delamination (W_d) (ii) energy required for axial cracks or petal formation (W_s) (iii) energy required for bending of petals (W_b) (iv) energy dissipated due to the friction between the crushing plate and petals (W_f). The final form of the energy balance equation is (Equation (7.4)),

$$P(\delta - 2\mu\delta_x) = \left(G_{IC} 2\pi r h\right) + \left[\frac{\pi h^3 \sigma^2 (\sin\theta)}{\sigma_u r}\left(\frac{2}{\sqrt{n}}\right)^2 (2tn)\right] + \int_0^{\pi/2} \frac{\sigma_u b t^2 d\theta}{8} \quad (7.4)$$

where P is the external load; δ is the crushing displacement; μ is the coefficient of friction between the petal and the crushing plate; $\delta_x = h\sin\theta$; G_{IC} is the critical strain energy release rate per unit interlaminar crack area (can be determined from experimental double cantilever beam test (DCB) as per ASTM D5528-01); h = crack length for the single stroke; r = mean radius of the tube; σ = circumferential stress; σ_u is the ultimate fracture strength in uni-axial tension; n is the number of petals; θ is the bending angle of petals and b is the total width of petals. In order validate the above models all the given variables in the respective equations should be known. Capturing these variables without conducting experiments is impossible. Hence, the validation of these models oftenly need more input data.

7. 12. Numerical prediction of energy absorption

The numerical simulation using the finite element technique has been adopted in a few cases to study the energy absorption. The static and dynamic axial collapse of CFRP tubes was studied numerically in [71]. The calculation of the dynamic response of the composite laminates under low-velocity impact was studied in ref. [72]. The numerical energy assessment of hybrid tubes made of pultruded tube overwrapped by braiding was studied by Han and his co-workers [62]. The peak load and the corresponding energy absorption characteristics of a square sandwich composite vehicle hollow body shell were discussed in [36]. The progressive crushing of the carbon fibre reinforced structural components of a Formula one racing car was studied in detail in [18]. Most of the above numerical modelling of the composite tubes was done with a single layer of shell elements. However, the numerical modelling of the delamination which causes the split of outer and inner plies of the composite tubes cannot be modelled with a single layer of shell elements. The consideration of the delamination approach is important to predict the correct energy absorption because it causes the separation of plies and loss in bending stiffness of each sub-laminate. Furthermore, many experimental studies [30, 41, 60, 73, 74] have proved that the occurrence of the peak load corresponds to the start of the circumferential delamination. However, often in the finite element models the modelling of delamination was not included. As an example, the finite element deformation patterns of hybrid pultruded composite tube and CFRP tubes (carbon fibre reinforced composite tubes) from literature are shown in Figure 7-21(a) and (b) respectively. These deformation patterns are completely different than from the experimental results.

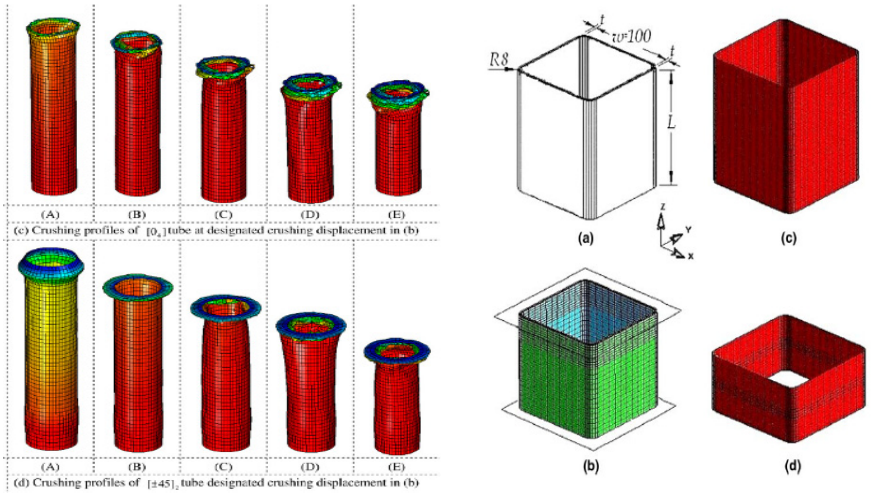

(a) **(b)**

Figure 7-21: Finite element deformation patterns with shell elements **(a)** hybrid pultruded composite tubes [62] **(b)** CFRP square tubes [71].

The reduction in compressive strength of composite laminates was studied numerically considering structural instability and delamination growth in [75, 76]. The influence of delamination failure on the concave cylindrical composite test specimen during an impact event using continuum damage model was studied in [77]. However, the approach of delamination was not considered for the circular and square composite tubes to predict the energy absorption in the past. Zarei et al. [78] proposed two layers of shell elements with surface-to-surface tie break contact to capture the de-cohesion between the bundles of plies. However, the actual deformation of a typical brittle composite tube exhibits multiple delaminations [76, 79-81]. For composite tube crushing a very few study has been considered the delamination modelling. However, these models lack in several aspects such as prediction of the correct peak crush force, deformation patterns and its length etc. As an example, deformation patterns and the corresponding load-deformation history from one of the models from literature are shown in Figure 7-22(a) and (b) respectively. In this model to initiate the delamination a triangular rigid wedge was used. Furthermore, the load-deformation curve is not complete. This study showed a validation of load-deformation curve for maximum of 2.5 mm deformation length (refer Figure 7-22(b)). However, in real situations the deformation length is tens of centimetres.

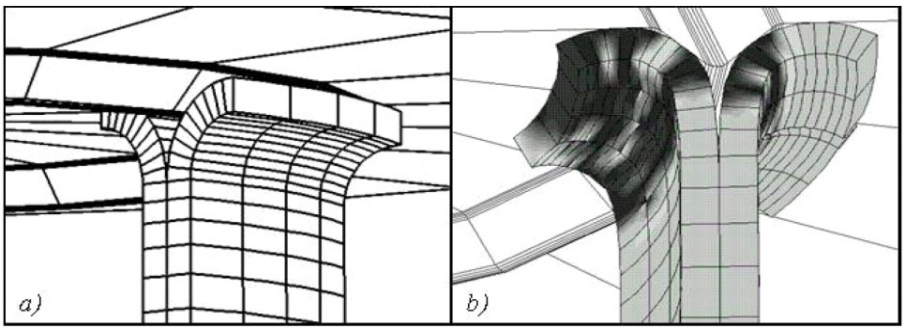

(a)

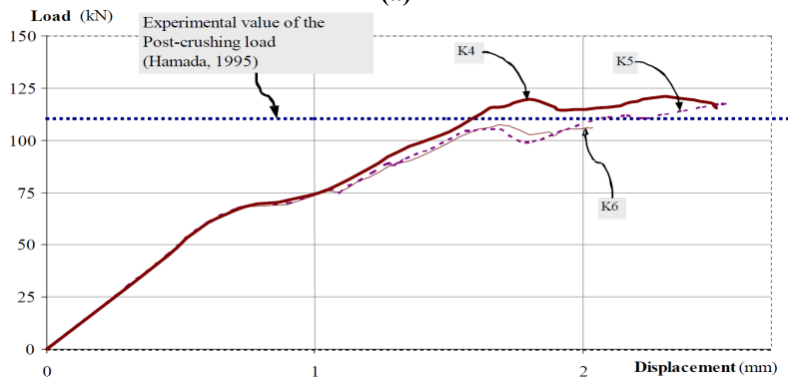

(b)

Figure 7-22: Finite element simulation with solid elements **(a)** deformation pattern **(b)** corresponding load deformation curve (reproduced from ref. [65]).

As mentioned in the previous section, an initiator (triggering mechanism) is required to induce the initial stable progressive crushing at low peak load. Normally, the 45° edge chamfering can be directly modelled numerically by the solid elements. However, the typical failure mechanisms of a brittle composite tube such as central delamination, bending of petals and axial cracks are hard to capture with the solid elements. Due to the above fact researchers have employed the shell elements for their numerical study of composite tubes. Unlike the solid elements, the 45° edge chamfering is tedious to model with the shell elements.

Strength based failure criteria are commonly used to predict the failures in a composite material. Few ply failure models have been proposed that can predict the failures for any given state of loading. Generally, for the impact and the crash analysis of a composite material, the approach of the continuum damage mechanics is preferred in which the failure is first identified and consequently, the degradation of the elastic properties are computed till final fracture. A good example of the above approach can be found in [82], in which a user material model was implemented in the explicit finite element code LS-DYNA to capture the tensile and compressive response of a braided composite material. However, there have been several studies proving that the well established and existing models available in commercial finite element codes can be adopted to predict the energy absorption behaviour of a composite tube. Han et al. [62] and Zarei et al. [78] used Material model 54 of LS-DYNA to predict the failure patterns and the energy absorption of the circular and square cross-sectional tubes respectively. Material model 54 [83] has the option of using either the Tsai-Wu failure or the Chang-Chang failure criteria for the individual lamina. The Chang-Chang failure criterion is the modified theory of the Hashin's failure criterion which accounts for the non-linear stress-strain behaviour. Although many failure criteria are used, the failure criterion proposed by Hashin [84] is extensively employed in many applications. The list of failure criteria [83, 85-87] which are available in the commercial codes (ABAQUS and LS-Dyna) are given in Table 7-2.

Table 7-2: Available material models for composites in ABAQUS and LS-Dyna [83, 85-87].

Name of the software	Material Model	Material Name	Solid element	Shell element	Strain rate	Plasticity	Failure	Type of composite
ABAQUS	Linear elastic orthotropic model		Y	Y				C,D
	Linear elastic orthotropic model with failure (Max, strain, max stress, Tsai-Hill, Tsai-Wu and Azzi-Tsai-Hill)			Y			Y	A,B,C,D
	Hashin model			Y			Y	A,B,C,D
LS-Dyna	Orthotropic elastic model	2	Y	Y			Y	C,D
	Elastic plastic with kinematic hardening	3	Y	Y	Y	Y	Y	B
	Chang-Chang brittle composite failure model	22	Y	Y			Y	C,D
	Temperature dependent orthotropic elastic model	23	Y	Y				C,D
	Orthotropic non linear elastic model	40		Y			Y	A,B,C,D
	Enhanced composite damage with Chang-Chang failure	54		Y			Y	C,D
	Enhanced composite damage with Tsai-Wu failure	55		Y			Y	C,D
	Laminated composite fabric	58		Y				C,D
	Composite damage (plasticity based)	59	Y	Y		Y	Y	B
	Brittle damage	96	Y		Y		Y	C,D
	Layered linear plasticity	114		Y	Y	Y	Y	B
	Gurson	120		Y				B
	Composite MSC	161	Y					A,C

A= Thermoplastic continuous fibres; B= Thermoplastic discontinuous fibres; C= Thermoset continuos fibres; D= Thermoset discontinuons fibres; Y= Available.

7. 13. Conclusions

In this chapter different failure modes (macroscopic and microscopic) of the composite tubes from literature are presented. As noticed the (specific) energy absorption of the composite tubes depends on many parameters. So, the energy absorption enhancing factors/parameters which are applicable to a particular architecture of the composite tube may not be applicable to other types. Since most of the investigations have been carried out on different architectures of the composite tubes, a thorough study on the unidirectional composite tubes which are intended for the chosen blast loading application (axial loading) has to be carried out. Most studies have used circular and square cross-sectional composite tubes. However, there are several shapes of composite tubes whose energy absorption capabilities have not been studied yet. Furthermore, many researchers have employed the edge chamfering of the structures as triggering mechanism. However, the effect of other triggering mechanisms on the energy absorption of uniform and non-uniform profiles of the composite tubes is yet to be captured.

Although different damage models for composite materials are available and implemented in the commercial codes, the validation of most published numerical investigations lacks in many aspects which are as follows:

(i) no simultaneous validation on time history of dynamic force, specific energy absorption, final deformation length and observed deformation patterns.
(ii) correct modelling of triggering pattern is avoided by introducing geometric imperfections, while these have (within normal production tolerances) a negligible influence on the crushing characteristics.
(iii) some models only show results for the very first millimeters of deformation length, while real deformation lengths are tens of centimeters (numerical convergence and stability).
(iv) most models fail for unidirectionally reinforced composite tubes, where deformation patterns are quite different from those for braided/woven tubes.
(v) little or no information about effect of element type, meshing quality and mesh size on the simulated crushing characteristics.

Capturing the above parameters for the design of sacrificial cladding structures is very important. The accuracy of these numerical predictions depends upon the correct modelling of the structural geometries (triggering profiles), integrating the right damage mechanisms and the accurate modelling of the physics of loading.

Hence, a detailed study on the above parameters and the corresponding working numerical models is absolutely necessary before investigating the unidirectional composite tubes for blast loading conditions.

In order to study the above mentioned aspects of the composite tubes, detailed experimental and numerical investigations have been carried out in two steps. As a first step, the experimental testing and numerical simulations have been carried out using commercially available pultruded composite tubes. The crushing peak and mean load characteristics of the composite tubes with different triggering profiles and their progressive failure modes are presented. In the second stage different uniform and non-uniform composite profiles have been investigated to identify a better cross-section and profile for maximum energy absorption. It was not feasible to obtain a small quantity of composite tubes with different geometrical shapes from any commercial manufacturer. Hence, due to the versatile advantages such as low tooling cost, start-up and low capital cost the hand lay-up technique was chosen to manufacture all composite tubes. The details of the above analyses are presented in Part III of this dissertation.

Bibliography

[1]. Karagiozova, D. and Jones, N., *Dynamic elastic-plastic buckling phenomena in a rod due to axial impact.* International Journal of Impact Engineering, 1996. **18**(7-8): p. 919-947.

[2]. Tarigopula, V., Langseth, M., Hopperstad, O. S. and Clausen, A. H., *An experimental and numerical study of energy absorption in thin-walled high strength steel sections.* WIT Transactions on Engineering Sciences, 2005. **49**(Impact loading of Lightweight structures): p. 495-507.

[3]. Peroni, L., Avalle, M., Petrella, V. and Monacelli, G., *Strain-rate effects on the energy absorption capability of crash boxes with different geometry.* Structures under SHOCK AND IMPACT, 2002. **11**: p. 259-268.

[4]. Jones, N., *Energy absorption effectiveness of thin-walled strucutres under static and dynamic axial crushing loads.* WIT Transactions on Engineering Sciences, 2005. **49**(Impact Loading of Light Weight structures): p. 273-287.

[5]. Hsu, S. S. and Jones, N., *Quasi-static and dynamic axial crushing of circular and square stainless steel tubes.* Structures under SHOCK AND IMPACT, 2000. **VII**: p. 169-178.

[6]. Langseth, M., Hopperstad, O. S. and Berstad, T., *Crashworthiness of aluminium extrusions: validation of numerical simulation, effect of mass ratio and impact velocity.* International Journal of Impact Engineering, 1999. **22**(9-10): p. 829-854.

[7]. Kotzialis, C., Derdas, C. and Kostopoulos, V., *Blast behaviour of plates with sacrificial cladding.* 5th GRACM International congress on computational mechanics, June 29 - July 1, Limassol, Cyprus., 2005.

[8]. Bogosian, D. D. and Crawford, J. E., *Energy absorbing retrofit systems for mitigating blast effects on occupants of conventional buildings.* 29th Explosive safety seminar, 2000.

[9]. Nurick, G. N., *Numerical and experimental results of blast loaded strucutres.* VIII International conference on Computational plasticity, 2005. **VIII**.

[10]. Lemanski, S. L., Nurick, G. N., Langdon, G. S., Simmons, M. S., Cantwell, W. J. and Schleyer, G. K., *Understanding the behaviour of fibre metal laminates subjected to localised blast loading.* Composite Structures, 2006. **76**(1-2): p. 82-87.

[11]. Weerth, D. E., *Blast resistant airline baggage container design.* 15th International Conference on Composite Materials (ICCM-15). Durban, 27 June - 1 July 2005., 2005.

[12]. Theobald, M. D. and Nurick, G. N., *Numerical investigation of the response of sandwich-type panels using thin-walled tubes subject to blast loads.* International Journal of Impact Engineering, 2007. **34**(1): p. 134-156.

[13]. Beardmore, P. and Johnson, C. F., *The potential for composites in structural automotive applications.* Composites Science and Technology, 1986. **26**(4): p. 251-281.

[14]. James, A., *Performance comparison of plastic composites with metals for vertical body panel applications.* SAE Technical paper, 1999. **(1999-01-08480)**.

[15]. Aljawi, A. A. N., *Numerical Simulation of axial crushing of circular tubes.* Engineering science, 2002. **14**(2): p. 101-115.

[16]. Abosbaia, A. S., Mahdi, E., Hamouda, A. M. S., Sahari, B. B. and Mokhtar, A. S., *Energy absorption capability of laterally loaded segmented composite tubes.* Composite Structures, 2005. **70**(3): p. 356-373.

[17]. Belingardi, G., Gugliotta, A. and Vadori, R., *Numerical simulation of fragmentation of composite material plates due to impact.* International Journal of Impact Engineering, 1998. **21**(5): p. 335-347.

[18]. Bisagni, C., Di Pietro, G., Fraschini, L. and Terletti, D., *Progressive crushing of fiber-reinforced composite structural components of a Formula One racing car.* Composite Structures, 2005. **68**(4): p. 491-503.

[19]. Bolukbasi, A. O. and Laananen, D. H., *Energy absorption in composite stiffeners.* Composites, 1995. **26**(4): p. 291-301.

[20]. Elgalai, A. M., Mahdi, E., Hamouda, A. M. S. and Sahari, B. S., *Crushing response of composite corrugated tubes to quasi-static axial loading.* Composite Structures, 2004. **66**(1-4): p. 665-671.

[21]. Farley, G. L., *Relationship between Mechanical - Property and Energy - Absoprtion Trends for Composite Tubes.* NASA TP-3284, ARL-TR-29, 1992, 1992.

[22]. Farely, G. L., *Energy absorption of composite materials.* Journal of Composite Materials, 1983. **17**: p. 167.

[23]. Farley, G. L., *Effect of fibre and maximum strain rate on the energy absorption of composite materials.* Journal of Composite Materials, 1986. **20**: p. 322.

[24]. Farley, G. L. and Jones, R. M., *Crushing characteristics of composite tubes with "near elliptical" cross sections.* Journal of Composite Materials, 1992. **26**: p. 1252.

[25]. Fawaz, Z., Zheng, W. and Behdinan, K., *Numerical simulation of normal and oblique ballistic impact on ceramic composite armours.* Composite Structures, 2004. **63**(3-4): p. 387-395.

[26]. Hamada, H. and Ramakrishna, S., *Effect of cooling rate on the energy absorption capability of carbon fibre /PEEK composite tubes.* Polymer composites, 1995. **3**: p. 1-6.

[27]. Hamada, H., Coppola, J. C., Hull, D., Maekawa, Z. and Sato, H., *Comparison of energy absorption of carbon/epoxy and carbon/PEEK composite tubes.* Composites, 1992. **23**(4): p. 245-252.

[28]. Hamada, H., Kameo, K., Sakaguchi, M., Saito, H. and Iwamoto, M., *Energy-absorption properties of braided composite rods.* Composites Science and Technology, 2000. **60**(5): p. 723-729.

[29]. Hamada, H. and Ramakrishna, S., *Scaling effects in the energy absorption of carbon-fiber/PEEK composite tubes.* Composites Science and Technology, 1995. **55**(3): p. 211-221.

[30]. Hamada, H., Ramakrishna, S. and Satoh, H., *Crushing mechanism of carbon fibre/PEEK composite tubes.* Composites, 1995. **26**(11): p. 749-755.

[31]. Her, S.-C. and Liang, Y.-C., *The finite element analysis of composite laminates and shell structures subjected to low velocity impact.* Composite Structures, 2004. **66**(1-4): p. 277-285.

[32]. Iannucci, L. and Willows, M. L., *An energy based damage mechanics approach to modelling impact onto woven composite materials--Part I: Numerical models.* Composites Part A: Applied Science and Manufacturing, 2006. **37**(11): p. 2041-2056.

[33]. Mamalis, A. G., Manolakos, D. E., Ioanniddis, M. B. and Papapostolou, *Finite element modelling of the crushing response of square carbon FRP tubes subjected to static and dynamic axial compression.* WIT Transactions on Engineering Sciences, 2005. **49**(Impact Loding of Lightweight structures): p. 373-386.

[34]. Mamalis, A. G., Manolakos, D. E., Demosthenous, G. A. and Ioannidis, M. B., *Energy absorption capability of fibreglass composite square frusta subjected to static and dynamic axial collapse.* Thin-Walled Structures, 1996. **25**(4): p. 269-295.

[35]. Mamalis, A. G., Manolakos, D. E., Demosthenous, G. A. and Ioannidis, M. B., *Analytical modelling of the static and dynamic axial collapse of thin-walled fibreglass composite conical shells.* International Journal of Impact Engineering, 1997. **19**(5-6): p. 477-492.

[36]. Mamalis, A. G., Manolakos, D. E., Ioannidis, M. B. and Kostazos, P. K., *Crushing of hybrid square sandwich composite vehicle hollow bodyshells with reinforced core subjected to axial loading: numerical simulation.* Composite Structures, 2003. **61**(3): p. 175-186.

[37]. Mamalis, A. G., Manolakos, D. E., Ioannidis, M. B. and Papapostolou, D. P., *Crashworthy characteristics of axially statically compressed thin-walled square CFRP composite tubes: experimental.* Composite Structures, 2004. **63**(3-4): p. 347-360.

[38]. Mamalis, A. G., Robinson, M., Manolakos, D. E., Demosthenous, G. A., Ioannidis, M. B. and Carruthers, J., *Crashworthy capability of composite material structures.* Composite Structures, 1997. **37**(2): p. 109-134.

[39]. Song, H.-W., Wan, Z.-M., Xie, Z.-M. and Du, X.-W., *Axial impact behavior and energy absorption efficiency of composite wrapped metal*

tubes. International Journal of Impact Engineering, 2000. **24**(4): p. 385-401.

[40]. Tao, W. H., Robertson, R. E. and Thornton, P. H., *Effects of material properties and crush conditions on the crush energy absorption of fiber composite rods.* Composites Science and Technology, 1993. **47**(4): p. 405-418.

[41]. Thornton, P. H., *Energy absorption in composite structures.* Journal of Composite Materials, 1979. **13**(247).

[42]. Ramakrishna, S., *Microstructural design of composite materials for crashworthy structural applications.* Materials & Design, 1997. **18**(3): p. 167-173.

[43]. Arnaud, P. and Hamelin, P., *Dynamic characterization of structures: A study of energy absorption in composite tubes.* Composites Science and Technology, 1998. **58**(5): p. 709-715.

[44]. Guden, M., Yuksel, S., Tasdemirci, A. and Tanoglu, M., *Effect of aluminum closed-cell foam filling on the quasi-static axial crush performance of glass fiber reinforced polyester composite and aluminum/composite hybrid tubes.* Composite Structures, 2007. **81**(4): p. 480-490.

[45]. Jimenez, M. A., Miravete, A., Larrode, E. and Revuelta, D., *Effect of trigger geometry on energy absorption in composite profiles.* Composite Structures, 2000. **48**(1-3): p. 107-111.

[46]. Ramakrishna, S. and Hull, D., *Energy absorption capability of epoxy composite tubes with knitted carbon fibre fabric reinforcement.* Composites Science and Technology, 1993. **49**(4): p. 349-356.

[47]. Mamalis, A. G., Manolakos, D. E., Demosthenous, G. A. and Ioannidis, M. B., *The static and dynamic axial crumbling of thin-walled fibreglass composite square tubes.* Composites Part B: Engineering, 1997. **28**(4): p. 439-451.

[48]. Mamalis, A. G., Manolakos, D. E., Ioannidis, M. B. and Papapostolou, D. P., *On the response of thin-walled CFRP composite tubular components subjected to static and dynamic axial compressive loading: experimental.* Composite Structures, 2005. **69**(4): p. 407-420.

[49]. Mamalis, A. G., Manolakos, D. E., Demosthenous, G. A. and Ioannidis, M. B., *The static and dynamic axial collapse of fibreglass composite automotive frame rails.* Composite Structures, 1996. **34**(1): p. 77-90.

[50]. Fairfull, A. H. and Hull, D., *Energy absorption of polymer matrix composite structures:Friction effects.* Structural Failure for International Symposium on Structural Failure MIT, 1988: p. 255.

[51]. Thornton, P. H. and Magee, C. L., *The interplay of geometric and materials variables in energy absorption.* Journal of Engineering material and Technology, 1977. **99**((Trans.ASME)): p. 114.

[52]. Thornton, P. H. and Edwards, P. J., *Energy absorption in composite tubes.* Journal of Composite Matter, 1982. **16**: p. 521-545.

[53]. Farley, G. L., *Effect of specimen geometry on the energy absorption of composite materials.* Journal of Composite Materials, 1986. **20**: p. 390.

[54]. Farley, G. L., *The effect of crushing speed on the energy-absorption capability of composite tubes.* Journal of Composite Materials, 1991. **25**: p. 1314.

[55]. Kirch, P. A. and Jannie, H. A., *Energy absorption of glass polyester structures* Techinical Paper Series, SAE, 1981. **810233**: p. 220.

[56]. Berry, J. and Hull, D., *Effect of speed on progressive crushing of epoxy glass cloth tubes.* Third International Conferrence.Mech.Prop.High Rates of Strain, Oxford, 1984: p. 463.

[57]. Warrior, N. A., Turner, T. A., Robitaille, F. and Rudd, C. D., *Effect of resin properties and processing parameters on crash energy absorbing composite structures made by RTM.* Composites Part A: Applied Science and Manufacturing, 2003. **34**(6): p. 543-550.

[58]. Farley, G. L., *Effect of fibre and matrix maximum strain rate on the energy absorption of composite materials.* Journal of Composite Materials, 1986. **20**: p. 322.

[59]. Farley, G. L., In Proceedings of the 43rd American Helicopter Society Annual Forum, St.Louis, USA, 1987: p. 613-627.

[60]. Farley, G. L., *Energy absorption of composite materials* Journal of Composite Materials, 1983. **17**: p. 167.

[61]. Hull, D., *A unified approach to progressive crushing of fibre-reinforced composite tubes.* Composites Science and Technology, 1991. **40**(4): p. 377-421.

[62]. Han, H., Taheri, F., Pegg, N. and Lu, Y., *A numerical study on the axial crushing response of hybrid pultruded and +/-45[degree sign] braided tubes.* Composite Structures, 2007. **80**(2): p. 253-264.

[63]. Zeng, T., Fang, D.-N. and Lu, T.-J., *Dynamic crashing and impact energy absorption of 3D braided composite tubes.* Materials Letters, 2005. **59**(12): p. 1491-1496.

[64]. Thornton, P. H., Harwood, J. J. and Beardmore, P., *Fiber reinforced plastic composites for energy absorption purposes.* Composite Science Technology, 1985. **24**: p. 275-298.

[65]. Pinho, S. T., Camanho, P. P. and de Moura, M. F., *Numerical simulation of the crushing process of composite materials.* International Journal of Crashworthiness, 2004. **9**(3): p. 263 - 276.

[66]. Fairfull, A. H. and Hull, D., *Effect of specimen dimensions on the specific energy absorption of fibre composite tubes.* In Proceedings of ICCM-VI, 1987: p. 3.36-3.45.

[67]. Thornton, P. H., *The crush behavior of pultruded tubes at high strain rates.* Journal of Composite Materials, 1989. **24**: p. 22.

[68]. Farley, G. L. and Jones, R. M., *Analogy for the effect of material and geometrical variables on energy absorption capability of composite tubes.* Journal of Composite Materials, 1992. **26**: p. 78.

[69]. Solaimurugan, S. and Velmurugan, R., *Influence of fibre orientation and stacking sequence on petalling of glass/polyester composite cylindrical shells under axial compression.* International Journal of Solids and Structures. 2007. **44**(21): p. 6999-7020.

[70]. Solaimurugan, S. and Velmurugan, R., *Progressive crushing of stitched glass/polyester composite cylindrical shells.* Composites Science and Technology, 2007. **67**(3-4): p. 422-437.

[71]. Mamalis, A. G., Manolakos, D. E., Ioannidis, M. B. and Papapostolou, D. P., *The static and dynamic axial collapse of CFRP square tubes: Finite element modelling.* Composite Structures, 2006. **74**(2): p. 213-225.

[72]. Y.P. Markopoulos, V. K., *On the Low Velocity Impact Response of Laminated Composite Plates Utilising the p-Version Ritz Method.* dvanced Composite Letters, 2003. **12**(5): p. 13.

[73]. Mamalis, A. G., Manolakos, D. E. and Viegelahn, G. L., *Crashworthy behaviour of thin-walled tubes of fibreglass composite material subjected to axial loading.* Journal of Composite Materials, 1990. **24**: p. 72.

[74]. Mamalis, A. G., Manolakos, D. E., Ioannidis, M. B. and Papapostolou, D. P., *On the experimental investigation of crash energy absorption in laminate splaying collapse mode of FRP tubular components.* Composite Structures, 2005. **70**(4): p. 413-429.

[75]. Suemasu, H., Sasaki, W., Ishikawa, T. and Aoki, Y., *A numerical study on compressive behavior of composite plates with multiple circular delaminations considering delamination propagation.* Composites Science and Technology, 2008. **68**(12): p. 2562-2567.

[76]. Wang, X. W., Pont-Lezica, I., Harris, J. M., Guild, F. J. and Pavier, M. J., *Compressive failure of composite laminates containing multiple delaminations.* Composites Science and Technology, 2005. **65**(2): p. 191-200.

[77]. Johnson, A. F. and Holzapfel, M., *Influence of delamination on impact damage in composite structures.* Composites Science and Technology, 2006. **66**(6): p. 807-815.

[78]. Zarei, H., Kröger, M. and Albertsen, H., *An experimental and numerical crashworthiness investigation of thermoplastic composite crash boxes.* Composite Structures, 2008. **85**(3): p. 245-257.

[79]. Palanivelu, S., Verhelst, R., Van Paepegem, W., Degrieck, J., Kakogiannis, D., Van Hemelrijck, D., Wastiels, J., De Wolf, K. and Vantomme, J., *Experimental and numerical study on axial crushing behaviour of pultruded composite tubes.* Proceeding of the 13th European conference on composite materials, Stockholm, Sweden, June 2-5, 2008.

[80]. Oh, J., Cho, M. and Kim, J.-S., *Buckling analysis of a composite shell with multiple delaminations based on a higher order zig-zag theory.* Finite Elements in Analysis and Design, 2008. **44**(11): p. 675-685.

[81]. Li, S., Reid, S. R. and Zou, Z., *Modelling damage of multiple delaminations and transverse matrix cracking in laminated composites due to low velocity lateral impact.* Composites Science and Technology, 2006. **66**(6): p. 827-836.

[82]. McGregor, C. J., Vaziri, R., Poursartip, A. and Xiao, X., *Simulation of progressive damage development in braided composite tubes under axial compression.* Composites Part A: Applied Science and Manufacturing. **In Press, Corrected Proof**.

[83]. *LS-DYNA keyword user's manual V971,.* LSTC, Livermore,CA, 2006.

[84]. Hashin, Z. and Rotem, A., *A fatigue failure criterion for fiber reinforced materials.* Journal of Composite Materials, 1973. **7**: p. 448.

[85]. *LS-DYNA Theory manual V971.* LSTC, Livermore,CA, 2006.

[86]. *ABAQUS User manual.* ABAQUS, Inc. and Dassault Systèmes 2007.

[87]. *ABAQUS Theory manual.* ABAQUS, Inc. and Dassault Systèmes, 2007.

Chapter 8

Experimental Axial Impact Study on Large-scale Pultruded Composite Tubes

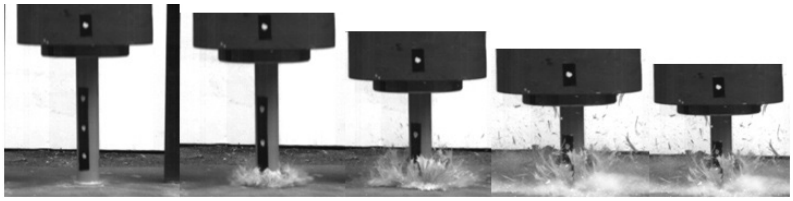

Overview

This chapter presents the experimental investigation on the progressive deformation behaviour of uni-directional pultruded composite tubes subjected to an axial impact load. Pultruded square and circular profiles with glass-polyester and glass-vinylester combinations were used for this study. Two types of triggering profiles were incorporated to investigate the effect of triggering on the energy absorption. All above combinations were investigated for three different impact velocities (9.3, 12.4 and 14m/s). The crushing peak and mean load characteristics of the composite tubes with different triggering profiles and their progressive failure modes are presented. The effects of the geometry profile, triggering, strain rate and the type of resin on energy absorption of the composite tubes were studied in detail.

8. 1. Introduction

As seen from the previous chapter the energy absorption of the composite tubes influenced by many variables. Hence, in this Chapter an axial impact study was conducted to understand the effect of cross-section, triggering profile, type of resin on the energy absorption of the composite tubes. Most of the published works [1-5] on field of the crushing of composite tubes used the circular and square cross-sections. Hence, in this study also the same cross-sections have used. Similarly, the polyester and vinylester resins were chosen to compare their performance. Two types of triggering (bevel triggering and tulip triggering) were chosen to study their influence on the deformation patterns and the corresponding energy absorption of

the composite tubes. All the above combinations have been studied for three impact velocities.

8. 2. Materials and experimental methods

8. 2. 1. Composite tubes

All the tubes which were used for the tests are manufactured by the pultrusion process (M/s EXEL, Belgium). The laminates were made with continuous 0° orientation fibres. To get the better surface finish the outer and inner layers were made up of random short glass fibres with approximate thickness of 0.1- 0.2 mm. The architectural construction of the circular pultruded profiles used for this study is schematically shown in Figure 8-1. Six different tube combinations SP1, SP2, CP1, CP2, CV1 and CV2 were studied experimentally. The SP1 refers to the square cross-sectional glass-polyester pultruded tube with triggering type 1. The SP2 refers to the square cross-sectional glass-polyester pultruded tube with triggering type 2. The CP1 and CP2 refer to the circular cross-sectional glass-polyester tube with triggering type 1 and 2 respectively. Similarly the CV1 and CV2 refer to the circular cross-sectional glass-vinylester tube with triggering type 1 and 2 respectively. The triggering type 1 is the 45° chamfering around the edges of the tubes (bevel triggering at one end of the tube) and the type 2 is a tulip pattern with an included angle of 60° between the edges. The details of the two triggering profiles for circular and square tubes are shown in Table 8-1. The motivation to choose these types was that, for type 1 profile the initial contact of the impactor will be uniform along the circumference of the tube at the time of impact, whereas in the case of type 2 the contact will take place at the sharp edges of the specimen. The first mechanism would enhance uniform circumferential interlaminar cracks causing the uniform delamination, whereas in case of triggering type 2, the initial cracks develop at the sharp edges of the tube which make first contact with the impactor. The circular and square test specimens with two types of triggering are shown in Table 8-1.

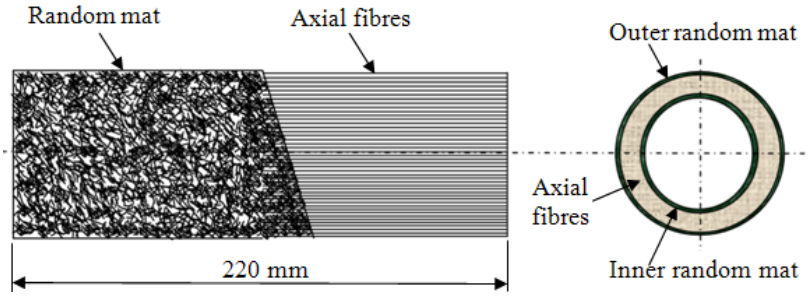

Figure 8-1: Architectural construction of the pultruded tubes.

Table 8-1: Dimensional and material details of the composite tube series.

S. No	Tube series	Cross-section	Triggering		Fibre	Resin	Dimensions (mm)	ρ_{linear} (g/mm)	Volume fraction (%)	Fibre volume fraction of 0° lay-up	Fibre volume fraction of random mat
			Type 1	Type 2							
1.	SP	Square	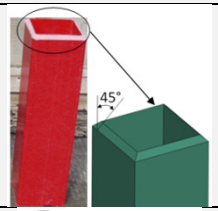	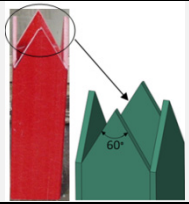	Glass	Polyester	$W = 60$ $t = 4.5$ $L = 220$	1.81	$V_m = 49.2$ $V_f = 50.8$	40.3 %	10.5 %
2.	CP	Circular	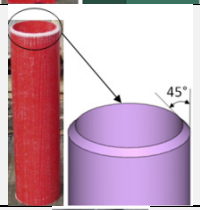	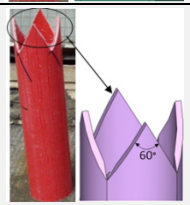	Glass	Polyester	$\phi = 50$ $t = 3$ $L = 220$	0.66	$V_m = 51.7$ $V_f = 48.3$	36.2 %	12.1 %
3.	CV	Circular			Glass	Vinylester	$\phi = 38$ $t = 3$ $L = 220$	0.60	$V_m = 49.7$ $V_f = 50.3$	41.4 %	9.0 %
W = outer width; t = wall thickness; L = length; ϕ = Outer diameter; V_m = Volume fraction of matrix; V_f = Volume fraction of fibre											

Studies conducted on the progressive crushing of circular cross-sectional tubes proved that tubes having a t/D ratio less than 0.015 will fail catastrophically (t – thickness of the tube; D – diameter of the tube) [6]. However, tubes with a t/D ratio in the range 0.015 to 0.25 will crush progressively. So the t/D ratio of the circular tubes was chosen 0.06 and 0.07 for CP and CV series respectively. For SP series, a t/W ratio of 0.075 (W- width of the tube) was chosen. The tolerances in the tube dimensions (outer width, outer diameter and thickness) were checked. The standard deviation of outer width and thickness of SP series and outer diameter and thickness of CP and CV series are 0.05, 0.05; 0.09, 0.12; 0.05 and 0.04 mm respectively.

To achieve the progressive failure of the composite tubes, the linear density (mass per unit length) of the tube was chosen as recommended in [7]. The resin and the fibre volume fraction were calculated based on ASTM D 2584. The details of the tube geometry, fibre, resin, tube dimensions, linear density and the corresponding volume fraction are mentioned in Table 8-1.

8. 2. 2. Experimental test set-up

All tests have been performed with the large scale drop weight test facility shown in Figure 8-2(a-b). The main horizontal supporting structure is attached to a vertical wall. The horizontal supporting structure carries the vertical guides along which the impactor slides. An impactor mass of 68.85 kg was used for all tests. The bottom surface of the impactor was made flat to fix the composite tube specimens. A scale was fixed parallel to the guiding rail to measure the drop height. The maximum drop height of the experimental setup is 12 m. However, for this experiment the impact height was limited up to 10 m. The bottom of the vertical sliding support is fixed to a 20 mm thick steel plate to withstand the total impact force during the impact test. The impact base plate was placed over a massive concrete basement.

Data acquisition and processing

The system was equipped with a high speed camera (Photron APX RS 250K) with maximum frame rate of 250,000 fps (Figure 8-2(c)). It was connected with a computer which records the images at specified instance of time during the impact event. The tracking area by the camera covered the entire impact basement. A special metal – halide lamp was used to maintain the light intensity at the area of the impact basement.

To capture the crash event of the composite tubes, a frame rate of 5000 fps was chosen. The corresponding pixel resolution of the screen was 1024 × 1024, with a remaining resolution of 384 × 400 for the area of impact. Markers were placed on the impactor as well as on the test specimen for digital image tracking. About half a meter height was covered by the focus lens of the high speed camera from the

basement of the impact system. The position of the impactor was recorded at every instance of impact time. From these data the corresponding velocities were calculated. Due to the clearance between the impactor guiding system and the impactor, a small change in the horizontal velocity was noticed. However compared to the magnitude of the vertical velocity it was negligible.

(a) **(b)** **(c)**

Figure 8-2: (a) Experimental set-up **(b)** Impactor **(c)** High speed camera.

As discussed in Chapter 3, the dynamic parameters such as test specimen deformation length, impactor velocity and the corresponding crushing force at the crushing end can be calculated using digital image correlation technique [8]. In this study, the same method was adopted to calculate the dynamic parameters. For each test a minimum of two tests have been conducted to calculate the crushing parameters.

8. 3. Experimental results and discussions

The details of the progressive deformation patterns and the corresponding load-deformation curves for the same composite tubes subjected to quasi-static loading can be found from ref. [9]. The progressive failure pattern of the different types of composite tubes was investigated with different impact velocities. Each set of composite tubes consists of square (SP1 and SP2) and circular tubes (CP1, CP2, CV1 and CV2). They were tested with different drop heights which correspond to 9.3 m/s, 12.4 m/s and 14 m/s initial impact velocities. Samples of a square and circular composite tube which have undergone the different phases of deformation are shown in Figure 8-3 and Figure 8-4 respectively. All the tubes exhibited the progressive crushing failure modes.

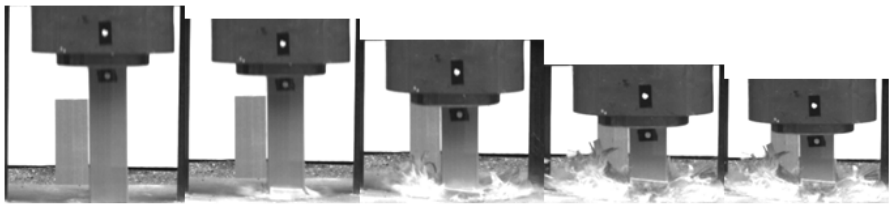

Figure 8-3: Different phases of square tube (SP1) crushing.

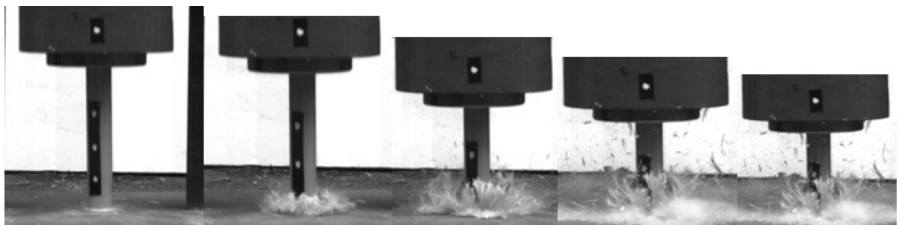

Figure 8-4: Different phases of circular tube (CV1) crushing.

8. 3. 1. Failure patterns for square tubes

For both types of square tubes (SP1 and SP2) after the circumferential delamination, the primary longitudinal cracks developed along the corners due to stress concentration. As a result each side of the tube has split into petals moving inwards and outwards. The major impact energy of both types of tubes was absorbed by lamina bending followed by the breakage of resin bonds. The separation of plies from each other was directly proportional to the number of interlaminar cracks which developed during the impact process. The complete surface delamination of inner and outer random fibre mat was observed from the core fibres. The de-cohesion of outer and inner skin is due to the uneven distribution of the bonding strength along the thickness of the tube. The lamina of each face of the square tube acted as a cantilever beam, which absorbed a considerable amount of energy by its bending mode. During the crash event, the bending angle of each petal was observed 90° for all square tubes. However due to the high stiffness of each petal the angle was gradually reduced when the impact force magnitude reached to zero (Figure 8-5). This mode was different from the previously reported modes [10] where all the petals deformed permanently for 90°. However, the inner laminae have undergone permanent bending as well as tearing mode (Figure 8-5 (a-b)). Unlike triggering type 1, triggering type 2 exhibited permanent bending of the laminae due to their lower stiffness. This can be clearly noticed from Figure 8-6.

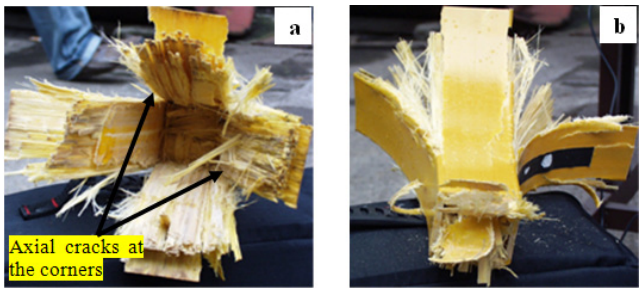

Figure 8-5: **(a & b)** - Failure pattern of SP1 tube series.

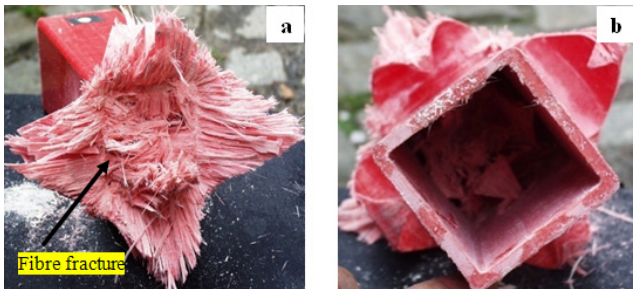

Figure 8-6: **(a & b)** - Failure pattern of SP2 tube series.

8. 3. 2. Failure patterns for circular tubes

Similar to square tubes, in all varieties of circular tubes (CP1, CP2, CV1 and CV2) the inner and outer petals were formed due to the circumferential delamination and consequently axial cracks parallel to the axis of the tube. The uniform geometry of the circular tube facilitated to form more axial cracks and thus more petals were formed. The major amount of impact energy was absorbed due to the increasing number of longitudinal cracks and subsequent bending of the laminates [11]. This phenomenon was clear in all cases in which the specific energy absorption of the circular tube was more than for the square tube. Unlike the square tubes. irrespective of the triggering and fibre volume fraction, the bending angles of the laminates were noticed greater than or equal to 90° (Figure 8-7 and Figure 8-8). For all tube series (SP1, SP2, CP1, CP2, CV1 and CV2) the bending of the inner petals reduced the acceleration of the impactor considerably due to the blockage of material within the profile.

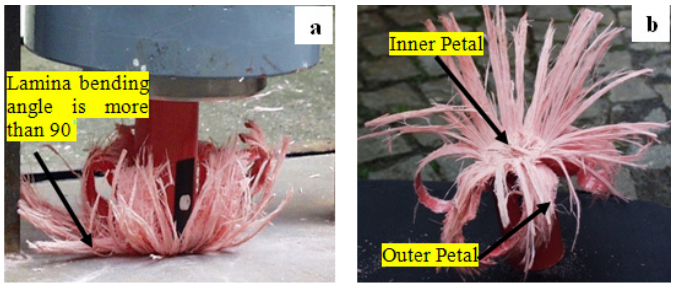

Figure 8-7: (a & b) - Failure pattern of CP1 and CP2 series.

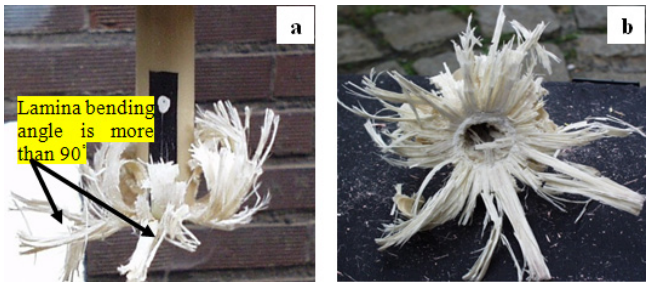

Figure 8-8: **(a & b)** - Failure pattern of CV1 and CV2 series.

8. 3. 3. Study of longitudinal cuts

After the impact testing, all samples were longitudinally cut to carry out a visual inspection of the crushed zone. The cut section of all tube series gave clear evidence that the major delamination took place at the mid thickness of the tube. A similar result was reported in [11, 12]. Other than the axial cracks, a smaller number of trans-laminar cracks (cracks which are perpendicular to the direction of the fibre orientation) were noticed for SP series. These axial and trans-laminar cracks were longer in length compared to circular cross sectional tubes. In contrast for CP and CV series, a larger number of axial and trans-laminar cracks was observed; however, the length of the axial and trans-laminar cracks were controlled by the uniform geometry of the circular tubes. As a result each laminate has split into a larger number of thinner layers. Due to the controlled axial trans-laminar cracks, more fibres of the CP and CV series have undergone fracture at the fixed end of the cantilever portion. In case of SP series less fibres had undergone fracturing due to the larger radius of the bending. This phenomenon can be clearly noticed from the difference between the amount of fibres and their angle of bending for square and circular tubes (refer Figure 8-9 and Figure 8-10). Unlike SP and CP series, in case of CV series there was no de-cohesion of the random mat from the core fibres noticed. The better adhesion property of vinylester resin attributed to the increasing uniform strength along the thickness of the tube.

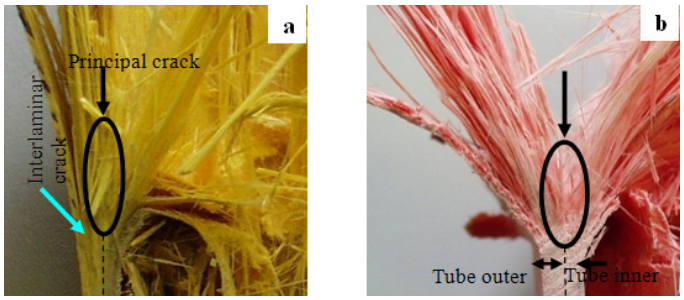

Figure 8-9: **(a)** SP1 tube **(b)** SP2 tube.

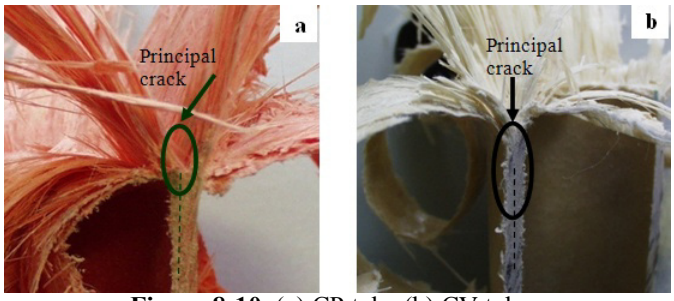

Figure 8-10: (a) CP tube (b) CV tube.

8. 3. 4. Force-deformation curves

The force-deformation curves of the tube series SP1, CP1 and CV1 for different initial impact velocities are shown in Figure 8-11 to Figure 8-13.

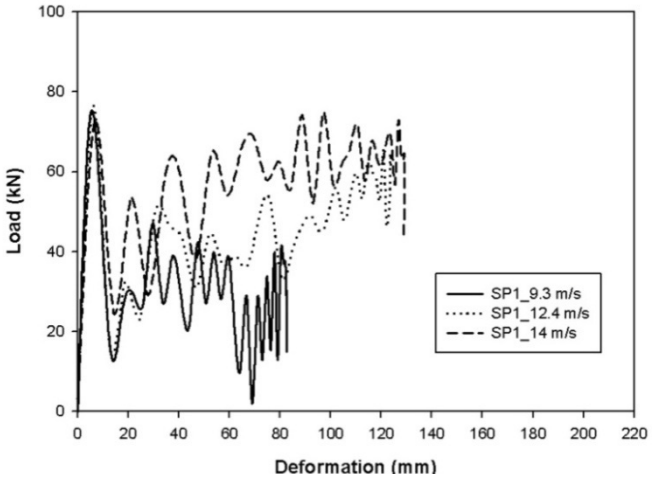

Figure 8-11: Force-deformation curves for SP1 series.

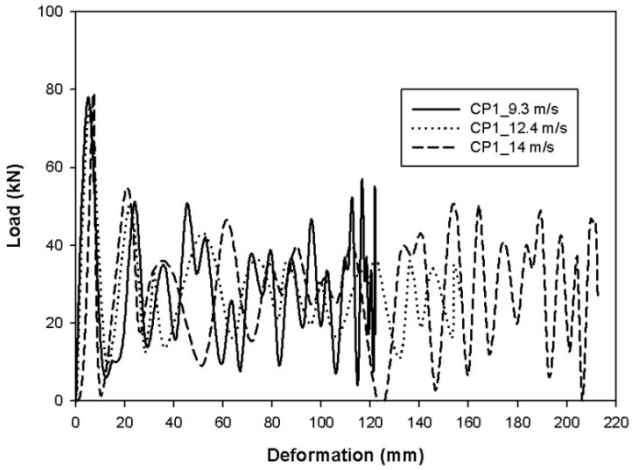

Figure 8-12: Force-deformation curves for CP1 series.

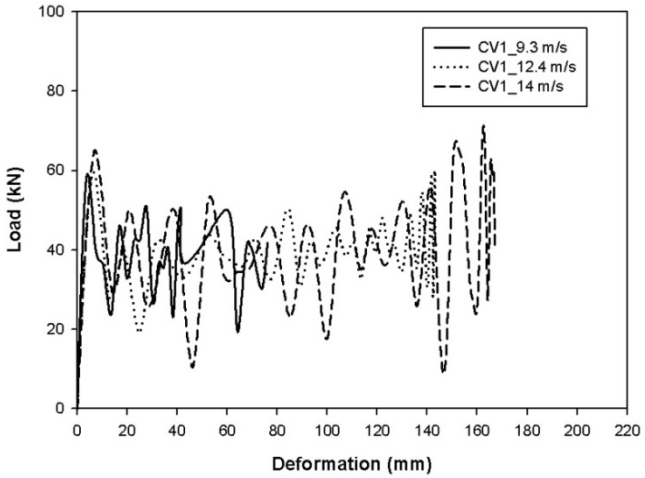

Figure 8-13: Force-deformation curves for CV1 series.

In all series, the force-deformation curves followed three phases. The first phase was the sudden increase in peak load at the initial stage of compression. During this stage the triggering length of the tube was completely crushed and followed by the start of the circumferential delamination. The area under the peak load in the force-deformation curve corresponds to the total energy spent on the initial circumferential delamination of the composite tube. After the circumferential delamination the peak load decreased abruptly. This corresponds to the second stage of the crushing. At the end of this second stage a significant amount of energy was consumed by bending of the petals followed by the shear deformation of plies that led to fibre fracture at the fixed end of the petal. The chronological order of delamination, axial cracks, bending of petals and due to that the shear fracture of the fibre continued for the subsequent stages of crushing. Due to the above failure modes, the crushing load of the tube oscillated around a mean value. This was the third stage of the crushing. The similar trend of all three stages was observed in case of triggering type 2 also. However due to the triggering tulips the time to reach the major delamination was different than for type 1 series and so a smaller slope of the peak load was observed. The magnitude of the peak crushing load and the corresponding mean crushing load are given in Table 8-2. The mean crushing load of all tube series was calculated based on Equation (3.6) which was given in Chapter 3. The ratio of the mean crush load to the peak crush load which indicates the efficiency of the crushing (η_c) is also given in Table 3. In case of the SP1 and CP1 series the tests at three different velocities (9.3, 12.4 and 14m/s) exhibited a very similar peak crushing load. However in case of CV1 series a minor increase in peak load was observed with increasing impact velocity. The CP1 and CV1 series exhibited approximately the same mean crush load for all three impact velocities. As a result the crush efficiency of these tube series remained approximately constant for all impact velocities. In case of SP1 the mean load of crushing increased with increasing impact velocities

and consequently the crush efficiency also increased. The increased mean crush load may be due to the blockage of the material at the inner profile of the tube.

8. 3. 5. Effect of triggering on peak load

The effect of triggering on the load-deformation curve for the tube series SP, CP and CV can be clearly noted from Figure 8-14, Figure 8-15 and Figure 8-16. For SP and CV tube series no appreciable difference in peak load was noticed between triggering type 1 and 2. However in case of CP series due to the triggering type 2, there was a 12 % reduction in peak load noticed. In all tube series with triggering type 2, the average slope to reach the peak load was uniform. The gradual increase in the load was due to the reduced stiffness of each tulip and so less energy was required for delamination. However in both cases the peak load occurred at a stage where the circumferential delamination took place. For the CP and CV series, a higher deformation length was noticed due to triggering type 2. However, in case of the SP series there was a negative effect observed and so the deformation length of triggering 1 was higher than for type 2. Apart from the peak load, a significant difference in the mean crush load was noticed for triggering type 2 series. Apart from the SP tube series, the mean crush load of CP2 and CV2 was smaller than CP1 and CV1. The lower mean crush load of the tube series may be due to the delayed major delamination and subsequently, less resistance offered by the triggering tulips. The comparison of peak and mean crush load of all tube series for the initial impact velocity of 9.3 m/s is given in Table 8-2.

Table 8-2: Summary of crushing parameters for different initial impact velocities.

Tube series	Impact velocity 9.3 m/s				Impact velocity 12.4 m/s				Impact velocity 14 m/s			
	Peak load (kN)	Mean load (kN)	Absorbed energy (kJ)	η_c (%)	Peak load (kN)	Mean load (kN)	Absorbed energy (kJ)	η_c (%)	Peak load (kN)	Mean load (kN)	Absorbed energy (kJ)	η_c (%)
SP1	73	31.01	2.563	42.5	77	43.18	5.341	56.4	73	55.95	7.218	76.5
SP2	73	37.20	2.680	51.9	-	-	-		-	-	-	-
CP1	78	28.34	3.462	36.4	76	28.10	4.455	37.2	79	28.3	6.029	35.8
CP2	69	26.05	3.470	37.8	-	-	-	-	-	-	-	-
CV1	59	38.66	2.938	65.5	60	38.52	5.508	64.5	65	39.01	6.515	59.8
CV2	63	34.62	3.448	55.3	-	-	-	-	-	-	-	-

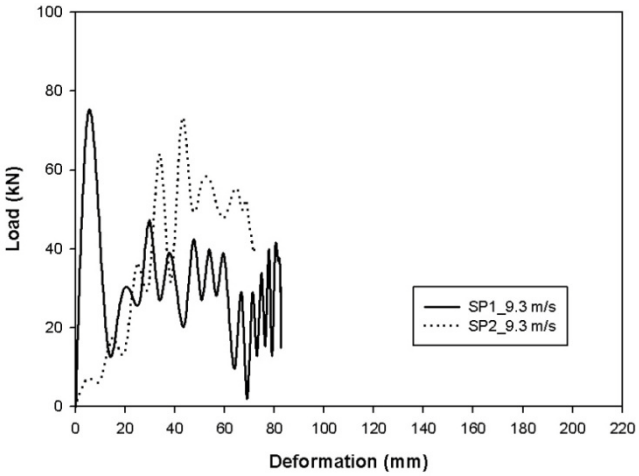

Figure 8-14: Comparison of SP1 and SP2 tubes.

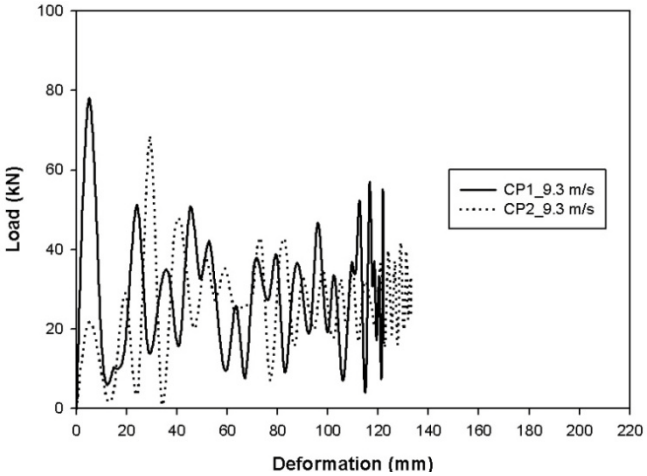

Figure 8-15: Comparison of CP1 and CP2 tubes.

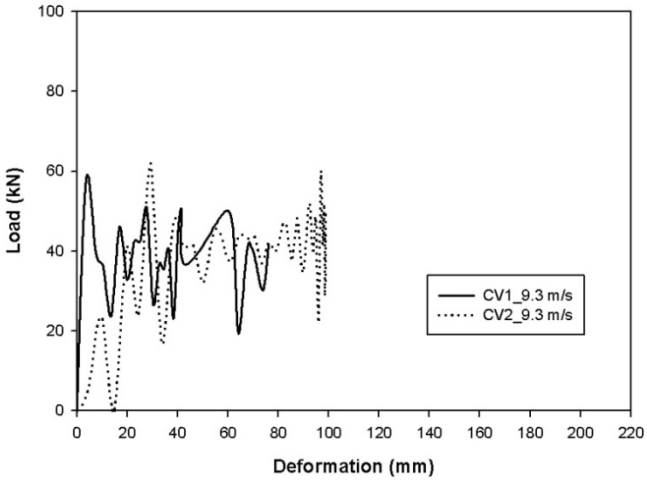

Figure 8-16: Comparison of CV1 and CV2 tubes.

8. 3. 6. Specific energy absorption

In order to determine the deformation length of the tube series two specimens were tested in each category. The maximum deformation lengths of the tubes were taken into account and thus minimum specific energy absorption of each case was calculated. The dissipated energy with respect to the deformed length of SP1, CP1 and CV1 tube series for the initial impact of velocity 9.3 m/s, 12.4 m/s and 14m/s are shown in Figure 8-17, Figure 8-18 and Figure 8-19. The increasing slope of the SP series indicated the dependency of the energy absorption on impact velocity. In contrast the CP and CV series followed approximately the same slope. The total energy absorption (E_d) of each case was calculated based on Equation (3.4) of Chapter 3 and the same is summarized in Table 8-2. To understand the energy absorption effectiveness of each tube, the specific energy absorption (SEA - normalized with respect to mass) was calculated (using Equation (3.7) of Chapter 3).

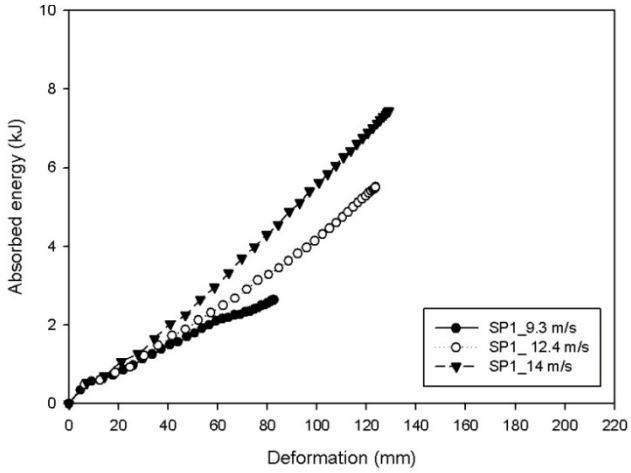

Figure 8-17: Energy absorption of SP1 series.

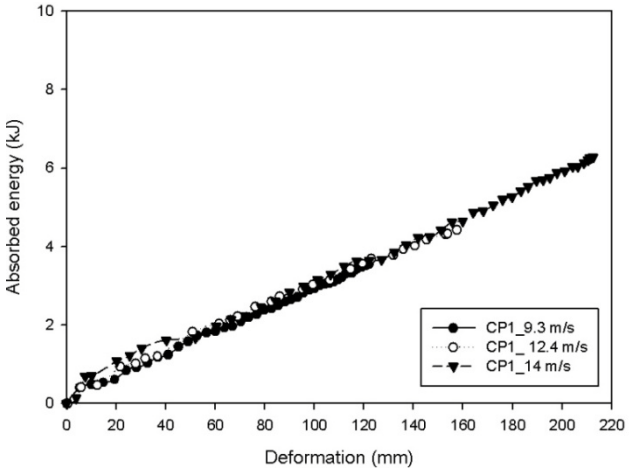

Figure 8-18: Energy absorption of CP1 series.

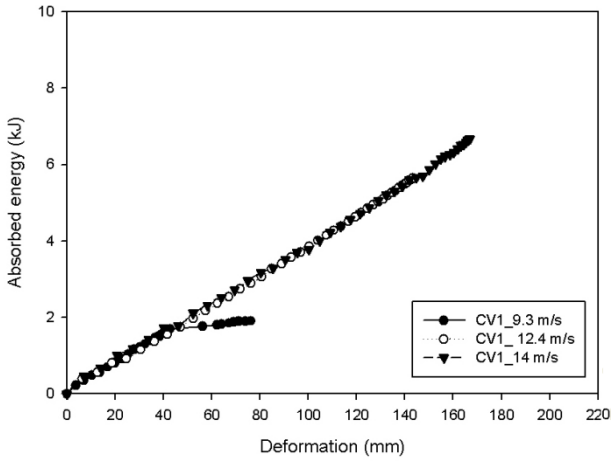

Figure 8-19: Energy absorption of CV1 series.

8. 3. 7. Effect of geometry and triggering on SEA

The comparison of the specific energy absorption of the SP, CP and CV series of triggering type 1 and 2 for the initial impact velocity of 9.3 m/s is presented in Figure 8-20. The specific energy absorption of circular tubes (CP and CV series) in all cases is higher than the square tubes (SP series). As discussed earlier, due to the uniform geometry the circular tube yielded a larger number of axial cracks. These cracks attributed to a higher specific energy absorption. In case of square tubes due to the higher stress concentration, the major axial cracks were formed at the four corners of the tube. Out of the total energy absorbed by the square tube in each category (SP1 and SP2), a significant amount of energy was absorbed by lamina bending followed by shear fracture at the fixed end of each sub-laminate.

The effect of triggering on SEA is also clearly explained by Figure 8-20. In case of CP and CV series, triggering type 1 absorbed more energy than triggering type 2. This is due to the fact that, during the impact event the controlled circumferential delamination followed by the axial cracks took place uniformly along the circumference of the tube. In case of triggering type 2, the delamination propagated at the sharp edges of the tube. The crushing of the triggering length of the tube delayed the major circumferential delamination. Compared to triggering type 1, an approximate time delay of 2-3 milliseconds was observed in all cases of triggering type 2. This can be noticed from the shift of peak load compared to type 1 in Figure 8-14, Figure 8-15 and Figure 8-16.

Due to the above effects the SEA of CP2 and CV2 series are 7.4% and 9.8% lower than CP1 and CV1 series for the case with the initial impact velocity of 9.3 m/s. However, in case of square tubes the SEA was higher for triggering type 2 than for triggering type 1. The increase in SEA of 16.5% was noticed for SP2 tubes

compared to SP1 tubes. Although a delay in delamination occurred between triggering type 1 and 2, in both SP1 and SP2 series a significant amount of energy was dissipated by lamina bending followed by the shear fracturing of the fibres. The stiffness of each side of the laminate of SP2 tubes was less than for SP1 series. The lower stiffness of each laminate attributed to the shear fracture of fibres at the base of the tulips followed by the major delamination. Due to this effect, each laminate of SP2 series exhibited the permanent bending angle of 90°, whereas in case of triggering type 1 it was approximately 45°.

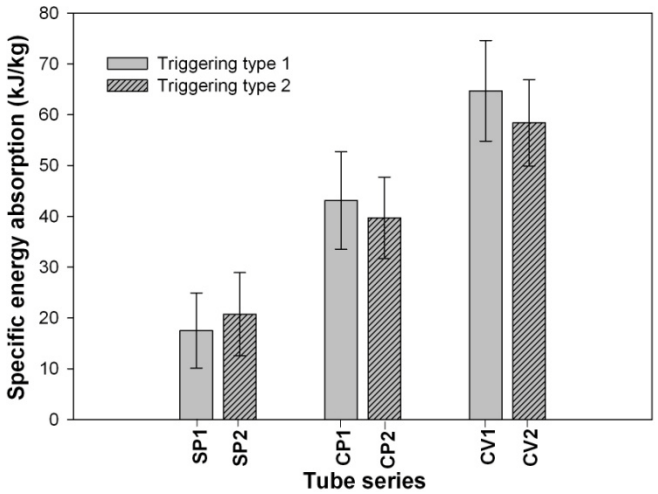

Figure 8-20: Effect of triggering on SEA (error bar indicates the standard deviation).

8. 3. 8. Effect of strain rate and resin type on SEA

The initial study of the tubes for the impact velocity of 9.3 m/s indicated that the specific energy absorption of tube series CP1 and CV1 exhibited more SEA than type 2. Therefore it was decided to study the strain rate effect on SEA using the type 1 series. From the experiments conducted, the SEA of each tube was calculated based on the higher deformation length of each series. From Figure 8-21, it can be noticed that the energy absorption of SP1 tube was sensitive to the impact velocity. There was a linear increase in SEA with 26% noticed from velocity to higher velocity. In case of CP series, there was a positive dependency noticed with respect to the strain rate; however, the difference in SEA was small. Similarly for CV series there was no appreciable increase in SEA from 9.3 m/s to 12.4 m/s, in contrast a negative dependency was observed for 14 m/s.

The effect of resin type on SEA can be concluded from the comparison of CP and CV series. In all cases, the CV1 tubes absorbed more energy than CP1 series. It is clearly evident from the fact that the SEA of CV1 series is 33% higher than for CP1

series for initial impact velocities of 9.3 m/s and 12.4 m/s. A difference of 27% was noted for the case with an initial impact velocity of 14 m/s. One reason for the increase in SEA could be the higher tensile strength and modulus of the vinylester which causes the better interlaminar strength. Furthermore, due to the smaller diameter of CV tubes more blockage of material (debris) occurred at the inner wall. This phenomenon also might have attributed to an increase in SEA.

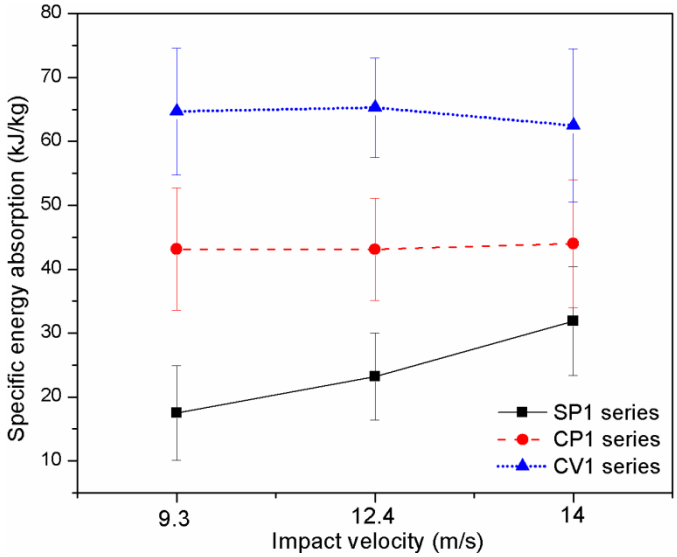

Figure 8-21: Effect of strain rate on SEA (error bar indicates the standard deviation).

8. 4. Conclusions

In this chapter, the impact energy absorption characteristics and the crushing mechanism using glass/polyester and glass/vinylester square and circular tubes with different thicknesses were investigated. The different t/D ratio and linear densities were chosen to achieve the progressive failure of the tubes. The effect of tube geometry, triggering, strain rate and the type of resin on the specific energy absorption was studied. From the experimental results obtained for three impact velocities it can be concluded that:

- In all cases, the circular tube was found to absorb more energy than the square tubes. For different impact velocities (9.3 m/s, 12.4 m/s and 14 m/s), the circular tubes with t/D ratio of 0.06 yielded approximately 59%, 45% and 28% increase in SEA compared to the square tube with t/W ratio of 0.075. The increase in SEA of the circular tube was due to the geometry of the tube which controls the deceleration of the impactor by progressive crushing.

- Out of the two types of triggering, the triggering type 1 (45° chamfering around the edge of the tube) absorbed more energy than the triggering type 2 (tulip pattern). In case of circular tubes the increase in SEA of 7 to 9% was observed due to triggering type 1. The increase in SEA was explained by the uniform circumferential delamination followed by the axial cracks of the tubes. However in case of square tubes, there was a negative effect observed due to the triggering type 1. The triggering type 2 showed 16.5 % increase in SEA compared to triggering type1. This is due to the fact that, in case of square tubes a significant amount of energy was absorbed by lamina bending followed by the shear fracture of the fibres. The lower laminate stiffness of triggering type 2 enhanced above said failure modes.
- The SEA of the square tube was found to be strain rate sensitive. The 26 % increase in SEA was noticed with increasing impact velocities. However, in case of circular tubes (made with glass polyester and glass vinylester) there was no significant increase in SEA noticed with increasing impact velocities.
- Finally studies from the glass polyester and glass vinylester tubes showed that tubes made of glass vinylester absorbed more energy than the glass polyester tubes. The increase in SEA was due to the better interlaminar strength, higher strain to failure of vinylester resin and the blockage of inner material due to the smaller diameter of the tube.

Bibliography

[1]. Farley, G. L., *Effect of fibre and matrix maximum strain rate on the energy absorption of composite materials.* Journal of Composite Materials, 1986. **20**: p. 322.

[2]. Farley, G. L., *Effect of specimen geometry on the energy absorption of composite materials.* Journal of Composite Materials, 1986. **20**: p. 390.

[3]. Hamada, H., Kameo, K., Sakaguchi, M., Saito, H. and Iwamoto, M., *Energy-absorption properties of braided composite rods.* Composites Science and Technology, 2000. **60**(5): p. 723-729.

[4]. Hull, D., *A unified approach to progressive crushing of fibre-reinforced composite tubes.* Composites Science and Technology, 1991. **40**(4): p. 377-421.

[5]. Mamalis, A. G., Manolakos, D. E., Ioannidis, M. B. and Papapostolou, D. P., *Crashworthy characteristics of axially statically compressed thin-walled square CFRP composite tubes: experimental.* Composite Structures, 2004. **63**(3-4): p. 347-360.

[6]. Hamada, H. and Ramakrishna, S., *Scaling effects in the energy absorption of carbon-fiber/PEEK composite tubes.* Composites Science and Technology, 1995. **55**(3): p. 211-221.

[7]. Thornton, P. H. and Edwards, P. J., *Energy absorption in composite tubes.* Journal of Composite Matter, 1982. **16**: p. 521-545.

[8]. Palanivelu, S., De Pauw, S., Van Paepegem, W., Degrieck, J., Kakogiannis, D., Wastiels, J., Van Hemelrijck, D., De Wolf, K. and Vontomme, J., *Validation of digitial image correlation technique for impact loading applications.* Proceedings of 9th International conference on the Mechanical and Physical Behaviour of Materials under Dynamic Loading, Brussels, Belgium, September 7-11., 2009.

[9]. Cedric, V., *Experimentele studie van het progressief falen van composietprofielen.* Master thesis, Vrij Universiteit Brussels, Brussels, Belgium, 2006-2007.

[10]. Mamalis, A. G., Manolakos, D. E., Ioannidis, M. B. and Papapostolou, D. P., *The static and dynamic axial collapse of CFRP square tubes: Finite element modelling.* Composite Structures, 2006. **74**(2): p. 213-225.

[11]. Solaimurugan, S. and Velmurugan, R., *Progressive crushing of stitched glass/polyester composite cylindrical shells.* Composites Science and Technology, 2007. **67**(3-4): p. 422-437.

[12]. Mamalis, A. G., Manolakos, D. E., Demosthenous, G. A. and Ioannidis, M. B., *The static and dynamic axial crumbling of thin-walled fibreglass composite square tubes.* Composites Part B: Engineering, 1997. **28**(4): p. 439-451.

Chapter 9

Numerical Axial Impact Study on Large-scale Pultruded Composite tubes

Overview

This chapter presents a numerical parametric study which was conducted to capture the typical failure patterns and the corresponding crushing performance of the circular and square cross-sectional pultruded glass polyester composite tubes. Numerical simulations have been performed using solid and shell elements. Furthermore, the importance of including the delamination modelling and the correct modelling of triggering geometry on the peak crush load and the corresponding crushing parameters of the composite tubes are discussed. The results from the different approaches have been compared and validated with the experimental results. In addition to that the effect of initial geometric imperfections and mesh sensitivity on the energy absorption, peak crushing load and the corresponding deformation pattern of the pultruded glass polyester composite tubes are presented.

9. 1. Numerical simulation

9. 1. 1. Salient features of numerical modelling

The commercially available finite element code ABAQUS V6.7-3 Explicit was used to study the energy absorption characteristics of the pultruded composite tubes. In ABAQUS V6.7-3 Explicit [1], the interface modelling can be done using the cohesive elements. Apart from the mechanical properties of a composite tube, the peak crushing load of a composite tube is also depending upon the shape of triggering. In this chapter, detailed studies have been conducted to address the numerical modelling issues of triggering mechanisms particularly for the type 1. To calculate the total energy absorption of a composite tube for a particular impact velocity, it is absolutely necessary to predict the total length of the deformation. Different approaches of the numerical modelling have been evaluated to achieve the appropriate deformation patterns, peak load and the corresponding energy absorption of the circular and square cross-sectional pultruded composite tubes using solid and shell elements.

9. 1. 2. Material data

The mechanical properties of the glass-polyester pultruded tube in principal directions are given in Table 9-1.

Table 9-1: Material properties of the glass polyester pultruded composite tube in principal directions.

Parameters	Symbol	Values
Material and elastic data		
Density (kg/m^3)	ρ	1850
Longitudinal modulus (GPa)	E_{11}	33.5
Transverse modulus (GPa)	E_{22}	8.0
In-plane shear modulus (GPa)	G_{12}	5.0
Out-of-plane shear modulus (GPa)	G_{23}	5.5
Poisson's ratio	υ_{12}	0.29
	υ_{23}	0.32
Glass polyester composite Strength		
Longitudinal tensile strength (MPa)	X_T	400
Longitudinal compressive strength (MPa)	X_C	200
Transverse tensile strength (MPa)	Y_T	30
Transverse compressive strength (MPa)	Y_C	50
In-plane shear strength (MPa)	S_L (S_{12})	30
Out-of-plane shear strength (MPa)	S_T (S_{23} and S_{13})	30

For the interface modelling (delamination) between plies, the properties of the polyester resin were considered. The mechanical properties of the polyester resin were adopted from [2] and the same are presented in Table 9-2.

Table 9-2: Mechanical properties of used polyester resin [2].

Resin	Relative density	Tensile modulus (GPa)	Ultimate tensile strength (MPa)
Norpol 631-610	1.12	2.6	51.2

9. 2. Numerical study with solid elements

9. 2. 1. Continuum damage model for solid composite laminates

In ABAQUS, the implementation of *Hashin damage model* is available only for shell elements. Hence, a user subroutine (VUMAT) was used to implement the same damage model for solid elements. The orthotropic elastic stress-strain relationship for the solid elements can be written as (Equation (9.1)) [3],

$$\begin{bmatrix} \sigma_{11} \\ \sigma_{22} \\ \sigma_{33} \\ \sigma_{12} \\ \sigma_{23} \\ \sigma_{13} \end{bmatrix} = \begin{bmatrix} C_{11} & C_{12} & C_{13} & 0 & 0 & 0 \\ C_{21} & C_{22} & C_{23} & 0 & 0 & 0 \\ C_{31} & C_{32} & C_{33} & 0 & 0 & 0 \\ 0 & 0 & 0 & 2G_{12} & 0 & 0 \\ 0 & 0 & 0 & 0 & 2G_{23} & 0 \\ 0 & 0 & 0 & 0 & 0 & 2G_{13} \end{bmatrix} \begin{bmatrix} \varepsilon_{11} \\ \varepsilon_{22} \\ \varepsilon_{33} \\ \varepsilon_{12} \\ \varepsilon_{23} \\ \varepsilon_{13} \end{bmatrix} \tag{9.1}$$

The following damage variables were introduced: d_f^t and d_f^c, associated with fibre tension and compression failure modes respectively; and d_m^t and d_m^c associated with the corresponding failure modes in the matrix. Global fibre and matrix damage variables were defined as (Equation (9.2)) [4],

$$\begin{aligned} d_f &= 1-(1-d_f^t)(1-d_f^c) \\ d_m &= 1-(1-d_m^t)(1-d_m^c) \end{aligned} \tag{9.2}$$

The damaged elastic constants, C_{ij}, were computed in terms of the initial elastic constants, C_{ij}^0, and the damage variables according to Equation (9.3).

$$
\begin{aligned}
C_{11} &= (1-d_f)C_{11}^0 \\
C_{22} &= (1-d_f)(1-d_m)C_{22}^0 \\
C_{33} &= (1-d_f)(1-d_m)C_{33}^0 \\
C_{12} &= (1-d_f)(1-d_m)C_{12}^0 \\
C_{23} &= (1-d_f)(1-d_m)C_{23}^0 \\
C_{13} &= (1-d_f)(1-d_m)C_{13}^0 \\
G_{12} &= (1-d_f)(1-s_m^t \cdot d_m^t)(1-s_m^c \cdot d_m^c)G_{12}^0 \\
G_{23} &= (1-d_f)(1-s_m^t \cdot d_m^t)(1-s_m^c \cdot d_m^c)G_{23}^0 \\
G_{13} &= (1-d_f)(1-s_m^t \cdot d_m^t)(1-s_m^c \cdot d_m^c)G_{13}^0
\end{aligned}
\tag{9.3}
$$

The factors s_m^t and s_m^t in the definitions of the shear moduli were introduced to control the loss of shear stiffness caused by matrix tensile and compressive failure respectively. The following values were assumed s_m^t = 0.9 and s_m^c = 0.5 [1, 4]. The following expressions are used to compute the initial (undamaged) elastic constants from the values of Young's modulus and Poisson's ratio (Equation (9.4)).

$$
\begin{aligned}
C_{11}^0 &= E_{11}^0(1-\nu_{23}\nu_{32})\Gamma \\
C_{22}^0 &= E_{22}^0(1-\nu_{13}\nu_{31})\Gamma \\
C_{33}^0 &= E_{33}^0(1-\nu_{12}\nu_{21})\Gamma \\
C_{12}^0 &= E_{11}^0(\nu_{21}+\nu_{31}\nu_{23})\Gamma \\
C_{23}^0 &= E_{22}^0(\nu_{32}+\nu_{12}\nu_{31})\Gamma \\
C_{13}^0 &= E_{11}^0(\nu_{31}+\nu_{21}\nu_{32})\Gamma \\
\Gamma &= 1/(1-\nu_{12}\nu_{21}-\nu_{23}\nu_{32}-\nu_{31}\nu_{13}-2\nu_{21}\nu_{32}\nu_{13}\nu)
\end{aligned}
\tag{9.4}
$$

The superscript "0" indicates the initial state or undamaged state of variables. The *Hashin damage model* [3] considers the following four failure modes, (i) *fibre rupture in tension* (ii) *fibre buckling and kinking in compression* (iii) *matrix cracking under transverse tension and shearing and* (iv) *matrix crushing under transverse compression and shearing*. The damage variables associated with fibre/matrix failure in tension/compression are set to one when the corresponding failure criterion is reached (Equation (9.5 to 9.8):

Fibre tensile failure $(\hat{\sigma}_{11} \geq 0)$:

$$F_f^t = \left(\frac{\hat{\sigma}_{11}}{X_T}\right)^2 + \left(\frac{\hat{\tau}_{12} + \hat{\tau}_{13}}{S_L}\right)^2 = 1, \quad d_f^t = 1 \tag{9.5}$$

Fibre compressive failure $(\hat{\sigma}_{11} \leq 0)$:

$$F_f^c = \frac{|\hat{\sigma}_{11}|}{X_C} = 1 \quad d_f^c = 1 \tag{9.6}$$

Matrix tensile failure $(\hat{\sigma}_{22} + \hat{\sigma}_{33} \geq 0)$:

$$F_m^t = \frac{(\hat{\sigma}_{22} + \hat{\sigma}_{22})^2}{Y_T^2} + \frac{\hat{\tau}_{12}^2 + \hat{\tau}_{13}^2}{S_{12}^2} + \frac{\hat{\tau}_{23}^2 - \hat{\sigma}_{22}\hat{\sigma}_{33}}{S_{23}^2} = 1 \quad d_m^t = 1 \tag{9.7}$$

Matrix compressive failure $(\hat{\sigma}_{22} + \hat{\sigma}_{33} \leq 0)$:

$$F_m^c = \left(\frac{Y_C^2}{4S_{12}^2} - 1\right)\left(\frac{\sigma_{22} + \sigma_{33}}{Y_C}\right) + \frac{(\sigma_{22} + \sigma_{33})^2}{4S_{23}^2} + \frac{\tau_{12}^2 + \tau_{13}^2}{4S_{12}^2} + \frac{\tau_{23}^2 - \sigma_{22}\sigma_{33}}{S_{23}^2} = 1 \quad d_m^c = 1 \tag{9.8}$$

An element is deleted when the fibre fail in tension $d_f^t = 1$.

9. 2. 2. Modelling

The complete length of the composite tube (220 mm) was modelled with solid three-dimensional stress-displacement continuum elements (C3D8R - a node linear brick with reduced integration and hourglass control). As mentioned earlier, the modelling of triggering type 1 (45° chamfering) with solid elements is straight forward and can be directly modelled using solid elements (refer Figure 9-1(a) and (b)). The used size of the solid element was 3 mm. In order to reduce the computation time the impactor and bottom crushing plate were modelled as analytical rigid surfaces (refer Figure 9-1(b)). An impactor mass of 68.85 kg was assigned to the centre of the top analytical rigid surface. The corresponding material section and its orientation (0° - along the axis of the tube) were assigned to the solid elements.

9. 2. 3. Adopted boundary conditions and contact controls

During the experimental testing, the non-triggered end of the composite tube was glued to the bottom end of the impactor due to easier alignment [5]. To simulate the same experimental condition, the non-triggered end of the tube was attached to the top analytical rigid body using "*tie*" constraints. To simulate the axial impact load only in vertical direction, apart from the vertical translation, all degrees of freedom of the top analytical rigid body were constrained. Furthermore, the initial impact

velocity was assigned to the top analytical rigid body. To represent the fixed crushing plate at the bottom, all the degrees of freedom of the bottom rigid body were also constrained. The "*surface-to-surface*" master-slave contact algorithm was established between the bottom rigid analytical surface and the composite tube with the friction coefficient equal to 0.2. In addition to that a self contact algorithm was also used for solid elements.

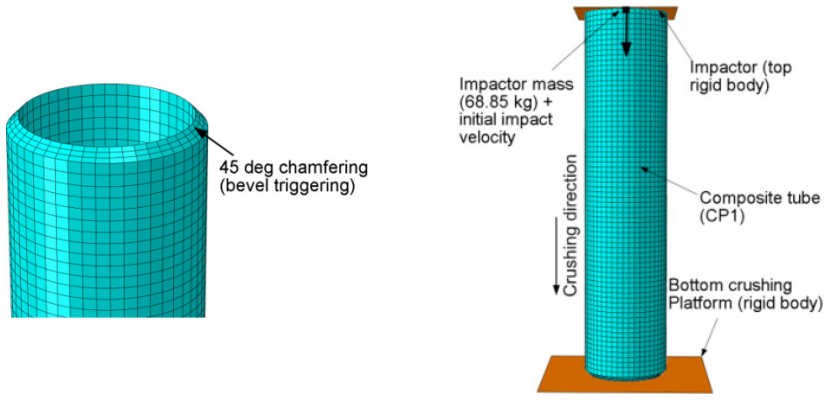

(a) **(b)**

Figure 9-1: (a) Triggering 1 profile with solid elements (45° chamfering). **(b)** Finite element model of CP1 tube

9. 2. 4. Results

The analysis was carried out for all cases of tube series involving CP1 (circular cross-sectional glass polyester composite tube with triggering type 1), CP2 (circular cross-sectional glass polyester composite tube with triggering type 2), SP1 (square cross-sectional glass polyester composite tube with triggering type 1) and SP2 (square cross-sectional glass polyester composite tube with triggering type 2) with three impact velocities (9.3 m/s, 12.4 m/s and 14 m/s). However, due to the similarity in approach, the results are discussed only for CP1 tube with an initial impact velocity of 9.3 m/s. The deformation and the corresponding reaction force of the tube were measured from the top analytical rigid surface. As an example, the sequence of the deformation patterns of CP1 tube is shown in Figure 9-2 and the corresponding force-deformation curve is presented in Figure 9-3. The deformation patterns are completely different from the experimental results. One of the reasons is that the delamination failure was not captured in the model because of using only solid elements.

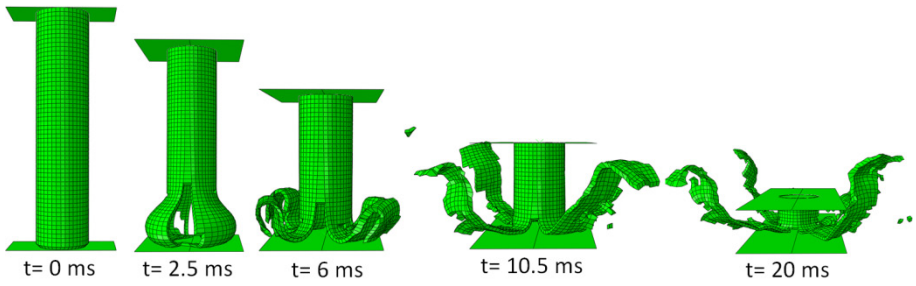

Figure 9-2: Deformation patterns of CP1 composite tube for an initial impact velocity of 9.13 m/s.

The initial crushing stages of the composite tube showed that the axial cracks were formed and propagated along the length of the tube. Due to this the composite tube crushed completely. Furthermore, the load-deformation curve was completely different from the experimental results. The predicted peak crush load of 35.5 kN was approximately 50% lower than the experimental value of 69 kN. The mean crush load of this case was significantly lower (refer Figure 9-3). This was due to the removal of elements due to the axial cracks and the corresponding lower stiffness offered by the tube. Furthermore, due to a very high bending stiffness of the tube the folding radius of the petals was larger (refer Figure 9-2); and no evidence was found for the inner and outer petals. Hence, a few studies have also been conducted with increasing number of elements through the thickness of the tubes; the number of elements varied from a minimum of 3 to maximum of 10. However, the results from these analyses showed very similar results. Further mesh convergence study from the element size 2 mm to 5 mm showed similar results.

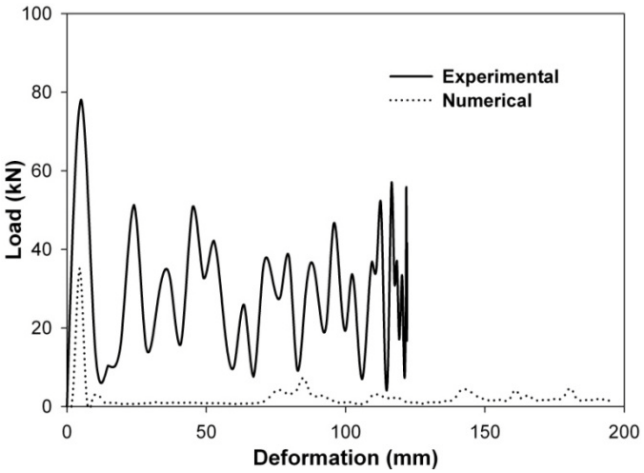

Figure 9-3: Force-deformation curve of CP1 composite tube for an initial impact velocity of 9.13 m/s

9. 3. Numerical study with cohesive and solid elements

9. 3. 1. Modelling

The results from the numerical simulations using only solid elements do not correlate with the experimental results. Nevertheless, further simulations were carried out including the delamination in the numerical models. The numerical simulation of the delamination phenomenon is normally performed by the virtual crack closure technique or using cohesive elements. Using the former approach, the energy release rate can be found from the nodal displacements and the nodal forces at the crack front. However, this method is very sensitive to the mesh refinement. Hence, in this work the cohesive elements approach was used to model the delamination between the plies. The experimental results provided evidence of circumferential (multiple) delaminations; with the major delamination taking place at the mid of the tube thickness. Hence, the thickness of the tube was divided into two equal thicknesses which represented the outer and inner sub laminate. Subsequently, they were modelled with solid elements. To model the delamination between the outer and inner sub laminates, a layer of zero thickness solid cohesive elements was added in between the outer and inner solid layers. Similar to the previous case the used element size for all layers was 3 mm. The details of the cohesive element are discussed in subsequent sections.

9. 3. 2. Cohesive elements

The details of the cohesive elements and their constitutive response and the damage model used for this study are discussed in this and the subsequent section. Often, the cohesive elements have been used to model the interface bonding where the thickness can be considered zero. The constitutive response [4] of these elements is based on the fracture mechanics approach which considers the amount of energy required to create new fracture surfaces. The behaviour of the interface prior to initiation of damage is often described as linear elastic in terms of a penalty stiffness that degrades under tensile and shear loading. However, the behaviour of these elements is unaffected by pure compression. In order to handle the complex contact conditions between the two (outer and inner) solid layers, a cohesive layer was modelled with zero thickness solid elements COH3D8 (cohesive; three dimensional element with 8 nodes). The traction-separation constitutive response was used which ensures that nominal strains are equal to the relative separation displacement of the cohesive layer. The elastic behaviour is assigned in terms of an elastic constitutive matrix that relates the nominal stresses to the nominal strains across the interface. The nominal stresses are the force components divided by the original area at each integration point, while the nominal strains are the separations divided by the

original thickness at each integration point. The nominal traction stress vector,*" t"*, consists of three components t_n (normal component), t_s and t_t (shear components). The corresponding separations are denoted by δ_n, δ_s and δ_t. Considering T_0 the original thickness of the cohesive element, the nominal strains and the elastic behaviour can be written as Equation (9.9) and (9.10).

$$\varepsilon_n = \frac{\delta_n}{T_0},\ \varepsilon_s = \frac{\delta_s}{T_0},\ \varepsilon_t = \frac{\delta_t}{T_0} \tag{9.9}$$

$$t = \begin{Bmatrix} t_n \\ t_s \\ t_t \end{Bmatrix} = \begin{bmatrix} K_{nn} & K_{ns} & K_{nt} \\ K_{ns} & K_{ss} & K_{st} \\ K_{nt} & K_{st} & K_{tt} \end{bmatrix} \begin{Bmatrix} \varepsilon_n \\ \varepsilon_s \\ \varepsilon_t \end{Bmatrix} = K\varepsilon \tag{9.10}$$

9. 3. 3. Damage model used

The general framework of the damage model using traction-separation consists of three ingredients: a damage initiation criterion, a damage evolution law (the rate at which the material stiffness is degraded once the damage initiation criterion is reached) and, finally, the choice of the element removal upon reaching a completely damaged state. The damage initiation refers to the beginning of the degradation of the response at any point in the material. In this work, the process of degradation was assumed to occur when a quadratic function involving the nominal stress ratios reaches the value of one (Equation (9.11)). The Macaulay brackets indicate that the stress state is not valid for pure compressive deformation.

$$\left\{\frac{\langle t_n \rangle}{t_n^0}\right\}^2 + \left\{\frac{t_s}{t_s^0}\right\}^2 + \left\{\frac{t_t}{t_t^0}\right\}^2 = 1 \tag{9.11}$$

A typical mode-independent traction-separation with linear softening response was used for this study. As shown in Figure 9-4, the evolution of the damage can be defined either by the dissipated energy (G_c) due to failure or effective displacement at the failure initiation $(\delta_n^0, \delta_s^0, \delta_t^0)$ and at complete failure state $(\delta_n^f, \delta_s^f, \delta_t^f)$. A scalar damage variable "*D*" captures the overall damage in the material. The initial value of "D" is "0". After the initiation of the damage, the value of "D" can evolve up to 1.0, due to further increase of the loading. During the damage process, the stress components can be calculated from the following relations,

$$t_s = \begin{cases} (1-D)\bar{t}_{n,} & \text{if } \ \bar{t}_n \geq 0 \\ \bar{t}_n & \text{otherwise} \end{cases} \tag{9.12}$$

$$t_s = (1-D)\bar{t}_s \tag{9.13}$$

$$t_t = (1-D)\bar{t}_t \tag{9.14}$$

where $\bar{t}_n, \bar{t}_s$ and $\bar{t}_t$ are the stress components calculated by the elastic traction-separation behaviour for the current strains without damage. For the cohesive elements modelling (linear softening response), the properties of polyester resin were considered (refer Table 9-2).

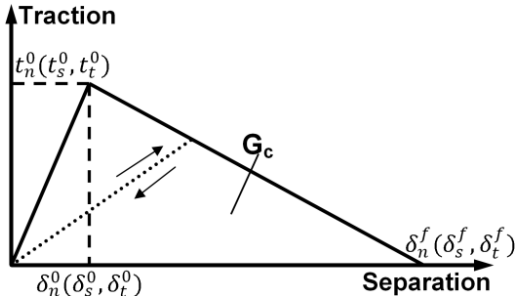

Figure 9-4: Traction-separation with linear softening response.

9. 3. 4. Adopted contact algorithm and boundary conditions

The "*tie*" constraint involving "*surface to surface*" discretization method was used to represent the outer solid layer, solid cohesive layer and the inner solid layer as a single entity. The contact algorithm of the tied connection performs the following functions during the analysis. At the time of initial calculation, the matching nodes and the adjacent elements are identified. Then, during the deformation, the matching pairs are constrained to move relative to each other based on the linear elastic and damage displacement law. The same size of element was chosen for inner solid, outer solid and the solid cohesive layer to ensure a straightforward connection between the master solid elements and the slave cohesive elements (refer Figure 9-5). Similar to the earlier approach (only solid elements case) the "*surface to surface*" contact algorithm was used for outer, inner and cohesive layer elements to the bottom analytical rigid surface. In addition to that, the self contact algorithm was also used for all the layers of elements.

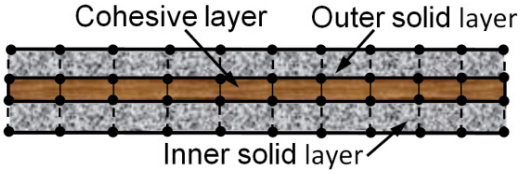

Figure 9-5: Tied connection between the solid layers and a cohesive layer.

9. 3. 5. Results

The computation time for this approach was larger than the previous case. The progressive deformation patterns for the composite tube CP1 is shown in Figure 9-6. Due to the use of cohesive elements a clear evidence for the central circumferential delamination was noticed at the mid-thickness of the tube. Furthermore, the axial cracks were formed at the inner and outer solid layers (refer Figure 9-6). However, the axial cracks on the outer and inner layers propagated along the tube length before contact with the crushing platform (refer Figure 9-6). Furthermore, the folding of the inner layer towards the axis of the tube was completely different from the experimental results. Due to a very high bending stiffness of the solid elements a kind of buckling was observed for the inner solid petals.

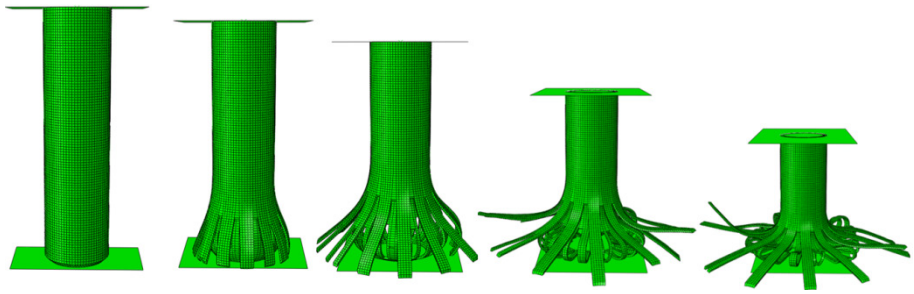

Figure 9-6: Deformation patterns of CP1 composite tube for an initial impact velocity of 9.13 m/s.

Because of the above phenomena the calculated load-deformation history from this case was very similar to the previous case (Figure 9-3). The number of solid layers was increased from 2 to 6 and the corresponding cohesive layers were increased from 1 to 5. However, the results from these studies showed no significant difference with the previous results.

9. 3. 6. Conclusions

In this section, a numerical study using solid elements was presented to predict the energy absorption characteristics and the corresponding failure patterns of composite tubes. The results from the circular cross-sectional pultruded profiles made of glass-polyester were presented. Apart from the general conclusion of the energy absorption of different profiles, the numerical modelling was focused to get the reasonable peak crush loads, energy absorption and the corresponding failure patterns of composite tubes. The importance of the delamination modelling on the energy absorption, peak crush load and the failure patterns is also studied using cohesive elements. From the conducted numerical simulations the following conclusions can be made: the deformation patterns of the composite tubes from the

used approaches (only solid elements and solid elements with cohesive elements) were different from the experimental results. The main reason for this difference was sudden propagation of axial cracks and different folding pattern of the inner petals. Because of a very high bending stiffness, the inner petals did not fold completely as like the experimental case. Furthermore, due to this very high bending stiffness of the elements and consequent stress concentration the elements were failed rapidly. As a result, the predicted load-deformation history from the numerical simulations was entirely different from the experimental results. Due to the above facts many researchers have adopted shell elements to predict the energy absorption of the composite tubes [6-8]. Although the problem of modelling the triggering type 1 geometry (45° chamfering at one end of the tube or bevel triggering) remains, it was decided to continue with the shell elements for further investigations.

9. 4. Numerical study with shell elements

As seen from the literature review of composite tubes (Chapter 7), most of the published models in the literature use a single layer of shell elements and solid elements. However, this approach will not predict the correct peak crush load and the corresponding crushing parameters. In order to prove this point similar to the approaches handled in the literature a single layer shell elements case is investigated. The results from the numerical models are compared with the experimental results.

9. 4. 1. Continuum damage model for shell composite laminates

For plane stress shell elements, the undamaged orthotropic plane stress material response was specified directly by the elastic stiffness matrix which is given in Table 9-1. The damage initiation criteria have the following forms [1, 4],

Fibre tension $(\hat{\sigma}_{11} \geq 0)$:

$$F_f^t = \left(\frac{\hat{\sigma}_{11}}{X_T}\right)^2 + \alpha\left(\frac{\hat{\tau}_{12}}{S_L}\right)^2 \tag{9.15}$$

Fibre compression $(\hat{\sigma}_{11} \leq 0)$:

$$F_f^c = \left(\frac{\hat{\sigma}_{11}}{X_C}\right)^2 \tag{9.16}$$

Matrix tension $(\hat{\sigma}_{22} \geq 0)$:

$$F_m^t = \left(\frac{\hat{\sigma}_{22}}{Y_T}\right)^2 + \left(\frac{\hat{\tau}_{12}}{S_L}\right)^2 \tag{9.17}$$

Matrix compression $(\hat{\sigma}_{22} \le 0)$:

$$F_m^c = \left(\frac{\hat{\sigma}_{22}}{2S_T}\right)^2 + \left[\left(\frac{Y_C}{2S_T}\right)^2 - 1\right] \cdot \left(\frac{\hat{\sigma}_{22}}{Y_C}\right) + \left(\frac{\hat{\tau}_{12}}{S_L}\right)^2 \tag{9.18}$$

In Equation (9.15), α is a coefficient that determines the contribution of the shear stress to the fibre tensile initiation criterion. The shear stress contribution was taken into account for the tensile failure, so the value of α was taken as 1. The $\hat{\sigma}_{11}$, $\hat{\sigma}_{22}$ and $\hat{\tau}_{12}$ are the components of the effective stress tensor. Then $\hat{\sigma}$ can be written as

$$\hat{\sigma} = M\sigma \tag{9.19}$$

where σ is the nominal stress and M is the damage operator, which can be written as

$$M = \begin{bmatrix} \frac{1}{(1-d_f)} & 0 & 0 \\ 0 & \frac{1}{(1-d_m)} & 0 \\ 0 & 0 & \frac{1}{(1-d_s)} \end{bmatrix} \tag{9.20}$$

d_f, d_m and d_s are the damage variables that characterize the fibre, matrix and shear damage which are derived from damage variables d_f^t, d_f^c, d_m^t and d_m^c corresponding to the four failure modes previously discussed (Equation (9.15) to (9.18)) as follows

$$d_f = \begin{cases} d_f^t & \text{if} \quad \hat{\sigma}_{11} \ge 0 \\ d_f^c & \text{if} \quad \hat{\sigma}_{11} < 0 \end{cases} \tag{9.21}$$

$$d_f = \begin{cases} d_m^t & \text{if} \quad \hat{\sigma}_{22} \ge 0 \\ d_m^c & \text{if} \quad \hat{\sigma}_{22} < 0 \end{cases}$$

$$d_s = 1-(1-d_f^t)(1-d_f^c)(1-d_m^t)(1-d_m^c)$$

Prior to any damage initiation the damage operator, M, is equal to the identity matrix. Once the damage occurs at any material point for at least one mode, the damage operator becomes significant in the criteria for damage initiation of other modes. The response of the material after damage initiation (describes the rate of degradation of the material stiffness once the initiation criterion is satisfied) is defined by the following equation

$$\sigma = C(d).\varepsilon \tag{9.22}$$

where C(d) is the damaged elasticity matrix and it can be written as (Equation (9.23)),

$$C(d)=\frac{1}{D}\begin{bmatrix}(1-d_f)E_1 & (1-d_f)(1-d_m)E_1 & 0\\ (1-d_f)(1-d_m)\upsilon_{12}E_2 & (1-d_m)E_2 & 0\\ 0 & 0 & D(1-d_s)G\end{bmatrix} \quad (9.23)$$

where $D=1-(1-d_f)(1-d_m)\upsilon_{12}\upsilon_{21}$; d_f reflects the current state of fibre damage, d_m reflects the current state of matrix damage, d_s reflects the current stage of shear damage, E_1 is the Young's modulus in the fibre direction, E_2 is the Young's modulus in the matrix direction, G is the shear modulus and υ_{12} and υ_{12} are Poisson's ratios.

In order to predict the correct energy absorption and the failure pattern, the numerical simulation should capture the micro-mechanical [9] and the macro-mechanical [10] failure mechanisms of a composite tube. However, as seen from previous sections capturing the above mechanism using solid elements is impossible. Hence, the different approaches of the numerical modelling to capture the above mechanisms were tried out using shell elements. The summary of the numerical approach and its results are discussed systematically from simple to complex models.

9. 4. 2. Case I – Simulation with a single layer of shell elements

Initially, a very basic model which consists of a single layer of shell elements was considered. The advantage of this approach is the reduced computation time. For both the circular and square cross-sectional tubes, the tube length of 220 mm was modelled with a single layer of meshed shell elements and that layer was located at the centre of the thickness of the composite tube. Similar to the earlier cases, the impactor and bottom crushing plate were modelled as analytical rigid surfaces. Very few quasi-static and impact numerical simulations [6, 11] have been conducted for the triggering type 1 using shell elements. To get the initial peak crushing force the accurate numerical modelling of triggering is very important. Most often the effect of the detailed modelling of triggering on the peak load is not discussed. As seen from the previous section, the modelling of triggering type 1 with solid elements is a straight forward and much more convenient solution than with shell elements. Normally the triggering type 1 is modelled with shell elements with gradually reduced thickness [6, 12] as shown in Figure 9-7(a) (Model A). However, this approach does not yield the correct geometry of the triggering geometry of the composite tube; rather it would yield a double chamfering triggering geometry (double bevel). To study the effect of triggering modelling, in addition to the Model A, one more possible modelling (Model B) was adopted where the shell elements are located as shown in Figure 9-7(b). The complete finite element models of CP1 and CP2 tubes are shown in Figure 9-8(a) and (b) respectively. The element size of 3 mm was chosen for all cases of the tube series. The effect of the size of element

(mesh sensitivity) on the numerical parameters such as peak crush load and the corresponding energy absorption is discussed in section 9. 10. For both the Model A and B, five elements with gradual reduction in thickness were placed vertically at the triggering portion of the tube. Unlike the triggering type 1, the triggering type 2 can be modelled with shell elements directly due to the constant thickness of the tulips (Figure 9-8b).

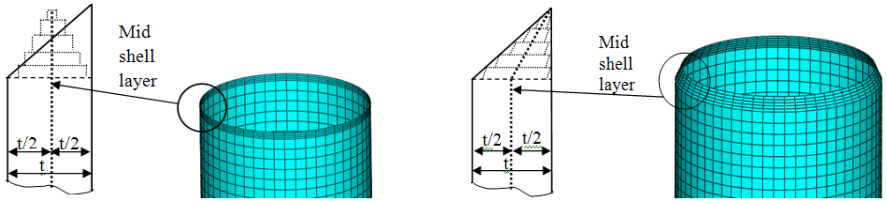

Figure 9-7:(a) Finite element modelling of triggering type 1- Model A. **(b)** Finite element modelling of triggering type 1- Model B.

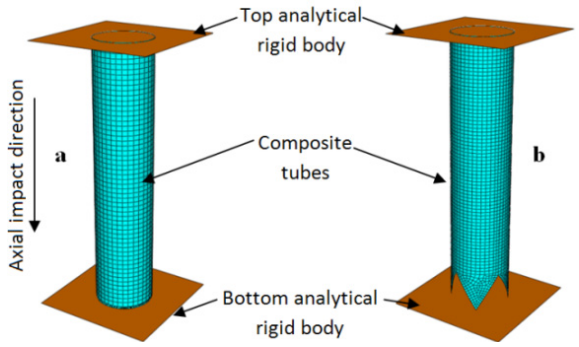

Figure 9-8: Finite element modelling with a single layer of shell elements **(a)** CP1 tube (Model A) **(b)** CP2 tube.

The adopted boundary conditions and the contact controls were the same as was discussed for solid elements approach.

9. 4. 3. Results

Due to the similarity in the results and similar to the earlier cases the results are discussed only for the initial impact velocity of 9.3 m/s. The results (deformation patterns and the force-deformation curves) obtained from the finite element analysis of the composite tubes are presented on the basis of triggering classifications.

CP1 and SP1 tube series – triggering type 1

The sequence of deformation patterns of CP1 tubes at different time intervals for Model B is given in Figure 9-9(a). For both circular and square tubes, no significant difference in the deformation pattern was noticed between the Models A and B. However, the deformation pattern of these approaches was entirely different from the experimental deformation pattern. For all three impact velocities of CP1 tubes, the simulation exhibited a local wall buckling failure mode followed by progressive end collapse (refer Figure 9-9(a)). For the CP1 tube, the peak crushing load of the Model A shows a higher value compared to Model B (refer Figure 9-10(a)). However, in the case of square tube, both models yielded approximately the same value (refer Figure 9-10(b)). In all cases, the deformation length obtained from the numerical analysis was less than the experimental results. This can be clearly noticed from Figure 9-10(a) and (b). Unlike the CP1 tube, the SP1 tube showed an unrealistic ductile deformation that resulted in end crushing and global wall buckling (Figure 9-9(b)). The maximum deformation of SP1 tube was 11 and 8 mm for Model A and B, respectively. From the above results, it can be concluded that both triggering modelling approaches (Model A and B) for CP1 and SP1 tubes were insufficient to capture the correct peak crushing load and the corresponding energy absorption. Furthermore, the numerical modelling with a single layer of shell elements was inadequate to capture the delamination phenomenon. The combined effect of these two phenomena (absence of delamination and inadequate triggering modelling) resulted far too high peak crush loads.

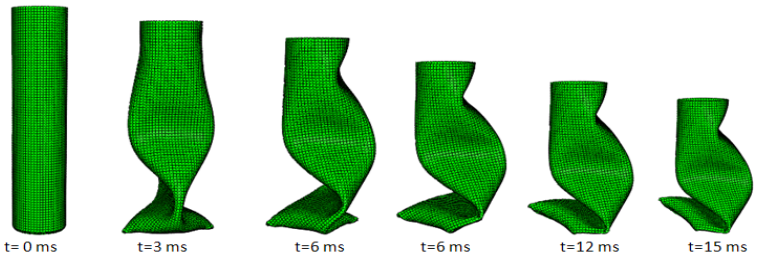

(a) CP1 tube with a single layer of shell elements – Model B

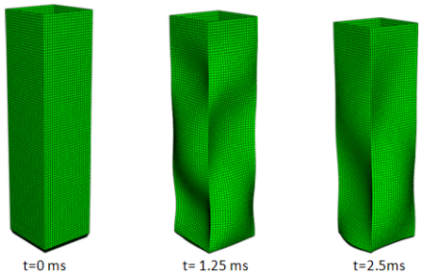

(b) SP1 tube with a single layer of shell elements

Figure 9-9: Deformation sequence of CP1 and SP1 tubes with a single layer of shell elements.

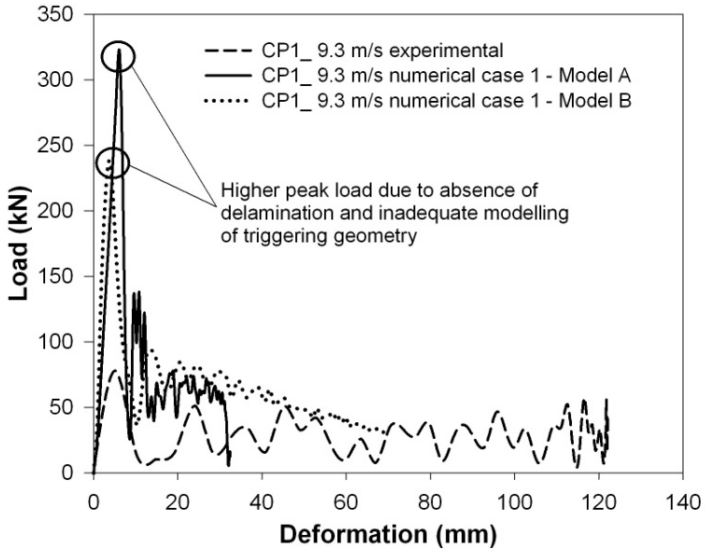

(a) CP1 tube with a single layer of shell elements

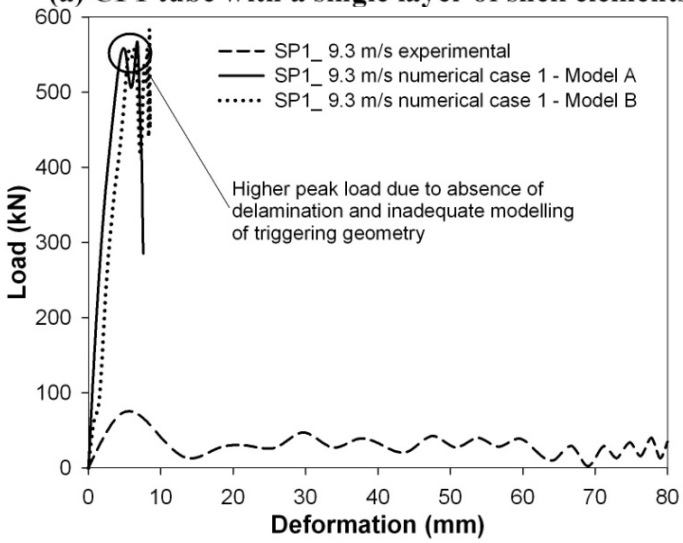

(b) SP1 tube with a single layer of shell elements

Figure 9-10: Comparison of load-deformation curve of CP1 and SP1 tubes with a single layer of shell elements.

CP2 and SP2 tube series – triggering type 2

The numerical crushing patterns of CP2 and SP2 showed that the tulips experienced the progressive folding at the initial time steps. The cross-sectional profile of the tube played a significant role on the tulip folding. In case of the circular tubes, due to the concave profile of the tulip the folding occurred towards the axis of the tube (Figure 9-11(a)) whereas the tulips of SP2 tube exhibited the outward folding (Figure 9-11(b)). However the total deformation lengths of both tube series were not comparable with the experimental values. Similar to the experimental results, the

triggering type 2 showed two peak loads; the first peak corresponded to the initial folding of the tulip and the second peak occurred during the deformation of the bottom end of the tulip portion of the tube. However, the magnitudes of these two peaks were higher than the experimental results (refer Figure 9-12(a) and (b)). This may be due to the fact that the models were not able to capture the delaminations which occurred at the edges and bottom end of the tulips of the composite tubes during the experimental testing [5]. For SP2 tube the magnitude of the initial peak was very high (Figure 9-12 (b)). This is due to the perfect geometry and the corresponding mesh patterns of tulips. Further study on the effect of (imperfect) geometry on the initial peak is discussed in section 9. 10. Similar to CP1 series, the CP2 series also exhibited local wall buckling mode after the crushing of the tulip pattern. The difference in the dissipated energy between the experimental and numerical results was due to the absence of the delamination phenomena. Unlike CP2 tube, there was no local buckling observed in case of SP2 tube. The maximum deformation of the tube was observed till the end of the tulips.

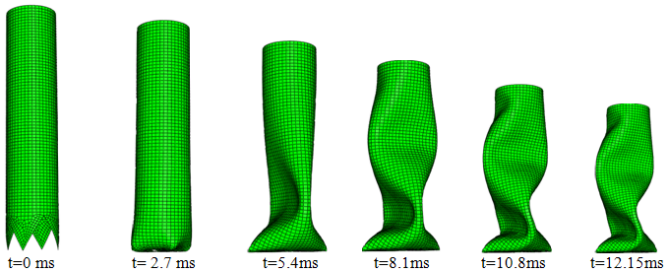

(a) CP2 tube with a single layer of shell elements.

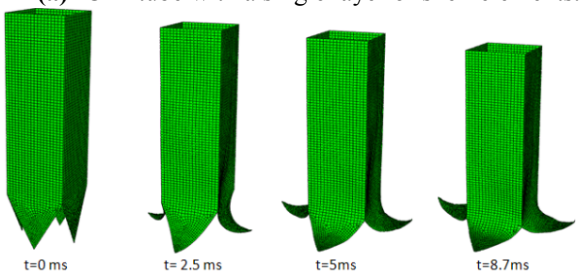

(b) SP2 tube with a single layer of shell elements.

Figure 9-11: Deformation sequence of CP2 and SP2 tubes with a single layer of shell elements.

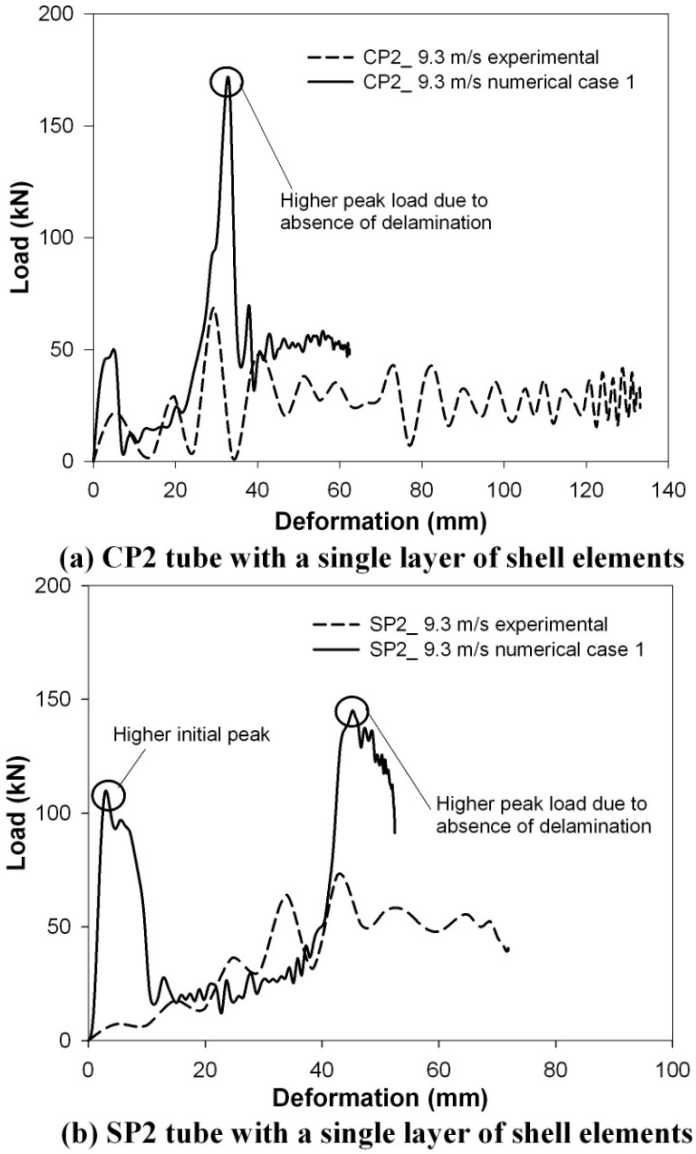

Figure 9-12: Comparison of load-deformation curve of CP2 and SP2 tubes with a single layer of shell elements.

9. 5. Case 2 - Two layers of shell elements with cohesive elements

9. 5. 1. Modelling

The modelling details and the corresponding boundary and contact conditions of this case were very similar to the one which was discussed in section 9. 3. for solid elements. Similar to Case 1, an attempt was made to model the correct geometry of triggering type 1. Two approaches (Model C and D) have been adopted and the

details of the numerical modelling are shown in Figure 9-13(a) and (b). However, for the triggering type 2, the triggering geometry can be directly captured due to the constant thickness of the tulip.

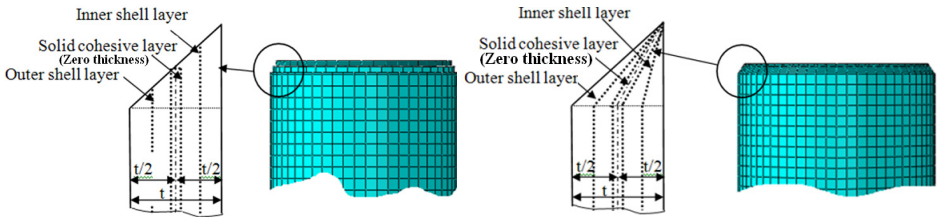

(a) Model C **(b)** Model D

Figure 9-13: Finite element modelling of CP1 tube with two layers of shell elements and a solid cohesive layer.

9. 5. 2. Results

CP1 and SP1 tube series – triggering type 1

For CP1 both SP1, the Model C and D were tried out for the initial impact velocity of 9.3 m/s. Similar to the results of Case 1, there was no significant difference in the deformation pattern noticed between Model C and D. Though the delamination was captured between the outer and inner shell layers due to the cohesive elements, the deformation pattern was very similar to the results of the single layer of shell elements. Both tubes (CP1 and SP1) exhibited the local wall buckling mode followed by the progressive end crushing. As an example the CP1 tube is shown in Figure 9-14. For CP1 tube, the two approaches of triggering modelling yielded much higher peak crushing loads (248 and 217 kN for Model C and D respectively) than the experimental value of 78 kN. The Model A and B of Case 1 for SP1 yielded the same value of peak crushing load. Hence, for SP1 tube the numerical analysis was carried out only for Model D. The magnitude of the peak loads (Figure 9-15(a) and (b)) showed that the finite element modelling of the triggering was not adequate to capture the delamination process and so the correct peak crushing loads. The comparison of the mean crush load and the corresponding energy absorption for all cases are given in Table 9-3.

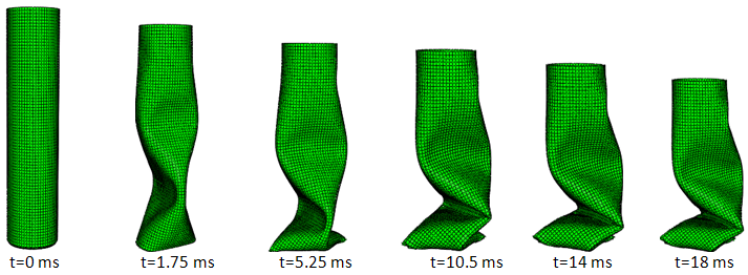

Figure 9-14: Deformation sequence of CP1 tube with two layers of shell elements and a solid cohesive layer.

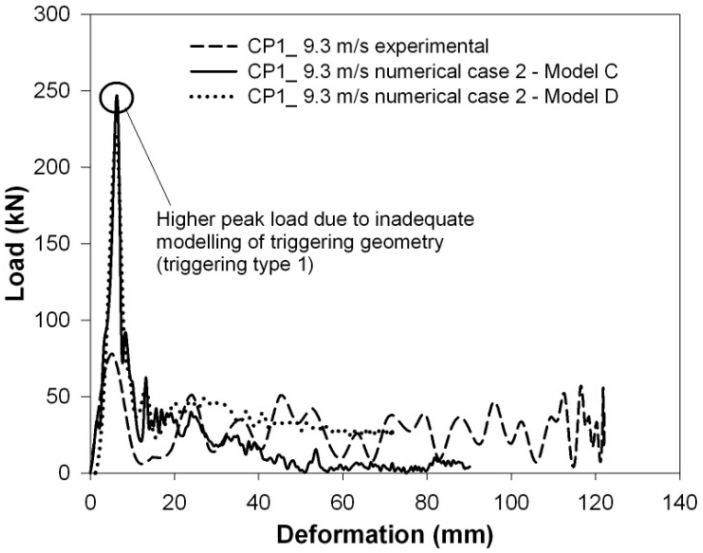

(a) CP1 tube with two layers of shell elements and a solid cohesive layer

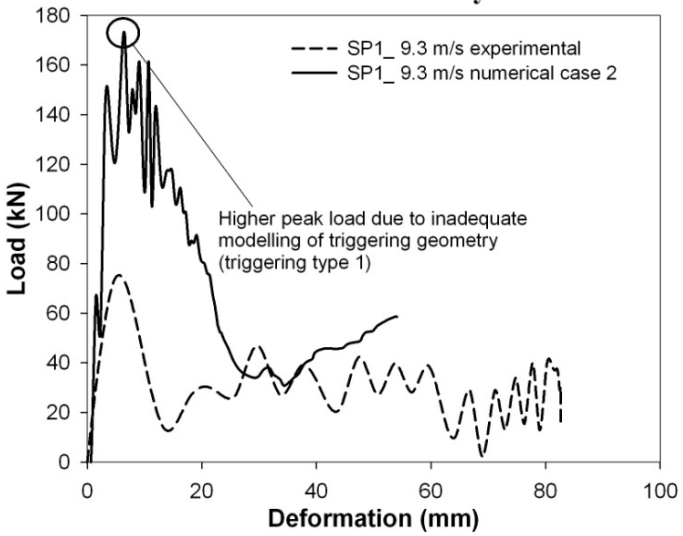

(b) SP1 tube with two layers of shell elements and a solid cohesive layer

Figure 9-15: Comparison of load-deformation curve of CP1 and SP1 tubes with two layers of shell elements and a solid cohesive layer.

CP2 and SP2 tube series – triggering type 2

The deformation sequence of CP2 and SP2 tubes are shown in Figure 9-16(a) and Figure 9-16(b) respectively. Figure 9-17(a) and (b) also show the corresponding energy absorption comparison with the experimental results. The initial increments of CP2 and SP2 tube series showed that the inner and the outer shell layer were subjected to delamination which separated both the outer and inner materials.

However, the later stages of these two tubes provided no clear separation of inner and outer materials; rather it showed the progressive end crushing of the tubes.

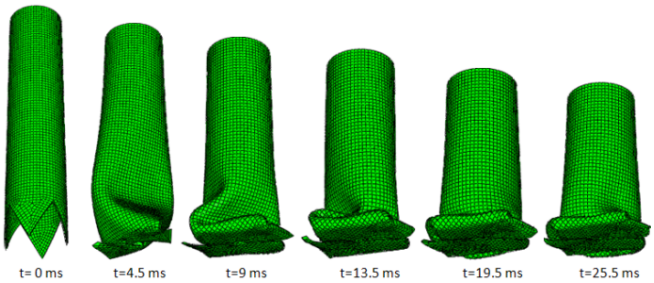

(a) CP2 tube with two layers of shell elements and a solid cohesive layer

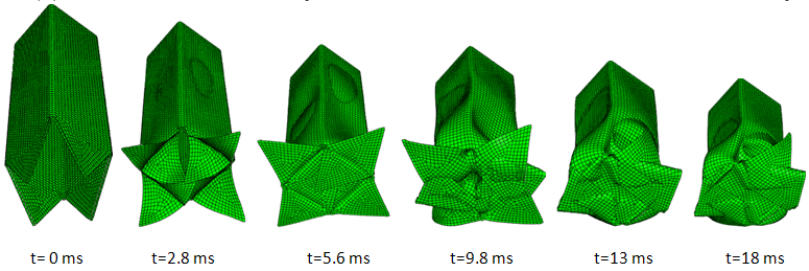

(b) SP2 tube with two layers of shell elements and a solid cohesive layer

Figure 9-16: Deformation sequence of CP2 and SP2 tube with two layers of shell elements and a solid cohesive layer.

Similar to the experimental results both the tube series showed two peaks; the magnitude of the peak crushing force was approximately 20% higher than the experimental result. However, these magnitudes are much lower than results from Case 1 (a single layer of shell elements approach). The difference in the experimental and numerical values is shown in Table 9-3. The average experimental deformation length of CP2 was approximately 20 mm higher than the numerical value. On the contrary the numerically predicted deformation length of SP2 tube was 13 mm higher than the experimental result. The mean crush force of CP2 tube showed the satisfactory result which can be noticed from Figure 9-17(a). However the SP2 tube yielded a lower mean crush load than the experimental data (refer Table 9-3). Similar to Case 1, the magnitude of the initial peak was higher. The effect of geometric imperfection on the magnitude of the initial peak load is discussed in section 9. 10.

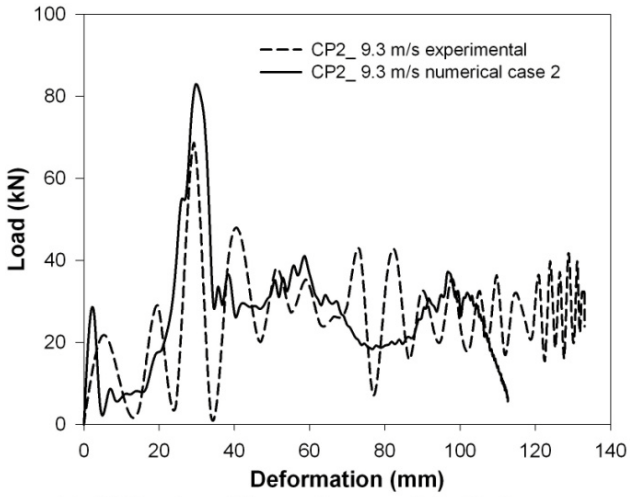

(a) CP2 tube with two layers of shell elements and a solid cohesive layer

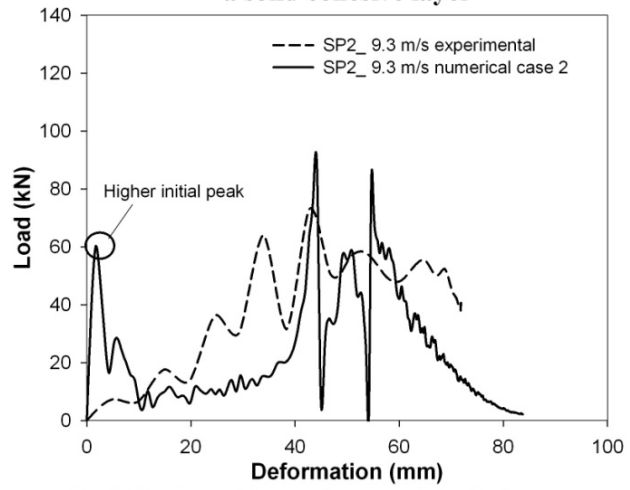

(b) SP2 tube with two layers of shell elements and a solid cohesive layer

Figure 9-17: Comparison of load-deformation curve of CP2 and SP2 tube with two layers of shell elements and a solid cohesive layer.

9. 6. Case 3 - Two layers of shell elements with cohesive elements and predefined seams

The previous sections dealt with the finite element modelling issues of triggering especially the triggering type 1 (45° chamfering around the edges of a composite tube) with a single and two layers of shell elements approach to predict the correct peak crush load and the corresponding energy absorption. Furthermore, it was also proved that the incorrect prediction of the peak crush load of a composite tube will provide an un-realistic deformation length and energy absorption. The approach of

two layers of shell elements with cohesive elements provided comparable peak and mean crush loads, deformation length and the corresponding energy absorption for the circular and square composite tubes with triggering type 2 (CP2 and SP2). The initial stages of these tubes exhibited a clear evidence of failure modes such as delamination, splitting of inner and outer plies and bending of plies. However, the later stages showed the buckling modes which were not similar to the experimental results. This was due to the reason that these models were inadequate to capture the axial cracks during crushing. Hence, an initial evaluation was made to study the effect of axial cracks on the deformation pattern of circular and square composite tubes for Case 2 (two layers of shell elements with cohesive elements). The axial cracks were modelled with pre-defined seams. Moreover, the effect of the number of pre-defined seams on the peak crushing load and the corresponding energy absorption of the composite tube series were also evaluated.

9. 6. 1. Modelling with seams

During the experimental crushing of a composite tube, the inner and outer petals were subjected to bending inside and outside of the tube followed by the circumferential delamination. The material splaying outwards flared into petals due to the phenomena of axial cracks and the material splaying inwards showed progressive folding without any petalling [5, 13, 14]. As a result, a considerable amount of energy was dissipated due to the axial cracks of the outer petals and significant amount of deceleration of the impactor was provided by the inner plies.

Seams

In order to simulate the axial cracks in the outer plies during the crushing process the seams were introduced at pre-defined locations in the outer shell layer of the composite tubes. A seam on the outer shell layer of the composite tube model defines an edge parallel to the axis of the tube that is originally closed; however, it can open during the analysis based on its assigned interface strength. During meshing, duplicate overlapping nodes are placed on the seam; these coincide nodes can break when the interface strength reaches its failure limit. In this analysis the matrix tensile strength was chosen as the interface strength between the nodes. Eventually, a seam pre-defines the surface along which the crack has to propagate. Creating duplicate nodes offers several advantages for fracture mechanics calculations. Using this approach the contour integral analysis and crack propagation analysis can be performed [1, 4]. Furthermore, this approach can be handled with a number of user defined variables (critical stress ahead of the crack tip, crack opening displacement etc). However, this work does not deal with the details of those analyses.

Table 9-3: Comparison of experimental and numerical simulation results.

Cases	**Peak crush load (kN) P_{max}**				**Mean crush load (kN) P_{mean}**				**Deformation length (mm) l_{max}**				**Absorbed energy (kJ) E_d**			
	CP1	**CP2**	**SP1**	**SP2**	**CP1**	**CP2**	**SP1**	**SP2**	**CP1**	**CP2**	**SP1**	**SP2**	**CP1**	**CP2**	**SP1**	**SP2**
Experimental	78	69	73	73	28.3	26.0	31.1	37.7	122	133	82.5	71	3.46	3.47	2.56	2.68
Numerical Case 1	238	165.8	554	145	-	47.7	-	56.0	-	62.3	-	52.5	-	2.99	-	2.97
Numerical Case 2	217	82.5	171	95	33.3	27.3	70.4	24.0	91	113	54	84	3.03	3.08	3.80	2.01
Numerical Case 3	103	67	139	81	24.6	19.0	35.9	25.5	98	125	70	90	2.41	2.30	2.51	2.30
Numerical Case 4	75	72	100	92	20.5	23.5	26.5	26.5	120	127	93	94	2.45	3.00	2.46	2.50
Numerical Case 5	82	64	95	69	25.7	24.3	43.3	24.9	130	140	70	98	3.34	3.40	3.03	2.46

A preliminary study on a composite tube using these seams showed that the peak crush load was affected by the introduction of seams. This was obvious, because the peak crush load of a composite tube with seams should be lower than the perfect composite tube. Hence, it is worth to investigate the effect of the number of pre-defined seams on the peak crush load of the composite tubes. During the experimental testing it was observed that the length of the axial cracks on the tubes was equivalent to the total length of deformation of the composite tubes [5]. However, before experimental testing the total deformation length of a composite tube for a particular initial impact velocity is unknown. Thus, the seams were introduced approximately for a length of 70 mm at the outer layer of the shell elements. Furthermore, the number of axial cracks differed for each CP tube series for the same impact velocity. Hence, the number of seams is varied from minimum 4 to a maximum of 16 for CP tube series. However, in case of the SP tube series during the experimental testing the axial cracks were formed only at the four corners of the tube due to the non-uniform geometry [5]. Hence for SP1 and SP2 tubes, the number of seams was restricted to 4 at the corners. The finite element modelling of the CP1 and SP2 tubes with predefined seams are shown in Figure 9-18. As explained in the previous sections, for CP1 tube, the Model D yielded a smaller peak crushing load than Model C. Hence, the approach of the introduction of pre-defined seam was carried out only for Model D for both CP1 and SP1 tubes.

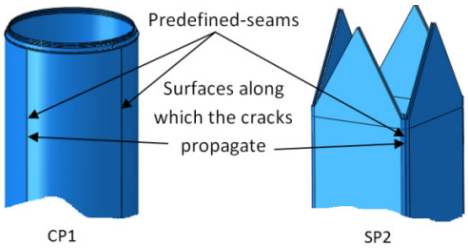

Figure 9-18: Finite element modelling of composite tubes with seams.

9. 6. 2. Results

CP1 and SP1 tube series – triggering type 1

The deformation pattern of CP1 tube with 16 seams on the outer shell layer (Figure 9-19(a)) and SP1 tube with 4 seams (Figure 9-19(b)) at the corners provided a clear evidence for the circumferential delamination which splits the outer and inner plies. Consequently, the axial cracks were formed along the axis of the tubes due to the predefined seams followed by the bending of inner and outer plies. The progressive folding of the inner layer towards the axis of the tube can be clearly noticed from Figure 9-19(a) and (b). Unlike the experimental results, the numerical results showed the complete splitting of outer layers at initial time steps. In case of circular tubes with triggering type 1 (CP1) and type 2 (CP2) there was no significant

difference in the failure pattern noticed for the same number of seams. Though the cohesive and seam element approach provided good results for the failure pattern, the predicted peak loads of both tube series CP1 and SP1 were higher than the experimental results due to inadequate triggering modelling (refer Figure 9-20(a) and Figure 9-20(b)). On the contrary the total length of deformation was less than the experimental results (98 and 70 mm against the experimental values 122 and 82.5 mm for CP1 and SP1 tubes respectively). The later stages of the CP1 tube exhibited the compression mode rather than uniform crushing. The comparison between the numerical and experimental results is given in Table 9-3.

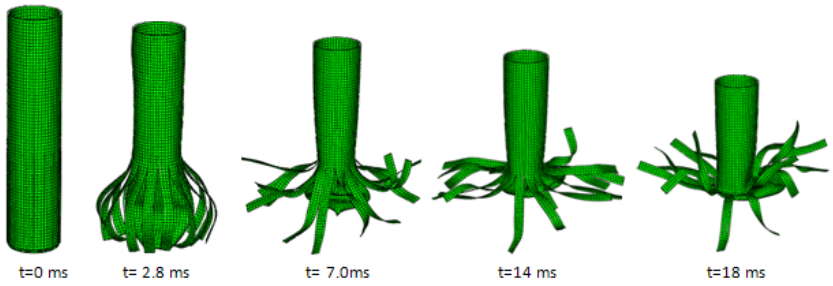

(a) CP1 tube with two layers of shell elements, a solid cohesive layer and pre-defined seams (16 nos).

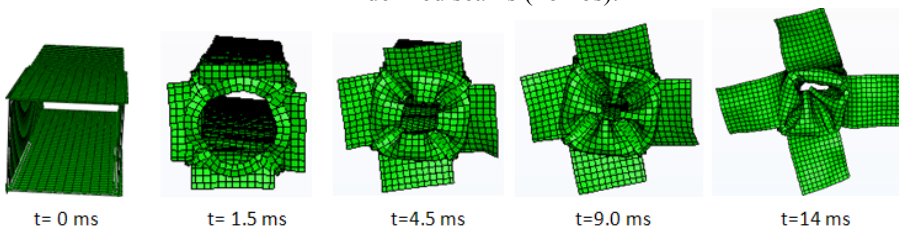

(b) SP1 tube with two layers of shell elements, a solid cohesive layer and pre-defined seams (4 nos).

Figure 9-19: Deformation sequence of CP1 and SP1 tubes with two layers of shell elements, a solid cohesive layer and pre-defined seams.

CP2 and SP2 tube series – triggering type 2

Similar to CP1 and SP1 tube series the delamination for CP2 and SP2 took place at the mid thickness of the tube due to the cohesive elements, the inner plies bent towards the centre line of the tube and outer plies bent towards the outside of tube. This can be noticed from the sequence of the deformation pattern of SP2 tube at different time intervals which is shown in Figure 9-21. There was a good correlation of peak crushing load and deformation length observed for CP2 tube (refer Figure 9-22(a)).

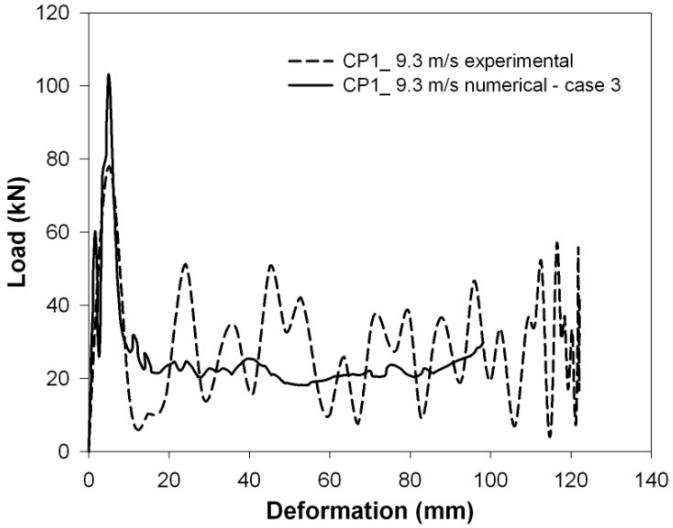

(a) CP1 tube with two layers of shell elements, a solid cohesive layer and pre-defined seams

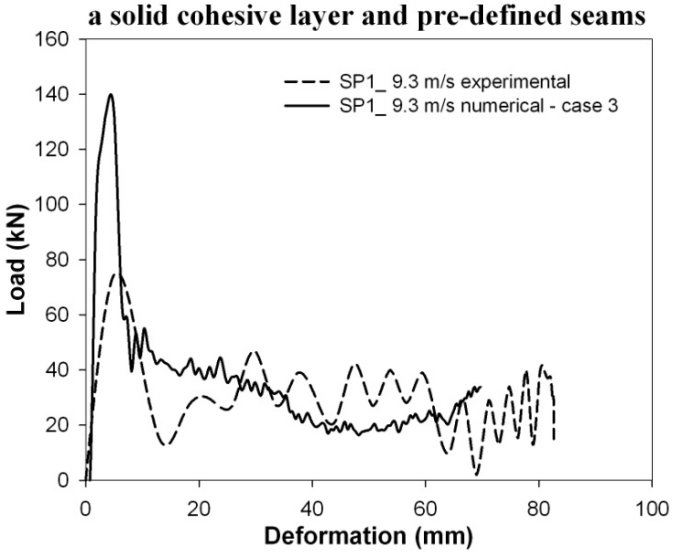

(b) SP1 tube with two layers of shell elements a solid cohesive layer and pre-defined seams

Figure 9-20: Comparison of load-deformation curve of CP1 and SP1 tubes with two layers of shell elements, a solid cohesive layer and pre-defined seams.

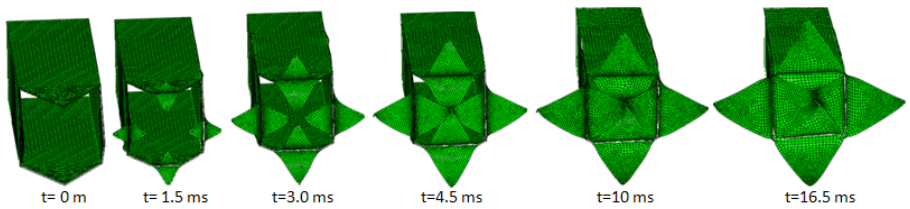

Figure 9-21: Deformation sequence of SP2 tube with two layers of shell elements, a solid cohesive layer and pre-defined seams.

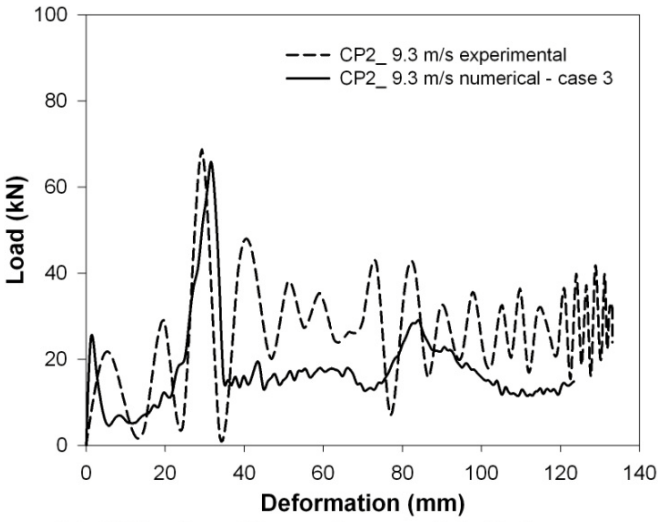

(a) CP2 tube with two layers of shell elements, a solid cohesive layer and pre-defined seams

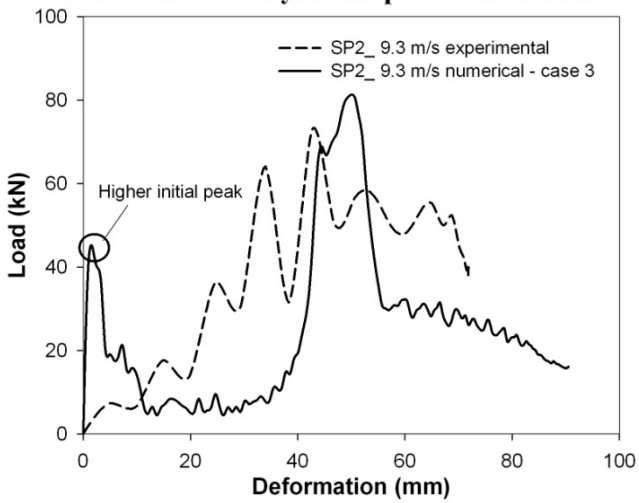

(b) SP2 tube with two layers of shell elements a solid cohesive layer and pre-defined seams

Figure 9-22: Comparison of load-deformation curve of CP2 and SP2 tubes with two layers of shell elements, a solid cohesive layer and pre-defined seams.

The numerical peak crushing load of SP2 was comparable with the experimental data; however, the slope of the curve to reach the peak crushing load was higher than the experimental data (refer Figure 9-22(b)). The initial peak crushing load corresponds to the phase at which the delamination takes place at the edges of the tulips. This can be noticed from the Figure 9-22(a) and (b) for CP2 and SP2 respectively. Though the peak crush load of SP2 tube was comparable with experimental values the magnitude of the initial peak was very high. This may be due to the perfect geometric shape of the tulips and the corresponding mesh pattern of the square tube. Further study on this phenomenon can be found in section 9. 10.

The mean crushing loads of tube series CP1, CP2 and SP2 were less than the experimental values. The higher peak crushing load of SP1 attributed to a higher mean crush load (refer Table 9-3). The differences in the energy absorption for all these cases are given in Table 9-3.

9. 7. Case 4 - Multiple layers of shell elements with cohesive elements and without seams

9. 7. 1. Modelling

The predicted peak crushing load from all the numerical simulations of two shell layers with cohesive elements was higher than the experimental values. This indicated that the numerical modelling of triggering, particularly for type 1 was insufficient to capture the accurate peak crush load. Moreover, during the experimental test in addition to the major circumferential delamination at the mid-thickness of the tube, multiple delaminations were observed in all sub-laminates during the bending of plies. This phenomenon significantly altered the bending stiffness of the plies [5, 13, 15]. Hence, the numerical modelling of the multiple delaminations is absolutely necessary to account for the energy dissipation in each ply which significantly contributes to the peak and mean crushing load of a composite tube. In order to isolate the effect of multiple delaminations on the energy absorption and deformation pattern, the thickness of the composite tubes was modelled with six layers of shell elements without seams. Accordingly the thickness of each shell layer was divided equally. Five layers of solid cohesive elements were placed in between the shell elements. The length of the inner most shell layer was 220 mm and the length of outer shells and cohesive layers were chosen to form the 45° edge chamfering. It can be noticed from the schematic representation (Figure 9-23) that the multiple layers of shell elements formed the correct geometry of the composite tube with triggering type 1. Similar to Case 3, the pure master-slave *"tied"* constraint was established between the shell layers and the solid cohesive layers. The element size of 3 mm was used for all the studies.

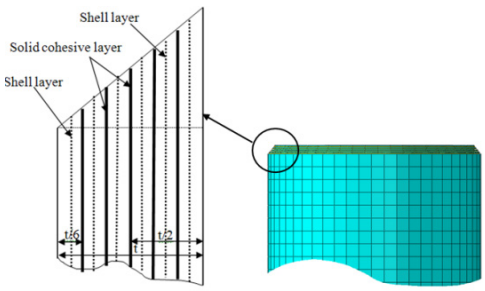

Figure 9-23: Finite element modelling of CP1 tube series with multiple layers of shell elements and solid cohesive layers.

9. 7. 2. Results

CP1 and SP1 tube series – triggering type 1

Due to the larger number of elements, the computation time was much larger than the previous cases. The deformation sequence of CP1 and SP1 tubes was very similar to Case 2 (initial progressive crushing at triggering location followed with local buckling). The numerical peak crushing load of the tube series CP1 was very close to the experimental results (Figure 9-24(a)). However, in the case of SP1 tube series there was a higher peak force (refer Figure 9-24(b)). The comparative study of the average crushing load and the energy absorption is given in Table 9-3. For the CP1 tube, the maximum deformation length of 120 mm was noted against the experimental value of 122 mm. In contrast to the CP1 tube, the SP1 tube exhibited more deformation length (94 mm) than the experimental value (82.5 mm).

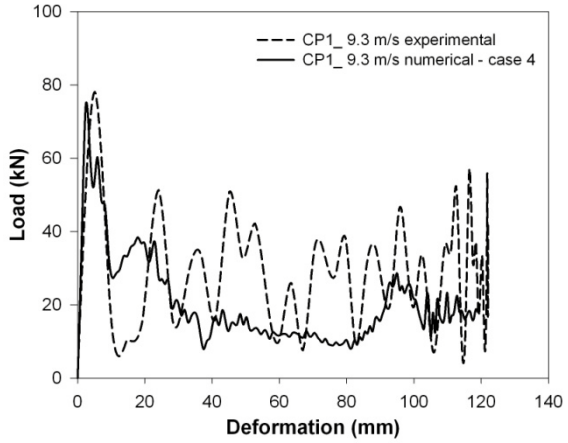

(a) CP1 tube with multiple layers of shell elements solid cohesive layers

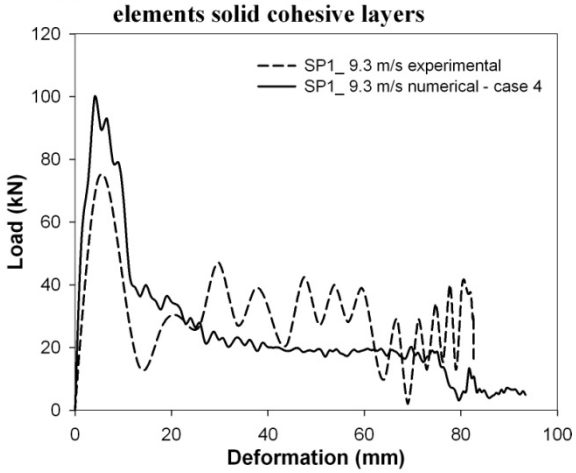

(b) SP1 tube with multiple layers of shell elements solid cohesive layers

Figure 9-24: Comparison of load-deformation curve of CP1 and SP1 tubes with multiple layers of shell elements and solid cohesive layers.

CP2 and SP2 tube series – triggering type 2

Though the numerical modelling of the two layers of shell elements with a solid cohesive layer (Case 2) captured the comparable peak crush load with the experimental results for triggering type 2 series, the deformation lengths of these types did not correlate well with the experimental data. Hence a numerical investigation was carried out with the multiple layers approach to study the deformation length and the corresponding energy absorption. The deformation pattern of CP2 and SP2 tube series at different time intervals are shown in Figure 9-25(a) and (b). The initial crushing stages of both tubes (CP2 and SP2) showed the clear evidence of delamination between the plies. In the later stages the tubes crushed progressively. The experimental crushing of the tubes showed that the axial cracks were formed in parallel with the bending of plies. However, in the numerical analysis there was no clear indication observed for the axial cracks. The same trend was observed for both cases of CP1 and SP1 tubes. In case of CP2 tube, there was a good correlation observed between the experimental and numerical results for the peak crushing load and the total deformation length (refer Figure 9-26(a)). However, the numerical peak crushing load and the total deformation of SP2 were higher than the experimental values (refer Figure 9-26(b)). Furthermore, the slope to reach the peak load was higher compared to the experimental data. This may be due to the reduced stiffness offered by the outer shell layers at the initial time increments. Similar to the Case 3, there was an initial peak observed before reaching the peak crush load. This phenomenon is explained in section 9. 10. which deals with initial geometric imperfection.

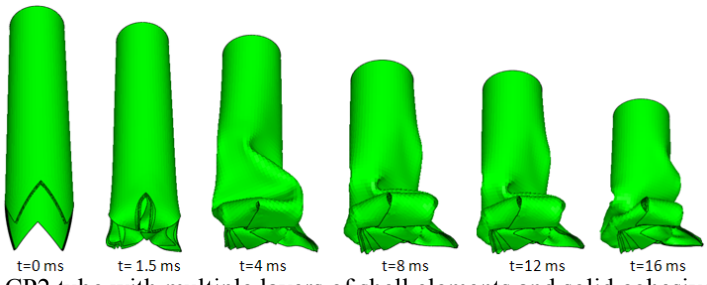

(a) CP2 tube with multiple layers of shell elements and solid cohesive layers

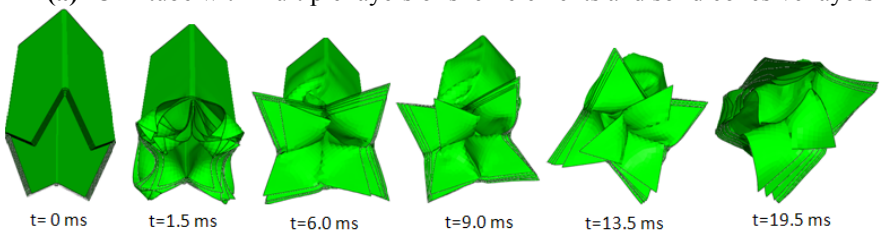

(b) SP2 tube with multiple layers of shell elements and solid cohesive layers.

Figure 9-25: Deformation sequence of CP2 and SP2 tubes with multiple layers of shell elements and solid cohesive layers.

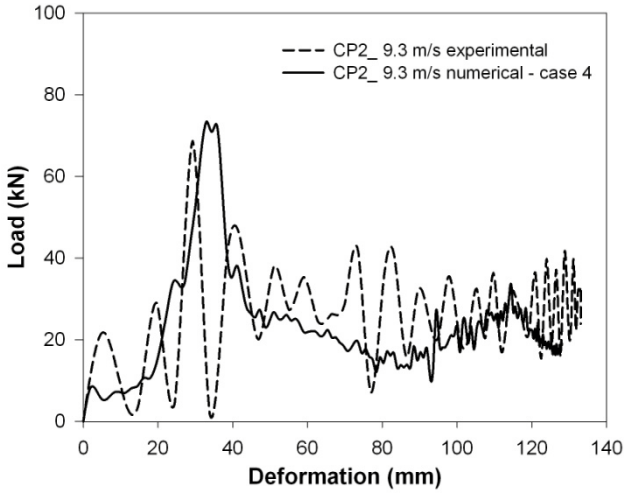

(a) CP2 tube with multiple layers of shell elements solid cohesive layers

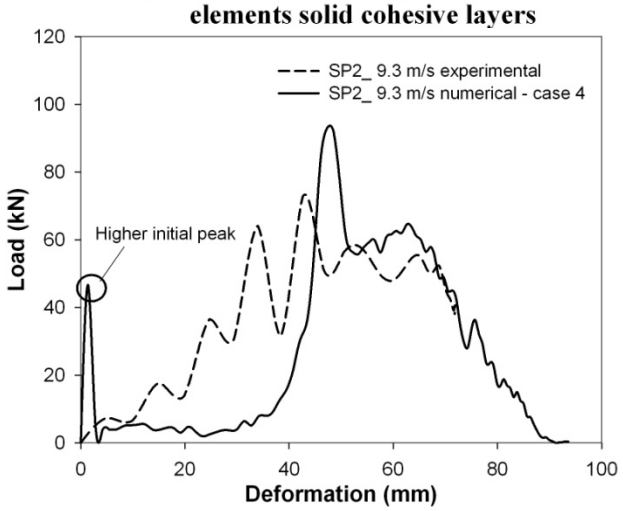

(b) SP2 tube with multiple layers of shell elements solid cohesive layers

Figure 9-26: Comparison of force-deformation curve of CP2 and SP2 tubes with multiple layers of shell elements and solid cohesive layers.

9. 8. Case 5 – Multiple layers of shell elements with cohesive elements and seams

9. 8. 1. Modelling

In order to achieve the correct peak crush load (especially for triggering type 1) with the multiple delaminations and to achieve the typical failure patterns of the composite tubes, the approach of multiple layers of shell elements with the combination of cohesive elements and seams was investigated. The number of shell

layers (six) was divided into half and the seams were assigned only to the outer shell layers.

9. 8. 2. Results

CP1 and SP1 tube series – triggering type 1

The deformation patterns of the CP1 tubes with 16 seams are shown in Figure 9-27(a). Due to the predefined seams the results of the initial time increments showed the complete splitting of the outer shell layers at the seams assigned locations, while the inner plies continued to fold inside. The later stages of the analysis gave a clear evidence of the bending of elements which belong to the outer shell layers. The numerical modelling approach with multiple layers of shell elements with cohesive elements and seams showed a very good correlation of the deformation patterns with the experimental results.

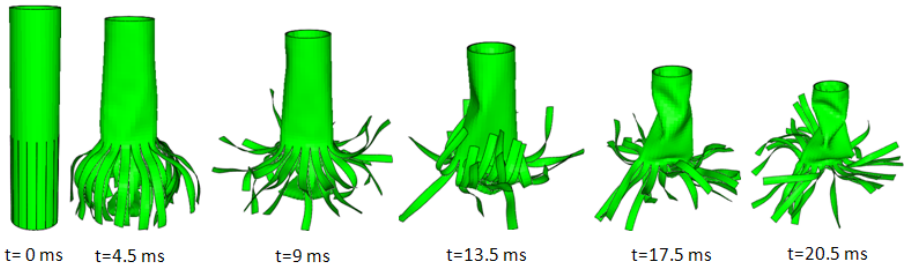

(a) CP1 tube with multiple layers of shell elements, solid cohesive layers and with 16 seams.

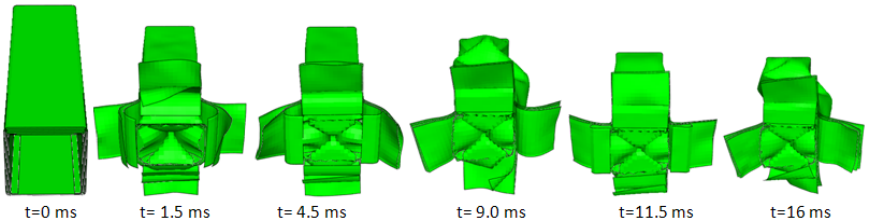

(b) SP1 tube with multiple layers of shell elements, solid cohesive layers and with 4 seams.

Figure 9-27: Deformation sequence of CP1 and SP1 tubes with multiple layers of shell elements, solid cohesive layers and pre-defined seams.

The effect of the number of predefined seams on the peak load was studied for CP1 tube. Two analyses were carried out with 8 and 16 seams for an impact velocity of 9.3 m/s. The corresponding force versus deformation histories of these two cases are presented in Figure 9-28(a). There was no significant difference in the magnitude of peak crush load observed between these two cases. However after 40 mm deformation length, a considerable difference in the mean load reduction was observed. The deformation pattern of SP1 tube at different time intervals is shown in Figure 9-28(b). Similar to CP1 tube, the SP1 tube also exhibited multiple

delaminations. The subsequent stages of SP1 tube showed that the inner plies were subjected to compression rather than uniform progressive folding. As a result the crushing force was increased considerably after attaining 50 mm of deformation length (refer Figure 9-28(b)). Consequently the total deformation length of the tube was lower compared to the Case 4 (70 mm against 93 mm).

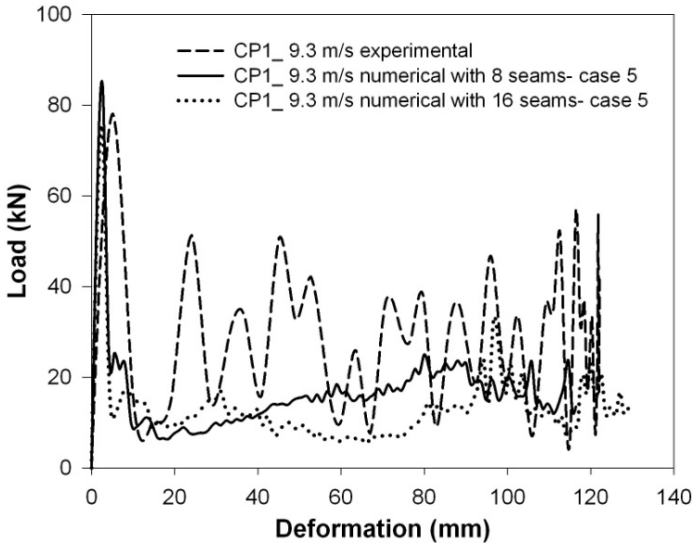

(a) CP1 tube with multiple layers of shell elements, solid cohesive layers and pre-defined seams

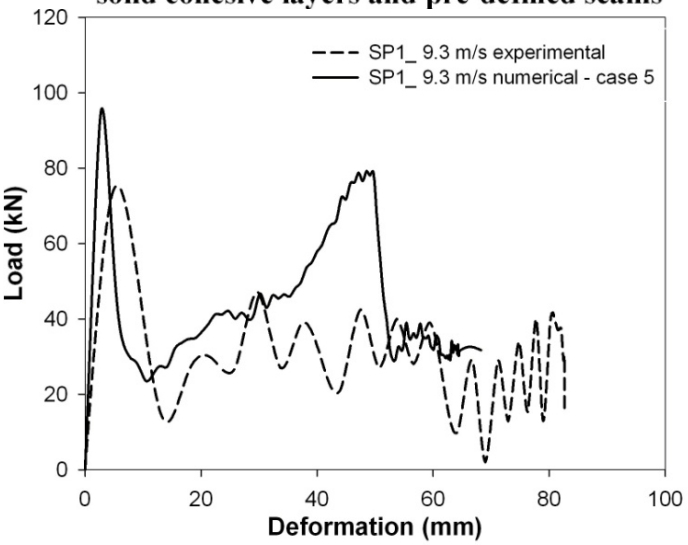

(b) SP1 tube with multiple layers of shell elements, solid cohesive layers and pre-defined seams

Figure 9-28: Comparison of load-deformation curve of CP1 and SP1 tubes with multiple layers of shell elements, solid cohesive layers and with pre-defined seams.

CP2 and SP2 tube series – triggering type 2

The experimental deformation pattern of the circular tubes (CP1 and CP2) yielded more than 10 major axial cracks along the axis of the tube. The effect of the number of seams on the peak crush load was studied with CP1 tube. To understand the deformation sequence in detail the CP2 tube was modelled only with 4 seams. The results of the numerical analysis at different time intervals are shown in Figure 9-29(a). Similar to the CP1 and SP1 series the initial stages of CP2 showed the clear evidence of the delaminations between all the shell layers. Consequently, the outer plies were subjected to outside bending and the inner materials bent inwards. This phenomenon can be well observed from Figure 9-29(a). The correlation of the experimental and the numerical results is shown in Figure 9-30(a). Similarly, the deformation pattern of SP2 tube at different time intervals showed the clear indication of all typical failure modes of a brittle composite tube (refer Figure 9-30(b)). As discussed earlier, the number of seams for SP2 tube was restricted to only 4 at the corners of the tube. For SP2, similar to Case 3 and 4, a delay in the peak crushing load and an initial peak crush load were observed (refer Figure 9-30(b)).

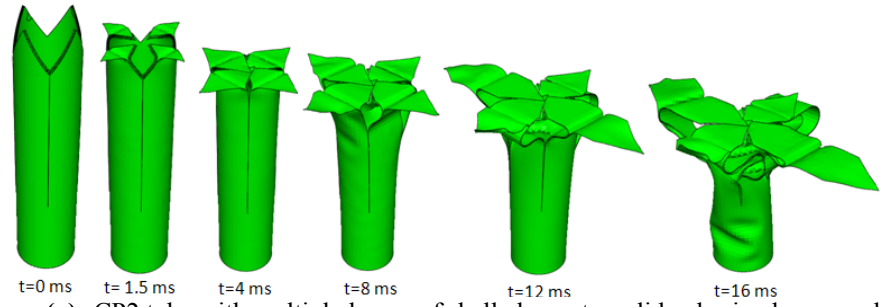

(a) CP2 tube with multiple layers of shell elements, solid cohesive layers and with 4 seams.

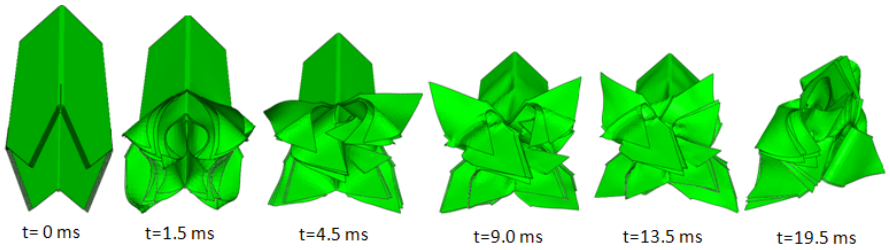

(b) SP2 tube with multiple layers of shell elements, solid cohesive layers and with 4 seams.

Figure 9-29: Deformation sequence of CP2 and SP2 tubes with multiple layers of shell elements, solid cohesive layers and with pre-defined seams.

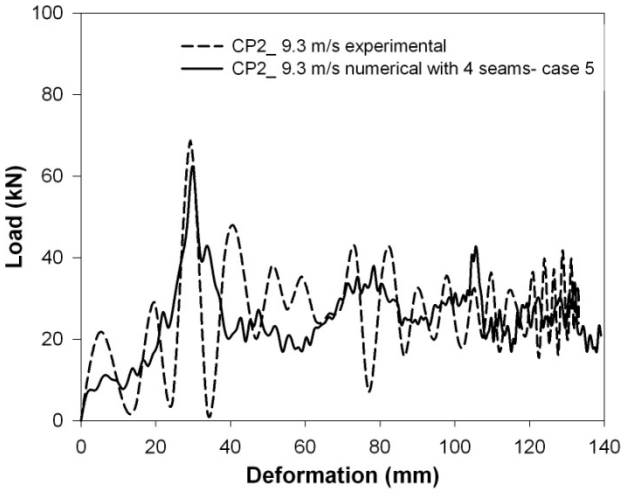

(a) CP2 tube with multiple layers of shell elements, solid cohesive layers and pre-defined seams

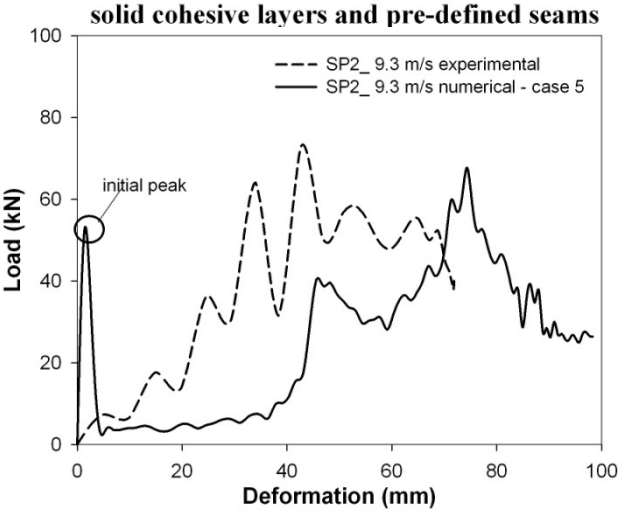

(b) SP2 tube with multiple layers of shell elements, solid cohesive layers and pre-defined seams

Figure 9-30: Comparison of load-deformation curve of CP2 and SP2 tubes with multiple layers of shell elements, solid cohesive layers and with pre-defined seams.

9. 9. Comparison of results

9. 9. 1. Comparison deformation patterns

From the above numerical parametric study, the approach from Case 1 (a single layer of shell elements) and Case 2 (two layers of shell elements with solid cohesive elements) provided deformation patterns which are entirely different from the experimental results. All tube series (CP1, CP2, SP1 and SP2) exhibited the local wall buckling followed by the end crushing. The initial stages of Case 2 approach

yielded a clear evidence of circumferential delamination for the tube series CP2 and SP2. However, other macro-failure mechanisms such as axial cracks and bending of plies were not clearly evident. The approach of Case 3 (two shell layers with cohesive elements and predefined seams) and Case 5 (multi layers shells with the cohesive elements and predefined seams) provided a good correlation of the deformation patterns for the circular and square composite tubes. Hence, in this section a comparison of the failure patterns of these cases are discussed with the experimental results. As discussed, from Case 3 and 5 there was no significant difference in the deformation pattern noticed between CP1 and CP2 tube series. So the failure patterns of the tube series CP1, SP1 and SP2 are only taken into consideration. The experimental failure pattern of these three tube series for the impact velocity of 9.3 m/s are again reproduced in Figure 9-31(a). Similarly the final deformation patterns of two layers (Case 3) and multiple layers (Case 5) of shell elements with cohesive elements and seams are shown in Figure 9-31(b) and Figure 9-31(c) respectively.

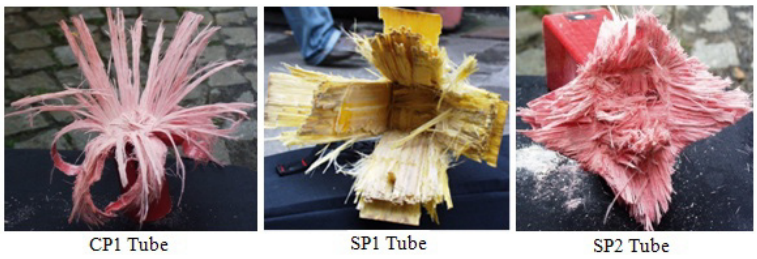

(a) Experimental deformation patterns of different composite tube series.

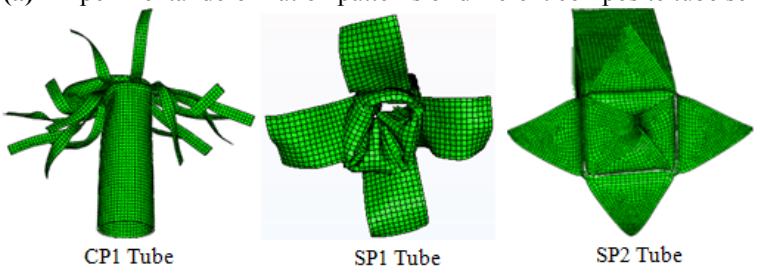

(b) Numerical deformation patterns of composite tubes with two layers of shell elements, cohesive elements and seams (Case 3).

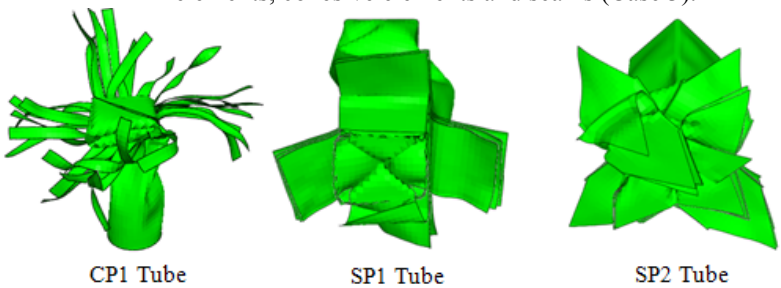

(c) Numerical deformation patterns of composite tubes with multiple layers of shell elements, cohesive elements and seams (Case 5).

Figure 9-31: Comparison of experimental and numerical deformation patterns.

The two layers of shell elements with cohesive elements and predefined seams approach showed the clear evidence of all the macro-failure mechanisms of the circular and square composite tubes. However, this approach cannot capture the multiple delaminations which occur at the time of failure of a composite tube. The approach with the multiple layers of shells with cohesive elements and seams provided a very good correlation of failure patterns for all cases of tube series. Similar to Case 3 approach, all the failure modes from Case 5 (delamination, axial cracks, bending of petals and fracturing) of a brittle composite tube are clearly evident.

9. 9. 2. Comparison of crush loads and energy absorption

The comparison of the peak crush load ($P_{\max}$), mean crush load (P_{mean}), total deformation length ($l_{\max}$) and the corresponding energy absorption (E_d) of the experimental and numerical approaches (Case 1 to 5) are given in Table 9-3. The CP1 and SP1 tubes with a single layer of shell elements approach (Case 1) were not considered for calculating the energy absorption due to the unrealistic peak forces and the deformation lengths. The single shell layer approach for the CP2 and SP2 tubes predicted the higher peak loads and the corresponding energy absorptions. Furthermore, this approach could not predict the correct deformation length of the tubes. As a result the mean crush loads of the tubes were higher than the experimental results. For the Case 2, out of two different approaches for triggering type 1 (Model C and D) the result of the Model D was considered. The comparison of peak crush load between the Cases 1 and 2 provided clear evidence of the influence of delamination on the peak crush load for all tube series. This can be clearly noticed for triggering type 2 tube series. Although the peak crush load from the Model D was less than the Model C (Case 2), the magnitude was higher than the experimental result. This gives the clear indication that the modelling of triggering was inadequate to capture the right peak crush load especially for triggering type 1. The energy absorption of this case for the circular tubes showed comparable values to the experimental results. Similar results have been obtained for Case 3 also.

The peak loads from the multiple delaminations approach (Case 4 and 5) provided closer values for all tube series compared to experimental data. This clearly indicates that the multiple delaminations have to be considered for the energy absorption calculations of composite tubes. The peak loads of SP1 tube series for these two approaches were lower than other approaches; however, the predicted peak loads were higher than the experimental values. The multiple layers of shell elements approach (Case 4 and 5) provided better energy absorption values compared to two layers of shell elements approach. The Case 5 (multiple layers with cohesive elements and pre-defined seams) approach predicted much closer values of energy absorption than any other approach which can be noticed from the Table 9-3.

9. 9. 3. Consolidated data for analysis

In this section, a list of used material data (both composite laminates and resin properties), proposed number of shell layers, number of seams and numerical input data such as damping and viscosity are given.

Table 9-4: Consolidated material and numerical data.

Parameters	Values
Material and elastic data for glass polyester	Refer Table 9-1
Glass polyester composite strength	Refer Table 9-1
Failure criteria for composite laminates	Hashin
Material and elastic data for polyester resin	Refer Table 9-2
Failure strength for polyester resin	Refer Table 9-2
Failure initiation criterion for cohesive elements	Quads
Damage evolution type	Fracture energy
Fracture energy for delamination (N/m)	300 [2]
Number of shell layers	One shell layer for 0.5 mm thickness
Number of seams	4 for square cross-sectional tube 8 – 12 for circular cross-sectional tube or based on experimental results.
Size of the shell elements	2 to 3 mm
Size of the cohesive elements	Same as shell element size. To avoid the numerical instability a smaller size can be used.
Inclusion of geometric imperfection	Not necessary for circular tubes; however, it is recommended for square cross-sectional tubes with tulip triggering.
Damage stabilization	0.0001 and 0.0005 for fibre and matrix (recommended values from Abaqus [1]).
Linear bulk viscosity parameter	0.06 (default value of Abaqus [1])
Quadratic bulk viscosity parameter	1.2 (default value of Abaqus [1]).
Frictional coefficient	0.2
Type of interaction of composite tube with crushing platform	Surface to surface [1].

9. 9. 4. Conclusions

In this section, a detailed numerical parametric study using shell elements was presented to predict the energy absorption characteristics and the corresponding failure patterns of composite tubes. The influence of triggering modelling on the peak crush load was explained with two different triggering mechanisms (45° edge chamfering and tulip pattern). Five different approaches have been employed to achieve the typical failure modes of brittle composite tubes. The concept of pre-defined seams was successfully employed to simulate the correct deformation patterns of the circular and square cross-sectional composite tubes. Using this approach, there was a very good correlation observed between the numerical and experimental deformation patterns. The typical failure modes of brittle composite tubes such as central delamination, bending of inner and outer plies, axial cracks and the fibre fracturing are clearly evident from the numerical deformation patterns. The effect of the number of pre-defined seams on the peak crush load and the corresponding energy absorption was evaluated. From the results of the numerical simulations it can be concluded that:

- The single layer of shell elements approach (Case 1) predicted approximately 140% and 100% higher peak crush loads for CP2 and SP2 tubes respectively. For CP2 with triggering type 1 (45° edge chamfering), Model B (triggering modelling approach) provided a lower peak crush load than Model A. However, the magnitude of the peak crush load from these two approaches was much higher than the experimental data. For SP1 tube there was no significant difference in peak load noticed between Model A and B. Furthermore, the deformation patterns of this approach for both triggering cases were entirely different from the experimental deformation patterns. This may be due to the fact that these models were not able to capture the delamination between the plies and inadequate modelling of the triggering profile (45° edge chamfering).
- The two layered shell elements with a solid cohesive layer (Case 2) approach showed clear evidence of the influence of the delamination phenomenon on the peak crush load of all composite tube series. The predicted peak crush load for the tube series CP2 and SP2 were 20% and 30 % higher than the experimental results. The difference may be due to the absence of multiple delaminations. In case of triggering type 1 series (CP1 and SP1) the difference between the experimental and numerical peak crush load was much higher. In addition to the absence of multiple delaminations, the inadequate modelling of triggering contributed to this very high difference. Similar to Case 1 approach the deformation patterns from Case 2 were different from the experimental deformation patterns.

- To capture the multiple delaminations and to model the correct geometry of the triggering type 1, the multiple layers of shell elements approach was handled (Case 4 and 5). Both these approaches provided peak crush loads which were closer to the experimental values for the tube series CP1, CP2, SP2. However the deformation pattern obtained from the former approach (Case 4) was similar to Case 1 and 2.
- The effect of axial cracks on the deformation patterns of the composite tubes was initially evaluated with two layers of shell elements and cohesive elements (Case 3). The same was implemented for Case 5 (multiple layers of shell layers elements with cohesive elements) which provided a very good correlation of deformation patterns with the experimental results. The above approaches Case 3 and 5 provided very good evidence of all macroscopic and microscopic deformation mechanisms of pultruded circular and square composite tubes. The corresponding energy absorption values were very close to the experimental values.

9. 10. Effect of initial geometric imperfections

As discussed in previous sections, the numerical impact studies on square tubes with tulip triggering (SP2) yielded an unrealistic initial peak load. This may be due to the perfect geometry of the triggering tulips. In order to evaluate the effect of geometric imperfections on this initial peak load the circular cross-sectional tube was considered in addition to the square cross-sectional composite tube. Different approaches from case 1 to 5 proved that the triggering modelling can influence the peak crush load of a composite tube (especially for triggering type 1). However, this effect was lower in case of tulip triggering (triggering type 2) due to the constant thickness of tulips. Hence, the pultruded glass-polyester circular and square cross-sectional tubes with triggering type 2 (CP2 and SP2) were selected for the study. Two approaches have been adopted to study this effect:

(i) the linear buckling mode shapes were similar to the Chapter 6 as the initial geometric imperfections of the composite tubes. However, due to the limitation of the used finite element code [1] this method of analysis was carried out only for a single layer of shell elements.

(ii) second method dealt with the finite element modelling of measured initial geometric imperfections from the manufactured composite tubes. In most of the practical applications, it was found that the buckling mode shapes of the cylindrical tubes are non-axisymmetric. Furthermore, the influence of the triggering profile on the linear buckling mode shapes was unknown. Due to the

above facts the complete 3D models of CP2 and SP2 tubes were considered for the linear buckling study.

9. 11. Geometric imperfections based on linear buckling approach

9. 11. 1. Buckling analysis and results

The details of this method and the corresponding imperfection analysis of a structure (empty beverage can) were well explained in Chapter 6. A similar approach has been handled here. In order to calculate the linear buckling modes of CP2 and SP2 tubes the finite element simulation of linear Eigen value buckling analysis was conducted. Consequently, the imperfections were introduced in the perfect composite tube geometry by adding these buckling modes. This perturbated geometry was used to study the effect on the peak crushing load and the corresponding energy absorption of the composite tubes for the axial impact loading case. The finite element modelling approach for the calculation of buckling mode shapes was very similar to the earlier model (refer Figure 9-32). In order to handle the complex contact pairs between the crushing platform and the composite tube, the "*subspace*" solver method was used to predict the Eigen values.

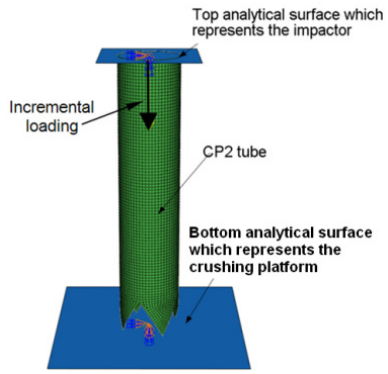

Figure 9-32: Finite element model of CP2 tube for linear buckling prediction.

The first five buckling mode shapes of CP2 and SP2 composite tubes and their corresponding Eigen values are shown in Figure 9-33(a) and (b) respectively. It can be noticed that for both composite tubes the successive Eigen frequencies are closely spaced. For such structures the first Eigen mode may not characterize the deformation that leads to the lowest buckling load, furthermore it can be concluded that the structures are imperfection sensitive. The calculated lowest buckling load for CP2 and SP2 composite tubes were 16.27 kN and 50.5 kN respectively.

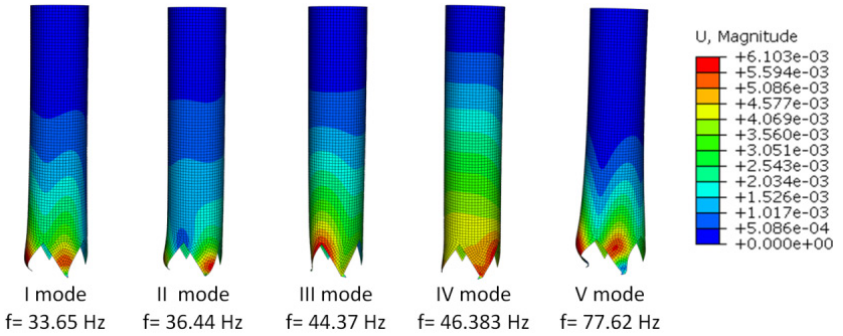

(a) Buckling mode shapes of CP2 tube with a single layer of shell elements.

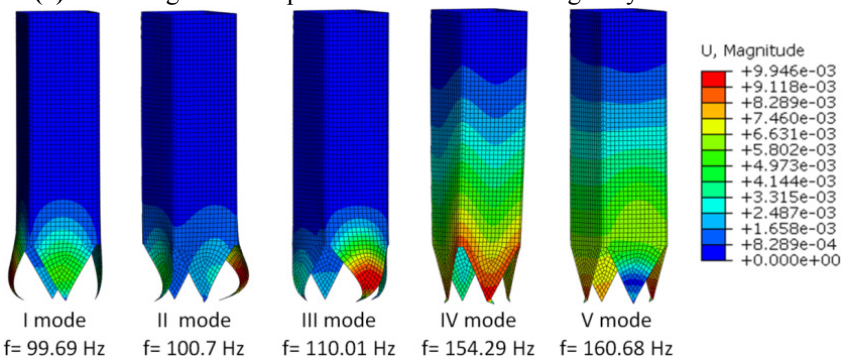

(b) Buckling mode shapes of SP2 tube with a single layer of shell elements.

Figure 9-33: Buckling mode shapes of circular and square cross-sectional composite tubes with triggering type 2.

9. 11. 2. Impact analysis and results

The impact modelling approach was very similar to Case 1 (a single layer of shell elements) which was discussed previously. However, the perturbation geometries of CP2 and SP2 tubes were considered for the study. For CP2 and SP2 composite tubes the Eigen values are closely spaced and so the first five modes were considered for the imperfections. Similar to the previous sections the result of this analysis was discussed only for the initial impact velocity of 9.3 m/s. The deformation sequences of CP2 composite tube with a geometric scaling factor (ω) of 5% of the tube thickness is shown in Figure 9-34(a). This deformation pattern is different from the pattern which is reported in Case 1 (without geometric imperfection) in section 9. 4. Due to the introduction of geometric imperfections from the linear mode shapes, the triggering tulips folded outwards. Consequently, a 5 to 7% increase in the peak load was noticed compared to the case without imperfection. Figure 9-35(a) shows the load-deformation history of CP2 tube with different scale factors. It can be noticed that for the scale factors 1, 2.5, 5, 10 and 100 % of the thickness of the tube no clear distinct difference was noticed in load-deformation curves. The peak crushing load was reduced from 180 kN to 107.6 kN for the case with the scale factor 1000 % of

thickness which is not possible in practical cases. However, compared to the perfect geometry analysis the slope to reach the peak crush load was decreased in all imperfection cases. The comparison of peak load, deformation length and the energy absorption for the different scale factors are given in Table 9-5. All cases with different scale factors yielded a lower deformation length than the case without geometric imperfection (refer Table 9-5). The reason for this lower deformation length was the deformation pattern. Due to the outward folding of the tulips the maximum deformation of the composite tube was restricted to the end of the tulips. This can be clearly noticed from Figure 9-34(a). Consequently, the local wall buckling mode occurred at the mid-length of the tube. As a result of the lower deformation length, the mean crush load of these cases was higher than the case without imperfection. However there was no significant difference in the energy absorption noticed.

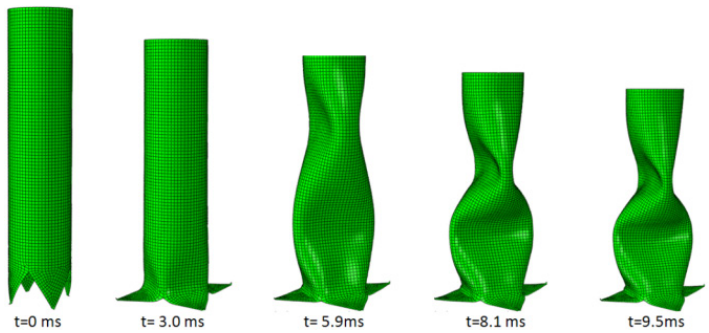

(a) Deformation patterns of CP2 tube (a single layer of shell elements) with linear buckling modes geometric imperfections (scale factor is 5% of thickness of the tube).

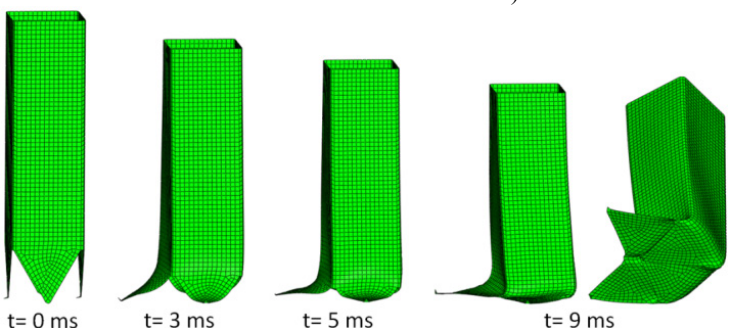

(b) Deformation patterns of SP2 tube (a single layer of shell elements) with linear buckling modes geometric imperfections (scale factor is 10% of thickness of the tube).

Figure 9-34: Deformation patterns of circular and square cross-sectional composite tubes.

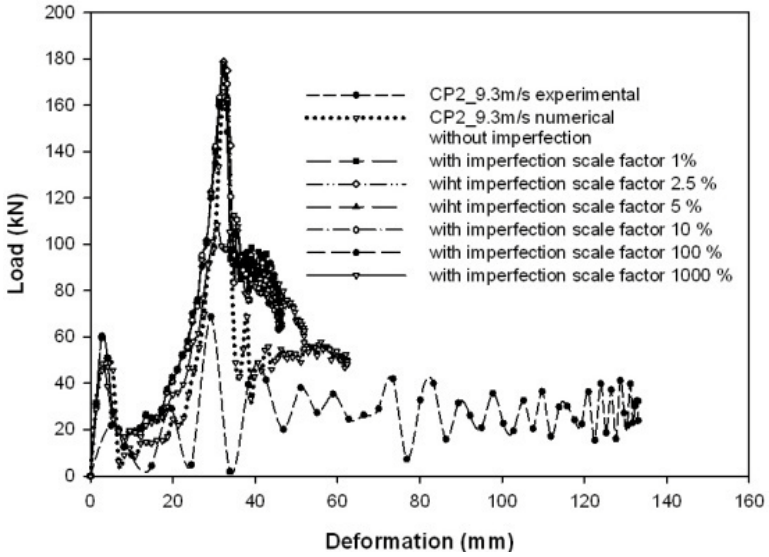

(a)

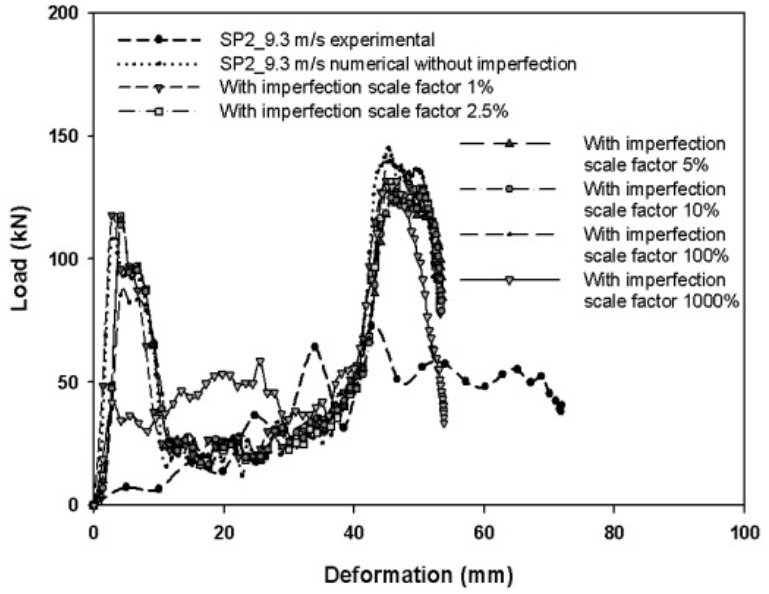

(b)

Figure 9-35: (a) The load-deformation histories of CP2 tube (Case 1- a single layer of shell elements) with different scale factors of geometric imperfections. **(b)** The load-deformation histories of SP2 tube (Case 1- a single layer of shell elements) with different scale factors of geometric imperfections.

Similar to CP2 composite tube, the deformation patterns of SP2 tube at different time intervals during the crushing process are shown in Figure 9-34(b). It can be noticed that the deformation pattern was again different from Case 1 which is reported in section 9. 4. The numerical analysis result of SP2 tube with perfect geometry showed the outward bending of all four tulips, whereas in case of the

linear buckling imperfection approach the introduction of buckling mode shapes caused two tulips to bend inside (towards the axis of the tube, refer Figure 9-34(b)). Furthermore, the load-deformation curves of all cases (imperfection scale factors from 1 to 1000 % of tube thickness, refer (Figure 9-35(b)) showed no distinctive difference from the perfect structure. In contrast for higher scaling factors such as 100 and 1000 % the peak crush load of the composite tube was increased. This may be due to the change in scaling the nodal position of tulips based on the mode shapes which caused a higher peak crush load. Furthermore, the magnitude of the initial peak considerably reduced for the cases with 100 % and 1000 % scale factors. This shows that the geometry of the tulips plays a vital role on the initial peak load. The summarized values of peak and mean crush load, deformation length and the energy absorption for different scale factors are given in Table 9-5.

Though the results from the linear buckling analysis showed that the composite tubes (CP2 and SP2) are sensitive to the initial geometry imperfections, the results from the axial impact loading analyses showed no significant difference in the predicted peak crush loads and the corresponding energy absorption.

Table 9-5: Summary of numerical impact parameters for CP2 and SP2 tubes (single layer of shell elements) with initial geometry imperfections (linear superposition of Eigen vectors).

Cases	Peak crush load (kN) P_{max}	Mean crush load (kN) P_{avg}	Deformation length (mm) l_{max}	Absorbed energy (kJ) E_d
Circular glass polyester tube with triggering type 2 (CP2)				
Experimental	69	26	133	3.47
Numerical results without imperfection	165.8	47.7	62.3	2.990
Numerical results with imperfection – linear superposition of Eigen vectors				
Scale factor 1 % of tube thickness	174.7	65.0	46.0	2.992
Scale factor 2.5 %	178.7	65.4	45.7	2.993
Scale factor 5 %	176.9	65.1	46.0	2.996
Scale factor 10 %	177.5	65.6	45.7	3.000
Scale factor 100 %	176.5	65.0	46.3	3.015
Scale factor 1000 %	107.695	57.2	52	2.976
Square glass polyester tube with triggering type 2 (SP2)				
Experimental	73	37.7	71	2.68
Numerical results without imperfection	145	56.0	52.5	2.971
Numerical results with imperfection – linear superposition of Eigen vectors				
Scale factor 1 % of tube thickness	135.7	56.8	53.2	2.995
Scale factor 2.5 %	131.2	54.4	53.2	2.895
Scale factor 5 %	123.2	54.0	53.5	2.894
Scale factor 10 %	125.7	55.7	52.0	2.900
Scale factor 100 %	139.5	55.0	52.0	2.863
Scale factor 1000 %	131.5	55.7	53.8	2.995

9. 12. Measured geometric imperfection approach

9. 12. 1. Initial geometric imperfections

The numerical impact studies (Case 1 to 5) on square tubes with tulip triggering (SP2) yielded an unrealistic initial peak load. This may be due to the assumed perfect geometry of triggering tulips and the corresponding mesh patterns. In order to evaluate the effect of geometric imperfection on this initial peak load and the corresponding crushing performance, a study was conducted with measured initial geometric imperfections. A representative specimen of tested composite tubes was sufficient to investigate the effect of initial geometric imperfections. Hence, a representative composite specimen from each series (CP2 and SP2) was taken for the study and consequently the initial geometric imperfections of these tubes were measured and recorded. The investigation of outer and inner surfaces of the tested composite tube specimens showed a good evidence of similar geometric imperfections throughout their length (220 mm). The outer diameter and the thickness were measured at regular intervals along radial and longitudinal directions of the tube. The inner surface measurement was used to determine the initial imperfections on the shell wall distribution. The difference between the outer and inner surface measurements was considered as the composite shell thickness distribution. The average measured thicknesses of CP2 and SP2 tubes were 2.953 mm and 4.554 mm respectively (nominal thickness are 3 mm and 4.5 mm). Figure 9-36(a) and Figure 9-37(a) show the typical polar diagrams of measured cross-sections of circular (CP2) and square (SP2) composite tubes. The deviation in inner and outer wall diameters can also be clearly noticed from these figures. Furthermore, Figure 9-36(b) and Figure 9-37(b) show the deviations in mid-thickness axis of the tubes with respect to the perfect circular and square composite tubes in thickness direction. The corresponding experimental results of these composite tubes were taken into consideration for the comparison of results.

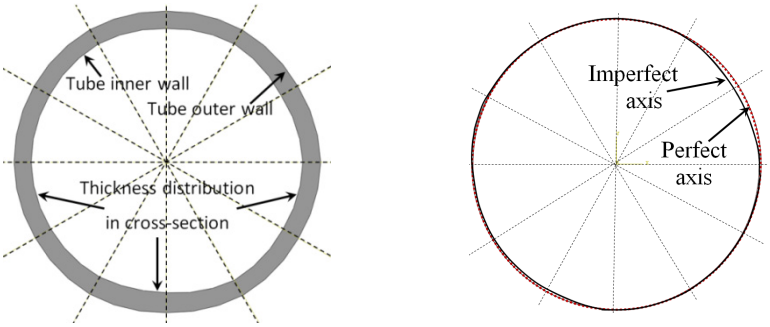

(a) Thickness distribution **(b)** Mean axis in thickness direction

Figure 9-36: Typical polar diagram of circular composite tube (CP2) measured cross-section.

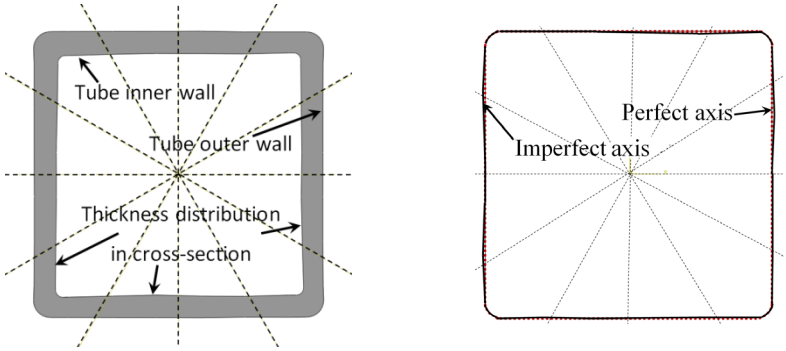

(a) Thickness distribution **(b)** Mean axis in thickness direction

Figure 9-37: Typical polar diagram of square composite tube (SP2) measured cross-section.

The modelling approach of each individual case 1 to 5 was very similar to the ones which were discussed in the previous sections.

9. 12. 2. Measured imperfection with Case 1

Initially the measured initial imperfection was modelled with a single layer of shell elements which represents the change in tube thickness at each and every location on the tube [16-18]. This approach may not attribute the correct prediction of design parameters for the case, where the initial geometric imperfections were evident only on the outer surface or inner surface of the composite tube. Furthermore, the peak crush load and the corresponding energy absorption prediction of composite tubes depend on correct modelling of complex deformation mechanisms such as delamination, axial cracks, bending of petals and fibre fracturing. As discussed earlier, the delamination phenomenon cannot be captured with the single layer of shell elements. However, to study the difference from the linear buckling approach, an analysis was carried out with the single layer of shell elements. The measured thickness of the tube was modelled with a single layer of shell elements. The element size of 3 mm was chosen similar to other cases.

The deformation patterns of CP2 tube at different time intervals with measured initial geometry imperfections are shown in Figure 9-38(a). The deformation pattern was similar to the linear buckling mode approach where triggering tulips exhibited the local wall buckling followed by outward bending of triggering tulips. However, the local wall buckling occurred close to the triggering tulips instead of at mid-length of the tube. Due to this effect the later time increments showed that the walls of the composite tube were squeezed to each other. This effect can be clearly noticed from Figure 9-38(a). The deformation length of this case was lower than earlier approaches (refer Figure 9-39(a)). This approach provided no distinctive difference

in the peak crush load compared to the perfect structure analysis. The comparison of all the numerical impact parameters for this case is given in Table 9-6.

Similarly the deformation patterns of SP2 tube with measured initial geometric imperfections are shown in Figure 9-38(b). A difference in the deformation pattern was noticed compared with the perfect SP2 tube analysis result. The imperfect shape of the square tube caused two tulips to bend outside (Figure 9-38(b)). The remaining two tulips were bent inside (towards the axis of the tube). As a result the deformation length of this tube was higher than the perfect structure (Figure 9-39(b)). Furthermore, it can be noticed from Figure 9-39(b) that the initial peak load of this imperfect tube was lower than the perfect structure. However, this magnitude was higher compared to the experimental value. In contrast, the peak crush load of imperfect SP2 tube (166.7 kN) was higher than the perfect tube (145 kN). The combination of imperfect geometry and the consequent deformation pattern of this tube might have attributed to the increase in the peak crush load. Furthermore, the single layer of shell elements cannot capture the delamination process which controls the peak crush load of a composite tube. As a result of the above mechanisms the approach with a single layer of shell elements with measured initial geometric imperfections of SP2 tube provided a higher value of the energy absorption (Table 9-6).

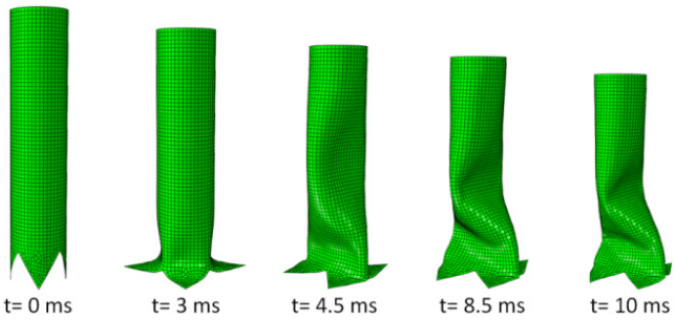

(a) Deformation patterns of CP2 tube (Case 1 - a single layer of shell elements) with measured initial geometric imperfections.

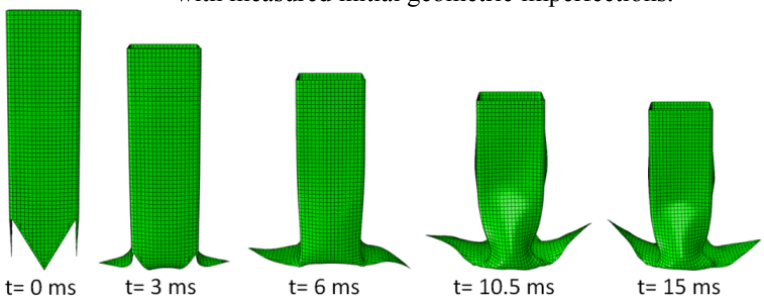

(b) Deformation patterns of SP2 tube (Case 1- a single layer of shell elements) with measured initial geometric imperfections.

Figure 9-38: Deformation patterns of composite tubes.

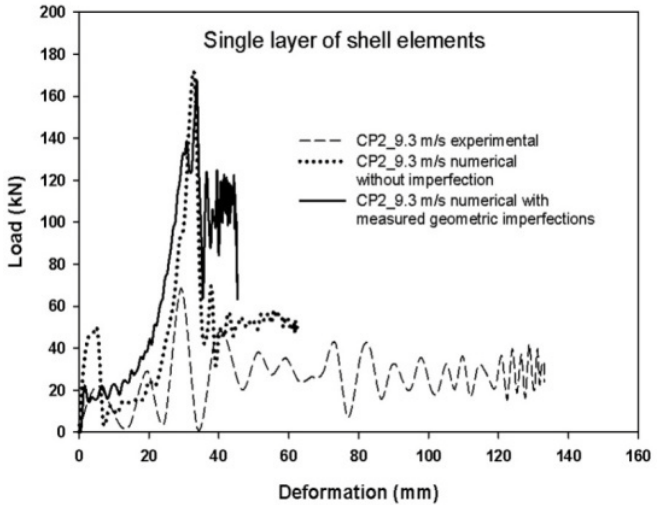

(a)

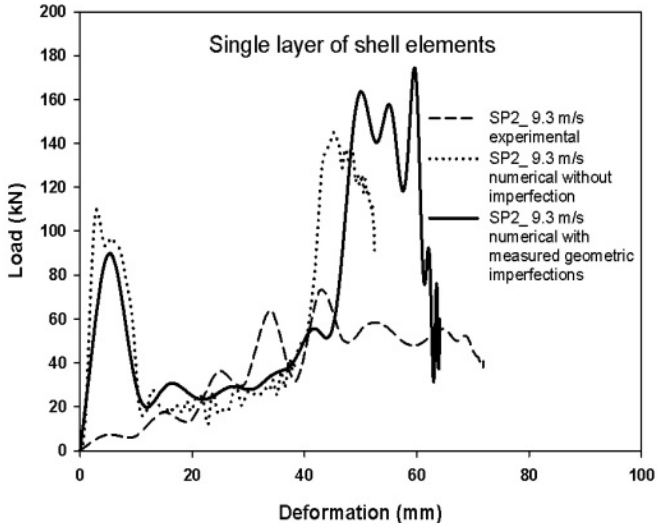

(b)

Figure 9-39: Comparison of load-deformation histories **(a)** CP2 tube (Case 1- a single layer of shell elements) with and without measured initial geometric imperfections**.(b)** SP2 tube (Case 1- a single layer of shell elements) with and without measured initial geometric

9. 12. 3. Measured imperfection with Case 2

The two approaches (superposition of linear buckling modes and measured initial geometric imperfections) with a single layer of shell elements provided higher peak crush loads for circular and square composite tubes with tulip triggering. Hence, the Case 2 (two layers of shell elements and a solid cohesive layer) approach was modelled with measured initial geometric imperfections. The measured thickness of

the tubes (Figure 9-36 (a) and Figure 9-37(a)) was divided into two halves. The inner and outer layers of the shell elements were located at the centre of each half. To capture the delamination phenomenon a solid cohesive elements layer was also placed between outer and inner shell layers. The results of the numerical analyses with measured initial geometric imperfections of CP2 and SP2 tubes are presented in Figure 9-40 and Figure 9-41 for the initial impact velocity of 9.3 m/s. The initial stages of CP2 tube with geometric imperfections showed a difference in the deformation pattern from the case without imperfection. The initial time increments of CP2 tube showed a local wall buckling mode followed by a uniform end crushing. Due to this effect the imperfect CP2 tube exhibited a higher mean crush load than the perfect tube geometry till 70 mm of deformation length (Figure 9-41(a)). However, the later stages of analysis showed a uniform end crushing mode (Figure 9-41(a)). This approach showed a significant difference in the peak crush load compared to the perfect geometry analysis. The peak crush load of this case was 71.6 kN which is very close to the experimental value 69 kN. The mean crush load of this case was close to the case without imperfection. As a result there was no distinct difference in the total energy absorption observed. The summary of all the impact parameters of this case is presented in Table 9-6.

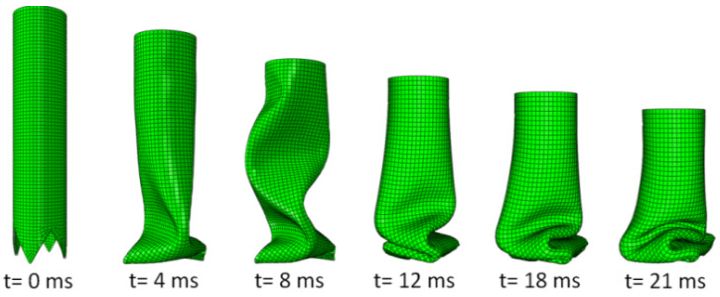

Figure 9-40: Deformation patterns of CP2 tube (Case 2 - two layers of shell elements and a solid cohesive layer) with measured initial geometric imperfections.

The numerical analysis result from the imperfect SP2 composite tube showed no significant difference in the deformation pattern and the peak crush load. However, there was a distinctive difference in the initial peak load noticed (Figure 9-41(b)). The magnitude of the initial peak load 60 kN (case without imperfection) was reduced to 40 kN (case with imperfection). Furthermore, this magnitude was lower than Case 1 - a single layer of shell elements approach (Figure 9-39(b)). This again shows the importance of considering delamination in the model. The load-deformation curve of the imperfect SP2 tube showed a difference in the slope of the curve to reach the peak crush load (Figure 9-41(b)). In addition to that there was a fluctuation in the load observed at the later stages of crushing. The calculated mean crush load of this case was very close to the case without imperfection (refer Table 9-6). Due to that the total absorbed energy for both cases (with and without imperfection) was very close.

Table 9-6: Summary of numerical impact parameters for CP2 and SP2 tubes with measured initial geometric imperfections.

Cases		Peak crush load (kN) P_{max}	Mean crush load (kN) P_{avg}	Deformation length (mm) l_{max}	Absorbed energy (kJ) E_d
Circular glass polyester tube with triggering type 2 (CP2)					
Experimental		69	26.0	133	3.47
Numerical study with the measured initial geometric imperfections					
Case 1	*Without imperfection*	165.8	47.7	62.3	2.99
	With imperfection	167.1	65.7	45.4	2.98
Case 2	*Without imperfection*	82.5	27.3	113	3.08
	With imperfection	71.6	25.6	117	2.99
Case 3	*Without imperfection*	67.0	19.0	125	2.30
	With imperfection	60.0	16.6	140	2.32
Case 4	*Without imperfection*	72.0	23.5	127	3.00
	With imperfection	66.1	23.3	133	3.10
Case 5	*Without imperfection*	64.0	24.3	140	3.40
	With imperfection	57.5	23.8	143	3.41
Square glass polyester tube with triggering type 2 (SP2)					
Experimental		73.0	37.7	71.0	2.68
Numerical study with the measured initial geometric imperfections					
Case 1	*Without imperfection*	145.0	56.0	52.5	2.97
	With imperfection	166.7	46.8	60.0	3.21
Case 2	*Without imperfection*	95.0	24.0	84.0	2.01
	With imperfection	93.0	25.8	82.5	2.13

Cases		Peak crush load (kN) P_{max}	Mean crush load (kN) P_{avg}	Deformation length (mm) l_{max}	Absorbed energy (kJ) E_d
Case 3	*Without imperfection*	81.0	25.5	90	2.30
	With imperfection	79.9	23.4	102	2.39
Case 4	*Without imperfection*	92.0	24.5	98	2.50
	With imperfection	76.8	23.5	104	2.44
Case 5	*Without imperfection*	69.0	24.9	98	2.46
	With imperfection	70.5	25.2	94	2.50

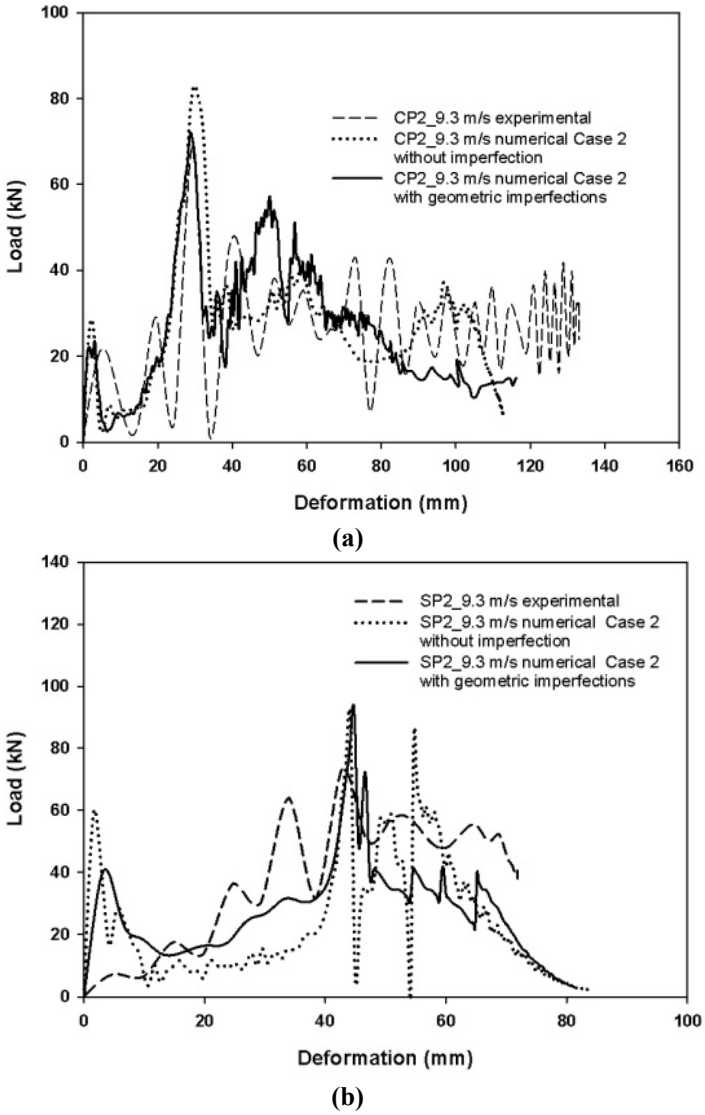

Figure 9-41: Comparison of load-deformation histories **(a)** CP2 tube (Case 2-two layers of shell elements with a solid cohesive layer) with and without initial geometric imperfections. **(b)** SP2 tube (Case 2-two layers of shell elements with a solid cohesive layer) with and without initial geometric imperfections.

9. 12. 4. Measured imperfection with Case 3

The deformation patterns of circular and square composite tubes with geometric imperfections were very similar to the cases without imperfection. The difference in the load-deformation histories of these two cases can be clearly noticed from Figure 9-42(a) and (b). For Case 2 the measured initial geometry imperfection of CP2 tube model predicted a peak load which was very close to the experimental data.

However, this model (case 3 with measured initial geometric imperfections) predicted a peak crush load which was lower than the experimental value (60 kN against 69 kN). Furthermore, the predicted total deformation length of the circular imperfect tube was higher than the case without imperfection (Figure 9-42). This may be due to the pre-defined seams in the numerical model. Due to the longer deformation length there was a reduction in mean crushing load from 19 kN to 16.6 kN observed. However there was no significant difference in the energy absorption noticed (refer Table 9-6). The total absorbed energy values were 2.30 kJ and 2.325 kJ for perfect and imperfect tube geometries of circular composite tubes respectively.

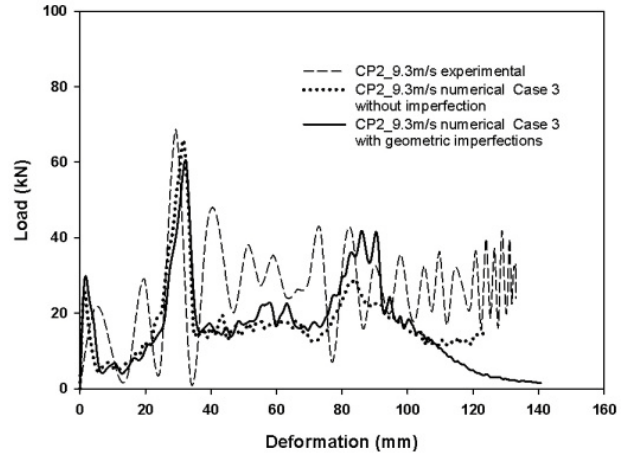

(a)

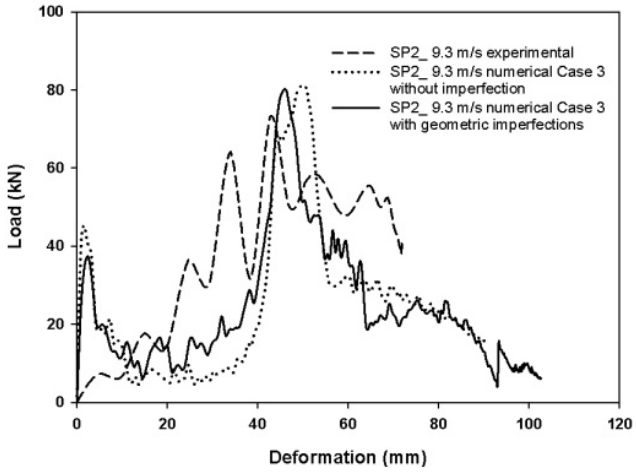

(b)

Figure 9-42: Comparison of load-deformation histories **(a)** CP2 tube (Case 3-two layers of shell elements with a solid cohesive layer and pre-defined seams) with and without initial geometric imperfections. **(b)** SP2 tube (Case 3-two layers of shell elements with a solid cohesive layer and pre-defined seams) with and without initial geometric imperfections.

Similarly for SP2 tube a very close peak crush load was noticed between the cases with and without imperfection (Figure 9-42(b)). The average crush load of this case was slightly lower than the case without imperfection. However, due to the higher deformation length the total absorbed energy for both cases was very close (Table 9-6). Similar to the other approaches, the initial peak load of this case was also reduced (Figure 9-42). This shows the influence of perfect geometry of tulips on the initial peak load.

9. 12. 5. Measured imperfection with Case 4

Similar to the earlier approach the deformation patterns of imperfect circular and square composite tubes showed no significant difference with the perfect tube geometry results. However, there was a difference in the load-deformation histories noticed. The load-deformation histories of these two composite tubes with initial geometry imperfections are shown in Figure 9-43(a) and (b). The peak crush load of CP2 tube with initial geometric imperfections showed a lower value than the perfect tube geometry which was already close to the experimental value (Figure 9-43(a)). The mean crush load of this approach was very close to the case without imperfection case. The summary of all the impact parameters is presented in Table 9-6.

Unlike the circular composite tube, there was a significant difference in the peak crush load noticed for the square tube with initial geometric imperfection. The SP2 tube with initial geometric imperfection obtained a peak crush load of 76.8 kN against 73 kN for the experimental result. The later crushing stages of this tube showed a higher mean crush load than the case without imperfection. An important conclusion can be made from Figure 9-43 that the magnitude of the initial peak crush load was considerably reduced as the number of shell element layers (with initial geometry imperfection) increased. Similar to other approaches there was no appreciable difference in the energy absorption noticed. The SP2 tube geometry with initial geometric imperfection showed 2.447 kJ against 2.5 kJ for the case without imperfection (Table 9-6).

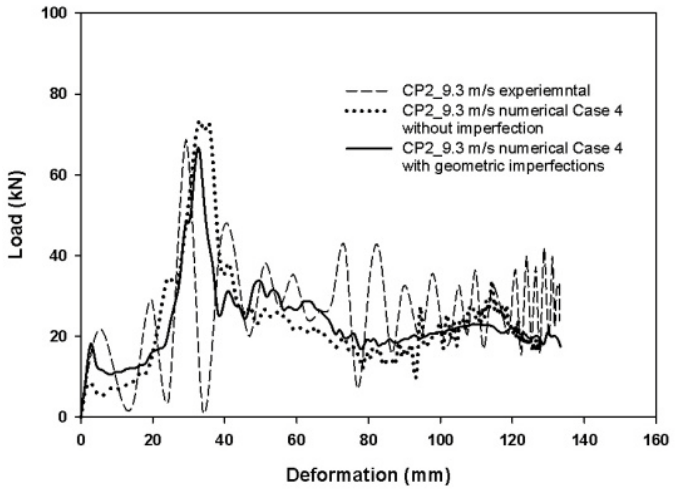

(a)

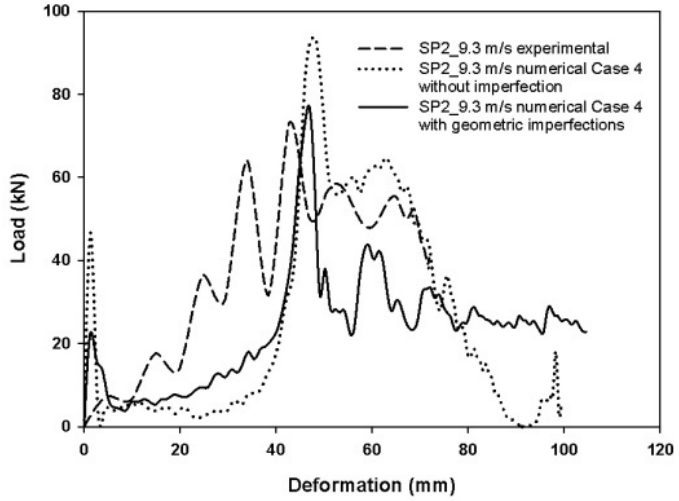

(b)

Figure 9-43: Comparison of load -deformation histories **(a)** CP2 tube (Case 4-multiple layers of shell elements with solid cohesive layers) with and without initial geometric imperfections.**(b)** SP2 tube (Case 4-multiple layers of shell elements with solid cohesive layers) with and without initial geometric imperfections.

9. 12. 6. Measured imperfection with Case 5

The load-deformation histories of CP2 and SP2 composite tube series are given in Figure 9-44(a) and (b) respectively. Similar to the previous approaches, there was no significant difference in the deformation pattern noticed with and without initial geometric imperfection approaches for Case 5. However, there was a distinctive difference in the peak crush load noticed for the circular composite tube (CP2) with initial geometric imperfections. The predicted peak load of CP2 tube was lower than

the experimental and perfect tube geometry numerical approach values (Figure 9-44(a)). The Case 5 approach with initial geometric imperfections yielded a peak load which was lower than any other approach. However, the mean crush load of this case was very close to the case without imperfection. Due to the comparable mean load and the deformation length this case provided a similar energy absorption value compared with the perfect structure. The comparison of the energy absorption with and without imperfection case is shown in Table 9-6.

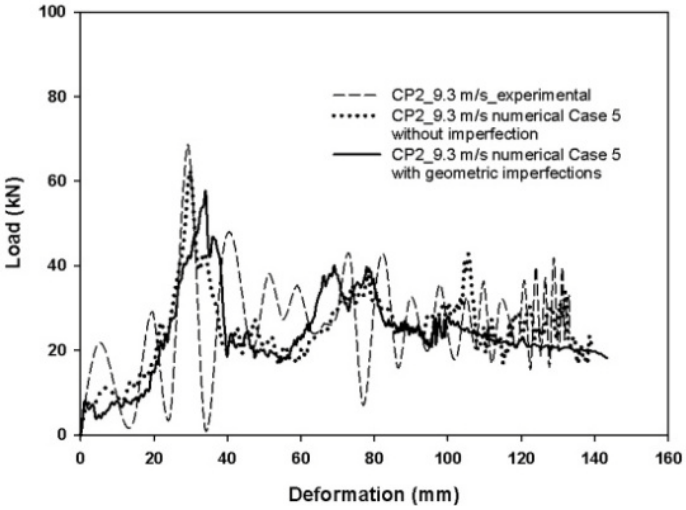

(a)

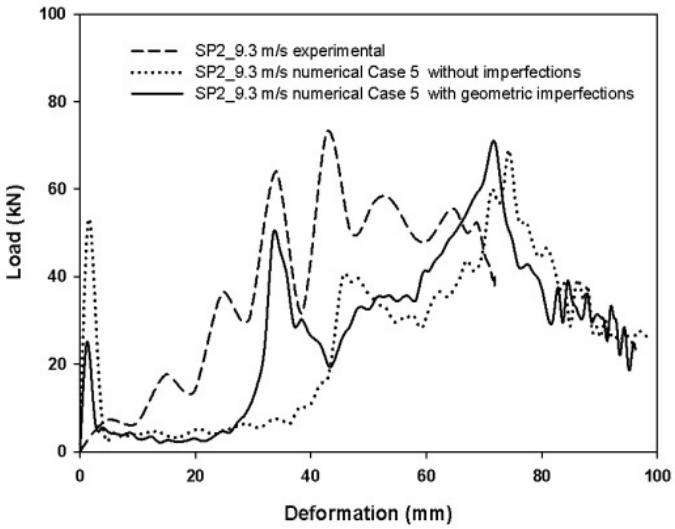

(b)

Figure 9-44: Comparison of load -deformation history **(a)** CP2 tube (Case 5- multiple layers of shell elements with solid cohesive layers and pre-defined seams) with and without initial geometric imperfections**.(b)** SP2 tube (Case 5 - multiple layers of shell elements with solid cohesive layers and pre-defined seams) with and without initial geometric imperfections.

9. 13. Mesh sensitivity

For any finite element calculation the quality of the results is affected by size, type of mesh (regular or irregular) and the aspect ratio of the chosen elements up to some extent. Choosing a finer and regular mesh will provide a more accurate solution. However, most of the real world structures are irregular in nature. Hence, it is impossible to achieve a very regular mesh for all structures. Furthermore, choosing a finer mesh will enhance the quality of the results. However, the finer mesh will increase the computation time and so it is expensive. In order to address the quality of the results with respect to the size of the element a mesh sensitivity study was carried out for case 1 to 5. Three different element lengths (l_e) were chosen (2 mm, 3.5 mm and 5 mm (refer Figure 9-45)) and consequently the analysis was carried out only on the perfect geometry of CP2 tube for the initial impact velocity of 9.3 m/s.

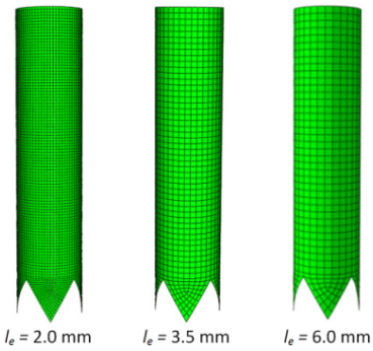

Figure 9-45: CP2 tube mesh with three different element lengths.

The results from the analysis for case 1 to 5 are shown in Figure 9-46 to Figure 9-48 and the comparison of results (peak crushing load, mean crushing load, deformation length and the energy absorption) are presented in Table 9-7. In case of a single layer of shell elements, the analyses with different element lengths showed no significant difference in the peak crush load and the deformation length (Figure 9-46(a)). As a result all these three cases predicted the same level of the energy absorption and mean crush load. Furthermore, as discussed earlier a significant difference between the experimental data and numerical prediction was due to the absence of delamination.

In case of two layers of shell elements with a solid cohesive layer (Case 2), the prediction using 2 mm element length yielded a peak crush load (67 kN) which is very close to the experimental value 69 kN (Figure 9-46(b)). The other two element lengths 3.5 mm and 5 mm predicted higher peak loads of 82.2 kN and 83.1 kN respectively. However the predicted deformation length was higher for the element length 5 mm. Due to the lower mean crush load of this case the calculated energy absorption was lower than other cases. The element length of 3.5 mm predicted a

higher energy absorption than other element lengths which was comparable with the experimental data. The magnitude of the initial peak which corresponds to deformation of the tulip portion of the composite tube was increased with decreasing element size. This phenomenon can be clearly noticed from Figure 9-46(b). This effect may be due to the different mesh pattern attributed by the element size and their skewness.

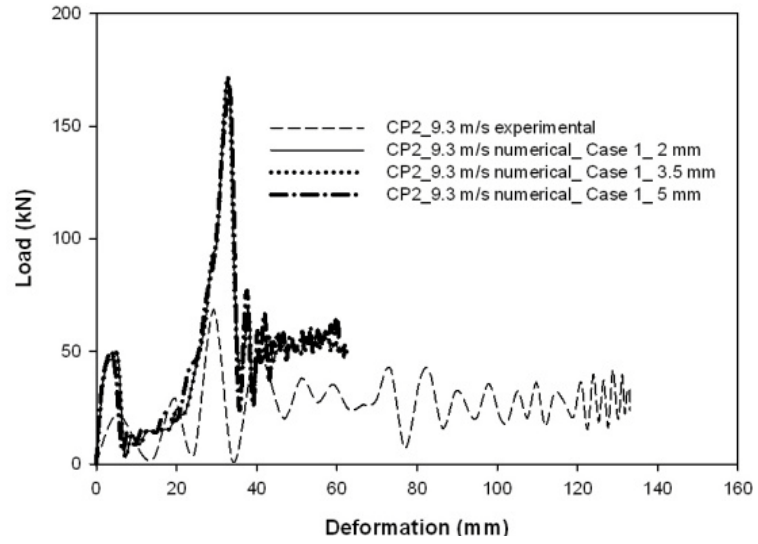

(a)

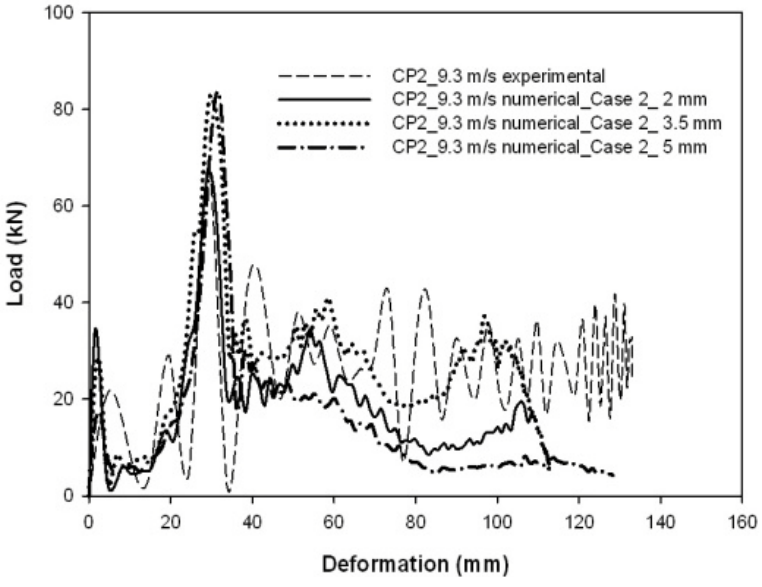

(b)

Figure 9-46: (a) Mesh sensitivity study of CP2 tube **(a)** for Case 1 **(b)** for Case 2.

The analysis of two layers of shell elements with solid cohesive elements and pre-defined seams (Case 3) with different element lengths showed good agreement of

peak crushing load with the experimental data (Figure 9-47(a)). Furthermore, there was no significant difference in initial peak load obtained during the crushing of tulips. This may be due to the lower stiffness offered by the outer layer of shell elements with pre-defined seams at initial time increments. The element length 5 mm predicted slightly a higher energy absorption than the other two element lengths. However the predicted energy absorption for all cases was lower than the experimental value (Table 9-7). The predicted peak load for Case 4 (multiple layers of shell elements with solid cohesive layers) with all three different element lengths was very close to the experimental value. This can be noticed from Figure 9-47(b). All the analyses showed a good consistency in their peak and mean crushing load.

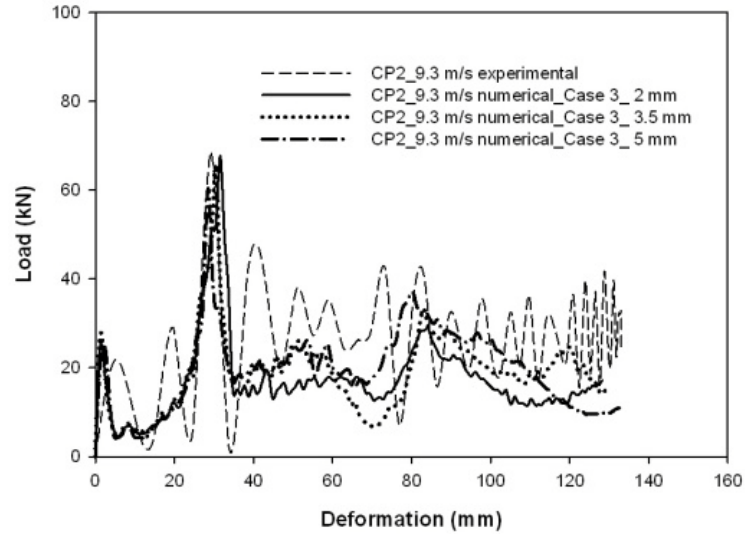

(a)

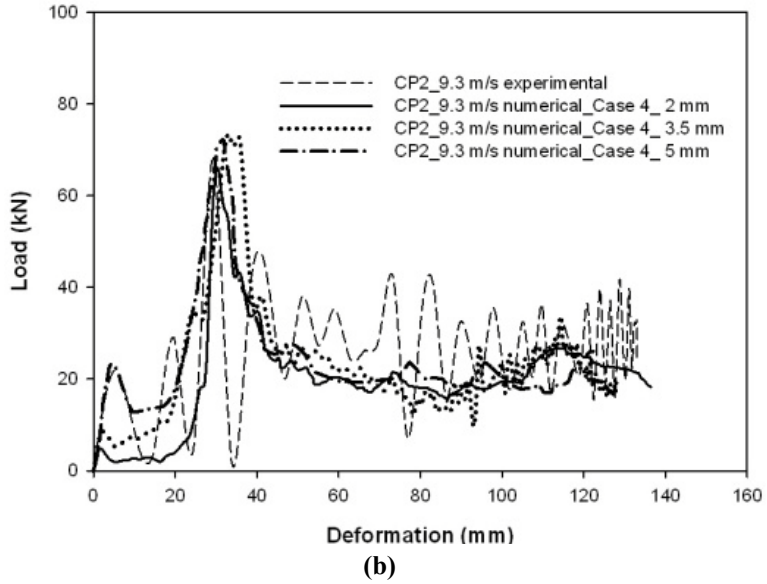

(b)

Figure 9-47: Mesh sensitivity study of CP2 tube **(a)** for Case 3 **(b)** for *Case 4*.

Finally the convergence study of Case 5 (multiple layers of shell elements with solid cohesive elements and pre-defined seams) predicted much closer values of the energy absorption than any other case (Table 9-7). It can be noticed from Figure 9-48 that the predicted peak crush loads with different element lengths were comparable with experimental data.

From the study above it can be concluded that the element length in the range of 3 to 4 mm predicted an average value which was closer to the experimental value. There was no significant difference in the deformation patterns noticed for the individual cases.

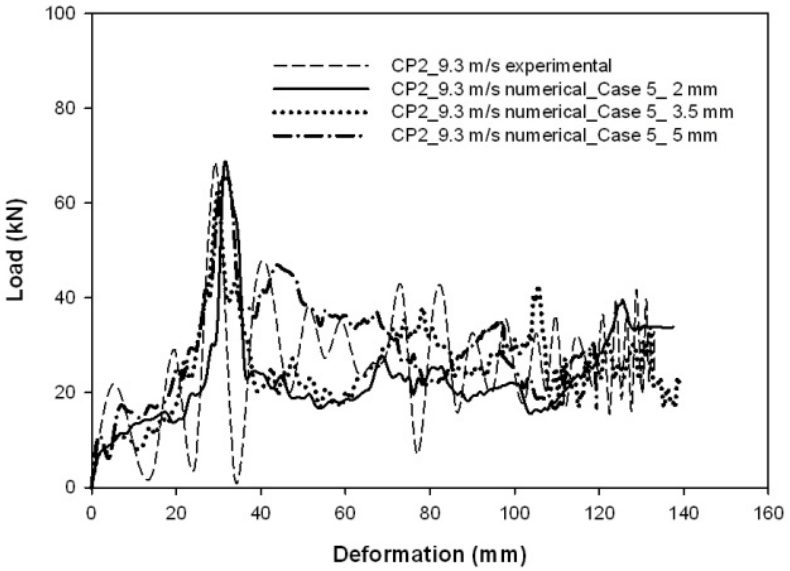

Figure 9-48: Mesh sensitivity study of CP2 tube (Case 5- multiple layers of shell elements with solid cohesive elements and pre-defined seams).

Table 9-7: Summary of numerical impact parameters for mesh sensitivity study.

	Cases	Peak crush load (kN) P_{max}	Mean crush load (kN) P_{avg}	Deformation length (mm) l_{max}	Absorbed energy (kJ) E_d
	Circular glass polyester tube with triggering type 2 (CP2)				
	Experimental	69	26.0	133	3.47
	Numerical convergence study results with different element length (l_e)				
Case 1	l_e =2.0 mm	165.81	47.72	62.4	2.978
	l_e =3.5 mm	165.81	47.70	62.4	2.977
	l_e =5.0 mm	165.65	49.17	60.4	2.970
Case 2	l_e =2.0 mm	67.0	19.13	108.3	2.072
	l_e =3.5 mm	82.2	27.30	112.7	3.081
	l_e =5.0 mm	83.10	15.17	128.32	2.010
Case 3	l_e =2.0 mm	67.7	17.34	128.20	2.224
	l_e =3.5 mm	65.75	18.93	130.0	2.461
	l_e =5.0 mm	60.5	19.70	133.10	2.623
Case 4	l_e =2.0 mm	66.2	20.30	136.0	2.743
	l_e =3.5 mm	73.4	23.33	128.0	2.987
	l_e =5.0 mm	72.07	24.26	122.0	2.960
Case 5	l_e =2.0 mm	65.9	22.90	137.5	3.150
	l_e =3.5 mm	64	24.94	139.0	3.467
	l_e =5.0 mm	65.3	29.60	120.0	3.553

9. 14. Conclusions

In this section, the effect of initial geometric imperfections and mesh size on the peak crushing load, failure pattern, deformation length and the corresponding energy absorption of the pultruded circular and square glass polyester composite tubes were presented. The tulip triggering pattern with an included angle of 60° between the edges was considered for the study. Two different approaches have been handled to study the effect of the initial geometry imperfections. The first approach dealt with superposition of linear combinations of typical buckling modes. The second approach was based on the measured initial geometric imperfections. Finally to study the effect of element size on the impact parameters (such as peak load, deformation length and the energy absorption) a mesh sensitivity study was conducted for all cases from simple to complex finite element models. From the results of the numerical studies it can be concluded that:

- The circular and square cross-sectional pultruded composite tubes with triggering type 2 (tulip pattern) exhibited non-axisymmetric buckling mode shapes. The closely spaced Eigen frequencies of the composite tubes showed that these structures are very sensitive to the initial geometric imperfections. However, the result from the impact analysis with the perturbated mesh (superposition of buckling mode shapes on the perfect geometry) revealed no significant change in the peak crush load and the energy absorption. Hence during the design of such a composite structure one must adopt utmost caution to deploy this approach (superposition of linear buckling mode shapes on perfect geometry to introduce the initial geometric imperfections) to predict the impact parameters (peak load and the energy absorption) with a single layer of shell elements approach. Furthermore, there was a difference in the deformation pattern noticed between the approaches with and without geometric imperfection.
- The measured initial geometric imperfections analysis with Case 1 (a single layer of shell elements) yielded higher peak crush loads and deformation lengths for circular and square composite tubes. However, in case of circular tubes there was no significant difference in the energy absorption noticed between the cases with and without imperfection. Square tubes with initial geometric imperfection showed higher energy absorption than the case without imperfection. This was due to higher peak crush load and deformation length. In both cases (circular and square) the imperfect geometry attributed to a lower magnitude of the initial peak load.
- The measured initial geometric imperfections analysis with Case 2 (two layers of shell elements with a solid cohesive layer) yielded a very close

peak crushing load compared to the experimental data for the circular tubes. However, there was no significant difference in the energy absorption noticed with perfect tube analysis. Similarly there was no appreciable difference in the peak crush load and the energy absorption observed for square composite tubes.

- Case 3 (two layers of shell elements with solid cohesive elements and pre-defined seams) with measured initial geometric imperfection provided no significant difference in the energy absorption. However, the peak crush load for the circular tube was reduced from 67 kN to 60 kN. For square tubes there was no significant difference in the peak load and deformation pattern observed due to the initial geometric imperfection.
- Similarly Case 4 (multiple layers of shell elements with cohesive elements) and Case 5 (multiple layers of shell elements with cohesive elements and with pre-defined seams) provided a lower magnitude of the peak crush load than the case without imperfection. However, there was no distinctive difference in the total absorbed energy noticed between the cases with and without imperfection. The magnitude of the initial peak for these approaches (with geometric imperfection) was much lower than other approaches. From the results it can be concluded that for square composite tube the perfect geometry of the tulips and the number of shell layers have a large influence on the initial peak load.
- Finally the effect of element size on the impact parameters has been evaluated with different element lsize (2 mm, 3.5 mm and 5 mm). The convergence study of different approaches on the perfect structure showed a good agreement with the experimental data. Furthermore there was no significant change in the deformation pattern due to the change in element length or size.

Bibliography

[1]. *ABAQUS User manual.* ABAQUS, Inc. and Dassault Systems 2007.

[2]. Warrior, N. A., Turner, T. A., Robitaille, F. and Rudd, C. D., *Effect of resin properties and processing parameters on crash energy absorbing composite structures made by RTM.* Composites Part A: Applied Science and Manufacturing, 2003. **34**(6): p. 543-550.

[3]. Hashin, Z. and Rotem, A., *A fatigue failure criterion for fiber reinforced materials.* Journal of Composite Materials, 1973. **7**: p. 448.

[4]. *ABAQUS Theory manual.* ABAQUS, Inc. and Dassault Systems, 2007.

[5]. Palanivelu, S., Van Paepegem, W., Degrieck, J., Van Ackeren, J., Kakogiannis, D., Van Hemelrijck, D., Wastiels, J. and Vantomme, J., *Experimental study on the axial crushing behaviour of pultruded composite tubes.* Polymer Testing, 2010. **29**(2): p. 224-234.

[6]. Han, H., Taheri, F., Pegg, N. and Lu, Y., *A numerical study on the axial crushing response of hybrid pultruded and +/-45[degree sign] braided tubes.* Composite Structures, 2007. **80**(2): p. 253-264.

[7]. McGregor, C., Vaziri, R. and Xiao, X., *Finite element modelling of the progressive crushing of braided composite tubes under axial impact.* International Journal of Impact Engineering. **37**(6): p. 662-672.

[8]. Mamalis, A. G., Robinson, M., Manolakos, D. E., Demosthenous, G. A., Ioannidis, M. B. and Carruthers, J., *Crashworthy capability of composite material structures.* Composite Structures, 1997. **37**(2): p. 109-134.

[9]. Mamalis, A. G., Manolakos, D. E., Ioannidis, M. B. and Papapostolou, D. P., *The static and dynamic axial collapse of CFRP square tubes: Finite element modelling.* Composite Structures, 2006. **74**(2): p. 213-225.

[10]. Arnaud, P. and Hamelin, P., *Dynamic characterization of structures: A study of energy absorption in composite tubes.* Composites Science and Technology, 1998. **58**(5): p. 709-715.

[11]. Mamalis, A. G., Manolakos, D. E., Ioanniddis, M. B. and Papapostolou, *Finite element modelling of the crushing response of square carbon FRP tubes subjected to static and dynamic axial compression.* WIT Transactions on Engineering Sciences, 2005. **49**(Impact Loding of Lightweight structures): p. 373-386.

[12]. Zarei, H., Kröger, M. and Albertsen, H., *An experimental and numerical crashworthiness investigation of thermoplastic composite crash boxes.* Composite Structures, 2008. **85**(3): p. 245-257.

[13]. Palanivelu, S., Van Paepegem, W., Degrieck, J., Kakogiannis, D., Van Ackeren, J., Van Hemelrijck, D., Wastiels, J. and Vantomme, J., *Comparative study of the quasi-static energy absorption of small-scale composite tubes with different geometrical shapes for use in sacrificial cladding structures.* Polymer Testing, 2010. **29**(3): p. 381-396.

[14]. Solaimurugan, S. and Velmurugan, R., *Influence of fibre orientation and stacking sequence on petalling of glass/polyester composite cylindrical shells under axial compression.* International Journal of Solids and Structures, 2007. **44**(21): p. 6999-7020.

[15]. Wang, X. W., Pont-Lezica, I., Harris, J. M., Guild, F. J. and Pavier, M. J., *Compressive failure of composite laminates containing multiple delaminations.* Composites Science and Technology, 2005. **65**(2): p. 191-200.

[16]. Bisagni, C., *Dynamic buckling of fiber composite shells under impulsive axial compression.* Thin-Walled Structures, 2005. **43**(3): p. 499-514.

[17]. Hilburger, M. W. and Starnes, J. H., *Effects of imperfections of the buckling response of composite shells.* Thin-Walled Structures, 2004. **42**(3): p. 369-397.

[18]. Tsouvalis, N. G., Zafeiratou, A. A., Papazoglou, V. J., Gabrielides, N. C. and Kaklis, P. D., *Numerical modeling of composite laminated cylinders in compression using a novel imperfections modeling method.* Composites Part B: Engineering, 2001. **32**(5): p. 387-399.

Chapter 10

Axial Crushing Study of Medium-scale Pultruded Composite Tubes

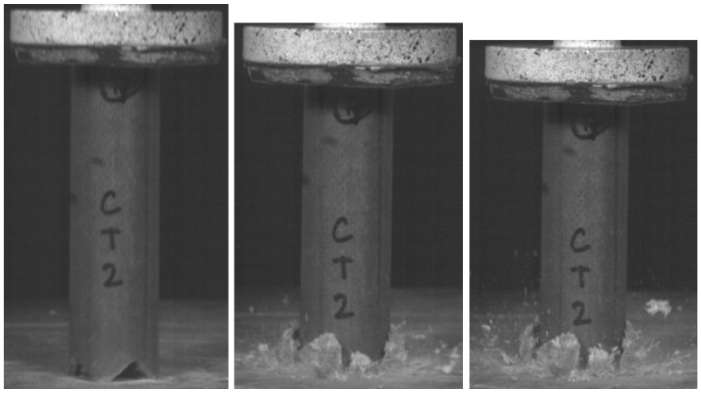

Overview

This chapter presents the experimental investigation on the progressive crushing behaviour of pultruded uni-directional cylindrical medium-scale composite tubes subjected to an axial quasi-static and impact load. Two types of triggering profiles were incorporated to investigate the effect of triggering on the energy absorption. Experimental tests have been conducted for three different impact velocities and with two different impactor masses. The crushing performance such as the deformation pattern, peak crush load and the corresponding energy absorption of these composite tubes are presented.

10. 1. Introduction

Chapter 8 presented the experimental axial impact study on large-scale pultruded composite tubes. Similarly, Chapter 9 presented the different approaches of numerical simulations and their corresponding results. As noticed from these chapters the geometrical dimensions of the used pultruded composite tubes are quite large (outer width = 60 mm; thickness = 4.5 mm for square cross-sectional glass polyester tube; outer ϕ = 50 mm and thickness 3 mm for glass polyester circular cross-sectional tube). Furthermore, from the experimental and numerical simulations

it was observed that the peak crush load for an individual composite tube was approximately 70 kN. This magnitude is very high; and the crushing of these composite tubes under blast loading needs a very large size (mass) of the charge. Furthermore, this size of the composite tube may not be required for the inner core of the proposed sacrificial cladding structure. However, these composite tubes have provided an opportunity to understand the experimental crushing performance (typical failure patterns and load-deformation histories) and the corresponding numerical modelling validation. On the other hand, for the actual deployment for the inner core of the proposed sacrificial cladding structure medium-scale composite tubes have been chosen. As mentioned earlier, the entire dissertation is focussed only on the axial loading (impact and blast) of the crushing structures (beverage cans and composite tubes). Therefore, similar to the earlier approach pultruded glass polyester composite tubes have been chosen but with smaller dimensions. Furthermore, the axial impact tests on large-scale circular and square cross-sectional tubes showed that the specific energy absorption of the circular cross-sectional composite tubes was higher than the square cross-sectional tubes. Therefore, only cylindrical composite tube (circular cross-section) was chosen for this study. Axial quasi-static and impact tests have been conducted to check the energy absorption performance of the composite tubes. Two different impactor masses and triggering mechanisms were used to conduct axial impact testing. All the above combinations were tried out for three different impact velocities. The deformation patterns, peak crush load and the corresponding energy absorption of these composite tubes are presented.

10. 2. Composite tube test specimens

All the tubes which were used for the tests are manufactured by the pultrusion process (M/s EXEL, Belgium). The laminates were made with continuous 0° orientation fibres. To get the better surface finish the outer and inner layers were made up of random short glass fibres with approximate thickness of 0.12- 0.35 mm. The architectural construction of these composite tubes was very similar to the one which was discussed in Chapter 8 (refer Figure 8-1 in Chapter 8). Two different tube combinations CT1 and CT2 were studied experimentally. The CT1 and CT2 refer to the cylindrical glass-polyester pultruded tube with triggering type 1 and type 2 respectively. The triggering type 1 is the 45° chamfering around the edges of the tubes (bevel triggering) and the type 2 is a tulip pattern with an included angle of 90° between the edges. Figure 10-1 illustrates the details of the triggering. The t/D ratio and linear density of the tubes are chosen as per the recommendations given in ref.[1, 2] The details of the tube geometry, fibre, resin, tube dimensions, linear density and the corresponding volume fraction are mentioned in Table 10-1. As an example, the used composite tubes are shown in Figure 10-2.

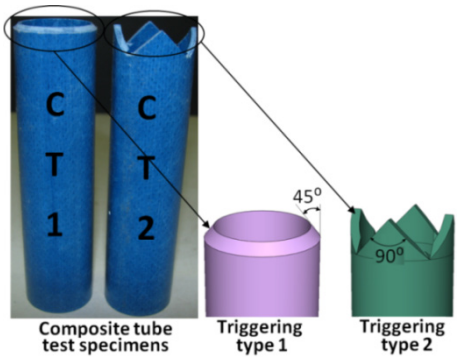

Figure 10-1: Glass polyester cylindrical composite tubes

Table 10-1: Dimensional and material details of the composite tube series.

Cross-section	Fibre	Resin	Dimensions (mm)	ρ_{linear} (g/mm)	Volume fraction (%)
Circular	Glass	Polyester	$\phi = 25$ $t = 2$ $L = 100$	0.235 for CT1 0.227 for CT2	$V_m = 49.7$ $V_f = 50.3$
ϕ - Outer diameter; t – thickness; L – length of tube; V_m – volume fraction of matrix; V_f – volume fraction of fibre.					

Figure 10-2: Cylindrical glass polyester composite tube test specimens.

10. 3. Quasi-static testing results

The typical quasi-static progressive deformation patterns of pultruded cylindrical glass polyester composite tubes with triggering type 1 and 2 (CT1 and CT2) for the crosshead displacement of 10 mm/min are shown in Figure 10-3(a) and Figure 10-3(b) respectively. Both tubes CT1 and CT2 showed the controlled progressive failure modes. For both tubes, the major circumferential delamination was started at the mid-wall thickness of the composite tube. Consequently, axial cracks were formed parallel to the axis of the tube. The uniform geometry of the circular cross-sectional tube facilitated to form a large number of axial cracks and thus more petals were formed. The major amount of the crushing energy was absorbed due to the increasing number of longitudinal cracks and the subsequent bending of the petals. During the crushing process a significant amount of fibre fracturing was also observed. As an example, the corresponding load-deformation histories of CT1 and

CT2 tubes are shown in Figure 10-4. As discussed in Chapter 8 and 9 the occurrence of the peak crush load corresponded to the major circumferential delamination (refer Figure 10-4). This can be noticed from the deformation length of the composite tubes corresponding to the peak crush load. For triggering type 2, due to the shape of the tulips the peak crush load occurred at around 10 mm of its deformation length. For these tubes, there was no significant difference in the peak load noticed for triggering type 1 and 2 (~13 kN). The post peak crush load of both composite tubes was approximately the same (refer Figure 10-4). A detailed comparison of quasi-static parameters with dynamic parameters is presented later.

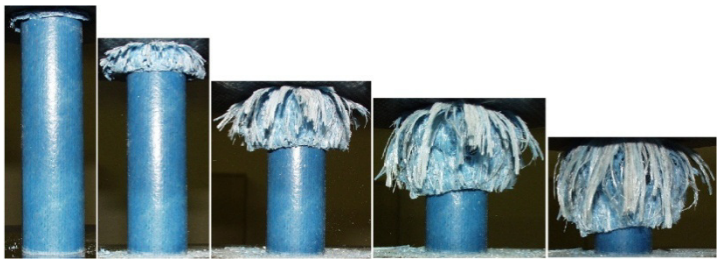

(a) Progressive deformation patterns of CT1 tube.

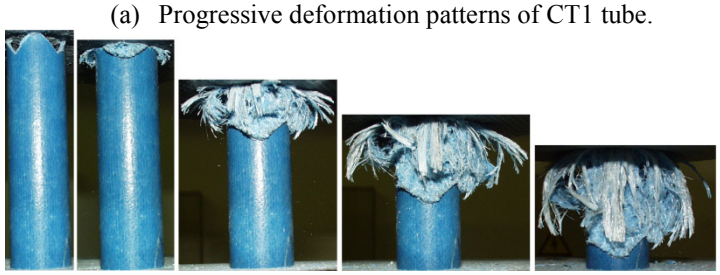

(b) Progressive deformation patterns of CT2 tube.

Figure 10-3: Progressive deformation patterns of cylindrical glass polyester composite tubes.

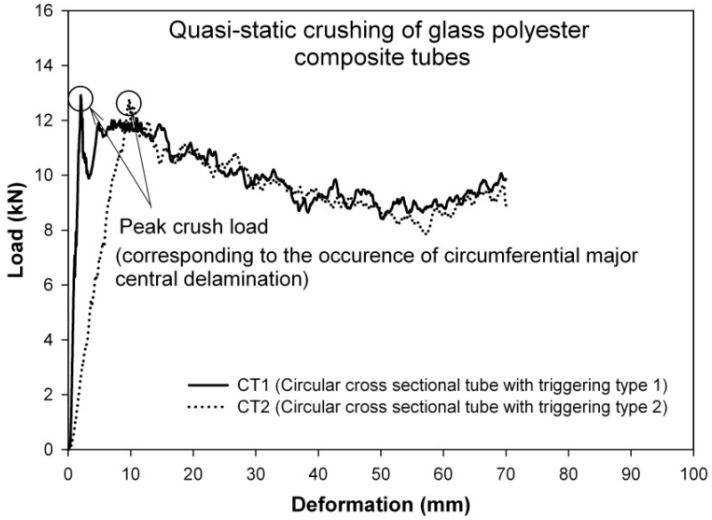

Figure 10-4: Quasi-static load-deformation curves for CT1 and CT2 tubes.

10. 4. Impact testing and results

10. 4. 1. Experimental test set-up

All tests have been performed with the medium-scale drop weight test facility which was discussed in Chapter 3 (refer Figure 10-5). Axial impact tests have been conducted with impact heights of 1.0 m, 1.5 m and 1.9 m which correspond to the initial impact velocities of 4.3 m/s, 5.3 m/s and 6.0 m/s. In order to study the effect of impactor mass on the crushing performance of the composite tubes, two impactor masses (7.6 kg and 10.6 kg) were used for conducting these tests. A high speed camera with a frame rate of 5000 fps was used to capture the deformation behaviour of these tubes. A sampling frequency of 200 kHz was chosen for all sensors (load cell, accelerometer and the inductive displacement sensor). A minimum of four composite tubes have been tested for each composite tube type (CT1 and CT2).

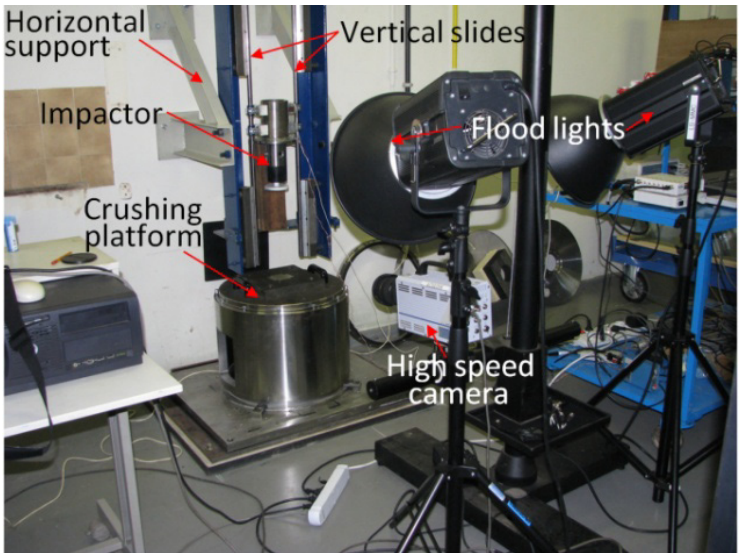

Figure 10-5: Experimental test set-up.

Samples of CT1 and CT2 composite tubes which have undergone the different phases of deformation are shown in Figure 10-6 and Figure 10-7 respectively. All composite tubes exhibited progressive crushing failure modes.

10. 4. 2. Failure patterns

The failure patterns of both composite tubes (CT1 and CT2) were very similar to the ones which were discussed in Chapter 8. For both composite tubes, due to the circumferential delamination and axial cracks the inner and outer petals were formed; subsequently, the bending of petals and fibre fracturing failure modes were

observed (refer Figure 10-6, Figure 10-7 and Figure 10-8). As an example, the final deformation patterns of CT1 and CT2 are shown in Figure 10-8. All the above said failure modes are clearly evident from these figures. A cut sectional view of these composite tubes showed a clear evidence for the circumferential major delamination at the mid-thickness of the composite tubes. The length of the axial cracks during the crushing process was well controlled by the circular geometry of the composite tubes (Figure 10-8). Unlike the results reported in the ref. [3-6] there was no evidence for the central triangular debris wedge which drives the continuous delamination at the mid-thickness of the tube. Furthermore, there was no evidence for the deposited matrix debris on the crushing platform after the test. Therefore, it can be concluded that to drive the continuous circumferential delamination the debris wedge is not necessary for the case of unidirectional pultruded composite tubes. Similar to the large-scale pultruded composite tube which was discussed in Chapter 8, the separation of the outer random mat fibre from the inner core fibre was noticed.

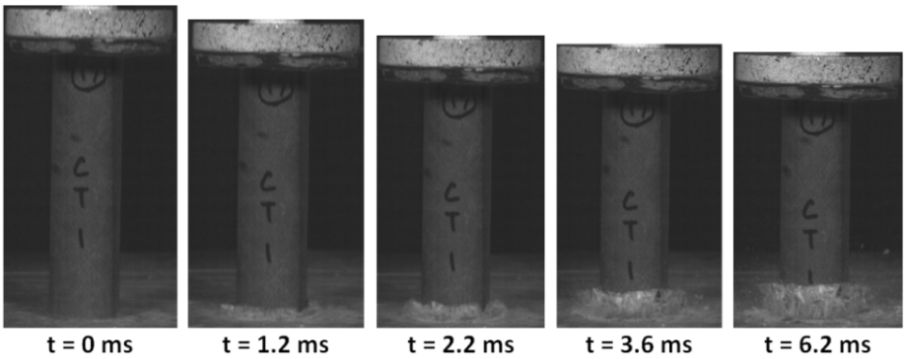

Figure 10-6: Progressive crushing phases of CT1 tube for dynamic loading.

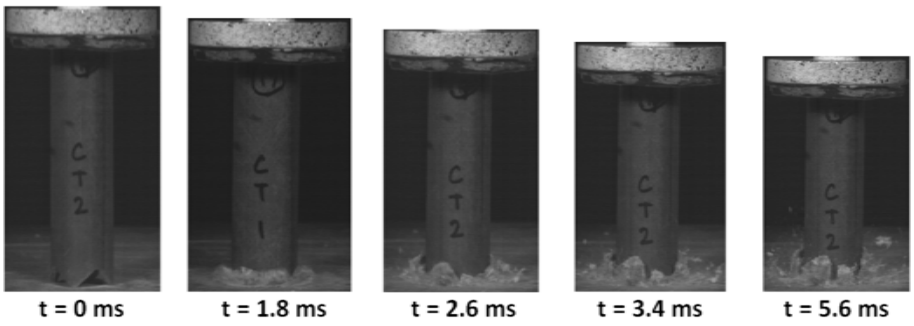

Figure 10-7: Progressive crushing phases of CT2 tube for dynamic loading.

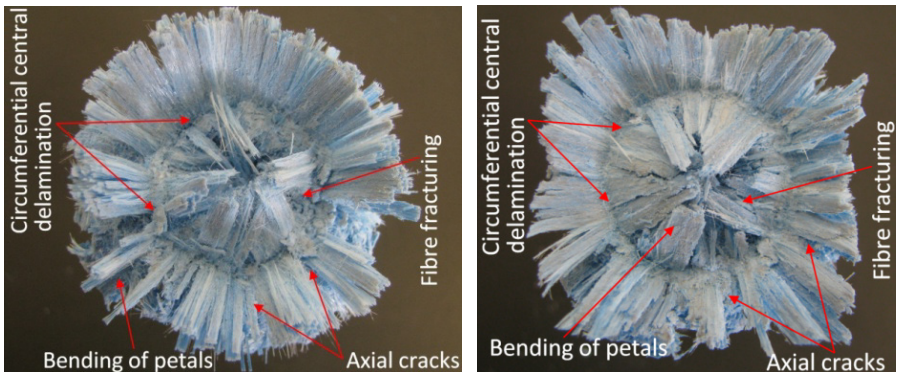

(a) CT1 tube (b) CT2 tube

Figure 10-8: Final deformation patterns of CT1 and CT2 composite tubes.

10. 4. 3. Force-deformation curves

As an example, the force-deformation curves of the composite tube series CT1 and CT2 for different initial impact velocities (4.3 m/s, 5.3 m/s and 6.0 m/s) with an impactor mass of 10.6 kg are shown in Figure 10-9 and Figure 10-10 respectively. It can be noticed that the scatter is low for different initial impact velocities. Similar to the large-scale pultruded composite tubes were three different phases noticed on the load-deformation curves (initial peak crush load, sudden drop after the peak and oscillation of crush load around a mean value). The details of all three phases are well discussed in Chapter 8.

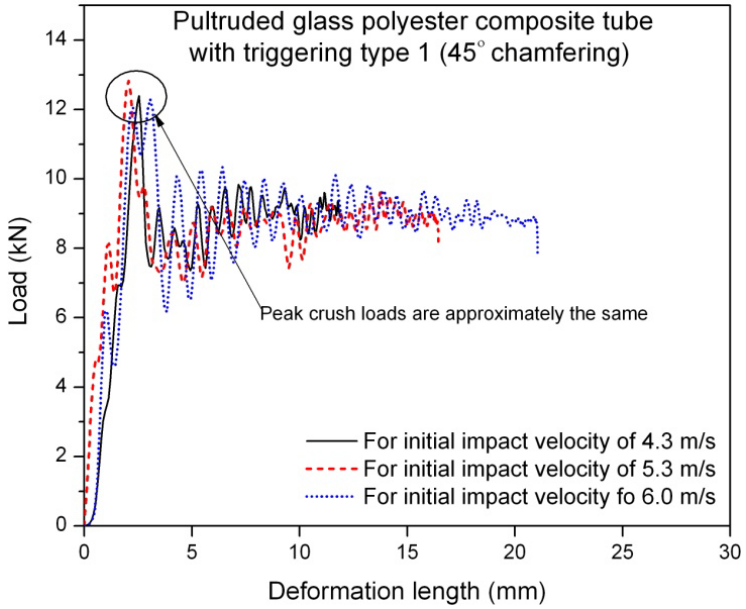

Figure 10-9: Load-deformation curves for CT1 tube series.

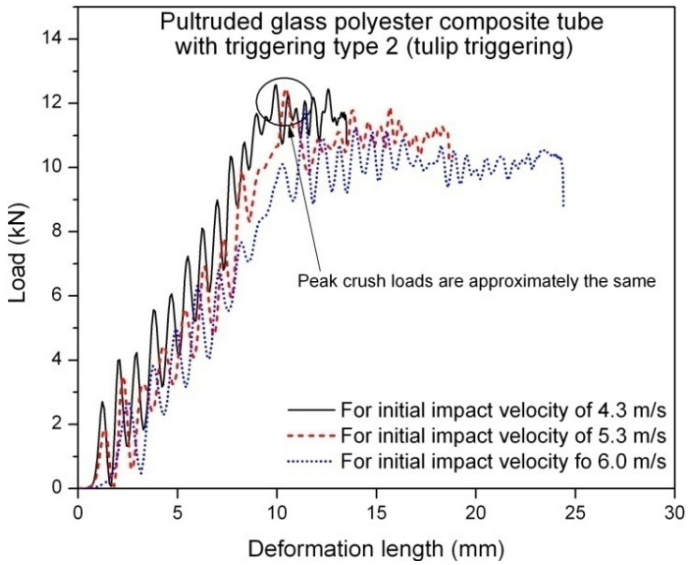

Figure 10-10: Load-deformation curves for CT2 tube series.

One important observation can be noticed from these figures. Irrespective of the initial impact velocity, the peak crush load of these composite tubes was approximately the same for triggering type 1 and 2. Hence, it can be concluded that for uni-directional fibre orientation the effect of strain-rate on the peak crush load is negligible. However, the peak crush load of these composite tubes should be verified for the blast loading condition and the same is presented in Chapter 11. The average magnitude of the peak crush load (four tests from each category) and the corresponding mean crush load are given in Table 10-2. For triggering type 1 (CT1), the peak crush load varied from a minimum of 12.4 kN to a maximum of 13.6 kN. Similarly for triggering type 2 it varied from a minimum of 11.6 kN to a maximum of 12.3 kN. It can be noticed that the peak crush load of the triggering type 1 was slightly higher than the triggering type 2. The ratio of the mean crush load to the peak crush load which indicates the efficiency of the crushing (η_c) is also given in Table 10-2. Furthermore, the mean crush load of the composite tube decreased with an increasing initial impact velocity.

10. 4. 4. Comparison of static and dynamic SEA

The calculated average total energy absorption and the corresponding specific energy absorption (from four test specimen) from each case are presented in Table 10-2. For both impactor masses (7.6 kg and 10.6 kg) the mean crush load decreased with increasing impact velocity. As a result the specific energy absorption was also decreased with increasing initial impact velocities. Few researches have investigated the effect of strain rate on the energy absorption [7-11]. They all suggested that the mechanism which controls the failure of the composite tube is a function of strain

rate or speed of crushing; furthermore, the crushing speed generally affects the energy absorbing capability of the fibre and the matrix. Hamada et al. [11] reported that for the same composite tube the dynamic specific energy absorption was lower than the quasi-static case. Hence, in order to study the effect of strain rate on the energy absorption of these composite tubes, a comparison was made between the static and dynamic SEA. The specific energy absorption for dynamic and quasi-static cases was calculated for the same deformation length (maximum deformation length corresponded to each dynamic test); and the results are presented in Figure 10-11(a-b) and Figure 10-12(a-b).

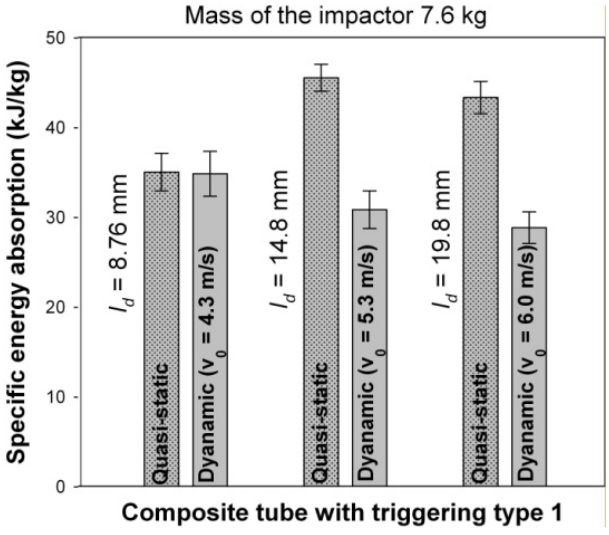

(a)

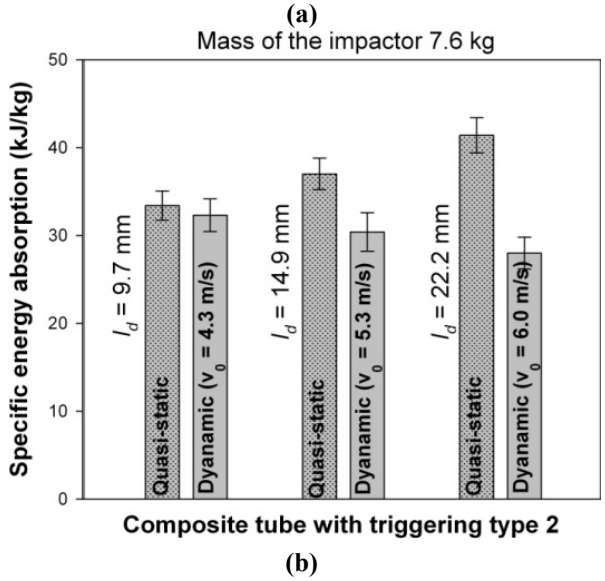

(b)

Figure 10-11: Comparison of quasi-static and dynamic SEA **(a)** Triggering type 1 **(b)** Triggering type 2 (l_d is the deformation length and error bar indicates the standard deviation).

From these figures, it can be noticed that the scatter in the SEA was low for both quasi-static and dynamic cases. Although the deformation patterns for quasi-static and dynamic cases remains the same, for most cases, the dynamic SEA was significantly lower than the quasi-static SEA.

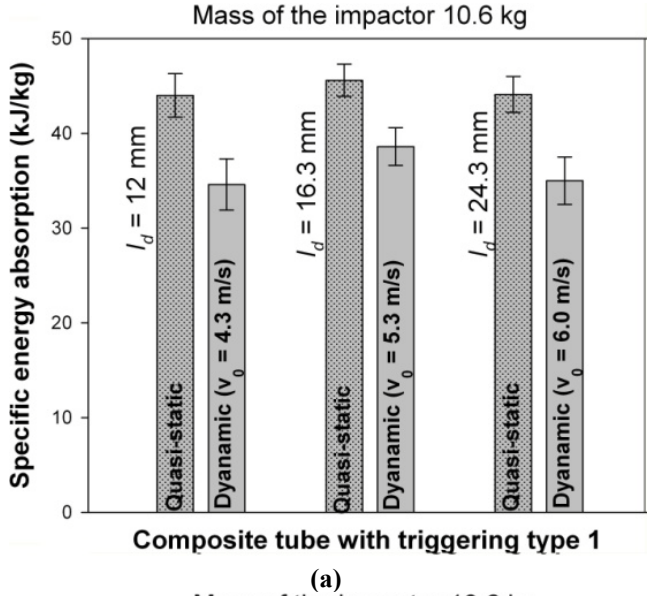

(a)

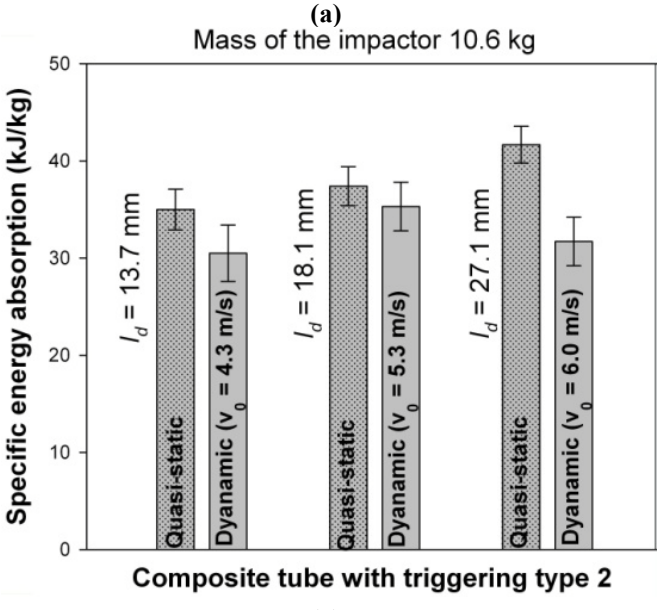

(b)

Figure 10-12: Comparison of quasi-static and dynamic SEA **(a)** Triggering type 1 **(b)** Triggering type 2 (l_d is the deformation length and error bar indicates the standard deviation).

Table 10-2: Summary of average crushing parameters.

Tube type	Initial impact velocity	Deformation length	Standard deviation for deformation length	Energy given by the impactor	Energy absorbed by the tube	Specific energy absorption	Peak crush load	Mean crush load	Crush efficiency
	(m/s)	(mm)	(mm)	(J)	(J)	(kJ/kg)	(kN)	(kN)	(%)
Mass of the impactor 7.6 kg									
CT1	4.38	8.76	1.1	73.5	72.3	35.2	12.6	8.28	65.7
CT2	4.37	9.72	1.8	73.2	72.0	31.6	12.1	7.43	61.4
CT1	5.36	14.85	2.9	110.2	108.2	31.0	12.4	7.29	58.8
CT2	5.31	14.88	2.7	108.2	107.3	29.8	12.0	7.01	58.4
CT1	6.03	19.8	3.7	139.6	138.0	29.7	12.7	7.00	55.1
CT2	6.08	22.2	3.2	140.1	140.12	26.8	11.6	6.30	54.4
Mass of the impactor 10.6 kg									
CT1	4.34	12.00	1.5	101.1	100.0	35.4	13.6	8.33	61.2
CT2	4.37	13.73	2.1	102.6	101.2	31.3	12.3	7.35	59.8
CT1	5.40	16.30	3.2	156.2	154.8	40.4	15.6	9.46	60.8
CT2	5.36	18.10	2.6	154.1	153.0	36.0	13.0	8.48	65.2
CT1	6.03	24.3	3.6	195.2	193.1	33.8	13.1	7.94	60.6
CT2	6.04	27.1	3.9	196.1	194.3	30.5	11.7	7.17	61.2

Because of a shorter deformation length, the dynamic SEA of triggering type 1 tube (with the impactor mass of 7.6 kg and with an initial impact velocity of 4.3 m/s) was equal to the quasi-static SEA (refer Figure 10-11(a-b). The average SEA was 35.4 kJ/kg and 35.2 kJ/kg for quasi-static and dynamic cases respectively. However, same initial impact velocity (4.3 m/s) with a higher impactor mass (10.6 kg) provided a lower SEA compared to the quasi-static value (44 kJ/kg and 35.4 kJ/kg for quasi-static and dynamic cases respectively). This was due to the additional kinetic energy provided by the impactor mass and subsequent longer deformation length of the test specimen. For the remaining impact velocities (5.3 m/s and 6.0 m/s) the difference between the quasi-static and dynamic SEA was significantly increased with increasing impact velocity (refer Figure 10-11 and Figure 10-12). However, for the case with the impactor mass of 10.6 kg the SEA for 4.3 m/s initial impact velocity case was lower compared to the 5.3 m/s case. The decreased SEA for 4.3 m/s case can be understood from the schematic diagram which is given in Figure 10-13. For all tests (with the impactor mass of 10.6 kg) the profile of the load-deformation curves followed four phases: (i) a steep increase to peak crush load (ii) sudden drop (iii) gradual increase in the load and (iv) a constant crush load with minor drop. All four phases can be noticed from Figure 10-13. Because of the lower deformation length the load deformation profile ended very close to phase III for the case with initial impact velocity of 4.3 m/s. As a result a lower SEA was noticed for compared to 5.3 m/s case.

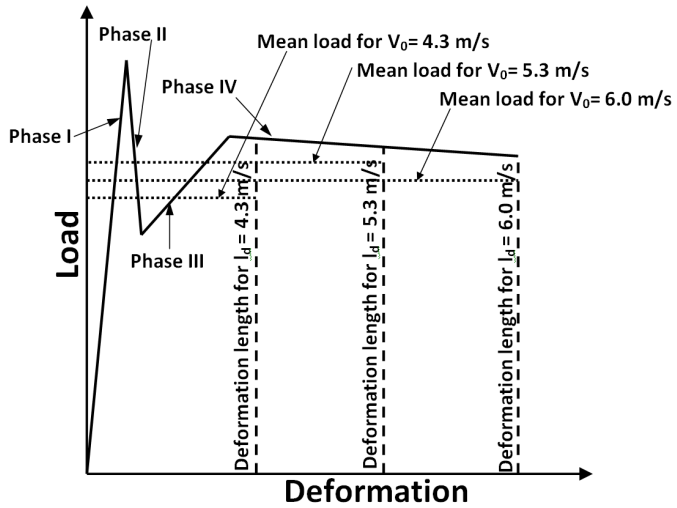

Figure 10-13: Schematic illustration of dynamic load-deformation curves.

The question of why the dynamic SEA decreases compared to the quasi-static SEA is to be answered. In quasi-static tests, after the circumferential delamination (which corresponds to the occurrence of the peak crush load) more petals were formed due to the axial cracks. The length of each petal or axial crack was controlled by the crosshead displacement of the Instron machine; and hence the length of the petal

was constant with respect to time. To rotate these petals at their base and subsequent bending a constant force was needed. Hence, the crushing force remains approximately the same after the peak crush load. However, during dynamic loading other than the geometry and material properties of the tube, the length of the axial cracks was determined by the combined effect of the inertia of the impactor and impact velocity. Furthermore, the lateral inertia of the composite tubes could play a role, but negligible for this case. Due to the above factors the length of the axial cracks which were formed (after the circumferential delamination) during the initial contact of the test specimen with the impactor, was longer compared to the quasi-static case. Hence, a relatively lower force was required to rotate the petals at their base and subsequently for the bending. Because of these phenomena the crush load dropped suddenly after the peak. Immediately after this event, a next cycle of circumferential delamination and axial cracks were formed. Due to the dynamic effect a smaller amount of energy was needed to create the next cycle of delamination and fracture surfaces (axial cracks). The increase in crush load corresponding to this process (refer Figure 10-13). However, by that time a significant amount of total energy from the impactor has been spent; and further it was continued until the total energy from the impactor dissipated by the composite tube. As an example, a comparison of the quasi-static and dynamic load-deformation curves (for the case with the initial impact velocity of 4.3 m/s) is shown in Figure 10-14. The peak crush load of these cases is approximately the same. However, there was a significant difference in the post peak crush load. For the dynamic case the drop in the load after the peak was higher compared to the quasi-static case. This means that once a longer length of (axial) crack was initiated; the rotation and subsequent bending of each petal needed a relatively lower force. In other words a lower force sufficient enough to create new fracture surfaces and the corresponding rotation of petals. Therefore, it can be stated that the magnitude of the crushing force depends upon the length of the axial crack (petal) and the lateral inertia of the petals.

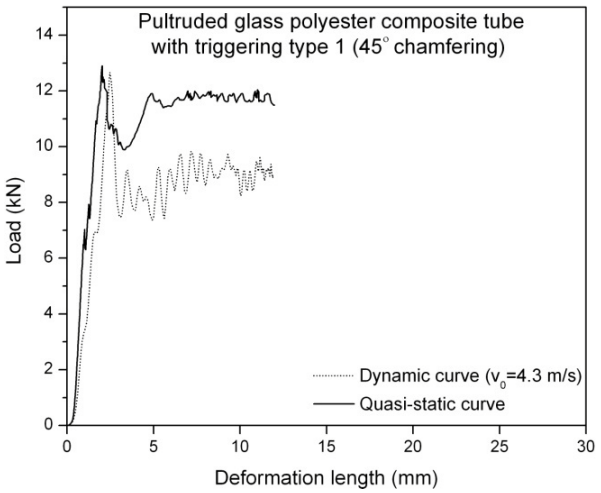

Figure 10-14: Comparison of quasi-static and dynamic load-deformation curves.

The effect of triggering on the SEA can be noticed from Figure 10-11 and Figure 10-12. For all cases, the SEA of triggering type 2 was lower than for triggering type 1. A higher deformation length of this case attributed for a lower SEA in all cases. However, for a few cases there was no significant difference noticed (for the case with the initial impact velocity of 5.3 m/s and 6.0 m/s with the impactor mass of 7.6 kg).

10. 5. Conclusions

In this chapter, the axial quasi-static and impact crushing performance of medium-scale pultruded cylindrical glass polyester composite tubes have been investigated. Axial quasi-static and impact tests have been conducted on these composite tubes with two different triggering mechanisms (45° chamfering and tulip triggering) and impactor masses of 7.6 kg and 10.6 kg. The above combinations have been tested for three different impact velocities (4.3 m/s, 5.3 m/s and 6.0 m/s). The effect of strain rate on the deformation patterns and the corresponding energy absorption were studied. From the conducted experimental tests the following conclusions can be made:

- In all cases the chosen composite tubes (CT1 and CT2) showed controlled and progressive crushing modes with circumferential delamination, axial cracks, lamina bending and fibre fracturing failure modes.
- The peak crush load of the composite tubes (CT1 and CT2) from quasi-static and impact experiments showed that these tubes are insensitive to the strain rate effect which is a good feature for the requirement of inner core of a sacrificial cladding structure. Use of these tubes will provide a constant peak force and the corresponding acceleration to the mounting structure irrespective of the magnitude of the (blast pressure) loading.
- The SEA of dynamic loading cases of these tubes decreased with increasing initial impact velocity. This was due to the decreased mean crush load for higher impact velocity cases.
- The dynamic SEA of all tubes was consistently lower than the quasi-static SEA. The major reason for this difference was the length of the axial cracks and the corresponding rotation of the petals. During a quasi-static loading the length of the axial cracks was controlled by the crosshead displacement. However, during the dynamic loading the inertia of the impactor, impact velocity and lateral inertia of the tube play a major role. When a (axial) crack was initiated, a relatively lower force was sufficient enough to create new fracture surfaces and the corresponding rotation of the petals.

Although the quasi-static and impact tests on the composite tubes with triggering type 1 and 2 showed the same peak crush load (12 to 13 kN), the same is to be verified for blast loading conditions. Furthermore, to use these tubes as inner core members the individual performance of these tubes for the blast loading should be understood. Hence, in order to check the deformation patterns and the corresponding crushing performance of these tubes close-range blast experiments have been conducted. The details of the conducted experiments and the corresponding results are discussed in the next chapter (Chapter 11).

Bibliography

[1]. Hamada, H. and Ramakrishna, S., *Scaling effects in the energy absorption of carbon-fiber/PEEK composite tubes.* Composites Science and Technology, 1995. **55**(3): p. 211-221.

[2]. Thornton, P. H. and Edwards, P. J., *Energy absorption in composite tubes.* Journal of Composite Matter, 1982. **16**: p. 521-545.

[3]. Pinho, S. T., Camanho, P. P. and de Moura, M. F., *Numerical simulation of the crushing process of composite materials.* International Journal of Crashworthiness, 2004. **9**(3): p. 263 - 276.

[4]. McGregor, C., Vaziri, R. and Xiao, X., *Finite element modelling of the progressive crushing of braided composite tubes under axial impact.* International Journal of Impact Engineering. **37**(6): p. 662-672.

[5]. Mamalis, A. G., Manolakos, D. E., Demosthenous, G. A. and Ioannidis, M. B., *Energy absorption capability of fibreglass composite square frusta subjected to static and dynamic axial collapse.* Thin-Walled Structures, 1996. **25**(4): p. 269-295.

[6]. Mamalis, A. G., Robinson, M., Manolakos, D. E., Demosthenous, G. A., Ioannidis, M. B. and Carruthers, J., *Crashworthy capability of composite material structures.* Composite Structures, 1997. **37**(2): p. 109-134.

[7]. Thornton, P. H., *The crush behavior of pultruded tubes at high strain rates.* Journal of Composite Materials, 1989. **24**: p. 22.

[8]. Arnaud, P. and Hamelin, P., *Dynamic characterization of structures: A study of energy absorption in composite tubes.* Composites Science and Technology, 1998. **58**(5): p. 709-715.

[9]. Farely, G. L., *The effect of crushing speed on the energy-absorption capability of composite tubes.* Journal of Composite Materials, 1991. **25**: p. 1314.

[10]. Farely, G. L., *Relationship between Mechanical - Property and Energy - Absoprtion Trends for Composite Tubes.* NASA TP-3284, ARL-TR-29, 1992, 1992.

[11]. Hamada, H., Kameo, K., Sakaguchi, M., Saito, H. and Iwamoto, M., *Energy-absorption properties of braided composite rods.* Composites Science and Technology, 2000. **60**(5): p. 723-729.

Chapter 11

Blast Loading on Medium-scale Pultruded Composite Tubes

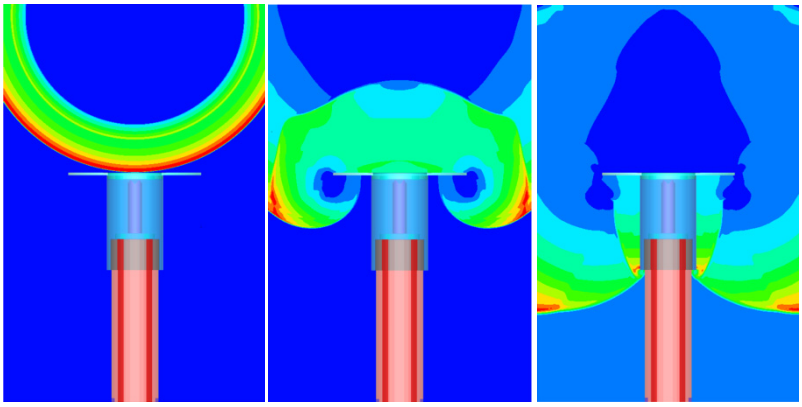

Overview

This chapter deals with close-range free air blast loading on medium-scale pultruded cylindrical glass/polyester composite tubes. Close-range free air blast tests have been conducted in detail to understand the crushing mechanisms and the corresponding energy absorption of single composite tubes with two different triggering mechanisms. The measured blast parameters from the experimental tests were compared with ConWep predicted data. A decoupled numerical analysis was carried out in Abaqus v6.10-1 explicit code using the experimentally measured reflected pressure time histories. The interaction of pressure waves with the test set-up and the corresponding effect on the loading of the structure (skin plate) were studied with Hydrocodes. The results from these numerical analyses are compared and validated with the experimental results.

11. 1. Introduction

Chapter 4 discussed close-range experimental blast loading on beverage cans and the corresponding crushing performance. This chapter discusses close-range blast loading on pultruded cylindrical glass polyester composite tubes. Few researchers [1-4] have investigated metals and its alloys for both outer skin and inner core. Nurick et al. [5] conducted tests with very close-range air blast and contact blast loads on sandwich structures comprising mild steel plates and aluminium alloy honeycomb cores. The honeycomb sandwich results are compared to the test results of structures with air as the core. This study concluded that the performance of the air core structure was better than honeycomb structures for small-scale explosion (impulse < 20 N.s); above 20 N.s the performance of honeycomb structures was better due to the energy absorption of the honeycomb core. Very recently Dharmasena et al. [6] studied explosive loading on sandwich panels with low density pyramidal lattice cores. Theobald et al. [3] studied the response of a sandwich cladding panel under blast loading. The sandwich inner cores are composed of square thin-walled metallic tubes using three primary layouts. The materials used for the inner core were annealed mild steel and 6063-T6 aluminium alloy. Similarly, Karagiozova et al. [4] studied the performance of circular and square shells made of aluminium alloy 6063 T5 subjected to explosive loads.

As seen in the previous paragraph different metals and its alloys have been tried out to minimize the peak force and the corresponding acceleration to the non-sacrificial structure. On the other hand, composite materials have relative advantages in terms of specific energy absorption, weight and maintenance [7-11]. Hence, this study focuses on the crushing performance of composite tubes for blast loading condition. As discussed in Chapter 4, before designing such a full-scale sacrificial cladding structure the knowledge of crushing performance (peak crush load, energy absorption, deformation pattern, strain rate effect on the material, etc.) of an individual sacrificial member is important. Despite a great deal of work on composite tubes under quasi-static and impact loading, there is almost no data available on the response of composite tubes subjected to air blast loading. Hence, to understand the above factors, close-range free air blast tests have been conducted with 40g of C4 with stand-off distances of 30 cm and 15 cm. The failure modes of composite tubes and the corresponding crushing characteristics have been studied for two different triggering mechanisms.

Similar to Chapter 4, to understand the parameters such as the inertia of the skin plate and surface area of the skin plate blast tests have been conducted with different masses of the skin plates. The effect of finite surface area and the corresponding resultant impulse was also explained. Similar to the blast loading on beverage cans, a part of the impulse was lost before it transferred to the non-sacrificial structure (for

40g C4 with 30 cm and 15 cm). This was due to the diffraction and ground reflection phenomena. However, due to the different charge mass (40g of C4) and stand-off distance (15 cm) the interaction of pressure waves with the experimental test set-up may differ. Hence, in order to understand the interaction of pressure waves and the corresponding impulse coupled and decoupled numerical studies have been conducted and the results from these studies are compared and validated with the experimental results.

11. 2. Experimental test set-up

The geometrical and material details of the composite tube test specimens and their nomenclature were given in Chapter 10. Furthermore, the working principle and the corresponding details of the experimental test set-up were given in Chapter 4. The schematic representation of the small-scale air blast test set-up which was used for conducting the blast tests is reproduced in Figure 11-1.

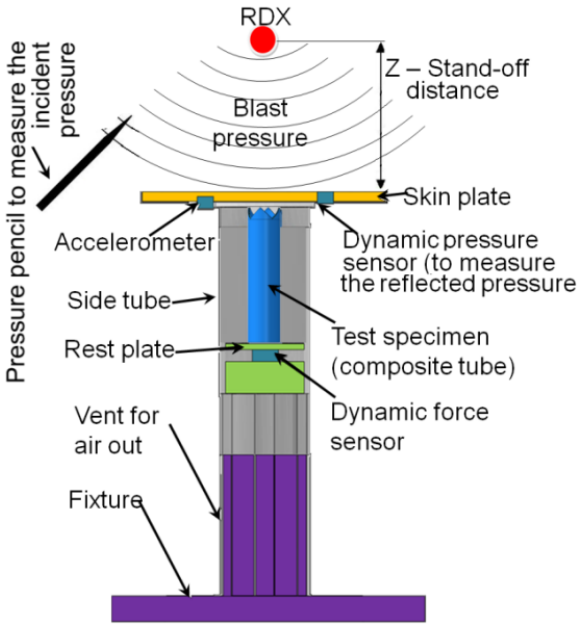

Figure 11-1: Schematic view of small-scale air blast test set-up.

Two types of skin plates (ϕ 250 mm) have been manufactured to study the clearing effect and inertia of the skin plate on the deformation length and the corresponding energy absorption of the composite tubes. The skin plates were made with aluminium (grade 2024 T3) and 3D stitched sandwich composite plates (top and bottom composite skin panels are made of bi-axially balanced glass fibre with polyester resin; core structure made of divinycell P foam; stitch made by aramid fibres; further details of the skin plate can be found from Chapter 15). The length of

the side tube was chosen 180 mm to have an adequate protection for the test specimen from the side pressure and to avoid oblique or offset loading during a blast event (refer Figure 11-2). The used materials for the side cover tubes were carbon-epoxy composite and PVC (polyvinyl chloride). To have a rigid crushing surface for the sandwich composite skin plates, a circular aluminium plate (ϕ 97 mm; 2 mm thick) was fixed to the bottom face of the skin plate in contact with the composite tube. The combined mass of the aluminium skin plate (top skin plate and the side tube) and the sandwich composite skin plates (top skin plate, side tube and circular aluminium plate) were 1.0 kg and 0.7 kg respectively.

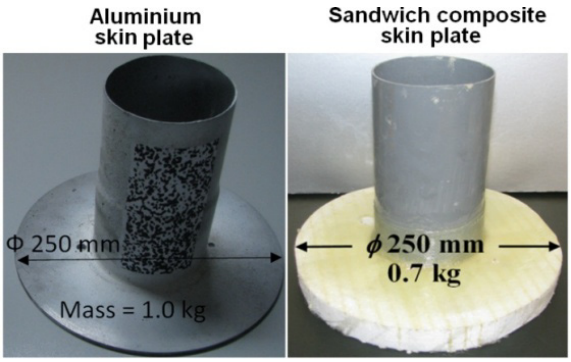

Figure 11-2: Aluminium and sandwich composite skin plates.

11. 3. Experimental results and discussions

In order to understand the crushing behaviour of a single composite tube and to compare the results with the beverage can, initially blast tests have been conducted with the same settings of 20g of C4 and with a stand-off distance of 30 cm. However, there was no deformation of the composite tubes for this loading. Hence, the charge mass was increased from 20g to 40g C4. A series of close-range free-air blast tests have been conducted with 40g of C4 and with stand-off distances of 30 cm and 15 cm. The charge was made spherical in shape. To achieve a zero incidence angle of the pressure waves, the charge was placed perpendicular and positioned to the centre of the top face of the skin plate. A sampling frequency of 5 MHz was chosen for all sensors (pressure sensors, accelerometer and the dynamic load cell). A minimum of five tests have been conducted for each loading case.

11. 3. 1. Pressure profiles and clearing effect

Pressure profiles

The nature of incident and reflected pressure is well discussed in Chapter 4. Furthermore, a list of commercial tools to predict the blast parameters and their

limitations are also explained (the fully reflected blast parameters given by these programs do not include the effects of clearing of the reflected pressure wave associated with a limited size of the reflected surface, mach effect and multiple reflections etc). Similar to Chapter 4, a comparison was made between the ConWep and measured blast experimental data with skin plates (refer Table 11-1). The input parameters for the ConWep were the same as the experimental test conditions (charge mass (40g), stand-off distance (30 cm and 15 cm) and the measurement of the reflected pressure (70 mm from the centre of the plate)). It can be noticed that a good correlation of peak reflected pressure was observed for both skin plates. However, there was a significant difference in the positive duration noticed. This was due to the limited surface area and the corresponding clearing of the reflected pressure waves. The corresponding experimental reflected impulses (area below the reflected pressure time curves) are given in Table 11-1. The incident pressure for a few tests with the sandwich composite skin plate (0.7 kg) was not measured due to the problem of physical connection with the adaptors. Furthermore, the reflected parameters for 40g C4 with stand-off distance of 15 cm could not be measured due to the consistent destroying of pressure sensors by the high pressures.

Figure 11-3 and Figure 11-4 show a comparison of the experimentally measured reflected over pressure-time histories with the aluminium skin plate (ϕ 250 mm; 1.0 kg), sandwich composite skin plate (ϕ 250 mm; 0.7 kg) and with the ConWep pressure profile. Due to the limited scatter, the first three tests are shown and for the simplification only the positive phase of the reflected pressure profile is shown. The influence of finite surface area on the positive phase duration can be understood again from these figures. The peak reflected pressure values (average of 8073 kPa and 7898 kPa with the aluminium and sandwich composite skin plates respectively) from the experimental tests showed a very good agreement to the ConWep predicted data (8275 kPa). However, the experimentally measured positive duration (average of 0.167 ms and 0.174 ms with the aluminium and sandwich composite skin plates respectively) was significantly lower than the ConWep predicted value (0.514 ms). This was due to the clearing of the reflected pressure waves (the pressure wave quickly passes around the edge of the skin plates due to the finite surface area of the skin plate) which ConWep does not take into account to calculate the positive duration of the reflected pressure wave.

Table 11-1: Summary of predicted and experimentally measured blast parameters (incident and reflected).

Type of composite tube	Experimental test No	Area of the circular skin plate (A_p)	Mass of the skin plate (m_p)	Mass of C4 (m_c)	Stand-off distance (Z)	Maximum incident over pressure (p^I_{max})	Maximum reflected over pressure (p^R_{max})	Positive duration (t_p)	Reflected impulse (I_{ref})
		m^2	Kg	g	cm	kPa	kPa	ms	kPa.ms
ConWep predicted		0.0491	-	40	30	1490	8275	0.514	257.0
Experimentally measured									
CT1 tubes	Test 1	0.0491 (ϕ250mm) Aluminium skin plate	1.0	40	30	860	8003	0.162	239.1
	Test 2					829	7863	0.168	210.1
	Test 3					784	7556	0.159	199.7
	Test 4					921	8023	0.170	231.1
	Test 5					821	7881	0.176	215.5
CT2 tubes	Test 6					791	8100	0.157	224.4
	Test 7					900	8047	0.169	220.5
	Test 8					856	9231	0.158	238.2
	Test 9					940	7994	0.180	225.3
	Test 10					882	8032	0.165	229.7
CT1 tubes	Test 11	0.0491 (ϕ250mm) Sandwich composite skin plate	0.7	40	30	790	7964	0.166	238.2
	Test 12					889	7599	0.171	241.5
	Test 13					805	7701	0.178	228.7
	Test 14					799	8081	0.165	195.5

Type of composite tube	Experimental test No	Area of the circular skin plate (A_p)	Mass of the skin plate (m_p)	Mass of C4 (m_c)	Stand-off distance (Z)	Maximum incident over pressure (p^I_{max})	Maximum reflected over pressure (p^R_{max})	Positive duration (t_p)	Reflected impulse (I_{ref})
		m^2	Kg	g	cm	kPa	kPa	ms	kPa.ms
CT2 tubes	Test 15					825	8019	0.174	234.6
	Test 16					879	8000	0.168	219.3
	Test 17					Not measured	7810	0.183	200.6
	Test 18					Not measured	8113	0.187	230.4
	Test 19					Not measured	7999	0.175	209.2
	Test 20					Not measured	7698	0.169	230.0
ConWep predicted		0.0491	-	40	15	5651	33090	0.098	537.6
The incident and reflected pressure time histories for the blast tests with 40g C4 and with stand-off distance of 15cm could not be measured due to consistent breakage of pressure sensors.									

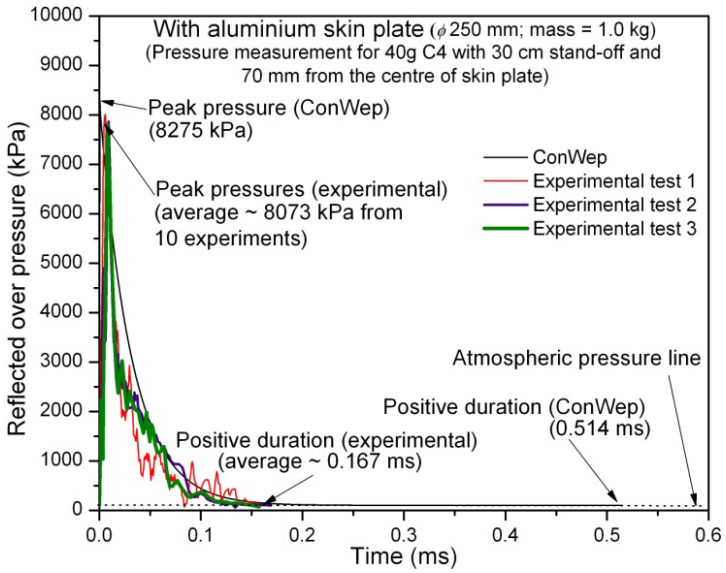

Figure 11-3: Comparison of experimentally measured pressure-time histories with ConWep data for 40g of C4 with a stand-off distance of 30 cm (experimental pressure time histories measured with aluminium skin plate (ϕ 250 mm; 1.0 kg of mass)).

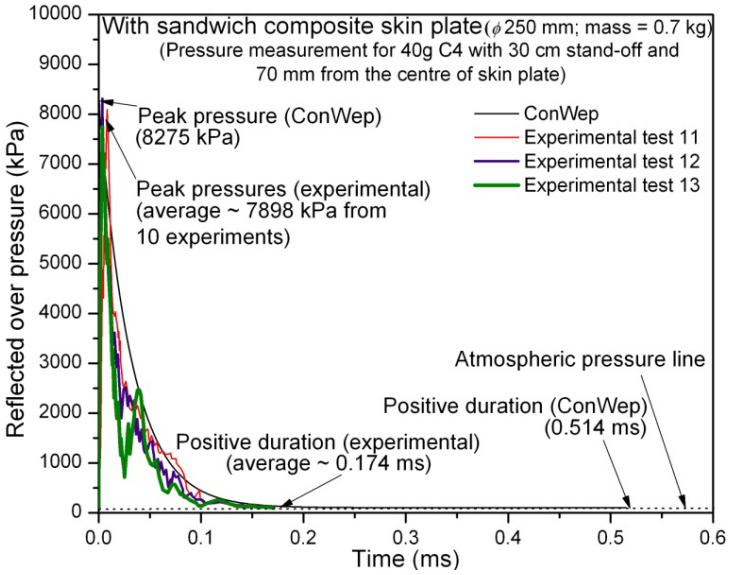

Figure 11-4: Comparison of experimentally measured pressure-time histories with ConWep data for 40g of C4 with a stand-off distance of 30 cm (experimental pressure time histories measured with sandwich composite skin plate (ϕ 250 mm; 0.7 kg of mass))

Effect of finite reflected surface area and associated clearing phenomenon on the equivalent load

Calculation of the impulse loading and subsequent analysis without including the finite surface area of the reflected surface will overpredict the efficiency of the sacrificial cladding structure. Figure 11-5(a) shows a comparison of the reflected pressure profiles (for 40g C4 with the stand-off distance of 30 cm) from three cases: (i) case A – calculated reflected pressure profile from ConWep assuming that the reflected surface is infinite (ii) case B – calculated reflected pressure profile from ConWep for the finite reflected surface area (ϕ 250 mm) (iii) case C – shows one of the experimental recordings of the reflected pressure-time profile measured with the aluminium skin plate (ϕ 250 mm; mass = 1.0 kg). A significant difference can be noticed from these three pressure profiles for the peak reflected pressure magnitude (P_{max}^{R}) and the corresponding positive duration (t_p). The magnitude of peak reflected pressure was 9135 kPa, 8275 kPa and 8073 kPa (average from 10 experiments) for case A, case B and case C respectively. The corresponding positive phase duration for these three cases was 0.514 ms, 0.514 ms and 0.167 ms. The peak reflected pressure for the case A was much higher than for the remaining cases (cases B and C). This difference was due to the consideration of infinite reflected surface which will not allow any diffraction and clearing of reflected pressure waves. Secondly, there was no change in the positive duration for finite and infinite reflected surfaces from ConWep. This again proves that the clearing of pressure waves is not considered in ConWep. The magnitude of peak reflected pressure from case B was very close to the experimentally measured value (case C). However, the positive duration for case B was significantly higher than for the case C (0.514 ms and 0.167 ms for case B and C respectively). The reason for this significant difference is due to the clearing effect of the pressure waves which is not accounted for in ConWep.

The effect of these pressure profiles on the loading of the structure can be further explained using Figure 11-5(b). Figure 11-5(b) shows the equivalent triangular impulse loading curves for these three cases. The calculated and measured total reflected impulse for these cases were 322 kPa.ms, 307 kPa.ms and 210 kPa.ms for case A, B and C respectively (area below the respective reflected pressure curve). The equivalent triangular impulse load was calculated based on the diffracting load case (engulfing). The actual peak pressure was taken as the peak of the equivalent impulse load, and the equivalent duration was selected to give an impulse per unit area the same as that of the actual [12]. The calculated new positive duration were 0.07 ms, 0.074 ms and 0.052 ms for case A, case B and case C respectively. The effect of not considering the actual reflected surface and the clearing effect can be further understood from this figure. The case A and B provide a higher impulse compared to case C; taking the impulse from case A and B will overpredict the efficiency of the inner core of a sacrificial cladding structure. Hence, the effect of

finite surface area and its clearing has to be taken into account for the design and correct efficiency calculation of the inner core structures.

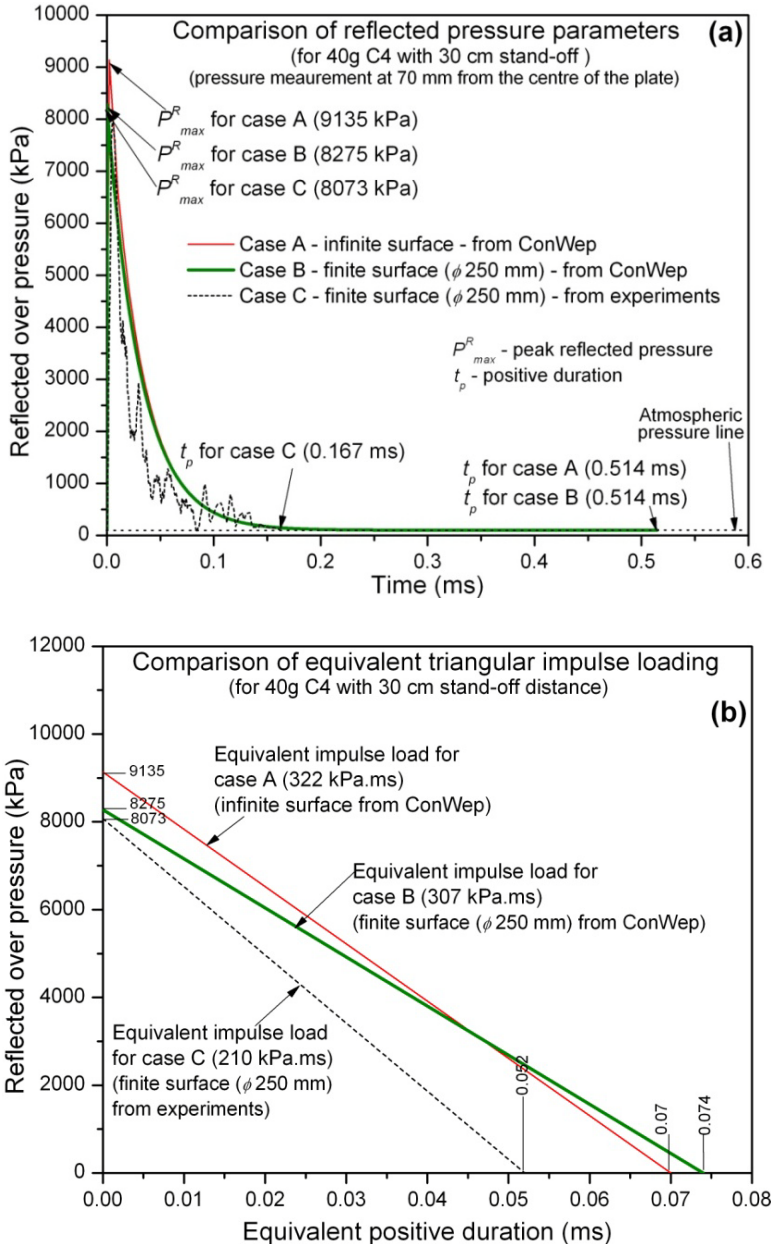

Figure 11-5: (a) Comparison of the reflected pressure parameters for finite and infinite reflected surfaces for 40 g C4 with a stand-off distance of 30 cm (comparison of the experimental and ConWep values). **(b)** Effect of finite surface and the corresponding clearing phenomenon on the equivalent triangular impulse loading for 40g C4 with a stand-off distance of 30 cm (comparison of the experimental and ConWep values).

11. 3. 2. Deformation patterns

The crushing patterns of circular composite tubes (with triggering type 1 and 2) from different blast tests with the aluminium and sandwich composite skin plate are shown in Figure 11-6(a – d). The deformation pattern of these composite tubes (delamination, axial cracks, lamina bending and fibre fracture) is very similar to their quasi-static and impact deformation patterns (refer Chapter 10). Both composite tubes (CT1 and CT2) exhibited progressive failure modes. For both tubes (CT1 and CT2) the inner and outer petals were formed due to the circumferential delamination and consequently axial cracks parallel to the axis of the tube. The uniform geometry of the circular tube facilitated to form more axial cracks and thus more petals were formed [13, 14].

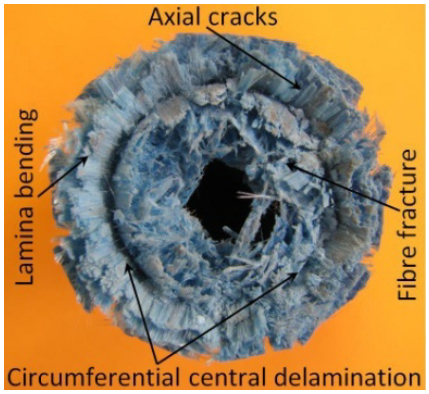

(a) Deformation pattern of composite tube with triggering type 1 for 40g of C4 with 30 cm stand-off distance.

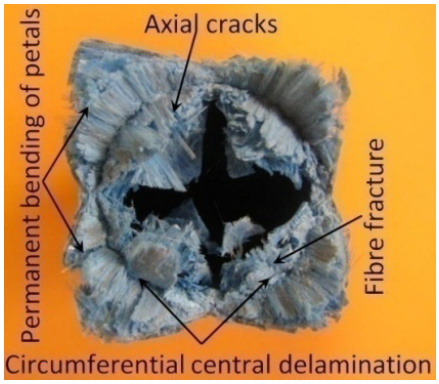

(b) Deformation pattern of composite tube with triggering type 2 for 40g of C4 with 30 cm stand-off distance.

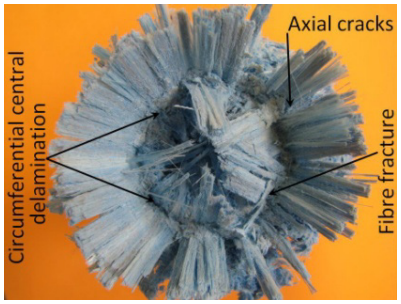

(c) Deformation pattern of composite tube with triggering type 2 for 40g of C4 with 15 cm stand-off distance.

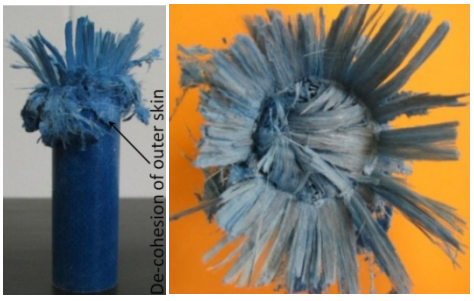

(d) Deformation pattern of composite tube with triggering type 2 for 40g of C4 with 15 cm stand-off distance.

Figure 11-6: Deformation patterns of composite tubes**: (a)** CT1 tube for 40g of C4 with stand-off distance of 30 cm. **(b)** CT2 tube for 40g of C4 with stand-off distance of 30 cm. **(c)** CT1 tube for 40g of C4 with stand-off distance of 15 cm. **(d)** CT2 tube for 40g of C4 with stand-off distance of 15 cm.

The major amount of blast energy was absorbed due to the increasing number of longitudinal cracks and subsequent bending of the laminates [15]. For all cases the bending of the inner petals reduced the acceleration of the skin plate considerably due to the blockage of material (inner petals) within the tube profile. After the blast testing, all samples were longitudinally cut to carry out a visual inspection of the crushed zone. The cut section of both tube series gave a clear evidence that the major delamination took place at the mid thickness of the tube [13, 14, 16]. Other than the longitudinal axial cracks, a larger number of trans-laminar cracks (cracks which are perpendicular to the direction of the fibre orientation) were observed. However the length of the axial and trans-laminar cracks was controlled by the uniform geometry of the circular tubes. The average deformation length for each case is reported in Table 11-2.

11. 3. 3. Crushing load curves

For the simplification the crushing compressive load and the deformation length are shown in positive values in all load-deformation graphs. As an example, the typical load-time histories (without filtering) of the composite tubes (CT1 and CT2) from the blast tests (40g C4 with stand-off distances of 30 cm and 15 cm) are shown in Figure 11-7(a) and (b). The results from the blast tests showed that these tubes are not sensitive to strain rate effect; because the peak crush load of these tubes from quasi-static, impact and blast tests was approximately the same (refer Chapter 10 and Figure 11-7). The average peak crush load (for 32 samples) of these composite tubes was 12.6 kN (refer Table 11-2). Hence, the deployment of these composite tubes for the inner core structure can provide a constant acceleration to the mounting (non-sacrificial) structure irrespective of the charge mass of the explosive used.

The peak crush load of both composite tubes (CT1 and CT2) occurred during the start of the major circumferential delamination; after the circumferential delamination the crush load decreased abruptly (refer Figure 11-7). For CT2 tubes the time to reach the major circumferential delamination was longer than for CT1 tubes due to the triggering profile and so a smaller slope of the peak crush load was observed (refer Figure 11-7(a) and (b)). Despite the change in the crush load pattern due to the triggering profile there was no consistency in the difference of the total duration of the transferred load to the non-sacrificial structure. For example, from Figure 11-7(a) it can be observed that the total duration of the transferred crush load was 2.36 ms and 2.0 ms for CT1 and CT2 tubes respectively; however, Figure 11-7(b) shows 3.5 ms and 3.78 ms for CT1 and CT2 tubes for 40g C4 with a stand-off distance of 15 cm.

Table 11-2: Summary of average crushing parameters.

Test No	Composite tube series	Mass of the skin plate (m_p)	Reflected (total) impulse delivered to the skin plate (I_{ref})	Impulse transferred to non-sacrificial structure (I_{trans})	% difference in impulse (ΔI)	Available energy from the blast to the skin plate for composite tube crushing (E_{trans})	Energy absorbed by the composite tube (E_{abs})	Peak (crush) load (P_{max})	Mean crush load (P_{mean})	Deformation length of composite tube (l_{max})	Standard deviation for l_{max}	Crush efficiency (η_d)	SEA
	-	Kg	kN.s	kN.s	%	J	J	kN	kN	mm	mm	(%)	(kJ/kg)
40g C4 with stand-off distance of 30 cm													
Reference test	-		0.0115	0.00762	33	-	-	38	-	-	-	-	-
Test 1-5	CT1	1.0	0.0106	0.00754	28	58.5	33.7	12.5	3.9	8.7	2.5	31	16.5
Test 6-10	CT2		0.0113	0.00808	29	63.6	34.4	12.1	3.4	10.2	3.1	28	14.9
Reference test	-		0.0108	0.00734	32	-	-	32	-	-	-	-	-
Test 11-15	CT1	0.7	0.0110	0.00760	31	83.7	55.4	13.1	4.0	13.2	3.6	32	17.9
Test 16-20	CT2		0.0107	0.00745	32	85.9	56.7	12.0	3.6	16.3	3.9	30	15.3
40g C4 with stand-off distance of 15 cm													
Reference test	-		-	0.0155	-	-	-	66	-	-	-	-	-
Test 21-23	CT1	1.0	-	0.0144	-	-	-	13.1	-	21.9	4.1	-	-
Test 24-26	CT2		-	0.0157	-	-	-	12.7	-	25.1	4.9	-	-
Reference test	-		-	0.0160	-	-	-	52	-	-	-	-	-
Test 27-29	CT1	0.7	-	0.0154	-	-	-	12.9	-	24.9	5.2	-	-
Test 30-32	CT2		-	0.0151	-	-	-	12.5	-	30.1	4.8	-	-

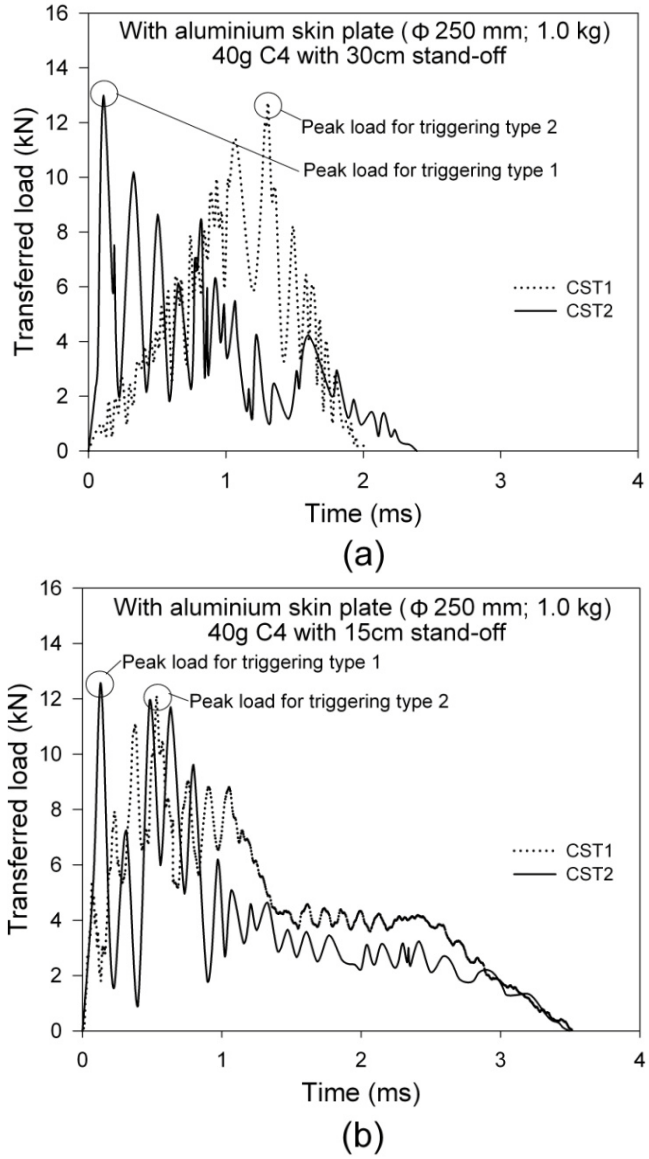

Figure 11-7: Force-time histories of composite tubes with aluminium skin plate (ϕ 250 mm; 1.0 kg of mass).**(a)** 40 g C4 with stand-off distance of 30 cm **(b)** 40 g C4 with stand-off distance of 15 cm.

Similar results have been obtained for the sandwich composite skin plate. The total energy absorption (E_{abs}) of each test specimen during the blast event was calculated and the average of each category is presented in Table 11-2. Similarly, the mean crush load P_{mean} (it is a measure of average force required to deform the material in a progressive manner) was calculated. The mean crushing load of the test specimen oscillated from a minimum of 3.4 kN to a maximum of 4.0 kN. The calculated crushing efficiency (the ratio of the mean crush load to the peak crush load which indicates the efficiency of the crushing (η_c)) of all tests is given in Table 11-2. The

summary of test specimen crushing parameters (peak crush load, mean crush load and the corresponding energy absorption) for all cases is given in Table 11-2.

To understand the energy absorption efficiency of each test specimen, the specific energy absorption (SEA - energy absorbed per unit mass of the crushed material) was calculated (refer Table 11-2). The test specimens which were tested with the aluminium skin plate (1.0 kg) exhibited a lower SEA compared to the sandwich composite skin plate. The average SEA of test specimens with aluminium skin plate was 16.5 kJ/kg and 14.9 kJ/kg for CT1 and CT2 respectively. Tests with sandwich composite skin plate (0.7 kg) provided 17.9 kJ/kg and 15.3 kJ/kg for CT1 and CT2 composite tubes respectively. In both cases the SEA of triggering type 1 was slightly higher than the triggering type 2. For the case with 40g C4 and 15 cm stand-off distance only the transferred impulse to the non-sacrificial structure could be measured. The acceleration of the skin plate, the incident and reflected pressures could not be measured due to the breakage of the sensors during blast loading. Hence, the deformation length of each test specimen was measured after each blast test and the average value is reported in Table 11-2. The measured data from the dynamic load cell (peak load and the transferred impulse) for this case is also reported in Table 11-2.

11. 3. 4. Effect of skin plate inertia

In order to understand the effect of skin plate inertia the energy delivered from the blast loading and the corresponding available energy for the crushing of the composite tube (after spending some energy to overcome the inertia of the skin plate) were calculated (the relations used to calculate these parameters were already discussed in Chapter 4). As an example, the explosive loading case of 40g C4 with the stand-off distance of 30 cm is presented here. Figure 11-8 shows the available energy from the blast to the skin plate for composite tube crushing. It is very clear that a significant amount of energy has been spent to overcome the inertia of the skin plates. The average energy available from the blast to the aluminium skin plate (after overcoming inertia) for composite tube crushing was 58.5 J and 60 J for CT1 and CT2 tubes respectively. The average energy available from blast to the sandwich composite skin plate was higher than for the aluminium skin plate. The sandwich composite skin plate provided 83.7 J and 85.9 J for CT1 and CT2 tubes respectively. It can be noticed that for the same charge and stand-off distance (40g C4 with the stand-off distance of 30 cm) the aluminium and sandwich composite skin plates provided different levels of energy with CT1 and CT2 tubes. Apart from the inertia of the skin plates the stiffness and the corresponding resistance provided by the composite tubes also played a role. Because of a lower stiffness of the tulips the energy given by the skin plates was higher for CT2 tubes. As a result, there was

a minor difference in the maximum attained velocity for these two triggering types (refer Figure 11-8). The average maximum velocity of the aluminium skin plate was 10.75 m/s and 11.36 m/s for CT1 and CT2 tubes respectively. Similarly, the sandwich composite skin plate provided 15.2 m/s and 16.0 m/s for CT1 and CT2 tubes respectively. Due to the different levels of the attained velocity of the skin plates, a significant difference in the deformation length (integrated twice from the acceleration signal) of the test specimens was noticed. The corresponding average deformation lengths for CT1 and CT2 tubes with the aluminium and sandwich composite skin plate are given in Table 11-2. Furthermore, the specific energy absorption of the composite tubes was slightly increased with the lower skin plate mass. For CT1 tubes the average SEA of 16.5 kJ/kg with the aluminium skin plate (1.0 kg) was increased to 17.9 kJ/kg with sandwich composite skin plate (0.7 kg). Similarly, for CT2 tubes the SEA value increased from 14.9 kJ/kg to 15.3 kJ/kg (refer Table 11-2).

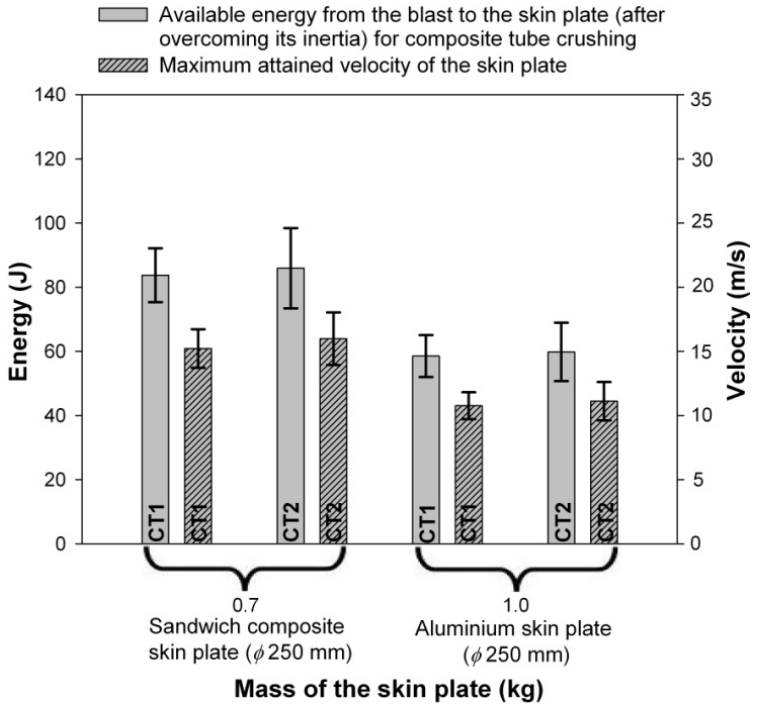

Figure 11-8: Effect of inertia of the skin plate on the available energy for the composite tube crushing and the corresponding maximum attained velocity of the skin plate (error bar indicates the standard deviation).

11. 3. 5. Impulse and energy transfer

In order to understand the effectiveness of the composite tubes the impulse delivered to the top face of the skin plate (total reflected impulse from the blast) and the corresponding transferred impulse at the bottom of the composite tube to the non-

sacrificial member (integration of the measured force-time history at the bottom of the composite tube) are compared. The calculated average values (for five experiments in each case) of I_{refl} and I_{trans} for 40g C4 with 30 cm and I_{trans} for 15 cm stand-off distance (four experiments in each case) are given in Table 11-2. Similar to the beverage can case the linear momentum is not conserved for 30 cm stand-off distance. A similar condition should have been obtained for 15 cm stand-off case. The average difference between the reflected impulse and the transferred impulse for the first 20 tests (40g C4 with 30 cm stand-off) is given in Table 11-2. It varied from a minimum of 28% to a maximum of 33%. As an example, one of the cases (test 6) with the aluminium skin plate (ϕ 250 mm; 1.0 kg) is discussed here. The reason for choosing the experimental test 6 is mentioned later. The applied load and the corresponding reflected impulse (from 40g C4 with stand-off distance of 30cm) given to the top face of the aluminium skin plate are shown in Figure 11-9(a); and the corresponding transferred load and impulse to the non-sacrificial structure (solid copper tube) are shown in Figure 11-9(c). Furthermore, the peak load from the reference test (average of two tests conducted without test specimen and only with skin plate directly placed on the dynamic load cell for the same loading parameters (40 g C4 with 30 cm stand-off distance)) is also given in Table 11-2. It can be noticed that the use of composite tubes reduced the peak load from 38 kN to about 13 kN considerably and the corresponding positive duration was extended significantly (0.16 ms to 2 ms – refer Figure 11-9(a) and (c)). However, the same figures (Figure 11-9(a) and (c)) also show the difference in the impulses ($\Delta I = I_{refl} - I_{trans}$= 0.0110 – 0.00805 = 0.00295 kN.s). Similarly, there was a significant difference noticed between the available energy from the blast to the skin plate (after overcoming inertia) for composite tube crushing (59.67 J) and the corresponding energy absorbed by the composite tube (35.1 J) (refer Figure 11-9(b), Figure 11-9(d)).

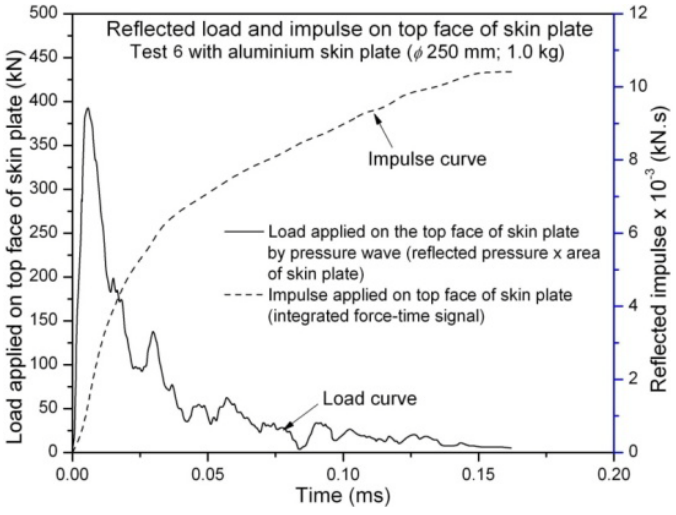

(a)

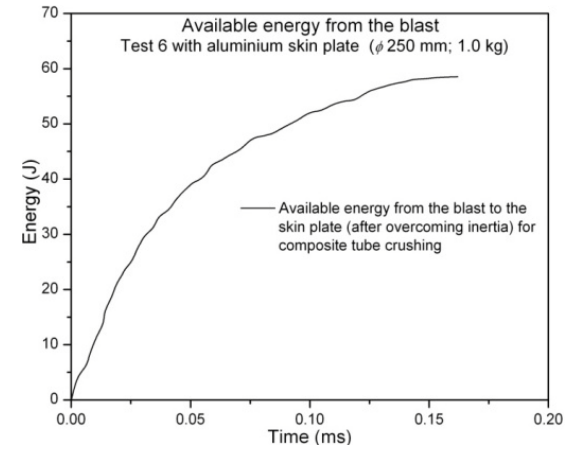

(b)

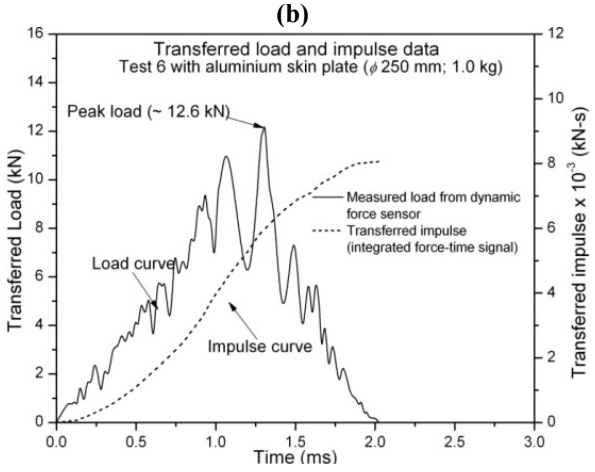

(c)

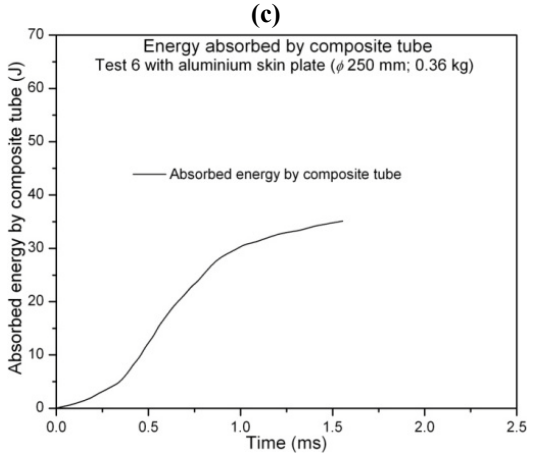

(d)

Figure 11-9: (a) Experimental reflected impulse (load-time history) for the aluminium skin plate (ϕ 250 mm; 1.0 kg of mass) **(b):** Energy delivered by the reflected pressure wave to the aluminium skin plate (ϕ 250 mm; 1.0 kg). **(c):** Transferred impulse (load-time history) to the non-sacrificial structure due to the composite tube crushing. **(d)**: Energy absorbed by the composite tube crushing.

Hence, similar to the beverage can case, a coupled Eulerian-Lagrangian analysis was carried out to study the interaction of the pressure waves with the test set-up using Hydrocodes. The influence of different parameters such as the diffraction of pressure waves due to the clearing effect and reflected pressure from the ground surface on the resultant impulse acting on the skin plate and the corresponding energy absorption of the test specimen are studied in detail.

11. 4. 2D Blast simulation and results

The modelling approach of the 2D simulation and its advantages were already explained in Chapter 5; and the same approach is adopted here. The used Equation Of States (EOS) and the corresponding properties were given in Chapter 5. Two models have been developed to capture the incident pressure for 40 g C4 at 30 cm and 15 cm stand-off distances. The contours of the simulated incident pressure at 30 cm and 15 cm from the detonation centre are shown in Figure 11-10(a) and Figure 11-10(b) respectively. These symmetric spherical data were written into a remap file and then imported into a 3D air model. The details of the 3D modelling are discussed in the next section.

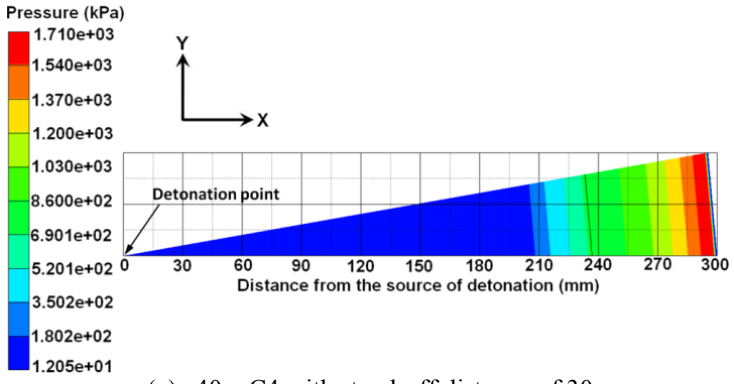

(a) 40 g C4 with stand-off distance of 30 cm

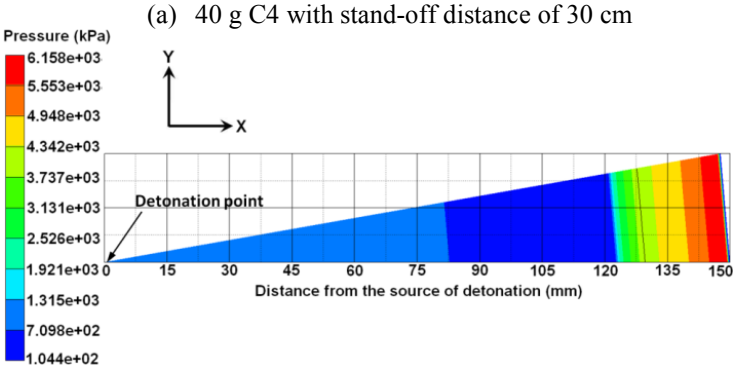

(b) 40 g C4 with stand-off distance of 15 cm

Figure 11-10: Wedge model (incident over-pressure contours for 40g of C4 with 30 cm and 15 cm stand-off distances).

11. 5. 3D Blast simulation and results

The equation of states and the material models for the aluminum skin plate, composite material, rigid support and their boundary conditions and the contact controls are the same as the ones which were discussed in Chapter 5. The boundary of the air model was chosen to have adequate air space in all directions from the centre of detonation. The dimensional details and the 3D computational modelling of the experimental set-up are shown in Figure 11-11. Accordingly the field data which were created from the 2D simulation were remapped (symmetrical about "Y" axis; 30 cm and 15 cm away from the top face of the skin plate) into the 3D air model. Similar to the analysis handled in Chapter 9, the medium scale pultruded composite tubes was modelled with four layers of shell elements (each layer is 0.5 mm thick). Accordingly, the Tsai-Wu failure criterion (standard failure criterion available in Autodyn) was used to capture the damage of the composite tubes (the equations for this damage model were already given in Chapter 5). The details of the used material properties for the composite tubes are given in Table 11-3.

Table 11-3: Material properties of glass/polyester composite laminates in principal directions.

Parameters	Symbol	Glass/polyester pultruded tubes
Material and elastic data		
Density (kg/m^3)	ρ	1850
Longitudinal modulus (GPa)	E_{11}	31.2
Transverse modulus (GPa)	E_{22}	9.36
In-plane shear modulus (GPa)	G_{12}	3.2
Out-of-plane shear modulus (GPa)	G_{23}	3.2
Poisson's ratio	ν_{12}	0.29
	ν_{23}	0.31
Strength properties		
Failure criteria	-	Hashin
Longitudinal tensile strength (MPa)	X_T	483
Longitudinal compressive strength (MPa)	X_C	409
Transverse tensile strength (MPa)	Y_T	34.9
Transverse compressive strength (MPa)	Y_C	92.2
In-plane shear strength (MPa)	S_L	73.3

Similarly, the delamination between all plies was modelled using the built-in "*tie-break*" function; and the corresponding interface function is given in Equation (11.1). The corresponding mechanical properties of polyester resin were adopted from ref. [17] and the same were already given in Chapter 9.

$$\left(\frac{\sigma_n}{\sigma_{nf}}\right)^2+\left(\frac{\sigma_s}{\sigma_{sf}}\right)^2 \geq 1 \qquad (11.1)$$

where σ_n is the normal stress at the interface; σ_s is the shear stress at the interface; σ_{nf} is the normal stress at the bond failure and σ_{sf} is the shear stress at the bond failure. In this study the values of both σ_{nf} and σ_{sf} are assumed to the same (51.2 MPa).

11. 5. 1. Results and discussions

Blast simulations with fully coupled Lagrangian and Eulerian formulation for the composite tube (40g of C4 with stand-off distances of 30 cm and 15 cm) were carried out. The interaction of the pressure waves with the aluminium skin plate was studied. The magnitude of the reflected pressure wave was calculated at the air grid which was very close to the top and bottom faces of the skin plate. In order to study the effect of grid size on the blast parameters, a mesh sensitivity study was conducted. The effect of air grid size on the peak reflected pressure values can be easily understood from Figure 11-12.

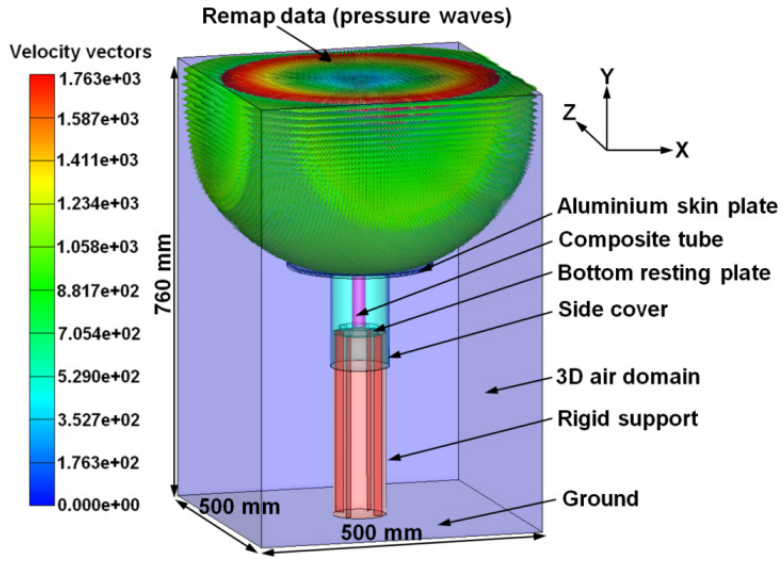

Figure 11-11: 3D computational model for simulating blast waves with aluminium skin plate.

The pressure values are calculated at the centre of the top face of the skin plate. For a smaller element size (0.25 mm and 0.5 mm), the magnitude of the peak reflected pressure (9165 kPa and 9087 kPa respectively) was very close to the ConWep value (9135 kPa). The corresponding positive phase durations are also shown in the same

figure. There was no significant difference in the positive duration noticed due to the change in size of the element (minimum of 0.223 ms; maximum of 0.227 ms). Based on this mesh sensitivity study an element size of 0.25 mm was used for all analyses.

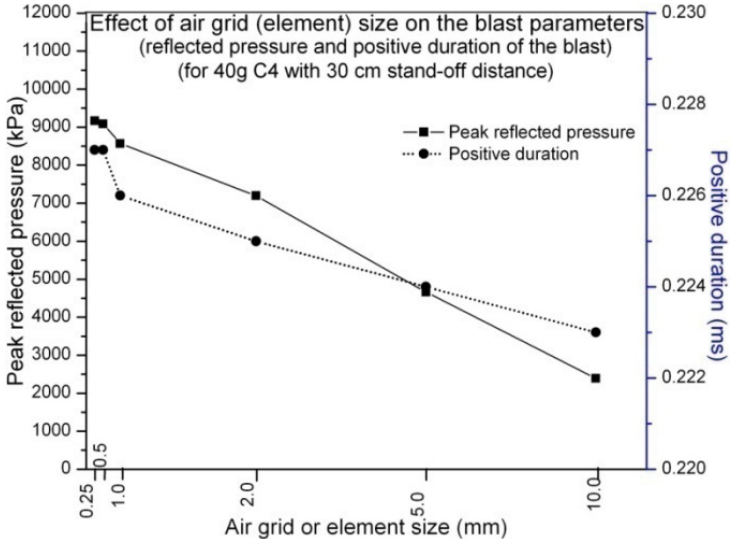

Figure 11-12: Mesh sensitivity study on the peak reflected pressure and its positive duration.

11. 5. 2. Reflected blast parameters for different stand-off distances

Reflected pressure profiles at the top face of the skin plate

The calculated pressure profiles from the top face of the aluminium skin plate (ϕ 250 mm; 1.0 kg) for 40g C4 with stand-off distances of 30 cm and 15 cm are given in Figure 11-13(a) and Figure 11-13(b) respectively. The reflected pressure profile was measured at five locations on the top face of the skin plate; and for the simplification, only the positive phase of the reflected pressure profile is considered for discussion. It can be noticed that the peak magnitude of the reflected pressure wave from the centre (9165 kPa for 30 cm stand-off and 40348 kPa for 15 cm stand-off) was gradually reduced to the periphery (6800 kPa for 30 cm stand-off and 16156 kPa for 15 cm stand-off) for both skin plates. Correspondingly, the positive phase duration varied from 0.227 ms to 0.17 ms for 30 cm stand-off; and for 15 cm stand-off, it varied from 0.14 ms to 0.12 ms. For 15 cm stand-off distance, after reaching the peak, the magnitude of the reflected pressure waves at each location on the top face of the skin plate was further increased due to the interaction with the incoming incident pressure waves (refer Figure 11-13b)). The peak reflected pressure at the centre and the average reflected pressure on the surface of the skin plate for 30 cm stand-off distance from the Autodyn simulations (9165 kPa and

8244 kPa respectively) were very close to the ConWep values (9135 kPa and 8033 kPa). Similarly, there was a good correlation observed for the simulated and experimentally measured peak reflected pressure (70 mm from the center of the skin plate) and the corresponding positive duration (refer Figure 11-13(a)). However, the average positive phase duration for this case (40g C4 with 30 cm stand-off) from the Autodyn simulation (0.2 ms) was much lower than the ConWep predicted value (0.514 ms). The reason for the above difference is due to the fact that ConWep (based on empirical relations) does not take into account the clearing of reflected pressure waves associated with the finite reflected surface area.

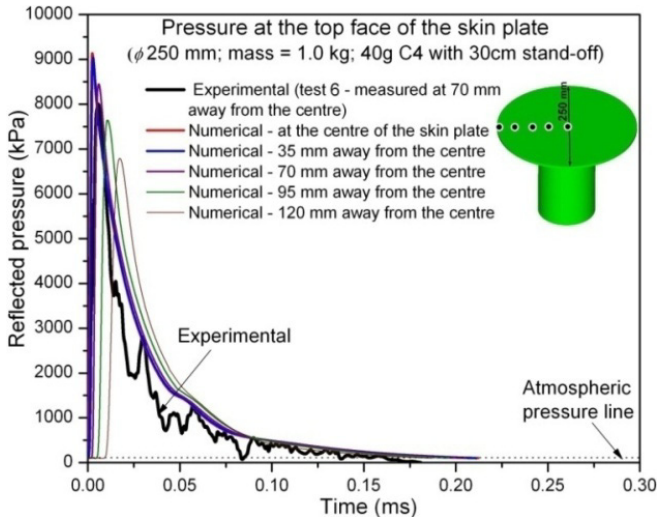

(a)

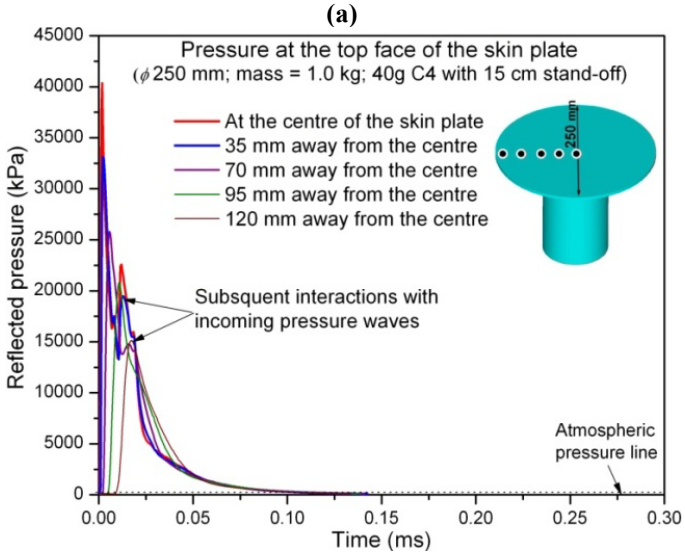

(b)

Figure 11-13: Reflected pressure-time histories at the top face of the aluminium skin plate (ϕ250 mm; 1.0 kg). **(a)** for 40g C4 with the stand-off distance of 30 cm. **(b)** for 40g C4 with the stand-off distance of 15 cm.

As an example, the reflected pressure contour and the positive duration for the ϕ250 mm skin plate (with 40g C4 with 30 cm stand-off distance) from ConWep are shown in Figure 11-14(a) and Figure 11-14(b) respectively. It can be noticed from Figure 11-14(b) that the minimum positive duration was 0.51 ms which corresponded to the centre of the plate; and the same value was observed for 70 mm from the centre of the plate. This result further proves that the effect of finite reflected surface is not completely accounted for in *ConWep*. In contrast to the case of 30 cm stand-off, a significant difference in the magnitude of the peak and average reflected pressure was noticed for 15 cm stand-off distance.

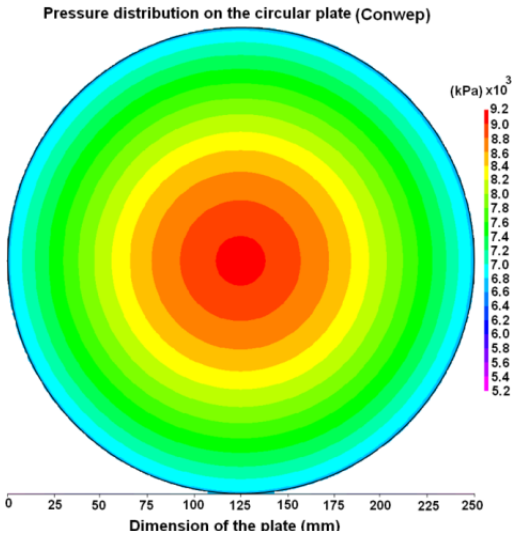

(a) Reflected pressure contours for 40g C4 with 30 cm stand-off distance

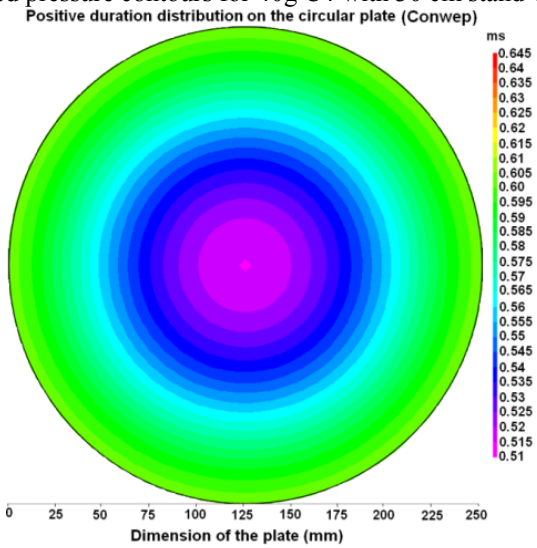

(b) Positive duration contours for 40g C4 with 30 cm stand-off distance

Figure 11-14: Contours of reflected parameters (for 40g C4 with a stand-off distance of 30cm) for a circular plate of ϕ250 mm from ConWep.

The peak reflected pressure 40348 kPa and average reflected pressure 27051 kPa from Autodyn are much lower than the values predicted by ConWep (47830 kPa and 34066 kPa for peak and average reflected pressures respectively). This shows that the reflected blast parameters predicted by ConWep for close range stand-off distances are not accurate enough. In addition to that ConWep does not include the additional impulse from multiple reflections of incoming waves which are shown in Figure 11-13(b). The calculated average impulse from the Autodyn simulation for 30 cm stand-off (242.8 kPa.ms (0.0119 kN.s)) was close to the average experimental impulse (223.98 kPa.ms (0.0110 kN.s) – from 20 tests). The calculated reflected impulse from Autodyn for 15 cm stand-off distance was 473.86 kPa.ms (0.0233 kN.s).

Clearing effect and interaction of diffracted pressure waves with the skin plate

The clearing of reflected pressure waves and the subsequent diffraction phenomenon can be explained by investigating the propagation and interaction of blast pressure waves with respect to time. As an example, the 30 cm stand-off distance case is discussed here. Figure 11-15 shows the interaction of the pressure waves (at the mid-plane representing X = 0 and Z = 0) with the top and bottom faces of the aluminium skin plate. These figures show a chronological event of interaction and diffraction of the pressure waves around the edges of the aluminium skin plate. As mentioned earlier the remapping of the 2D blast wave was fed into the 3D computational model. After remapping, the analysis was started when the pressure reached 0.25 mm above the top face of the skin plate (this corresponds to time t = 0 ms). The magnitude of the pressure wave increased suddenly when the incident pressure was obstructed by the top face of the skin plate. Due to the spherical wave front, a higher magnitude was observed at the centre of the top face of the skin plate. This event started at approximately 0.8 μs at the centre of the top face of the plate and it lasted for approximately 1.9 μs. After that the amplitude reduced exponentially. During this period a significant amount of pressure waves (especially the pressure wave at the periphery of the top face of the skin plate) diffracted around the top edge of the skin plate (clearing phenomenon). Due to this clearing the magnitude of the reflected pressure wave was reduced significantly in short time. Furthermore, a clear evidence of the diffracted pressure waves acting on the bottom face of the aluminum skin plate can be noticed in Figure 11-16. After some time these waves were pushed downwards by the incoming direct pressure from the explosion (refer Figure 11-15); as a result, the magnitude of the diffracted pressure wave reduced significantly.

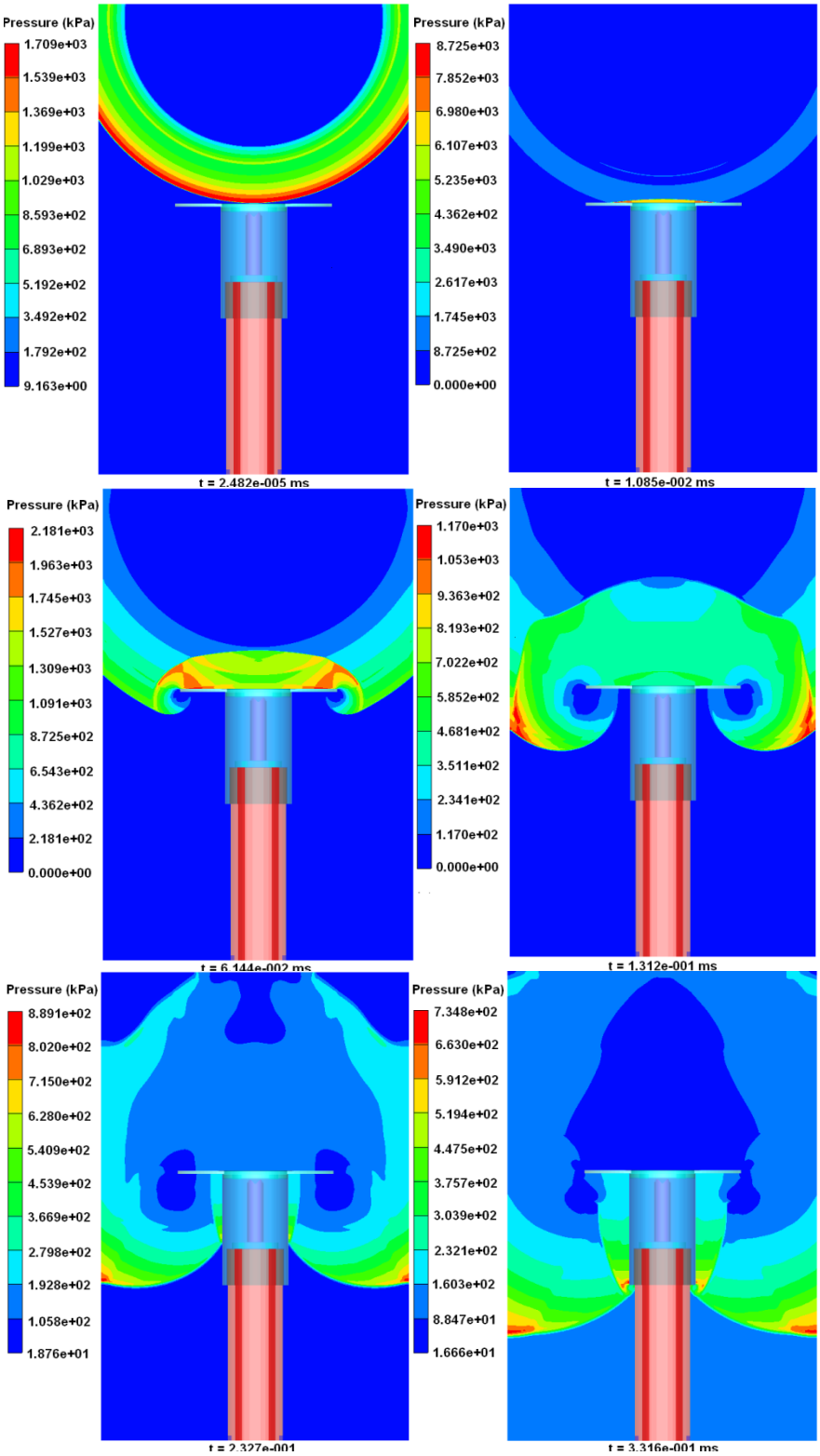

Figure 11-15: Interaction of blast pressure waves with the aluminium skin plate.

The later time increments show that the downward propagated waves significantly acted on the side tube and subsequently, at the bottom face of the skin plate for a long time due to a larger radius and higher magnitude of the pressure waves. The calculated pressure-time history of the pressure waves at the bottom face of the aluminum skin plate is shown in Figure 11-16(a). The rise in pressure at the bottom face was noticed approximately 0.125 ms later than the rise in pressure at the top face of the aluminium skin plate. This was due to the time taken for the pressure waves to reach the edges and to create the subsequent diffraction phenomenon.

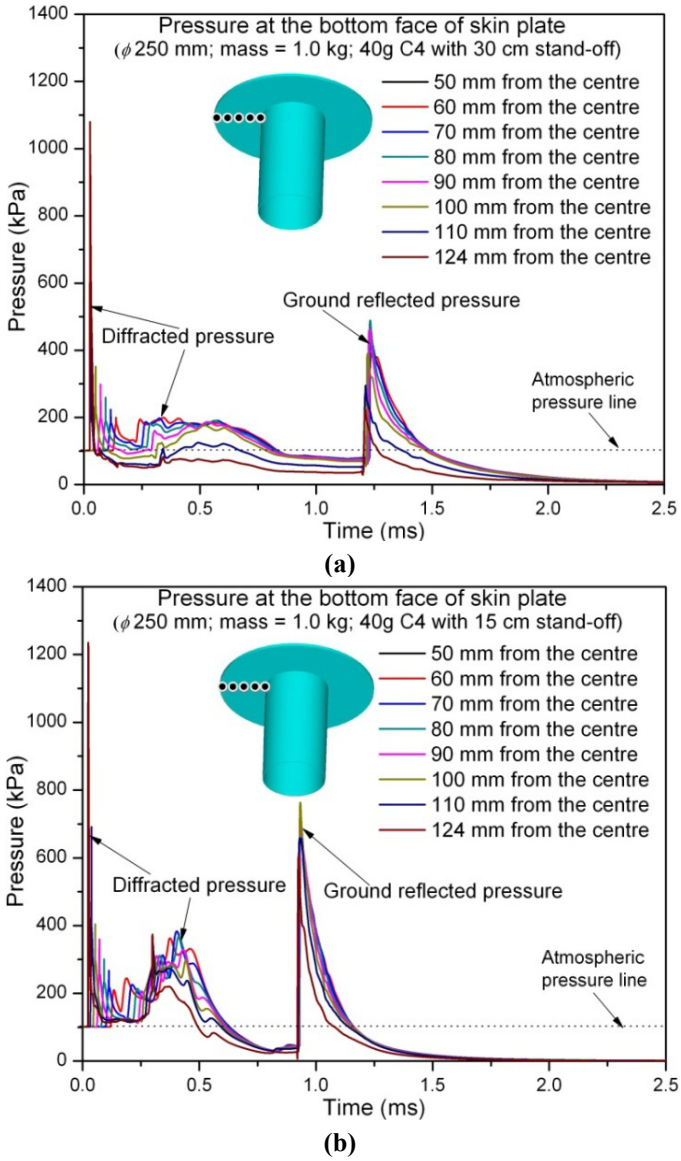

Figure 11-16: Pressure time histories of the diffracted pressure acting at the bottom face of the aluminium skin plate (ϕ250 mm; 1.0 kg) **(a)** for 40g C4 with 30 cm stand-off distance; **(b)** for 40g C4 with 15 cm stand-off distance.

It can be noticed that the magnitude of the diffracted pressure and its duration at the bottom face was significant. The initial magnitude of the diffracted pressure wave decreased from the outer edge of the skin plate to the side tube (1045 kPa for 124 mm from the centre of the skin plate to 200 kPa for 50 mm from the centre of the skin plate). However, after 0.25 ms the magnitude of the diffracted pressure decreased from inner to outer radius (from side tube to outer edge of the skin plate). This was due to the subsequent interaction of pressure waves from the side tube to the bottom face of the skin plate (refer Figure 11-16). This result was different from the case with 20g of C4 with stand-off distance of 30 cm. Although evidence for the down propagated pressure wave acting on the bottom face of the skin plate was noticed for the 20g C4 case, the magnitude was very less (refer Figure 5-18 and Figure 5-19 in Chapter 5). The difference may be due to a smaller radius and a lower velocity of the blast waves for 20g of C4. A similar interaction of pressure wave with the side tube and the bottom face of the skin plate was observed for the case with 40g C4 and 15 cm stand-off distance. The corresponding pressure time histories are shown in Figure 11-16(b).

Interaction of ground reflected pressure wave with bottom face of the skin plate

Similar to the beverage can case, the later time increments of the analysis showed the interaction of ground reflected pressure with the skin plate. As an example, the numerical evidence of the interaction of pressure waves from the ground reflection for 30 cm stand-off distance is shown in Figure 11-17. The reflection of the pressure waves at the ground surface lasted about 0.6 ms and 0.45 ms for 30 cm and 15 cm stand-off distances respectively. The average magnitude of the reflected pressure wave at the ground was approximately 2010 kPa and 2803 kPa for 30 cm and 15 cm stand-off distances respectively. The reflected pressure time histories at the ground surface for the case with 40g C4 with 15 cm stand-off distance are shown in Figure 11-18. These values were calculated for a radial distance of 250 mm from the centre of the test set-up (refer Figure 11-18). The reflected pressure magnitude was reduced significantly when the pressure wave started to move upwards. Due to the finite radius of the incoming pressure wave and subsequent interaction with the skin plate and the side tube, the pressure wave close to the test set-up reaches the ground surface later than the pressure wave at the periphery (away from the test set-up) as indicated in Figure 11-19(a). Because of the direct pressure wave from the explosion the magnitude of the pressure at the periphery was higher than the one which was close to the solid copper tube. As a result the magnitude of the reflected pressure wave at the periphery was higher (refer Figure 11-18). Furthermore, the magnitude was amplified by the interactions with the incoming pressure wave.

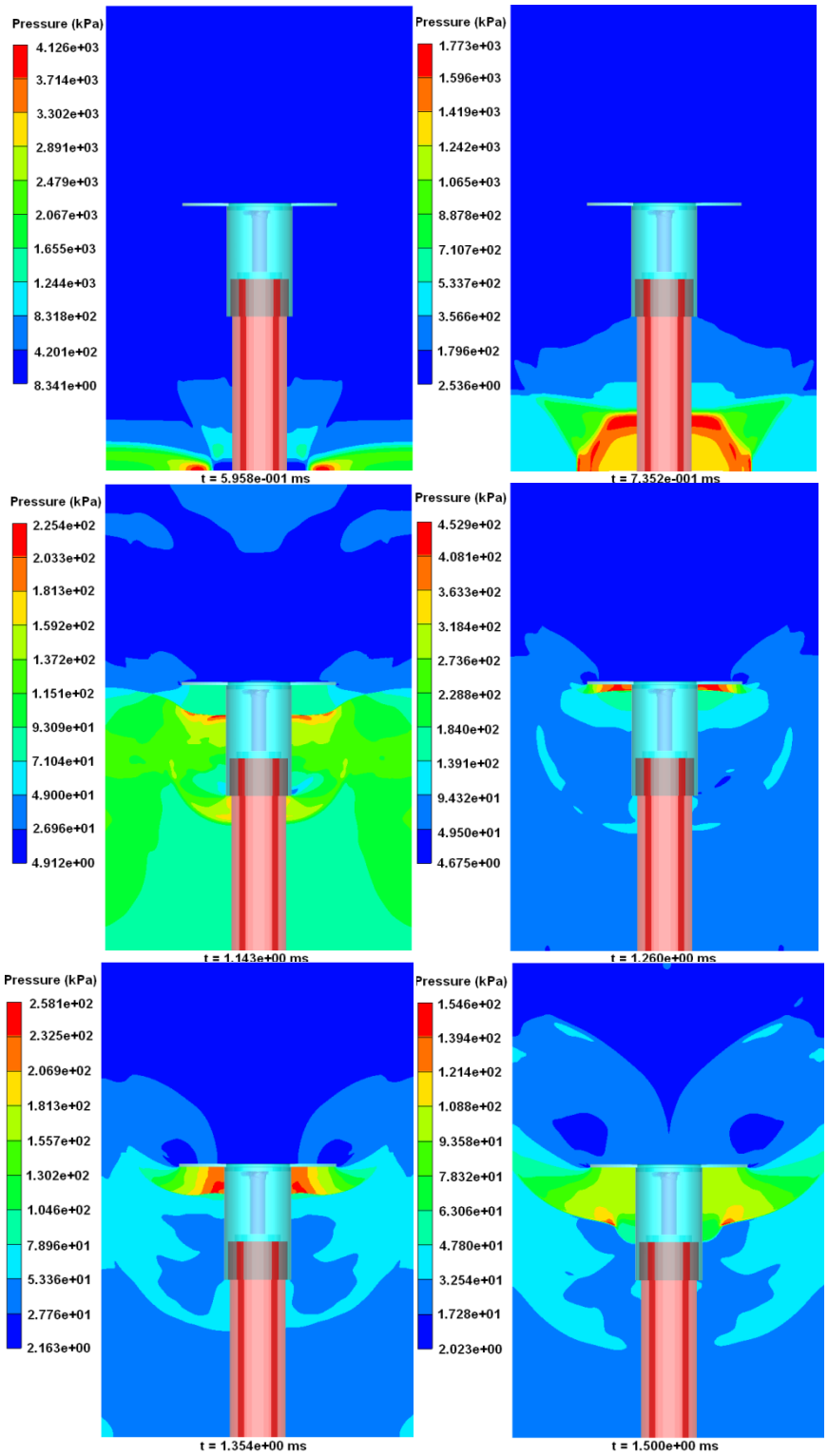

Figure 11-17: Interaction of the reflected pressure wave with the skin plate from the ground surface for 40g C4 with the stand-off distance of 30 cm.

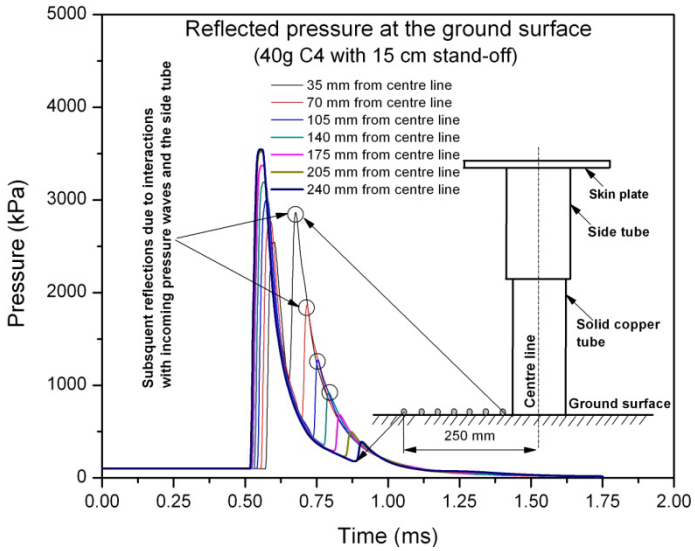

Figure 11-18: Reflected pressure time histories at the ground surface for 40g C4 with stand-off distance of 15 cm.

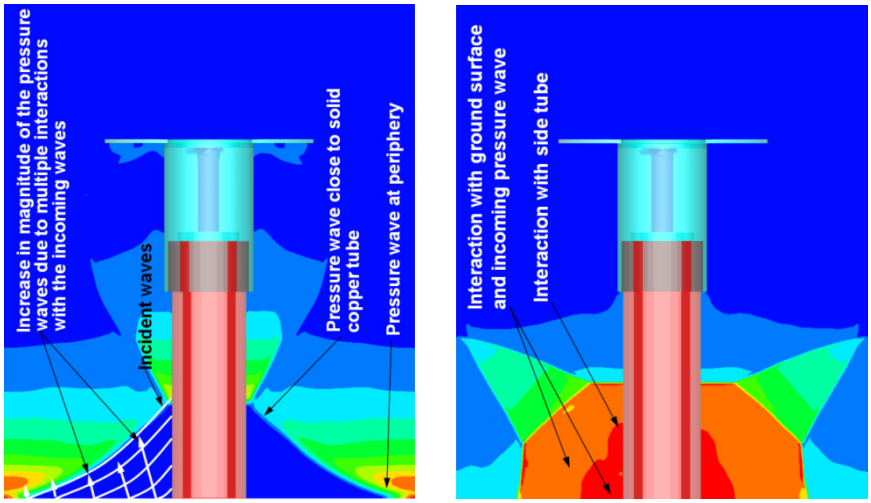

(a) **(b)**

Figure 11-19: Subsequent reflections due to interaction with incoming pressure waves and the side tube

On the contrary, the initial magnitude of the reflected pressure close to the test set-up was lower; however, the magnitude was further increased to a significant value due to the interaction with the incoming pressure wave and with the side tube (refer Figure 11-18 and Figure 11-19(b)). The reflected pressure wave at the ground surface propagated rapidly back to the bottom face of the skin plate and during the propagation the magnitude was reduced (approximately 260 kPa and 500 kPa for 30 cm and 15 cm stand-off distances respectively). The rapid propagation of this reflected pressure wave to the skin plate might be accelerated by the negative

pressure (below atmospheric pressure) below the skin plate. The reflected pressure wave from the ground acts on the bottom face of the skin plate around 1.22 ms and 0.92 ms for 30 cm and 15 cm stand-off distances respectively; subsequently, the pressure wave spreads laterally without a significant diffraction around the skin plate (refer Figure 11-17 for 30 cm stand-off distance). Due to the reflection phenomenon the magnitude of the pressure wave was increased to approximately two times its incident value (refer Figure 11-16(a-b)). The calculated average reflected pressure was 385 kPa and 690 kPa for 30 cm and 15 cm stand-off distance respectively (refer Figure 11-16(a) and Figure 11-16(b)). The calculated average impulse due to the diffraction and ground reflection was 75.8 kPa.ms (0.00372 kN.s) and 139.3 kPa.ms (0.00683 kN-s) for 30 cm and 15 cm stand-off distances respectively.

The impulse from the diffraction and ground reflection was opposite to the direction of the reflected impulse at the top face of the skin plate. Therefore, the resultant impulse imparted to the top skin plate and the corresponding transferred impulse (I_{trans}) to the solid copper tube was equal to the difference between the reflected impulse and the combined impulse from the diffraction and ground reflection ($I_{resultant} = I_{ref} - I_{diffraction} - I_{ground\ reflection}$). The calculated combined impulse from diffraction and ground reflection at the bottom face of the skin plate from Figure 11-16(a) and Figure 11-16(b) was approximately 31% and 29.4% of the total reflected impulse at the top face of the aluminium skin plate (ϕ 250 mm; 1.0 kg) for 30 cm and 15 cm stand-off distance respectively. Now, these values (31% and 29.4%) can be compared with the average difference in impulse ($\Delta I = I_{refl} - I_{trans}$) observed during the experimental testing. The average difference in the experimental impulse varied from a minimum of 28% to a maximum of 33% (refer Table 11-2). From the results of the above analyses it can be concluded that approximately 30% of the total impulse was lost due to the diffraction and ground reflection phenomena.

This can be further validated by comparing the impulse and energy; hence, for the case with 40g C4 with stand-off distance of 30 cm presented here. Table 11-4 shows a comparison of the experimental and coupled numerical simulation data. The reflected impulse from the numerical simulation (242.8 kPa.ms) was approximately 7.5% higher than the average experimental results (224.7 kPa.ms). Because of the higher reflected impulse the corresponding available energy from the blast was higher (63.6 J and 67.9 J for the experimental and numerical simulation respectively). Similarly, there was a difference observed for the transferred impulse and the corresponding energy absorbed by the composite tube (refer Table 11-4).

Table 11-4: Comparison of the experimental and coupled numerical simulation results for 40g C4 with a stand-off distance of 30 cm (with composite tubes with triggering type 2).

	Experimental (average)	Numerical
Reflected impulse (kPa.ms)	224.7	242.8
Energy available from the blast (J)	63.6	67.9
Transferred impulse (kPa.ms)	164.6	170.0
Energy absorbed (J)	34.6	38.1
Deformation length (mm)	10.2	12.5

11. 6. Decoupled numerical simulation and results

Due to the fact that the combined impulse from diffraction and ground reflection acted in the opposite direction of the reflected impulse, only 70% of the total (reflected) impulse was transferred to the non-sacrificial structure. The above finding is also validated for the decoupled numerical analysis. A parametric study on the crushing characteristics of pultruded glass polyester composite tubes for an axial impact loading case was reported in Chapter 9. The same study proved that to predict the correct crushing parameters of a pultruded composite tube the use of multiple layers of shell elements, correct modelling of triggering and delamination modelling between the composite laminates are absolutely necessary. Hence, the same modelling procedure is adopted. In order to avoid the influence of the number of shell layers and the corresponding triggering modelling on the peak crush load [18, 19] the composite tube with triggering type 2 (CT2) was chosen for the numerical investigation (experimental test 6). The experimentally measured reflected impulse of this case (test 6) was very close to the average experimental impulse.

The details of the finite element modelling with the CT2 composite tube are shown in Figure 11-20(a-b). It was assumed that the thickness of each individual ply of the composite tube is 0.5 mm; accordingly, the composite tube was modelled with four layers of shell elements (4-node, quadrilateral, stress/displacement shell element with reduced integration and with finite membrane strain formulation). The meshed shell elements were located at the centre of the thickness of each composite laminate (refer Figure 11-20(b)). The integration points representing all layers were located evenly through the thickness of the tube using Simpson integration rule. A minimum of 3 integration points was located for each shell layer. The material properties of the shell sections in principal directions were defined by introducing a local cylindrical coordinate system. The material properties for the glass polyester pultruded composite tubes are given in Table 11-3. Subsequently, the "*Hashin failure criterion*" was used to capture the failure in the composite laminate. The

corresponding pultruded composite strengths are given in Table 11-3. In order to capture the delamination between these shell layers three layers of zero thickness solid cohesive elements have been placed (COH3D8 - three dimensional cohesive elements with 8 nodes). The elastic behaviour is assigned in terms of an elastic constitutive matrix that relates the nominal stresses to the nominal strains across the interface (traction-separation constitutive response). Furthermore, the process of degradation was assumed to occur when a quadratic function involving the nominal stress ratios reaches the value of one [18, 19]. For the cohesive elements modelling the properties of polyester resin were considered; and the same properties were given in Chapter 9.

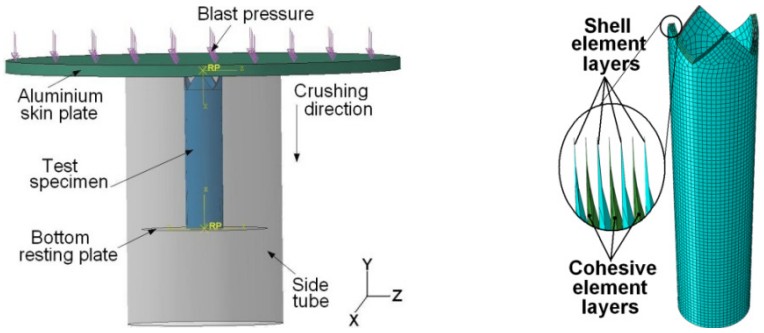

Figure 11-20: Details of the finite element models: **(a)** Finite element model with aluminium skin plate (ϕ 250 mm; 1.0 kg. **(b)** Composite tube modelling with four layers of shell elements and zero thickness solid cohesive layers.

The aluminium skin plate and the side tube were modelled with solid C3D8R elements (8 node, linear brick elements with reduced integration and hourglass control). The corresponding *Johnson-Cook* material parameters for aluminium (grade 2024 T3) were adopted from [20] and the same are given in Chapter 3. For simplification, the PVC side tube was also modelled with aluminium material (grade 2024 T3). The equivalent mass of the PVC was considered for the modelling of the aluminium side tube. The bottom resting plate was modelled as an analytical rigid surface. To simulate the axial blast load only in vertical direction [along "Y" direction] the translational degrees of freedom of the aluminium skin plate in "X" and "Z" direction were arrested; the rotational degree of freedom with respect to the "Y" axis was also arrested and the bending of the aluminium skin plate with respect to the "X" and "Z" axis were allowed. To represent the fixed supporting plate at the bottom, all degrees of freedom of the bottom rigid body were also arrested. To simulate the same experimental condition, a "*surface-to-surface*" master-slave contact algorithm was established between the composite tube to the top and bottom plates with a friction coefficient equal to 0.2. In addition to that, a self-contact algorithm was also introduced for the shell and cohesive layers.

It was assumed that the proportion of the impulse due to diffraction and ground reflection phenomena (30%) is constant. The equivalent triangular reflected impulse for this case was 224 kPa.ms. The impulse due to diffraction and ground reflection was 67.2 kPa.ms (considering 30% difference). Therefore the resultant impulse acting on the top face of the skin plate was 156.8 kPa.ms; The approximate new positive duration for this equivalent triangular impulse load is 0.039 ms; the corresponding equivalent triangular impulse load is shown in Figure 11-21. The deformation of the composite tube was obtained from the displacement of the skin plate and the reaction load was extracted from the interface load between the composite tube and the bottom analytical rigid surface. Analyses have been carried out for the aluminium and sandwich composite skin plates. However, due to the similarity in the modelling approach the aluminium skin plate case is presented here.

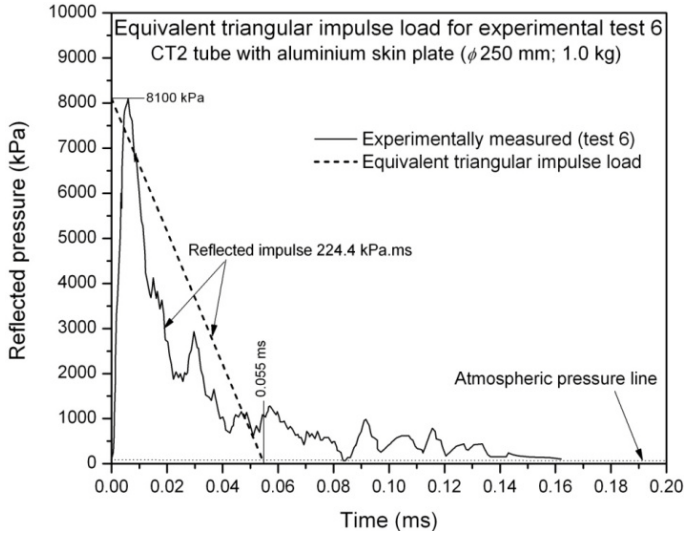

Figure 11-21: Equivalent triangular impulse load for the experimentally measured reflected pressure profile (test 6).

The results of this analysis are presented in Figure 11-22 and Figure 11-23. The final deformation length (11.1 mm) was very close to the experimental result (10.2 mm) The typical failure patterns of the pultruded composite tube (circumferential delamination, axial cracks, lamina bending and fibre fracturing) are evident from these figures. Similarly, a comparison of the experimental and numerical transferred impulse and the corresponding energy are shown in Figure 11-23(a) and Figure 11-23(b) respectively. Although there was a difference noticed during the initial time steps for the numerical simulation the final values of the transferred impulse and the corresponding energy absorption can be very well compared with the experimental results. The difference in the impulse and the energy profile was attributed by the difference in load time history from the numerical simulation. Therefore, the results from the coupled and decoupled numerical analyses once

again prove that the difference in impulse was caused by the diffraction and ground reflection phenomena

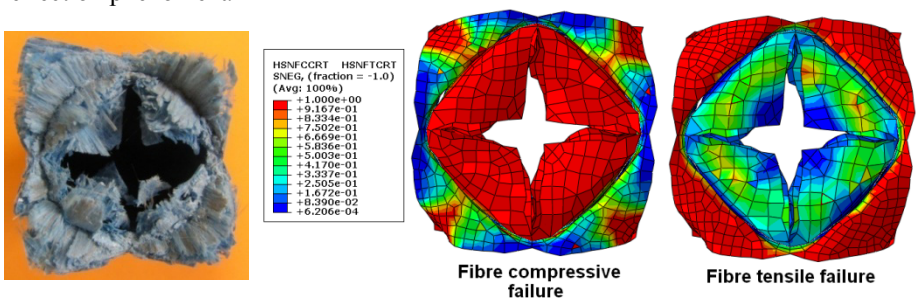

(a) Experimental **(b)** Numerical

Figure 11-22: Comparison of the experimental and numerical deformation patterns.

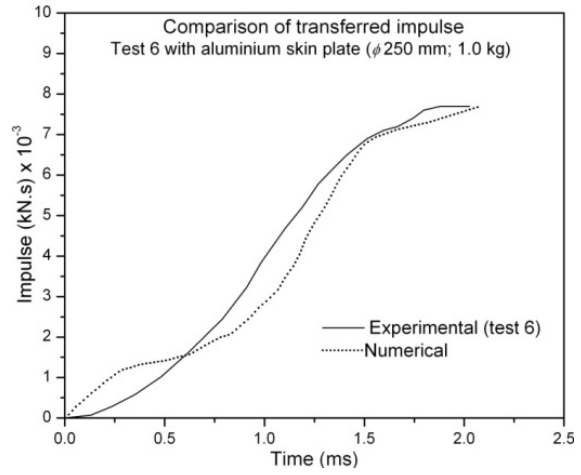

(a)

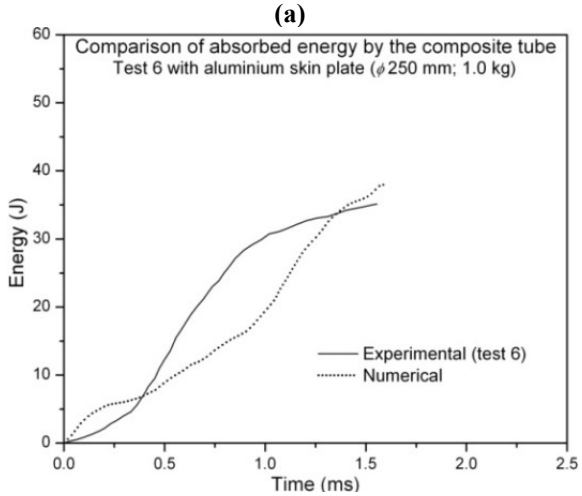

(b)

Figure 11-23: Comparison of the experimental and numerical results with decoupled analysis **(a)** transferred impulse to the non-sacrificial structure **(b)** absorbed energy by the composite tube.

11. 7. Conclusions

In this section, the experimental and numerical blast energy absorption characteristics and the corresponding crushing mechanisms of pultruded glass/polyester cylindrical composite tubes were investigated. Close-range free-air blast tests have been conducted with 40g of C4 with stand-off distances of 30 cm and 15 cm. Experiments were carried out with two different skin plates to understand the effect of inertia of the skin plates on the energy absorption of a sacrificial core structure. The experimentally measured blast parameters were compared with predicted values from ConWep. The importance of consideration of the clearing effect of the reflected pressure with a finite surface of skin plate was studied. The failure patterns of the composite tubes with two different triggering mechanisms and the corresponding energy absorption levels were studied in detail. From the conducted experiments and numerical simulations the following conclusions can be made:

Experimental

- The experimentally measured peak reflected pressure values with aluminium and sandwich composite skin plates for 40g C4 with 30 cm stand-off distance are comparable with the ConWep predicted value. However, there was a significant difference in the positive phase duration noticed between ConWep and the experimentally measured values. The reason for this difference was the clearing of pressure waves associated with the finite reflected surface area of the outer skin plate.
- The finite reflected surface area and the corresponding clearing of pressure waves has to be considered for the resultant impulse loading on a sacrificial structure.
- The inertia of the outer skin layer of a sacrificial cladding structure plays a vital role for the crushing length of the test specimens. A lower mass with high bending stiffness of the skin plate would maximize the energy absorption of the inner core structure.
- The peak crush load of the composite tubes with two different triggering mechanisms from quasi-static, impact and free air blast experiments showed strain rate insensitivity. Hence, the use of these composite tubes for the inner core structure can provide a constant acceleration to the mounting structure irrespective of the charge mass of the explosive used.
- The deformation patterns of the composite tubes with 45° chamfering and tulip triggering from the experimental blast tests showed a very similar deformation pattern compared to quasi-static and impact test results. The composite tubes showed circumferential delamination, axial cracks, lamina bending and fibre fracturing failure modes.

Numerical

- The magnitude of the peak reflected blast pressure from the 3D computational model was very close to the ConWep predicted and the experimentally measured values for 40g C4 with the stand-off distance of 30 cm. Furthermore, the numerically calculated average positive duration was comparable with the experimental data. However, the predicted positive duration from ConWep was significantly higher than the experimentally measured and numerically calculated values. The reason for this difference was the diffraction associated with the clearing of pressure waves for the finite reflected surface. On the other hand, the numerically calculated blast parameters for 40g C4 with 15 cm stand-off distance do not correlate with the ConWep predicted values.
- For a close-range blast loading (40g C4 with a stand-off distance of 30 cm and 15 cm) ConWep and Autodyn V-12.1 showed a non-uniform distribution of the reflected pressure and its positive duration on the top face of the skin plate.
- The 3D computational model showed a clear evidence of clearing of the reflected pressure waves with finite surface area of the reflected surface (aluminium skin plate). The diffracted pressure from the top face quickly passed around the edges and acted on the bottom face of the skin plate. In addition to the diffracted pressure, the incident pressure wave at the boundary of the skin plate also played a role (engulfing phenomenon).
- The effect of ground surface reflection on the bottom face of the skin plates was also studied. The calculated average reflected pressure due to ground reflection was 385 kPa and 690 kPa (above the atmospheric pressure) for 30 cm and 15 cm stand-off distance respectively.
- The effective impulse from the diffraction and ground reflection was significant compared to the reflected impulse; an average value of 30% of the reflected impulse acted on the bottom face due to diffraction and ground reflection. This percentage was the same for 20g C4 with 30 cm stand-off distance which was discussed in Chapter 5. This shows that irrespective of the charge mass and stand-off distances conducting blast tests with the presented experimental test set-up will provide a 30% loss in the reflected impulse. However, this also depends upon the area of the skin plate.
- The failure initiation and the final deformation patterns of the cylindrical glass polyester pultruded composite tubes from numerical simulation were very similar to the experimental results. All the typical failure modes such as circumferential delamination, axial cracks, lamina bending and fibre fracturing were clearly evident from the numerical simulation.

11. 8. Need for alternative composite tubes

As seen from the experimental and numerical results the maximum deformation lengths of the composite tubes with 40g C4 with 30 cm and 15 cm stand-off distance were 16 mm and 30 mm respectively. The peak crush load of these composite tubes (~13 kN) was approximately three to four times higher than from the empty beverage cans (3 to 4 kN). The effectiveness of the inner core depends on the transferred peak force to the non-sacrificial structure and the corresponding crushing duration. Since the deformation length and the corresponding crushing duration of the composite tubes were lower, the chance of transferring a relatively higher force in shorter duration to the mounting structure is quite high. This point can be supported by comparing the results with the beverage can. The approximate peak force and the crushing duration for the beverage can were 3.5 kN and 8 ms respectively (with sandwich composite skin plate ϕ 250 mm; 0.36 kg) for 20g C4 with a stand-off distance of 30 cm. Whereas for the composite tubes these values were 13 kN and 3.65 ms (40g C4 with 15 cm stand-off distance and 0.7 kg mass of skin plate) respectively. Furthermore, if the inner core member is very stiff then a high bending stiffness of the skin plate is absolutely necessary to crush the inner core. Consequently, this option will increase the mass of the skin plate (even deploying the sandwich structure concept) which is not desirable in terms of the available energy for the crushing of the inner core, because, a considerable amount of energy will be lost to overcome the inertia and subsequently for the acceleration of the skin plate.

On the other hand, these composite tubes can be deployed for the inner core of a sacrificial cladding structure which is designed for very high blast pressure loading such as very close-range and contact blast loading applications. Accordingly, the *Department of Mechanics of Materials and Constructions, Vrije Universiteit Brussels*, Belgium, (one of the partners in this FWO project) has successfully conducted experiments on these composite tubes under contact blast loading condition using a so-called *suspended pendulum set-up* in collaboration with Prof. Gerald Nurick from University of Cape town, South Africa (refer Figure 11-24). Further details on the use of this suspended pendulum set up and method of calculation of the blast parameters can be found from the refs.[4, 5, 21-28]. As an example, the deformation patterns of composite tubes are shown in Figure 11-24.

Achieving the above deformation lengths of the composite tubes (41 mm and 45.5 mm) in air blast loading needs a very high bending stiffness and a lower mass of the skin plate. However, achieving this combination is impossible. Furthermore, achieving a reflected pressure to provide such a longer deformation length of the test specimen is very difficult. Either the size of the charge to be increased for a long stand-off distance or blast tests have to be performed at very close stand-off distance

using a relatively smaller charge mass. Using the earlier approach will need a large quantity of explosive to perform more tests; and blast parameters cannot be measured for using the later approach. Hence, in order to avoid these limitations composite tubes with a lower stiffness are absolutely necessary for the inner core. Furthermore, as discussed in Chapter 7, the different uniform and non-uniform profiles of the unidirectional composite tubes have to be checked for the maximum energy absorption. However, we could not able to find low stiff composite tubes from the commercial market; therefore it was decided to manufacture them in-house. Hence, unidirectional glass polyester composite tubes with nine different shapes have been manufactured. Similar to the earlier approach, initially the nine different shapes have been evaluated for quasi-static loading conditions; then the qualified shapes have been considered for the impact and blast tests. The next part of the dissertation presents the results from the above studies.

Figure 11-24: Details of the striker mass and the failed composite tubes.

Bibliography

[1]. Guruprasad, S. and Mukherjee, A., *Layered sacrificial claddings under blast loading Part II - experimental studies.* International Journal of Impact Engineering, 2000. **24**(9): p. 975-984.

[2]. Hanssen, A. G., Enstock, L. and Langseth, M., *Close-range blast loading of aluminium foam panels.* International Journal of Impact Engineering, 2002. **27**(6): p. 593-618.

[3]. Theobald, M. D. and Nurick, G. N., *Experimental and numerical analysis of tube-core claddings under blast loads.* International Journal of Impact Engineering. **37**(3): p. 333-348.

[4]. Karagiozova, D., Nurick, G. N. and Chung Kim Yuen, S., *Energy absorption of aluminium alloy circular and square tubes under an axial explosive load.* Thin-Walled Structures, 2005. **43**(6): p. 956-982.

[5]. Nurick, G. N., Langdon, G. S., Chi, Y. and Jacob, N., *Behaviour of sandwich panels subjected to intense air blast - Part 1: Experiments.* Composite Structures, 2009. **91**(4): p. 433-441.

[6]. Dharmasena, K. P., Wadley, H. N. G., Williams, K., Xue, Z. and Hutchinson, J. W., *Response of metallic pyramidal lattice core sandwich*

panels to high intensity impulsive loading in air. International Journal of Impact Engineering. **In Press, Corrected Proof**.

[7]. Arnaud, P. and Hamelin, P., *Dynamic characterization of structures: A study of energy absorption in composite tubes.* Composites Science and Technology, 1998. **58**(5): p. 709-715.

[8]. Farley, G. L., *Energy absorption of composite materials* Journal of Composite Materials, 1983. **17**: p. 267-279.

[9]. Hamada, H., Kameo, K., Sakaguchi, M., Saito, H. and Iwamoto, M., *Energy-absorption properties of braided composite rods.* Composites Science and Technology, 2000. **60**(5): p. 723-729.

[10]. Mamalis, A. G., Manolakos, D. E., Demosthenous, G. A. and Ioannidis, M. B., *Analytical and experimental approach to damage and residual strength of fibreglass composite automotive frame rails during manufacturing.* Composite Structures, 1995. **32**(1-4): p. 325-330.

[11]. Thornton, P. H. and Edwards, P. J., *Energy absorption in composite tubes.* Journal of Composite Matter, 1982. **16**: p. 521-545.

[12]. Gilbert F. Kinney, K. J. G., *Explosive shocks in air.* Springer-Verlag, 1985.

[13]. Palanivelu, S., Van Paepegem, W., Degrieck, J., Kakogiannis, D., Van Ackeren, J., Van Hemelrijck, D., Wastiels, J. and Vantomme, J., *Comparative study of the quasi-static energy absorption of small-scale composite tubes with different geometrical shapes for use in sacrificial cladding structures.* Polymer Testing, 2010. **29**(3): p. 381-396.

[14]. Palanivelu, S., Van Paepegem, W., Degrieck, J., Van Ackeren, J., Kakogiannis, D., Van Hemelrijck, D., Wastiels, J. and Vantomme, J., *Experimental study on the axial crushing behaviour of pultruded composite tubes.* Polymer Testing, 2010. **29**(2): p. 224-234.

[15]. Solaimurugan, S. and Velmurugan, R., *Progressive crushing of stitched glass/polyester composite cylindrical shells.* Composites Science and Technology, 2007. **67**(3-4): p. 422-437.

[16]. Palanivelu, S., Van Paepegem, W., Degrieck, J., Vantomme, J., Kakogiannis, D., Van Ackeren, J., Van Hemelrijck, D. and Wastiels, J., *Crushing and energy absorption performance of different geometrical shapes of small-scale glass/polyester composite tubes under quasi-static loading conditions.* Composite Structures, 2010. **93**(2): p. 992-2007.

[17]. Warrior, N. A., Turner, T. A., Robitaille, F. and Rudd, C. D., *Effect of resin properties and processing parameters on crash energy absorbing composite structures made by RTM.* Composites Part A: Applied Science and Manufacturing, 2003. **34**(6): p. 543-550.

[18]. Palanivelu, S., Van Paepegem, W., Degrieck, J., Kakogiannis, D., Van Ackeren, J., Van Hemelrijck, D., Wastiels, J. and Vantomme, J., *Parametric study of crushing parameters and failure patterns of pultruded composite tubes using cohesive elements and seam, Part I: Central delamination and triggering modelling.* Polymer Testing, 2010. **29**(6): p. 729-741.

[19]. Palanivelu, S., Van Paepegem, W., Degrieck, J., Van Ackeren, J., Kakogiannis, D., Wastiels, J., Van Hemelrijck, D. and Vantomme, J., *Parametric study of crushing parameters and failure patterns of pultruded composite tubes using cohesive elements and seam: Part II - Multiple delaminations and initial geometric imperfections.* Polymer Testing, 2010. **29**(7): p. 803-814.

[20]. Lesuer, D., *Experimental Investigations of Material Models for Ti-6Al-4V Titanium and 2024-T3 Aluminum.U.S. Department of Transportation.DOT/FAA/AR-00/25,Sept. 2000*

[21]. Langdon, G. S., Cantwell, W. J. and Nurick, G. N., *The blast response of novel thermoplastic-based fibre-metal laminates - some preliminary results and observations.* Composites Science and Technology, 2005. **65**(6): p. 861-872.

[22]. Langdon, G. S., Cantwell, W. J. and Nurick, G. N., *Localised blast loading of fibre-metal laminates with a polyamide matrix.* Composites Part B: Engineering, 2007. **38**(7-8): p. 902-913.

[23]. Langdon, G. S., Lemanski, S. L., Nurick, G. N., Simmons, M. C., Cantwell, W. J. and Schleyer, G. K., *Behaviour of fibre-metal laminates subjected to localised blast loading: Part I--Experimental observations.* International Journal of Impact Engineering, 2007. **34**(7): p. 1202-1222.

[24]. Nurick, G. N., Gelman, M. E. and Marshall, N. S., *Tearing of blast loaded plates with clamped boundary conditions.* International Journal of Impact Engineering, 1996. **18**(7-8): p. 803-827.

[25]. Nurick, G. N. and Martin, J. B., *Deformation of thin plates subjected to impulsive loading--A review: Part I: Theoretical considerations.* International Journal of Impact Engineering, 1989. **8**(2): p. 159-170.

[26]. Nurick, G. N. and Martin, J. B., *Deformation of thin plates subjected to impulsive loading--a review Part II: Experimental studies.* International Journal of Impact Engineering, 1989. **8**(2): p. 171-186.

[27]. Nurick, G. N., Olson, M. D., Fagnan, J. R. and Levin, A., *Deformation and tearing of blast-loaded stiffened square plates.* International Journal of Impact Engineering, 1995. **16**(2): p. 273-291.

[28]. Nurick, G. N. and Shave, G. C., *The deformation and tearing of thin square plates subjected to impulsive loads--An experimental study.* International Journal of Impact Engineering, 1996. **18**(1): p. 99-116.

Part III

This part deals with the quasi-static, impact and small-scale blast testing on β - type structure (small-scale in-house composite tubes)

Chapter 12

Quasi-Static Energy Absorption of Small-scale In-house Composite Tubes

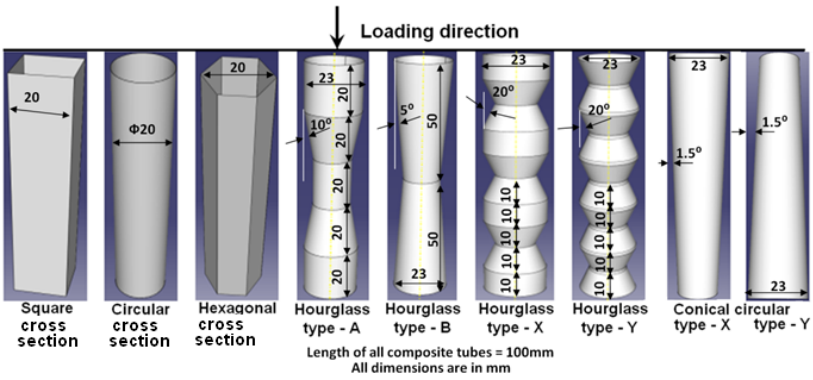

Overview

This chapter presents the quasi-static crushing performance of nine different geometrical shapes of small-scale composite tubes. The idea is to understand the effect of geometry, dimension and triggering mechanism on the progressive deformation of small-scale composite tubes. Different geometrical shapes of the composite tubes have been manufactured by hand lay-up technique using uni-directional E-glass fabric (with single and double plies) and polyester resin. Dedicated quasi-static tests (144 tests) have been conducted to understand the crushing behaviour, deformation patterns and the corresponding energy absorption of each composite tube. The effect of dimensions and the triggering mechanism on each geometrical shape was evaluated with two different t/D (thickness to diameter) ratios and two triggering profiles From this unique study, it was found that the crushing characteristics and the corresponding energy absorption of the special geometrical shapes (hourglass type - A, hourglass type - B, conical circular type - X and conical circular type - Y) are better than the standard geometrical shapes such as square and hexagonal cross-sections. Furthermore, the tulip triggering attributed to a lower peak crush load followed by a steady mean crush load compared to the 45° chamfering triggering profile which resulted into a higher energy absorption in most of the geometrical shapes of the composite tubes.

12. 1. Introduction

The selection of the composite tubes for the inner core of the sacrificial cladding structure involves two major requirements: (i) controlled, uniform and progressive crushing during loading (ii) maximum energy absorption. Therefore, a major question arises about the cross-section, geometry of the composite tube and its variables (material and architectural) which can provide the above said requirements. A clear overview of the various variables which alter the energy absorption of composite structures can be found in [1]. The progressive crushing process which yields a higher energy absorption depends on the mechanical properties of the fibre and the resin, fibre and resin volume fractions, laminate stacking sequence, fibre orientation and the geometry of the tube [1, 2]. However, keeping the same variables for the above parameters (except geometry), different levels of the specific energy absorption can be achieved by changing the geometry of the composite structure [3]. Hence, a suitable geometrical shape of the composite tubes which controls the progressive crushing process and maximizes the energy absorption has to be defined for the inner core structure of the proposed sacrificial cladding structure. The effect of the composite specimen dimensions and its geometry on the energy absorption were studied in [4, 5] using circular and square cross-sectional composite tubes. The general conclusion of these studies is that the D/t (diameter to thickness) ratio significantly affects the energy absorption capability of these composite tubes. Thornton [5] and Thornton et al. [6] demonstrated experimentally that composite tubes with circular cross-sections show a higher energy absorption capability than tubes with rectangular or square cross-sections. Mamalis et al. [7, 8] reported that the square and rectangular cross-sectional composite tubes have 0.8 and 0.5 times the specific energy absorption of circular composite specimens. The reason for the lower energy absorption is due to higher stress concentrations at the corner edges of the tubes which leads to the formation of axial cracks only at those locations. Jimenez et al. [9] conducted a study on open sections such as “I” sectional composite tubes. The result of this research showed that the energy absorption capability of the “I” sectional profile is 15% smaller than the square cross-sectional composite tube; and the corresponding peak crush load during the crushing process was 60% lower. Studies by Mamalis et al. [8, 10] on conical shells showed that the specific energy absorption decreases as the semi-apical angle of the frusta increases. Furthermore, they concluded that the transition point between the stable and unstable collapse with respect to the semi-apical angle lies in the range of 15 to 20 degrees.

Hull [3] stated that the shape and the dimensions of the composite structure are one of the five important variables affecting the specific energy absorption. Very few studies have been carried out on special shapes of composite structures which are intended for specific applications. Mamalis et al. [11] investigated the energy

absorption characteristics of a special shaped (horizontal hourglass) automotive rail frame made of glass/vinylester composite. They reported that the specific energy of the progressively collapsed rail beams is almost constant as the ratio t/L (thickness/length) of the shell increases. Farley and Jones [8, 12] investigated the effect of reducing the included angle in carbon/epoxy elliptical composite tubes. They found that the specific energy absorption increases with decreasing the included angle. The specific energy absorption improved about 10% to 30% corresponding to the reduction of the included angle from 180° to 90°. Elgalai et al. [13] investigated the crushing response of carbon/epoxy and glass/epoxy composite tubes in quasi-static axial loading. They reported that the introduction of corrugation significantly enhanced the energy absorption capability of composite tubes. Zarei et al. [14] studied the energy absorption characteristics of a hexagonal box with vertical ribs. These test specimens were manufactured from woven fiberglass/polyamide plates using thermoforming welding method. Abdewi et al. [15] studied the quasi-static axial and lateral crushing of radial corrugated glass/epoxy composite tubes. They concluded that the radial corrugation significantly influenced the energy absorption of the composite tubes.

As noticed in the previous paragraphs different forms of energy absorbing composite structures are studied for specific applications. However, the dimensions of these composite test specimens are generally larger than the inner core structures of the proposed sacrificial cladding structure. Furthermore, there are several shapes of composite tubes whose energy absorption capabilities have not been studied yet. Few examples of such geometrical shapes (Hourglass type - A, Hourglass type - B, Hourglass type - X, Hourglass type- Y and Conical circular type - X) are shown in Figure 12-1. Hence, in order to study the influence of geometry on the energy absorption, nine different geometrical shapes have been chosen (Figure 12-1). Due to a higher performance to cost ratio and the acceptance in many applications the E-glass fabric and the polyester resin were chosen. Similar to the previous studies the fibre orientation along the axis of the tube was chosen for better energy absorption [16, 17]. In order to scale these composite tubes for different energy absorption values and to study the influence of t/D ratio, two different t/D ratios have been considered for the study. To produce a significant deceleration during the crush event, the failed tubes should exhibit delamination, bending, axial cracking and fibre fracturing modes [1, 2, 16, 18-21]. To induce a stable progressive crushing many researchers [1, 4, 5, 10, 21-23]employed the edge chamfering of the structures as triggering mechanism. Few studies have been conducted with square tubes and “I” sectional tubes to study the effect of triggering on the energy absorption [9, 20]. However, the effect of triggering mechanisms on the energy absorption of other geometrical shapes is yet to be captured. Hence, it is worth to investigate the role of different triggering mechanisms on the energy absorption of uniform and non-uniform geometrical shapes. To study the effect of triggering on the crushing

behaviour and the corresponding energy absorption two different triggering mechanisms (45° chamfering around the edge and tulip triggering with an included angle between the edges of 90°) were chosen.

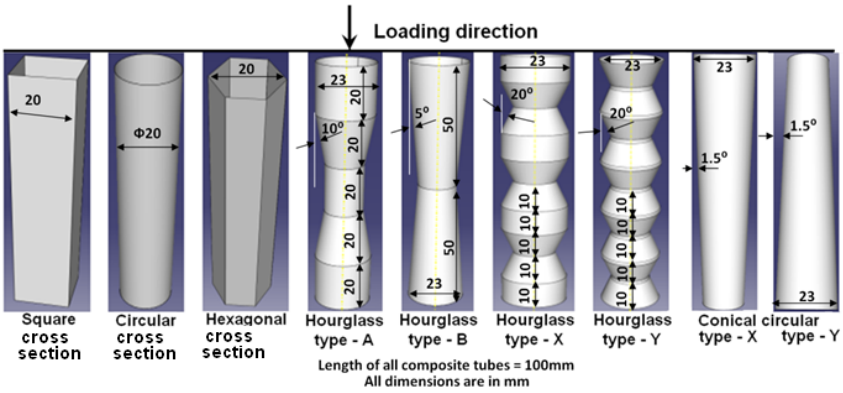

Figure 12-1: Details of the cross-sections, geometry and the (inner) dimensions of the composite tubes.

A large amount of quasi-static investigations [2, 13, 16, 22, 24-26] has been carried out to study the energy absorption characteristics of metal and composite structures. The advantage of this method is the very slow speed of the crushing process and it helps to capture the deformation behaviour of the test specimens. This quasi-static testing can help to leave out many choices of the composite tubes which can exhibit non-progressive or catastrophic failure modes and hence the lower energy absorption. Furthermore, it can give a preliminary idea about the deployment of the different geometrical shapes of the composite tubes for different blast loading conditions. The qualified set of geometrical shapes from this quasi-static evaluation can be further considered for dynamic studies (impact and blast). Hence, in order to understand the crushing behaviour and the corresponding energy absorption of these small-scale composite tubes the quasi-static axial crushing tests were conducted. The test parameters such as the specific energy absorption, peak crush load, mean crush load and the efficiency of the crushing process are presented. All the composite tube specimens have been manufactured by hand lay-up using E-glass fabric, polyester resin and polyurethane foam mandrels, as explained in subsequent section.

12. 2. Materials and manufacturing of composite tubes

12. 2. 1. Materials and dimensional details of the composite tubes

The composite tubes tested in this investigation were fabricated by hand lay-up using a uni-directional E-glass fabric (Roviglass R475/17). In the fibre direction $\vec{e}_{11}$,

the reinforcement was 475 g/m^2, while in the direction $\vec{e}_{22}$, the reinforcement was 17 g/m^2 (refer Figure 12-2(a) and Figure 12-3). The Synolite 1408-P-1 polyester resin (low viscous, pre-accelerated, promoted thixotropic medium reactive unsaturated polyester resin) was used to manufacture the composite tubes. Studies conducted on the progressive crushing of circular cross-sectional composite tubes proved that tubes having a t/D ratio less than 0.015 will fail catastrophically [21]. However, tubes with a t/D ratio in the range of 0.015 to 0.25 will crush progressively. Hence, the t/D and t/W (thickness to width) ratio of the tubes were chosen as per the above recommendation for 1 mm and 2 mm thickness tubes (refer Table 12-1). The average diameter was considered for t/D calculation for the composite tubes with non-uniform cross-section along their length and the calculated average values (from 4 test specimens) for each composite tube series are given in Table 12-1. The length of all the composite tubes was restricted to 100 mm. A polyurethane foam with density of 104 kg/m^3 was used to make all the mandrels (refer Figure 12-2(b)).

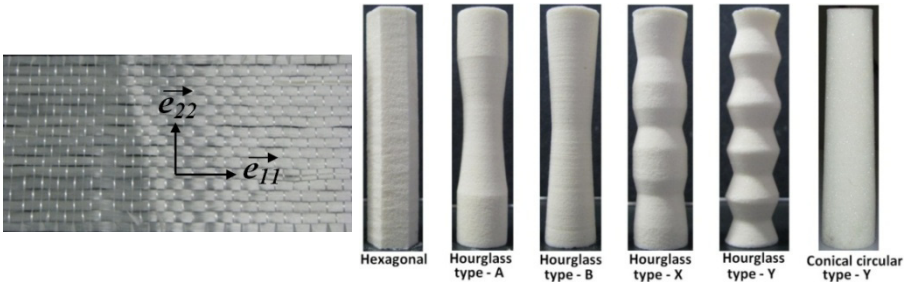

(a) Unidirectional E-glass fabric.

(b) Example of polyurethane foam mandrels.

Figure 12-2: Uni-directional E-glass fabric and finished polyurethane foam mandrels.

12. 2. 2. Fabrication

Sophisticated methods for manufacturing of composite tubes need a considerable amount of resources. Furthermore, it may not be feasible to obtain a low quantity of composite tubes with different geometrical shapes from any commercial manufacturer. Hence, due to the versatile advantages such as low tooling cost, start-up and low capital cost the hand lay-up technique was chosen to manufacture all composite tubes. The steps involved in the fabrication of the composite tubes are as follows: (i) initially, the polyurethane foam mandrels were made as per the inner dimensions of the composite tubes. The fabricated polyurethane foam mandrels for a few geometrical shapes were shown in Figure 12-2(b). (ii) secondly, the E-glass fibre mat was cut into the developed length for each geometrical shape of the composite tubes. (iii) in the third stage, these polyurethane foam mandrels were mounted on a rotating rod which was clamped at both ends (the filament winding machine was used for this purpose).

Table 12-1: Nomenclature, geometry and dimensional details of the composite tube series.

S.No	Tube series	Cross-section / Geometry of the composite tube	t/D or t/W ratio	Length) (mm)	ρ_{linear} (g/mm)
		Wall thickness of the tube 1 mm (S = Single)			
1	SST1	Square cross-sectional tube with triggering type 1	0.045	100	0.1232
2	SST2	Square cross-sectional tube with triggering type 2			0.1229
3	CST1	Circular cross-sectional tube with triggering type 1	0.045		0.0993
4	CST2	Circular cross-sectional tube with triggering type 2			0.0947
5	HST1	Hexagonal cross-sectional tube with triggering type 1	0.045		0.1018
6	HST2	Hexagonal cross-sectional tube with triggering type 2			0.1025
7	HAST1	Hourglass type - A with triggering type 1	0.043		0.1050
8	HAST2	Hourglass type - A with triggering type 2			0.1011
9	HBST1	Hourglass type - B with triggering type 1	0.045		0.0895
10	HBST2	Hourglass type - B with triggering type 2			0.0883
11	HXST1	Hourglass type - X with triggering type 1	0.043		0.1078
12	HXST2	Hourglass type - X with triggering type 2			0.0984
13	HYST1	Hourglass type - Y with triggering type 1	0.046		0.1041
14	HYST2	Hourglass type - Y with triggering type 2			0.1118
15	CXST1	Conical circular type - X with triggering type 1	0.045		0.1208
16	CXST2	Conical circular type - X with triggering type 2			0.1225
17	CYST1	Conical circular type - Y with triggering type 1	0.045		0.1244
18	CYST2	Conical circular type - Y with triggering type 2			0.1139

S.No	Tube series	Cross-section / Geometry of the composite tube	t/D or t/W ratio	Length) (mm)	ρ_{linear} (g/mm)
		Wall thickness of the tube 2 mm (D = Double)			
19	SDT1	Square cross-sectional tube with triggering type 1	0.083	100	0.2005
20	SDT2	Square cross-sectional tube with triggering type 2			0.2084
21	CDT1	Circular cross-sectional tube with triggering type 1	0.083		0.1668
22	CDT2	Circular cross-sectional tube with triggering type 2			0.1598
23	HDT1	Hexagonal cross-sectional tube with triggering type 1	0.083		0.1670
24	HDT2	Hexagonal cross-sectional tube with triggering type 2			0.1596
25	HADT1	Hourglass type - A with triggering type 1	0.08		0.1886
26	HADT2	Hourglass type - A with triggering type 2			0.1826
27	HBDT1	Hourglass type - B with triggering type 1	0.083		0.1552
28	HBDT2	Hourglass type - B with triggering type 2			0.1534
29	HXDT1	Hourglass type - X with triggering type 1	0.08		0.1682
30	HXDT2	Hourglass type - X with triggering type 2			0.1633
31	HYDT1	Hourglass type - Y with triggering type 1	0.084		0.1601
32	HYDT2	Hourglass type - Y with triggering type 2			0.1679
33	CXDT1	Conical circular type - X with triggering type 1	0.083		0.1988
34	CXDT2	Conical circular type - X with triggering type 2			0.1884
35	CYDT1	Conical circular type - Y with triggering type 1	0.083		0.2006
36	CYDT2	Conical circular type - Y with triggering type 2			0.1856

(Example of the nomenclature of the circular cross-sectional composite tube: **CST1**– **C**ircular, **S**ingle ply (1 mm thick) and **T**riggering type **1**; **CDT2 - C**ircular, **D**ouble plies (2 mm thick) and **T**riggering type **2**)

Subsequently, the E-glass fibre mat was placed and wrapped around the polyurethane foam mandrel; and further, the polyester resin was applied on that. Special care was taken not to alter the fibre orientations during the wrapping and resin application process. The polyester resin was cured with 1% Butanox M-50 before applying on the mandrel and the E-glass fabric. In order to get a better surface finish, the composite tubes were kept rotating for at least two hours after the manufacturing. Finally, the composite tubes were post-cured for 24 hours at room temperature followed by 24 hours at 60° C and 24 hours at 80° C as per the supplier recommendation. After curing, the polyurethane foam inside the composite tube was removed by using special tools. The used number of E-glass fabric layers to achieve 1 mm and 2 mm thicknesses of the composite tubes was one and two respectively. Later the triggering geometry was introduced on one side of the composite tubes; and the details of the triggering (type 1 and type 2) are shown in Figure 12-3(a) and Figure 12-3(b). The motivation to choose these triggering types was already explained in Chapter 10. Totally, 36 composite tube series were tried out to study the deformation patterns and their corresponding energy absorption behaviour. The nomenclature and the corresponding dimensional details of the composite tube series are given in Table 12-1. The average linear density (mass per unit length) measured from four tubes for each composite tube series is reported in Table 12-1. The finished samples of a few composite tube series are shown in Figure 12-4.

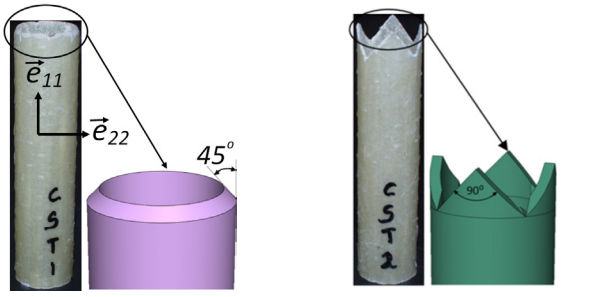

(a) Triggering type 1 (b) Triggering type 2

Figure 12-3: Details of triggering.

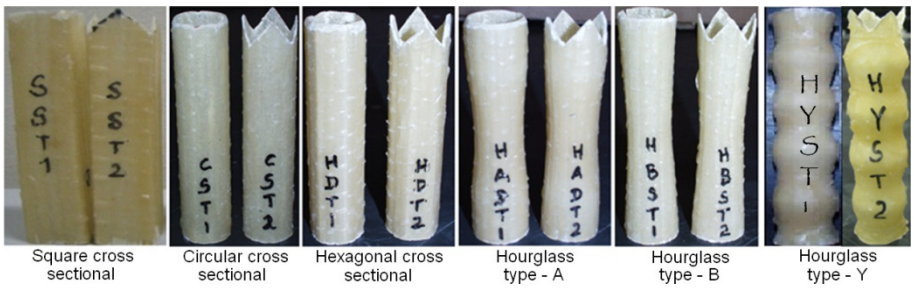

Figure 12-4: Examples of finished composite tube specimens with triggering.

12. 3. Experimental results and discussions

The deformation patterns and the corresponding load-deformation histories of all the composite tubes were studied for quasi-static axial compressive loading condition. An electro-mechanical Instron 4505 machine was used for conducting all the quasi-static crushing tests. In addition to the measurement of the crushing load and the crosshead displacement (which is equivalent to the deformation length of the test specimen), a LVDT was used to measure the initial deformation length of each test specimen up to 10 mm. The arrangement of the LVDT on the Instron machine is shown in Figure 12-5. The measurement of the displacement from the LVDT can provide us an accurate deformation length which corresponds to the peak crush load of a composite tube (this measurement can eliminate the effect of the joint stiffness due to the clearance of the mounting pins and the sockets of the top and bottom crushing plates). The sampling rate of the load cell, LVDT and the crosshead displacement measurement of the Instron machine was the same. However, there was an insignificant difference in the deformation length noticed between these two measurements (LVDT and crosshead displacement).

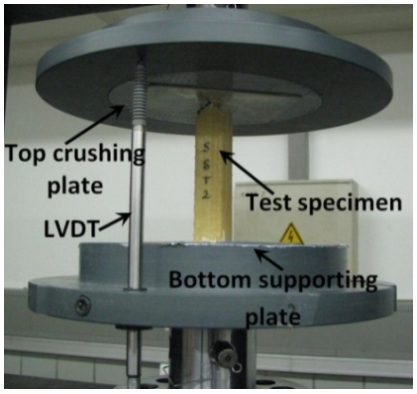

Figure 12-5: LVDT set-up.

The cross-head displacement of 10 mm/min was chosen to conduct all the quasi-static tests. For each composite tube series a minimum of four tests has been conducted. Totally 144 tests have been conducted to study the crushing performance of small-scale composite tubes. The crushing characteristics, deformation patterns and the corresponding load-deformation histories of all the composite tube specimens are presented in this section based on their geometry, thickness and their triggering profiles. For the simplification, the compressive load and the compressive deformation length are indicated in positive numbers in all the load-deformation curves. The scatter in the crushing parameters for all the composite tubes is low despite using the hand lay-up process to manufacture the composite tubes. As an example, the load-deformation curves of 2 mm thickness circular cross-sectional composite tubes with triggering type 2 (tulip triggering) are shown in Figure 12-6.

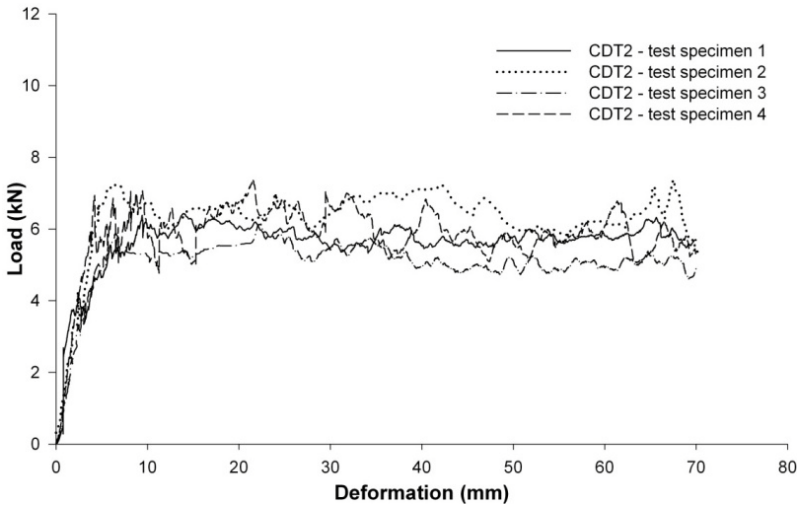

Figure 12-6: Example of a limited scattering of crushing characteristics of 2 mm thickness circular cross-sectional composite tubes with triggering type 2 (tulip triggering).

Therefore, in the coming sections only one representative curve for each type of composite tubes is presented; and the maximum scale of load axes is 6 kN and 12 kN for 1 mm and 2 mm wall thickness composite tubes respectively. For all composite tube series, there was no significant difference in the final deformation observed between triggering type 1 and 2. Furthermore, the effect of transverse fibres ($\vec{e}_{22}$) on the crushing performance of the composite tubes is negligible.

12. 4. Square cross-sectional tubes

12. 4. 1. 1 mm thickness tubes (SST1and SST2)

The deformation patterns of square tubes (both triggering type 1 and 2) with t/W ratio of 0.045 are shown in Figure 12-7(a - top) and Figure 12-7(b - top). Both series of composite tubes (SST1 and SST2) exhibited a catastrophic failure mode due to their geometry and thickness. The initial stages of the crushing showed a progressive crushing of the triggering profiles. However, immediately after the crushing of the triggering profiles a sudden growth of the axial cracks was observed along its entire length. In all eight test specimens (4 test specimens for each triggering) the axial cracks were observed only at the corner locations. This is due to the stress concentration at the corners of the square composite tubes [7, 8]. Furthermore, the axial cracks were formed only at the interface location of one roving to another. This evidence can be clearly noticed from Figure 12-7(a - top). Due to the sudden growth of the axial cracks, the composite tubes lost their load bearing capacity in the later stages of crushing. As an example, the corresponding load-deformation histories for

one specimen of these two composite tubes are shown in Figure 7(b - top). For both tubes the crushing load dropped immediately after the peak crush load. There was an appreciable difference in the peak crush load noticed between triggering type 1 and 2. The peak crush load of triggering type 1 was higher than for triggering type 2. This may be due to the lower stiffness offered by each tulip and the consequent reduction in the strength. The average peak crush load for triggering type 1 was 2.2 kN and the average peak crush load of triggering type 2 was 1.5 kN. For triggering type 2, the slope to reach the peak crush load was uniform. For both composite tube series there was no clear evidence of delamination noticed. Furthermore, there was no difference in the deformation pattern.

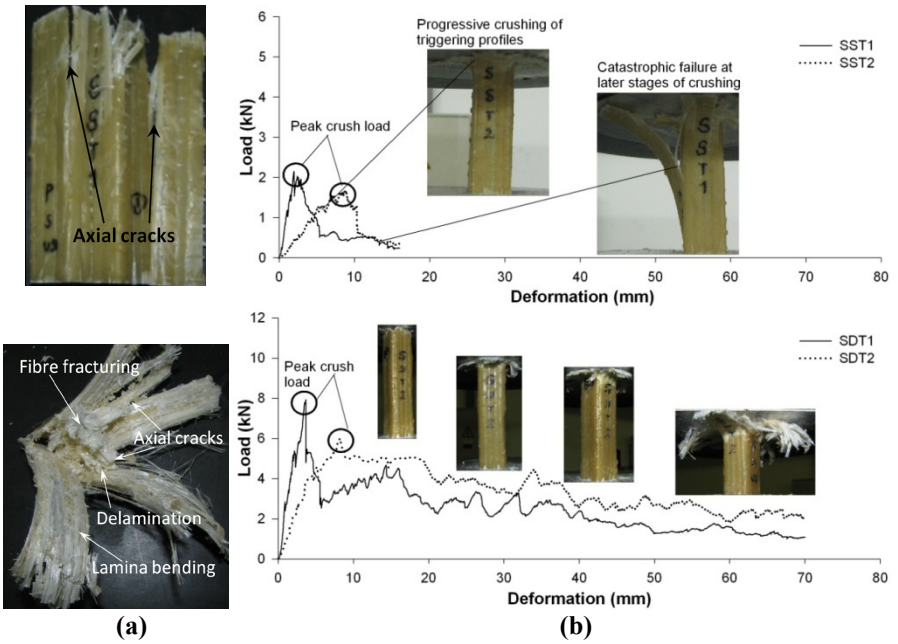

Figure 12-7: Deformation patterns and the crushing performance of the square cross-sectional composite tubes **(a)** Final deformation patterns (top - SST1; bottom - SDT2).(**b)** Load - deformation histories (top - SST1 and SST2; bottom - SDT1 and SDT2).

12. 4. 2. 2 mm thickness tubes (SDT1and SDT2)

Similar to 1 mm thickness tubes, the deformation patterns and the corresponding load-deformation histories of square tubes with 2 mm thickness are shown in Figure 12-7(a - bottom) and Figure 12-7(b - bottom). Unlike 1 mm thickness composite tubes, the 2 mm thickness composite tubes (SDT1 and SDT2) showed uniform and progressive crushing failure modes throughout their length. For both square tubes, after the circumferential delamination (which occurred at the mid thickness of the

tube), the primary axial cracks developed along the corners due to stress concentrations. As a result, each side of the composite tube has split into petals moving inwards and outwards [10, 16, 21]. The major crushing energy of both types of composite tubes was consumed by lamina bending followed by the breakage of resin bonds. The separation of plies from each other occurred at the mid-thickness of the tube wall due to the delamination process. The typical failure modes of brittle composite tubes such as delamination, axial cracks, lamina bending and the fibre fracturing were evident (refer Figure 12-7(a - bottom) and Figure 12-7(b - bottom)) throughout the crushing process. The load-deformation histories of these two composite tubes (SDT1 and SDT2) are shown in Figure 12-7(b - bottom). Similar to the earlier cases which are discussed in previous chapters, the load-deformation curves of both composite tubes followed three phases. The first phase was the increase in load at the initial stage of the compression. During this stage the triggering region of the composite tube was completely crushed; subsequently, the circumferential delamination was started. The area under the load-deformation curve up to the peak crush load corresponds to the total energy spent on the initial circumferential delamination of the composite tube. After the circumferential delamination the peak crush load decreased abruptly. This corresponds to the second stage of the crushing. At the end of this second stage a significant amount of energy was consumed by bending of the petals followed by the shear deformation of the plies that led to fibre fracture. The chronological order of the delamination, axial cracks, bending of petals and the shear fracture of the fibre continued for the subsequent stages of the crushing. Due to the above failure modes, the crushing load of the tube oscillated around a mean value. This was the third stage of the crushing. For triggering type 2, due to the triggering tulips the deformation length to reach the major delamination was different from triggering type 1 tubes and so a smaller slope of the peak crush load was observed. Similar to 1 mm thickness tubes, there was a significant difference in the peak crush load observed between triggering type 1 and type 2. The composite tube with triggering type 1 showed a higher peak crush load than triggering type 2. Furthermore, for triggering type 1 the load dropped considerably after the peak crush load. However, in case of triggering type 2 the drop in the load after the peak crush load was linear. The average peak crush loads were 7.47 kN and 6.22 kN for triggering type 1 and 2 respectively.

◯12. 5. Circular cross-sectional tubes

12. 5. 1. 1 mm thickness tubes (CST1 and CST2)

Unlike square tubes with 1 mm thickness, the circular tubes (CST1 and CST2) showed the controlled progressive failure modes. The progressive deformation patterns and the corresponding load-deformation histories are shown in Figure

12-8(a - top) and Figure 12-8(b - top). Though the composite tube was made by a single layer of E-glass fabric, the circumferential delamination started at the mid-wall thickness of the composite tube. This evidence can be noticed from Figure 12-8(a - top). The longitudinal cut sections of these composite tubes confirmed the same. Consequently, axial cracks were formed parallel to the axis of the tube. The uniform geometry of the circular tube facilitated to form a large number of axial cracks and thus more petals were formed. The major amount of the crushing energy was absorbed due to the increasing number of longitudinal cracks and subsequent bending of the petals [2]. The bending angle of the petals was larger than for the square tubes. This might be due to a lower resistance offered by each petal. During the crushing process a considerable amount of fibre fracturing was also observed. Similar to the square tube the axial cracks were formed only at the interface location of each roving. The peak crush load for the triggering type 1 was higher than for triggering type 2. The average peak crush loads were 3.09 kN and 2.9 kN for triggering type 1 and 2 respectively. Due to the triggering profile the peak crush load for triggering type 2 occurred later than for the triggering type 1. The results from the circular geometry gave a clear indication that even though the composite tube dimensions remain the same (i.e., t/D and t/W ratio for circular and square tubes) the geometry of the composite tube plays a vital role for the progressive crushing.

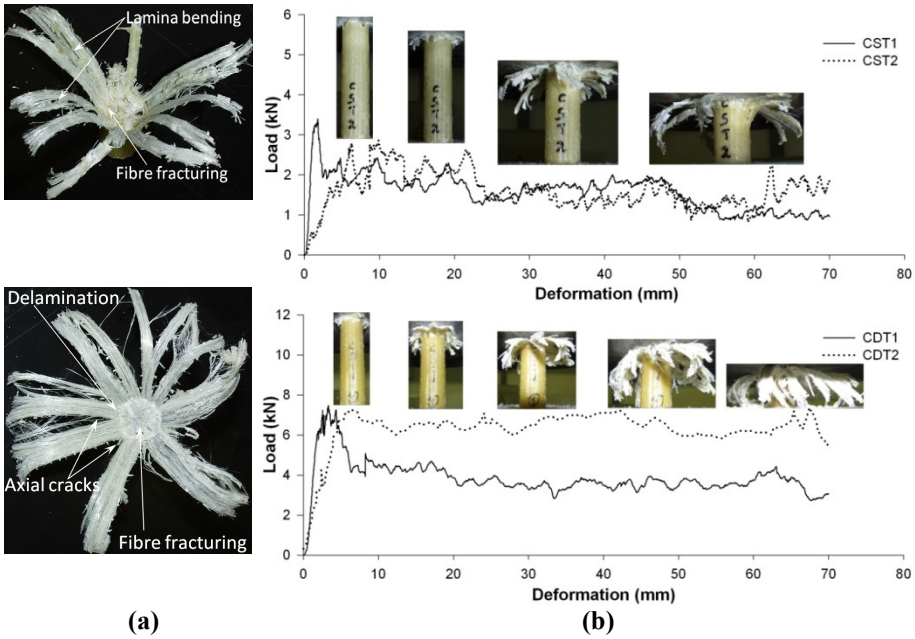

Figure 12-8: Deformation patterns and the crushing performance of the circular cross-sectional composite tubes. **(a)** Final deformation patterns (top - CST2; bottom - CDT1). **(b)** Load - deformation histories (top - CST1 and CST2; bottom - CDT1 and CDT2).

12. 5. 2. 2 mm thickness tubes (CDT1 and CDT2)

Similar to 1 mm thickness circular cross-sectional composite tubes, the 2 mm thickness circular cross-sectional composite tubes (CDT1 and CDT2) showed the progressive deformation failure modes. For both tubes the inner and outer petals were formed due to the circumferential delamination. Consequently, the axial cracks were formed parallel to the axis of the tube. The circumferential delamination occurred at the mid-thickness of the tube. Similar to 1 mm thickness composite tubes more axial cracks were observed. During the crushing process a significant amount of fibre fracturing was also observed. These failure modes can be easily noticed from Figure 12-8(a - bottom) and Figure 12-8(b - bottom). These composite tubes (CDT1 and CDT2) showed a very stable and progressive crushing throughout the crushing process. Similar to the 1 mm thickness circular composite tube with triggering type 1 (CST1), the 2 mm thickness circular composite tube with triggering type 1 (CDT1) showed a sudden drop in the crushing load after the peak crush load. For the triggering type 2 the crushing load remained the same throughout the crushing length which is a good indicator for the better energy absorption. For both series of composite tubes the number of axial cracks varied from 10 to 14. Similar to square tubes there was a difference in the peak crush load noticed between the triggering type 1 and 2. The average peak crush loads were 7 kN and 6.35 kN for the triggering type 1 and triggering type 2 respectively.

〇12. 6. Hexagonal cross-sectional tubes

12. 6. 1. 1 mm thickness tubes (HST1 and HST2)

The crushing performance of 1 mm thickness hexagonal cross-sectional composite tubes (HST1 and HST2) was very similar to 1 mm thickness square tubes. A local-kink in the fibres was observed after the crushing of the triggering profile (refer Figure 12-9(b - top). Subsequently, the longitudinal cracks were initiated and propagated through the entire length of the composite tubes (Figure 12-9(a - top). However, there was a difference noticed for the location of the axial cracks. For the square tubes with 1 mm thickness (SST1 and SST2) the axial cracks were formed at the corner locations of the composite tubes consistently. However, in case of hexagonal composite tubes there was no consistency in the location of axial cracks at the corner locations; these locations were changed arbitrarily. Later stages of the crushing process showed a wall buckling mode. This effect can be clearly noticed from Figure 12-9(b - top). The corresponding load-deformation histories of these composite tubes can be noticed from Figure 12-9(b - top). Similar to other composite series, there was a significant difference in the peak crush load observed

between triggering type 1 and triggering type 2. The average peak crush loads were 2.52 kN and 2.0 kN for triggering type 1 and triggering type 2 respectively.

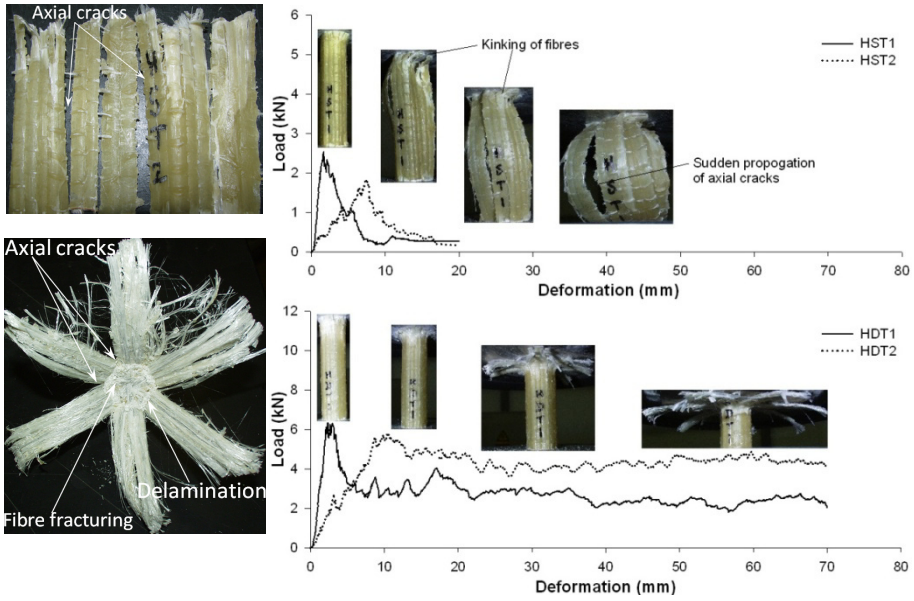

(a) **(b)**

Figure 12-9: Deformation patterns and the crushing performance of the hexagonal cross-sectional composite tubes.**(a)** Final deformation patterns (top – HST2; bottom - HDT1). **(b)** Load - deformation histories tubes (top - HST1 and HST2; bottom - HDT1 and HDT2).

12. 6. 2. 2 mm thickness tubes (HDT1 and HDT2)

The deformation pattern of the hexagonal cross-sectional composite tubes with 2 mm thickness is shown in Figure 12-9(a - bottom) and Figure 12-9(b - bottom). Similar to the square and circular cross-sectional composite tubes the hexagonal tubes also exhibited a uniform and progressive crushing failure mode. The typical failure modes (circumferential delamination, axial cracks, lamina bending and fibre fracturing) of these composite tubes can be clearly noticed from Figure 12-9(a - bottom). The number of axial cracks for these cases (HDT1 and HDT2) was limited to six. Unlike 1 mm thickness hexagonal composite tubes (HST1 and HST2) the 2 mm thickness hexagonal tubes showed the axial cracks only at the corner locations (refer Figure 12-9(a - bottom). The stress concentrations at these corner locations of the composite tubes caused the axial cracks. The corresponding load-deformation histories of these composite tubes with triggering type 1 and 2 are shown in Figure 12-9(b - bottom). The average peak crush loads were 6.30 kN and 5.72 kN for the triggering type 1 and triggering type 2 respectively. Furthermore, the triggering type

2 profile showed a steady and higher mean crush load than triggering type 1 which resulted into a higher energy absorption.

12. 7. Hourglass type - A shaped (circular cross-sectional) tubes

12. 7. 1. 1 mm thickness tubes (HAST1 and HAST2)

The deformation behaviour of the hourglass type - A was similar to the circular composite tubes. The hourglass type - A with 1 mm thickness tubes (HAST1 and HAST2) showed the typical crushing failure modes such as the circumferential delamination, axial cracks, bending of petals and fibre fracturing. However, there was a difference in the amount of fibre fracturing observed for the hourglass type - A composite tubes with triggering type 1. A considerable amount of fibres showed fracturing at the mid-length of the composite tubes. This was due to the geometrical shape of these composite tubes. The controlled circumferential delamination attributed to the fibres to split into two halves, and consequently folded inwards and outwards. The reduced cross-section of the composite tubes at the mid length facilitated the blockage of a large amount of fibres which were folded inwards (refer Figure 12-10(a - top)). As a result of this phenomenon, there was a significant difference in the load-deformation histories noticed compared to the circular composite tubes with 1 mm thickness. The mean crush load of these tubes (with triggering type 1) was increased after achieving 20 mm of deformation length (Figure 12-10(b - top)). However, for triggering type 2 the tulip profiles attributed to the breakage of the fibres in short length. Due to the latter phenomenon there was no considerable blockage of fibre debris at its mid-length. Therefore, the mean crush load was controlled only by the geometry and hence, the mean load dropped at its mid-length (Figure 12-10(b)). Similar to other cases the peak crush load for the triggering type 2 was lower than for triggering type 1. The average peak crush loads were 3.1 kN and 2.5 kN for the triggering type 1 and 2 respectively.

12. 7. 2. 2 mm thickness tubes (HADT1 and HADT2)

The crushing behaviour of the hourglass type - A composite tubes with 2 mm thickness (HADT1 and HADT2) was very similar to the 1 mm thickness composite tube series (HAST1 and HAST2). The deformation patterns and the crushing performance of these composite tubes are given in Figure 12-10(a - bottom) and Figure 12-10(b - bottom). The typical failure patterns are well evident from these figures. Similar to HAST1, there was an increase in mean crush load noticed after 20

mm deformation length for HADT1. The average peak crush load for these cases was 7 kN and 6.55 kN for HADT1 and HADT2 composite tubes respectively.

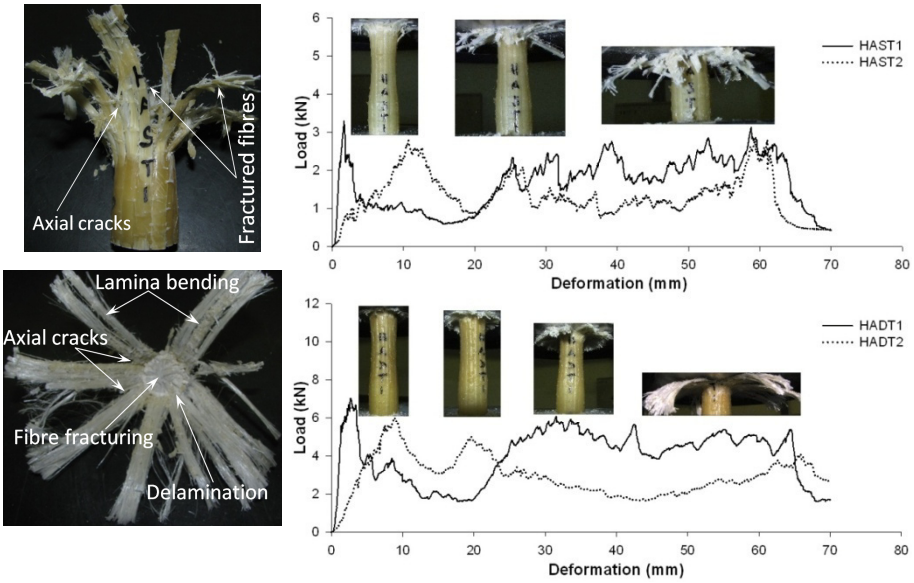

Figure 12-10: Deformation patterns and the crushing performance of the hourglass type - A shaped composite tubes. **(a)** Final deformation patterns (top - HAST1; bottom - HADT2).**(b)** Load - deformation histories (top - HAST1 and HAST2; bottom -HADT1 and HADT2).

12. 8. Hourglass type - B shaped (circular cross-sectional) tubes

12. 8. 1. 1 mm thickness tubes (HBST1 and HBST2)

The deformation patterns of the hourglass type - B shaped composite tubes with 1 mm thickness (HBST1 and HBST2) are shown in Figure 12-11(a - top) and Figure 12-11(b - top). The crushing behaviour of these tubes was similar to the circular cross-sectional composite tubes. Similar to the hourglass type - A tubes, a significant amount of fibre fracturing was also observed (Figure 12-11 (a - top)) due to the reduced cross-section. However, due to the gradual reduction in the cross-section of the composite tube the increased mean crush load after 20 mm deformation length was linear. This phenomenon can be noticed for the composite tube with triggering type 1 (HBST1) in Figure 12-11(b - top). However, for triggering type 2 the tulip profiles attributed to a steady mean crush load (refer Figure 12-11(b - top)). Similar to other cases, the peak crush load for triggering type 1 was higher than for the

triggering type 2 (Figure 12-11 (b - top)). The average peak crush loads were 2.99 kN and 2.55 kN for triggering type 1 and 2 respectively.

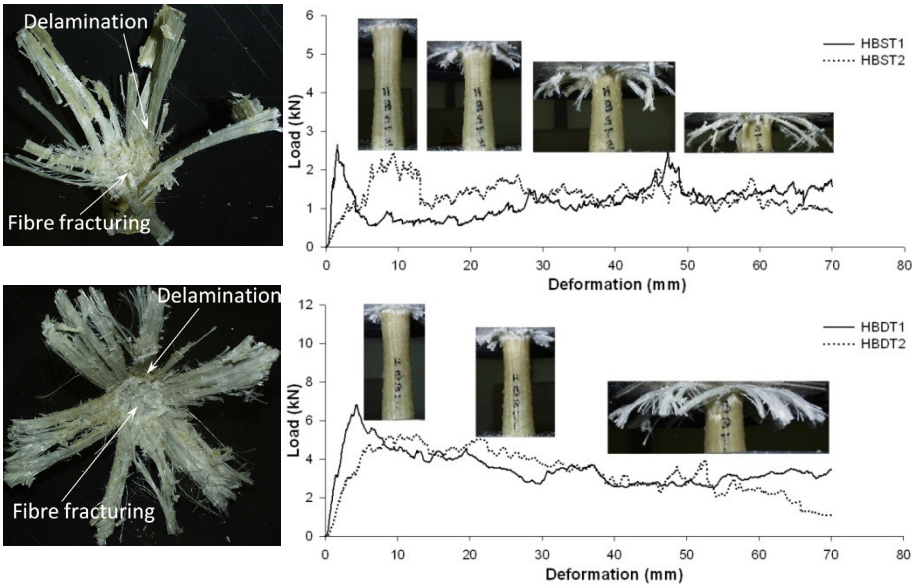

Figure 12-11: Deformation patterns and the crushing performance of the hourglass type – B shaped composite tubes.**(a)** Final deformation patterns (top - HBST1; bottom - HBDT2).**(b)** Load - deformation histories (top - HBST1 and HBST2; bottom - HBDT1 and HBDT2).

12. 8. 2. 2 mm thickness tube (HBDT1 and HBDT2)

The deformation pattern and the corresponding load-deformation histories of the hourglass type - B shaped composite tubes (HBDT1 and HBDT2) are shown in Figure 12-11(a - bottom) and Figure 12-11(b - bottom). The failure patterns of these composite tubes with triggering type 1 and triggering type 2 were very similar to those of the circular composite tubes. Unlike the 1 mm thickness composite tubes (HBST1 and HBST2), the load-deformation histories of these composite tubes (HBDT1 and HBDT2) showed no increase in the mean crush load due to the geometry. This shows that the hourglass type - B geometry does not play a major role for the mean crush load for the higher t/D ratio composite tubes. However, this conclusion should be verified for other conical angles. In this investigation a conical angle of 5° was used for this category of tubes (refer Figure 12-1). The peak crush load of this case showed a significant difference between the triggering type 1 and triggering type 2. The average peak crush load for these cases are 6.42 kN and 5.52 kN for triggering type 1 and triggering type 2 respectively.

12. 9. Hourglass type - X shaped (circular cross-sectional) tubes

12. 9. 1. 1 mm thickness tubes (HXST1 and HXST2)

The crushing performance of the HXST1 and HXST2 composite tubes was completely different from the previous cases. These composite tubes showed non-uniform crushing failure modes. The initial stages of the HXST1 and HXST2 tubes showed the progressive crushing of the triggering profile. However, the later stages of crushing showed a growth of axial cracks at the major diameter locations and further propagated throughout their length. This may be due to the higher compressive radial stress at those locations. The number of the axial cracks varied from 2 to 4 for each composite tube. As a result of this phenomenon, each tube segment showed local wall buckling. Due to this effect the crush load was increased considerably. Subsequently, the fibres at the major diameter location were subjected to fracturing. These failure modes can be observed from Figure 12-12(a -top). The sequence of the formation of the axial cracks at the major diameter and the subsequent local wall buckling and the fibre fracturing continued to the next major diameter region of the composite tubes. The load-deformation histories of these composite tubes showed a lower peak crush load than any other composite tubes series (Figure 12-12(b - top)). The reason for the lower magnitude of the peak crush load was due to the absence of the progressive deformation patterns such as delamination. The average peak crush load of these composite tubes with triggering type 1 and triggering type 2 were 1.25 kN and 1.05 kN respectively.

12. 9. 2. 2 mm thickness tubes (HXDT1 and HXDT2)

The crushing behaviour of 2 mm thickness composite tubes (HXDT1 and HXDT2) was similar to 1 mm thickness composite tubes (HXST1 and HXST2). The initial stages of the crushing of these composite tubes showed a clear evidence of delamination between the inner and the outer plies. However, the later stages of the crushing showed no progressive deformation failure modes (refer Figure 12-12(a - bottom)). Similar to 1 mm thickness tubes (HXST1 and HXST2), the axial cracks initiated at the major diameter locations of the composite tubes. Consequently, the fibres at the major diameter locations showed local wall buckling followed by fibre fracturing (Figure 12-12(b - bottom)). During the local wall buckling mode the fibres at the minor diameter location were pulled towards the axis of the composite tube. The process continued throughout its length. The major amount of the energy was absorbed by the local wall buckling mode and the corresponding fibre fracturing mode. As a result, the total absorbed energy for these composite tube series was lower than for other series. For these composite tubes there was no significant

difference in the peak crush load noticed for triggering type 1 and triggering type 2. The average peak crush loads were 3.85 kN and 3.7 kN for triggering type 1 and triggering type 2 respectively.

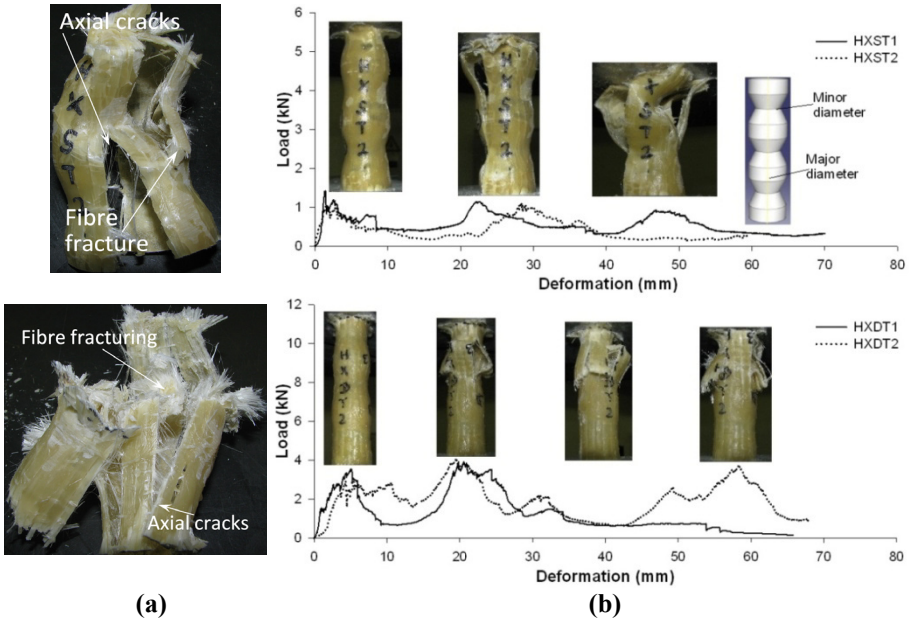

Figure 12-12: Deformation patterns and the crushing performance of the hourglass type - X shaped composite tubes.**(a)** Final deformation patterns (top - HXST1; bottom - HXDT2).**(b)** Load - deformation histories (top - HXST1 and HXST2; bottom - HXDT1 and HXDT2).

12. 10. Hourglass type - Y shaped (circular cross-sectional) tubes

12. 10. 1. 1 mm thickness tubes (HYST1 and HYST2)

The performance of the hourglass type - Y geometry composite tubes (HYST1 and HYST2) was very similar to hourglass type - X geometry tubes. The formation of the axial cracks at the major diameter region due to the compressive radial stress followed by the local wall buckling failure can be noticed from Figure 12-13(a - top). This process continued and propagated to the other end of the composite tube. Due to their geometry (no alignment of triggering profiles to the direction of compressive loading), there was no delamination failure mode observed for these composite tubes. The peak crush load of these composite tubes corresponded to the formation of the axial cracks at the major diameter regions. Furthermore, the effect of the sequential failure modes of these composite tubes can be easily understood from the load-deformation histories (Figure 12-13(b - top)). The peak crush load for

these cases was lower than for other composite tube series. Furthermore, there was no significant difference in the peak crush load noticed for triggering type 1 and triggering type 2. The average peak crush loads were 1.5 and 1.4 kN for triggering type 1 and 2 respectively.

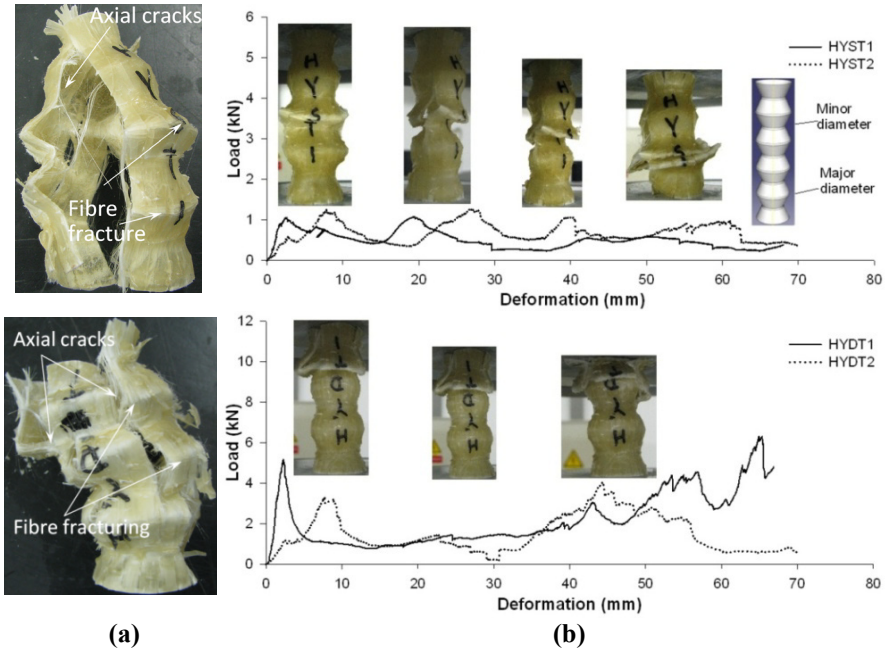

(a) **(b)**

Figure 12-13: Deformation patterns and the crushing performance of the hourglass type - Y shaped composite tubes.**(a)** Final deformation patterns (top - HYST1; bottom - HYDT1).**(b)** Load - deformation histories (top - HYST1 and HYST2; bottom - HYDT1 and HYDT2).

12. 10. 2. 2 mm thickness tubes (HYDT1 and HYDT2)

The deformation patterns and the corresponding load-deformation histories of the 2 mm thickness composite tubes (HYDT1 and HYDT2) are shown in Figure 12-13(a - bottom) and Figure 12-13(b - bottom). The failure sequences of these composite tubes were very similar to the 1 mm thickness composite tubes (HYST1 and HYST2). However, there was a significant difference in the peak crush load noticed for triggering type 1 and 2. The average peak crush loads were 4.6 kN and 3.43 kN for triggering type 1 and 2 respectively.

12. 11. Conical circular type - X

12. 11. 1. 1 mm thickness tubes (CXST1 and CXST2)

The crushing performance of these composite tubes (CXST1 and CXST2) was similar to the circular composite tubes. The typical failure patterns of these composite tubes showed the evidence of the circumferential delamination at its mid-thickness, axial cracks, lamina bending and fibre fracturing. The final deformation patterns and the corresponding sequential failure stages are shown in Figure 12-14(a - top) and Figure 12-14(b - top). For this type of tubes, there was no significant difference in the peak crush load observed for triggering type 1 and 2. The average peak crushing loads were 4.0 kN and 3.9 kN for triggering type 1 and 2 respectively. Due to the gradually reduced cross-section of the composite tubes (towards the bottom side) the mean crush load was increased after 50 mm deformation length. Furthermore, a considerable amount of fibre fracturing occurred at the later stages of the crushing process.

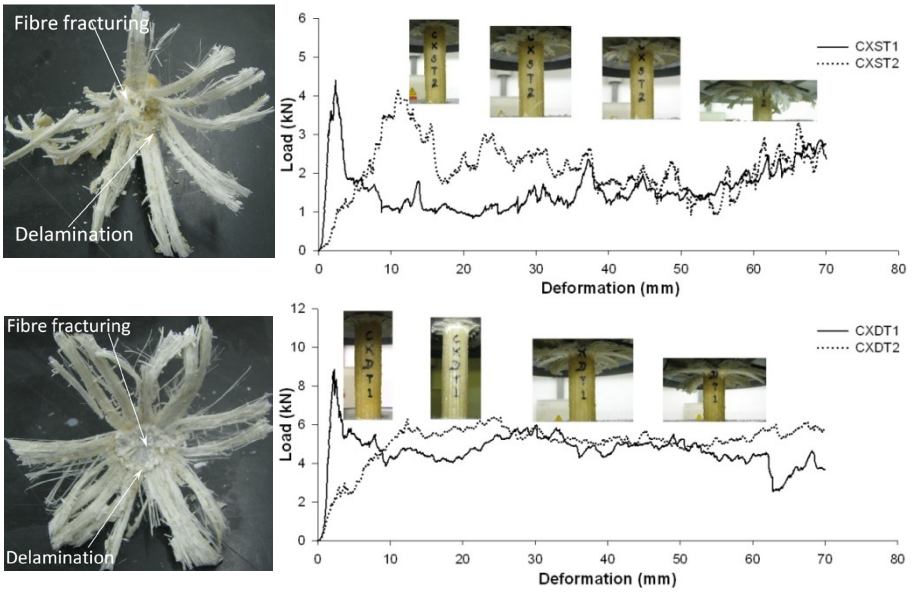

(a) **(b)**

Figure 12-14: Deformation patterns and the crushing performance of the conical circular type - X shaped composite tubes. **(a)** Final deformation patterns (top - CXST1; bottom - CXDT2).**(b)** Load - deformation histories (top - CXST1 and CXST2; bottom - CXDT1 and CXDT2).

12. 11. 2. 2 mm thickness tubes (CXDT1 and CXDT2)

The deformation patterns and the corresponding load-deformation histories of the conical circular type - X geometry composite tubes with 2 mm thickness (CXDT1

and CXDT2) are shown in Figure 12-14(a - bottom) and Figure 12-14(b - bottom). It can be noticed that the deformation patterns of these composite tubes are similar to the circular tubes (CDT1 and CDT2). However, the peak crush load for these composite tubes (CXDT1 and CXDT2) was higher than for the circular composite tubes. The peak crush load loads were 8.65 kN and 7.65 kN for triggering type 1 and 2. This may be due to the increased cross-section at the triggering ends (refer Figure 12-1). After reaching the peak crush load, the mean crush load of triggering type 2 tubes (CXDT2) was constant throughout the crushing process. As a result of this process the total absorbed energy of this case was higher than for the triggering type 1.

12. 12. Conical circular type - Y

12. 12. 1. 1 mm thickness tubes (CYST1 and CYST2)

The deformation patterns and the corresponding load-deformation curves of CYST1 and CYST2 composite tube series are shown in Figure 12-15(a - top) and Figure 12-15(b - top). The conical circular type - Y geometry with triggering type 1 and 2 exhibited progressive crushing failure modes. Similar to other series, the initial circumferential delamination occurred at the mid thickness of the composite tubes. Subsequently, the axial cracks, lamina bending and fibre fracturing were also observed. The initial crushing stages of these composite tubes showed a significant amount of fibre fracturing failure modes. This might be attributed to the reduced cross-sectional profile at the initial stages of crushing (Figure 12-15(a - top)). The final length of the crushed fibres was shorter than for other composite tube series. The magnitude of the peak crush load for these cases was higher than for the circular composite tubes. This may be due to a higher t/D ratio (0.052) of these composite tubes at their triggering ends. The peak crush loads were 4.45 kN and 4.1 kN for the triggering type 1 and 2 respectively. Due to the advantage of the triggering profile the type 2 showed a higher mean crush load. As a result, the total energy absorption for this case (CYST2) was higher than for the triggering type 1 (CYST1).

12. 12. 2. 2 mm thickness tube (CYDT1 and CYDT2)

Similar to 1 mm thickness composite tubes, the deformation patterns and the crushing performance of 2 mm thickness composite tubes with two types of triggering (CYDT1 and CYDT2) are shown in Figure 12-15(a - bottom) and Figure 12-15(b - bottom). The peak crush load of these composite tube series also showed higher values. However, there was no significant difference in the peak crush load noticed between the triggering type 1 and triggering type 2 tube series. The average

peak crush loads were 9.34 kN and 9.10 kN for triggering type 1 and 2 respectively. As a result of the higher peak crush load and the corresponding mean crush load, the total absorbed energy for these composite tube series was higher than for other composite tube series.

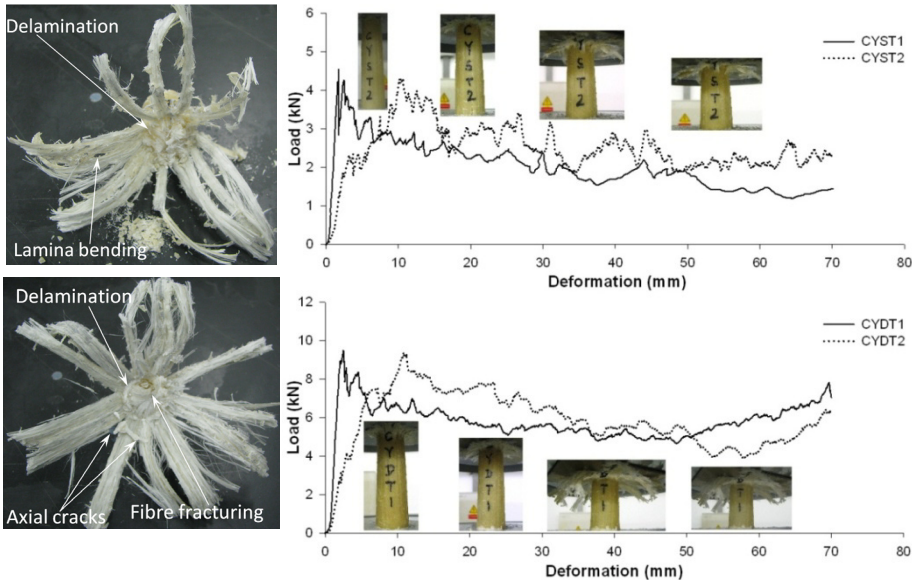

Figure 12-15: Deformation patterns and the crushing performance of the conical circular type - Y shaped composite tubes.**(a)** Final deformation patterns (top - CYST1; bottom - CYDT2).**(b)** Load - deformation histories (top - CYST1 and CYST2; bottom - CYDT1 and CYDT2).

12. 13. Comparison of crushing performance

In order to qualify the different geometry of the composite tubes based on their performance, the crushing parameters are presented and compared in this section. To calculate the energy absorption of each composite tube series a deformation length of 70 mm was considered for all composite tube series. To understand the energy absorption effectiveness of each composite tube, the specific energy absorption (SEA - normalized with respect to mass) was calculated. As seen earlier the peak crush load and the mean crush load were significantly influenced by the triggering geometry. Hence the effect of triggering on these performance parameters is also presented. The mean crush load (P_{mean}) of each composite tube and the corresponding crushing efficiency (η_c) were calculated (refer Table 12-2).

Table 12-2: Summary of the average crushing parameters of all composite tube series.

Tube cross-section / geometrical shapes	1 mm thickness							2 mm thickness						
	Tube series	η_c (%)	Mean load (kN)	Peak load (kN)	C_v for peak load (%)	SEA (kJ/kg)	C_v for SEA (%)	Tube series	η_c (%)	Mean load (kN)	Peak load (kN)	C_v for peak load (%)	SEA (kJ/kg)	C_v for SEA (%)
Square cross-section	**SST1**	-	-	2.22	12.6	-	-	**SDT1**	33.0	2.46	7.47	7.0	12.3	12.7
	SST2	-	-	1.50	16.6	-	-	**SDT2**	53.1	3.43	6.22	4.5	16.2	9.5
Circular cross-section	**CST1**	51.1	1.58	3.09	9.6	15.90	10.1	**CDT1**	70.0	4.90	7.00	8.5	30.4	4.2
	CST2	55.7	1.61	2.90	7.0	17.00	8.8	**CDT2**	75.4	5.21	6.35	9.4	35.2	4.6
Hexagonal cross-section	**HST1**	-	-	2.52	10.0	-	-	**HDT1**	43.3	2.73	6.30	9.5	16.4	13.4
	HST2	-	-	2.00	12.5	-	-	**HDT2**	48.4	2.77	5.72	5.0	17.4	12.7
Hourglass type - A	**HAST1**	53.5	1.66	3.10	6.7	15.45	7.7	**HADT1**	56.9	3.98	7.00	6.0	21.1	4.5
	HAST2	54.0	1.35	2.50	16.0	15.14	9.2	**HADT2**	45.0	2.95	6.55	8.3	18.2	6.7
Hourglass type - B	**HBST1**	39.5	1.18	2.99	7.0	13.21	9.8	**HBDT1**	54.4	3.49	6.42	7.4	20.1	6.8
	HBST2	51.9	1.35	2.55	13.7	15.20	6.5	**HBDT2**	60.1	3.32	5.52	6.1	22.6	7.1
Hourglass type - X	**HXST1**	44.0	0.55	1.25	18.0	5.14	34	**HXDT1**	30.4	1.17	3.85	17.0	6.96	30.0
	HXST2	31.8	0.35	1.05	15.2	3.63	58	**HXDT2**	50.5	1.87	3.70	12.0	11.4	26.0
Hourglass type - Y	**HYST1**	30.6	0.46	1.50	17.7	4.44	45	**HYDT1**	45.4	2.09	4.60	14.0	13.0	17.8
	HYST2	47.8	0.67	1.40	23.0	6.04	41	**HYDT2**	43.7	1.50	3.43	12.6	8.94	26.8
Conical circular type - X	**CXST1**	40.0	1.59	4.00	8.8	13.19	15	**CXDT1**	54.0	4.67	8.65	4.3	23.5	5.8
	CXST2	54.3	2.12	3.90	8.0	17.30	9.2	**CXDT2**	66.4	5.08	7.65	4.7	26.9	6.7
Conical circular type - Y	**CYST1**	45.2	2.01	4.45	6.0	16.20	8.3	**CYDT1**	61.9	5.78	9.34	4.1	28.8	4.1
	CYST2	60.7	2.49	4.10	5.4	21.80	7.6	**CYDT2**	64.3	5.85	9.10	4.9	31.5	4.3

12. 13. 1. For 1 mm thickness composite tube series

Effect of tube geometry and triggering type on SEA

The specific energy absorption of different geometrical shapes of the composite tubes with 1 mm thickness (for triggering type 1 and 2) is shown in Figure 12-16(a); and the corresponding average peak crush loads are shown in Figure 12-16(b). It can be noticed that the scatter of the crushing parameters is low despite using the hand lay-up technique for manufacturing the composite tubes. The square and hexagonal cross-sectional tubes with 1 mm thickness were not considered for the specific energy absorption due to their catastrophic failure. For composite tubes with 1 mm thickness, the specific energy absorption for the conical circular type - Y was higher than for any other composite tube series. The average maximum value attained by this composite tube series with triggering type 2 was 21.8 kJ/kg. This value was reduced considerably for triggering type 1 (16.20 kJ/kg). Similarly, the other composite tube series such as circular cross-sectional, hourglass type - B, and hourglass type - Y showed similar results (Figure 12-16(a)). The reason for the higher SEA of triggering type 2 is the higher mean crush load. As a result of this phenomenon the crushing efficiency for the composite tubes with triggering type 2 was higher than for the triggering type 1 (refer Table 12-2).

However, the hourglass type - A showed no significant difference in SEA for triggering type 1 (15.45 kJ/kg) and type 2 (15.14 kJ/kg). The SEA levels of hourglass type - X (5.14 and 3.63 kJ/kg for triggering type 1 and 2 respectively) and hourglass type - Y (4.44 and 6.04 kJ/kg for triggering type 1 and 2 respectively) were much lower than other geometrical shapes. The reasons for the lower specific energy absorption were the non-progressive failure modes and the absence of the delamination. The ranking from a higher to a lower specific energy absorption based on the geometry and the triggering for 1 mm thickness composite tubes is given below.

For triggering type 1: Conical circular type - Y > Circular cross-section = Hourglass type - A > Hourglass type - B = Conical circular type - X > Hourglass type - X > Hourglass type - Y.

For triggering type 2: Conical circular type - Y > Conical circular type - X > Circular cross-section > Hourglass type - B > Hourglass type - A > Hourglass type - Y > Hourglass type - X.

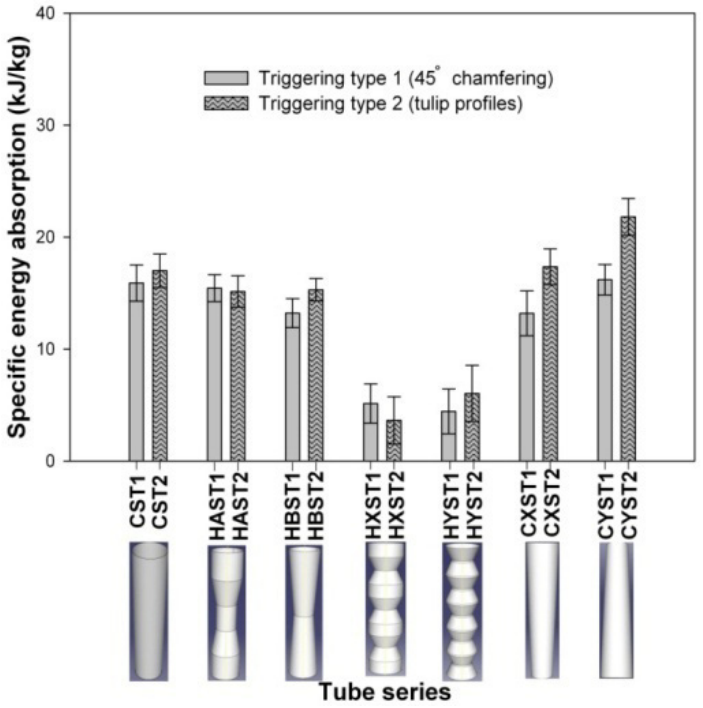

(a)

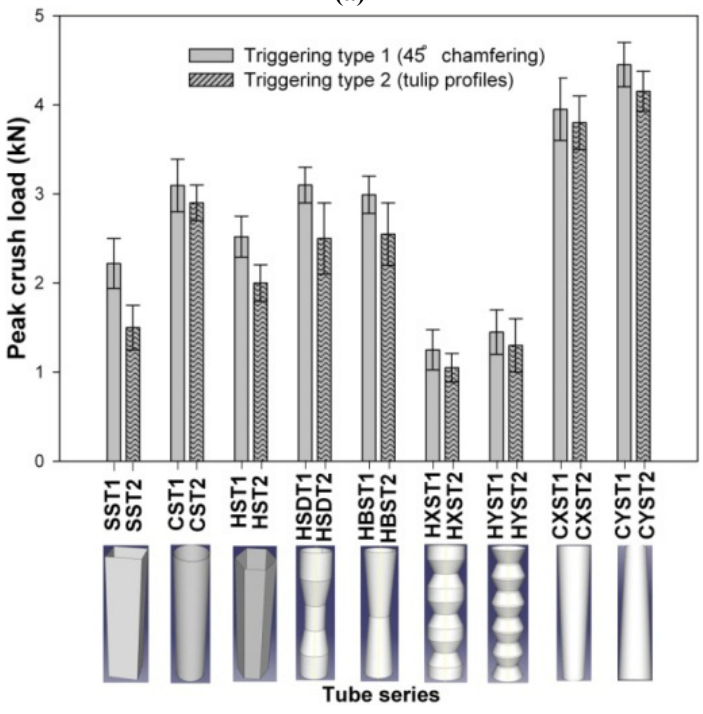

(b)

Figure 12-16: Comparison of the specific energy absorption and peak crush load for 1 mm thickness composite tube series. **(a)** Comparison of the specific energy absorption. **(b)** Comparison of peak crush load.

Effect of tube geometry and triggering type on peak crush load

The effect of tube geometry and the triggering type on the peak crush load can be clearly noticed from Figure 12-16(b). The conical circular type - Y geometry showed higher peak crush loads (4.45 and 4.10 kN for triggering type 1 and 2) than any other composite tube geometry. The peak crush load of hourglass type - A (3.10 kN) and hourglass type - B (2.99 kN) with triggering type 1 can be compared with the circular tube (3.09 kN). Due to the absence of the circumferential delamination, the hourglass type - X and hourglass type - Y geometrical shapes showed lower peak crush loads. In all tube series the peak crush load for triggering type 2 was lower than for triggering type 1; and the corresponding SEA for triggering type 2 tubes is higher than for triggering type 1 (except hourglass type - A and hourglass type - X). This was due to the lower stiffness offered by each tulip during the crushing process followed by short interlaminar cracks. Keeping a lower peak crush load for the inner core member may attribute to achieve the deformation easily during an explosion event and so the magnitude of the peak crush load transferred to the non-sacrificial structure can be minimised. Hence, the selection of triggering type 2 geometry would provide appropriate results at a lower peak crush load. However, the performance of this profile should be verified for blast loading condition. From these results an important conclusion can be made; the same geometry of the composite tube can be extended to different (blast) loading requirements by changing the triggering profile. However, the peak crush loads of these profiles and the influence of other parameters have to be studied and confirmed for dynamic load cases.

12. 13. 2. For 2 mm thickness composite tube series

Effect of tube geometry and triggering type on SEA

The comparison of the specific energy absorption and the corresponding peak crush load distributions are given in Figure 12-17(a) and Figure 12-17(b) respectively. It can be noticed that the scatter of the crushing parameters is even lower compared to 1 mm thickness tubes. Unlike 1 mm thickness composite tubes the circular cross-sectional tube showed a higher specific energy absorption value (35.2 kJ/kg with triggering type 2) than any other composite tube series. The reason for the higher specific energy absorption was higher crush efficiency (75.4 %). Apart from hourglass type - X and hourglass type - Y, the SEA of hourglass type - A, hourglass type - B, conical circular type - X and conical circular type - Y is significantly higher than the standard profiles such as square and hexagonal cross-sectional tubes (refer Figure 12-17(a)). The increased thickness from 1 mm to 2 mm for hourglass type - X and hourglass type - Y has not facilitated to achieve the progressive failure modes. Due to the absence of progressive failure modes and circumferential delamination the SEA of these two tube series is lower. Therefore, these two

geometrical shapes can be excluded for further investigations. Similar to 1 mm thickness tubes, for most cases the SEA for triggering type 2 was higher than for triggering type 1. The ranking from a higher to a lower specific energy absorption based on the geometry and the triggering type for 2 mm thickness composite tubes is given below.

For triggering type 1: Circular > Conical circular type - Y > Conical circular type - X > Hourglass type - A > Hourglass type - B > Hexagonal > Hourglass type - Y > Square > Hourglass type - X

For triggering type 2: Conical circular type - Y > Circular tubes > Conical circular type - X > Hourglass type - B > Hexagonal > Hourglass type - A > Square > Hourglass type - X > Hourglass type - Y

It can be noticed that the ranking is not the same as for 1 mm thickness composite tube series. This shows again the influence of the dimensions (t/D and t/W) of the composite tubes on the specific energy absorption.

Effect of tube geometry and triggering type on peak crush load

The effect of the tube geometry on the peak crush load can be clearly seen from Figure 12-17(b). Similar to 1 mm thickness tubes, the peak crush load for conical circular type - Y was higher than for other tube series (9.34 kN and 9.10 kN for triggering type 1 and 2 respectively). Due to the absence of delaminations, the peak crush load of hourglass type - X (3.85 kN and 3.70 kN for triggering type 1 and 2 respectively) and hourglass type - Y (4.60 kN and 3.43 kN for triggering type 1 and 2 respectively) was lower. The peak crush load of these cases corresponded to the formation of axial cracks at their major diameter location. The peak crush load of the hourglass type - A (7 kN and 6.55 kN for triggering type 1 and 2 respectively) was comparable with circular cross-sectional tube (7 kN and 6.35 kN for triggering type 1 and 2 respectively). Similar to 1 mm thickness tubes the peak crush load for triggering type 2 was lower than for triggering type 1 for all composite tube series.

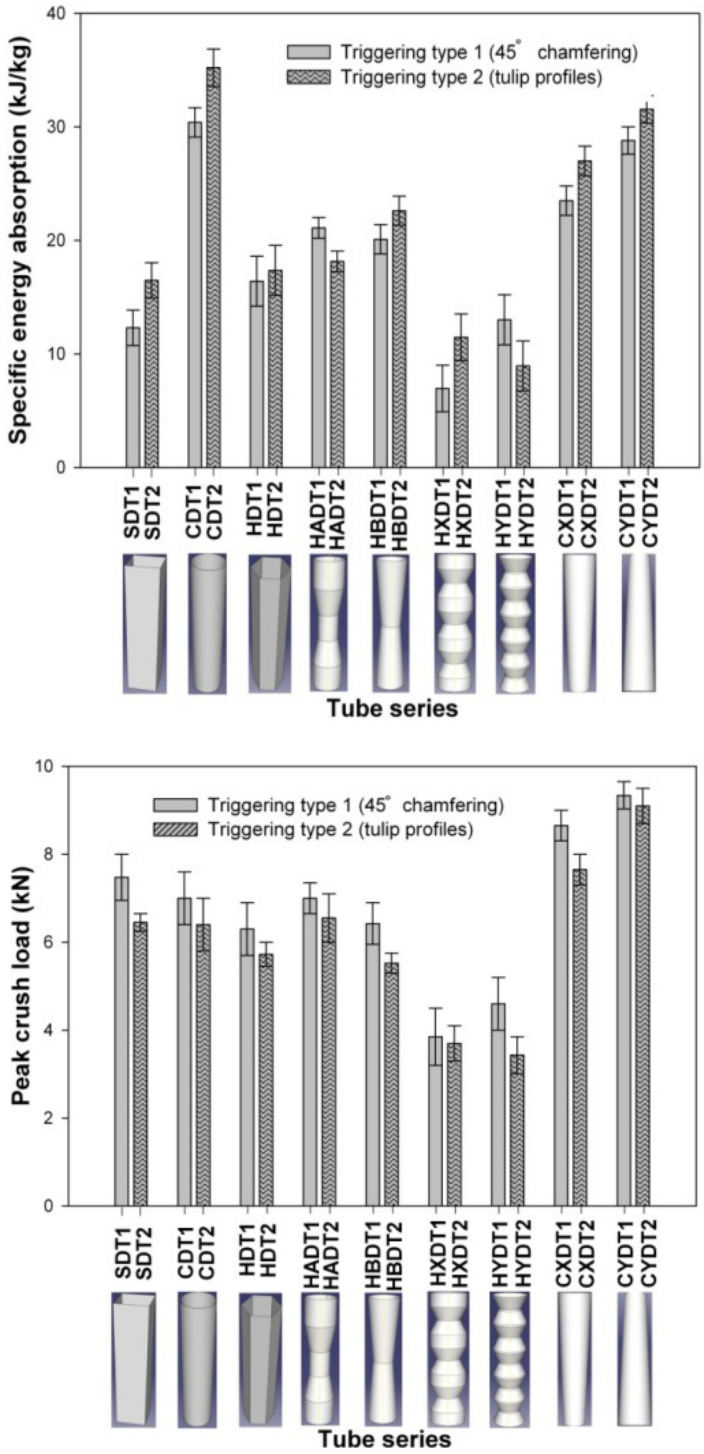

Figure 12-17: Comparison of specific energy absorption and peak crush load for 2 mm thickness composite tube series.**(a)** Comparison of specific energy absorption **(b)** Comparison of peak crush load.

12. 14. Conclusions

In this chapter, the crushing behaviour and the corresponding energy absorption capabilities of small-scale composite tubes have been studied. Nine different geometrical shapes with two different triggering mechanisms (45° chamfering and tulip pattern with an included angle of 90°) were considered for the study. Furthermore, the effect of dimension (t/D and t/W ratio) on each geometrical shape was captured with two different thicknesses (1 and 2 mm). From the quasi-static experimental results it can be concluded that:

- The circular cross-sectional, hourglass type - A, hourglass type - B, conical circular type - X and conical circular type - Y composite tubes with 1 mm thickness (with triggering type 1 and 2) showed uniform and progressive crushing failure modes. The macro-failure mechanisms associated with these composite tubes were circumferential delamination, axial cracks, lamina bending and fibre fracturing. However, the composite tubes with the standard profiles such as the square and hexagonal cross-sections with the same t/W and t/D ratio (0.045) showed a catastrophic failure mode. The major reason for the catastrophic failure was the initiation and sudden propagation of the axial cracks throughout the tube length. This shows that the geometry of the composite tubes plays a significant role for the progressive crushing. Though the hourglass type - X and hourglass type - Y geometrical shapes do not show the catastrophic failure mode, the total energy absorption for these composite tubes was lower than for other tube series. The reason for the lower energy absorption was the absence of the circumferential delamination.
- The square and the hexagonal cross-sectional composite tubes with a higher t/W and t/D ratio (0.083) showed uniform and progressive crushing failure modes. From these results it can be concluded that in addition to the geometry, the t/D or t/W ratio of a composite tube also plays a major role for uniform and progressive crushing. The increased thickness from 1 mm to 2 mm for the hourglass type - X and hourglass type - Y has not facilitated to get all the typical progressive failure patterns of the composite tubes. Similar to 1 mm thickness composite tubes the hourglass type - X and the hourglass type - Y showed the axial cracks, wall-buckling and the fibre fracturing failure modes.
- Comparison with two different thicknesses and triggering types showed that the consideration of the special geometrical shapes such as the hourglass type - A, hourglass type - B, conical circular type - X and conical circular type - Y will provide higher specific energy absorption values than the standard geometrical profiles such as the square and hexagonal cross-sectional tubes. Furthermore, this study has given a clear indication that the

hourglass type - X and the hourglass type - Y can be excluded for further investigations.

- For all composite tube series (both 1 mm and 2 mm) the peak crush load for the composite tubes with triggering type 1 was higher than for triggering type 2. However, for most cases the crushing efficiency of the triggering type 2 was higher than that of triggering type 1. This was due to the "flat-topped" shape of the load-deformation curves of the respective composite tube series due to tulip triggering. Furthermore, the specific energy absorption for triggering type 2 profile was significantly higher than for triggering type 1. The steady mean crush load of the triggering profile (tulips) attributed to a higher specific energy absorption for each case. Hence, the triggering mechanism is an important factor to be considered to achieve good values of the specific energy absorption.

Bibliography

[1]. Ramakrishna, S., *Microstructural design of composite materials for crashworthy structural applications.* Materials & Design, 1997. **18**(3): p. 167-173.

[2]. Solaimurugan, S. and Velmurugan, R., *Progressive crushing of stitched glass/polyester composite cylindrical shells.* Composites Science and Technology, 2007. **67**(3-4): p. 422-437.

[3]. Hull, D., *A unified approach to progressive crushing of fibre-reinforced composite tubes.* Composites Science and Technology, 1991. **40**(4): p. 377-421.

[4]. Farley, G. L., *Effect of specimen geometry on the energy absorption of composite materials.* Journal of Composite Materials, 1986. **20**: p. 390.

[5]. Thornton, P. H. and Edwards, P. J., *Energy absorption in composite tubes.* Journal of Composite Matter, 1982. **16**: p. 521-545.

[6]. Thornton, P. H., Harwood, J. J. and Beardmore, P., *Fiber reinforced plastic composites for energy absorption purposes.* Composite Science Technology, 1985. **24**: p. 275-298.

[7]. Mamalis, A. G., Manolakos, D. E., Ioannidis, M. B. and Papapostolou, D. P., *On the response of thin-walled CFRP composite tubular components subjected to static and dynamic axial compressive loading: experimental.* Composite Structures, 2005. **69**(4): p. 407-420.

[8]. Mamalis, A. G., Robinson, M., Manolakos, D. E., Demosthenous, G. A., Ioannidis, M. B. and Carruthers, J., *Crashworthy capability of composite material structures.* Composite Structures, 1997. **37**(2): p. 109-134.

[9]. Jimenez, M. A., Miravete, A., Larrode, E. and Revuelta, D., *Effect of trigger geometry on energy absorption in composite profiles.* Composite Structures, 2000. **48**(1-3): p. 107-111.

[10]. Mamalis, A. G., Manolakos, D. E., Demosthenous, G. A. and Ioannidis, M. B., *Energy absorption capability of fibreglass composite square frusta*

subjected to static and dynamic axial collapse. Thin-Walled Structures, 1996. **25**(4): p. 269-295.

[11]. Mamalis, A. G., Manolakos, D. E., Demosthenous, G. A. and Ioannidis, M. B., *The static and dynamic axial collapse of fibreglass composite automotive frame rails.* Composite Structures, 1996. **34**(1): p. 77-90.

[12]. Farley, G. L. and Jones, R. M., *Crushing characteristics of composite tubes with "near elliptical" cross sections.* Journal of Composite Materials, 1992. **26**: p. 1252.

[13]. Elgalai, A. M., Mahdi, E., Hamouda, A. M. S. and Sahari, B. S., *Crushing response of composite corrugated tubes to quasi-static axial loading.* Composite Structures, 2004. **66**(1-4): p. 665-671.

[14]. Zarei, H., Kröger, M. and Albertsen, H., *An experimental and numerical crashworthiness investigation of thermoplastic composite crash boxes.* Composite Structures, 2008. **85**(3): p. 245-257.

[15]. Abdewi, E. F., Sulaiman, S., Hamouda, A. M. S. and Mahdi, E., *Quasi-static axial and lateral crushing of radial corrugated composite tubes.* Thin-Walled Structures, 2008. **46**(3): p. 320-332.

[16]. Farley, G. L., *Energy absorption of composite materials* Journal of Composite Materials, 1983. **17**: p. 267-279.

[17]. Farley, G. L., *Effect of fibre and maximum strain rate on the energy absorption of composite materials.* Journal of Composite Materials, 1986. **20**: p. 322-331.

[18]. Hamada, H., Coppola, J. C., Hull, D., Maekawa, Z. and Sato, H., *Comparison of energy absorption of carbon/epoxy and carbon/PEEK composite tubes.* Composites, 1992. **23**(4): p. 245-252.

[19]. Mamalis, A. G., Manolakos, D. E., Demosthenous, G. A. and Ioannidis, M. B., *The static and dynamic axial crumbling of thin-walled fibreglass composite square tubes.* Composites Part B: Engineering, 1997. **28**(4): p. 439-451.

[20]. Thornton, P. H., *The crush behavior of pultruded tubes at high strain rates.* Journal of Composite Materials, 1989. **24**: p. 22.

[21]. Solaimurugan, S. and Velmurugan, R., *Influence of fibre orientation and stacking sequence on petalling of glass/polyester composite cylindrical shells under axial compression.* International Journal of Solids and Structures, 2007. **44**(21): p. 6999-7020.

[22]. Fairfull, A. H. and Hull, D., *Effect of specimen dimensions on the specific energy absorption of fibre composite tubes.* In Proceedings of ICCM-VI, 1987: p. 3.36-3.45.

[23]. Thornton, P. H., *Energy absorption in composite structures.* Journal of Composite Materials, 1979. **13**(247).

[24]. Abosbaia, A. A. S., Mahdi, E., Hamouda, A. M. S. and Sahari, B. B., *Quasi-static axial crushing of segmented and non-segmented composite tubes.* Composite Structures, 2003. **60**(3): p. 327-343.

[25]. Mahdi, E., Hamouda, A. S. M. and Sen, A. C., *Quasi-static crushing behaviour of hybrid and non-hybrid natural fibre composite solid cones.* Composite Structures, 2004. **66**(1-4): p. 647-663.

[26]. Hsu, S. S. and Jones, N., *Quasi-static and dynamic axial crushing of circular and square stainless steel tubes.* Structures under SHOCK AND IMPACT, 2000. **VII**: p. 169-178.

Chapter 13

Effect of Foam-filling on Small-scale In-house Composite Tubes

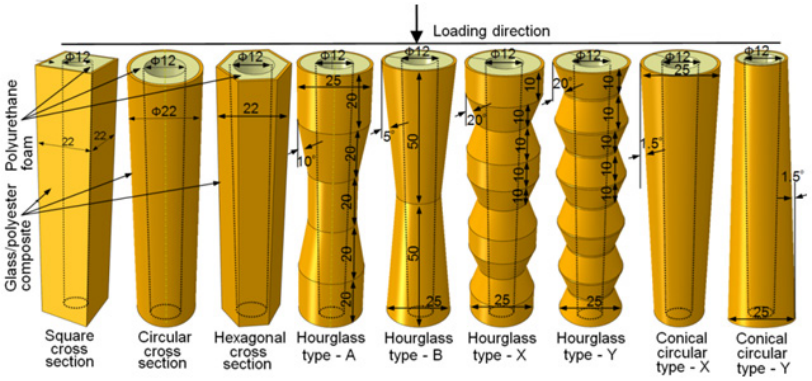

Overview

This chapter presents the quasi-static crushing performance of nine different geometrical shapes of small-scale glass/polyester composite tubes filled with polyurethane closed-cell foam. The effect of polyurethane foam on the crushing characteristics and the corresponding energy absorption is addressed for each geometrical shape of the composite tube. Composite tubes with two different thicknesses (1 mm and 2 mm) have been considered to study the influence of polyurethane foam on the crushing performance. From the present study, it was found that the presence of polyurethane foam inside the composite tubes suppressed the circumferential delamination process and fibre fracturing; consequently, it reduced the specific energy absorption of composite tubes. Furthermore, the polyurethane foam attributed to a higher peak crush load for each composite tube. However, the presence of polyurethane foam inside the composite tubes significantly increased the stability of the crushing phenomena especially for the square and hexagonal cross-sectional composite tubes with 1 mm wall thickness.

13. 1. Introduction

The previous study (from Chapter 12) was focused on the effect of geometry and the corresponding dimensions on the energy absorption of nine different geometrical shapes of hollow composite tubes. These tubes were manufactured by hand lay-up technique using unidirectional E-glass fabric, polyester resin and polyurethane foam mandrels. The scatter in the crushing parameters was very low, despite using hand lay-up technique for manufacturing these composite tubes (refer Chapter 12). After manufacturing of these composite tubes, the polyurethane foam inside each composite tube was removed manually by using special tools which is a time consuming task. Leaving the polyurethane foam inside the composite tube can save considerable quantity of time; furthermore, the additional mass due to the polyurethane foam inside the composite tubes is negligible compared to the mass of the hollow composite tubes. In addition to that, during the previous study a few geometrical shapes of the composite tubes (square and hexagonal cross-sectional tube with 1 mm wall thickness) without polyurethane foam exhibited catastrophic and non-uniform crushing failure modes. The effect of polyurethane foam on the stability of the crushing process is unknown for such geometrical shapes (with uni-directional fibre orientation) of the composite tubes. Furthermore, a comparison of results with the previous study can conclude whether or not to use composite tubes with polyurethane foam for the inner core of the proposed sacrificial cladding structure. Therefore, it is worth to investigate the effect of polyurethane foam on the crushing performance of these tubes.

Many studies [1-5] have been conducted to study the effect of metallic and non-metallic foams on the energy absorption of thin-walled metal tubes. The general conclusion of these researches is that the number of folds formed in foam-filled tubes increased with foam filling and also with increasing foam filler density. As a result, the energy absorption of foam-filled tubes was higher than the sum of the energy absorption of the empty tube and the filler. Furthermore, the interaction of tube wall and foam resulted into an axisymmetric mode (concertina) of deformation. In contrast to the metal tubes, very few studies [6-9] have been conducted on composite tubes with foam-filler material. Guden et al. [7] studied the effect of aluminium closed-cell foam filling on the quasi-static crushing behaviour of E-glass woven fabric polyester composite tubes and thin-walled aluminium/glass polyester composite hybrid tubes. They concluded that the foam filling of hybrid tubes resulted into an axial splitting of the outer composite tubes due to the resistance imposed by the aluminium tube. Babbage and Malick [6] investigated the quasi-static crushing behaviour of epoxy foam-filled aluminum tubes overwrapped with filament-wound E-glass/epoxy composite layers. The conclusion of that research was that the overwrap increased the performance (peak crush load, mean crush load and the corresponding energy absorption) of the square and circular cross-sectional

tubes. Harte et al. [8] investigated the energy absorption behaviour of foam-filled (polyurethane foam and polymethyl-acrylamid foam) circular cross-sectional braided composite tubes. In this work, an analytical model for energy absorption calculation is proposed considering the progressive failure collapse by axisymmetric buckling. Mamalis et al. [9] studied the crushing performance of aluminium and polyurethane foam-filled square cross-sectional glass/vinylester composite tubes. The square tube filled with polyurethane foam exhibited a brittle peripheral rupture, followed by the penetration of the lower part into the upper part which resulted into a lower energy absorption value. However, the tube filled with aluminium foam showed progressive crushing failure modes (delamination, axial cracks, bending of lay-ups and fibre fracturing) which resulted into a higher energy absorption value.

In order to understand the crushing behaviour and the corresponding energy absorption of the small-scale composite tubes with polyurethane foam, quasi-static axial crushing tests were conducted. The dimensional, material and architectural parameters of the composite tubes are the same as in the previous study (refer Chapter 12). The details of the adopted geometrical shapes and the corresponding dimensions for 1 mm thickness tubes with polyurethane foam are given in Figure 13-1. From the quasi-static tests, parameters such as the specific energy absorption, peak crush load, mean crush load and the efficiency of the crushing process are presented. Due to the manufacturing process a hole in the polyurethane foam (ϕ 12 mm) was present inside the composite tubes for the whole length (refer Figure 13-1).

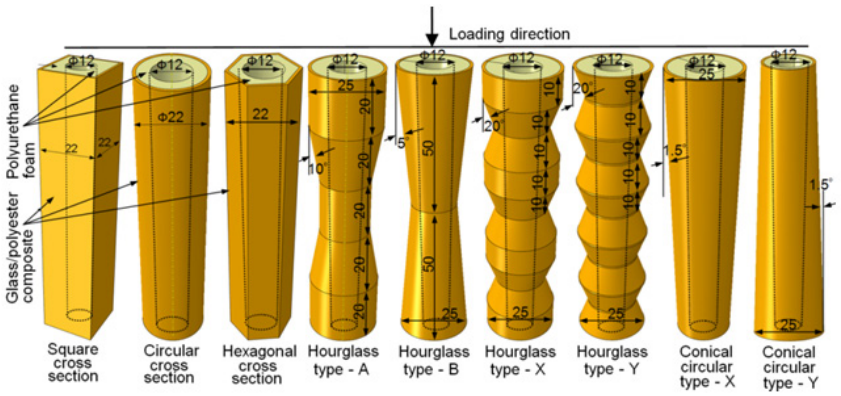

Figure 13-1: Different geometrical shapes of the composite tubes (1mm thickness) and their dimensions considered for the study.

13. 2. Experimental testing and results

The small-scale composite tubes tested in this investigation were fabricated by hand lay-up using a uni-directional E-glass fabric (Roviglass R475/17), Synolite 1408-P-1 polyester resin and polyurethane foam with density of 104 kg/m^3 (closed-cell > 90 %

of volume). The steps involved in manufacturing of these composite tubes and the corresponding post-curing details can be found in Chapter 12. To induce the progressive crushing a triggering geometry (45° chamfering) was introduced on one side of the composite tubes only (refer Figure 13-2). Totally, 19 composite tube series were tried out to study the deformation patterns and the corresponding energy absorption behaviour. The nomenclature and the corresponding dimensional details of the composite tube series are given in Table 13-1. The average linear density (mass per unit length) measured from four tubes for each composite tube series is reported in Table 13-1.

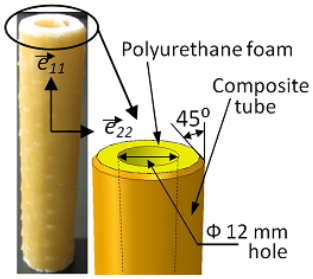

Figure 13-2: Details of triggering.

For simplification, the compressive parameters (load, deformation, stress and strain) are indicated in positive numbers. For each composite tube series a minimum of four tests has been conducted and the average of all the four tests has been taken into account to calculate the crushing parameters of the composite tubes. To discuss the typical load-deformation behaviour of the composite tubes a representative measurement from each composite tube series is presented. In order to measure the compressive behaviour of the polyurethane foam uni-axial compressive tests have been conducted on polyurethane foam as per ASTM 1621-91 (refer Figure 13-3). The figure shows the typical elasto-plastic behaviour with the linear elastic regime, the plateau regime and the densification regime.

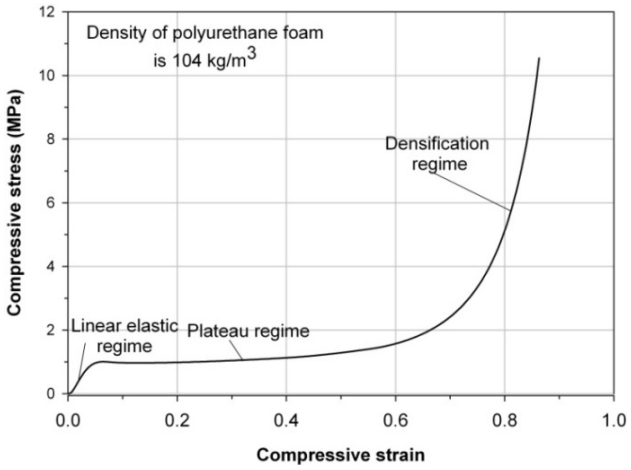

Figure 13-3: Compressive behaviour of polyurethane foam.

Table 13-1: Nomenclature, geometry and dimensional details of the composite tube series.

S.No	Tube series	Cross-section / Geometry of the composite tube	t/D or t/W ratio (excluding polyurethane foam)	Length (mm)	ρ_{linear} (g/mm) (including polyurethane foam)
		Wall thickness of the composite tube = 1 mm			
1	***SSF***	Square cross-sectional tubes	0.045	100	0.1537
2	***CSF***	Circular cross-sectional tubes	0.045		0.1454
3	***HSF***	Hexagonal cross-sectional tubes	0.045		0.1317
4	***HASF***	Hourglass type - A tube	0.043		0.1293
5	***HBSF***	Hourglass type - B tubes	0.045		0.1346
6	***HXSF***	Hourglass type - X tubes	0.043		0.1440
7	***HYSF***	Hourglass type - Y tubes	0.046		0.1366
8	***CXSF***	Conical circular type - X tubes	0.045		0.1336
9	***CYSF***	Conical circular type - Y tubes	0.045		0.1172
		Wall thickness of the composite tube = 2 mm			
10	***SDF***	Square cross-sectional tubes	0.083	100	0.2376
11	***CDF***	Circular cross-sectional tubes	0.083		0.1775
12	***HDF***	Hexagonal cross-sectional tubes	0.083		0.2117
13	***HADF***	Hourglass type - A tubes	0.080		0.2093
14	***HBDF***	Hourglass type - B tubes	0.083		0.2460
15	***HXDF***	Hourglass type - X tubes	0.080		0.2117
16	***HYDF***	Hourglass type - Y tubes	0.084		0.1994
17	***CXDF***	Conical circular type - X tubes	0.083		0.1990
18	***CYDF***	Conical circular type - Y tubes	0.083		0.2040
19	***CDF-****partial*	Circular cross-sectional tubes with partially removed	0.083		0.1729

(Example of the nomenclature of the circular cross-sectional composite tubes: (i) ***CSF*** – ***C***ircular cross-section, ***S***ingle ply (1 mm thick), ***F***- polyurethane ***F***oam filled; (ii) ***CDF*** – ***C***ircular cross-section, ***D***ouble plies (2 mm thick), ***F***- polyurethane ***F***oam filled)

13. 3. Square cross-sectional tubes with polyurethane foam

The deformation patterns of polyurethane foam-filled square cross-sectional composite tubes with 1 mm thickness are shown in Figure 13-4(a - top) and Figure 13-4(b - top). These composite tubes exhibited progressive failure modes. After the crushing of the triggering profile major longitudinal cracks (axial cracks) were observed at the corners of the tube. This is due to the stress concentrations at those locations [10, 11]. The axial cracks were formed only at the interface locations of one roving to another (Figure 13-4(a - top)). Simultaneously, the polyurethane foam inside the composite tube was subjected to compression. Subsequently, the interface between the polyurethane foam and the composite tube walls was subjected to compressive shear failure. As a result, thin layers of polyurethane foam stayed on the inner surface of each composite wall segment (Figure 13-4(a)). The major crushing energy of the composite tubes was consumed by lamina bending followed by the breakage of resin bonds. Before reaching the densification regime, the polyurethane foam was loaded in pure compression. The longitudinal cut section of these tubes confirmed the same. However, after reaching about 60 mm of deformation length the polyurethane foam showed a compressive shear failure mode. The load-deformation history of these composite tubes showed three phases (Figure 13-4(b - top)). The first phase corresponds to the crushing of the triggering profile, simultaneous compression of polyurethane foam and initiation of axial cracks. During the second phase the load decreased abruptly due to the propagation of axial cracks. At the end of this second stage a significant amount of the energy was consumed by friction, bending of the petals and the breakage of resin bonds. These failure modes continued for the subsequent stages of crushing and hence, the load of the tube oscillated around a mean value; this was the third stage of the crushing. The average peak crush load (from 4 test specimens) for this case was 4.24 kN. The presence of polyurethane foam increased the performance of the tubes significantly. A previous study on 1 mm thickness square cross-sectional composite tubes without polyurethane foam showed a catastrophic failure mode (refer Chapter 12). This shows the strengthening and the stability effect of polyurethane foam on the crushing performance of square cross-sectional composite tubes. For these tubes there was no clear evidence of circumferential delamination during the crushing of the triggering profiles.

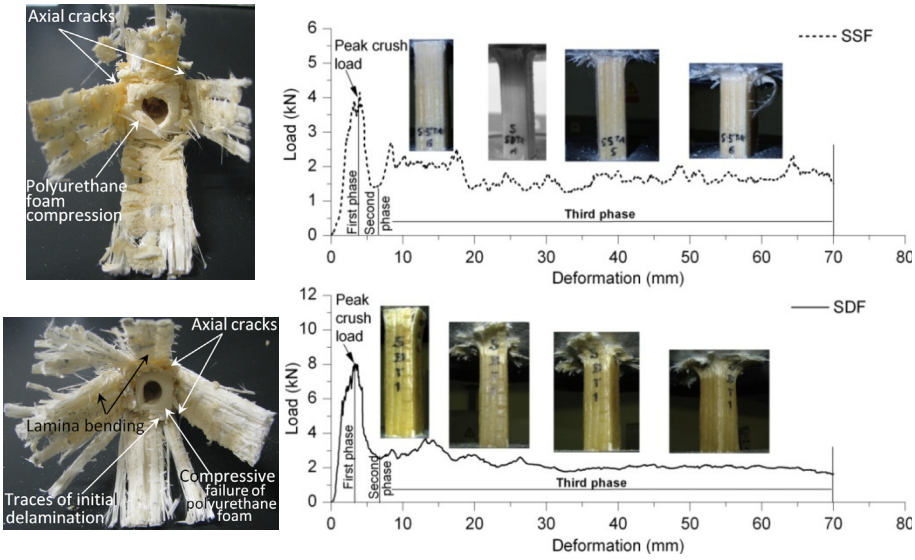

(a) **(b)**

Figure 13-4: Deformation patterns and the crushing performance of the square cross-sectional composite tubes filled with polyurethane foam.**(a)** Final deformation patterns(top - SSF; bottom – SDF) **(b)** Load - deformation histories (top -SSF; bottom - SDF).

Similar to the 1 mm thickness tubes, the polyurethane foam-filled 2 mm thickness square cross-sectional composite tubes showed uniform and progressive crushing failure modes throughout their length (Figure 13-4(a - bottom) and Figure 13-4(b - bottom)). The initial crushing stages of these tubes showed a clear evidence of circumferential delamination at the mid thickness of the tubes. However, the delamination did not continue for later crushing stages. After the initial circumferential delamination, the primary axial cracks developed along the corners due to stress concentrations. As a result, each side of the composite tube wall has split into petals moving inwards and outwards [12-14]. However, the polyurethane foam prevented the flow of inner petals towards the axis of the tube. As a result, further delamination was suppressed. Due to the above phenomenon all the petals started to move outwards (away from the tube axis). This failure mode is different from what has been reported in ref. [9]. The mean crush load and the corresponding energy absorption of this case (SDF) was considerably lower than from the previous results (refer Chapter 12). The reason for the lower energy absorption was the absence of continuous delamination followed by fibre fracturing. The average peak crush load for this case was 9.05 kN which is slightly higher than the case of composite tubes without polyurethane foam (refer Chapter 12).

13. 4. Circular cross-sectional tubes with polyurethane foam

The typical progressive deformation pattern and the corresponding load-deformation curve for 1 mm thickness circular cross-sectional composite tubes filled with polyurethane foam are shown in Figure 13-5(a - top) and Figure 13-5(b - top). These tubes showed a clear evidence of delamination at the triggering location. Furthermore, the number of axial cracks for this case was higher than for the square cross-sectional tubes. The uniform geometry of the circular cross-sectional tube facilitated a large number of axial cracks (varied from 10 to 13) and thus more petals were formed [10, 15]. The major amount of the crushing energy was absorbed by the increasing number of longitudinal cracks and the subsequent bending of petals [14]. Due to the resistance of the polyurethane foam the delamination was suppressed immediately after crushing of the triggering profile. As a result all petals started to bend outwards and consequently, no fibre fracturing was observed. The average peak crush load of this case (CSF) was 4.78 kN which was higher than the case of tubes without polyurethane foam [16]. The progressive deformation patterns and the failure modes of CDF tubes were very similar to CSF tubes (refer Figure 13-5(a - bottom) and Figure 13-5(b - bottom)). The number of axial cracks for this case varied from 8 to 10 for each composite tube. The average peak crush load of this case (CDF) was 7.82 kN.

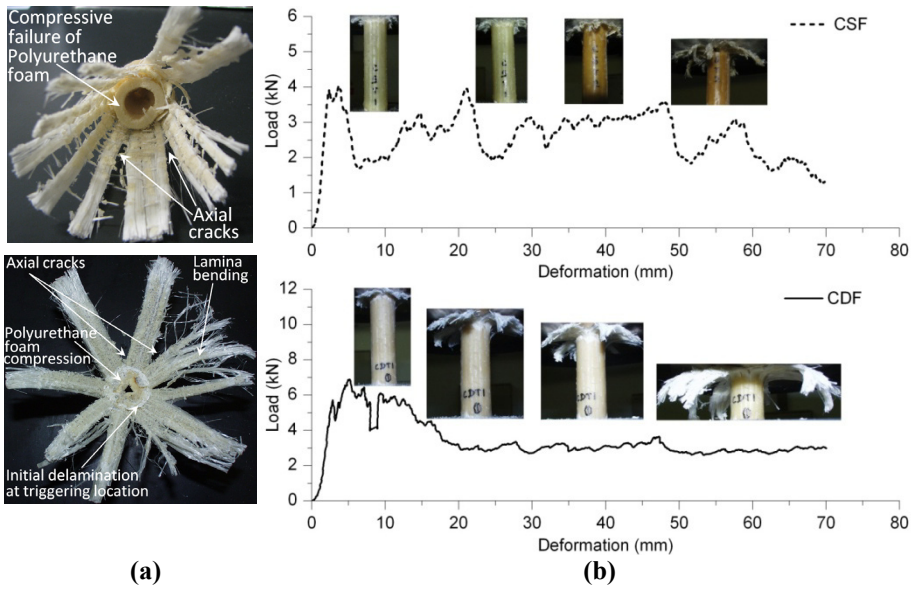

(a) **(b)**

Figure 13-5: Deformation patterns and the crushing performance of the circular cross-sectional composite tubes filled with polyurethane foam. **(a)** Final deformation patterns (top - CSF; bottom - CDF). **(b)** Load - deformation histories (top - CSF; bottom - CDF).

13. 5. Hexagonal cross-sectional tubes with polyurethane foam

The crushing performance of 1 mm thickness hexagonal cross-sectional composite tubes (HSF) with polyurethane foam was very similar to the case of 1 mm thickness square cross-sectional composite tubes (SSF). However, these tubes showed a clear evidence of delaminations at the triggering locations similar to the 1 mm thickness circular cross-sectional tubes. The axial cracks occurred only at the corner locations of the tube (refer Figure 13-6(a)). This result is different from the previous study (which was discussed in Chapter 12). The hexagonal composite tubes (1 mm thickness) without polyurethane foam exhibited a catastrophic failure mode and the location of axial cracks at the corners was not consistent [16]. The presence of polyurethane foam inside the composite tube increased the stability of the composite tube walls and controlled the failure process significantly (refer Figure 13-6(b - top)). The average peak crush load of these composite tubes is 3.51 kN. The progressive deformation patterns (axial cracks, lamina bending and foam compression) of the 2 mm thick hexagonal cross-sectional composite tubes are shown in Figure 13-6(a - bottom) and Figure 13-6(b - bottom). Similar to the 1 mm thickness tubes (HSF) the number of axial cracks for this case (HDF) was limited to six. The average peak crush load of this case was 8.88 kN.

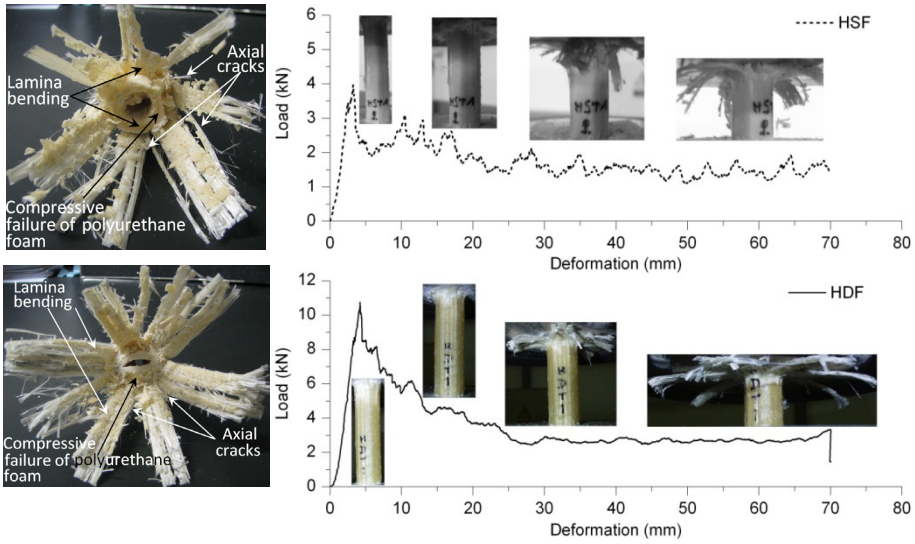

Figure 13-6: Deformation patterns and the crushing performance of the hexagonal cross-sectional composite tubes filled with polyurethane foam. **(a)** Final deformation patterns (top - HSF; bottom - HDF). **(b)** Load - deformation histories (top - HSF; bottom - HDF).

13. 6. Hourglass type - A shaped (circular cross-sectional) tubes with polyurethane foam

The progressive crushing behaviour of the hourglass type - A shaped composite tubes with polyurethane foam (HASF and HADF) was very similar to the circular cross-sectional composite tubes (refer Figure 13-7(a)). A considerable amount of compressive shear failure of the polyurethane foam occurred at the plane B which is indicated in Figure 13-7(b - top). This was due to the composite tube geometry. The reduced cross-section from plane A to B directed the polyurethane foam compression at an angle of 10° (Figure 13-1). Due to a lower thickness of the polyurethane foam from plane B to C and the subsequent compression of foam from the top end of the tube, a significant amount of compressive shear failure was noticed at location plane B. The sectional cut of these tubes confirmed the same. Furthermore, the failed polyurethane foam was accumulated and subjected to compression at the mid-length of the composite tube (due to a reduced cross-section from plane B to C). Because of this process, the crush load of this composite tube increased considerably after achieving 50 mm of deformation length (Figure 13-7(b)). The average peak crush load was 3.79 kN and 8.91 kN for HASF and HADF tubes respectively.

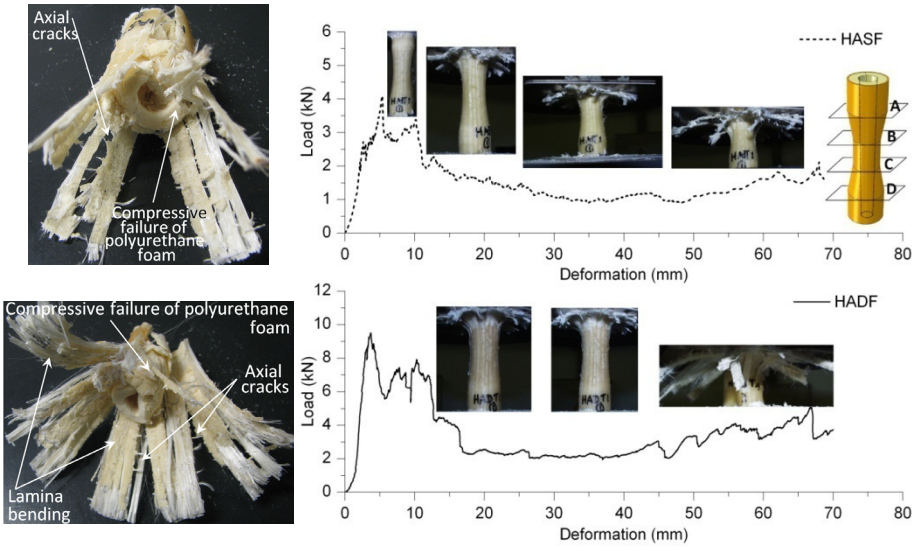

(a) **(b)**

Figure 13-7: Deformation patterns and the crushing performance of the hourglass type - A composite tubes filled with polyurethane foam. **(a)** Final deformation patterns (top - HASF; bottom - HADF). **(b)** Load - deformation histories (top - HASF; bottom - HADF)

13. 7. Hourglass type - B shaped (circular cross-sectional) tubes with polyurethane foam

The deformation patterns of the hourglass type - B shaped composite tubes (HBSF and HBDF) are shown in Figure 13-8(a) and Figure 13-8(b). For these tubes a significant amount of polyurethane foam was blocked at the mid length of the tube. The reduced cross-section of the tube attributed to this blockage. This evidence can be noticed from Figure 13-8(b); the crush load increased significantly after 50 mm of deformation length. The average peak crush load was 3.94 kN and 7.15 kN for HBSF and HBDF tubes respectively. Similar to other composite tube series, there was no fibre fracturing observed due to the absence of continuous delamination.

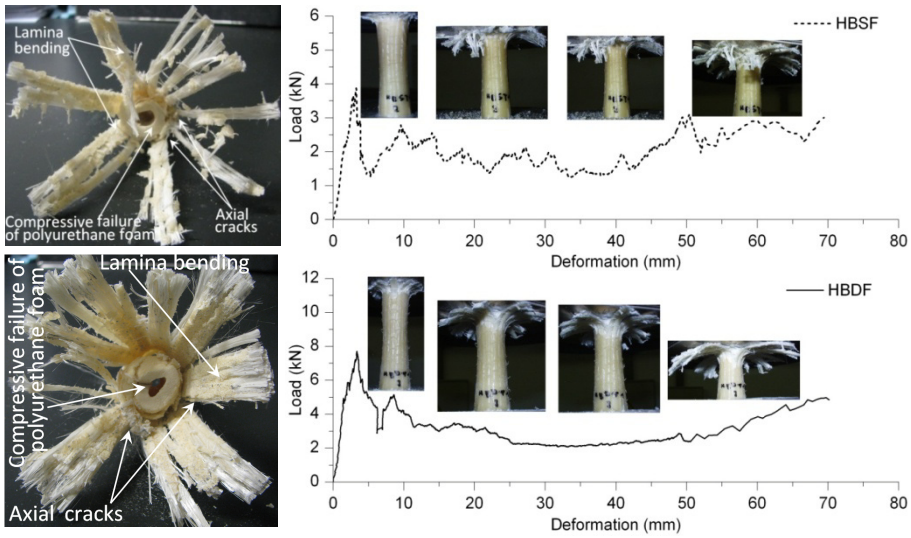

Figure 13-8: Deformation patterns and the crushing performance of the hourglass type - B composite tubes filled with polyurethane foam. **(a)** Final deformation patterns (top - HBSF; bottom - HBDF). **(b)** Load - deformation histories (top - HBSF; bottom - HBDF).

13. 8. Hourglass type - X shaped (circular cross-sectional) tubes with polyurethane foam

The initial crushing stages of HXSF and HXDF tubes showed the progressive crushing of the triggering profile followed by formation of axial cracks (Figure 13-9(a) and Figure 13-9(b)). The number of axial cracks (6 to 8) was higher than for the case without polyurethane foam. The additional stability of polyurethane foam might have attributed to this increased number of axial cracks. In later stages, the fibres at the minor diameter location were pulled towards the axis of the tube due to

a lower thickness of the polyurethane foam (at the minor diameter locations) and the geometrical shape of the tube. As a result, each composite wall segment underwent a local wall buckling mode (Figure 13-9(b)). At this stage a significant increase in crush load was noticed (Figure 13-9(b)). Subsequently, the fibres (at the major diameter location) were subjected to fracturing due to higher radial shear stresses (refer Figure 13-9(b)). Due to this phenomenon a considerable amount of polyurethane foam shearing was observed. This sequence of failures continued to the next major diameter region of the composite tubes. The load-deformation histories of these composite tubes showed lower peak crush loads (2.39 kN and 4.81 kN for HXSF and HXDF respectively).

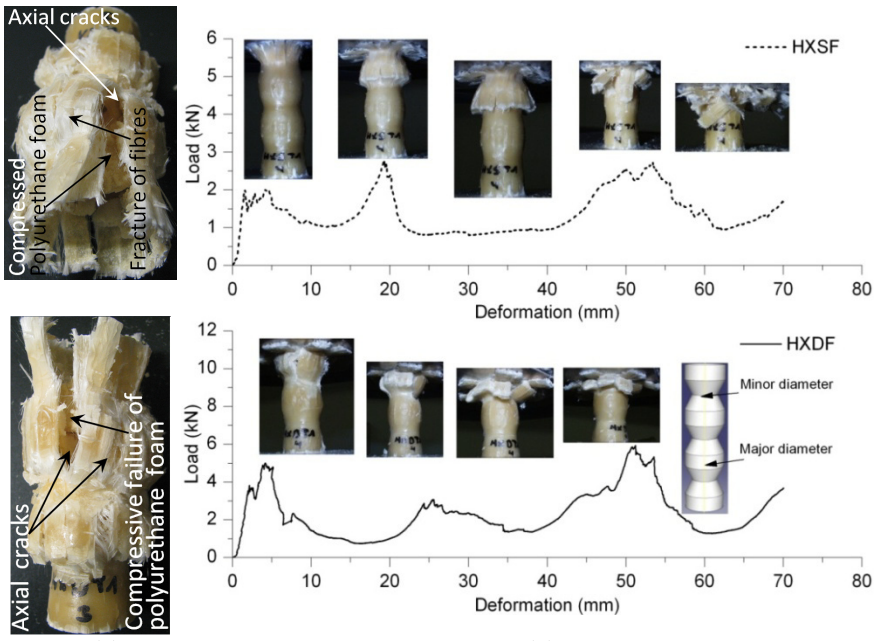

Figure 13-9: Deformation patterns and the crushing performance of the hourglass type - X composite tubes filled with polyurethane foam. **(a)** Final deformation patterns (top - HXSF; bottom - HXDF). **(b)** Load - deformation histories (top - HXSF; bottom - HXDF).

13. 9. Hourglass type - Y shaped (circular cross-sectional) tubes with polyurethane foam

The crushing performance of the hourglass type - Y shaped composite tubes (HYSF and HYDF) filled with polyurethane foam was very similar to the hourglass type - X geometry tubes (refer Figure 13-10(a) and Figure 13-10(b)). Due to the tube geometry (no alignment of triggering profiles to the direction of the compressive

loading), there was no initial delamination failure mode observed for these composite tubes. The peak crush load of these composite tubes corresponds to the formation of axial cracks at the major diameter regions and polyurethane foam compression. The average peak crush load for these composite tubes was 1.40 kN and 3.51 kN for HYSF and HYDF composite tubes respectively.

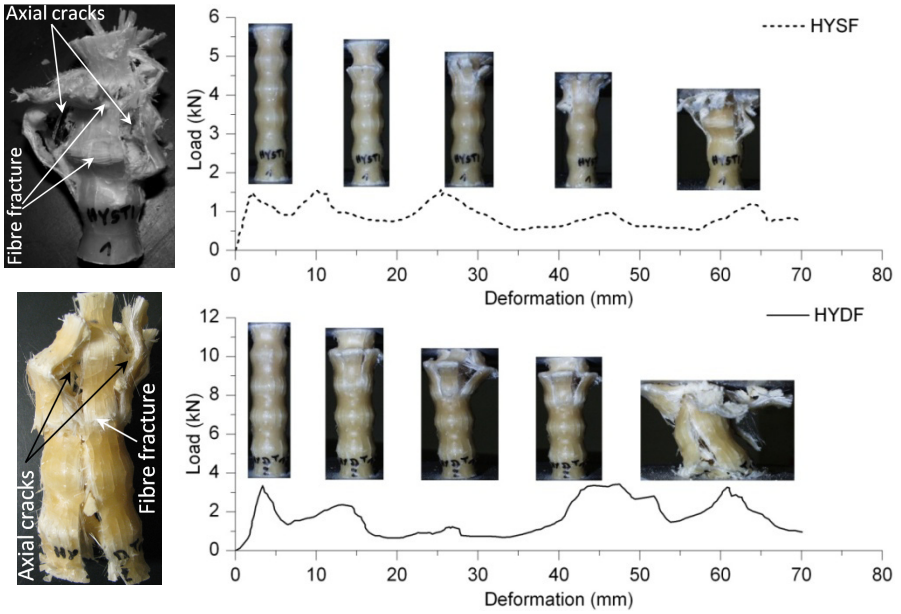

Figure 13-10: Deformation patterns and the crushing performance of the hourglass type - Y composite tubes filled with polyurethane foam. **(a)** Final deformation patterns (top - HYSF; bottom - HYDF) **(b)** Load - deformation histories (top - HYSF; bottom - HYDF).

13. 10. Conical circular type - X tubes with polyurethane foam

The crushing performance of these composite tubes (CXSF and CXDF) was similar to the circular cross-sectional composite tubes (CSF and CDF). The final deformation patterns and the corresponding sequential failure stages are shown in Figure 13-11(a) and Figure 13-11(b). For a few composite tubes (both CXSF and CXDF), the tubes split into two halves due to the gradual reduction in cross-section towards the bottom side and the subsequent compression of polyurethane foam (Figure 13-11(a - top)). This may be due to a lower hoop stress of the tube at the reduced cross-section and subsequent compression of polyurethane foam. However, this phenomenon occurred at the end of the crushing and hence, there was no

significant effect on the load-deformation curve observed. The average peak crush loads were 4.15 kN and 10.6 kN for CXSF and CXDF composite tubes respectively.

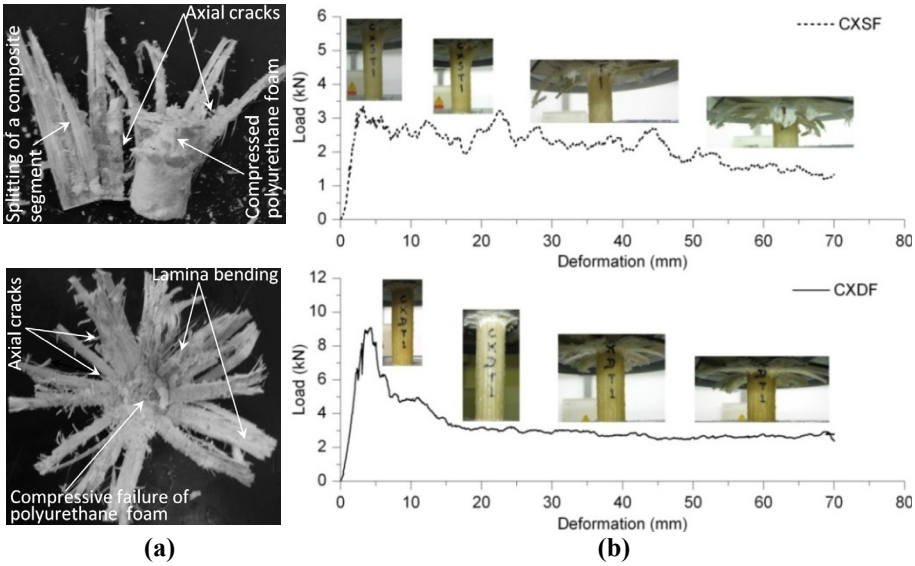

Figure 13-11: Deformation patterns and the crushing performance of the conical circular type - X composite tubes filled with polyurethane foam. **(a)** Final deformation patterns (top - CXSF; bottom - CXDF). **(b)** Load - deformation histories (top - CXSF; bottom - CXDF).

13. 11. Conical circular type - Y tubes with polyurethane foam

The deformation patterns and the corresponding load-deformation curves of CYSF and CYDF composite tube series are shown in Figure 13-12(a) and Figure 13-12(b). The 1 mm and 2 mm thickness conical circular type -Y geometry with polyurethane foam exhibited progressive crushing failure modes. Furthermore, during the crushing of the triggering profiles a clear evidence of delamination was noticed. Similar to the other composite tube series the typical failure modes such as the axial cracks, lamina bending and foam compression were observed. For the 2 mm thickness composite tubes, the initial crushing of the triggering profile and the simultaneous compression of foam attributed to a higher peak crush load. However, the load was reduced suddenly after the peak crush load. The reduced crush load corresponded to the formation and propagation of axial cracks. This may be due to the combined effect of a higher t/D ratio (0.092) of the composite tube and a lower thickness of polyurethane foam at the triggering locations. The number of axial cracks varied from 8 to 12 for each case.

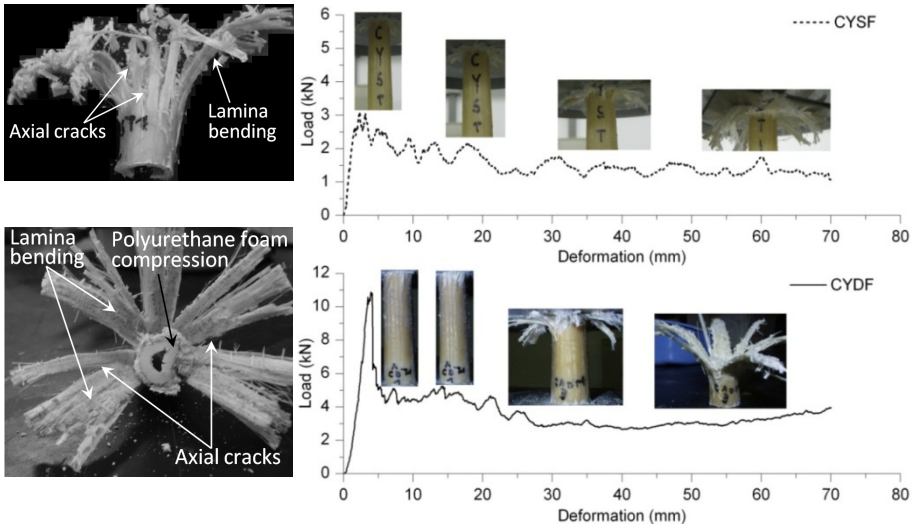

(a) **(b)**

Figure 13-12: Deformation patterns and the crushing performance of the conical circular type - Y composite tubes filled with polyurethane foam. **(a)** Final deformation patterns (top - CYSF; bottom - CYDF). **(b)** Load - deformation histories (top - CYSF; bottom - CYDF).

13. 12. Circular cross-sectional tubes with partially removed polyurethane foam

As seen earlier, the delamination process was suppressed by the polyurethane foam for all tube series. Hence, an experiment was made to study the effect of foam length on the delamination process. The idea is to allow the delamination failure for a certain length and then to study the effect of polyurethane foam on the deformation pattern. The circular cross-sectional tube with 2 mm thickness was chosen for this study; subsequently, the polyurethane foam at the crushing side was removed for 3 different lengths (10 mm, 20 mm and 30 mm). Although, the three cases were conducted (refer Figure 13-13(a - top)) only one of the cases (30 mm of foam removal) is discussed here due to the similarity of the results. The results of these tests showed the following behaviour. During the crushing of the triggering profiles the circumferential delamination took place at the mid-thickness of the tube which split the tube wall thickness into two halves. As a result the inner petal moved inwards and the outer petals moved outwards. Consequently, the formation of axial cracks occurred parallel to the axis of the tube. Due to the above phenomena the petals showed lamina bending and fibre fracturing failure modes. However, the delamination process was suppressed when the crushing length reached the polyurethane foam similar to earlier cases. As an example, the final deformation pattern of one of the tubes is presented in Figure 13-13(a - bottom). The

corresponding load-deformation curve also shows similar evidence (refer Figure 13-13(b)). The mean crush load of this tube was reduced significantly after reaching 30 mm of deformation length. This was due to the absence of continuous delamination and fibre fracturing and the mean crush load of the tube after 30 mm of deformation was only controlled by axial cracks, lamina bending and the polyurethane foam compression.

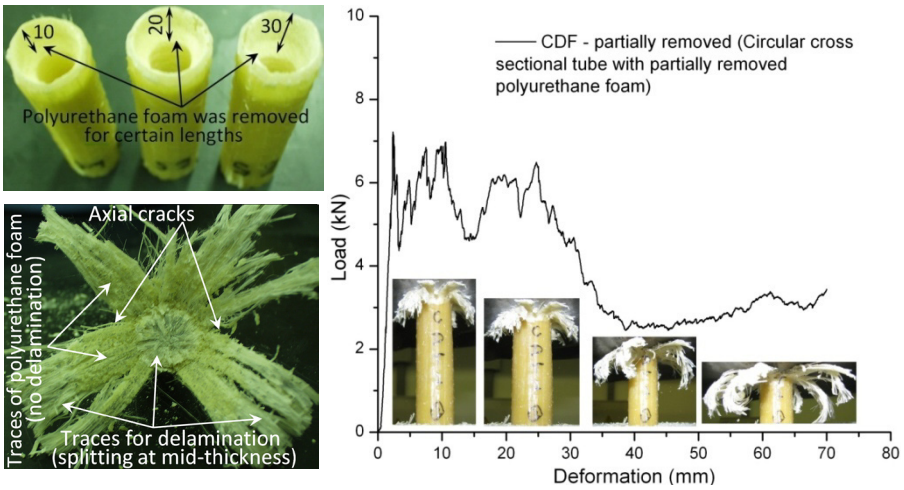

(a) **(b)**

Figure 13-13: Details of test specimen, deformation pattern and the corresponding crushing performance of circular cross-sectional tubes with partially removed polyurethane foam (30 mm foam removal case).**(a)** top - test specimens; bottom - final deformation pattern **(b)** Load - deformation history.

13. 13. Comparison of longitudinal cut sections

After the quasi-static testing, the crushed tube specimens were cut longitudinally (along the length) to carry out the visual inspection of the crushed zone. The cut section of all the tubes gave a clear evidence that the polyurethane foam was subjected to a shear fracture followed by compression. The failure patterns of these tubes (both 1 mm and 2 mm thickness with polyurethane foam) are compared with the tubes without polyurethane foam (Figure 13-14(a-d)). As an example, representative specimens from 1 mm and 2 mm thickness tubes (both without and with polyurethane foam) are shown in Figure 13-14. It can be noticed that the tubes without polyurethane foam showed a clear evidence of circumferential delamination at its mid thickness, lamina bending, axial cracks and fibre fracturing failure modes. However, for the tubes with polyurethane foam the delamination was suppressed after the crushing of the triggering profile. Furthermore, the polyurethane foam has undergone a pure compression mode (plateau) before it reaches the densification regime. The later stages of the polyurethane foam showed a clear evidence of shear

fracture failure mode. In all tube series except the hourglass type - X and hourglass type - Y, the shear fracture plane was located at an angle of 45° with respect to the tube axis (refer Figure 13-14(b) and Figure 13-14(d)). This may be due to the presence of a cylindrical cavity (hole with ϕ 12 mm) throughout its length. Furthermore, there was no fibre fracturing mode observed at later stages of crushing due to the absence of delamination.

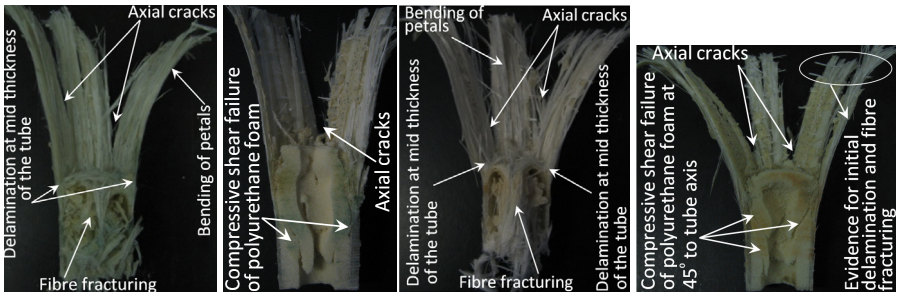

(a) **(b)** **(c)** **(d)**

Figure 13-14: Comparison of longitudinal cut sections of composite tubes: **(a)** 1mm thickness tube without polyurethane foam. **(b)** 1mm thickness tube filled with polyurethane foam. **(c)** 2 mm thickness tube without polyurethane foam. **(d)** 2 mm thickness tube filled with polyurethane foam.

13. 14. Effect of polyurethane foam on SEA and peak crush load

A comparison of the crushing parameters of different geometrical shapes of the composite tubes filled with polyurethane foam is presented in this section. Similar to the previous study the following three parameters were calculated (i) mean load (P_{mean}) (ii) specific energy absorption (SEA) (iii) crush efficiency (η_c). The calculated average values (from 4 test specimens) of each composite tube series are given in Table 13-2.

13. 14. 1. 1 mm thickness composite tubes with polyurethane foam

The average specific energy absorption of different geometrical shapes of 1 mm thickness composite tubes filled with polyurethane foam is shown in Figure 13-15(a); and the corresponding average peak crush loads are shown in Figure 13-15(b). In order to compare the results with empty composite tubes (without polyurethane foam), the results from Chapter 12 are included in the same figure.

Table 13-2: Summary of the average crushing parameters of all composite tube series with polyurethane foam.

Tube cross-section / geometrical shapes	1 mm thickness					2 mm thickness				
	Tube series	Peak load (kN)	Mean load (kN)	SEA (kJ/kg)	η_c (%)	Tube series	Peak load (kN)	Mean load (kN)	SEA (kJ/kg)	η_c (%)
 Square cross-section	***SSF***	4.24	1.42	9.200	34	***SDF***	9.05	2.57	10.82	29
 Circular cross-section	***CSF***	4.78	2.44	14.79	52	***CDF***	7.82	3.49	19.67	45
 Hexagonal cross-section	***HSF***	3.51	1.48	11.22	42	***HDF***	8.88	3.50	14.50	40
 Hourglass type -A	***HASF***	3.79	1.45	11.27	39	***HADF***	8.91	3.29	15.78	38
 Hourglass type -B	***HBSF***	3.94	1.87	12.10	48	***HBDF***	7.15	2.80	15.17	39
 Hourglass type -X	***HXSF***	2.39	0.96	6.670	42	***HXDF***	4.81	2.01	9.230	42
 Hourglass type -Y	***HYSF***	1.40	0.61	5.030	43	***HYDF***	3.51	1.51	7.370	43
 Conical circular type - X	***CXSF***	4.15	1.89	12.13	47	***CXDF***	10.6	3.43	17.12	33
 Conical circular type - Y	***CYSF***	3.31	1.15	11.18	34	***CYDF***	10.1	4.03	19.63	41
 Circular cross-sectional tube with partially removed foam **- *CDF- partially removed***							7.68	3.71	21.44	52

The nomenclature of the composite tubes without polyurethane foam is very similar to the nomenclature of composite tubes with polyurethane foam; the letter "**F**" is not included in the name series to represent the tubes without polyurethane foam. It can be noticed that the scatter of the crushing parameters is low despite using hand lay-up technique for manufacturing the composite tubes. The presence of polyurethane foam inside the composite tube significantly improved the stability during the crushing process and subsequent energy absorption for the square and hexagonal cross-sectional tubes. The average SEA of square and hexagonal cross-sectional composite tubes was 9.2 kJ/kg and 11.22 kJ/kg respectively. The square and hexagonal cross-sectional composite tubes without polyurethane foam showed a catastrophic failure mode (refer Chapter 12). The initiation and sudden propagation of axial cracks caused this failure (refer Chapter 12). Similarly, the presence of polyurethane foam improved the crushing performance of hourglass type - X and hourglass type - Y tubes. The average SEA of these tubes is 6.67 kJ/kg and 5.03 kJ/kg for hourglass type - X and hourglass type - Y respectively. However, there was no significant difference in the crushing pattern observed during the crushing process due to the presence of polyurethane foam. These tubes exhibited a non-uniform crushing failure similar to the tubes without polyurethane foam (refer Chapter 12).

On the contrary, the presence of polyurethane foam inside the composite tubes significantly reduced the SEA of the remaining geometrical shapes (circular cross-sectional, hourglass type - A, hourglass type - B, conical circular type - X and conical circular type - Y) which exhibited uniform and progressive crushing failure modes (Figure 13-15(a)). The main reason for the lower specific energy absorption of these composite tubes is the absence of continuous delamination and subsequent fibre fracturing. The effect of polyurethane foam on the peak crush loading of each geometrical shape of the composite tubes can be clearly understood from Figure 13-15(b). The peak crush load of the composite tubes with polyurethane foam was higher than for the tubes without polyurethane foam. The reason for the higher peak crush load was simultaneous polyurethane foam compression during the crushing of the triggering profile. The average values are 4.78 kN, 3.79 kN, 3.94 kN, 4.15 kN and 3.31 kN for circular cross-sectional, hourglass type - A, hourglass type - B, conical circular type - X and conical circular type - Y respectively. Keeping a lower failure load for the inner core member of the sacrificial cladding structure can reduce the magnitude of the peak load transferred to the non-sacrificial structure. Hence, the tubes without polyurethane foam can provide good energy absorption values at lower peak crush loads. However, the effect of strain rate on the peak crush loads should be verified for dynamic load cases. Due to the reduced cross-section at the crushing end and the absence of a continuous delamination process the peak crush load of the conical circular type - Y with polyurethane foam was lower than without polyurethane foam.

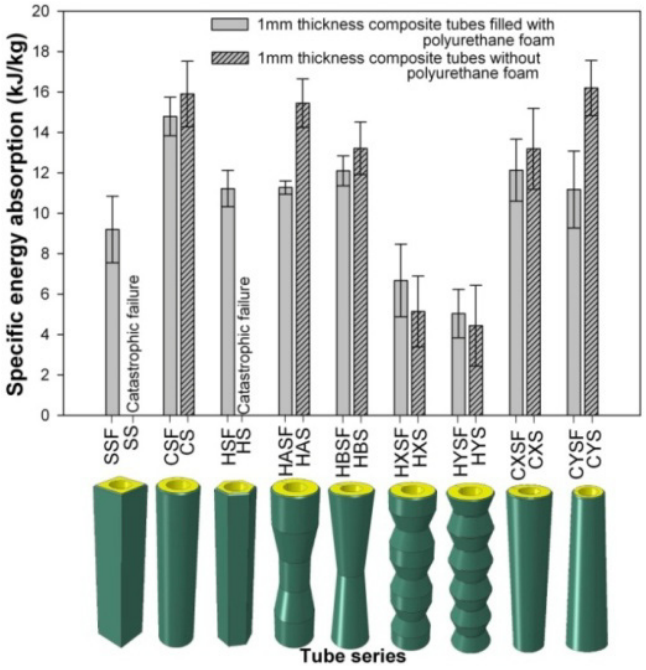

(a)

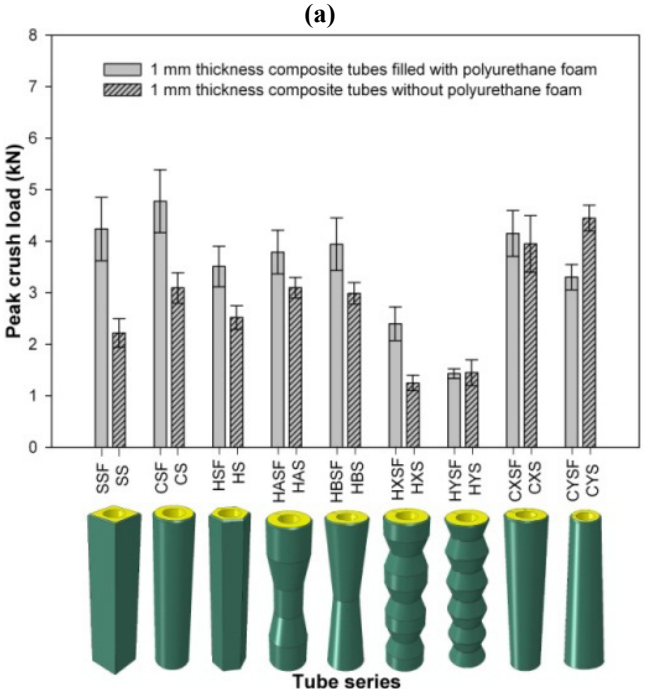

(b)

Figure 13-15: Comparison of the specific energy absorption and peak crush load for 1 mm thickness composite tubes series with and without polyurethane foam (error bar indicates standard deviation).**(a)** Comparison of specific energy absorption for 1 mm thickness composite tubes.**(b)** Comparison of peak crush load for 1 mm thickness composite tubes.

13. 14. 2. 2 mm thickness composite tubes with polyurethane foam

The comparison of the specific energy absorption and the corresponding peak crush load for 2 mm thickness composite tubes filled with polyurethane foam are given in Figure 13-16(a) and Figure 13-16(b) respectively. Similar to the 1 mm thickness composite tubes, these results are compared with the tubes without polyurethane foam. The scatter of the crushing parameters is again low compared to the 1 mm thickness tubes. It can be noticed that in all composite tube series except the hourglass type - X, the specific energy absorption of the tubes with polyurethane foam was lower than the tubes without polyurethane foam. This difference was significant for the circular cross-sectional (19.67 kJ/kg and 30.4 kJ/kg for with and without foam respectively), hourglass type - A (15.78 kJ/kg and 21.1 kJ/kg for with and without foam respectively), hourglass type - B (15.17 kJ/kg and 22.5 kJ/kg for with and without foam respectively), conical circular type - X (17.12 kJ/kg and 23.5 kJ/kg for with and without foam respectively) and conical circular type - Y tubes (19.63 kJ/kg and 28.8 kJ/kg for with and without foam respectively). The tubes without polyurethane foam exhibited a larger number of axial cracks followed by continuous circumferential delamination (refer Chapter 12). Hence, a significant quantity of energy was consumed by the delamination process which split each segment or petal. Although the tubes with polyurethane foam showed many axial cracks similar to the cases without foam, the absence of delamination attributed to lower SEA values. This fact is again proved for the circular cross-sectional tubes with partially removed polyurethane foam (30 mm polyurethane foam removal). The SEA of this tube (21.44 kJ/kg) is higher than for the CDF tube series (19.67 kJ/kg). The energy absorption of the hourglass type - X and hourglass type - Y was lower than other tube series (Figure 13-16(a)). Hence, these tube series can be excluded for further dynamic investigations.

Similar to the 1 mm thickness tubes, a significant difference was observed between composite tubes with and without polyurethane foam. The peak crush load of the tubes with polyurethane foam was higher than for the tubes without polyurethane foam (refer Figure 13-16(b)). The compressive resistance of the polyurethane foam led to an increased peak crush load.

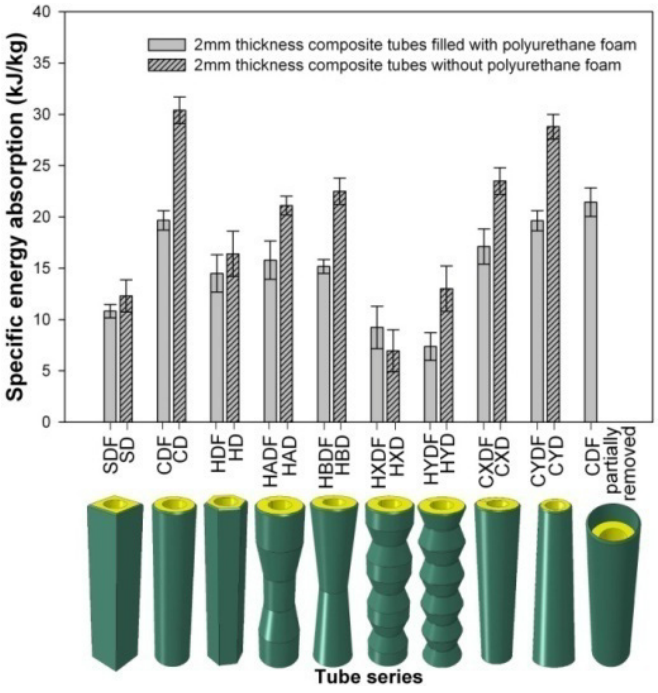

(a)

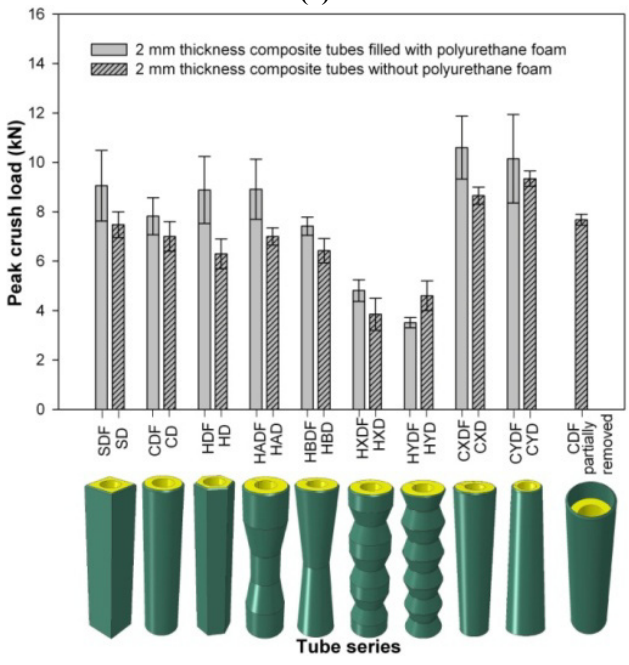

(b)

Figure 13-16: Comparison of specific energy absorption and peak crush load for 2 mm thickness composite tubes series with and without polyurethane foam (error bar indicates standard deviation).**(a)** Comparison of specific energy absorption for 2 mm thickness composite tubes.**(b)** Comparison of peak crush load for 2 mm thickness composite tubes.

13. 15. Conclusions

In this chapter, the effect of polyurethane foam filling on the crushing performance of small-scale composite tubes has been evaluated. Nine different geometrical shapes and two different thicknesses have been considered for the study. The crushing behaviour and their corresponding energy absorption values were captured by quasi-static axial compression tests. From the quasi-static experimental results it can be concluded that:

- both 1 mm and 2 mm thickness composite tubes filled with polyurethane foam showed uniform and progressive crushing failure modes. The macro-failure mechanisms associated with these composite tubes were axial cracks, bending of petals and simultaneous shear failure of foam followed by compression. A considerable amount of energy was consumed by friction between the crushing plate and the petals. This was due to the accumulation of a thin layer of polyurethane foam on the surface of the petals.
- for all composite tube series (except 1 mm thickness square cross-sectional tubes and hourglass type - Y series) the circumferential delamination was observed during the crushing of the triggering profile. However, the delamination failure did not continue for later stages of crushing. This was due to the resistance offered by the polyurethane foam against the inward flow of petals (towards the axis of the tube).
- the presence of polyurethane foam inside the composite tube improved the stability and strengthening of the composite tube walls. The square and hexagonal cross-sectional tubes with 1 mm thickness are the evidence for this. The same tubes (square and hexagonal cross-sections) without polyurethane foam failed catastrophically.
- the peak crush load of the composite tubes with polyurethane foam is significantly higher than for the tubes without polyurethane foam. In addition to the triggering end crushing, the simultaneous compression of polyurethane foam attributed to this increasing peak crush load.
- The presence of polyurethane foam reduced the specific energy absorption significantly for the composite tubes which can already provide progressive and stable failure patterns without polyurethane foam. The reason for the reduction in the specific energy absorption was the difference in the deformation patterns (presence of polyurethane foam prevented the circumferential delamination and subsequent fibre fracturing). Furthermore, the architecture of the composite tubes also played a role (in this study the reinforcement fibres are oriented along the axis of the tube; and so a lower hoop strength is obtained). Hence, before deploying the foam-filling in a composite structure for energy absorption applications one should be aware that any changes in the failure pattern due to foam-filling can alter the

crushing performance of the composite structure. Furthermore, the resistance offered by the polyurethane foam against the inner petals is also depending upon the density of the foam. This parameter should be studied further.

Bibliography

[1]. Aktay, L., Toksoy, A. K. and Güden, M., *Quasi-static axial crushing of extruded polystyrene foam-filled thin-walled aluminum tubes: Experimental and numerical analysis.* Materials & Design, 2006. **27**(7): p. 556-565.

[2]. Hall, I. W., Guden, M. and Claar, T. D., *Transverse and longitudinal crushing of aluminum-foam filled tubes.* Scripta Materialia, 2002. **46**(7): p. 513-518.

[3]. Toksoy, A. K. and Güden, M., *The strengthening effect of polystyrene foam filling in aluminum thin-walled cylindrical tubes.* Thin-Walled Structures. **43**(2): p. 333-350.

[4]. Zarei, H. R. and Kröger, M., *Optimization of the foam-filled aluminum tubes for crush box application.* Thin-Walled Structures, 2008. **46**(2): p. 214-221.

[5]. Hanssen, A. G., Langseth, M. and Hopperstad, O. S., *Static and dynamic crushing of circular aluminium extrusions with aluminium foam filler.* International Journal of Impact Engineering, 2000. **24**(5): p. 475-507.

[6]. Babbage, J. M. and Mallick, P. K., *Static axial crush performance of unfilled and foam-filled aluminum-composite hybrid tubes.* Composite Structures, 2005. **70**(2): p. 177-184.

[7]. Guden, M., Yüksel, S., Tasdemirci, A. and Tanoglu, M., *Effect of aluminum closed-cell foam filling on the quasi-static axial crush performance of glass fiber reinforced polyester composite and aluminum/composite hybrid tubes.* Composite Structures, 2007. **81**(4): p. 480-490.

[8]. Harte, A.-M., Fleck, N. A. and Ashby, M. F., *Energy absorption of foam-filled circular tubes with braided composite walls.* European Journal of Mechanics - A/Solids, 2000. **19**(1): p. 31-50.

[9]. Mamalis, A. G., Manolakos, D. E., Ioannidis, M. B., Chronopoulos, D. G. and Kostazos, P. K., *On the crashworthiness of composite rectangular thin-walled tubes internally reinforced with aluminium or polymeric foams: Experimental and numerical simulation.* Composite Structures, 2009. **89**(3): p. 416-423.

[10]. Palanivelu, S., Van Paepegem, W., Degrieck, J., Van Ackeren, J., Kakogiannis, D., Van Hemelrijck, D., Wastiels, J. and Vantomme, J., *Experimental study on the axial crushing behaviour of pultruded composite tubes.* Polymer Testing, 2010. **29**(2): p. 224-234.

[11]. Mamalis, A. G., Manolakos, D. E., Demosthenous, G. A. and Ioannidis, M. B., *Analytical and experimental approach to damage and residual strength of fibreglass composite automotive frame rails during manufacturing.* Composite Structures, 1995. **32**(1-4): p. 325-330.

[12]. Farley, G. L., *Energy absorption of composite materials* Journal of Composite Materials, 1983. **17**: p. 267-279.

[13]. Mamalis, A. G., Manolakos, D. E., Demosthenous, G. A. and Ioannidis, M. B., *Energy absorption capability of fibreglass composite square frusta subjected to static and dynamic axial collapse.* Thin-Walled Structures, 1996. **25**(4): p. 269-295.

[14]. Solaimurugan, S. and Velmurugan, R., *Progressive crushing of stitched glass/polyester composite cylindrical shells.* Composites Science and Technology, 2007. **67**(3-4): p. 422-437.

[15]. Farley, G. L., *Effect of specimen geometry on the energy absorption of composite materials.* Journal of Composite Materials, 1986. **20**: p. 390.

[16]. Palanivelu, S., Van Paepegem, W., Degrieck, J., Kakogiannis, D., Van Ackeren, J., Van Hemelrijck, D., Wastiels, J. and Vantomme, J., *Comparative study of the quasi-static energy absorption of small-scale composite tubes with different geometrical shapes for use in sacrificial cladding structures.* Polymer Testing, 2010. **29**(3): p. 381-396.

Chapter 14

Axial Impact and Blast Testing on Small-scale In-house Composite Tubes

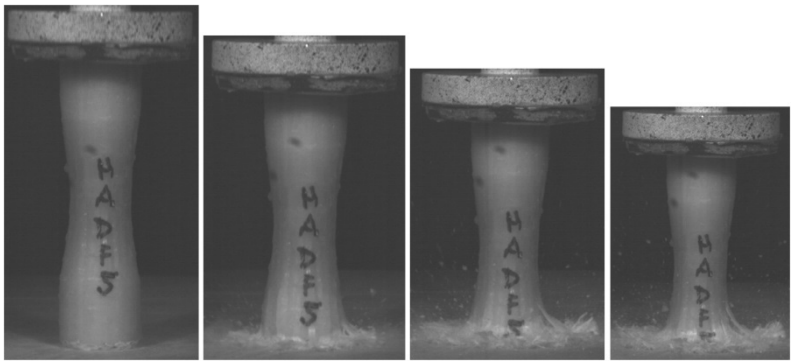

Overview

The first part of this chapter presents the axial impact crushing performance of six different shapes of uni-directional small-scale in-house glass polyester composite tubes. Axial impact tests have been conducted with two different wall thicknesses of the composite tubes and two impactor masses. Furthermore, the effect of polyurethane foam-filling on the crushing performance of composite tubes was evaluated. The above combinations have been studied for the initial impact velocities of 3.1 m/s, 3.8 m/s, 4.4 m/s, 4.9 m/s and 5.3 m/s. From this study three profiles have been finalized for the blast testing (circular cross-section, hourglass type – A and conical circular type – Y). The second part of this chapter deals with close-range blast loading on these three shapes of the composite tubes. Close-range blast tests have been conducted with 25g of C4 with a stand-off distance of 30 cm. A comparison of the crushing performance of different shapes of the composite tubes from the above studies is presented.

14. 1. Introduction

As seen in the previous chapters (Chapter 12 and 13) the energy absorption levels of the square cross-section, hourglass type – X and hourglass type –Y tubes were considerably lower than for the other shapes of the chosen composite tubes [1, 2]. Hence, these three shapes have not been considered for the axial impact testing. The hexagonal cross-sectional hollow composite tube with 1 mm wall thickness for quasi-static loading showed a catastrophic failure mode. However, the polyurethane foam-filling on the same tube improved the stability of the tube wall and lead to progressive crushing. However, this finding has to be validated for dynamic loading conditions. Hence, in addition to the remaining shapes (circular cross-sectional, hourglass type – A, hourglass type –B, conical circular type – X and conical circular type – Y) the hexagonal cross-section has been considered for the axial impact study (refer Figure 14-1). The geometry, dimensions, material and the method of manufacturing of the composite tubes were the same (refer Chapter 12 for more details). Similar to the quasi-static study, two different wall thicknesses were chosen (1 mm and 2 mm). Furthermore, in order to check the effect of polyurethane foam-filling on the crushing performance of these composite tubes, axial impact tests have been conducted with hollow and foam-filled tubes [3]. The quasi-static study showed that the specific energy absorption of triggering type 2 (tulip triggering) was higher than for triggering type 1 (45° chamfering on one end of the tube) [2]. However, the triggering type 1 was chosen for the study due to the easier manufacturing procedure.

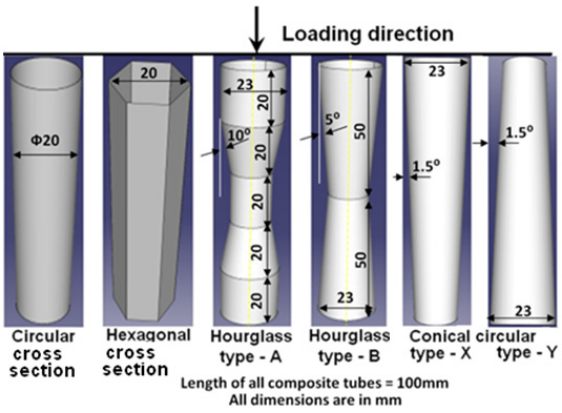

Figure 14-1: Different geometrical shapes of the composite tubes (1mm thickness) and their dimensions considered for the study.

14. 2. Impact testing and results

The details of the used experimental test set-up and the measurement of data were given in Chapter 3. Furthermore, the dimensions and, nomenclature of the used composite tubes (hollow and polyurethane foam-filled), triggering details and the

corresponding material data were given in Chapter 12 and 13. The 1 mm wall thickness composite tubes were tested with an impactor mass of 7.6 kg and with three different initial impact velocities (3.1 m/s, 3.8 m/s and 4.4 m/s). In order to have a higher deformation length, the 2 mm wall thickness tubes were tested with the impactor mass of 10.6 kg. Similarly, these tubes (2 mm wall thickness) were tested for four different initial impact velocities (3.8 m/s, 4.4 m/s, 4.9 m/s and 5.4 m/s). For each category a minimum of four tests have been conducted and the average parameters are reported.

14. 2. 1. Composite tubes with 1 mm wall thickness

Hollow tubes (composite tubes without polyurethane foam)

Apart from the hexagonal cross-sectional tubes the progressive deformation patterns of all types of composite tubes are very similar to their quasi-static deformation patterns. As an example, the final deformation pattern for each tube is given in Figure 14-2(a-f).

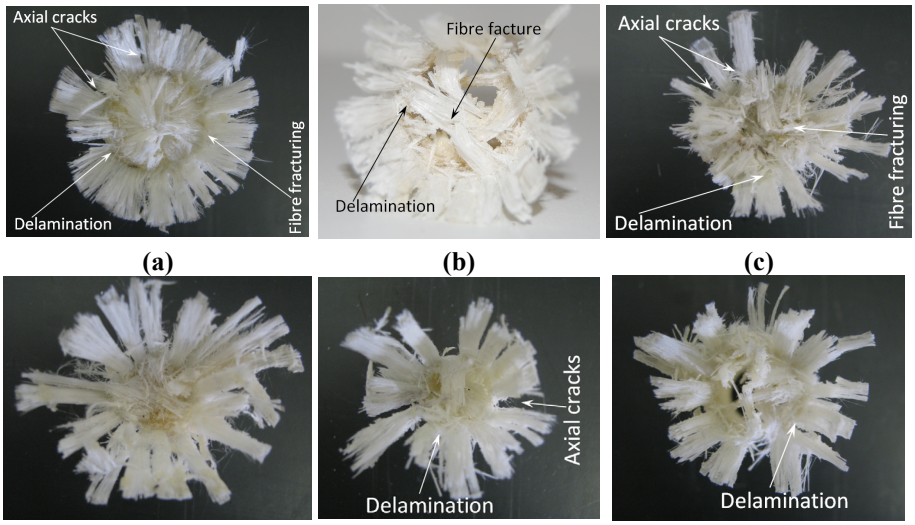

Figure 14-2: Deformation patterns for hollow composite tubes with 1 mm wall thickness **(a)** circular cross-section **(b)** hexagonal cross-section **(c)** hourglass type – A **(d)** hourglass type –B **(e)** conical circular type – X and **(f)** conical circular type – Y.

For all tubes, the major delamination was formed at the mid-thickness of the composite tube [4-12]. Subsequently, the axial cracks, lamina bending and fibre fracturing failure modes were observed (refer Figure 14-2 (a-f)). Unlike in the quasi-static study, the hexagonal cross-sectional composite tubes showed progressive crushing failure modes for the initial impact velocities of 3.1 m/s and 3.8 m/s.

However, 50% of the hexagonal cross-sectional composite tubes showed a catastrophic failure mode (formation and sudden propagation of axial cracks throughout the length of the composite tube) for the case with the initial impact velocity of 4.4 m/s. Similar to the quasi-static study, the hourglass type – A and hourglass type – B showed significant fibre fracturing. This was due to the shape of these tubes. There were a large number of axial cracks observed for all cases compared to the quasi-static tests. This may be due to a combined effect of dynamic loading and a low strength in the hoop direction of the composite tube. All axial cracks were formed at the interface location of each roving.

As an example, the load-deformation histories (from one of the tests) for all tube series for the case with an initial impact velocity of 4.4 m/s are shown in Figure 14-3(a-f) and the corresponding progressive crushing sequences of these tubes are also shown in the same figures. As discussed in Chapter 10, the crushing load for all cases dropped significantly due to the combined effect of impactor mass, impact velocity and less lateral inertia of the composite tubes. However, for the conical circular type – Y the reduction in the post peak crush load was lower compared to other cases (refer Figure 14-3(f)). The crushing load was remained approximately the same. This may be due to the shape of the composite tube. An experiment was done with this type of composite tubes (conical circular type –Y) to check the effect of triggering. A few composite tubes in this case (conical circular type –Y) were tested without triggering. Because of its profile (natural chamfer in the profile of the tube) the tested tubes showed progressive crushing failure modes.

Furthermore, due to the transverse force a significant quantity of fibre fracturing was also observed (the crushing force on the tube can be resolved into two components due to the fact that the fibres were not oriented in the crushing direction). However, for the comparison of crushing parameters with other tube categories the results from this investigation (without triggering) were not considered. A similar investigation was repeated for conical circular type – X shaped composite tubes. However, these composite tubes showed axial splitting without any delamination. This was due to the diverging profile of the composite tube in the crushing direction (refer Figure 14-1). Among all composite tube categories (1 mm wall thickness), the circular cross-section showed very controlled deformation patterns; the corresponding deformation pattern can be noticed from Figure 14-2(a). Due to that the circular cross-section showed superior specific energy absorption (among 1 mm wall thickness tubes). A comparison of all the parameters is given in Table 14-1.

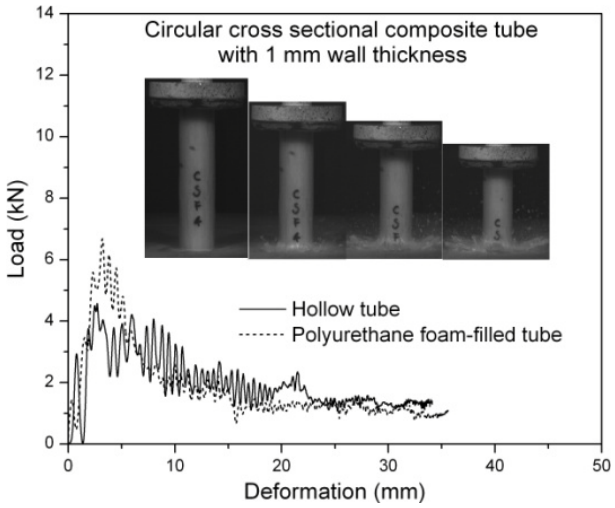
Circular cross sectional composite tube
with 1 mm wall thickness
Load (kN)
Deformation (mm)
Hollow tube
Polyurethane foam-filled tube

(a)

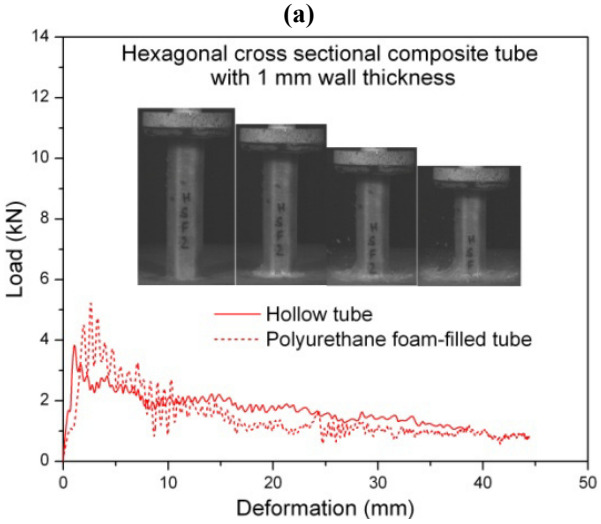
Hexagonal cross sectional composite tube
with 1 mm wall thickness
Load (kN)
Deformation (mm)
Hollow tube
Polyurethane foam-filled tube

(b)

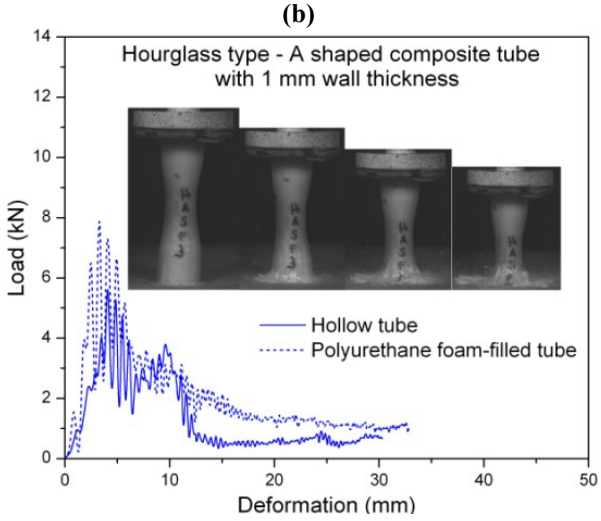
Hourglass type - A shaped composite tube
with 1 mm wall thickness
Load (kN)
Deformation (mm)
Hollow tube
Polyurethane foam-filled tube

(c)

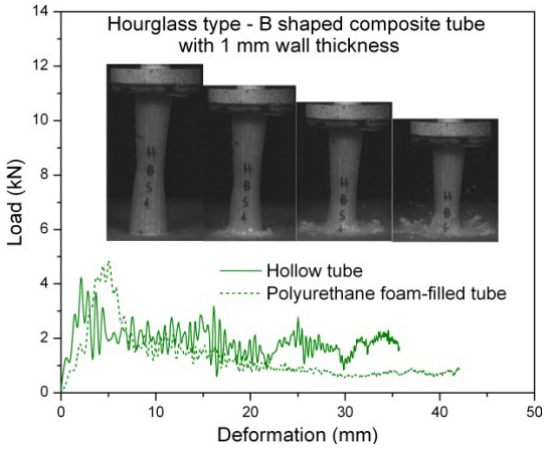

(d)

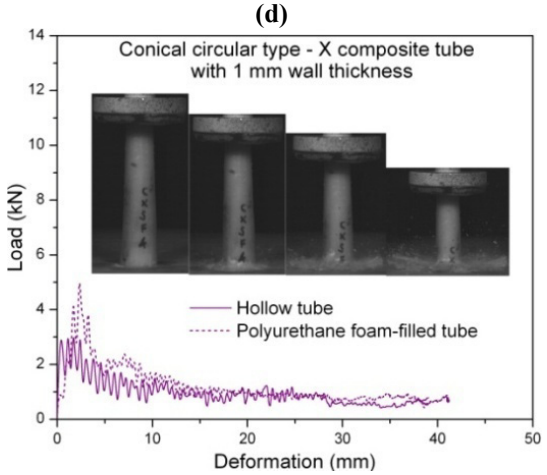

(e)

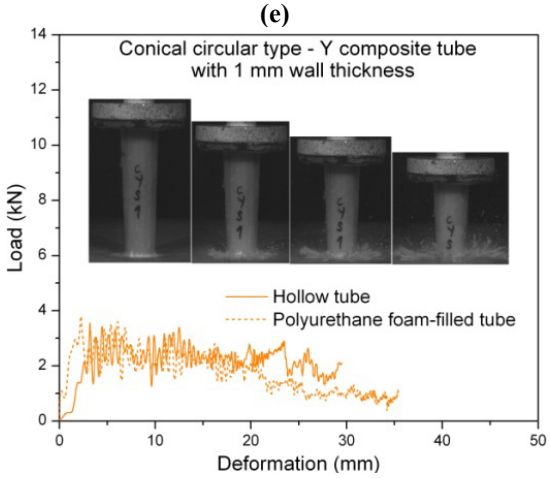

(f)

Figure 14-3: Load-deformation curves of hollow and polyurethane foam-filled composite tubes with 1 mm wall thickness **(a)** circular cross-section **(b)** hexagonal cross-section **(c)** hourglass type – A **(d)** hourglass type –B **(e)** conical circular type – X and **(f)** conical circular type – Y.

Polyurethane foam-filled composite tubes

As seen from the quasi-static study, leaving the polyurethane foam inside the composite tubes reduced the specific energy absorption due to the suppressed failure patterns such as delamination and fibre fracture. However, the effect of inclusion of the polyurethane foam inside the composite tubes for the dynamic loading condition is not known. Hence, in order to investigate this effect and to compare the results with hollow tubes, axial impact tests have been conducted for the same initial impact velocities (3.1 m/s, 3.8 m/s and 4.4 m/s) and with the same impactor mass (7.6 kg). As an example, the final deformation patterns from all six tube series are given in Figure 14-4(a-f). It can be noticed that all tubes crushed progressively; furthermore, the deformation patterns of these composite tubes are very similar to the quasi-static test results. An investigation on the crushed tubes showed clear evidence for an initial delamination at the triggering location and it was propagated for a certain length. However, the further delamination was suppressed due to the presence of polyurethane foam. Due to that the later crushing stages of these tubes showed axial splitting (axial cracks) of fibres (refer Figure 14-4(a-f)). The number of major axial cracks for each type of tube was different. The circular cross-sectional, hourglass type – A, hourglass type –B and conical circular type – Y tubes showed a reduced number of axial cracks (varied from a minimum of 7 to a maximum of 12). However, the remaining two cases (hexagonal cross-section and conical circular type – X) showed a large number of axial cracks (refer Figure 14-4(b) and Figure 14-4(e)). The later crushing stages of polyurethane foam showed compressive and shear failure modes.

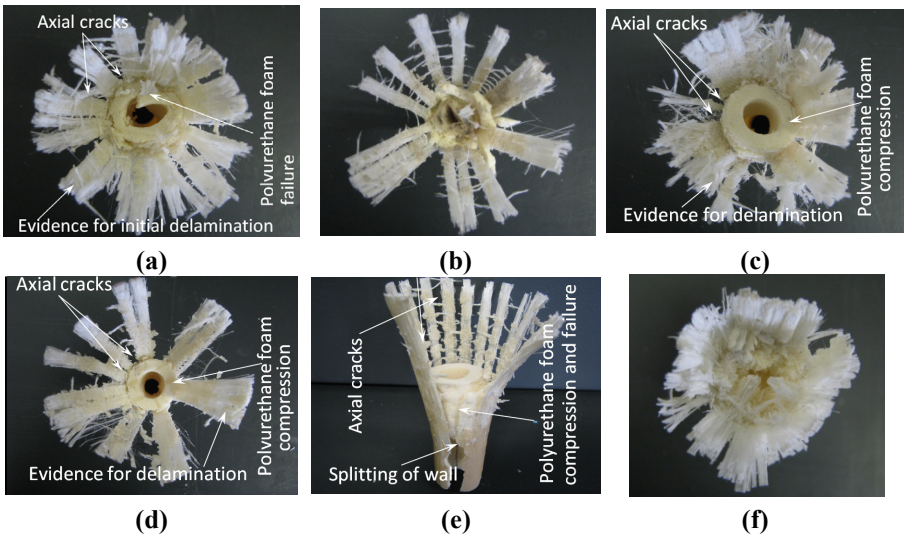

Figure 14-4: Deformation patterns for polyurethane foam-filled composite tubes with 1 mm wall thickness **(a)** circular cross-sectional **(b)** hexagonal cross-section **(c)** hourglass type – A **(d)** hourglass type –B **(e)** conical circular type – X and **(f)** conical circular type – Y.

Due to their profiles the hourglass type – A and hourglass type –B showed a significant amount of compressive shear failure of the polyurethane foam at their mid length. Similarly, for conical circular type – X the compression of the polyurethane foam caused an axial splitting of the composite tube wall (refer Figure 14-4(e)). For conical circular type – Y, 50% of the test specimens showed continuous delaminations and corresponding fibre fracture due to the lower thickness of the polyurethane foam at the crushing end of the composite tubes.

A comparison of the load-deformation histories of the polyurethane foam-filled composite tubes and hollow tubes is given in Figure 14-3(a-f). From these graphs, it can be noticed that the peak crush load of the polyurethane foam-filled composite tubes was consistently higher than for the hollow tubes. In addition to the initial delamination the compressive resistance of the polyurethane foam attributed to a higher peak crush load. However, the mean crush load or the post peak crush load of these composite tubes dropped after achieving the deformation length of about 8 to 10 mm. This was due to the axial splitting of the composite tube wall and subsequently the crushing load was controlled by the axial splitting, lamina bending and the friction between the crushing platform and the petals. Due to the above facts the deformation lengths of foam-filled tubes were longer than for the hollow tubes (refer Figure 14-3(a-f)). A comparison of the specific energy absorption and the corresponding peak crush load for these two cases (hollow and foam-filled composite tubes with 1 mm wall thickness) are presented later.

Table 14-1: Summary of the average crushing parameters of hollow and polyurethane foam-filled composite tubes.

Tube cross-section / geometrical shapes	Tube series	**1 mm wall thickness tubes tested with mass of the impactor 7.6 kg**						Tube series	**2 mm wall thickness tubes tested with mass of the impactor 10.6 kg**					
		Initial impact velocity (m/s)	Deformation length (mm) (l_{max})	Standard deviation for l_{max} (mm)	Peak load (kN)	SEA (kJ/kg)	η_c (%)		Initial impact velocity (m/s)	Deformation length (mm) (l_{max})	Standard deviation for l_{max} (mm)	Peak load (kN)	SEA (kJ/kg)	η_c (%)
Hollow circular cross-sectional composite tube	**CS**	3.1	10	2.4	4.4	29.7	69.0	**CD**	3.8	14.0	1.7	8.8	25.8	61.8
		3.8	18	3.6	4.7	26.7	62.6		4.4	18.0	3.0	8.6	25.0	65.4
		4.4	30	6.7	4.1	16.7	58.6		4.9	23.5	5.3	10.8	23.3	49.8
									5.3	29.1	5.8	9.5	20.8	52.1
Polyurethane foam-filled circular cross-sectional composite tube	**CSF**	3.1	13.5	3.0	5.0	22.2	50.8	**CDF**	3.8	10.0	1.5	9.0	26.5	83.6
		3.8	23	4.3	5.6	18.7	41.5		4.4	13.0	2.4	9.6	25.3	81.0
		4.4	36	6.4	5.9	11.9	34.8		4.9	21.0	5.1	9.9	25.0	60.1
									5.3	27.0	4.9	11.6	23.3	46.6
Hollow hexagonal cross-sectional composite tube	**HS**	3.1	30.5	8.2	4.3	16.2	27.2	**HD**	3.8	16.0	2.5	8.6	21.7	53.7
		3.8	47.3	10.4	5.1	15.5	22.8		4.4	22.0	4.0	8.9	21.0	51.5
									4.9	27.0	6.2	7.9	19.4	59.0
									5.3	35.0	6.5	9.4	18.9	44.6
Polyurethane foam-filled hexagonal cross-sectional composite tube	**HSF**	3.1	44	10.5	5.0	16.0	16.3	**HDF**	3.8	14.0	2.1	8.7	25.6	60.7
		3.8	64	14.3	5.2	8.0	16.4		4.4	18.0	4.2	9.0	26.0	62.3
									4.9	20.0	4.4	9.8	25.4	63.2
									5.3	28.0	5.0	10.7	23.1	48.3

Tube cross-section / geometrical shapes	Tube series	**1 mm wall thickness tubes tested with mass of the impactor 7.6 kg**						Tube series	**2 mm wall thickness tubes tested with mass of the impactor 10.6 kg**					
		Initial impact velocity (m/s)	Deformation length (mm) (l_{max})	Standard deviation for l_{max} (mm)	Peak load (kN)	SEA (kJ/kg)	η_c (%)		Initial impact velocity (m/s)	Deformation length (mm) (l_{max})	Standard deviation for l_{max} (mm)	Peak load (kN)	SEA (kJ/kg)	η_c (%)
Hourglass type – A shaped composite tube 	**HAS**	3.1	25	4.6	5.3	18.0	25.8	**HAD**	3.8	14.2	3.0	8.9	24.1	59.3
		3.8	36	7.8	4.7	16.3	31.5		4.4	20.3	5.6	8.5	22.5	59.1
		4.4	41	8.0	5.0	14.7	35.6		4.9	31.2	7.5	8.9	17.6	45.3
									5.3	36.1	8.7	9.3	17	43.7
Polyurethane foam-hourglass type – A shaped composite tube 	**HASF**	3.1	22	3.0	6.5	16.0	24.3	**HADF**	3.8	9.00	1.9	10.4	22.8	79.0
		3.8	31	6.9	6.2	12.3	27.8		4.4	16.0	3.5	10.4	23.7	60.6
		4.4	36	9.1	6.5	10.2	31.2		4.9	18.0	3.0	9.8	24.8	70.2
									5.3	21.0	4.2	9.0	25.0	76.7
Hollow hourglass type – B shaped composite tube 	**HBS**	3.1	17	3.9	4.2	18.5	46.9	**HBD**	3.8	16.1	3.2	8.7	22.6	53.5
		3.8	22	4.3	4.0	14.0	59.1		4.4	22.3	5.4	8.4	20.4	54.7
		4.4	30	7.6	4.5	11.8	53.4		4.9	24.0	4.9	8.6	18.7	60.4
									5.3	28.2	6.3	9.1	17.6	57.4
Polyurethane foam-hourglass type – B shaped composite tube 	**HBSF**	3.1	24	4.5	5.2	13.0	26.8	**HBDF**	3.8	11.3	2.3	9.9	26.1	67.1
		3.8	42	7.2	5.3	9.5	24.5		4.4	16.4	4.6	8.7	23.3	70.9
		4.4	49	10.3	5.8	8.3	26.0		4.9	27.2	7.0	9.8	19.0	46.5
									5.3	31.0	8.4	9.2	18.0	50.5

Tube cross-section / geometrical shapes	Tube series	**1 mm wall thickness tubes tested with mass of the impactor 7.6 kg**						Tube series	**2 mm wall thickness tubes tested with mass of the impactor 10.6 kg**					
		Initial impact velocity (m/s)	Deformation length (mm) (l_{max})	Standard deviation for l_{max} (mm)	Peak load (kN)	SEA (kJ/kg)	η_c (%)		Initial impact velocity (m/s)	Deformation length (mm) (l_{max})	Standard deviation for l_{max} (mm)	Peak load (kN)	SEA (kJ/kg)	η_c (%)
		3.1	18	4.0	3.8	17.4	49.7		3.8	19.5	3.4	8.4	24.5	46.4
Hollow conical circular type - X composite tube	**CXS**	3.8	30	8.8	4.0	8.9	44.4		4.4	25.3	6.9	8.5	20.1	46.2
		4.4	53	12.0	3.2	9.3	43.2	**CXD**	4.9	30.2	9.1	8.3	18.5	49.7
		-	-		-	-	-		5.3	37.1	11.0	8.6	18.2	45.2
Polyurethane foam-filled conical circular type-X composite tube	**CXSF**	3.1	16	4.9	5.1	16.1	40.9		3.8	16.5	4.3	9.4	26.2	48.5
		3.8	41	10.4	4.5	8.6	29.5	**CXDF**	4.4	20.3	5.5	9.3	24.3	52.6
		4.4	58	13.6	5.3	8.0	23.8		4.9	25.4	4.3	9.1	21.4	54.0
									5.3	30.0	6.4	9.0	18.8	45.1
Hollow conical circular type - Y composite tube	**CYS**	3.1	17	4.1	3.9	20.8	59.2		3.8	17.1	2.8	8.6	28.6	50.3
		3.8	23	5.6	3.6	19.4	62.7	**CYD**	4.4	20.3	4.3	8.8	27.1	55.4
		4.4	30	7.7	4.0	18.6	75.5		4.9	24.5	5.1	8.4	24.0	60.1
									5.3	30.3	7.4	8.9	22.5	53.3
Polyurethane foam-filled conical circular type-Y composite tube	**CYSF**	3.1	20	4.7	4.0	21.7	42.1		3.8	15.2	3.0	9.6	30.2	51.3
		3.8	26	5.2	4.3	20.4	48.9	**CYDF**	4.4	17.1	3.9	9.3	28.6	62.4
		4.4	35	7.0	4.1	19.1	63.5		4.9	24.3	5.4	9.2	24.7	55.9
									5.3	27.4	7.0	9.5	23.1	55.9

14. 2. 2. Composite tubes with 2 mm wall thickness

Hollow tubes (composite tubes without polyurethane foam)

The deformation patterns of 2 mm wall thickness hollow composite tubes are very similar to 1 mm wall thickness tubes. All tubes showed controlled and progressive crushing failure modes; and the corresponding typical failure patterns of these composite tubes can be noticed from Figure 14-5(a-f).

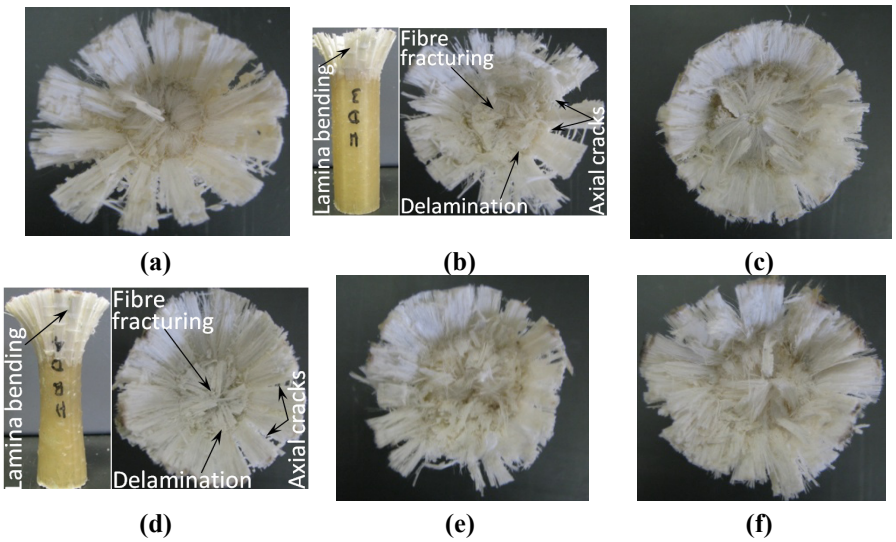

Figure 14-5: Deformation patterns of hollow composite tubes with 2 mm wall thickness **(a)** circular cross-sectional **(b)** hexagonal cross-section **(c)** hourglass type – A **(d)** hourglass type –B **(e)** conical circular type – X and **(f)** conical circular type – Y.

Similarly, the load-deformation curves of these composite tubes for the case with the initial impact velocity of 5.4 m/s are shown in Figure 14-6(a-f). Similar to the 1 mm wall thickness tubes all three different phases are clearly evident.

Polyurethane foam-filled composite tubes

The deformation patterns of the polyurethane foam-filled composite tubes are given in Figure 14-7(a-f). A significant difference can be noticed on these figures compared to the hollow composite tubes. In addition to the polyurethane foam compression a continuous delamination was present for all cases. The presence of continuous delamination was due to a combination of two effects: (i) additional hoop strength (2 mm wall thickness) of the composite tube and (ii) the inertia effect of the impactor. In order to check this result a few experiments were conducted with the impactor mass of 7.6 kg. The results from these studies also showed the same deformation patterns. In addition to the typical failure modes of the composite tubes,

the compressive and shear failure of the polyurethane foam attributed to a higher energy absorption.

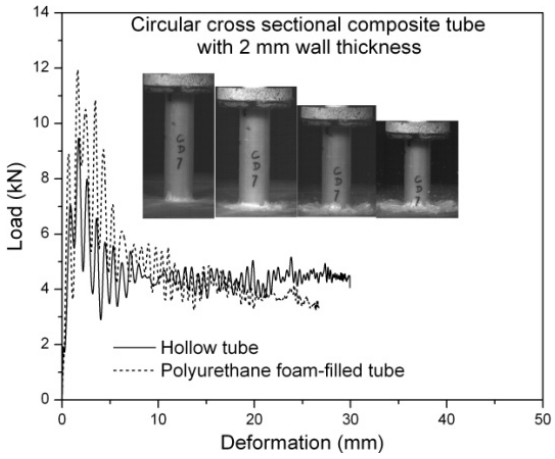

(a)

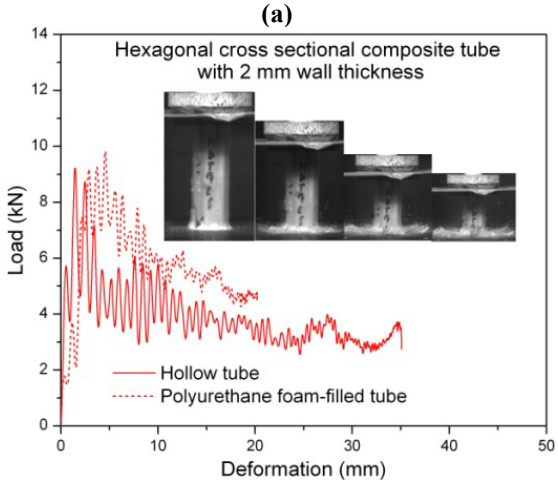

(b)

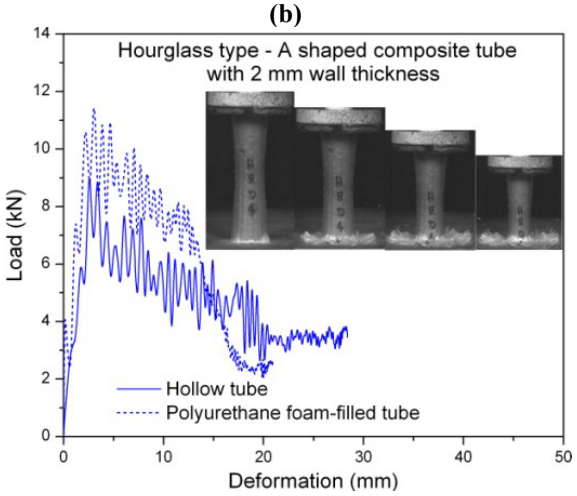

(c)

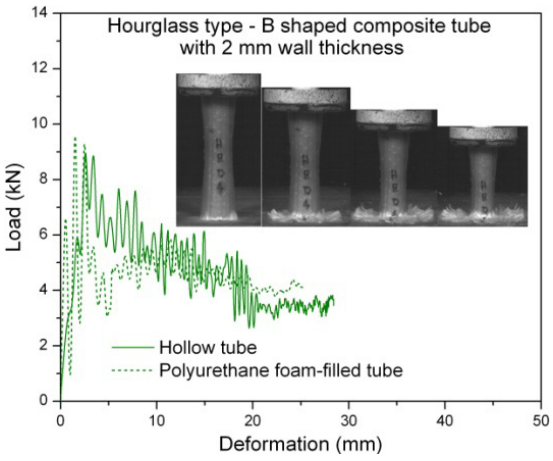

(d)

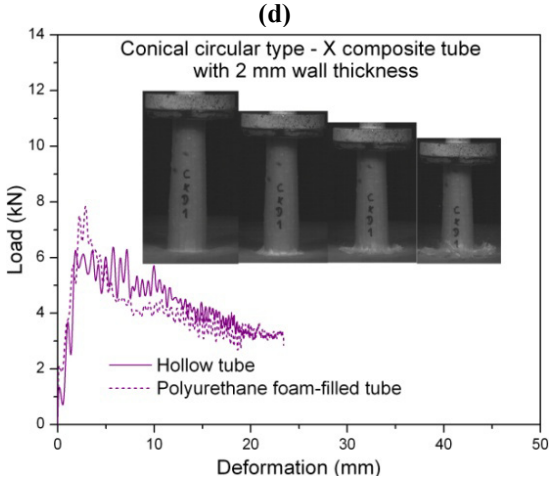

(e)

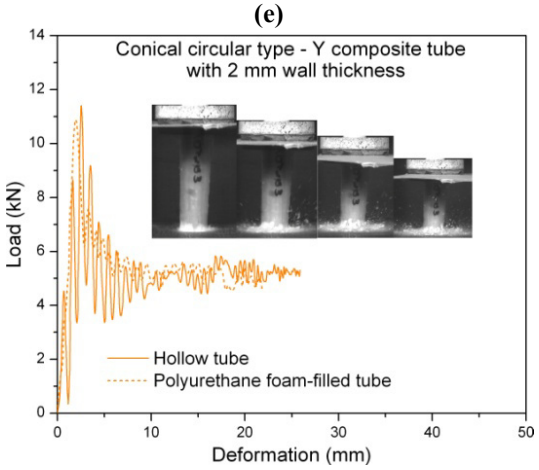

(f)

Figure 14-6: Load-deformation curves of hollow and polyurethane foam-filled composite tubes with 2 mm wall thickness **(a)** circular cross-section **(b)** hexagonal cross-section **(c)** hourglass type – A **(d)** hourglass type –B **(e)** conical circular type – X and **(f)** conical circular type – Y.

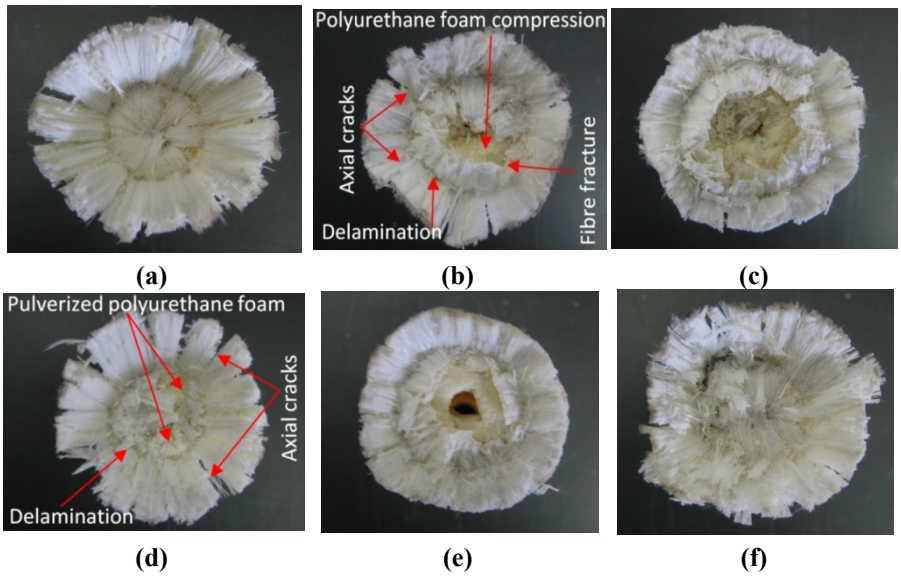

Figure 14-7: Deformation patterns for polyurethane foam-filled composite tubes with 2 mm wall thickness **(a)** circular cross-sectional **(b)** hexagonal cross-section **(c)** hourglass type – A **(d)** hourglass type –B **(e)** conical circular type – X and **(f)** conical circular type – Y.

In order to compare the results with hollow tubes, the load-deformation histories of these tubes (polyurethane foam-filled 2 mm wall thickness composite tubes) are given in Figure 14-6(a-f). Similar to 1 mm wall thickness composite tubes, the peak crush loads of these composite tubes are higher than for the hollow tubes due to the additional resistance of the polyurethane foam. Furthermore, the mean crush load of the polyurethane foam-filled composite tubes after the peak crush load was higher compared to the hollow tubes. In addition to the typical energy absorption mechanisms (delamination, axial cracks, lamina bending, fibre fracture and friction) the compressive and shear resistance of the polyurethane foam attributed to increase the mean crush load. As a result the total deformation lengths of these tubes are consistently shorter than for the hollow tubes (refer Figure 14-6(a-f)).

14. 2. 3. Comparison of crushing parameters

1mm wall thickness tubes

A comparison of the specific energy absorption and the corresponding peak crush load for hollow and foam-filled composite tubes is presented in this section. 50% of the hexagonal cross-sectional composite tubes failed catastrophically for the tests with the initial impact velocity of 4.4 m/s. Hence, this particular case (hexagonal tube with the initial impact velocity of 4.4 m/s) was not considered for the calculation of the specific energy absorption. Figure 14-8 shows the specific energy

absorption values of different shapes of composite tubes. The specific energy absorption of the circular cross-sectional tube (29.7 kJ/kg) was higher than for other composite tubes for the initial impact velocity of 3.1 m/s. However, for a higher impact velocity (4.4 m/s) the SEA value dropped significantly (16.7 kJ/kg) compared to other profiles such as hourglass type – A, conical circular type – X and conical circular type - Y. For conical circular type – Y the reduction in the SEA was not significant compared to other profiles. The average SEA of these tubes was 21.7 kJ/kg, 20.4 kJ/kg and 19.1 kJ/kg for the initial impact velocity of 3.1 m/s, 3.8 m/s and 4.4 m/s respectively.

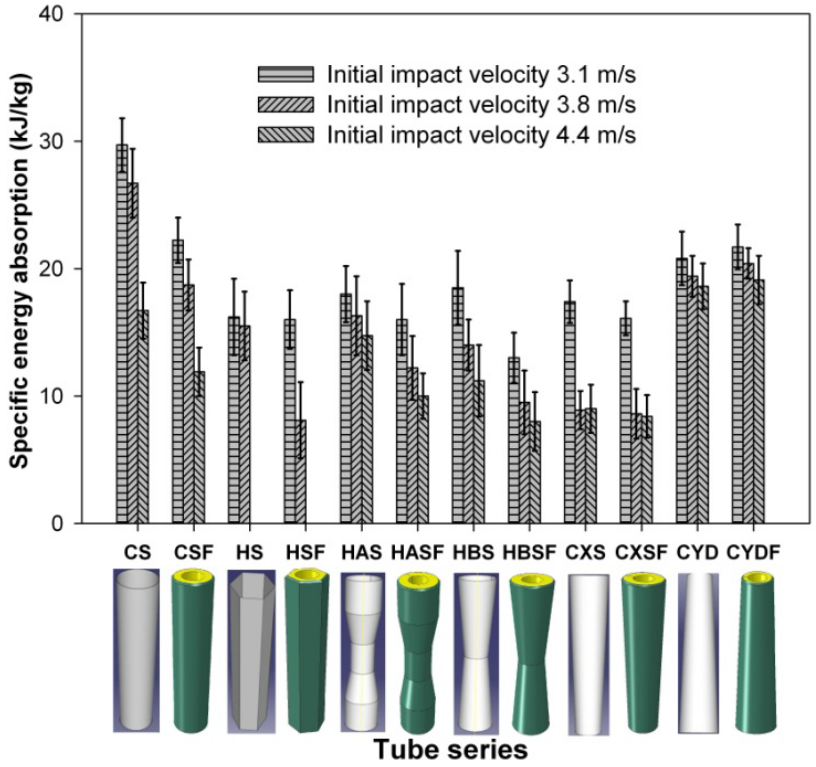

Figure 14-8: Comparison of the specific energy absorption for hollow and polyurethane foam-filled composite tubes with 1 mm wall thickness (error bar indicates the standard deviation).

The specific energy absorption of hourglass type – A, hourglass type – B and conical circular type – X are comparable for the initial impact velocity of 3.1 m/s (18 kJ/kg, 18.5 kJ/kg and 16.1 kJ/kg for hourglass type – A, hourglass type – B and conical circular type – X respectively). However, for higher impact velocities such as 3.8 m/s and 4.4 m/s the specific energy absorption of hourglass type – A was higher than for the remaining two profiles (refer Figure 14-8 and Table 14-1). In all cases, the specific energy absorption was reduced with increasing initial impact

velocity. This was due to the reduction in the mean crush load and the reason for this reduction was already discussed in Chapter 10.

The specific energy absorption of the polyurethane foam-filled composite tubes is significantly lower than for the hollow tubes for all impact velocities (refer Figure 14-8). This was due to the absence of continuous delamination and the corresponding mean crush load was determined by the axial splitting of the tube wall, lamina bending and the friction between the petals and the crushing platform. However, for conical circular type – Y the specific energy absorption of the polyurethane foam-filled composite tubes was higher than for the hollow tubes. Because of the geometry and the corresponding lower thickness of the polyurethane foam at the crushing end, the delamination continued for a longer length. This evidence can be noticed from Figure 14-4(f). The continuous delamination and the corresponding fibre fracture caused an increase the mean crush load and the corresponding specific energy absorption. Similarly, the peak crush load of these composite tubes (1 mm wall thickness) is shown in Figure 14-9.

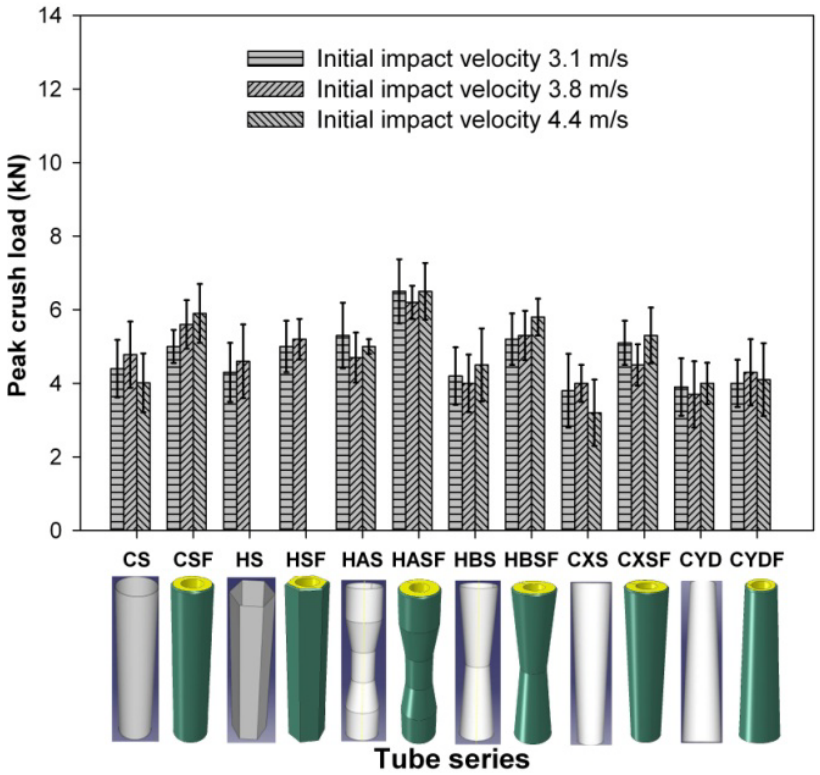

Figure 14-9: Comparison of peak crush load for hollow and polyurethane foam-filled composite tubes with 1 mm wall thickness (error bar indicates the standard deviation).

For all cases the peak crush load of the polyurethane foam-filled composite tubes was higher than for the hollow tubes. In addition to the initial delamination the compressive resistance of the polyurethane foam attributed to increase in the peak crush load. The peak crush load of the hourglass type – A and hourglass type – B showed higher values compared to other tube series. For hourglass type – A, the peak crush load varied from a minimum of 5.0 kN to a maximum of 5.3 kN for hollow tubes; a minimum of 6.2 kN to 6.5 kN for foam-filled composite tubes. Similarly the hourglass type – B showed maximum values of 4.5 kN and 5.8 kN for hollow and foam-filled tubes respectively. The dynamic peak crush load of all tubes except the conical circular type – Y was higher than for the quasi-static loading (refer Chapter 12). This may be due to the difference in the material properties of the tubes which were manufactured for the quasi-static and dynamic tests (fibre and matrix volume fractions). In addition to that there may be an influence from the circumferential fibres for dynamic loading. However, to conclude the above statements a thorough study is needed.

2mm wall thickness tubes

Similar to 1 mm wall thickness tubes, a comparison of the specific energy absorption of hollow and foam-filled composite tubes with 2 mm wall thickness is shown in Figure 14-10.

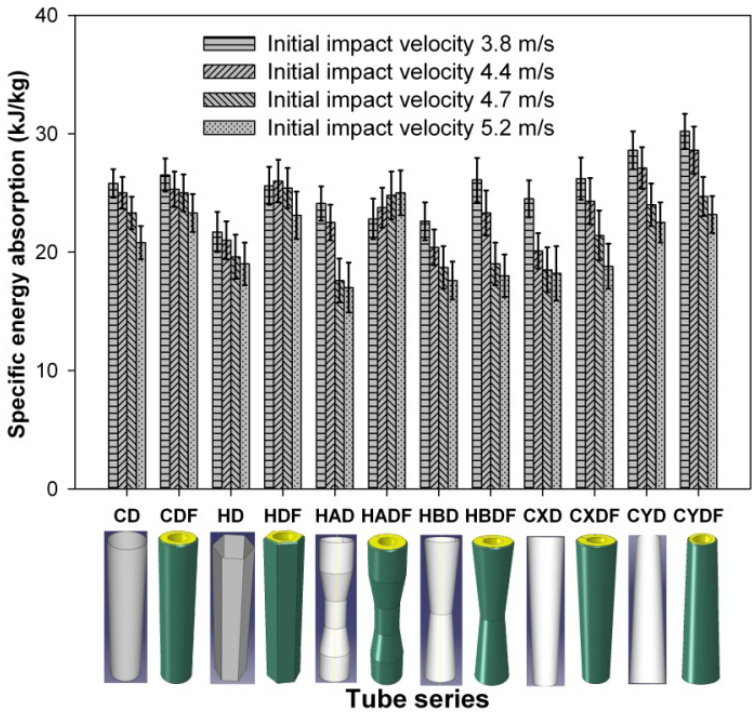

Figure 14-10: Comparison of the specific energy absorption for hollow and polyurethane foam-filled composite tubes with 2 mm wall thickness (error bar indicates the standard deviation).

The corresponding peak crush loads are shown in Figure 14-11. It can be noticed that the scatter in the parameters is low compared to the 1 mm wall thickness tubes. From Figure 14-10, it is clearly evident that the dynamic specific energy absorption decreases with increasing velocity. Unlike 1 mm thickness tubes, the reduction in the dynamic SEA was linear for all cases. Among the six different profiles the conical circular type – Y showed superior specific energy absorption values (30.2 kJ/kg, 28.6 kJ/kg, 24.7 kJ/kg and 23.1 kJ/kg for 3.8 m/s, 4.4 m/s, 4.9 m/s and 5.3 m/s respectively). The specific energy absorption of all remaining tube series was comparable for the initial impact velocity of 3.8 m/s (25.8 kJ/kg, 21.7 kJ/kg, 24.1 kJ/kg, 22.6 kJ/kg, 24.5 kJ/kg for circular, hexagonal, hourglass type – A, hourglass type – B, and conical circular type – X respectively).

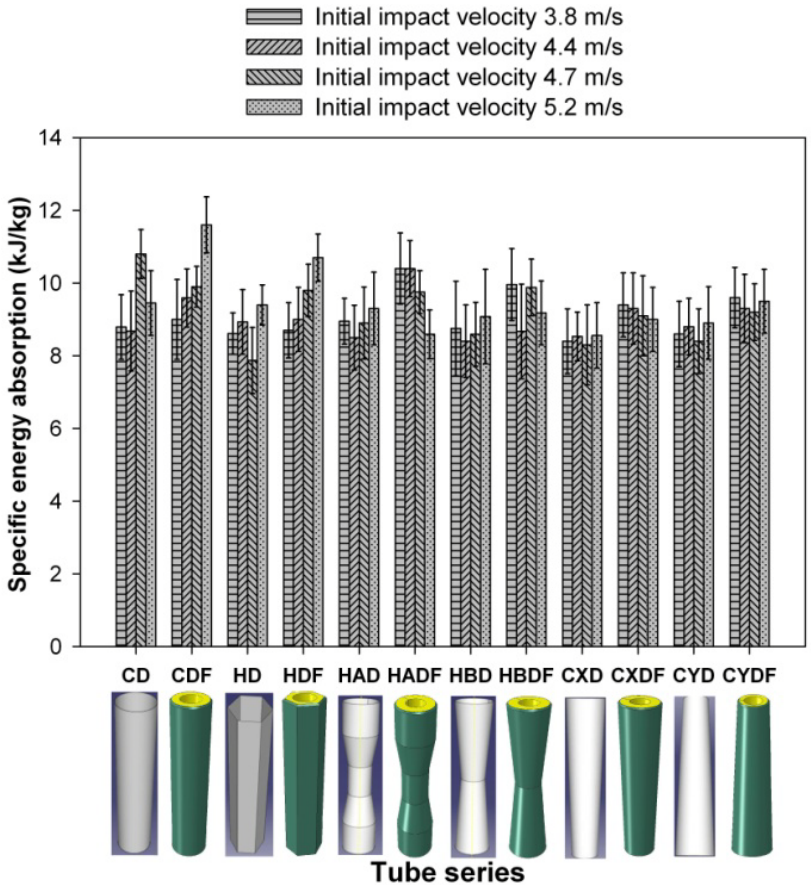

Figure 14-11: Comparison of peak crush load for hollow and polyurethane foam-filled composite tubes with 2 mm wall thickness (error bar indicates the standard deviation).

Unlike 1 mm wall thickness tubes, the specific energy absorption of 2 mm wall thickness polyurethane foam-filled composite tubes was higher than for hollow tubes. The reason for increasing the specific energy absorption was the presence of

continuous delamination and fibre fracturing in addition to the polyurethane foam compressive shear failure mode. Similarly from Figure 14-11, it can be noticed that the peak crush load of the foam-filled composite tubes was higher than for the hollow tubes. In addition to the circumferential delamination the compressive resistance of the polyurethane foam attributed increase the peak crush load.

14. 2. 4. Conclusions

This section presented the axial impact crushing performance of six different shapes of unidirectional small-scale in-house glass polyester composite tubes. Based on the quasi-static study six different profiles (circular, hexagonal, hourglass type – A, hourglass type – B, conical circular type – X and conical circular type – Y) have been used for the axial impact tests. Furthermore, the effect of polyurethane foam-filling on the crushing performance of these composite tubes was evaluated. Tests have been conducted with two different wall thicknesses and with different initial impact velocities. From the results of the conducted experiments the following conclusions can be made:

- the deformation patterns of hollow and polyurethane foam-filled composite tubes with 1 mm wall thickness were very similar to the quasi-static test results. All types of hollow tubes exhibited typical brittle composite failure modes such as delamination, axial cracks, lamina bending and fibre fracturing. For polyurethane foam-filled tubes, the circumferential delamination was observed during the crushing of the triggering profile. However, due to the presence of polyurethane foam the continuous delamination and fibre fracturing were suppressed at later crushing stages. Because of the difference in the deformation pattern the specific energy absorption of hollow tubes with 1 mm wall thickness was higher than for the polyurethane foam-filled tubes. In contrast, the specific energy absorption of foam-filled conical circular type – Y tubes was higher compared to the hollow tubes. The conical profile and a lower thickness polyurethane foam at the crushing end attributed for continuous delamination and fibre fracturing failure modes. Due to the additional resistance offered by the polyurethane foam, the peak crush load of the polyurethane foam-filled composite tubes was higher than for the hollow tubes.
- Unlike 1 mm thickness tubes, the 2 mm thickness composite tubes filled with polyurethane foam showed a higher specific energy absorption consistently for all shapes of the composite tubes. In addition to the polyurethane foam compressive shear failure, the continuous delamination and fibre fracturing of this case attributed to an increasing specific energy

absorption. Similar to 1 mm wall thickness tubes the peak crush load of foam-filled tubes was higher.

14. 3. Blast testing and results

14. 3. 1. Introduction

The first section of this chapter presented the axial impact crushing performance of six different shapes of small-scale in-house composite tubes (circular cross-sectional, hexagonal cross-sectional, hourglass type – A, hourglass type – B, conical circular type – X and conical circular type – Y). The specific energy absorption of circular cross-section, hourglass type - A and conical circular type –Y composite tubes was higher than the remaining profiles. Hence, these three profiles have been chosen to study the deformation patterns and the corresponding energy absorption for axial blast loading condition. Furthermore, close-range blast loading of mediums-scale pultruded glass polyester composite tubes (Chapter 11) listed out the difficulties of using the 2 mm wall thickness composite tubes. Based on these studies uni-directional glass polyester composite tubes with 1 mm wall thickness have been chosen. The geometry, dimensions, materials and manufacturing method of the composite tubes were the same (refer Chapter 12 for more details). Furthermore, in order to check the effect of polyurethane foam-filling on the deformation pattern additional blast tests have been conducted only on polyurethane foam-filled circular cross-sectional composite tubes. Similar to the quasi-static testing the triggering type 1 and 2 (45° chamfering and tulip pattern with an included angle of 90°) were adopted. Close-range blast tests have been conducted for 25 g C4 with a stand-off distance of 30 cm.

14. 3. 2. Measured blast parameters

The details of the used experimental test set-up and the measurement of data were given in Chapter 4 and 11. Furthermore, the dimensions of the composite tubes, nomenclature of the used composite tubes (hollow and polyurethane foam-filled), triggering details and the corresponding material data were given in Chapter 12 and 13. As known from Chapter 4 and 11, a lower inertia of the skin plates can provide a higher deformation length and the corresponding crushing duration can be extended. Hence, to study the crushing performance of these composite tubes (circular cross-section, hourglass type – A and conical circular type – Y) in detail, a skin plate with a mass of 0.65 kg (ϕ 250 mm) was used. The materials to manufacture the skin plates and the side tubes and the corresponding details were given in Chapter 4. A series of close-range blast tests have been conducted with the charge mass of 25 g of

C4 and with a stand-off distance of 30 cm. However, in addition to the above mentioned tests, a few tests have been also conducted with the aluminium skin plate (1.0 kg; ϕ 250 mm) to check and verify the deformation patterns of the composite tubes. For those tests only the deformation patterns of the composite tubes are presented. Hence, detailed results were captured and presented only for 25 g of C4 with a stand-off distance of 30 cm. A sampling frequency of 5 MHz was chosen for all sensors (pressure sensor, accelerometer and the dynamic load cell). The details of the used sensors were given in Chapter 4. For each category a minimum of five tests have been conducted and the average parameters are reported. Similar to the earlier cases, a comparison of the measured reflected parameters (reflected pressure and the corresponding positive duration) with the *ConWep* data are given in Table 14-2. The average peak reflected pressure from the experimental tests was comparable with the *ConWep* values. However, similar to the earlier cases there was a significant difference in the positive duration noticed (refer Table 14-2).

Table 14-2: Summary of predicted and experimentally measured reflected blast parameters.

Type of composite tube	Experimental test No	Area of the circular skin plate (A_p)	Mass of the skin plate (m_p)	Mass of C4 (m_c)	Stand-off distance (Z)	Maximum reflected over pressure (p^R_{max})	Positive duration (t_p)
		m^2	kg	g	cm	kPa	ms
ConWep		0.0491	-	25	30	5891	0.55
CST1 tubes	Test 1 to 5	0.0491 (ϕ 250mm)	0.65	25	30	6003	0.24
CST2 tubes	Test 5 to 10					6102	0.23
HAST1 tubes	Test 11 to 15					5900	0.21
HAST2 tubes	Test 16 to 20					6032	0.22
CXST1 tubes	Test 21 to 25					5834	0.22
CXST2 tubes	Test 26 to 30					6067	0.23

14. 3. 3. Deformation patterns

Hollow tubes:

The deformation patterns of the circular, hourglass type – A and conical circular type - Y composite tubes with aluminium (ϕ 250 mm; 1.0 kg) and sandwich composite skin plate (ϕ 250 mm; 0.65 kg) are given in Figure 14-12(a-f). Similar to the earlier experiments with the beverage can and medium-scale pultruded composite tubes, the deformation length of the small-scale in-house composite tubes has increased with the lower inertia of the skin plate (0.65 kg). Furthermore, the deformation patterns of these tubes were very similar to the quasi-static and impact experimental results. However, there was a difference noticed for the bending angle of the petals. The bending angle of the petals was approximately 20° to 30° for these composite tubes (refer Figure 14-12(a-f)). For quasi-static testing the bending angle of the petals was greater than or equal to 90° (refer Chapter 12); and for impact experiments this value was approximately 40° to 75°. The reduced bending angle of the petal was due to resulting high dynamic load for a very short duration from the blast.

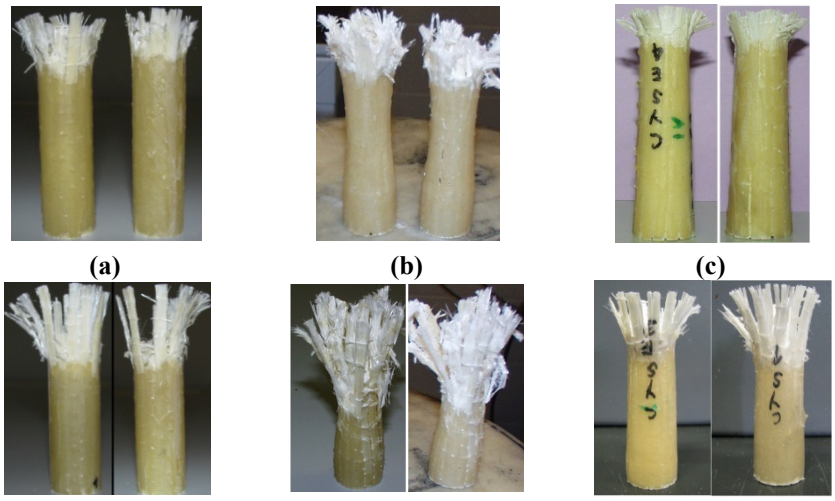

Figure 14-12: Deformation patterns of in-house composite tubes with 1 mm wall thickness subjected to 25 g of C4 with 30 cm stand-off distance **(a-c)** circular cross-section, hourglass type – A and conical circular type – Y respectively with the aluminium skin plate (ϕ 250 mm; 1.0 kg) **(d-f)** circular-cross-section, hourglass type – A and conical circular type - Y respectively with the sandwich composite skin plate (ϕ 250 mm; 0.65 kg)

The typical failure modes of the brittle composite tubes (circumferential delamination, axial cracks, lamina bending and fibre fracturing) can be noticed from Figure 14-13(a-b) for the circular and hourglass type – A composite tubes. For all

composite tubes (circular, hourglass type – A and conical circular type – Y) there was significant fibre fracturing noticed for the inner petals.

In order to check these failure modes for a different charge mass two tests have been conducted with 15 g of C4 and 30 cm stand-off distance for the circular and hourglass type - A composite tubes. These tests also showed the same results (refer Figure 14-14). Hence, it can be concluded that irrespective of the charge mass and stand-off distance the failure patterns of the chosen small-scale in-house composite tubes remains the same.

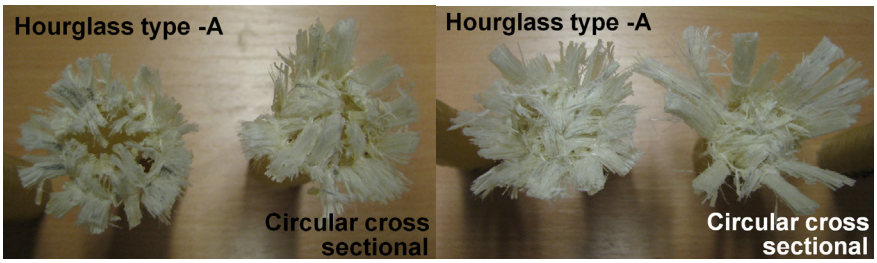

(a) **(b)**

Figure 14-13: (a) Progressive deformation patterns of the circular and hourglass type – A composite tubes for 25 g C4 with the stand-off distance of 30 cm **(a)** with the aluminium skin plate (ϕ 250 mm; 1.0 kg) **(b)** with the sandwich composite skin plate (ϕ 250 mm; 0.65 kg).

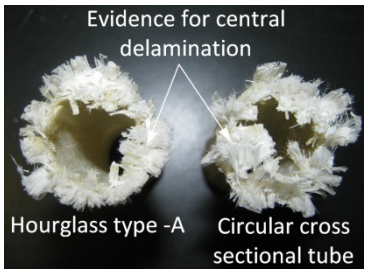

Figure 14-14: Deformation patterns of the circular cross-sectional and hourglass type – A composite tube with 1 mm wall thickness for 15 g of C4 with a stand-off distance of 30 cm.

As noticed from Chapter 12, the square and hexagonal cross-sections with 1 mm wall thickness showed a catastrophic failure. However, the same hexagonal cross-sectional tubes showed progressive failure modes for the impact loading (refer section 14. 2. 1.). Hence, in order to check the performance of these tubes (square and hexagonal cross-section) few blast tests were carried out (with the aluminium skin plate). However from these tests showed similar results as the quasi-static tests (sudden growth and propagation of axial cracks throughout the length of the composite tube). As an example, the deformation patterns of the square cross-sectional composite tube are given in Figure 14-15.

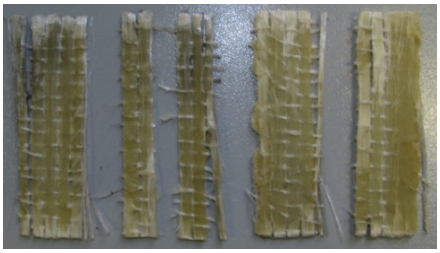

Figure 14-15: Deformation patterns of the square cross-sectional composite tube with 1 mm wall thickness (for 25 g C4 with the stand-off distance of 30 cm and with the aluminium skin plate (ϕ 250 mm; 1.0 kg)).

Polyurethane foam filled composite tubes:

In order to check the influence of the polyurethane foam-filling on the deformation patterns of the composite tubes, blast tests have been conducted only on the circular cross-sectional composite tubes. Blast tests have been conducted with 25 g of C4 with a stand-off distance of 30 cm. These tests showed consistent results similar to the quasi-static and impact tests: a continuous delamination was suppressed due to the resistance offered by the polyurethane foam and subsequently the composite tubes underwent axial splitting and lamina bending; due to this process the circumferential fibres were fractured. The influence of the skin plate mass on the total deformation length and the corresponding final failure patterns of these composite tubes are shown in Figure 14-16(a) and (b) respectively.

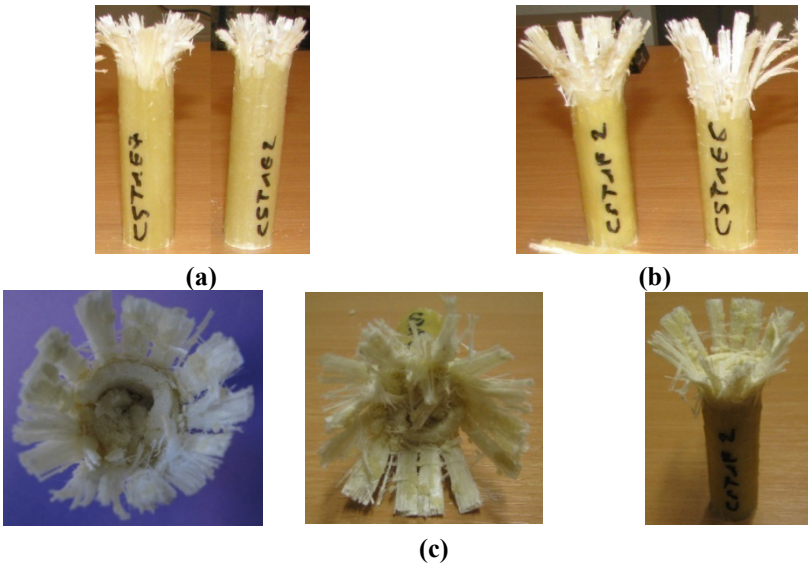

Figure 14-16: Deformation patterns of polyurethane foam-filled circular cross-sectional composite tubes for 25 g C4 with 30 cm stand-off distance **(a)** with the aluminium skin plate (ϕ 250 mm; 1.0 kg) **(b-c)** sandwich composite skin plate (ϕ 250 mm; 0.65 kg).

14. 3. 4. Crushing load curves

The crushing load-time curves of hollow tubes with circular cross-section, hourglass type – A and conical circular type – Y are presented in this section. Similar to the earlier chapters, the crushing compressive load and the deformation length are shown in positive values in all load-deformation graphs. As an example, the typical load-time histories of the circular cross-sectional, hourglass type – A and conical circular type – Y with triggering type 1 and triggering type 2 are shown in Figure 14-17(a), (b) and (c) respectively. In all cases, a significant fluctuation in the load-time histories was noticed due to the dynamic loading. Furthermore, similar to the quasi-static and impact cases there was a distinct difference in the load-time curves observed for triggering type 1 and 2. Due to the triggering profile and the delayed circumferential delamination the peak crush load for triggering type 2 occurred later than for the triggering type 1. However, there was no direct advantage noticed due to the use of different triggering profiles. Both tubes (triggering type 1 and 2) in each category altered a high force short duration pulse from the blast to a low force long duration pulse. The typical positive duration of the blast of 0.225 ms (refer Table 14-1) was extended to approximately 6 to 7 ms (refer Figure 14-17(a-b)). At the same time the peak force was reduced from 14.89 kN (measured from the reference tests conducted without test specimens and only with the skin plate directly placed on the load cell for the same loading parameters (25 g C4 with 30 cm stand-off distance)) to an approximate value of 4 kN for all cases.

14. 3. 5. Comparison of parameters

In order to compare the effectiveness of each composite tube series all crushing variables of the composite tubes (mean crush load, specific energy absorption, crushing efficiency etc.) are presented in Table 14-3. From the specific energy absorption results it can be concluded that the performance of the composite tubes with both triggering types (triggering type 1 and 2) is the same.

The specific energy absorption of the conical circular type – Y (9.29 kJ/kg and 9.27 kJ/kg for triggering type 1 and 2 respectively) was higher than the remaining two categories (circular and hourglass type – A) and it was comparable with the circular cross-sectional tubes (9.13 kJ/kg and 9.14 kJ/kg for triggering type 1 and 2 respectively). However, due to longer deformation lengths the hourglass type – A showed lower SEA values (7.85 kJ/kg and 7.80 kJ/kg for triggering type 1 and 2 respectively). The peak crush load of these tubes showed similar values (refer Table 14-3). Hence, deploying the circular cross-sectional or conical circular type - Y for the inner core of a sacrificial cladding structure can provide similar results using a less material compared to hourglass type – A.

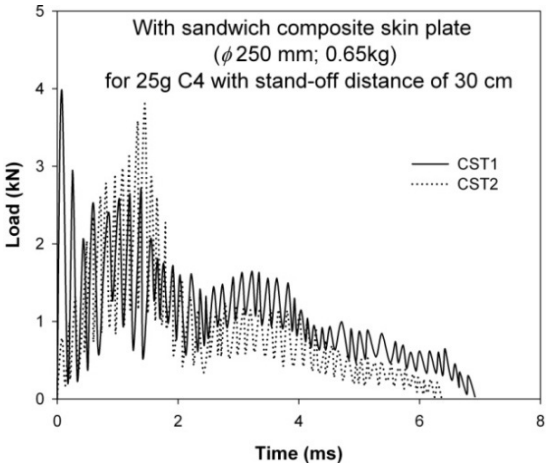

(a)

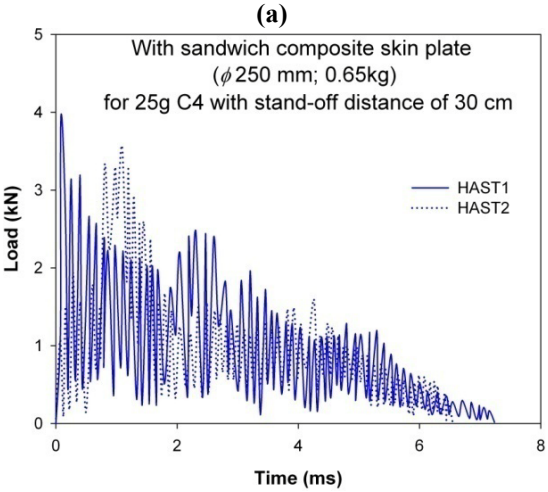

(b)

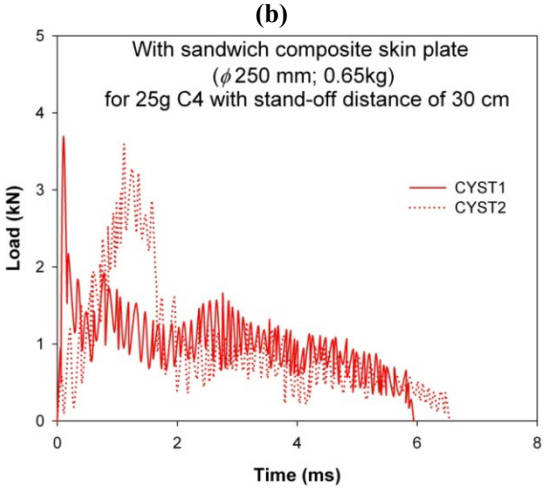

(c)

Figure 14-17: Load-time history of the composite tube series for 25 g C4 with 30 cm stand-off distance **(a)** circular cross-sectional composite tubes **(b)** hourglass type – A composite tubes **(c)** conical circular type – Y composite tubes.

Table 14-3: Summary of average crushing parameters.

Test No	Composite tube series	Mass of the skin plate (m_p)	Reflected (total) impulse delivered to the skin plate (I_{ref})	Impulse transferred to non-sacrificial structure (I_{trans})	% difference in impulse (ΔI)	Available energy from the blast to the skin plate for composite tube crushing (E_{trans})	Energy absorbed by the composite tube (E_{abs})	Peak (crush) load (P_{max})	Mean crush load (P_{mean})	Deformation length of composite tube (l_{max})	Standard deviation for (l_{max})	Crush efficiency (η_d)	SEA
	-	kg	kN.s	kN.s	%	J	J	kN	kN	mm	mm	(%)	(kJ/kg)
25g C4 with stand-off distance of 30 cm													
Reference test	-		0.0093	0.0063	32.3	-	-	14.66	-	-	-	-	-
Test 1-5	CST1		0.0089	0.0060	33.1	60.0	28.3	4.10	0.883	31	4.5	21.5	9.13
Test 6-10	CST2		0.0092	0.0064	30.5	64.5	32.3	3.85	0.871	36	7.2	22.6	9.14
Test 11-15	HAST1	0.65	0.0088	0.0059	32.2	58.9	27.2	4.35	0.812	33	8.1	18.7	7.85
Test 16-20	HAST2		0.0091	0.0064	29.4	64.8	32.3	3.99	0.799	40	6.3	20.0	7.80
Test 21-25	CYST1		0.0090	0.0059	34.0	62.1	26.0	3.96	0.913	28	6.9	23.2	9.29
Test 26-30	CYST2		0.0087	0.0063	27.4	60.3	31.2	3.82	0.899	34	7.6	23.9	9.27

Similar to the earlier chapters (Chapter 4 and 11), there was a difference noticed for the reflected and transferred impulse and energy values (refer Table 14-3). This difference was due to the combined effect of diffraction and ground reflection of the pressure waves on the skin plate.

14. 3. 6. Conclusions

This section presented the axial crushing performance of uni-directional small-scale in-house glass polyester composite tubes under close-range blast loading. Three different shapes (circular cross-section, hourglass type – A and conical circular type – Y) with 1 mm wall thickness have been considered for the study. Blast tests with different charges and skin plate masses showed that the deformation patterns of hollow and foam-filled tubes were the same as compared to quasi-static and impact testing results. The hollow tubes showed typical failure modes such as the circumferential delamination, axial cracks, lamina bending and fibre fracturing; similarly, the polyurethane foam-filled tubes showed axial splitting, lamina bending and polyurethane foam compression and shear failure modes. All three types of tubes significantly altered the high force short duration pulse from the blast, to a low peak long duration pulse. The peak crush load and the corresponding duration for which the load was transferred to the non-sacrificial structure were approximately the same for all three profiles. However, the specific energy absorption of hourglass type - A was lower than for the circular cross-sectional and conical circular type- Y tubes. Hence, deploying either conical circular type – Y or circular cross-section section can provide better results with less material investment.

Bibliography

[1]. Palanivelu, S., Van Paepegem, W., Degrieck, J., Kakogiannis, D., Van Ackeren, J., Van Hemelrijck, D., Wastiels, J. and Vantomme, J., *Comparative study of the quasi-static energy absorption of small-scale composite tubes with different geometrical shapes for use in sacrificial cladding structures.* Polymer Testing, 2010. **29**(3): p. 381-396.

[2]. Palanivelu, S., Van Paepegem, W., Degrieck, J., Vantomme, J., Kakogiannis, D., Van Ackeren, J., Van Hemelrijck, D. and Wastiels, J., *Crushing and energy absorption performance of different geometrical shapes of small-scale glass/polyester composite tubes under quasi-static loading conditions.* Composite Structures, 2010. **93**(2): p. 992-2007.

[3]. Palanivelu, S., Van Paepegem, W., Degrieck, J., Vantomme, J., Kakogiannis, D., Van Ackeren, J., Van Hemelrijck, D. and Wastiels, J., *Comparison of the crushing performance of hollow and foam-filled small-scale composite tubes with different geometrical shapes for use in*

sacrificial cladding structures. Composites Part B: Engineering, 2010. **41**(6): p. 434-445.

[4]. Mamalis, A. G., Manolakos, D. E. and Demosthenous, G. A., *Crushing behaviour of thin-walled, non-circular, glass fibre-reinforced composite tubular components due to bending.* Composites, 1992. **23**(6): p. 425-433.

[5]. Mamalis, A. G., Manolakos, D. E., Demosthenous, G. A. and Ioannidis, M. B., *Energy absorption capability of fibreglass composite square frusta subjected to static and dynamic axial collapse.* Thin-Walled Structures, 1996. **25**(4): p. 269-295.

[6]. Mamalis, A. G., Manolakos, D. E., Ioannidis, M. B. and Papapostolou, D. P., *Crashworthy characteristics of axially statically compressed thin-walled square CFRP composite tubes: experimental.* Composite Structures, 2004. **63**(3-4): p. 347-360.

[7]. Mamalis, A. G., Robinson, M., Manolakos, D. E., Demosthenous, G. A., Ioannidis, M. B. and Carruthers, J., *Crashworthy capability of composite material structures.* Composite Structures, 1997. **37**(2): p. 109-134.

[8]. Solaimurugan, S. and Velmurugan, R., *Progressive crushing of stitched glass/polyester composite cylindrical shells.* Composites Science and Technology, 2007. **67**(3-4): p. 422-437.

[9]. Farley, G. L. and Jones, R. M., *Analogy for the effect of material and geometrical variables on energy absorption capability of composite tubes.* Journal of Composite Materials, 1992. **26**: p. 78.

[10]. Thornton, P. H., *The crush behavior of pultruded tubes at high strain rates.* Journal of Composite Materials, 1989. **24**: p. 22.

[11]. Hamada, H., Coppola, J. C., Hull, D., Maekawa, Z. and Sato, H., *Comparison of energy absorption of carbon/epoxy and carbon/PEEK composite tubes.* Composites, 1992. **23**(4): p. 245-252.

[12]. Ramakrishna, S. and Hull, D., *Energy absorption capability of epoxy composite tubes with knitted carbon fibre fabric reinforcement.* Composites Science and Technology, 1993. **49**(4): p. 349-356.

Part IV

This part deals with large-scale blast testing on α and β type structures (empty beverage cans and small-scale pultruded composite tubes)

Chapter 15

Large-Scale Blast Testing on Array of Empty Metal Beverage Cans

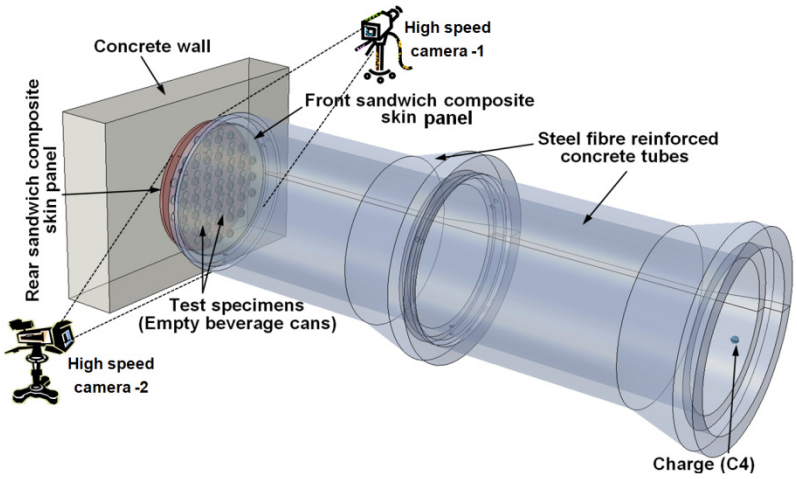

Overview

This chapter presents the large-scale blast testing on representative sacrificial cladding structures made of empty recyclable metal beverage cans and sandwich composite skin panels. To measure the protection efficiency of these structures large-scale air blast experiments have been conducted with different charge masses of C4. To create a perfectly plane shock wave the shock tube concept was used using concrete sewage pipes. The experimentally measured reflected blast parameters were compared with the coupled numerical simulation results. In order to understand the progressive crushing stages of the beverage cans a decoupled numerical analysis was conducted. The experimental and numerical crushing performance of the empty beverage cans is studied in detail.

15. 1. Introduction

In order to deploy the gained knowledge from the small-scale blast studies and to check the performance of the empty beverage cans, large-scale blast tests were conducted. To create a perfectly plane shock wave the a shock tube concept was used using segments of concrete sewage pipes. The coupled numerical simulations were carried out in Autodyn v12.1 in order to calculate the minimum length of the pipe which provides a perfectly plane shock wave at the other end (crushing end); accordingly, the detonation and propagation of the air blast was modelled in concrete sewage pipes. Air blast experiments have been conducted on two configurations of the empty beverage cans with different charge masses of C4. During the experimental tests, the reflected pressure, acceleration of the skin panel, transmitted impulse and high-speed images of crushing were recorded. The crushing performance of the empty metal beverage cans was studied in detail. In order to understand the initiation and the corresponding progressive crushing stages of the beverage cans in detail, a numerical simulation was conducted using the commercial explicit code Abaqus v6.9-2. The results from the numerical simulations were compared and validated with the experimental results.

15. 2. Experimental test set-up

Large-scale air blast tests were conducted in collaboration with the ***Royal Military Academy of Belgium*** at the Brasschaat testing domain (refer Figure 15-1). A schematic global view of the experimental test set-up is shown in Figure 15-2. The empty metal beverage cans were mounted on a rear skin panel (sandwich composite panel) behind which three dynamic load cells were connected to a concrete wall to measure the transferred impulse to the concrete structure. All the skin panels used for the large-scale blast tests were manufactured by M/s Acrosoma, Belgium [1] (further details of the skin panels are given in the next section). The locations of the force sensors are equidistant from the centre of the rear skin panel and the angle between these sensors is 120°. Another skin panel (front skin panel) was assembled on the front side of the empty beverage cans (test specimens). The front skin panel was instrumented with three pressure sensors and two accelerometers to measure the reflected pressure and the acceleration of the skin panel respectively (refer Figure 15-3). The crushing face of the front skin panel was in-line with the end of the concrete pipe which was close to the concrete wall (refer Figure 15-4). The C4 charge was placed at the other end of the concrete pipe (stand-off distance was 4.2 m – refer Figure 15-3). Blast experiments have been conducted on two configurations of the beverage cans (25 and 37 beverage cans) with different charge masses (75 g, 100 g, 150 g and 200 g of C4). Two high speed cameras were used to capture the crushing behaviour of the beverage cans from two different points of view during the blast tests.

Figure 15-1: Test site at Royal Military Academy, Brasschaat, Belgium.

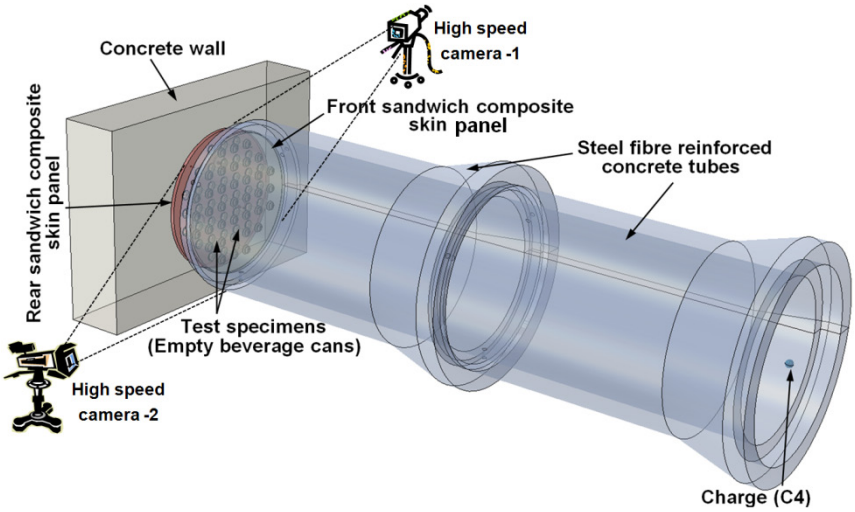

Figure 15-2: Schematic view of the large-scale experimental test facility.

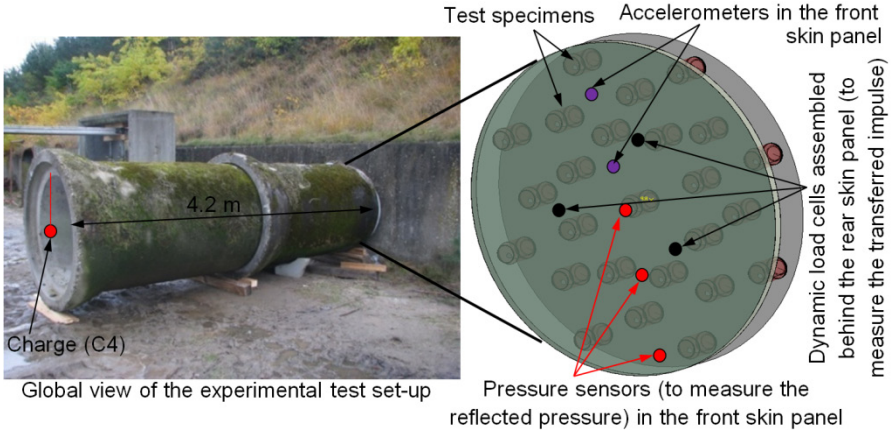

Figure 15-3: Arrangement of the large-scale test set-up.

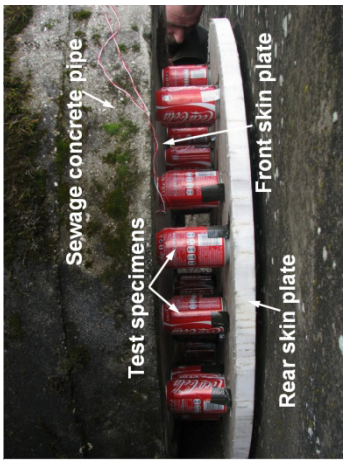

Figure 15-4: Side view of assembly.

15. 2. 1. Skin panels

All (sandwich composite) skin panels were manufactured by M/s Acrosoma, Belgium [1]. The sandwich composite skin panels were made of three materials (refer Figure 15-5). The outer face sheets (top and bottom) are made of bi-axially balanced glass fibre fabric with polyester resin; the core structure is made of divinycell P foam. The outer face sheets are stitched together straight through the foam with aramid fibres. This prevents the delamination between the face sheets and the core structure (refer Figure 15-5).

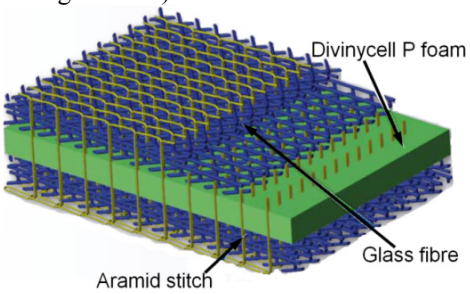

Figure 15-5: Internal architecture of the skin panel [1].

The diameter of the rear skin panel was 1.0 m. In order to have a small clearance for an easy assembly of the front skin panel with the concrete pipe, the diameter of the front skin panel was chosen to be ϕ 0.96 m (refer Figure 15-6). Furthermore, the location of the pressure sensors (to measure the reflected pressure) and the accelerometers (to measure the acceleration of the skin panel) are shown in Figure 15-6. The mass of the front skin panel was approximately 7.15 kg including all sensors. To hold the test specimens in horizontal position on the rear skin panel during blast loading soft foam holders were assembled on the rear skin panel (refer Figure 15-7(a-b)). The stiffness of this foam was very less; hence, the resistance provided by the foam during the blast loading can be neglected.

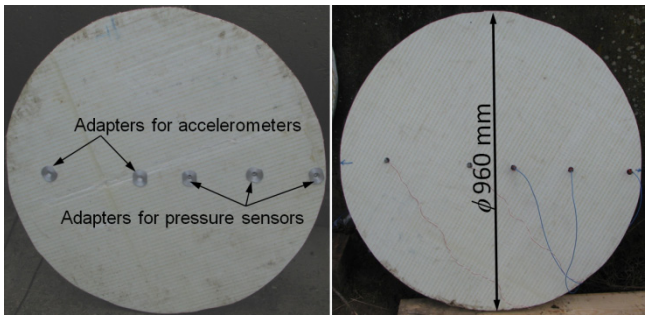

Figure 15-6: Details of front sandwich composite skin panels.

(a) **(b)**

Figure 15-7: (a) Soft-foam assembly on the rear skin panel to hold the test specimens (b) Assembly of test specimens.

15. 2. 2. Preliminary lab-scale blast test on skin panels

In order to evaluate the performance of the sandwich composite skin panels preliminary lab-scale blast tests were conducted. The chosen size of the sandwich composite skin panel was 400 × 400 mm (refer Figure 15-8(a)). The details of the charge mass, stand-off distance (30 g C4 with 30 cm) and the boundary conditions are shown in Figure 15-8(b). A minimum of 4 tests were conducted on a single panel. After the test the entire skin panel was intact. However, there was an evidence of delamination within the foam structure at the centre of the skin panel. In addition to that the foam at the edge location was removed after the blast tests (refer Figure 15-9(a)). In order to compare the performance of Acrosoma sandwich panels a test was conducted on a reference panel (4.5 mm thick bi-axially balanced glass epoxy composite panel). The final deformation pattern of this composite panel after the first test (with the same 30 g of C4 and 30 cm stand-off distance) is shown in Figure 15-9(b). The delamination failure mode was observed on the entire panel; furthermore, significant fibre breakage was also observed at the centre of the composite panel. The results from these tests encouraged to use the Acrosoma sandwich panels for the large-scale blast tests.

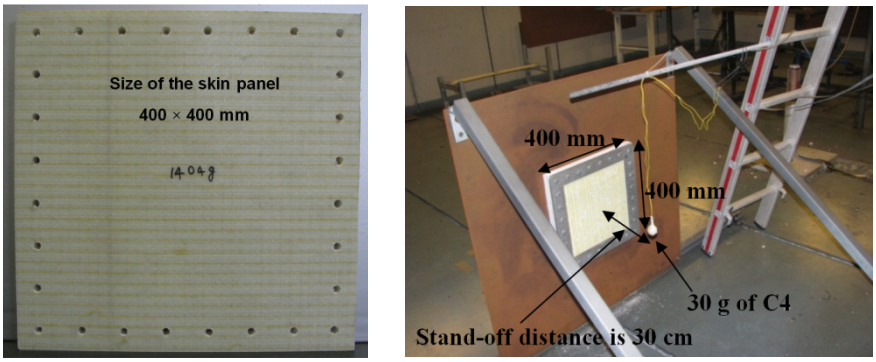

(a) **(b)**

Figure 15-8: (a) Sandwich composite skin panel **(b)** Experimental blast test set-up.

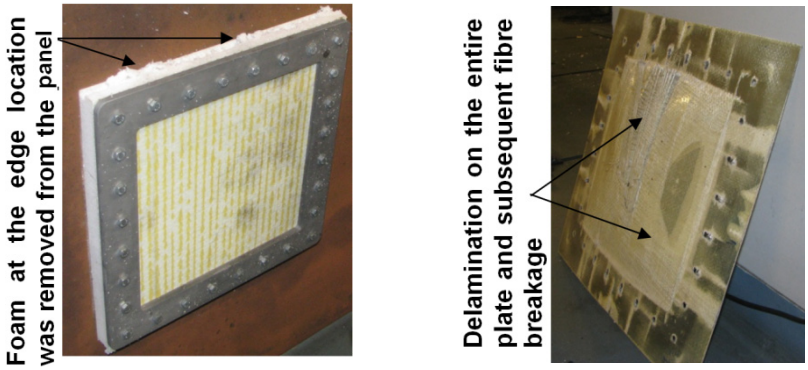

(a) **(b)**

Figure 15-9: Comparison of deformation patterns of Acrosoma sandwich panels and a reference panel **(a)** Acrosoma sandwich panel **(b)** Reference panel – 4.5 mm thick bi-axially balanced glass epoxy composite panel.

15. 2. 3. Instrumentation

Accelerometers and pressure sensors

The details of the used dynamic load cells (*PCB 202B*), pressure sensors (*PCB 102A*) and accelerometers (*PCB 350 B02*) were already given in Chapter 4. The used number of pressure sensors and accelerometers was 3 and 2 respectively. In order to assemble these sensors on the front skin panel, adapters have been made (refer Figure 15-10(a) and (b) for pressure sensor and accelerometer respectively). The pressure sensors and the accelerometers were placed equidistant from the centre to the edge of the skin panel (refer Figure 15-6). Similarly, the assembly of load cells can be understood from Figure 15-11(a-c). In order to have a flat surface and to prevent the penetration of the load cells within the concrete wall and the rear skin panel, the load cells have been assembled in between two steel plates (refer Figure 15-11(a-c)).

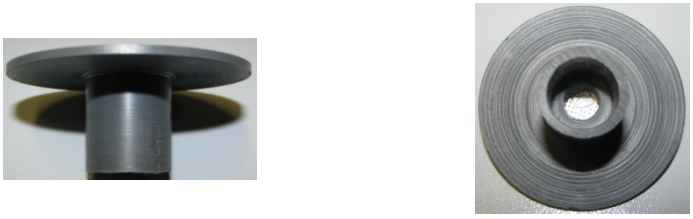

(a) **(b)**

Figure 15-10: (a) Adaptor for accelerometer (b) Adaptor for pressure sensor.

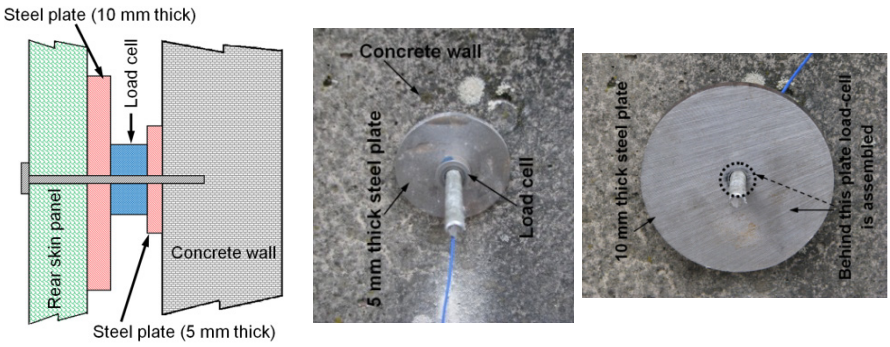

(a) **(b)** **(c)**

Figure 15-11: (a-c) Load cell assembly.

15. 2. 4. Configurations of the empty beverage cans

Two configurations (configuration 1 and 2) have been selected to study the crushing performance of the empty beverage cans (refer Figure 15-12(a-b). Configuration 1 consists of 25 beverage cans and the configuration 2 consists of 37 cans. The positions of the beverage cans for these two configurations are given in Figure 15-12(a) and (b) respectively. These configurations are based on the results from the small-scale blast tests (based on the surface area and the corresponding impulse for each test specimen). Small-scale blast tests with a skin panel mass of 0.36 kg (ϕ 250 mm) provided an average deformation length of 60 mm. In order to achieve a similar deformation length of the test specimens the same parameters (mass as well as area of the skin panel) have to be maintained. Totally, 16 test specimens can be accommodated for the same parameters (assuming the surface area exposed to each test specimen was 0.049 m^2). However, due to a lower mass of the chosen large-scale front skin panel (7.15 kg), it was decided to use a minimum of 25 beverage cans. Furthermore, due to the internal reflections of the pressure wave inside the concrete pipe, the expected pressure at the other end of the concrete pipe was higher. Based on the above assumptions the configurations (25 and beverage cans) were finalized for the large-scale blast testing.

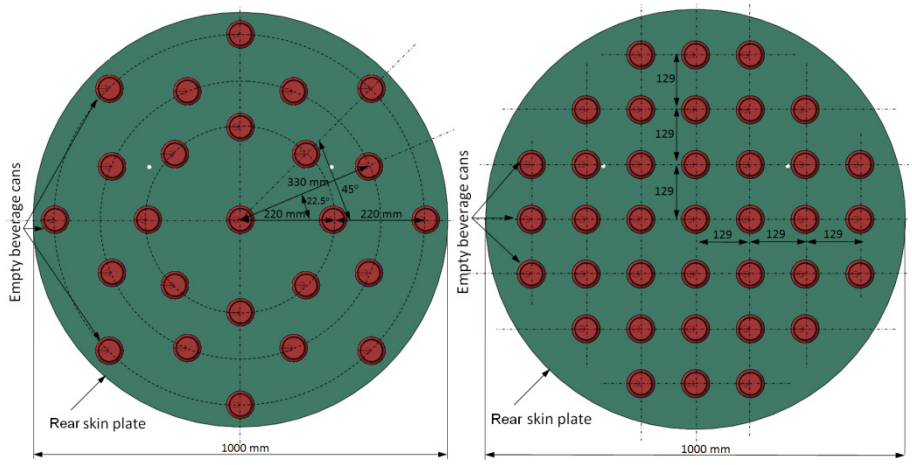

(a) **(b)**

Figure 15-12: Different configurations of empty beverage cans **(a)** for 25 cans **(b)** for 37 cans.

15. 3. Coupled numerical simulations and results

Before conducting large-scale blast tests the minimum length of the concrete sewage pipe to provide a perfectly plane shock wave should be known. Hence, coupled numerical simulations have been conducted for different charge masses and with different lengths of concrete sewage pipes to identify the length which was required to have a perfectly plane shock wave. The commercially available code Autodyn v12.1 was used for this purpose [2]. The coupled numerical modelling details for the small-scale blast tests on the beverage cans were discussed in Chapter 5 [3]. To reduce the computation time the concrete pipes and the front skin panel were modelled with a rigid material. The length of a single concrete pipe was 2.1 m. Hence, the discrete length dictated by the length of one concrete tube. Similar to the approach handled in Chapter 5, the air and C4 were modelled using the *multi-material Euler formulation* [2, 4, 5]. The initiation, detonation and the expansion of C4 were modelled using the *Jones-Wilkins-Lee* (JWL) Equation of state (EOS) and the details of this equation and the corresponding used material properties of C4 were already discussed in Chapter 5. Similarly, the volume filled inside the concrete pipes with ambient air was modelled using the ideal gas equation of state (refer Chapter 5). Different lengths and charge masses have been considered to achieve a perfectly plane shock wave at the other end of the concrete pipe. A fixed boundary condition was used for the skin panel to calculate the reflected pressure time histories. As an example, one of the cases (100 g C4 with 4.2 m stand-off distance) is presented here. Figure 15-13 shows the detonation of C4 and the corresponding propagation of the pressure wave inside the concrete pipes. It can be noticed from

the same figure that a perfectly plane shock wave was formed at the other end of the concrete pipe.

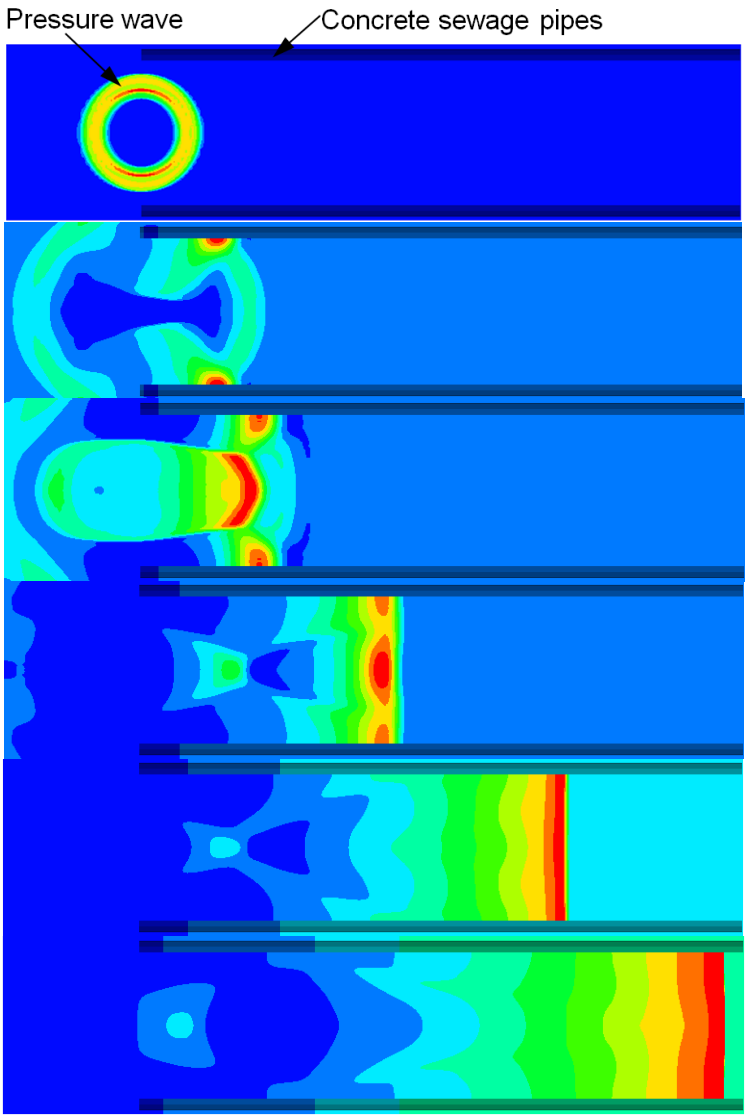

Figure 15-13: Propagation and interaction of pressure waves with the concrete sewage pipes.

The interaction of the pressure wave with the concrete pipe continuously amplified the magnitude of the pressure wave. Similarly Figure 15-14(a-c) shows the final pressure contours available at the other end of the concrete pipes for different charge masses (75 g, 150 g and 200 g of C4 respectively). Furthermore, the magnitude of the pressure was increased with increasing C4 charge masses. Although a perfectly plane shock wave was formed at the other end of the concrete pipe for all charge masses, the magnitude of the pressure close to the inner wall surface of the concrete

pipe was higher (refer Figure 15-14(a-c)). This may be due to a continuous interaction and corresponding reflection of the pressure waves at the inner wall surface of the concrete pipes.

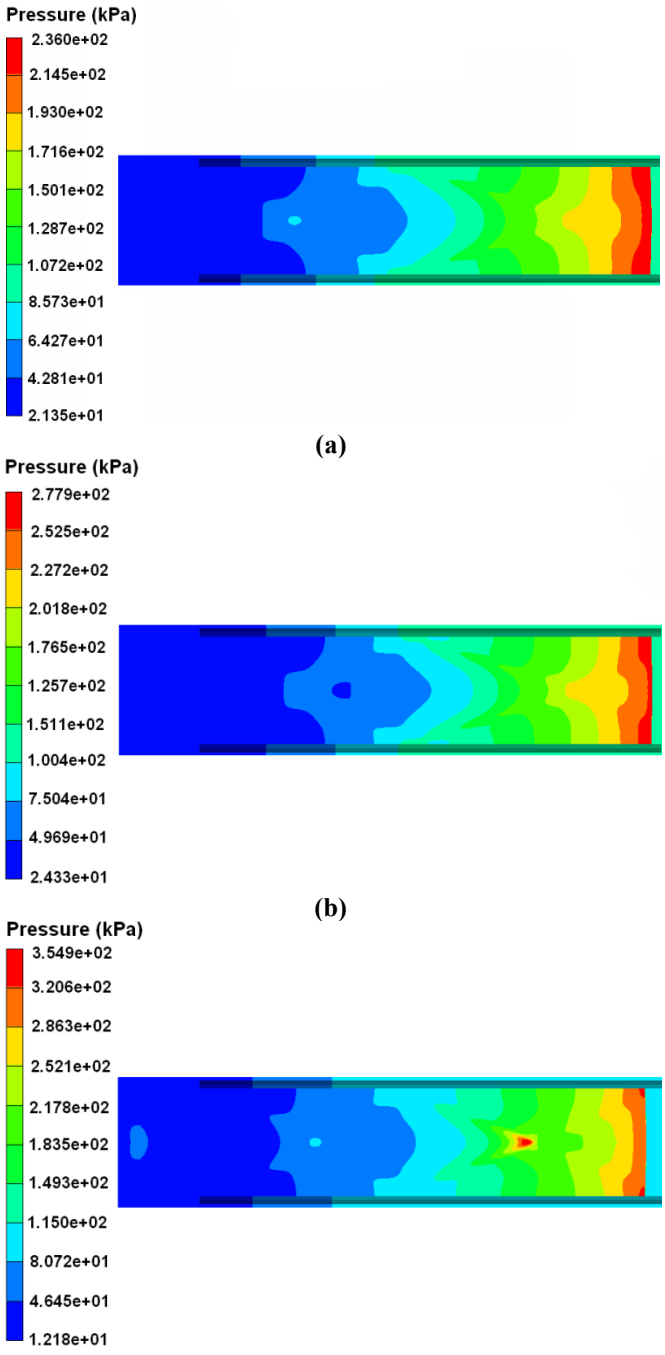

Figure 15-14: Pressure contours at the end of the concrete pipes **(a)** for 75 g of C4 **(b)** 150 g of C4 **(c)** 200 g of C4.

The calculated reflected pressure-time histories for all cases (75 g, 100 g, 150 g and 200 g of C4) are presented in Figure 15-15(a-d). The reflected pressure was calculated at the air grids which were very close to the front skin panel which was modelled at the other end of the concrete pipe. The pressure profiles were measured along the diameter of the tube at equal intervals. The pressure profile for 75 g of C4 was very uniform along the diameter of the concrete pipe (refer Figure 15-15(a)). However, for the remaining charges (100 g, 150 g and 200 g of C4) there were minor fluctuations in the pressure profiles noticed. This may be due to the subsequent reflections from the incoming pressure waves and the chosen boundary condition (a fixed boundary condition was used for the skin panel). The average peak reflected pressure was increased with increasing charge mass.

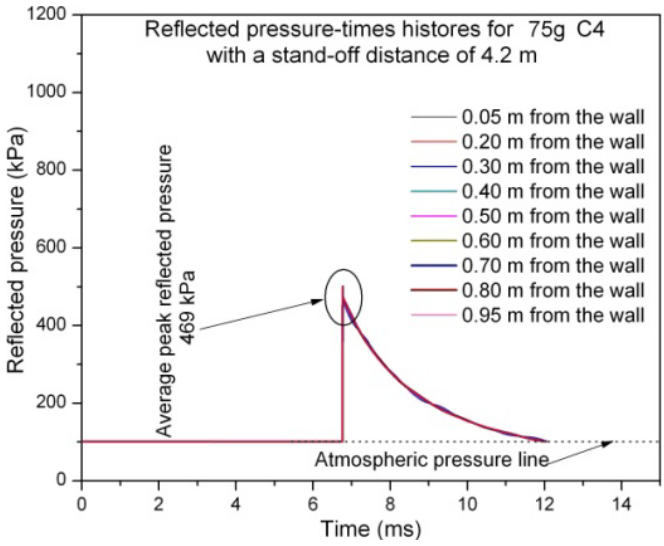

(a)

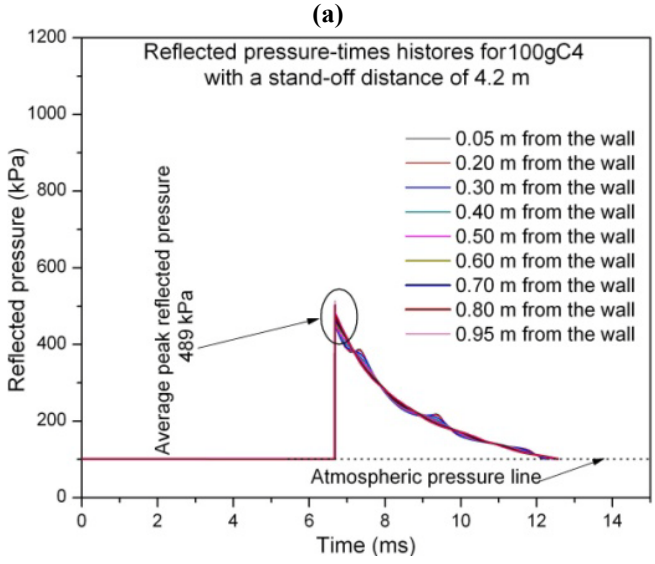

(b)

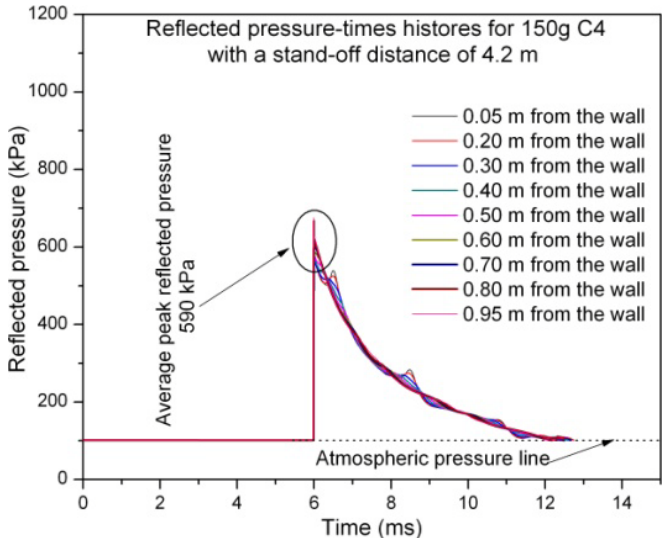

(c)

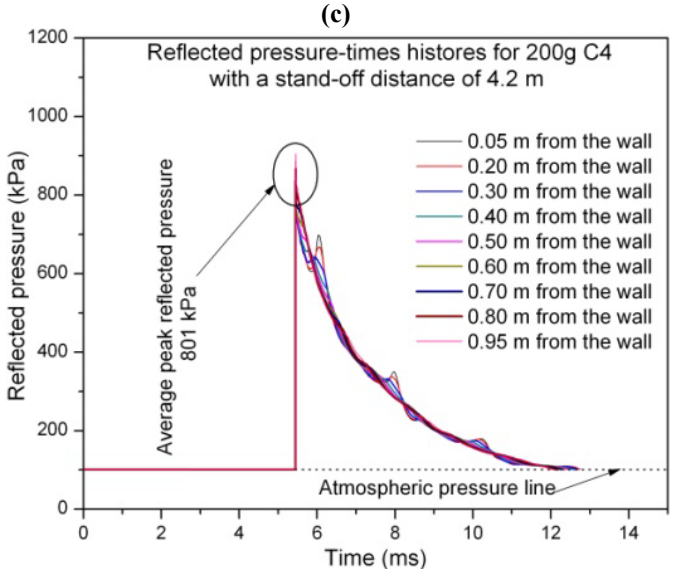

(d)

Figure 15-15: Reflected pressure-time histories **(a)** for 75 g of C4 **(b)** 100 g of C4 **(c)** 200 g of C4 **(d)** 200 g of C4.

The calculated average peak reflected pressure was 469 kPa, 489 kPa, 590 kPa and 801 kPa for 75 g, 100 g, 150 g and 200 g of C4 respectively. Similarly, the corresponding positive duration was increased (5.3 ms, 5.7 ms, 6.2 ms and 7.1 ms for 75 g, 100 g, 150 g and 200 g of C4 respectively). The consolidated reflected blast parameters (time of arrival, reflected pressure, positive duration and the corresponding reflected impulse) from the Autodyn simulations for all cases are presented in Table 15-1.

Table 15-1: Summary of blast parameters from the Autodyn simulations for the stand-off distance of 4.2 m.

Parameters	Charge mass of C4 (g)			
	75	100	150	200
Time of arrival (ms)	6.8	6.6	6.0	5.6
Average peak reflected pressure (kPa)	469	489	590	801
Average positive duration (ms)	5.3	5.7	6.8	7.2
Reflected impulse (kPa.ms)	604	653	908	1264

15. 4. Experimental results

Experimental blast tests have been conducted with two configurations of the beverage cans (configuration 1 and 2 with 25 and 37 beverage cans respectively). Two tests have been conducted for each category. For configuration 1, only two charges have been used for conducting the tests (75 g and 150 g of C4); for the second configuration tests have been conducted with 4 different charge masses (75 g, 100 g, 150 g and 200 g of C4). Similar to the small-scale blast tests the spherical shape of the C4 was ensured by using moulds (refer Figure 15-16).

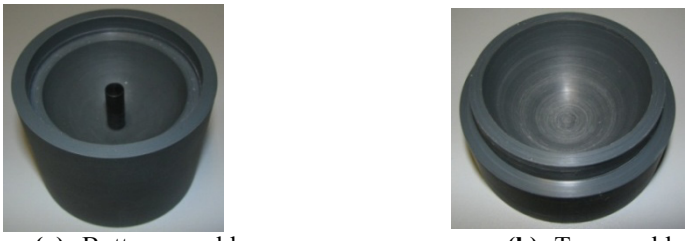

(a) Bottom mould **(b)** Top mould

Figure 15-16: Mould for C4.

For all tests the empty beverage cans were crushed progressively during the explosive loading. After the detonation of C4, the air inside the concrete pipes was accelerated to the other end of the pipe (crushing end) and consequently the air pressure inside the concrete pipes was increased due to multiple reflections on the inner wall of the concrete pipes. As a result the front skin panel was accelerated and subsequently, it crushed the beverage cans. As an example, the progressive deformation patterns of the beverage cans for 150 g of C4 are shown in Figure 15-17 and Figure 15-18 from the high speed cameras 1 and 2 respectively. The high speed images of all tests showed that the front skin panel has distributed the pressure evenly to the inner core structures (beverage cans). However, due to a radial clearance between the concrete pipe and the front skin panel there was a clearing of pressure waves noticed even before the acceleration and the corresponding movement of the front skin panel (inner diameter of the concrete pipe and outer

diameter of the front skin panel were 1.0 m and 0.96 m respectively). This phenomenon can be noticed from the third image of Figure 15-18. The clearing of pressure waves further increased during the crushing of the beverage cans (refer Figure 15-18). During the crushing stages of the beverage cans the movement of the skin panel was uniform and approximately followed the axis of the concrete pipe; furthermore, there was no local bending of the front skin panel noticed. However, when the test specimens reached their maximum deformation length there was a local bending of the front skin panel noticed. This was due to the resistance offered by the beverage cans and the corresponding foam deformation of the front skin panel. This evidence can be noticed from the last image of Figure 15-17. In addition to that significant global bending and corresponding vibration of the rear skin panel were noticed.

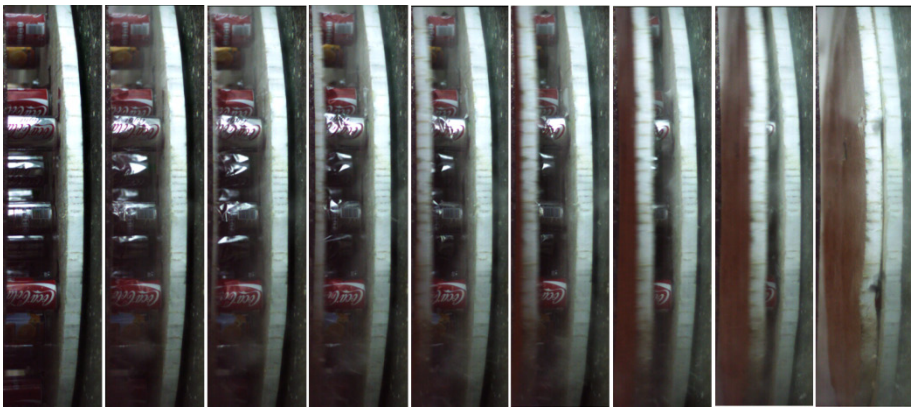

Figure 15-17: Progressive crushing stages of the beverage cans for 150 g of C4 (from high speed camera 1 –right side of the test set-up).

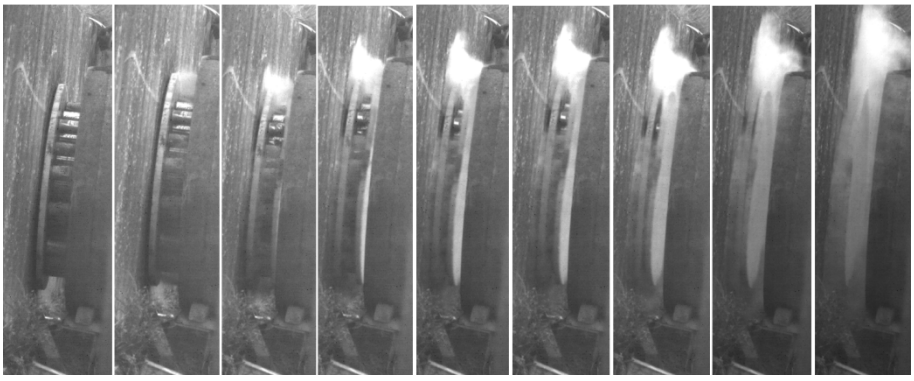

Figure 15-18: Progressive crushing stages of the beverage cans for 150 g of C4 (from high speed camera 2 – left side of the test set-up).

As noticed from the quasi-static and impact test results (from Chapter 3), the crush load was increased significantly when the beverage cans reached their maximum deformation length (approximately 80 mm). Similarly, during the large-scale blast

tests the resistance offered by the test specimens increased at their maximum deformation lengths. However, due to the available energy from the blast the front skin panel was further accelerated. Because of this process the unsupported part of the rear skin panel started to bend towards the concrete wall (global bending) until the rear skin panel touched the concrete wall (the rear skin panel was fixed to the concrete wall through load cells at three points (refer Figure 15-11)). Subsequently, there was significant vibration of the rear skin panel noticed. This was due to the combined effect of the spring back effect of the beverage cans (stored elastic strain energy given back to the front skin panel after achieving their maximum deformation lengths) and the negative phase of the blast. The above discussed phenomena can be understood from Figure 15-19.

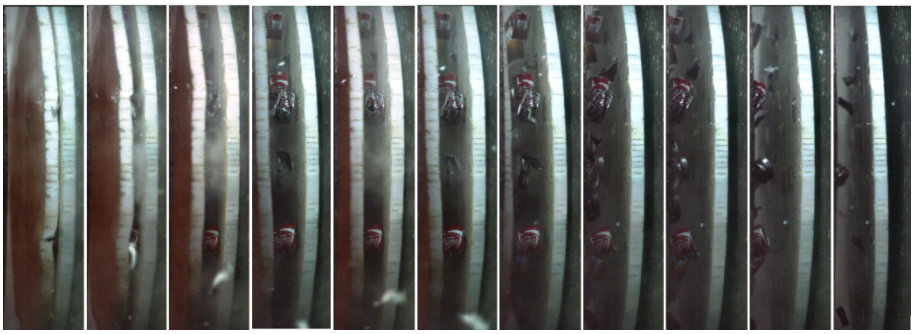

Figure 15-19: Global bending and vibration of the rear skin panel during the crushing process of beverage cans (for 150 g C4).

15. 4. 1. Deformation patterns

As seen from the high speed images of the previous section, the beverage cans showed progressive crushing failure modes for all tests. As an example, global views of the deformation patterns of the beverage cans are shown in Figure 15-20(a-d). A large number of test specimens showed perfect axial crushing. However, several test specimens showed offset crushing modes (approximately 30% of the beverage cans for each test). This was due to the clearing of the pressure wave at one side of the front skin panel (because of the radial clearance between the front skin panel and the concrete pipe). For most of the test specimens, the crushing initiated at the interface location of top-shoulder and mid-wall region and progressed to the bottom of the beverage can. A similar deformation pattern was also observed for the axial impact and small-scale blast tests (refer Chapter 3 and 4). A close inspection of these test specimens showed evidence of the asymmetric failure pattern (diamond mode). Due to a difference in the axial loading the number and length of the triangular lobes were different for each beverage can. Furthermore, the length of the first lobe was always higher than the remaining lobes. This may be due to a higher impact velocity of the front skin panel on these test specimens.

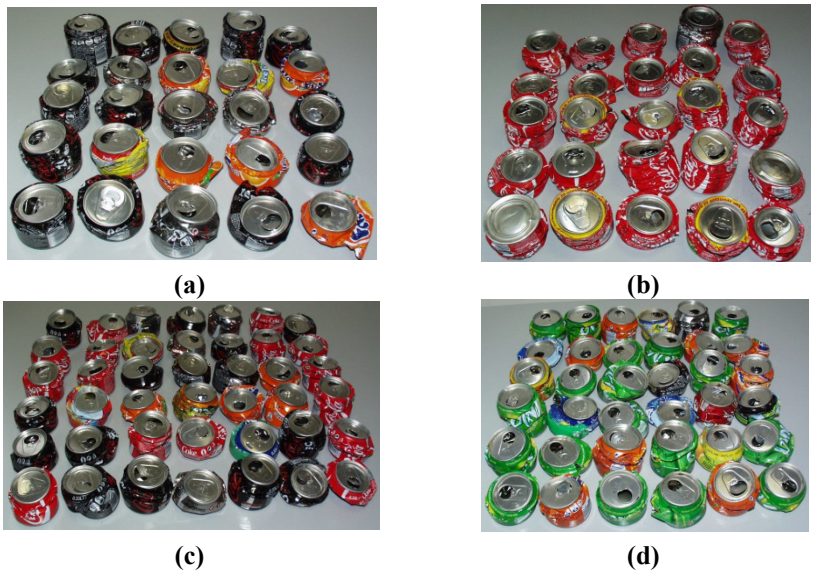

(a) **(b)**

(c) **(d)**

Figure 15-20: (a-b) Deformation pattern of empty beverage cans from two different tests (configuration 1- 25 cans) for 150 g of C4 **(c-d)** Deformation pattern of empty beverage cans from two different tests (configuration 2 - 37 cans) for 150 g of C4.

As an example, the final deformation patterns of a few beverage cans are shown in Figure 15-21(a-d) for 75 g, 100 g, 150 g and 200 g of C4 respectively. From these figures it is very clear that these beverage cans showed asymmetric or diamond mode deformation patterns consistently [6, 7]. The number of triangular lobes varied from a minimum of 7 to a maximum of 13. For lower charge masses such as 75 g and 100 g of C4, there was no significant deformation observed of the top-shoulder and bottom of the beverage cans (refer Figure 15-22(a-b)). However, for higher charge masses such as 150 g and 200 g of C4, there was a significant deformation observed at both top shoulder and bottom of the beverage cans. This may be due to a higher pressure loading on the front skin panel and the corresponding higher impact velocities of the front skin panel. Test specimens which were assembled at the bottom part of the rear skin panel showed a complete bottom out as shown in Figure 15-22(a-b). This was due to the lower clearance between the front skin panel and the concrete pipe. The inner bottom surface of the concrete pipe was used to support the front skin panel and to position the skin panel in front of the test specimens as shown Figure 15-23. Due to that the radial clearance between the concrete pipe wall and the top radius of the front skin panel was higher than for the bottom surface. During the blast loading, the pressure waves at the top surface cleared more easily than at the bottom surface. As a result, there might have been a difference in the reflected impulse for the front skin panel at the top and bottom surfaces. Due to a lower clearance, the bottom surface of the skin panel might have been subjected to a higher impulse and hence have lead to a longer deformation lengths for the test specimens which were assembled at the bottom surface.

Figure 15-21: Final deformation patterns of beverage cans. **(a)** for 75 g of C4 **(b)** for 100 g of C4 **(c)** for 150 g of C4 and **(d)** for 200 g of C4.

Figure 15-22: Final deformation patterns of beverage cans assembled at the bottom surface **(a)** for 100 g of C4 **(b)** for 150 g of C4.

For each case, the deformation lengths of the beverage cans varied in a certain range. However, the average values of the deformation lengths are reported here. After the test, the average deformation length of each beverage can was measured at

four locations on the circumference of the beverage cans at equal intervals. The measured average deformation lengths of the beverage cans are reported in Table 15-2. For configuration 1, the average deformation length of the beverage can was 71.8 mm and 81.3 mm for 75 g and 150 g of C4 respectively. For configuration 2, the average deformation length was 68.6 mm, 75.9 mm, 76.8 mm and 83.3 mm for 75 g, 100 g, 150 g and 200 g of C4 respectively.

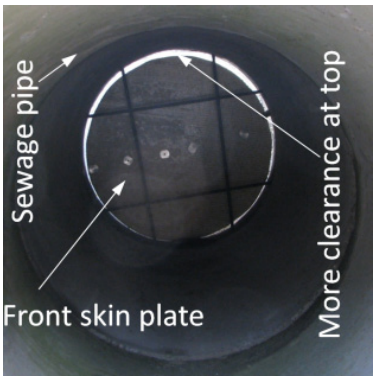

Figure 15-23: Radial clearance between the concrete sewage pipe and the front skin panel.

15. 4. 2. Reflected pressure profiles – a comparison

The very first test with 150 g of C4 showed that the negative phase is a very important parameter to be considered and taken into account for such tests. During the test, immediately after crushing the test specimens, the front skin panel was pulled back along the same path due to the negative phase of the blast. This can be noticed from Figure 15-24. Because of this the front skin panel was thrown back to the other end of the concrete pipe (charge end). Since the negative phase duration was longer, the associated impulse should also be higher. The assembled sensors (three pressure sensors and two accelerometers) and the wiring harness on the front skin panel were damaged after the first test.

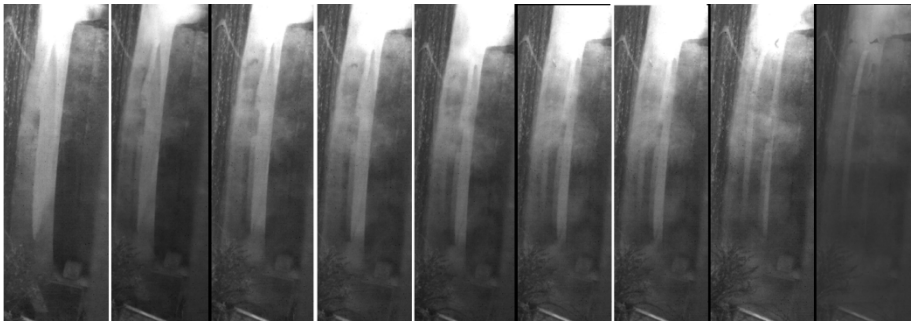

Figure 15-24: Movement of the front skin panel during the negative phase of the blast.

Table 15-2: Summary of crushing parameters.

Charge mass	No. of beverage cans	Stand-off distance	Load cells data	Peak crush load from each load cell	Total peak crush load	Time for load transfer	Average time	Reflected impulse (from Autodyn)	Transferred impulse	Total transferred impulse	Average deformation length
(g)		(m)		(kN)	(kN)	(ms)	(ms)	(kN.ms)	(kN.ms)	(kN.ms)	(mm)
Test with configuration 1 (25 beverage cans)											
75	25	4.2	Load cell 1	25.8	76.7	12.0	11.6	531	110.2	327.1	72.6
			Load cell 2	27.1		11.8			114.2		
			Load cell 3	23.8		11.0			102.7		
			Load cell 1	25.6	73.0	11.6	11.9		118.8	338.9	71.0
			Load cell 2	23.5		12.1			116.5		
			Load cell 3	23.9		11.9			103.6		
150			Load cell 1	25.7	64.3	7.12	6.7	679	62.8	193.2	79.7
			Load cell 2	19.9		6.0			61.9		
			Load cell 3	18.7		6.9			68.5		
			Load cell 1	23.9	58.3	5.8	6.8		70.3	185.6	83.0
			Load cell 2	19.6		7.5			59.4		
			Load cell 3	14.8		7.0			55.9		
Test with configuration 2 (37 beverage cans)											
75	37	4.2	Load cell 1	26.5	69.0	14.2	13.9	531	98.5	287.3	66.2
			Load cell 2	24.3		14.4			101		
			Load cell 3	18.2		12.9			87.8		
			Load cell 1	25.7	72.7	13.8	12.4		87	280.0	71.0
			Load cell 2	27.0		11.3			94		
			Load cell 3	20.0		12.1			99		

Charge mass	No. of beverage cans	Stand-off distance	Load cells data	Peak crush load from each load cell	Total peak crush load	Time for load transfer	Average time	Reflected impulse (from Autodyn)	Transferred impulse	Total transferred impulse	Average deformation length
(g)		(m)		(kN)	(kN)	(ms)	(ms)	(kN.ms)	(kN.ms)	(kN.ms)	(mm)
100			Load cell 1	28.3	80.0	12.4	12.1	599	98.6	298.8	74.5
			Load cell 2	24.3		11.6			98.14		
			Load cell 3	27.7		12.3			102.1		
			Load cell 1	29.7	90.0	10.1	11.5		97.4	273.7	77.3
			Load cell 2	32.4		11.8			88.7		
			Load cell 3	28.8		12.6			87.6		
150			Load cell 1	33.1	89.6	8.4	8.5	679	103.5	288.8	79.5
			Load cell 2	26.7		9.2			92.5		
			Load cell 3	29.8		7.9			92.8		
			Load cell 1	30.1	83.7	8	8.6		89.4	270.6	74.1
			Load cell 2	27.7		7.7			100.7		
			Load cell 3	25.9		10.2			80.5		
200			Load cell 1	29.7	88.9	8.75	8.0	860	88.2	267.9	82.2
			Load cell 2	32.3		8.3			85.2		
			Load cell 3	26.9		7			94.5		
			Load cell 1	30.4	85.2	7.7	8.3		79.8	254.1	84.4
			Load cell 2	28.5		10.5			84.2		
			Load cell 3	26.7		6.9			90.1		
Reference test											
150	-	4.2	Load cell 1	48.5	138.3	5.4	4.4	679	87.9	256.6	-
			Load cell 2	46.9		3.6			83.4		
			Load cell 3	42.9		4.2			85.3		

However, the required information such as the reflected pressure time histories and the corresponding acceleration of the skin panel were captured during the positive phase of the blast. This large negative phase was not expected before conducting the test. Hence, to capture the complete data (reflected pressure histories and the acceleration) from the remaining tests an attempt was made to hold the front skin panel at the crushing end of the concrete pipe after crushing the test specimen. After the assembly of the front skin panel in front of the beverage cans, two vertical and horizontal steel bars (ϕ 18 mm) were inserted before the front skin panel as shown in Figure 15-23. The idea was not to disturb the plane wave front and at the same time during the negative phase the front skin panel should be retained at the crushing end so that the pressure sensors and the accelerometers will be safeguarded. The adopted scheme worked well; however, during the negative phase the impact of the front skin panel on the steel bars damaged the front skin panel as well as the steel bars. As per the assembly sequence, these steel bars have to be removed after each test to place the front skin panel in front of the test specimens (no accessibility on the sides for placing the skin panel); however, after a significant deformation of the steel bars it was tedious to remove them from their positions. Hence, it was decided to check and compare the experimentally measured reflected pressure time histories with the Autodyn simulation results. If the correlation between the experimentally measured and numerically calculated parameters is acceptable, further tests can be continued without using the data measuring sensors. Figure 15-25 shows a comparison of the reflected pressure time histories for 150 g of C4. The average peak reflected pressure measured from three pressure sensors was 550 kPa. Similarly, the average reflected pressure profile from Autodyn is also shown in the same figure. The magnitude of the peak reflected pressure from the Autodyn simulation was 590 kPa; the corresponding positive duration was 6.2 ms. Although there was a good correlation observed for the peak reflected pressure, the reflected impulse from the numerical simulation was significantly higher than from the experimental results (refer Table 15-3).

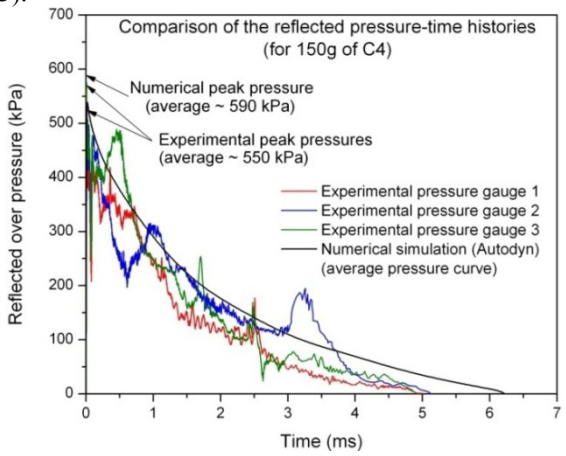

Figure 15-25: Comparison of experimentally measured and numerically calculated reflected pressure time histories for 150 g C4.

Table 15-3:Comparison of the experimental and numerical results.

Parameters	Pressure sensor 1	Pressure sensor 2	Pressure sensor 3
Experimental			
Peak reflected pressure (kPa)	561.5	525.2	530.8
Positive duration (ms)	5.2	4.9	5.1
Reflected impulse (kPa.ms)	627.1	685.3	737.6
Numerical simulation without considering the radial clearance			
Peak reflected pressure (kPa)		590	
Positive duration (ms)		6.2	
Reflected impulse (kPa.ms)		908	
Numerical simulation with considering the radial clearance			
Peak reflected pressure (kPa)		564	
Positive duration (ms)		5.24	
Reflected impulse (kPa.ms)		679	

The experimental average impulse was 683 kPa.ms and the corresponding numerical impulse was 908 kPa.ms (without considering the radial clearance between the concrete pipe and the front skin panel). The difference in the reflected impulse may be due to the clearing of the reflected pressure waves through the radial clearance between the front skin panel and the concrete pipe. Figure 15-26 shows evidence of the clearing of the reflected pressure waves before the front skin panel was accelerated (through the radial clearance between the front skin panel and the inner surface of the concrete sewage pipe). Furthermore, as discussed in the previous section due to a larger clearance at the top part of the front skin panel the corresponding clearance of the reflected pressure wave at that location was significant (refer Figure 15-26).

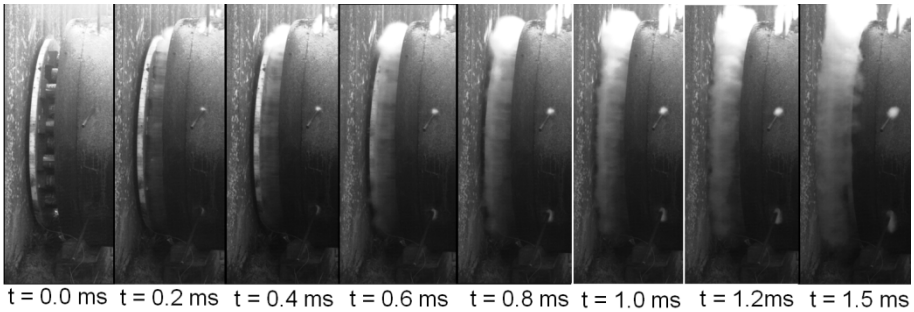

Figure 15-26: Experimental evidences for clearing of reflected pressure waves through the radial clearance (between the front skin panel and the concrete sewage pipe) before the movement of the front skin panel (time t = 0 corresponds to the arrival of the reflected pressure reached at the front skin plate).

In addition to that there was minor leakage of the pressure waves observed through the holes which were used to insert the steel bars (to retain the front skin panel).

However, compared to the clearing of the reflected pressure waves through the radial clearance this effect may be neglected. In order to check the influence of this phenomenon on the total reflected impulse, additional numerical simulations were performed considering the radial clearance (20 mm) between the front skin panel and the concrete sewage pipe. Although an offset clearing was present during the experimental tests a uniform clearance was considered for the numerical simulations. The corresponding schematic representation is shown in Figure 15-27.

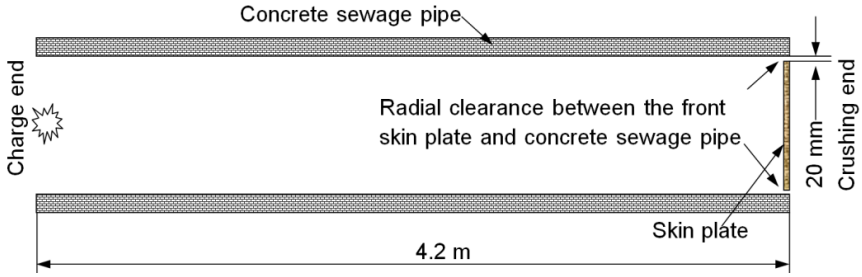

Figure 15-27: Schematic representation showing the radial clearance between the front skin panel and the concrete pipe.

The results from the numerical simulations also confirmed the clearing of the pressure wave. Figure 15-28 shows a magnified view of the pressure front in the radial clearance area. In order to check the clearing pressure magnitude and its duration a pressure time history was calculated at the mid-length of the radial clearance. The magnitude and the corresponding duration of the clearing pressure wave are significant for each charge mass (refer Figure 15-29). The magnitude of the peak clearing pressure was 224 kPa, 239 kPa, 267 kPa and 314 kPa for 75 g, 100 g, 150 g and 200 g of C4 respectively; and the corresponding positive duration also increased with increasing charge mass.

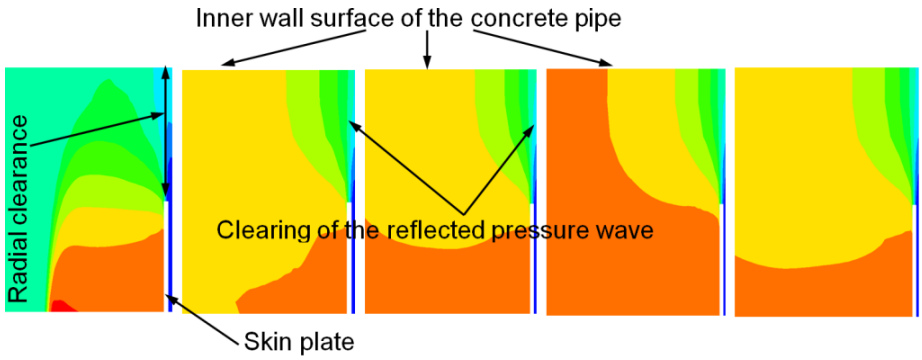

Figure 15-28: Numerical evidence for clearing of the reflected pressure wave through the radial clearance (between the front skin panel and the concrete sewage pipe) for the case with 150 g of C4.

A comparison of the average reflected pressure time histories from the experimental data and the Autodyn simulation is given in Figure 15-30 for 150 g of C4. It can be noticed that the average reflected pressure curve from the numerical simulation follows the experimental mean reflected pressure curve very well. The average numerical profile from this case was different from the previous case (without considering the radial clearance) which was shown in Figure 15-25. The case with the radial clearance showed a fluctuation in the reflected pressure time history similar to the experimental curves. However, for the earlier case the reflected pressure time curve followed a perfect exponential decay. The positive duration from the latter case (with radial clearance) also provided a good correlation for the positive duration (5.1 ms and 5.24 ms for the experimental and numerically calculated values respectively). A comparison of the experimental and the numerical simulation results considering the clearance (between the top skin panel and the concrete sewage pipe inner wall surface) is given in Table 15-3. The calculated reflected impulse from this case was very close to the experimental value (679 kPa.ms and 683.3 kPa.ms for the numerically calculated and experimentally measured impulse respectively).

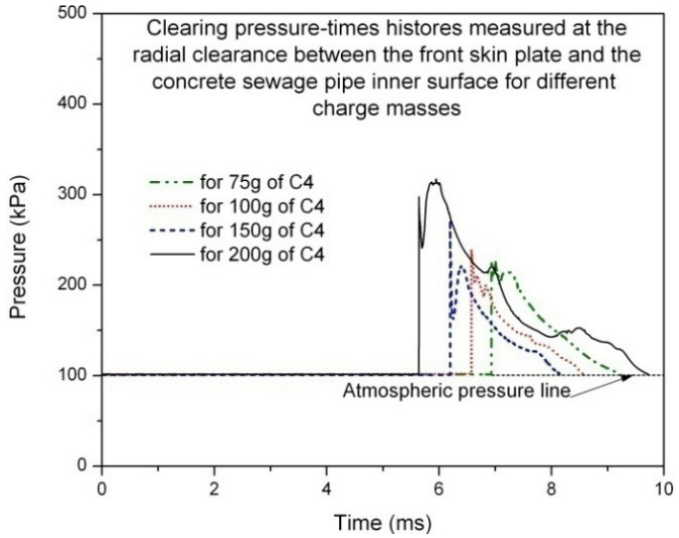

Figure 15-29: Calculated clearing pressure time histories at the radial clearance between the front skin panel and the inner surface of the concrete pipe.

The numerical simulation results from the case with radial clearance (between the front skin panel and the concrete pipe) encouraged to continue the tests without measuring the reflected blast parameters. Similar to 150 g of C4, the numerical simulations were conducted for the remaining cases. The corresponding average reflected parameters are given in Table 15-4.

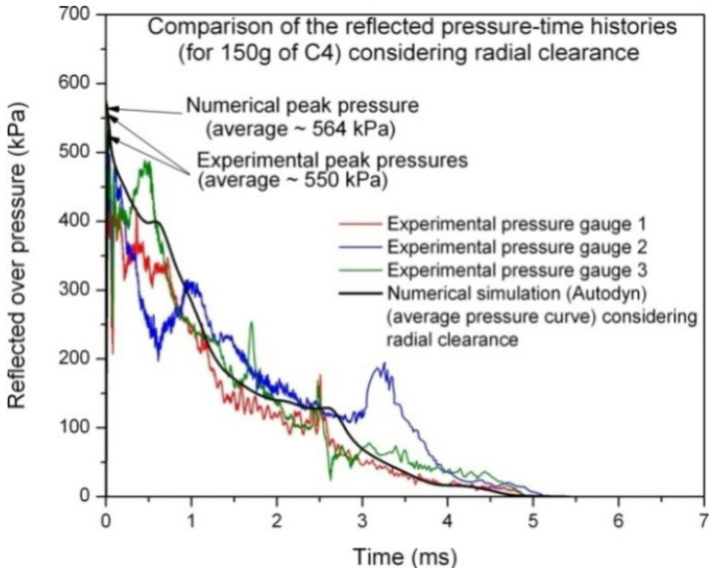

Figure 15-30: Comparison of the experimentally measured and numerically calculated (reflected) pressure time histories for 150 g C4 considering a radial clearance between the front skin panel and concrete pipe.

Table 15-4: Summary of blast parameters from Autodyn simulations considering a radial clearance between the front skin panel and the concrete pipe.

Parameters	Charge mass of C4 (g)			
	75	100	150	200
Time of arrival (ms)	6.8	6.6	6.0	5.6
Average peak reflected pressure (kPa)	446	469	564	724
Average positive duration (ms)	4.6	4.9	5.24	6.5
Reflected impulse (kPa.ms)	531	599	679	860

15. 4. 3. Crushing load curves

As an example, the experimentally measured (transferred) load-time histories from the dynamic load cells for four different charge masses (75 g, 100 g, 150 g and 200 g) with two configurations are given in Figure 15-31(a-d). It can be seen from these figures that the scatter in the signals was low (except the case with 150 g of C4) and the data measured by the load cells were consistent. The performance of the configuration 1 (with 25 beverage cans) was significant for 75 g of C4 loading case. The positive duration of the blast of 4.6 ms was extended to approximately 12 ms. The average peak crush load transferred to the non-sacrificial structure (concrete wall) was 74.85 kN from two tests. The corresponding average transferred impulse was 333 kPa.ms. However, the efficiency of configuration 1 decreased with increasing charge mass.

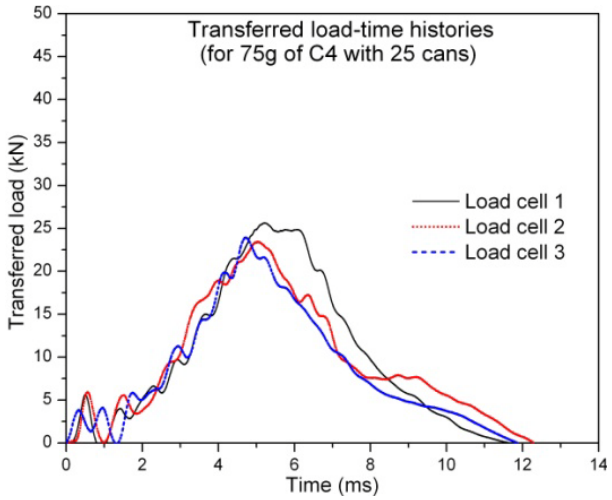
Transferred load-time histories
(for 75g of C4 with 25 cans)
Transferred load (kN)
Time (ms)
Load cell 1
Load cell 2
Load cell 3

(a)

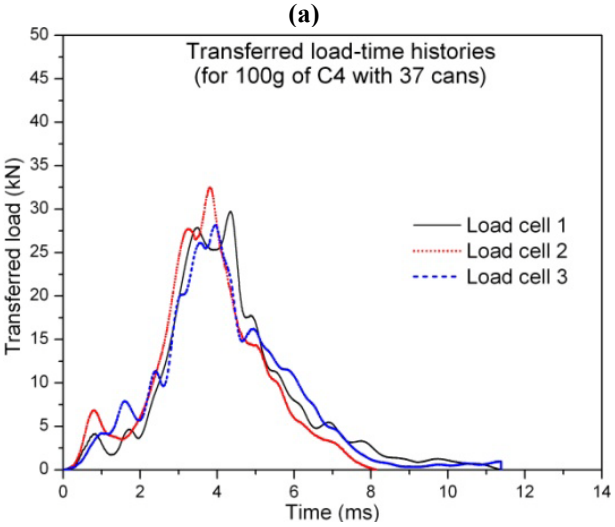
Transferred load-time histories
(for 100g of C4 with 37 cans)
Transferred load (kN)
Time (ms)
Load cell 1
Load cell 2
Load cell 3

(b)

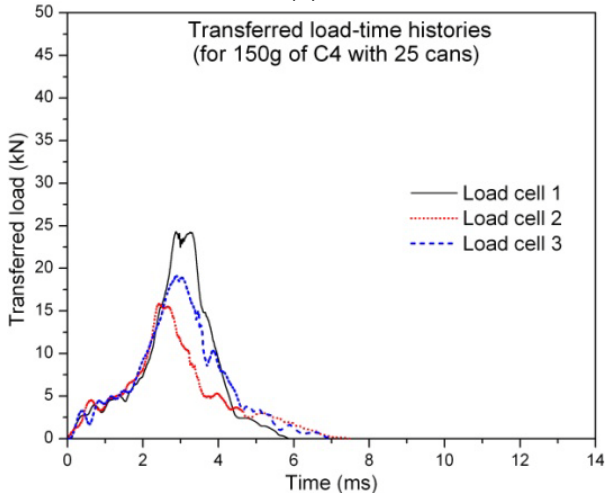
Transferred load-time histories
(for 150g of C4 with 25 cans)
Transferred load (kN)
Time (ms)
Load cell 1
Load cell 2
Load cell 3

(c)

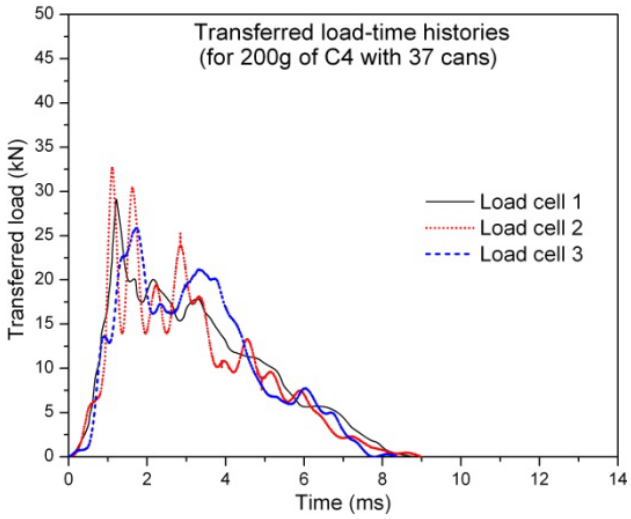

(d)

Figure 15-31: Transferred load histories to the non-sacrificial structure **(a)** 75 g of C4 with 25 beverage cans **for (b)** 100 g C4 with 37 cans **(c)** 150 g C4 with 25 cans **(d)** 200 g of C4 with 37 cans.

For example, for the case with 150 g C4 the duration for the transferred load (crushing duration) significantly reduced to 6.75 ms which was only slightly higher than the positive duration of the blast (5.24 ms). The reason was that the 25 beverage cans (configuration 1) were not sufficient enough to dissipate the total energy from the blast. In addition to that the bending stiffness of the rear skin panel played a major role. The initial crushing stages of this case showed a progressive crushing of the beverage cans until the maximum deformation length. When the beverage cans reached their maximum deformation length a significant quantity of elastic strain energy was absorbed. However, the remaining energy from the blast further accelerated the front skin panel towards the rear skin panel. As a result the local stiffness of the front skin panel reduced due to the presence of the test specimens and hence local bending was observed throughout the front skin panel. This can be noticed from Figure 15-34. A similar local bending effect was also observed for the rear skin panel (refer Figure 15-34).

Subsequently, the overhanging part of the rear skin panel came in contact with the concrete wall. Thus a significant quantity of reaction load was transferred to the concrete wall through the rear skin panel directly to the concrete wall. Therefore, the calculated impulse from the measured signals (integrated load time histories measured from the load cells) was significantly lower than the reflected impulse on the front skin panel. At the end of the process, the stored elastic strain energy in the beverage cans was given back to the front skin panel. In addition to that the entrapped air inside the beverage cans might have played a role for the spring back of the test specimens. A similar result was also observed for other charge masses

(100 g and 200 g of C4). For 200 g of C4 due to the high reaction load, the rear skin panel started to bend globally from the initial stages of crushing and subsequently it was in contact with the concrete wall (refer Figure 15-33).

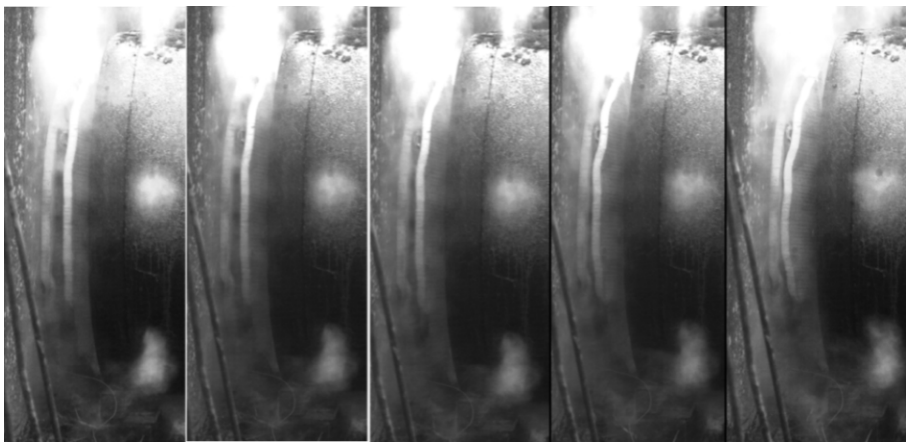

Figure 15-32: Experimental evidence for the local bending of the front skin panel and contact of rear skin panel with the concrete wall.

Figure 15-33: Experimental evidence for a global bending of the rear skin panel and subsequent contact with the concrete wall.

The average peak crush load of configuration 2 showed a clear indication of strain rate dependency. The peak crush loads of the configuration 2 were 70 kN, 85 kN, 86.7 kN and 87 kN for 75 g, 100 g, 150 g and 200 g of C4 respectively. However, for the configuration 1, the peak crush load for 75 g of C4 (74.8 kN) was higher than for 150 g of C4 (61.3 kN). This may be due to the difference in the material and geometry parameters of the chosen beverage cans. For quasi-static and impact tests the chosen beverage cans were restricted to only one manufacturer. However, due to the large needed quantity, selection of the beverage cans from a single manufacturer was difficult. The calculated average parameters for all cases are given in Table 15-2.

In order to compare the effectiveness of the proposed sacrificial cladding structure and to understand the behaviour of the skin panels a blast test was conducted only on the skin panels without any test specimens (for 150 g of C4). Two sandwich panels (front and rear) were placed next to each other. The results from this experiment showed no significant deformation of the skin panels and the corresponding load-time histories are shown in Figure 15-34. It can be noticed that the use of beverage cans significantly altered a high magnitude load to a low magnitude load (approximately 138.3 kN to 85 kN).

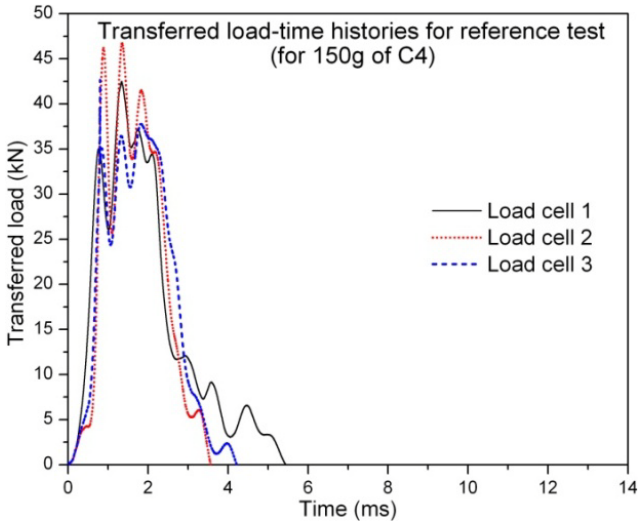

Figure 15-34: Transferred load-time histories for the reference test (with 150 g of C4).

The blast tests with the concrete pipes showed that the limiting charge for the large-scale blast tests was 150 g of C4. A very first test with 200 g of C4 initiated two major longitudinal cracks at the charge end; further tests with the same charge mass of C4 showed that propagation of the cracks for longer lengths. Finally, the concrete pipe at the charge end split into two halves (refer Figure 15-35(a-c)).

(a) **(b)** **(c)**

Figure 15-35: Failure of the concrete sewage pipe **(a)** Propagation of the longitudinal crack **(b)** Evidence for water ingress **(c)** Complete failure.

In addition to the blast pressure the water ingress into these pipes might have caused this problem (the used concrete sewage pipes were not brand new ones; these tubes were lying in open atmosphere for few years).

15. 5. Decoupled numerical simulation and results

15. 5. 1. Modelling

Out of all cases, the experiments with 150 g of C4 with 25 cans showed a significant difference between the reflected and transferred impulse. Hence, in order to investigate this phenomenon and to understand the crushing behaviour of the empty beverage cans in detail, a decoupled numerical simulation was conducted for the case with 150 g C4 with 25 cans. The modelling details of the large-scale blast test were very similar to the small-scale decoupled numerical study which was discussed in Chapter 4. The modelling details of the beverage can (used elements, geometry and the materials details, used material model (*Johnson-Cook*)) were similar to the one which was discussed in Chapter 3. It was assumed that the energy absorbed by the front and rear skin panels was negligible compared to the beverage cans. Hence, for the front and rear skin panels the material properties of glass epoxy were adopted (refer Table 4-12 of Chapter 4). The numerical modelling of the sandwich composite skin panel was done as per the assembly sequence. The top and bottom composite skin faces were modelled with shell elements (refer Figure 15-36). The meshed shell elements were located at the centre of the thickness of each composite laminate (refer Chapter 4 for the remaining details of the modelling of the skin panels). The strength model of the divinycell P foam was represented by means of the compressive crush characteristics (refer Figure 15-37). It was assumed that the top and bottom composite plates and divinycell P foam are tied together due to the 3D stitch by aramid fibres. This was also supported by the experimental observations. Accordingly a tied connection was established at the interfaces of all these parts. Similar to the experimental conditions, the dynamic load cells were modelled as rigid bodies to measure the load time histories. The concrete wall was modelled as a rigid body; subsequently a reference point was introduced to capture the total impulse transferred to the concrete wall. Accordingly, three more rigid bodies were modelled as per the dimensions of the load cell (refer Figure 15-36). An equivalent triangular time dependent pressure was applied to the top face of the top skin panel [8-11]

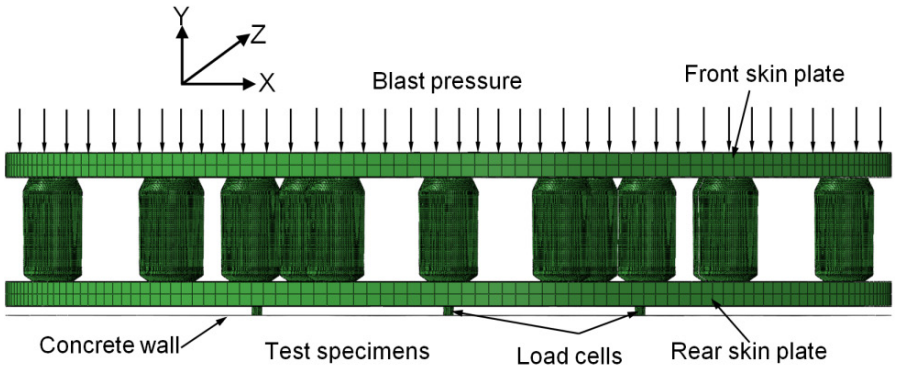

Figure 15-36: Finite element modelling details.

To simulate the axial blast load only in vertical direction the translational degrees of freedom of the aluminium skin panel in "X" and "Z" axis was arrested; the rotational degree of freedom with respect to the "Y" axis was also arrested and the bending of the front and rear skin panels with respect to the "X" and "Z" axis were allowed. The bottom surfaces of the beverage cans were connected to the top skin of the rear skin panel using "*tie*" constraints. Similar connections were established for the load-cells to the rear skin panel and the concrete wall (refer Figure 15-36). In order to represent the fixed concrete wall all degrees of freedom of the rigid wall were arrested. The analysis was carried out for the equivalent triangular impulse load for 150 g C4. The deformation of the beverage can was obtained from the displacement of the top skin panel and the reaction load was extracted from the load cells. The commercially available explicit code ABAQUS V6.9-2 was used to carry out this analysis [12, 13].

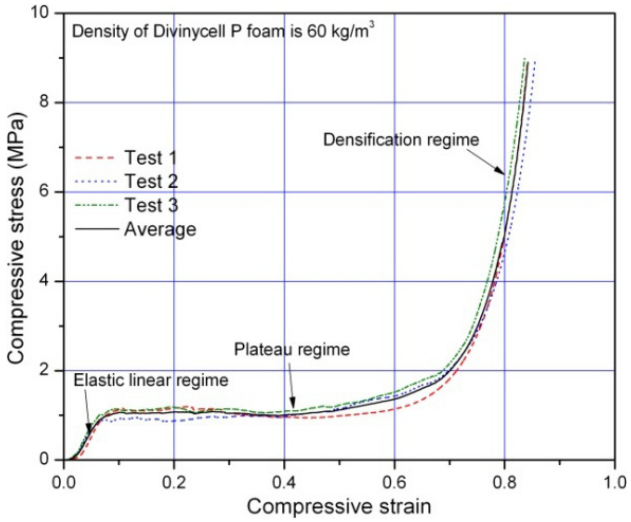

Figure 15-37: Compressive crushing characteristic of the divinycell P foam.

15. 5. 2. Results

The results from this numerical simulation showed that all beverage cans had undergone uniform and progressive crushing failure modes (refer Figure 15-38, Figure 15-39 and Figure 15-40).

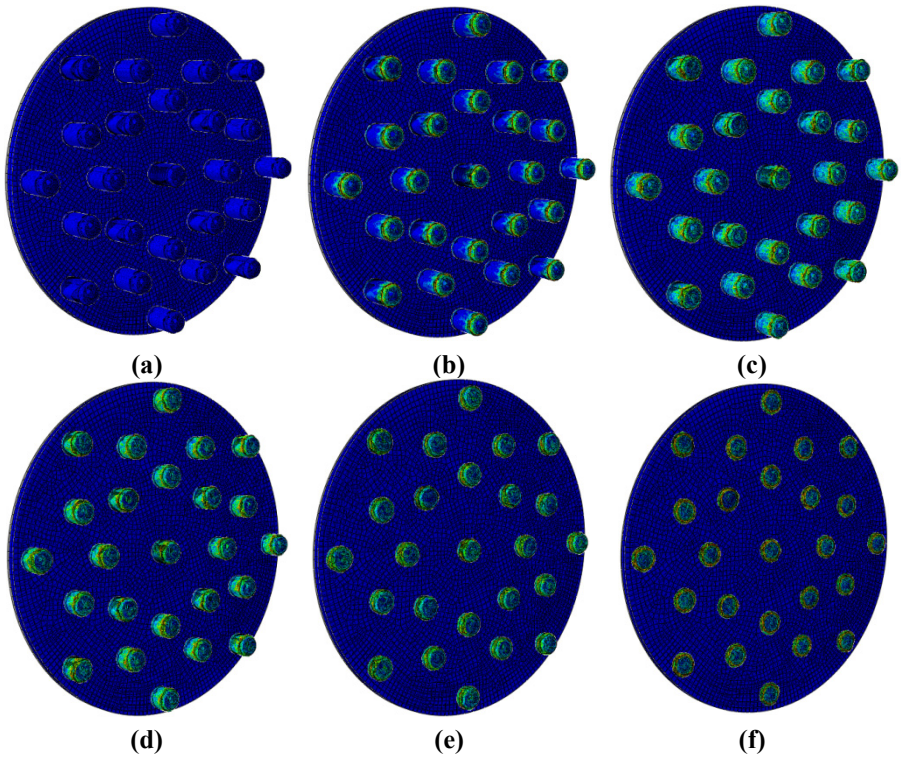

Figure 15-38: Progressive deformation patterns of the empty beverage cans subjected to 150 g of C4 pressure loading (isometric view).

For all beverage cans the initiation of crushing started at the interface location of the top-shoulder and mid-wall region (refer Figure 15-38(a-f) and Figure 15-39). Unlike the experimental results, the crushing length of the beverage cans was very uniform. This was due to the applied time dependent uniform pressure on the top face of the front skin panel. The initial time increments showed that the front skin panel underwent a significant compression. Due to the applied blast pressure on the front face of the front skin panel the core foam reached its densification regime and it continued to stay in that regime until the test specimens reached their maximum deformation length. There was no significant compression observed in the rear skin panel until the core foam of the front skin panel reached its densification regime. The compression of the core foam of the rear skin panel started when the front skin panel reached its densification regime. This evidence can be noticed from Figure 15-39. However, the compressive behaviour of the core foam was very uniform

through the entire surface of both front and rear skin panel. When the deformation length of the beverage cans reached its maximum value, the entire rear skin panel started to bend. Subsequently, the rear skin panel came into contact with the concrete wall. A similar evidence was also noticed from the experimental results. Furthermore, a local compression of the skin plates (both front and rear) was significant at the mounting locations of the test specimens (refer Figure 15-40).

Unlike the experimental results, the spring back lengths of the beverage cans were very less after reaching their maximum deformation length. This may be due to the effect of entrapped air inside the beverage cans. As noticed from Chapter 3 the influence of air inside the beverage can is significant when the deformation length of the beverage can reaches beyond 80 mm. For this case the high speed images of the experimental tests showed that all beverage cans reached their maximum deformation length (rear face of the front skin panel was in contact with front face of the rear skin panel; the same evidence of bottoming out of the beverage cans can be noticed from Figure 15-17 and Figure 15-18). However, the measured final deformation lengths were lower than the bottom out length of the beverage can (refer Table 15-2). Furthermore, the final experimental deformation patterns of the beverage cans (refer Figure 15-21) were very similar to the impact cases (a significant spring back or expansion of triangular lobes due to entrapped air inside the beverage cans). This proves that the entrapped air inside the beverage cans played a role for the spring back and the corresponding final deformation lengths of the beverage cans. Conducting a numerical simulation with air inside the beverage can needs a very high computing facility. In contrast, the chance of entrapped of air inside the beverage cans for this case would seem less because of the observed high flexibility of the front and rear skin panels. However, a thorough numerical analysis is required to conclude on this statement.

Further investigations on the front and rear skin panels showed that these skin panels were severely stressed at the mounting locations and the beverage cans crushing areas. As an example, the fibre and matrix failure modes of the bottom face of the rear skin panel and bottom face of the front skin panel are shown in Figure 15-41(a-d) and Figure 15-42(a-b). It can be noticed that the tensile failure of fibres and matrix were significant. The elements at the load cell mounting locations showed a complete failure. The same evidence was observed from the experimental results; the foam core at the mounting locations delaminated from the face plates. Similarly, for the front skin panel high chances of failure can be expected for the areas which were in contact with the beverage cans (the assembly configuration 1 can be observed from Figure 15-42). Similarly, the stress distribution of the foam core (divinycell P foam) of the rear skin panel is shown in Figure 15-43.

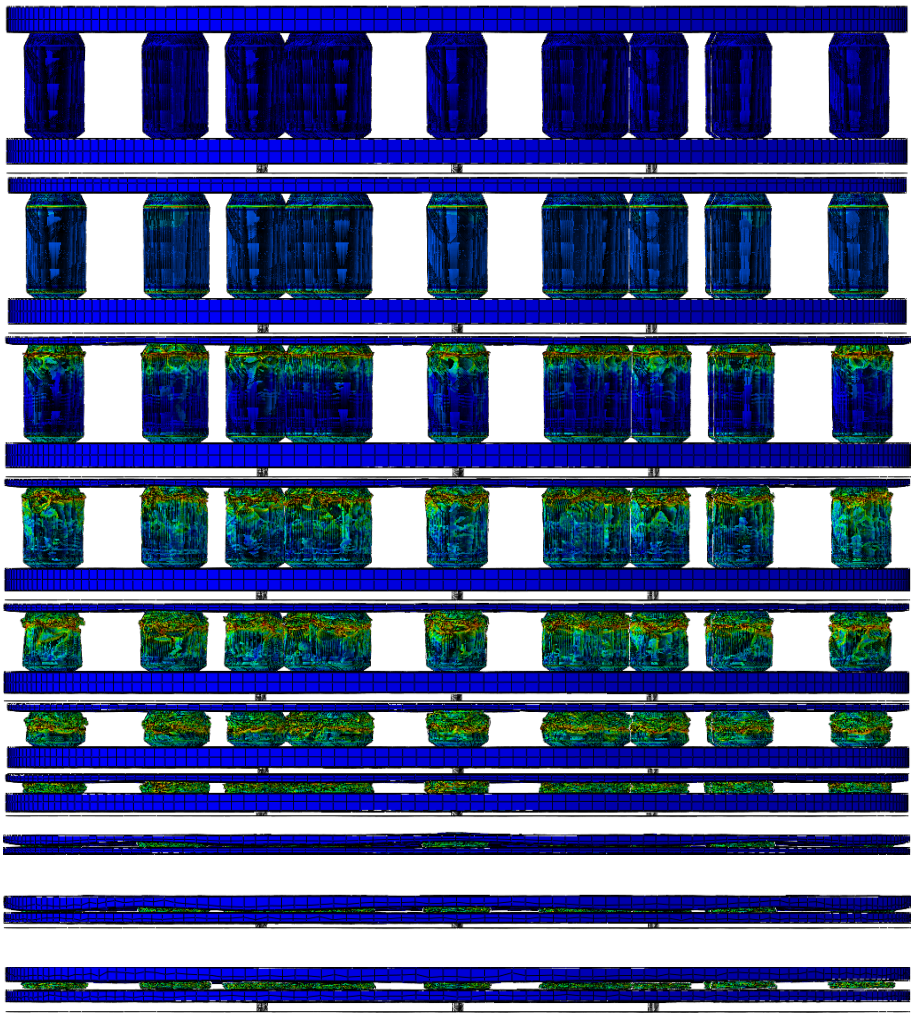

Figure 15-39: Progressive deformation patterns of the empty beverage cans subjected to 150 g of C4 pressure loading (side view).

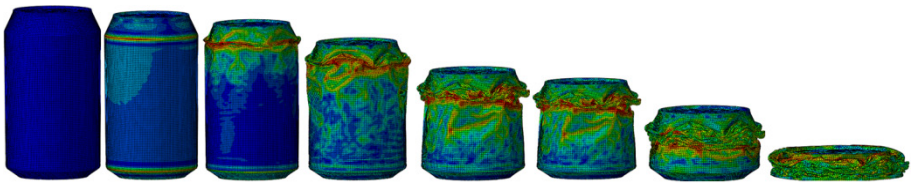

Figure 15-40: Progressive deformation patterns of an empty beverage can subjected to 150 g of C4 pressure loading.

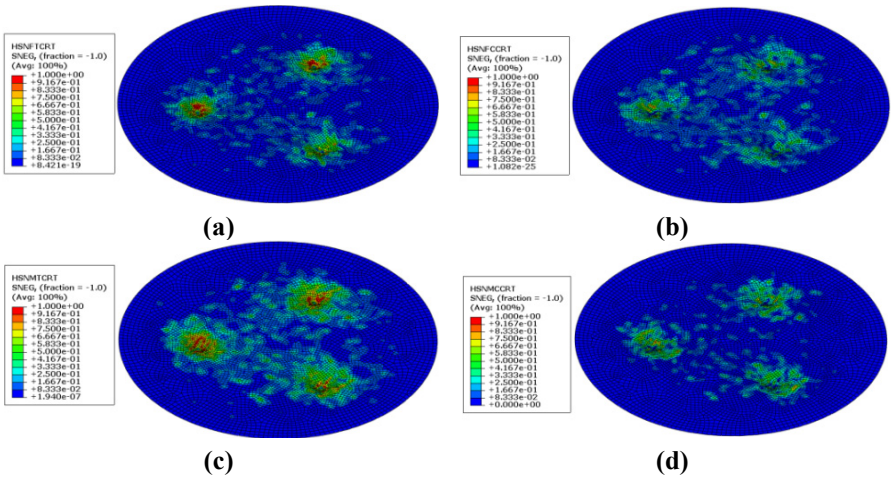

Figure 15-41: Tensile and compressive failures of back face of rear skin panel (a) fibre tensile failure (b) fibre compressive failure (c) matrix tensile failure (d) matrix compressive failure (magnification factor 5).

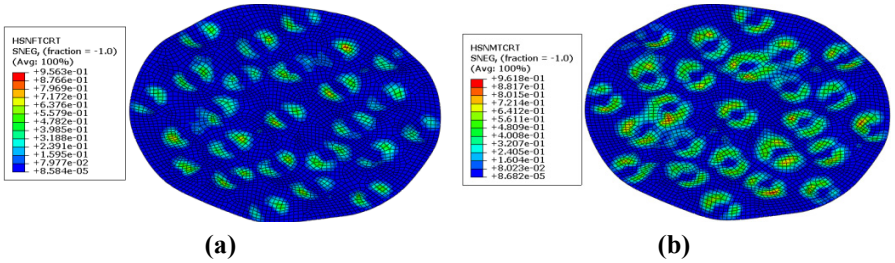

Figure 15-42: Fibre and matrix failures of bottom face of the top skin panel (a) fibre tensile failure (b) matrix tensile failure (magnification factor 5).

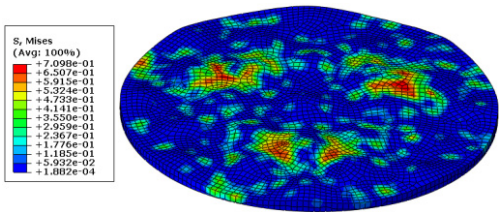

Figure 15-43: Stress distribution on core foam (divinycell P foam) of the rear skin panel (magnification factor 5).

The numerically calculated load time histories from the three load cell positions were approximately identical. As an example, one of the numerically calculated load time histories is compared with the experimental results in Figure 15-44. The calculated peak crush load from the numerical simulation for all three load cell positions was approximately 26.1 kN; subsequently, the total magnitude of the peak crush load was 78.5 kN. This value can be very well compared with the experimental average value 81.4 kN. However, the slope to reach the peak crush

load from the numerical simulation was significantly different from the experimental results (refer Figure 15-44). This may be due to a difference in the sequence of the experimental and numerical deformation patterns. As noticed in the previous sections, the clearing of the reflected pressure wave (between the concrete pipe and the front skin plate) led to relatively shorter deformations lengths for the test specimens which were assembled at the top surface compared to the test specimens which were assembled at the bottom surface of the rear skin panel. This also means that the initiation and the corresponding progressive crushing stages of all test specimens were not the same. Due to a higher reflected pressure at the bottom surface of the front skin panel the crushing initiation of the beverage cans which were assembled at the bottom surface of the rear skin panel might have started earlier than from the rest of the test specimens; gradually further crushing initiation progressed to the test specimens which were assembled at the top surface of the rear skin panel. The sequence of crushing of test specimens from the lower surface to the upper surface might have caused a lower slope to reach the peak crush load. However, in the numerical simulation the slope to reach the peak crush load was higher because of the applied uniform pressure and the corresponding simultaneous crushing of the test specimens. In addition to the above, the difference in the initial stiffness provided by the front skin panel might have caused this increasing slope. As mentioned earlier due to the unavailability of the material properties of glass polyester (of the used sandwich composite skin panels), the glass epoxy material properties were adopted for the numerical simulation. Furthermore, the effect of "Z" stitches is not included in the numerical model.

Furthermore, the drop in the post peak crush load was significant compared to the experimental results. Unlike the experimental results, the numerical simulation showed two peaks and the magnitude of the second peak was higher than the first one. The first peak corresponded to the initiation of progressive deformation of the beverage cans; the second peak corresponded to the additional load transferred during the global bending and subsequent contact of the rear skin panel with the concrete wall. The non-consideration of the negative phase in the numerical model might have attributed for a higher magnitude. As seen from the previous sections the front skin panel was pulled back to the charge end immediately after achieving the maximum deformation lengths. Subsequently, only one peak was observed consistently for all experimental tests. This again proves that the negative phase cannot be excluded to predict the correct crushing parameters for this case.

The total duration of the crushing event from the numerical simulation (4.9 ms) was shorter than the experimental average value (6.75 ms). In addition to that the total deformation length of the beverage cans from the numerical simulation was higher than the experimental results (81.3 mm and 98.7 mm for the experimental and numerical deformation lengths respectively). This also shows that the influence of

the entrapped air inside the beverage cans cannot be neglected to predict the accurate crushing parameters. As noticed from the Chapter 3 for the impact case, the entrapped air inside the beverage can extended the impact duration. The load measured from the rigid body showed that a total impulse value of 537 kN.ms was transferred to the concrete wall. This value was higher than the applied impulse (an equivalent triangular impulse load on the top face of the top skin panel). The reason for the additional impulse was the spring back effect of the beverage cans (stored elastic energy during crushing was given back to the front skin panel). A comparison of the experimental (average values) and numerical parameters is given in Table 15-5.

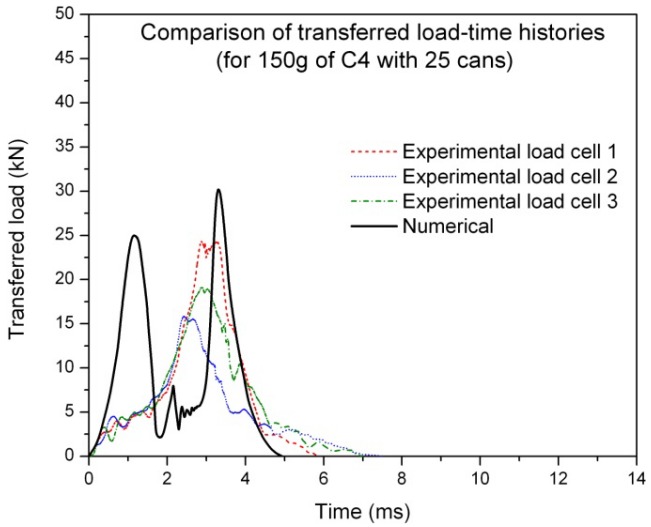

Figure 15-44: Comparison of the experimentally measured and numerically calculated load time histories.

Table 15-5: Comparison of the experimental (average) and numerical results.

Parameters	Experimental average	Numerical
Reflected impulse (kN.ms)	491.6	491.6 (input)
Peak crush load (kN)	81.4	78.5
Total impulse duration (ms)	6.75	4.9
Transferred impulse through load cells (kN.ms)	189.4	207.5
Total transferred impulse to the non-sacrificial structure (kN.ms)	Not measured	540
Deformation length of the test specimens (mm)	81.3	98.7

15. 6. Conclusions

To understand the blast mitigation performance of the proposed sacrificial cladding structure using empty metal beverage cans and sandwich skin panels, large-scale air blast experiments have been conducted with different charge masses of C4 (75 g, 100 g, 150 g and 200 g). Two configurations of beverage cans were used to perform the blast tests (configuration 1 and 2 with 25 and 37 beverage cans respectively). To create a perfectly plane shock wave the shock tube concept was adopted using concrete sewage pipes. The coupled numerical simulations were carried out in Autodyn v12.1 in order to calculate the minimum length of the tube which provides the perfectly plane shock wave at the other end. The results from the numerical simulations showed a good correlation with the experimental data. Furthermore, in order to understand the crushing process of the beverage cans a decoupled numerical analysis was carried out in Abaqus v6.9-2. For all tests, the empty beverage cans showed a progressive deformation pattern. From the conducted experimental and numerical results the following conclusions can be made.

- The adopted concept of using two segments of concrete sewage pipes (4.2 m in length) provided a perfectly plane shock wave at the other end of the tube (crushing end). However, the set-up using the concrete pipes is limited to the charge mass of 150 g of C4 (this also depends on the tensile failure strength of the combined concrete matrix and the steel fibres). A higher charge mass of C4 can be used for tubes which are made with higher strength material such as steel. Furthermore, the negative phase of such experiments plays a major role. It was observed that the front skin panel pulled back in the same line of crushing during the negative phase. Hence, proper precautions should be taken to prevent the breakage of data measuring sensors and their wiring harness.
- The coupled numerical simulations using Autodyn predicted very close results compared to the experimental results. The peak reflected pressure, positive duration and the corresponding reflected impulse from the coupled numerical simulations were very close to the experimental results (for the case with 150 g of C4). The radial clearance between the front skin panel and the inner surface of the concrete pipe played a significant role for the total reflected impulse. Due to the clearing of the reflected pressure wave (through the radial clearance) the total reflected impulse was reduced. Hence, to predict accurate blast parameters the same experimental boundary conditions have to be used in the numerical model.
- For all charge masses, the beverage can showed uniform and progressive crushing deformation patterns. A large number of test specimens showed the asymmetric deformation mode (diamond mode). For all tests, several specimens experienced offset loading due to the pressure difference

between the top and bottom surface of the front skin panel (due to the clearing of reflected pressure waves associated with the radial clearance between the front skin panel and the concrete pipe). The use of empty beverage cans reduced the peak load which was transferred to the non-sacrificial structure (concrete wall) and extended the crushing time significantly.

- For higher charge masses such as 100 g, 150 g and 200 g of C4, the proposed number of beverage cans (25 and 37) were not sufficient to absorb all the energy from the blast. Due to the higher energy, local bending of the front skin panel and global bending of the rear skin panel were noticed. Due to that the rear skin panel came into direct contact with the concrete wall for a longer time. As a result, a significant part of the load was directly transferred to the concrete wall. Therefore, there was a difference in the reflected impulse and the transferred impulse noticed. Hence, for the future tests the rear skin panel (sandwich composite panel) should be replaced with an alternative material/structure with an adequate bending stiffness.
- During the crushing of the beverage cans it was observed that a significant quantity of elastic strain energy was stored when the beverage cans reached their maximum deformation lengths and it was given back to the front skin panel. Hence, the final deformation lengths of the beverage cans were shorter due to the spring back effect. In addition to the elastic strain energy the air entrapped inside the beverage can might have played a role.
- The conducted decoupled numerical simulation showed clear evidence that the crushing started at the interface location of top-shoulder and mid-wall region of the beverage cans. Unlike the experimental results, the deformation length of all the beverage cans was the same due to the applied uniform time dependent reflected pressure. Furthermore, the compression of the foam core of the skin panels increased with increasing deformation length of beverage cans. Similar to the experimental results, the transferred impulse measured from the load cells showed a difference with the reflected impulse due to the contact of the rear skin panel with the concrete wall.
- The calculated impulse at the load cell positions from the numerical simulation was higher than from the experimental results. Furthermore, unlike the experimental results two peaks in the load time histories were noticed. This may be due to the oblique loading of the beverage cans due to the clearing of the reflected pressure wave and non-consideration of the negative phase in the numerical simulation. Hence, to predict the accurate crushing parameters the correct loading and boundary conditions should be captured in the numerical model.

From the above results, it can be concluded that the empty metal beverage cans can be considered as a potential member to protect civil engineering structures from air blast load. However, further investigations on these beverage cans under large-scale blast testing are absolutely necessary to cater into different blast loading regimes.

Bibliography

[1]. http://www.acrosoma.com (dated 02-06-2011).
[2]. Autodyn, *Theory manual.* M/s Century Dynamics, 2007.
[3]. Palanivelu, S., Van Paepegem, W., Degrieck, J., Reymen, B., Ndambi, J.-M., Vantomme, J., Kakogiannis, D., Wastiels, J. and Van Hemelrijck, D., *Close-range blast loading on empty recyclable metal beverage cans for use in sacrificial cladding structure.* Engineering Structures, 2011. **33**(6): p. 1966-1987.
[4]. Chapman, T. C., Rose, T. A. and Smith, P. D., *Blast wave simulation using AUTODYN2D: A parametric study.* International Journal of Impact Engineering, 1995. **16**(5-6): p. 777-787.
[5]. Tham, C. Y., *Numerical simulation on the interaction of blast waves with a series of aluminum cylinders at near-field.* International Journal of Impact Engineering, 2009. **36**(1): p. 122-131.
[6]. Abramowicz, W. and Jones, N., *Dynamic progressive buckling of circular and square tubes.* International Journal of Impact Engineering, 1986. **4**(4): p. 243-270.
[7]. Wierzbicki, T. and Abramowicz, W., *On the crushing mechanism of thin-walled structures.* ASME Journal of Applied mechanics, 1983. **50**: p. 727-34.
[8]. Krauthammer, T., *Modern protective structures.* CRC Press, New York, 2008.
[9]. Kinney, G. F. and Graham, K. J., *Explosive shocks in air.* Springer-Verlag, 1985.
[10]. Smith, P. D. and Hetherington, J. G., *Blast and ballistic loading of structures.* Butterworth-Heinemann Ltd., 1994.
[11]. Bangash, M. Y. H., *Shock, impact and Explosion.* Springer, London, 1993.
[12]. *ABAQUS User manual.* ABAQUS, Inc. and Dassault Systems 2007.
[13]. *ABAQUS Theory manual.* ABAQUS, Inc. and Dassault Systems, 2007.

Chapter 16

Large-scale Blast Tests on Array of Pultruded Small-scale Composite tubes

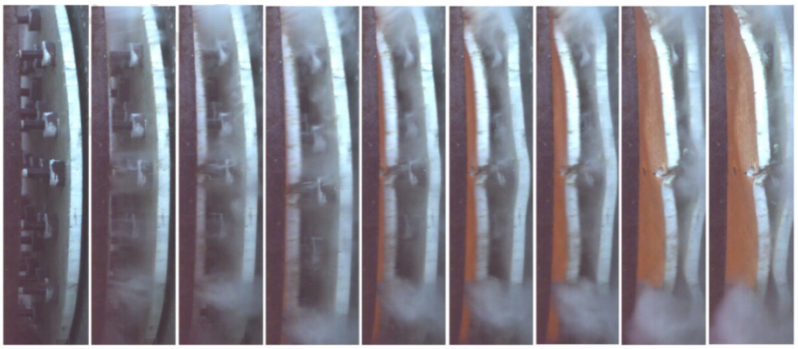

Overview

This chapter presents the large-scale blast testing on a representative sacrificial cladding structure made of pultruded small-scale glass polyester composite tubes and sandwich composite skin panels. To measure the protection efficiency of the structures large-scale air blast experiments have been conducted with 100 g and 150 g of C4. Similar to the beverage cans two configurations of the composite tubes were chosen for the study. From these studies, the crushing performance and the corresponding deformation patterns of the composite tubes are presented.

16. 1. Introduction

A significant amount of quasi-static [1-7] and axial impact investigations [8-13] have been carried out to study the crushing performance of composites. However, there is almost no data available on the response of composite tubes subjected to air blast loading. Chapter 11 and 14 dealt about the blast loading on (unidirectional) pultruded medium scale and small-scale in-house glass polyester composite tubes respectively. The general conclusion of these studies was that the crushing deformation patterns of unidirectional composite tubes remain similar to the axial quasi-static and impact loading cases. Furthermore, these studies revealed that the strain rate sensitivity of the uni-directional composite tubes is negligible for impact

and small-scale blast tests. In order to verify the above findings and to check the blast mitigation performance of the composite tubes, large-scale air blast tests have been conducted. Similar to the large-scale tests on the beverage cans, two configurations of the composite tubes (25 and 37 composite tubes) have been chosen to study the crushing performance of the composite tubes. As discussed in the previous chapter the adopted large-scale test set-up is limited to the charge mass of 150 g of C4. Hence, large-scale blast tests have been conducted with 100 g and 150 g of C4. The deformation patterns and the corresponding crushing performance of the pultruded small-scale composite tubes are presented.

16. 2. Composite tubes

As per the initial testing plan the calculated total length of the composite tube for the large-scale blast testing was ± 40 m. Manufacturing 40 m length of the tube in the laboratory is difficult; because of the adopted procedure maximum length of the tube can be manufactured at one time is 500 mm; repeating the procedure to achieve 40 m is laborious task. Hence, the manufacturing task was subcontracted to a company from Italy (M/s Bea service). All pultruded small-scale composite tubes used for the large-scale blast testing were manufactured by M/s Bea service, Italy (refer Figure 16-1). Each composite tube was reinforced with 18 streams of 4800 tex glass roving (P192 type from M/s OCV). The volume fraction of the fibre was approximately 50%. The POLYLITE® 413-010 resin (un-accelerated, non-thixotropic, medium reactive orthophthalic polyester resin) was used to manufacture the composite tubes. In order to achieve a uniform and progressive deformation pattern the t/D ratio (0.045) was chosen as similar to the small-scale in-house composite tubes which were discussed in Chapter 12 [14]. The dimensional and material details of the composite tubes are given in Table 16-1. The composite tubes have been cut for 100 mm length (refer Figure 16-1). To induce the failure at lower force, the 45° chamfering (triggering mechanism) was introduced at one end of the composite tubes. Similar to the earlier approaches preliminary quasi-static and impact investigations have been performed to check the progressive crushing deformation patterns of these tubes.

.

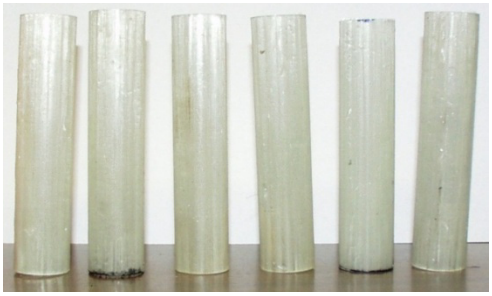

Figure 16-1: Composite tube test specimens (100 mm long).

Table 16-1: Dimensional and material details of the composite tube series.

Cross-section	Fibre	Resin	Dimensions (mm)	ρ_{linear} (g/mm)	Volume fraction (%)
Circular	Glass	Polyester	$\phi = 22$ $t = 1$ $L = 100$	0.14 without foam 0.15 with foam	$V_m = \sim 50$ $V_f = \sim 50$
ϕ - Outer diameter; t – thickness; L – length of tube; V_m – volume fraction of matrix; V_f – volume fraction of fibre.					

Thickness variation of the composite tube

Before using these composite tubes for quasi-static and impact testing the dimensional parameters were carefully checked. The wall thickness of the composite tubes at both ends has been measured. Unfortunately, the thickness of the composite tubes was not uniform at all around the circumference. The thickness varied from a minimum of 0.72 mm to a maximum of 1.3 mm. As an example, the typical thickness distributions of two composite tubes are shown in Figure 16-2. The location "A" which is indicated in Figure 16-2 shows a lower thickness compared to other locations. Except a very few, all the composite tubes had a similar thickness distribution. The composite tubes had arrived two weeks before the large-scale test. Hence, there was not enough time to replace with new tubes and so the tests were continued with these tubes.

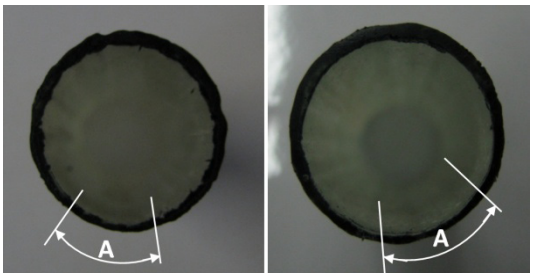

Figure 16-2: Thickness distribution of the composite tubes around their circumference.

16. 3. Preliminary test results

Axial quasi-static crushing tests were carried out on these composite tubes (both non-uniform and uniform thicknesses) using an Instron machine. A crosshead displacement of 10 mm/min was used. Due to the non-uniform thickness distribution, most composite tubes showed catastrophic failure (after the central delamination the initiation and sudden propagation of axial cracks was observed throughout the length of the composite tubes at the lower thickness locations). However, the composite tubes with uniform thickness (approximate thickness of 1.0 to 1.27 mm) showed controlled and progressive failure modes. As an example, the catastrophic and progressive failures modes and the corresponding load deformation

curves are shown in Figure 16-3(a-b) and Figure 16-4(a-b) for non-uniform thickness and uniform thickness composite tubes respectively.

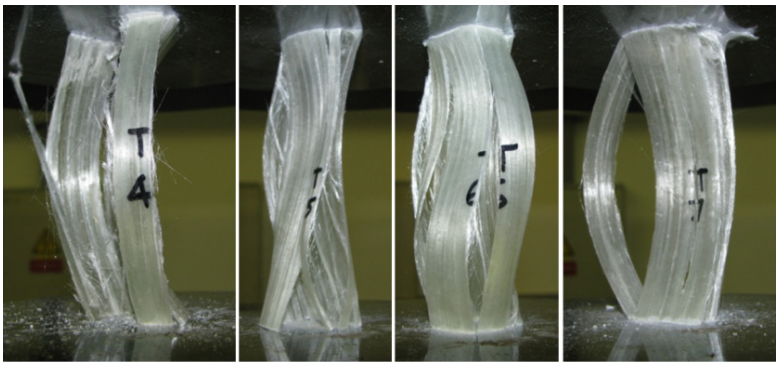

(a) Catastrophic failure of composite tubes with non-uniform thickness.

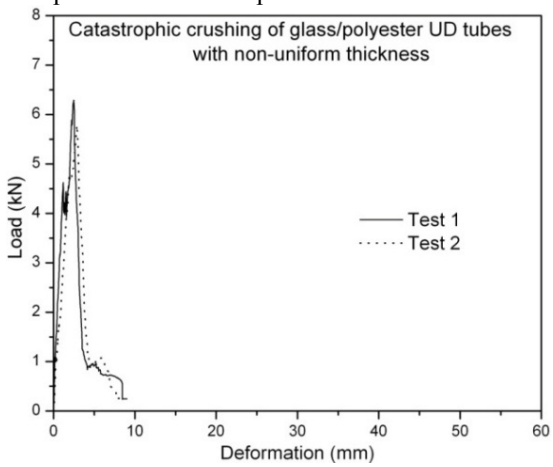

(b) Load-deformation curves of composite tubes with non-uniform thickness.

Figure 16-3: Catastrophic failure modes of composite tubes with non-uniform thickness and the corresponding load-deformation curves.

The final deformation patterns of the uniform wall thickness composite tubes are shown in Figure 16-5. The typical progressive deformation patterns of brittle composite tubes are well evident. In order to make use of these tubes for the large-scale blast testing several modifications have been tried out. To prevent the sudden propagation of axial cracks the composite tubes were taped by (i) a heat shrink and (ii) tape. The composite tubes were reinforced with heat shrink/tape over the whole length, except the length at the crushing end to initiate the failure. Due to a low stiffness, the use of heat shrink did not prevent the buckling of the side wall after the formation of axial cracks along the length of the specimen (refer Figure 16-6(a)). The taped composite tubes showed encouraging results for crosshead displacements of 5 mm/min and 10 mm/min. The corresponding progressive crushing patterns of the taped tubes are shown in Figure 16-6(b-c) for two varieties of tapes respectively. However, the progressive crushing of the taped composite tubes was not consistent

for higher crosshead displacements such as 100 mm/min and 200 mm/min. The inward buckling of the tube wall remained even after using the tape.

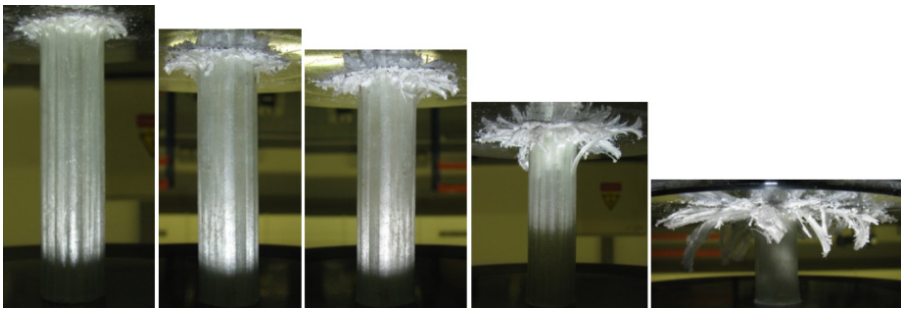

(a) Progressive failure modes of composite tubes with uniform thickness**.**

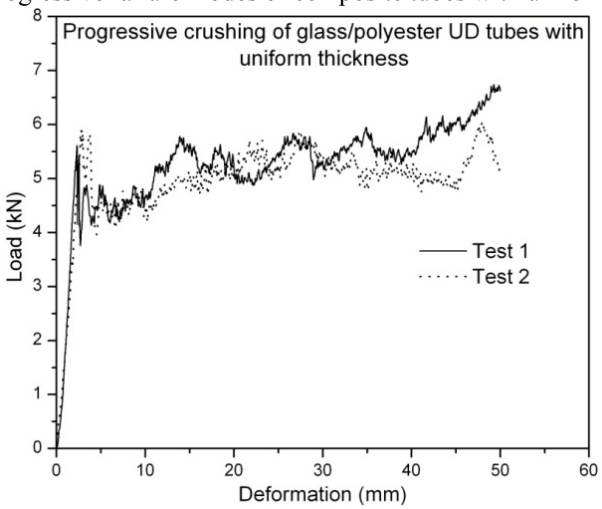

(b) Load-deformation curves of composite tubes with uniform thickness.

Figure 16-4: Progressive crushing modes of composite tubes with uniform thickness and the corresponding load-deformation curves.

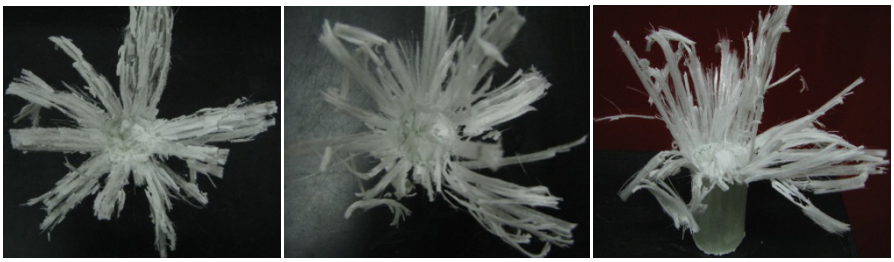

Figure 16-5: Final deformation patterns of uniform thickness composite tubes.

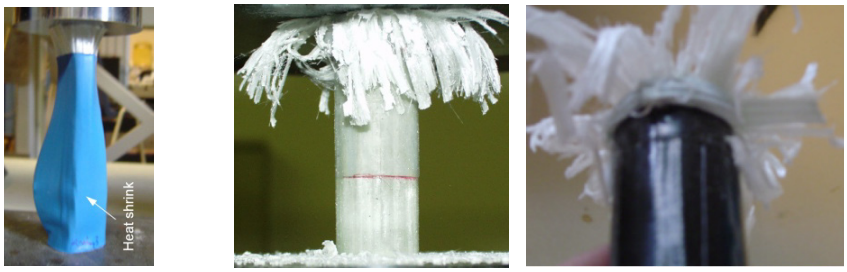

(a) **(b)** **(c)**

Figure 16-6: (a) Composite tube with a heat shrink **(b** and **c)** taped composite tube.

As a second step, to prevent the inward buckling these composite tubes were filled with polyurethane foam (refer Figure 16-7(a)). The used polyurethane foam is available in the market and it is normally used for insulation purposes (refer Figure 16-7(b)); the density of the used polyurethane foam was approximately 30 kg/m^3. Triggering (45° chamfering) was introduced at one end of the tube after drying of the polyurethane foam (Figure 16-7(a)). Axial quasi-static and impact tests have been conducted to check the crushing performance of these composite tubes (progressive or non-progressive). Quasi-static tests have been conducted for different crosshead displacements such as 10 mm/min, 100 mm/min and 200 mm/min. Impact tests have been conducted for two different heights (0.5 m and 0.75 m) which corresponded to the initial impact velocities of 3.13 m/s and 3.83 m/s.

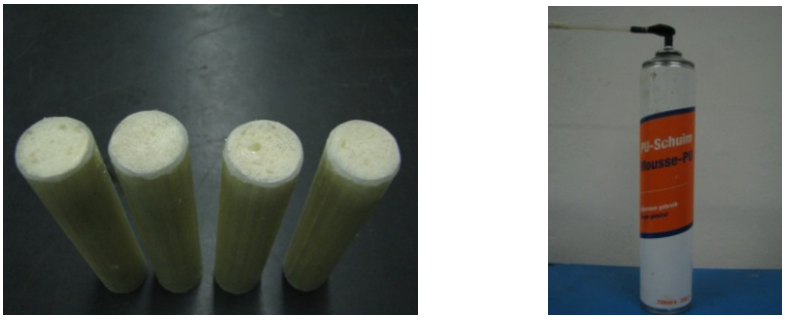

(a) **(b)**

Figure 16-7: (a) Polyurethane foam-filled tubes **(b)** Standard polyurethane foam available in the market

Polyurethane foam-filled composite tubes tested for 10 mm/min crushed progressively (refer Figure 2(a)). The delamination failure was noticed in all tubes due to a lower resistance of the foam. For a higher loading rate (100 mm/min and 200 min/min) the progressive crushing was not consistent (out of 3 tubes one failed catastrophically after achieving 30 mm of deformation length due to the splitting of walls). This may be due to the non-uniformity in the polyurethane foam density and the corresponding offset loading. Hence, to avoid the wall splitting of wall the polyurethane foam-filled composite tubes were taped once again. Axial quasi-static

tests have been repeated for the crosshead displacement of 100 mm/min and 200 mm/min rate of loading. The polyurethane foam-filled and taped tubes showed consistent progressive failure modes (refer Figure 16-8(b)). The corresponding load-deformation curves are shown in Figure 16-9. The peak crush load of these composite tubes was not consistent due to the difference in the triggering. The same configuration (polyurethane foam-filling and taping) was also verified for the axial impact loading condition with the initial impact velocity of 3.13 m/s and 3.83 m/s (refer Figure 16-10). The obtained results are different from what was discussed in Chapter 13. The polyurethane foam filling for 1 mm wall thickness small-scale in-house glass polyester composite tubes showed no continuous delamination and fibre fracturing failure modes.

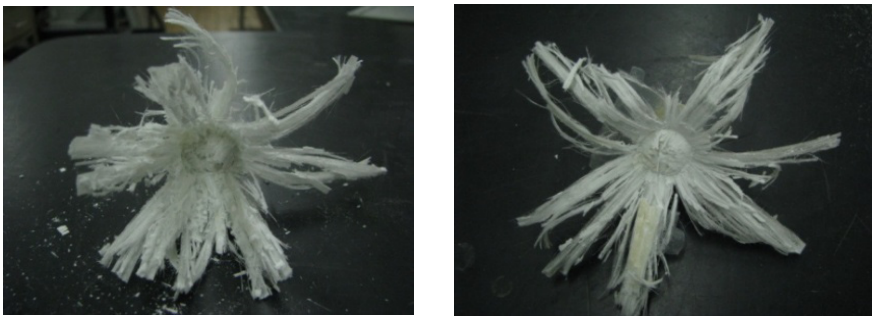

(a) Deformation pattern of the polyurethane foam-filled composite tube (10 mm/min)

(b) Deformation pattern of the polyurethane foam-filled and taped composite tube (200 mm/min)

Figure 16-8: Deformation patterns of the polyurethane foam-filled composite tubes.

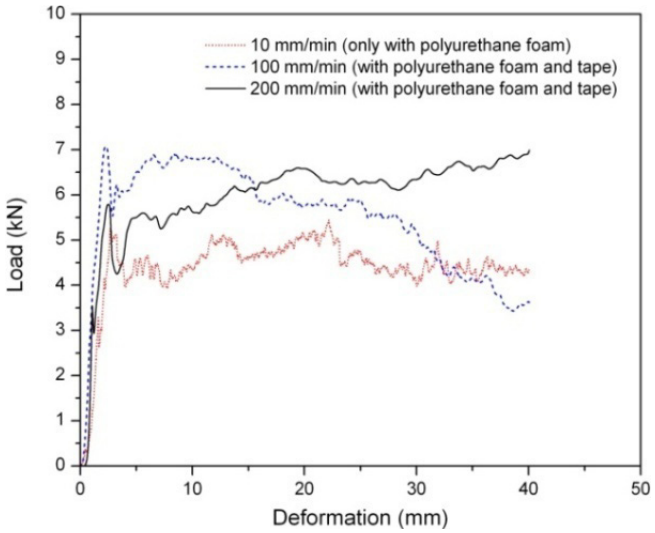

Figure 16-9: Load-deformation curves of the polyurethane-foam filled composite tubes.

The resistance offered by the polyurethane foam (with density of 107 kg/m^3) inside the composite tube prevented the continuous delamination. For the pultruded small-scale composite tubes the density of the used polyurethane foam was 30 kg/m^3. Due to its low density the polyurethane foam has accommodated the inward flow (towards the axis of the tube) of inner petals.

Figure 16-10: Deformation patterns of composite tubes (polyurethane foam-filled and taped) from impact tests.

In order to check the deformation patterns of the polyurethane foam-filled and taped composite tubes, small-scale blast tests have been conducted for 25 g of C4 with a stand-off distance of 30 cm. The mass and the diameter of the skin panel were 0.65 kg and ϕ 250 mm respectively. The results from these tests showed similar deformation patterns compared to quasi-static and impact results (delamination, axial cracks, lamina bending and fibre fracture). The corresponding deformation patterns are shown in Figure 16-11. Furthermore, the wrapped tape around the composite tubes also showed few major axial cracks; and the length of these cracks was equal to the deformation length of the composite tubes.

Figure 16-11: Deformation patterns of composite tubes (filled with polyurethane foam and taped) from small-scale blast tests (for 25g of C4 with 30 cm stand-off distance).

Hence, based on the above studies it was decided to use the polyurethane foam-filled and taped tubes for the large-scale blast tests. This configuration is good for easy mounting of the composite tubes on the (back) skin panel; furthermore, the buckling

of the composite tubes can be avoided with this configuration if any offset loading occurs during the blast event.

16. 4. Experimental test set-up

The details of the used large-scale experimental test set-up (concrete sewage pipes, materials and dimensions of the front and rear skin panel [15]) were discussed in Chapter 15. The same experimental test facility was used to conduct all tests. Furthermore, the configurations of assembling test specimens are the same (configuration 1 and 2 with 25 and 37 polyurethane foam-filled and taped composite tubes respectively). Similar to the beverage can tests, soft foam holders were used in order to assemble the composite tubes on the rear skin panel (refer Figure 16-12(a-b)). In order to prevent the penetration of glass fibre into the front skin panel, the thin aluminium plates (90 × 90 mm × 0.5 mm) were assembled on the crushing side of the front skin panels (refer Figure 16-13). Blast experiments have been conducted on two configurations of the composite tubes (25 and 37 tubes) and two different charge masses (with 100 g and 150 g of C4).

(a) **(b)**

Figure 16-12: Large-scale blast experimental test set-up**.(a)** Acrosoma panel with composite tubes (25 tubes configuration) **(b)** Side view of assembly

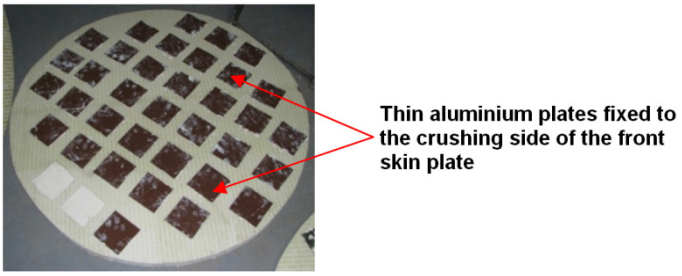

Figure 16-13: Front skin sandwich panel with the aluminium sheets.

16. 5. Experimental results

Large-scale experimental blast tests have been conducted to study the crushing and corresponding blast mitigation performance of polyurethane foam-filled and taped small-scale pultruded glass polyester composite tubes. Two tests have been conducted for each configuration.

16. 5. 1. Deformation patterns

For all six tests the composite tubes showed uniform and progressive crushing failure modes such as delamination, axial cracks, lamina bending, fibre fracturing and compression of polyurethane foam. As an example, the progressive crushing stages for configuration 1 (25 composite tubes) from one of the high speed cameras are shown in Figure 16-14 for 150 g C4. For all these tests both the front and rear skin panels experienced local and global bending modes. This effect can be noticed from the same figure. This was due to a high stiffness of the composite tubes and the corresponding effective contact area with the front and rear skin panels.

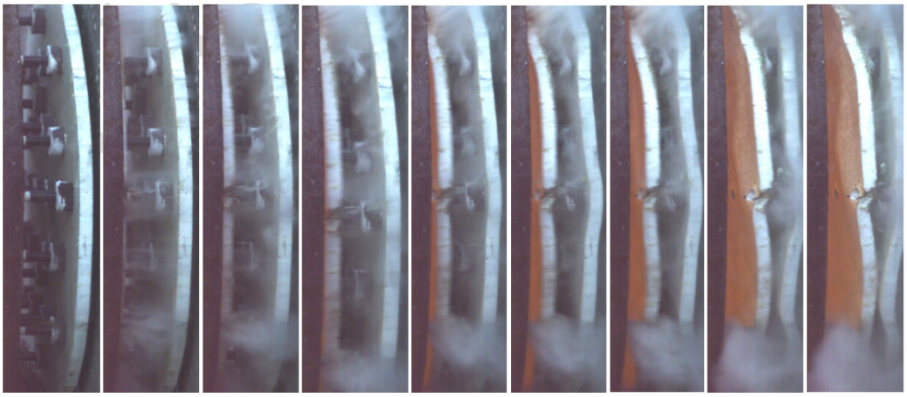

Figure 16-14: Progressive crushing stages of the 25 composite tubes (25 numbers) for 150 g of C4.

Due to the small contact area the skin panels were highly stressed during the crushing process. After each test the front and rear skin panels were checked. The mounting locations of the rear skin panels showed a noticeable deformation at the mounting locations. Similarly, most of the aluminium thin plates which were fixed to the front skin panel peeled off from their positions (refer Figure 16-15(a)); this was due to the local and global bending of the front skin panel. Furthermore, at few locations the penetration of the composite tube into the aluminium plate and the front skin panel was observed (refer Figure 16-15(b)). This was due to the high hardness of the glass fibre and the corresponding sharp edges of the composite tubes. Although the composite tubes were stiffer than the beverage cans, a significant part of the impulse was transferred directly to the concrete wall due to an

inadequate bending stiffness of the front and rear skin panels (leading to a direct contact of the rear skin panel with the concrete wall).

The global deformation patterns of the composite tubes with 150 g of C4 are shown in Figure 16-16(a) and (b) for configuration 1 and 2 respectively. As an example, the final deformation patterns of two composite tubes from each case are shown in Figure 16-17(a-d). It can be noticed from these figures that the deformation patterns of the composite tubes are consistent; and all typical failure modes are clearly evident. The average deformation length for configuration 1 was higher (55.7 mm) than for configuration 2 (33.7 mm).

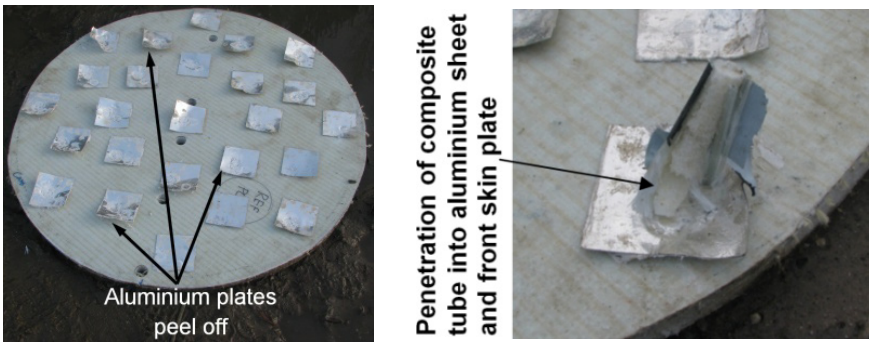

(a) **(b)**

Figure 16-15: (a) The aluminium plates peel off from the front skin panel. **(b)** Penetration of the composite tubes into the aluminium and front skin panel.

(a) **(b)**

Figure 16-16: Global deformation patterns of the composite tubes **(a)** configuration 1 (25 composite tubes) with 150 g of C4 **(b)** configuration 2 (37 composite tubes) with 150 g of C4.

Similar to the quasi-static and impact tests, the presence of the polyurethane foam and the tape prevented the axial splitting of the tube wall. In addition to that the low density of the polyurethane foam did not affect the continuous delamination and subsequent fibre fracturing failure modes which are very good irreversible energy dissipation mechanisms.

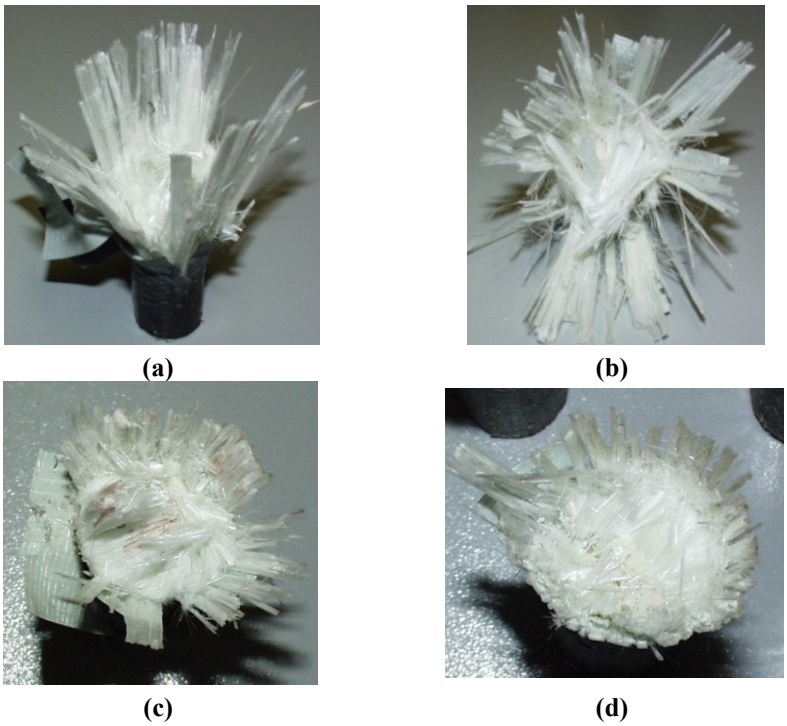

(a) **(b)**

(c) **(d)**

Figure 16-17: Final deformation patterns of composite tubes **(a-b)** for 150 g of C4 with configuration 1 (25 composite tubes). **(c-d)** for 150 g of C4 with configuration 2 (37 composite tubes).

16. 5. 2. Crushing load curves

The experimentally measured load time histories for three different cases are shown in Figure 16-18(a-c) for 100 g of C4 with 25 composite tubes, 150 g of C4 with 25 composite tubes and 150 g of C4 with 37 composite tubes respectively. The corresponding consolidated average parameters for these cases are given in Table 16-2. For the case with 100 g of C4 the data from one test could not be measured due to some problems. Hence, for this case the data from only one test is presented. From Figure 16-18(a-c) and Table 16-2, it can be noticed that irrespective of the charge mass the peak crush load for configuration 1 (25 composite tubes) remained the same. The peak crush loads for 100 g of C4 and 150 g of C4 were 87.75 kN (from one test) and 86 kN (from two tests) respectively. For configuration 2, the average peak crush load of 103.1 kN was noticed due to a higher number of composite tubes. Similarly, the positive duration was extended approximately to 8.2 ms, 9.5 ms and 9.2 ms for 100 g C4 with 25 composite tubes, 150 g C4 with 25 composite tubes and 150 g C4 with 37 composite tubes respectively.

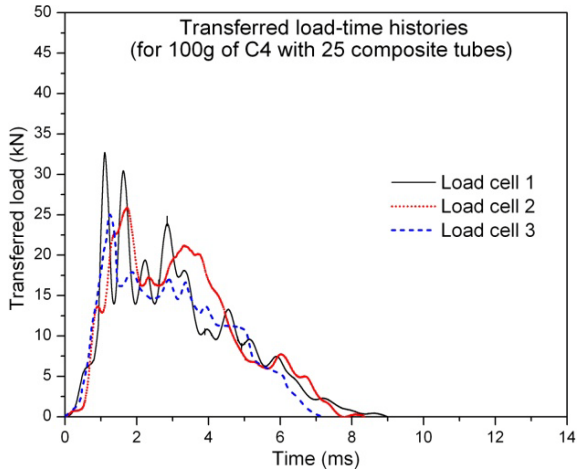

(a)

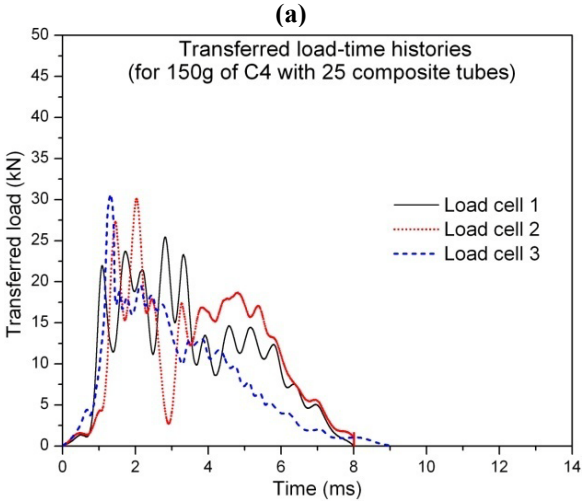

(b)

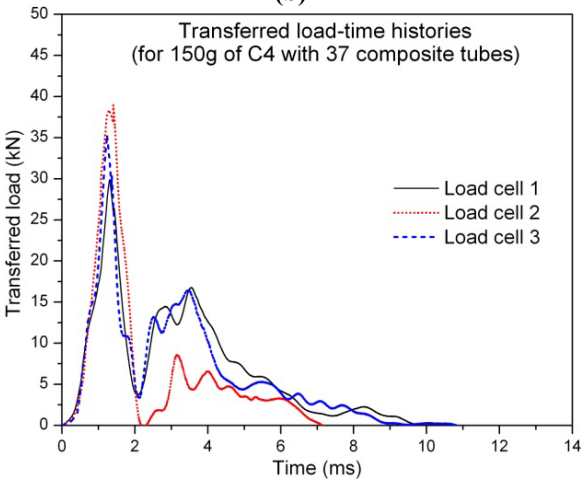

(c)

Figure 16-18: Transferred load time histories **(a)** for 100 g of C4 with 25 tubes **(b)** for 150 g of C4 with 25 tubes **(c)** for 150 g of C4 with 37 tubes.

Table 16-2: Summary of crushing parameters.

Charge mass	No. composite tubes	Stand-off distance	Load cells data	Peak crush load	Total peak crush load	Time for load transfer	Average time	Reflected impulse (from Autodyn)	Transferred impulse	Total transferred impulse	Average deformation length
(g)		(m)		(kN)	(kN)	(ms)	(ms)	(kN.ms)	(kN.ms)	(kN.ms)	(mm)
Test with configuration 1 (25 composite tubes)											
100	25	4.2	Load cell 1	29.5	87.7		8.2	599	85.2	249.3	25.8
			Load cell 2	32.3					88.1		
			Load cell 3	25.9					76.0		
150	25	4.2	Load cell 1	25.4	86.6	8.1	8.4	679	87.3	267.3	33.6
			Load cell 2	30.1		8.0			89.9		
			Load cell 3	31.1		9.2			90.1		
			Load cell 1	36.1	85.4	11.6	10.7		95.0	247.3	31.1
			Load cell 2	27.2		10.0			71.1		
			Load cell 3	22.1		10.7			81.2		
Test with configuration 2 (37 composite tubes)											
150	37	4.2	Load cell 1	30.3	104.4	10.4	9.4	679	72.5	196.1	55.2
			Load cell 2	38.1		7.15			53.8		
			Load cell 3	36.0		10.8			69.8		
			Load cell 1	27.5	101.9	8.16	8.95		65.9	185.2	49.8
			Load cell 2	40.9		10.7			61.0		
			Load cell 3	33.5		7.99			58.3		
Reference test											
150	-	4.2	Load cell 1	48.5	138.3	5.4	4.4	679	87.9	256.6	-
			Load cell 2	46.9		3.6			83.4		
			Load cell 3	42.9		4.2			85.3		

Similar to the beverage can cases, there was a difference observed between the reflected impulse and the transferred impulse. The configuration 1 with 100 g and 150 g of C4 showed higher transferred impulses than for configuration 2 with 150 g of C4. The reason was that the lower number of composite tubes (for configuration 1) provided a lower resistance to the front skin panel and the corresponding reaction load to the rear skin panel. The initial stages of crushing showed a local bending of both skin panels; the later high speed images showed a global bending of the rear skin panel. Therefore, a significant load was directly transferred to the concrete wall. However, for the case with 37 composite tubes (configuration 2) the reaction load to the rear skin panel was larger due to a larger number of composite tubes. Due to a larger reaction load and an inadequate bending stiffness, the rear skin panel was subjected to global bending during the initial stages of crushing and it came into contact with the concrete wall (refer Figure 16-19). Hence, a significant part of the load directly transferred to the concrete wall. Therefore, the transferred impulse (integrated load time histories) measured from the load cells was lower for configuration 2 compared to configuration 1. Due to a lack of material property there was no numerical simulation conducted on this case.

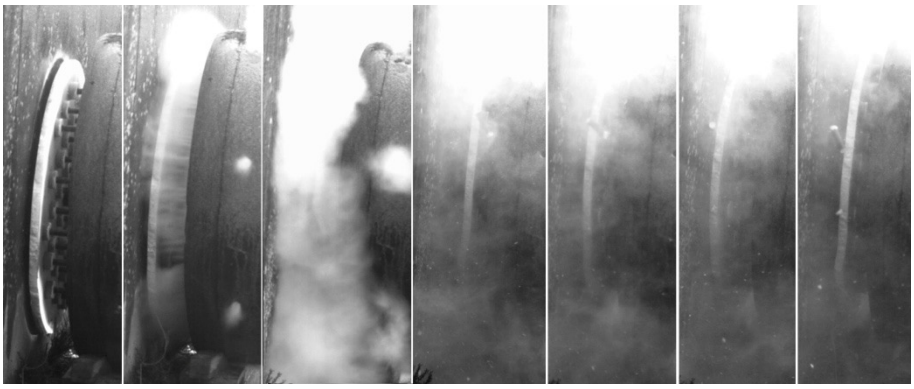

Figure 16-19: Global bending of rear skin panel and the corresponding contact with the concrete wall.

16. 6. Conclusions

Similar to the beverage cans, large-scale blast tests have been conducted to understand the blast mitigation performance of the pultruded small-scale glass polyester composite tubes. Tests have been conducted on two configurations of the composite tubes (25 and 37) with two charge masses of C4 (100 g and 150 g). From the conducted experimental tests the following conclusions can be made.

- For thin-walled composite tubes, in addition to several parameters such as t/D ratio, linear density and triggering mechanisms, the uniform distribution of the wall thickness plays a significant role to achieve progressive

deformation patterns. A non-uniform distribution of the wall thickness can result into catastrophic failure modes. For the chosen composite tubes (pultruded small-scale glass polyester composite tubes) the catastrophic failure modes were avoided by the polyurethane foam-filling and taping on the outer surface of the composite tubes.

- The conducted axial quasi-static, impact and large-scale blast experiments have showed that the deformation patterns of these composite tubes remain the same. The typical brittle composite tube failure modes such as delamination, axial cracks, lamina bending and fibre fracturing were clearly evident.
- The failure pattern of a foam-filled composite tube highly depends upon the density of the filled foam material. A high density of the foam can suppress few failure modes and associated energy absorption. However, a low density foam material can improve the wall strength and stability of the composite tube during crushing; furthermore it can allow to achieve the typical failure modes of the composite tubes and the corresponding energy absorption.
- The average peak crush load of the configuration 1 and 2 (25 and 37 composite tubes respectively) was 86.5 kN and 103.1 kN respectively. These values are higher than for the beverage can configurations.
- Similar to the blast tests on the beverage cans, the tests on the composite tubes showed that the bending stiffness of the rear skin panel was not adequate. Hence, a local and global bending of the rear skin panel and the corresponding direct contact with the concrete wall were noticed. As a result there was a significant difference in the reflected and transferred impulses (calculated from the load cell signals)
- The strain rate insensitivity of small-scale pultruded composite tubes is not directly evident from these tests. The reason was, the offset loading of the composite tubes due to the clearing of the reflected pressure waves. Therefore, more number of tests has to be repeated with an improved rear skin panel and with an adequate bending stiffness.

Bibliography

[1]. Farley, G. L. and Jones, R. M., *Crushing characteristics of composite tubes with "near elliptical" cross sections.* Journal of Composite Materials, 1992. **26**: p. 1252.

[2]. Farley, G. L. and Jones, R. M., *Analogy for the effect of material and geometrical variables on energy absorption capability of composite tubes.* Journal of Composite Materials, 1992. **26**: p. 78.

[3]. Palanivelu, S., Van Paepegem, W., Degrieck, J., Vantomme, J., Kakogiannis, D., Van Ackeren, J., Van Hemelrijck, D. and Wastiels, J.,

Crushing and energy absorption performance of different geometrical shapes of small-scale glass/polyester composite tubes under quasi-static loading conditions. Composite Structures, 2010. **93**(2): p. 992-2007.

[4]. Mamalis, A. G., Manolakos, D. E. and Viegelahn, G. L., *Crashworthy behaviour of thin-walled tubes of fibreglass composite material subjected to axial loading.* Journal of Composite Materials, 1990. **24**: p. 72.

[5]. Mamalis, A. G., Manolakos, D. E. and Demosthenous, G. A., *Crushing behaviour of thin-walled, non-circular, glass fibre-reinforced composite tubular components due to bending.* Composites, 1992. **23**(6): p. 425-433.

[6]. Hamada, H., Kameo, K., Sakaguchi, M., Saito, H. and Iwamoto, M., *Energy-absorption properties of braided composite rods.* Composites Science and Technology, 2000. **60**(5): p. 723-729.

[7]. Solaimurugan, S. and Velmurugan, R., *Influence of fibre orientation and stacking sequence on petalling of glass/polyester composite cylindrical shells under axial compression.* International Journal of Solids and Structures, 2007. **44**(21): p. 6999-7020.

[8]. Thornton, P. H., *The crush behavior of glass fiber reinforced plastic sections.* Composites Science and Technology, 1986. **27**(3): p. 199-223.

[9]. Thornton, P. H., *The crush behavior of pultruded tubes at high strain rates.* Journal of Composite Materials, 1989. **24**: p. 22.

[10]. Palanivelu, S., Van Paepegem, W., Degrieck, J., Van Ackeren, J., Kakogiannis, D., Van Hemelrijck, D., Wastiels, J. and Vantomme, J., *Experimental study on the axial crushing behaviour of pultruded composite tubes.* Polymer Testing, 2010. **29**(2): p. 224-234.

[11]. Mamalis, A. G., Manolakos, D. E., Demosthenous, G. A. and Ioannidis, M. B., *The static and dynamic axial collapse of fibreglass composite automotive frame rails.* Composite Structures, 1996. **34**(1): p. 77-90.

[12]. Mamalis, A. G., Manolakos, D. E., Ioannidis, M. B. and Kostazos, P. K., *Crushing of hybrid square sandwich composite vehicle hollow bodyshells with reinforced core subjected to axial loading: numerical simulation.* Composite Structures, 2003. **61**(3): p. 175-186.

[13]. Mamalis, A. G., Manolakos, D. E., Ioannidis, M. B. and Papapostolou, D. P., *On the response of thin-walled CFRP composite tubular components subjected to static and dynamic axial compressive loading: experimental.* Composite Structures, 2005. **69**(4): p. 407-420.

[14]. Hamada, H. and Ramakrishna, S., *Scaling effects in the energy absorption of carbon-fiber/PEEK composite tubes.* Composites Science and Technology, 1995. **55**(3): p. 211-221.

[15]. http://www.acrosoma.com (dated 02-06-2011).

Chapter 17

Conclusions and Outlook

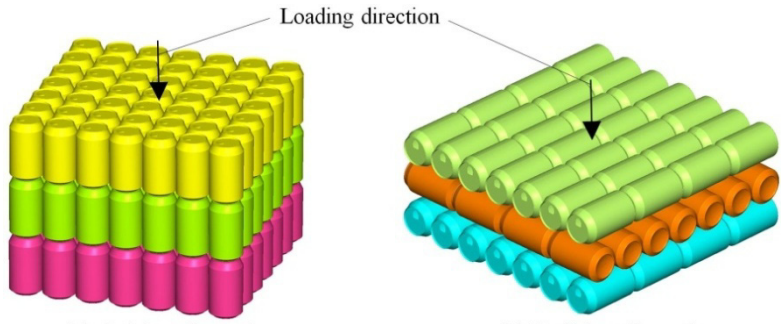

(a) Axial configuration (b) Radial configuration

Overview

This chapter presents the conclusions for all four major parts of the dissertation, together with some recommendations for the future work.

17. 1. Conclusions

Protecting the civilian population against blast attacks is a complex and comprehensive task. During a blast event, the catastrophic failure of critical load bearing members of civil engineering structures causes major human causalities. Currently, different design approaches are in practice to prevent the catastrophic failure of main load bearing members of civil engineering structures from such high dynamic events. Out of different proposals the concept of sacrificial cladding structure is adopted in this dissertation. In relation with that two types of structures, namely, α and β type were investigated to address the different needs of the proposed inner core of the sacrificial cladding structure. This chapter presents the conclusions of the work and also some proposals to guide possible future work in this field.

This dissertation consists of four major parts. In all four parts extensive experimental and numerical investigations have been carried out for quasi-static, impact and blast loading conditions. Understanding the behaviour of materials/structures under these loads is very important to design an energy absorbing element. The first part introduced the experimental and numerical axial

quasi-static, impact and small-scale blast loading on the α - type structure (empty metal beverage can); furthermore, to measure the dynamic parameters a contactless method using digital image correlation technique is proposed. The second and third parts are devoted to β - type structures (composite tubes). Similar to the first part, analyses (axial quasi-static, impact and small-scale blast loading) were carried out for large-scale and medium scale pultruded composite tubes and the same are presented in the second part. The third part of the dissertation dealt with small-scale in-house glass polyester composite tubes. Finally, the fourth part presented large-scale blast tests on representatives of the proposed sacrificial cladding structures made of α and β - type structures.

Conclusion from Part I (for α - type structure)

In Chapter 3, it is found from the conducted axial quasi-static and impact experiments that the empty metal beverage cans are sensitive to the strain rate effect. The crushing deformation patterns of the beverage cans are not uniform for lower rates of loading (10 mm/min and 50 mm/min for quasi-static condition; impact test with 1.4 m/s). In contrast, because of D/t ratio the beverage cans showed a perfect asymmetric deformation patterns (diamond mode) for higher impact velocities (2.2 m/s, 3.1 m/s, 3.8 m/s, 4.4 m/s and 4.9 m/s). It has also been found that the number of triangular lobes and their widths and the corresponding mean crush load increased with increasing initial impact velocities. In addition to that, the strain hardening of the beverage can material influences the mean crush load significantly. It is interesting to note the effect of entrapped air inside the beverage can for 50% of the cases with the initial impact velocity of 4.9 m/s. The energy balance plot of this case showed that the entrapped air inside the beverage can dissipated 3% of the total energy and the same is confirmed from a numerical simulation using surface based fluid cavity approach with an *Ideal gas* Equation Of State. Further investigations with the numerical simulations for the impact of the beverage cans gave an opportunity to understand the impact process in detail. The developed numerical model using the *Johnson-Cook* material model provided a very good correlation with the experimental results. Similarly, to predict the energy absorption capability of the beverage cans an analytical model is proposed including the strain rate and strain hardening effects. The results from this model are in a very good agreement with the experimental results. However, for a particular initial impact velocity this model requires few inputs such as the folding length and the number of triangular folds. If the experimental failure patterns are established, then an accurate prediction of the crushing parameters is possible using this model. If not, these parameters can be varied and accordingly a range of crushing parameters can be proposed. Finally, a contactless method using the *Digital Image Correlation (DIC)* technique is proposed to measure the dynamic parameters such as deformation length, impact velocity and reaction force at the crushing end of the test specimen. Axial impact tests with two test specimens (empty beverage can and polyurethane foam) showed that the

accuracy of this method highly depends upon the frame rate and the material/structure deformation behaviour.

In Chapter 4, the blast energy absorption characteristics and the corresponding crushing mechanisms of empty recyclable metal beverage cans are studied for 20 g of C4 with a stand-off distance of 30 cm. Close-range blast tests with three different skin panels representing the outer skin panels of the proposed sacrificial cladding structure showed that the surface roughness of the reflected surface plays a significant role for the reflected blast parameters. Another interesting fact noticed during these tests is the clearing of the reflected pressure wave associated with the finite reflected surface area (the reflected pressure waves quickly passes around the edges of the skin panel and hence a shorter positive duration is obtained). Due to this effect, the total impulse is significantly reduced compared to the value predicted by the empirical relations (*ConWep*). Hence, the clearing factor should be accounted for the design of a sacrificial cladding structure with a finite reflected surface area. Furthermore, these tests proved that to achieve a better performance of the sacrificial cladding structure, the mass of the skin panel should be low with an adequate bending stiffness. Besides, the conducted tests showed a non-conservation of linear momentum (there is a difference in the reflected and transferred impulse).

In Chapter 5, the importance of considering the interaction of the blast pressure wave with a structure and the corresponding resultant blast loading are presented. The developed 2D and 3D computational models using the Eulerian and Lagrangian approach provided a complete idea about the interaction of the blast pressure with the developed small-scale test set-up and the corresponding loading on the inner core structure. It is proved that the difference between the reflected and transferred impulse was due to a combined effect of the diffracted and ground reflected pressure waves. The same finding is also validated with a decoupled numerical study. It is also shown that the accuracy of the blast parameters is highly affected by the size of the air grid. In Chapter 6, an analytical model is given to predict the energy absorption of the beverage cans for blast loading conditions. However, to include the strain rate effect of the beverage can's material the maximum velocity of the skin panel during the blast should be known; hence, a method is proposed to calculate the maximum velocity and the corresponding strain rate using an arbitrary value of the mean crush load. The results from this model are in a very good agreement with the experimental results. Since the beverage cans are available freely from the market, the initial geometric imperfections conceived during the usage should not be neglected. Although the usage patterns vary from person to person, two representative patterns with two different numerical approaches (superposition of linear buckling modes and measured geometric imperfection) are considered. Based on the results from these numerical studies it is proved that the initial geometric

imperfections of the beverage cans can be neglected and they do not influence the overall crushing performance of the beverage cans.

Conclusion from Part II (for β - type structure)

In Chapter 8, the influence of cross-section, triggering, type of resin and the strain rate on the specific energy absorption of large-scale pultruded glass polyester and glass vinylester composite tubes are presented. The typical failure modes (delamination, axial cracks, lamina bending and fibre fracture) of these composite tubes are studied. It is observed that the specific energy absorption (SEA) of the circular cross-sectional composite tubes is higher than for the square cross-sectional tubes. Similarly, the circular cross-sectional composite tubes with bevel triggering showed a higher SEA value compared to those with tulip triggering. In contrast, the tulip triggering showed a higher SEA value for square cross-sectional tubes. This is due to the differences in the proportion of the energy absorption associated with each failure mode. It is noticed that the peak crush load of the circular and square cross-sectional composite tubes remained the same for different initial impact velocities (9.3 m/s, 12.4 m/s and 14 m/s).

In Chapter 9, the limitations of the currently used modelling approaches for the crushing of composite tubes are presented; and the corresponding difficulties of using solid elements and shell elements are explained. Many studies from the literature have used a single solid or shell element layer to capture the crushing characteristics of the composite tubes with bevel triggering (45° chamfering). However, this approach will not give accurate prediction of the crushing parameters for unidirectional composite tubes. A parametric numerical study reveals that to capture the accurate crushing parameters of a uni-directional composite tube, the correct modelling of the triggering and the corresponding delaminations between the laminates are absolutely necessary. It is shown that among the different approaches, the concept using multiple shell layers with cohesive elements and seams predicted accurate crushing parameters and the correct deformation patterns of the pultruded glass polyester composite tubes.

In Chapter 10, axial quasi-static and impact tests on cylindrical medium-scale pultruded glass polyester composite tubes are presented with two triggering profiles. Similar to the large-scale tubes, axial impact tests with different initial impact velocities and impactor masses showed that the pultruded tubes are insensitive to the strain rate effect, which is a good feature for the requirement of inner core of a sacrificial cladding structure. A comparison of the quasi-static and dynamic specific energy absorption is given for these composite tubes. In all cases, the dynamic specific energy absorption decreases with increasing initial impact velocities; furthermore, it is observed that the dynamic SEA was significantly lower than the quasi-static one for the same deformation lengths. The major reason for this

difference is the length of the axial cracks. During a quasi-static loading the length of the axial cracks is controlled by the crosshead displacement. However, for dynamic loading the length of the axial cracks is controlled by the inertia of the impactor, impact velocity and the lateral inertia of the composite tube. When an (axial) crack is initiated during dynamic loading, a relatively lower force is sufficient enough to create new fracture surfaces and the corresponding bending of the petals. Similarly, the crushing performance of these tubes for an axial air blast loading is presented in Chapter 11 for 40 g C4 with 30 cm and 15 cm stand-off distances. This study again proves that the deformation patterns of the pultruded composite tubes remain the same for quasi-static, impact and blast loading conditions. Furthermore, it is observed that irrespective of the charge mass and stand-off distances the developed small-scale blast test set-up will provide an approximately 30% difference in the reflected and transferred impulse. Finally, this study indicates that to enhance the blast mitigation performance the use of low stiffness composite tubes is absolutely necessary.

Conclusion from Part III (for β - type structure)

In Chapter 12, the effect of cross-sections, geometrical shapes, t/D ratio and triggering types on the specific energy absorption of nine different shapes of small-scale in-house glass polyester composite tubes is presented. This study proves that the geometry of the composite tube and its t/D ratio play a major role to achieve the progressive deformation patterns and the corresponding higher energy absorption. This study also showed that the change of t/D ratio of the composite tubes certainly will change the ranking of the composite tubes from lower to higher specific energy absorption or vice versa. In Chapter 13, the effect of polyurethane foam-filling on the crushing performance of the same composite tubes is presented. This study shows that the presence of polyurethane foam inside the composite tubes improved the stability and strengthening of the composite tube walls. However, the presence of polyurethane foam reduced the specific energy absorption significantly for the composite tubes which can already provide progressive and stable failure patterns without polyurethane foam. This is due to the difference in the deformation patterns. The presence of polyurethane foam inside the composite tube prevents the circumferential delamination and subsequent fibre fracturing. Hence, before deploying the foam-filling in a composite structure for energy absorption applications one should be aware that any changes in the failure pattern due to foam-filling can alter the crushing performance of the composite structure. The resistance offered by the polyurethane foam for the inner petals is depending upon the density of the foam.

Further investigations for the above composite tubes (hollow and foam-filled) under dynamic loading (axial impact and blast) are presented in Chapter 14. This study proves that for lower t/D ratio of hollow and foam-filled composite tubes, the failure

patterns remain the same as for the quasi-static tests and the corresponding specific energy absorption decreases due to dynamic effects. However, the crushing performance of the foam-filled composite tubes with a higher t/D ratio is significantly increased due to the inertia of the impactor and increased hoop strength of the composite tubes. This study also concludes that the conical circular type –Y and circular cross-sectional composite tubes will provide a better blast mitigation performance with a less material investment.

Conclusion from Part IV (for both α and β type structures)

In Chapter 15, the large-scale blast testing on representative sacrificial cladding structures made of empty beverage cans and sandwich composite skin panels is presented. To create a perfectly plane shock wave the shock tube concept is successfully employed using concrete sewage pipes. The numerically calculated blast parameters are in a very good agreement with the experimentally measured values. However, this study proves that to reach an accurate or acceptable numerical solution with the experimental results, the boundary conditions of the experimental tests should be captured in the numerical model. The above statement can be supported with the results from the coupled and decoupled numerical simulations. The use of the beverage cans significantly altered a high magnitude, short duration blast load to a low peak, long duration pulse. However, it is important to note that the measurement of the transferred load signals to the concrete wall is significantly affected by the bending stiffness of the rear mounting structure (rear skin panel). Similarly, in Chapter 16 the large-scale blast testing on representative sacrificial cladding structures made of small-scale pultruded glass polyester composite tubes is presented. The performance of these composite tubes is very similar to the beverage cans; however a higher peak crush load (transferred load) is noticed due a higher stiffness of the composite tubes. This study also proves that, a uniform wall thickness distribution of the composite tubes plays a significant role to achieve controlled and progressive deformation patterns during crushing. The polyurethane foam-filling and taping of the composite tubes seems to be a working solution to achieve the progressive deformation patterns for non-uniform thickness composite tubes. Large-scale blast tests with different charge masses of C4 show that the empty metal beverage cans and composite tubes can be considered as potential members to protect civil engineering structures from air blast load. Nevertheless, further investigations on the beverage cans and composite tubes for the large-scale blast testing are absolutely necessary to cater into different blast loading regimes.

17. 2. Outlook

In addition to the conducted experimental and numerical investigations to understand the crushing performance of α and β type structures, a complete design

of the proposed sacrificial cladding structure needs more attention in terms of ability to absorb energy from an oblique blast, assembly architecture of the front skin and rear skin panels and inner core members, retaining the front skin panel after crushing of the inner core etc. In addition to that there are some other experimental and numerical studies that can be done to understand the performance of these structures completely. In the following paragraphs some ideas have been put forward for future researchers who are interested in building further on this work.

Oblique blast loading

The present configuration of the proposed sacrificial cladding structure has dealt only with axial blast pressure loading on the skin panel and inner core. However, in real life situations this condition cannot be expected always. Hence, investigating the performance of the proposed sacrificial cladding structure for oblique pressure loading and the corresponding performance will provide a better understanding of these structures as a whole. Based on the results, the design architecture of the inner core especially for the composite tubes can be revisited. This dissertation has dealt only with uni-directional composite tubes. The performance of these uni-directional composite tubes can be significantly affected by oblique blast loading conditions. Hence, a detailed study is absolutely necessary. On the other hand, the use of beverage cans can handle the oblique blast loading up to some extent due a larger diameter and the corresponding contact area with the front skin panel.

Macro-foam configuration

As discussed in the Introduction, the beverage cans can be adopted in different configurations of macro foam depending upon the blast loading magnitudes. Two different possible configurations are reproduced in Figure 17-1(a-b). To use these configurations, detailed impact and blast loading investigations on the progressive collapse and the corresponding interactions between the beverage cans have to be performed. Preliminary impact tests on the axial configuration using two beverage cans top of each other showed a promising result. Similar to the conventional metal foams, the first beverage can underwent progressive crushing modes until it reaches the densification regime then the subsequent crushing was started for the second beverage can.

Efficiency enhancement

As have seen from the large-scale blast testing on the beverage cans, a significant quantity of elastic strain energy was given back to the front skin panel after achieving the maximum deformation length of the beverage cans; the entrapped air inside the beverage can plays a significant role for this phenomenon. Capturing the effect of entrapped air inside the beverage can during the experimental testing is extremely difficult. On the other hand, conducting a numerical simulation for the array of cans including the effect of air inside the beverage cans needs a significant

computing power. Furthermore, for a good energy absorption structure/material, the energy conversion during the crushing process should be irreversible [1]. As seen from Chapter 3, the effect of entrapped air can be eliminated by introducing few holes at the bottom of the beverage cans [2]. Hence, it is proposed to introduce a few holes at the bottom of the beverage can for the future tests.

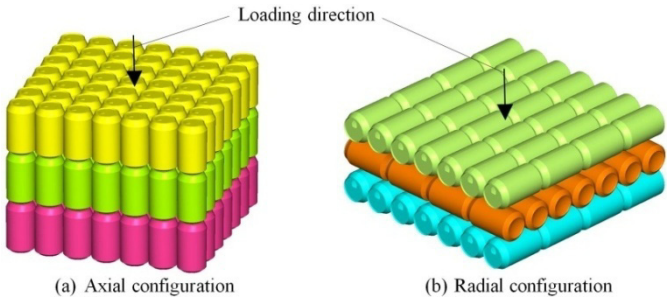

Figure 17-1: Two configurations of macro foam arrangement of empty recyclable metal beverage cans.

Assembly architecture

The assembly architecture of the front skin panel, inner core and the rear skin panel needs important attention. The movement and the corresponding velocity of the front skin panel in opposite the direction during the negative phase of blast are significant. Hence, in order to avoid the impact of the front skin panel with other structures and human beings during the negative phase of a blast, a robust solution has to be worked out.

Fire protection

The efficiency of the front skin panel may go down if it is exposed to a severe fire during blast loading (this may happen when the charge is situated very close to the front skin panel). Hence, a fire resistant coating on the front skin panel is absolutely necessary. The IPC (Inorganic Phosphate Cement) material developed by *Vrije Universiteit Brussel* can be used for this purpose and it can resist temperatures up to 1000° C [3]. The thickness of the IPC coating can be decided based on the performance variables. However, the use of IPC coating may affect the surface smoothness of the front skin panel. As seen from Chapter 4, for close stand-off distance the surface roughness plays a significant role for the blast parameters [4]. Hence, a detailed study has to be carried out to check the influence of the IPC coating on the front skin panel.

Alternative method of analysis and design

To predict the accurate crushing parameters of uni-directional composite tubes the use of multiple shell layers and cohesive layers are absolutely necessary [5, 6]. However, conducting coupled or decoupled numerical simulations using this approach to design a real-scale sacrificial cladding structure needs too much

computing power. Alternatively, similar to the beverage cans analytical models can be developed for the inner composite tubes to calculate the crushing performance. An analytical model suggested by Solaimurugan et al. [7] can be a starting point for the used uni-directional composite tubes due to the strain rate insensitivity. Secondly, few studies [8-10] on composite materials using meshless methods (SPH – Smooth Particle Hydrodynamics) showed promising results with a relatively less computational time. Therefore, this approach can also be considered as an alternative method for the future research.

Optimization of composite tubes and skin panel

Many methods are available to achieve single–objective and multi–objective optimization of variables. Any given geometry of the composite tube can be optimized to achieve a maximum crushing performance using the available parameters. The same concept can also be extended to the skin panels.

Green fibres

During the last decade there has been a renewed interest in the natural fibre as a substitute for glass, motivated by potential advantages of weight saving, lower raw material price, and 'thermal recycling' or the ecological advantages of using resources which are renewable. On the other hand natural fibres have their shortcomings, and these have to be solved in order to be competitive with glass. Natural fibres have lower durability and lower strength than glass fibres. However, recently developed fibre treatments have improved these properties considerably [11, 12]. Hence, the natural fibres can be used as an alternative for the glass fibres. Preliminary quasi-static and impact tests conducted by the author on uni-directional flax fibre reinforced polyester composite tubes showed encouraging results (refer Figure 17-2). Therefore, for future investigation the flax fibre can be considered for use in the inner core of the proposed sacrificial cladding structures.

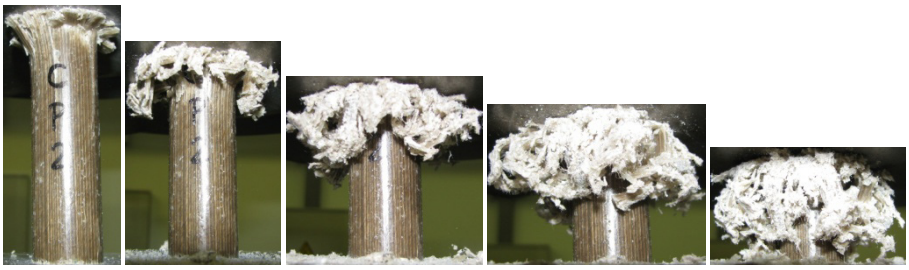

Figure 17-2: Progressive crushing stages of uni-directional flax polyester composite tubes for quasi-static loading.

Bibliography

[1]. Lu, G. and Yu, T. X., *Energy absorption of structures and materials.* Woodhead Publishing Ltd., 2003.

[2]. Palanivelu, S., Van Paepegem, W., Degrieck, J., De Pauw, S., Vantomme, J., Wastiels, J., Kakogiannis, D. and Van Hemelrijck, D., *Low velocity axial impact crushing performance of empty recyclable metal beverage cans.* International Journal of Impact Engineering, 2011. **38**(7): p. 622-636.

[3]. http://vubonite.com/Kernel/IndexStage3_HR.aspx (dated 02-06-2011).

[4]. Palanivelu, S., Van Paepegem, W., Degrieck, J., Reymen, B., Ndambi, J.-M., Vantomme, J., Kakogiannis, D., Wastiels, J. and Van Hemelrijck, D., *Close-range blast loading on empty recyclable metal beverage cans for use in sacrificial cladding structure.* Engineering Structures, 2011. **33**(6): p. 1966-1987.

[5]. Palanivelu, S., Van Paepegem, W., Degrieck, J., Kakogiannis, D., Van Ackeren, J., Van Hemelrijck, D., Wastiels, J. and Vantomme, J., *Parametric study of crushing parameters and failure patterns of pultruded composite tubes using cohesive elements and seam, Part I: Central delamination and triggering modelling.* Polymer Testing, 2010. **29**(6): p. 729-741.

[6]. Palanivelu, S., Van Paepegem, W., Degrieck, J., Van Ackeren, J., Kakogiannis, D., Wastiels, J., Van Hemelrijck, D. and Vantomme, J., *Parametric study of crushing parameters and failure patterns of pultruded composite tubes using cohesive elements and seam: Part II - Multiple delaminations and initial geometric imperfections.* Polymer Testing, 2010. **29**(7): p. 803-814.

[7]. Solaimurugan, S. and Velmurugan, R., *Influence of fibre orientation and stacking sequence on petalling of glass/polyester composite cylindrical shells under axial compression.* International Journal of Solids and Structures, 2007. **44**(21): p. 6999-7020.

[8]. Chen, Y. and Kulasegaram, S., *Numerical modelling of fracture of particulate composites using SPH method.* Computational Materials Science, 2009. **47**(1): p. 60-70.

[9]. Johnson, G. R., *Numerical algorithms and material models for high-velocity impact computations.* International Journal of Impact Engineering. **In Press, Corrected Proof**.

[10]. Hiermaier, S. J., *Structures Under Crash and Impact - Continuum mechanics, discretization and experimental characterization.* Springer, 2007.

[11]. http://www.fao.org/DOCREP/004/Y1873E/y1873e0a.htm (dated 02-06-2011).

[12]. http://en.wikipedia.org/wiki/Flax (dated 02-06-2011).